



UNIVERSITÀ
DEGLI STUDI
DI PADOVA

UNIVERSITÀ DEGLI STUDI DI PADOVA

Dipartimento di Ingegneria Industriale

Corso di dottorato di ricerca in Ingegneria Industriale

Curricolo: Ingegneria Meccanica

Ciclo XXXII

**Development and assessment of energy methods
for structural durability**

Coordinatore: Ch.mo Prof. Paolo Colombo

Supervisore: Ch.mo Prof. Giovanni Meneghetti

Dottorando: Daniele Rigon

Alla mia famiglia

A Chiara

Ai miei amici

Table of Contents

Table of Contents	i
Abstract	1
Sommario	3
List of Figures	7
List of Tables	21
Chapter 1: Introduction	23
1.1 Peak stress Method	24
1.1.1 Notch Stress Intensity Factors approach	24
1.1.2 Equivalent Peak Stress definition	29
1.2 Thermal Energy dissipation due to fatigue	34
1.2.1 Methods for fatigue life and fatigue limit estimation by thermography	36
1.2.2 Methods for fatigue crack growth and identification of the plastic zone	39
1.2.3 Specific thermal energy dissipated per cycle evaluated by using the cooling gradient technique	41
1.3 Metallic materials produced by additive manufacturing	46
1.4 References	49
Chapter 2: Peak Stress Method for multiaxial loading.....	57
2.1 Theoretical framework.....	57
2.1.1 Definition of PSM-Based design stress for multiaxial loadings by using the SED criterion	59
2.1.2 Special cases of equivalent peak stress	61
2.2 Geometries and PSM Fe-models	65
2.2.1 Steel welded joints.....	65
Siljander et al. [19].....	72
Razmjoo [20], tube-to-flange joints	74
Yousefi et al. [21]	77
Bäckström et al. [22].....	78
Dahle et al. [17]	79
Sonsino et al. [23,24]	79
Bertini et al. [25] and Frenzo and Bertini [26].....	80
Takahashi et al. [27,28].....	81
2.2.2 Aluminium welded joints	82
Kueppers and Sonsino [16].....	82
Costa et al. [30].....	83
2.3 Assessment of weld toe and weld root failures.....	86
2.3.1 Steel welded joints.....	86
2.3.2 Aluminium welded joints	94
2.4 Discussion.....	97
2.5 Conclusions	98
2.6 References	99
Chapter 3: The use of the Specific Heat Loss per cycle to correlate the fatigue strength of severely notched stainless steel specimens.....	103

3.1	Introduction and Theoretical background	104
3.2	Material and Methods	107
3.2.1	Experimental protocol.....	107
3.2.2	Data post-processing.....	111
3.3	Energy-based synthesis of fatigue test results.....	113
3.4	Thermal energy dissipation close to the notch tip.....	120
3.5	Analysis of energy distribution	123
3.6	Discussion	129
3.7	Conclusions.....	130
3.8	references	132
Chapter 4: Analysis of the energy dissipation on AISI 304L stainless steel subjected to multiaxial cyclic loading.....		135
4.1	Introduction.....	135
4.2	Materials and Methods.....	137
4.2.1	Material and specimen's geometry	137
4.3	Testing setup: bending and torsion fatigue tests	140
4.4	Testing setup: Axial and torsion fatigue tests	142
4.5	Fatigue test results.....	144
4.5.1	Long-term temperature acquisition and damage analysis of type A specimens.....	144
4.5.2	Evaluation of the Specific heat loss per cycle Q	158
4.5.3	Synthesis of multiaxial fatigue test results in terms of Q	174
4.6	Conclusions.....	178
4.7	References.....	179
Chapter 5: Analysis of the energy dissipation on thin-walled tubular C45 steel specimens subjected to multiaxial loading		183
5.1	Introduction.....	183
5.2	Materials and methods	185
5.2.1	Infrared camera setup.....	187
5.2.2	Digital Image Correlation system setup.....	187
5.3	Damage analysis	192
5.4	Fatigue test results.....	195
5.4.1	Cooling gradient evaluation and evolution of Q during fatigue tests	196
5.4.2	Strain energy density dissipated in a cycle ΔW	212
5.4.3	Synthesis of the fatigue test results in terms of Q	219
5.5	Discussion	221
5.6	Conclusions.....	222
5.7	references	223
Chapter 6: Analysis of defects influence on structural durability of maraging steel specimens produced by additive manufacturing		225
6.1	Introduction.....	226
6.1.1	Static mechanical properties of AMed maraging steel 300	228

6.1.2	Fatigue strength of AMed maraging steel 300	229
6.2	Theoretical background	231
6.2.1	Rapid estimation of a_0	234
6.3	Materials and Methods	235
6.4	Fatigue test results	242
6.4.1	Fracture surface analysis	243
6.4.2	Evaluation of a_0	253
6.4.3	Fatigue test results expressed in terms of ΔK_{corr}	255
6.4.4	Sharp V-notch results	260
6.5	Conclusions	263
6.6	References	264
	Conclusions	267
	Bibliography	269
	Ringraziamenti	287

Abstract

Fatigue life assessment is the key task of the design of mechanical components subjected to service loads for avoiding failure occurring in the form of incipient cracks which may cause damages to the entire mechanical system or even worse to people.

The nowadays industrial applications increasingly require mechanical components having complex geometry subjected to complex loading conditions. Considering the guidelines of the fatigue design of welded joints as an example, the standards report several stress-based fatigue design curves each one related to the most common welded structural details under a given loading direction. For this reason, by adopting the nominal approach, if the welded detail is different from those reported in the standards, the choice of the proper design fatigue curve might not be done for certain.

This dissertation deals with fatigue assessment of metallic material and components by adopting local energy-based parameter which can quantify the local damage due to stress gradient caused by notches as well as defects. More precisely, the extension of the applicability of three energy-based approaches to several factors that influence the fatigue strength of material and components in addition to those already covered is the aim of the present dissertation.

The first energy-based method, the so-called Peak Stress Method deals with the fatigue assessment of welded joints by means of a numerical FE-oriented application of the Notch- Stress Intensity Factors (N-SIFs). The equivalent peak stress (the fatigue damage parameter used for assessing the fatigue strength of welded joints) can be obtained by invoking the averaged Strain Energy Density (SED) criterion. The second one deals with the fatigue characterization of metallic component by assuming the specific heat loss per cycles as a fatigue damage parameter which can be evaluated in a standard constant amplitude fatigue test by adopting an easy experimental technique based on temperature measurements of material surface. The third one deals with the fatigue characterization of metallic materials produced by additive manufacturing, one of the most attractive and studied technology nowadays. Since these materials are affected by the presence of irregular defects, energy-related fracture mechanics approaches seem to be the most suitable for fatigue life assessment.

In the *first chapter*, the state of the art of energy-based methods for fatigue and fracture mechanics characterization are described along with their theoretical frameworks.

In the *second chapter*, the theoretical framework for extending the applicability of Peak Stress Method to the fatigue strength assessment of welded joints subjected to multiaxial loading conditions has been presented. Then, several multiaxial fatigue data taken from the literature relevant to both aluminum and steel welded joints were analysed by using the PSM for validating the theoretical prediction. The equivalent

peak stress has shown to correlate with good approximation about all the experimental data.

The *third chapter* deals with the analysis of the thermal energy dissipated during fatigue tests on severely notched AISI 304L stainless steel specimens. For the first time, the specific heat loss per cycle (Q parameter) was evaluated experimentally on 4-mm-thick, hot-rolled AISI 304L stainless steel specimens, characterized by 3, 1 and 0.5 mm notch tip radii by means of a FLIR SC7600 infrared camera during fully reversed axial fatigue tests. The new fatigue test results were successfully included in the existing heat energy-based scatter band previously calibrated on plain and bluntly notched specimens. Finally, an analysis of the heat energy dissipated around the notch tip has been presented and discussed with the aim of proposing a semi-automatic procedure to evaluate the thermal energy dissipated distribution.

The *fourth and fifth chapters* deal with the analysis of the thermal energy dissipation on both AISI 304L and C45 steels specimens subjected to multiaxial loads. The specific heat loss per cycle was measured during constant amplitude multiaxial fatigue tests adopting two different phase shift angles of the applied loads and two biaxiality ratios. All the fatigue test results on both materials are in good agreement with the relevant scatter band previously calibrated except for the out of phase multiaxial fatigue results relevant to the AISI 304L steel. These results seem to be justified by the strain-induced martensitic transformation in metastable austenitic stainless steel, significantly present in out of phase cyclic loading condition.

In the *sixth chapter*, the influence of the defect on fatigue behaviour of maraging steel specimens has been investigated. Axial fatigue tests were carried out on three batches of AMed maraging steel specimens produced by two different AM systems. Furthermore, axial fatigue tests were carried out on wrought maraging steel specimens both in annealed and in aged condition. After failure, the $\sqrt{\text{area}}$ of the killer defects was examined by SEM observations of the fracture surfaces. A stress intensity factor-based design curve for all the test series was obtained taking into account the short crack effect by means of the El-Haddad-Smith-Topper model. Due to the lack of expensive experimental data to determine the relevant material length parameter a_0 , a novel rapid method to approximately evaluate a_0 has been proposed. In particular, it consists in matching El-Haddad-Smith-Topper model with Murakami's expression of the threshold range of mechanically short cracks. The advantage of the adopted engineering approach is that only Vickers hardness of the material is necessary. Theoretically, this rapid method can be also adopted to estimate the size of the control volume of the averaged SED approach due to the analogy of the latter to the material length parameter a_0 . In the end, the stress intensity factor-based design curve was adopted to estimate the fatigue strength of sharp V-shaped notches characterized by a reduced notch opening angle.

Sommario

La valutazione della vita a fatica è di fondamentale importanza per la progettazione di componenti meccanici sottoposti a carichi ciclici al fine di evitare che si verifichino rotture le quali possono causare danni all'intero sistema meccanico o addirittura alle persone.

Le applicazioni industriali odierne richiedono componenti meccanici con geometria sempre più complessa sottoposti a condizioni di carico sempre più complesse. Considerando come esempio le linee guida della progettazione a fatica dei giunti saldati, le norme riportano diverse curve di progettazione a fatica basate su tensioni nominali le quali sono correlate ai più comuni dettagli strutturali saldati sottoposti ad un determinato tipo di carico. Per questo motivo, se i dettagli saldati da verificare sono diversi da quelli riportati in normativa, può risultare incerta la scelta della curva di fatica di progetto adottando l'approccio nominale.

La presente tesi si occupa della valutazione della fatica del materiale e dei componenti metallici adottando grandezze fisiche locali basate sull'energia che possono quantificare il danno locale dovuto ai gradienti di tensione che si verificano in prossimità di intagli e difetti. Più precisamente, l'obiettivo della presente tesi dottorato è quello di estendere l'applicabilità di tre approcci basati sull'energia includendo diversi fattori che influenzano la resistenza a fatica.

Il primo metodo basato sull'energia, il cosiddetto metodo Peak Stress Method, si occupa della valutazione della fatica dei giunti saldati mediante un'applicazione numerica agli elementi finiti dei Notch Stress Intensity Factors (N-SIFs). La tensione equivalente picco (ovvero il parametro di danneggiamento utilizzato per valutare la resistenza a fatica dei giunti saldati) può essere ottenuto richiamando il criterio della densità di energia di deformazione (SED) mediata. Il secondo metodo riguarda la caratterizzazione della fatica di componenti metallici assumendo come parametro di danneggiamento a fatica la perdita di calore specifica in un ciclo Q che può essere valutata in prove standard di fatica ad ampiezza costante adottando una semplice tecnica sperimentale basata su misurazioni della temperatura della superficie del materiale. Il terzo riguarda la caratterizzazione a fatica dei materiali metallici prodotti mediante manifattura additiva, una delle tecnologie più interessanti e studiate al giorno d'oggi. Poiché questi materiali sono affetti dalla presenza di difetti irregolari, gli approcci alla meccanica della frattura legati all'energia sembrano essere i più adatti per la valutazione della vita a fatica.

Nel *primo capitolo* viene descritto lo stato dell'arte dei suddetti metodi assieme alle loro basi teorico-analitiche.

Nel *secondo capitolo*, è stata presentata la trattazione teorica per estendere l'applicabilità del PSM alla valutazione della resistenza a fatica dei giunti saldati sottoposti a condizioni di carico multiassiale. Successivamente, sono stati analizzati,

mediante il PSM, diversi dati di fatica multiassiale presenti in letteratura, relativi a giunti saldati sia in alluminio che in acciaio per convalidare la previsione teorica. La tensione equivalente di picco ha dimostrato di correlare con buona approssimazione quasi tutti i dati sperimentali.

Il *terzo capitolo* tratta dell'analisi dell'energia termica dissipata durante le prove di fatica su campioni di acciaio inossidabile AISI 304L fortemente intagliati. La perdita di calore specifica per ciclo (parametro Q) è stata valutata sperimentalmente su campioni di acciaio inossidabile AISI 304L laminati a caldo di spessore 4 mm, caratterizzati da raggi di fondo intaglio pari a 3, 1 e 0,5 mm mediante una telecamera a infrarossi FLIR SC7600 durante prove di fatica assiale alternata. I nuovi risultati dei test di fatica risultano in ottimo accordo con la banda di dispersione basata sull'energia termica dissipata, precedentemente calibrata sul materiale liscio e dolcemente intagliato. Infine, è stata presentata e discussa la distribuzione dell'energia termica dissipata intorno all'apice dell'intaglio.

Il *quarto e il quinto capitolo* trattano dell'analisi della dissipazione dell'energia termica su provini sia in acciaio AISI 304L che in acciaio C45 sottoposti a carichi multiassiali. La perdita di calore specifica per ciclo è stata misurata durante i test di fatica multiassiale ad ampiezza costante adottando due diversi angoli di sfasamento tra carichi applicati e due rapporti di biassialità. Tutti i risultati dei test di fatica su entrambi i materiali sono in buon accordo con la relativa banda di dispersione precedentemente calibrata, ad eccezione dei risultati di fatica multiassiale relativi all'acciaio AISI 304L sollecitato con carichi sfasati di 90°. Questi risultati sembrano essere giustificati dalla trasformazione martensitica indotta dalla deformazione in acciaio inossidabile austenitico metastabile che si manifesta significativamente condizioni di carico ciclico sfasato.

Nel *sesto capitolo* è stata studiata l'influenza dei difetti sul comportamento a fatica dei campioni di acciaio maraging prodotto mediante manifattura additiva (AM). Sono stati effettuati test di fatica assiale su tre lotti di campioni di acciaio maraging prodotto con diverse macchine AM. Inoltre, sono stati effettuati test di fatica assiale su campioni dello stesso acciaio prodotto con tecnologia tradizionale sia allo stato ricotto che invecchiato. Dopo rottura, il parametro $\sqrt{\text{area}}$ dei difetti killer è stato valutato mediante analisi al SEM delle superfici di frattura. È stata proposta una curva di progettazione basata sullo Stress Intensity Factor (ΔK_{corr}) per ogni serie di test tenendo conto dell'effetto delle cricche corte con il modello di El-Haddad-Smith-Topper. A causa della mancanza di costosi dati sperimentali necessari per determinare il parametro a_0 , è stato proposto un nuovo metodo approssimato per stimare a_0 . In particolare, esso consiste nell'abbinare il modello El-Haddad-Smith-Topper con l'espressione di Murakami del ΔK di soglia delle cricche corte. Il vantaggio dell'approccio ingegneristico proposto è che la sola durezza Vickers del materiale è necessaria ai fini di stimare a_0 . Teoricamente, questo metodo rapido può anche essere utilizzato per stimare la dimensione del volume di controllo dell'approccio del SED mediato per via dell'analogia di quest'ultimo con il parametro a_0 . Infine, la curva di

progettazione basata sul ΔK_{corr} è stata utilizzata anche per stimare la resistenza a fatica di provini intagliati a V con angolo di apertura ridotto prodotti mediante manifattura additiva.

List of Figures

Figure 1.1 Assumptions of the NSIF-based approach in fatigue design of welded joints with reference referring to a tube-to-flange fillet-welded joint under multiaxial fatigue loading. The sharp V-notch opening angle 2α is typically 0° at the weld root and 135° at the weld toe. [Figure taken from [19]].	25
Figure 1.2. Polar reference system centred at the weld toe of a typical tube-to-flange welded joint geometry subjected to multiaxial bending and torsion loading. [Figure taken from [19]]	26
Figure 1.3. Typical 2D FE mesh to apply the PSM according to Eq. (11); the example reported in the figure shows a tube-to-flange fillet welded joint. The four-node, quadrilateral, harmonic PLANE 25 elements available in Ansys® Element Library were adopted to generate the free mesh shown in the figure. The Y-axis coincides with the axis of the tube. [Figure taken from [19]].	27
Figure 1.4: Comparison between the fatigue design scatter band and experimental fatigue results relevant to structural steel welded joints obtained under mode I+II [19,27,31–36] (figure taken from [39]).	33
Figure 1.5: Comparison between the fatigue design scatter band and experimental fatigue results relevant to structural steel welded joints obtained under mode III. [19,33,40] (figure taken from [39]).	33
Figure 1.6. Qualitative thermal increments in specimens under fatigue loading at different applied stresses. The three phases are shown.	37
Figure 1.7. Determination of the fatigue limit from the initial temperature gradient $\Delta T/\Delta N$ a) and stabilised temperature ΔT (phase 2 of fig. 6) b). Pictures were taken from [44].	37
Figure 1.8: $\Delta\phi_{\max}$ data for fatigue limit estimation. Figure taken from [67].	39
Figure 1.9: Waveform of temperature measurement close to a circular hole under cyclic axial load. Figure taken from [71].	40
Figure 1.10: Energy dissipation evolution during a loading cycle of a simplified bilinear material model. Figure taken from [74].	41
Figure 1.11: Energy balance of a material subjected to cyclic loading (a) Qualitative representation of temperature evolution during a fatigue test and evaluation of the cooling gradient immediately after a test stop (b).	42
Figure 1.12: Fatigue tests results in terms of specific heat energy. The scatter band was calibrated only on data published in [77].	43
Figure 1.13: Fatigue data analysed in terms of specific heat loss. Scatter bands are defined for 10% and 90% survival probabilities [62].	44

Figure 1.14: Fatigue data of Fig. 13 analysed in terms of the temperature-corrected energy parameter Q. Scatter bands are defined for 10% and 90% survival probabilities. [62].....	45
Figure 1.15: Fatigue test results in terms of SWT parameter for DMLS specimens tested in the as-built (not-treated NT) and aged (heat-treated T) conditions with different building orientations (0° and 90°) (from [125]). Comparison with fatigue test results obtained by Van Swam et al. [126] by testing vacuum melted maraging steel 300 under push-pull loading.....	48
Figure 2.1: Typical 2D FE mesh to apply the PSM according to Eq. (11); the example reported in the figure shows a tube-to-flange fillet welded joint. The four-node, quadrilateral, harmonic PLANE 25 elements available in Ansys® Element Library were adopted to generate the free mesh shown in the figure. The Y-axis coincides with the axis of the tube. [Figure taken from [1]].....	58
Figure 2.2: 2D FE mesh to apply the PSM according to Eq. (10); the example reported in the figure shows a tube-to-flange full penetration welded joint [16] with a large toe radius ($\rho = 13$ mm). Four-node, quadrilateral, harmonic PLANE 25 elements available in Ansys® Element Library were adopted to generate the free mesh shown in the figure. The Y-axis is the axis of the tube. [Figure taken from [1]].....	62
Figure 2.3 3D FE mesh to apply the PSM according to Eq. (11); the example reported in the figure shows a box-beam fillet-welded joint [17]. Eight node brick SOLID 185 elements (with K-option 2 set to 3) available in Ansys® Element Library were adopted to generate the 3D mesh of the submodel shown in the figure. [Figure taken from [1]].....	63
Figure 2.4. 3D FE mesh to apply the PSM according to Eq. (18c); the example reported in the figure shows a plate having a box-welded (wrap-around) joint [27,28]. Eight node brick SOLID 185 elements (with K-option 2 set to 3) available in Ansys® Element Library were adopted to generate the 3D mesh of the submodels shown in the figure. [Figure taken from [1]].....	64
Figure 2.5: Nominal loading paths adopted in out-phase multiaxial fatigue tests in [19]. [Figure taken from [1]].....	73
Figure 2.6 Fatigue assessment of tube-to-flange welded joints (model 1) according to the PSM. Comparison between the proposed multiaxial fatigue design scatter band and experimental fatigue results from [19]. [Figure taken from [2]].....	86
Figure 2.7 Fatigue assessment of tube-to-flange welded joints (model 2a and 2b) according to the PSM. Comparison between the proposed multiaxial fatigue design scatter band and experimental fatigue results from [20]. [Figure taken from [2]].....	87
Figure 2.8: Fatigue assessment of tube-to-flange welded joints with partial penetration (model 3), according to the PSM. Comparison between the proposed multiaxial fatigue design scatter band and experimental fatigue results from [21]. [Figure taken from [2]].....	87

Figure 2.9 Fatigue assessment of square hollow section (SHS) beam fillet-welded onto a square plate (SP), (model 4) according to the PSM. Comparison between the proposed multiaxial fatigue design scatter band and experimental fatigue results from [22]. [Figure taken from [2]].....	88
Figure 2.10 Fatigue assessment of box-beam steel fillet welded joints (model 5) according to the PSM. Comparison between the proposed multiaxial fatigue design scatter band and experimental fatigue results from [17]. [Figure taken from [2]]	88
Figure 2.11: Fatigue assessment of tube-to-flange full-penetration welded joints (model 6) according to the PSM. Comparison between the proposed multiaxial fatigue design scatter band and experimental fatigue results from [23,44], expressed in terms of number of cycles to (a) crack initiation and (b) break-through. [Figure taken from [2]].....	89
Figure 2.12: Fatigue assessment of tube-to-flange welded joints (model 7a and 7b) according to the PSM. Comparison between the proposed multiaxial fatigue design scatter band and experimental fatigue results from [25,26]. [Figure taken from [2]].....	90
Figure 2.13: Fatigue assessment of plates having a box-fillet-welded (wrap-around) joints (model 8a and 8b) according to the PSM. Comparison between the proposed multiaxial fatigue design scatter band and experimental fatigue results from [27,28]. [Figure taken from [2]]	91
Figure 2.14: Fatigue assessment of square hollow section (SHS) beam fillet-welded onto a square plate (SP), (model 4) based on the nominal stress approach, as formulated for the case of multiaxial loadings according to IIW Recommendations [37]. Comparison between the design curve and experimental fatigue results from [22]. [Figure taken from [2]].....	91
Figure 2.15 Experimental fatigue results relevant to tube-to-flange steel welded joints (model 1) taken from [19] and expressed in terms of shear (for pure torsion) or normal (for all other cases) nominal stress range. See Fig. 6 for comparison. [Figure taken from [2]].....	92
Figure 2.16: Experimental fatigue results relevant to tube-to-flange steel welded joints with partial penetration (model 3) taken from [21] and expressed in terms of shear (for pure torsion) or normal (for all other cases) nominal stress range. See Fig. 8 for comparison. [Figure taken from [2]].....	92
Figure 2.17: Crack initiation experimental fatigue results relevant to tube-to-flange full-penetration steel welded joints (model 6) taken from [23,24] and expressed in terms of shear (for pure torsion) or normal (for all other cases) nominal stress range. See Fig. 11a for comparison. [Figure taken from [2]]	93
Figure 2.18: Fatigue assessment of tube-to-flange welded joints made of aluminium alloy according to the PSM. Comparison between the proposed multiaxial fatigue design scatter band and experimental fatigue results from [16]. [Figure taken from [1]]	94

Figure 2.19 Fatigue assessment of overlap-tubes welded joints made of aluminium alloy according to the PSM. Comparison between the proposed multiaxial fatigue design scatter band and experimental fatigue results from [30]. [Figure taken from [1]]	95
Figure 2.20: Experimental fatigue results relevant to tube-to-flange welded joints made of aluminium alloy taken from [16] and expressed in terms of nominal shear (for pure torsion) or normal (for all other cases) stress range. See Fig. 18 for comparison. [Figure taken from [1]].....	95
Figure 2.21: Experimental fatigue results relevant to overlap-tubes welded joints made of aluminium alloy taken from [30] and expressed in terms of nominal normal stress range. See Fig. 19 for comparison [Figure taken from [1]]	96
Figure 3.1: Fatigue tests results in terms of specific heat energy. The scatter band was calibrated only on data published in [6].....	105
Figure 3.2: Material control volume at a notch tip according to [12] ($r_0=0.2$, $2\alpha=135^\circ$).	106
Figure 3.3: Experimental set-up adopted (a) and evaluation of the cooling gradient (from Eq. (1)) during a fatigue test (b).	106
Figure 3.4: Specimen's geometry (units in mm) (a) and microstructure of the AISI 304L stainless steel (b).	108
Figure 3.5: Test setup consisting of a FLIR SC7600 infrared camera, a AM4115ZT Dino-lite digital microscope and the specimen clamped in the test machine.....	109
Figure 3.6: Inspection phase of technical crack initiation.....	110
Figure 3.7: A crack observed at the number of cycles of technical crack initiation	110
Figure 3.8: Digital microscope image on the left and infrared image on the right used for evaluating the effective spatial resolution before each test.	111
Figure 3.9: Schematic representation of the 3-dimensional array $\bar{T}(a)$. Flowchart of the data analysis to obtain the energy distribution at the notch tip. (b).....	112
Figure 3.10: Fatigue data analysed in terms of net-section stress amplitude. Scatter band was calibrated in [6].	113
Figure 3.11. Typical temperature evolution measured at a distance of 5 mm from the notch apex by using thermocouples.	113
Figure 3.12: Temperature maps observed during the fatigue tests.	114
Figure 3.13: Typical cooling gradients at the notch tip measured during the fatigue tests. T_{max} is the maximum temperature inside a circle area as it is shown in Fig. (4).	115
Figure 3.14: Definition of the time t^* when the machine is assumed to stop cycling and the cooling gradient is evaluated.	116

Figure 3.15 Mean temperature field $T_m(r,\theta)$, and radial paths adopted to calculate Q^* from Eq. (2) (a). Radial temperature profile measured at $\theta = 0^\circ$ (b).....	116
Figure 3.16: Typical cooling gradient of T_{max} measured during the fatigue tests carried out on notched specimens with $r_n = 0.5\text{mm}$ (a). Typical cooling gradient of $T^*(t)$ for the same fatigue test on the same notched specimen (b).....	117
Figure 3.17: Q versus N/N_i , measured during the fatigue tests (a) and Q^* (from equation (4)) versus N/N_i , measured during the fatigue tests (b).....	118
Figure 3.18: Example of Q and Q^* trends evaluated before the technical crack initiation	118
Figure 3.19 Fatigue data reported in figure 8 analysed in terms of specific heat loss per cycle. Scatter band is defined for 10% and 90% survival probabilities (from [6])	119
Figure 3.20: Example of raw data of the energy distribution $Q(x,y)$ (a) and along the coordinate $y=0$ (along the notch bisector (b). The filtered energy distribution $Q_{flt}(x,y)$ (c) and the relevant distribution along the notch bisector ($y=0$) (d). (a-d) data are referred to the acquisition obtained at $N = 8.12 \cdot 10^3$ cycles of the specimen characterised by $r_n=0.5$ mm, $\sigma_{an}=130$ MPa, and $N_f = 6.76 \cdot 10^4$	121
Figure 3.21: Heat energy distributions at the notch tip: (a,b,) $r_n=3$ mm, $\sigma_{an}=170$ MPa, $N_f=1.85 \cdot 10^4$ cycles; (c,d) $r_n=1$ mm, $\sigma_{an}=150$ MPa, $N_f=1.67 \cdot 10^4$ cycles; (e,f) $r_n=0.5$ mm, $\sigma_{an}=100$ MPa, $N_f=1.35 \cdot 10^5$ cycles	122
Figure 3.22. Temperature distribution measured along the notch tip from the lateral view (see Fig. (3a)) (a) and the corresponding energy distribution (b)	123
Figure 3.23: a) AISI 304L steel 2D bar subjected to self-heating just in a portion of volume constrained at $T = 0^\circ\text{C}$ and the ends. b) Qualitative representation of temperature profile after stabilization according to Eq. (9) and (10).	125
Figure 3.24. Temperature profile obtained from FE steady-state thermal analysis of the bar shown in (Fig. 22a).....	125
Figure 3.25. Temperature profile on four point (See Fig. 22a) obtained by FE transient analysis.....	126
Figure 3.26: Steady-state temperature ($T_m(x,y)$) field (a) and distribution along the notch bisector ($y=0$) (b). Filtered steady-state temperature ($T_{m,flt}(x,y)$) field (c) and the relevant distribution along the notch bisector ($y=0$) (d). The relevant fatigue test details are reported in Fig. 7.....	127
Figure 3.27: Filter Laplacian field (a) and comparison with the not filtered and the filtered Laplacian distributions along the notch bisector ($y=0$) (b).	128
Figure 3.28: Contour plot of the nodal temperature solutions (a) and comparison between the experimental steady-state temperature and nodal solutions along three different path (b,c,d).	128

Figure 4.1. Fatigue test results of plain and notched AISI 304L in terms of specific heat loss Q (a). Qualitative representation of temperature evolution during a fatigue test and evaluation of the cooling gradient immediately after a test stop (b).....	136
Figure 4.2: (a) Specimen's geometry for bending-torsional fatigue tests; (b) specimen's geometry for axial-torsional fatigue tests (dimensions are given in mm)	138
Figure 4.3: Microstructure of cold drawn AISI 304L stainless steel in the longitudinal and transversal planes both close to the edge and in the bulk of the raw bars.....	138
Figure 4.4: Flexible test bench designed for dynamic combined plane bending and torsion on AISI 304L specimens of Fig. (3a) (a). Picture of the relevant test bench placed at the laboratory of Machine Design of University of Padova (b).	139
Figure 4.5: Test bench configurations.....	141
Figure 4.6: Experimental setup of the Matelect DCM-2 DCPD crack growth monitor device.....	142
Figure 4.7: Picture of the experimental setup of multiaxial fatigue testing on type (B) specimens (Fig. 3b).....	143
Figure 4.8. Picture of the specimens (B) of Fig. (3b), used for combined axial and torsional fatigue tests.....	143
Figure 4.9: Fatigue test results in terms of nominal net-section stress amplitude. ..	144
Figure 4.10: Example of long-term temperature acquisition by using thermocouples (a) and potential ratio signal obtained by means of DCPD method (b) on plane bending fatigue tests.....	145
Figure 4.11: Example of long-term temperature acquisition by using thermocouples (a) and potential ratio signal obtained by means of DCPD method (b) on plane bending fatigue tests.....	146
Figure 4.12: Example of long-term temperature acquisition by using thermocouples (a) and potential ratio signal obtained by means of DCPD method (b) on pure torsion fatigue tests.	147
Figure 4.13: Example of long-term temperature acquisition by using thermocouples (a) and potential ratio signal obtained by means of DCPD method (b) on pure torsion fatigue tests.	148
Figure 4.14: Example of long-term temperature acquisition by using thermocouples (a) and potential ratio signal obtained by means of DCPD method (b) on multiaxial B+T, $\varphi=0^\circ$, $\Lambda=1$ fatigue tests.	149
Figure 4.15: Example of long-term temperature acquisition by using thermocouples (a) and potential ratio signal obtained by means of DCPD method (b) on multiaxial B+T, $\varphi=0^\circ$, $\Lambda=1$ fatigue tests.	150
Figure 4.16: Example of long-term temperature acquisition by using thermocouples (a) and potential ratio signal obtained by means of DCPD method (b) on multiaxial B+T, $\varphi=90^\circ$, $\Lambda=1$ fatigue tests	151

Figure 4.17: Example of long-term temperature acquisition by using thermocouples (a) and potential ratio signal obtained by means of DCPD method (b) on multiaxial B+T, $\varphi=0^\circ$, $\Lambda=\sqrt{3}$ fatigue tests.....	152
Figure 4.18: Example of long-term temperature acquisition by using thermocouples (a) and potential ratio signal obtained by means of DCPD method (b) on multiaxial B+T, $\varphi=0^\circ$, $\Lambda=\sqrt{3}$ fatigue tests.....	153
Figure 4.19: Example of long-term temperature acquisition by using thermocouples (a) and potential ratio signal obtained by means of DCPD method (b) on multiaxial B+T, $\varphi=90^\circ$, $\Lambda=\sqrt{3}$ fatigue tests.....	154
Figure 4.20: Cracks orientation due to cyclic plane bending.....	155
Figure 4.21. Crack orientation due to cyclic pure torsion bending at LCF a) Low-Medium HF b) and HCF regime c).....	156
Figure 4.22: Crack orientation due to cyclic combined bending and torsional fatigue loading characterized by $\Lambda= 1$, $\varphi=0^\circ$	157
Figure 4.23: Crack orientation due to cyclic combined bending and torsional fatigue loading characterized by $\Lambda= \sqrt{3}$, $\varphi=0^\circ$	157
Figure 4.24: Crack orientation due to cyclic combined bending and torsional fatigue loading characterized by $\Lambda= 1$, $\varphi=90^\circ$	158
Figure 4.25: Crack orientation due to cyclic combined bending and torsional fatigue loading characterized by $\Lambda= \sqrt{3}$, $\varphi=90^\circ$	158
Figure 4.26: Example of cooling gradient measured in plane bending fatigue test and relevant Q evolution.	159
Figure 4.27: Example of cooling gradient measured in plane bending fatigue test and relevant Q evolution.	160
Figure 4.28: Example of cooling gradient measured in pure torsional fatigue test and relevant Q evolution.	161
Figure 4.29: Example of cooling gradient measured in pure torsional fatigue test and relevant Q evolution.	162
Figure 4.30: Example of cooling gradient measured in B+T, $\varphi=0^\circ$, $\Lambda=1$ fatigue test and relevant Q evolution.	163
Figure 4.31: Example of cooling gradient measured in B+T, $\varphi=0^\circ$, $\Lambda=1$ fatigue test and relevant Q evolution.	164
Figure 4.32: Example of cooling gradient measured in B+T, $\varphi=90^\circ$, $\Lambda=1$ fatigue test and relevant Q evolution.	165
Figure 4.33: Example of cooling gradient measured in B+T, $\varphi=90^\circ$, $\Lambda=1$ fatigue test and relevant Q evolution.	166
Figure 4.34: Example of cooling gradient measured in B+T, $\varphi=0^\circ$, $\Lambda=\sqrt{3}$ fatigue test and relevant Q evolution.	167
Figure 4.35: Example of cooling gradient measured in B+T, $\varphi=0^\circ$, $\Lambda=\sqrt{3}$ fatigue test and relevant Q evolution.	168
Figure 4.36 Example of cooling gradient measured in B+T, $\varphi=90^\circ$, $\Lambda=\sqrt{3}$ fatigue test and relevant Q evolution.	169

Figure 4.37: Example of cooling gradient measured in B+T, $\varphi=90^\circ$, $\Lambda=\sqrt{3}$ fatigue test and relevant Q evolution.	170
Figure 4.38: Synthesis of Q evolutions during plane bending fatigue tests.	171
Figure 4.39: Synthesis of Q evolutions during pure torsional fatigue tests.	171
Figure 4.40: Synthesis of Q evolutions during combined bending and torsional fatigue test with $\varphi=0^\circ$ and $\Lambda=1$	172
Figure 4.41: Synthesis of Q evolutions during combined bending and torsional fatigue test with $\varphi=90^\circ$ and $\Lambda=1$	172
Figure 4.42: Synthesis of Q evolutions during combined bending and torsional fatigue test with $\varphi=0^\circ$ and $\Lambda=\sqrt{3}$	173
Figure 4.43: Synthesis of Q evolutions during combined bending and torsional fatigue test with $\varphi=90^\circ$ and $\Lambda=\sqrt{3}$	173
Figure 4.44: Synthesis of fatigue test results in terms of Q, compared to the scatter band calibrated in [8].....	174
Figure 4.45: Infrared images at time t^* (see Fig. (1b)) for uniaxial (a), torsional (b), multiaxial $\Lambda = \sqrt{3}$ in-phase (c) and out of phase (d) loading conditions on type B specimens. The temperature value was averaged within the red rectangular area for each frame.....	175
Figure 4.46: Example of cooling gradient measured in uniaxial fatigue test (specimen B)	175
Figure 4.47: Example of cooling gradient measured in pure torsional fatigue test (specimen B).....	176
Figure 4.48: Example of cooling gradient measured in A+T, $\varphi=0^\circ$, $\Lambda=\sqrt{3}$ fatigue test (specimen B).....	176
Figure 4.49: Example of cooling gradient measured in A+T, $\varphi=90^\circ$, $\Lambda=\sqrt{3}$ fatigue test (specimen B).....	176
Figure 4.50: Evolution of Q during uniaxial and multiaxial fatigue test on type B specimens	177
Figure 4.51: Comparison between the results obtained on specimen A and specimen B expressed in terms of Q.....	177
Figure 5.1: Qualitative representation of temperature evolution during a fatigue test and evaluation of the cooling gradient immediately after a test stop (a).....	184
Figure 5.2: Qualitative representation of temperature evolution during a fatigue test and evaluation of the cooling gradient immediately after a test stop (a). Energy-based scatter band calibrated in [13] (b).	184
Figure 5.3: Microstructure of quenched and tempered C45 steel in both longitudinal and transversal planes.	186
Figure 5.4: Specimen's geometry adopted for multiaxial fatigue testing.	186
Figure 5.5: Black painted specimens surface (a) and experimental setup for evaluating the specific heat loss per cycles (b) at Fatigue Lab of NTNU (Norway).	188

Figure 5.6: Portion of surface area framed by the infrared camera with the relevant temperature map recorded by the infrared camera. The selected rectangular area at the net section of the specimens for extracting the mean temperature value.	189
Figure 5.7: Schematic illustration of the experimental setup for evaluating Q and ΔW (a) and picture of the DIC system adopted (b).....	190
Figure 5.8: Example of speckle pattern.....	191
Figure 5.9: Examples of DIC calibration images of the calibration target.	191
Figure 5.10: Picture taken by the DIC cameras. The correlation algorithm was run within the black rectangular area adopting a subset size of 50 pixels.	191
Figure 5.11: crack paths relevant to uniaxial (a,b) and pure torsion (c,d) loading conditions.	192
Figure 5.12: crack paths relevant to multiaxial A+T, $\Lambda=1$, $\varphi=0^\circ$ (a,b) and A+T, $\Lambda=\sqrt{3}$, $\varphi=0^\circ$ (c,d) loading conditions	193
Figure 5.13: crack paths relevant to multiaxial A+T, $\Lambda=1$, $\varphi=90^\circ$ (a,b) and A+T, $\Lambda=\sqrt{3}$, $\varphi=90^\circ$ (c,d) loading conditions	194
Figure 5.14: Fatigue test results in terms of nominal net-section stress amplitude.....	195
Figure 5.15: Example of cooling gradient measured of axial fatigue test and relevant Q evolution.....	197
Figure 5.16: Example of cooling gradient measured of axial fatigue test and relevant Q evolution.....	198
Figure 5.17: Example of cooling gradient measured of pure torsion fatigue test and relevant Q evolution.....	199
Figure 5.18: Example of cooling gradient measured of pure torsion fatigue test and relevant Q evolution.....	200
Figure 5.19: Example of cooling gradient measured in A+T, $\varphi=0^\circ$, $\Lambda=1$ fatigue test and relevant Q evolution	201
Figure 5.20: Example of cooling gradient measured in A+T, $\varphi=0^\circ$, $\Lambda=1$ fatigue test and relevant Q evolution.	202
Figure 5.21: Example of cooling gradient measured in A+T, $\varphi=0^\circ$, $\Lambda=\sqrt{3}$ fatigue test and relevant Q evolution.	203
Figure 5.22: Example of cooling gradient measured in A+T, $\varphi=0^\circ$, $\Lambda=\sqrt{3}$ fatigue test and relevant Q evolution.	204
Figure 5.23: Example of cooling gradient measured in A+T, $\varphi=90^\circ$, $\Lambda=1$ fatigue test and relevant Q evolution.	205
Figure 5.24: Example of cooling gradient measured in A+T, $\varphi=90^\circ$, $\Lambda=1$ fatigue test and relevant Q evolution.	206
Figure 5.25: Example of cooling gradient measured in A+T, $\varphi=90^\circ$, $\Lambda=\sqrt{3}$ fatigue test and relevant Q evolution.	207

Figure 5.26: Example of cooling gradient measured in A+T, $\varphi=90^\circ$, $\Lambda=\sqrt{3}$ fatigue test and relevant Q evolution.	208
Figure 5.27: Synthesis of Q evolutions during axial and pure torsion fatigue tests.....	209
Figure 5.28: Synthesis of Q evolutions during combined axial and torsional fatigue test with $\varphi=0^\circ$ and $\Lambda=1$	210
Figure 5.29: Synthesis of Q evolutions during combined bending and torsional fatigue test with $\varphi=0^\circ$ and $\Lambda=\sqrt{3}$	210
Figure 5.30: Synthesis of Q evolutions during combined bending and torsional fatigue test with $\varphi=90^\circ$ and $\Lambda=1$	211
Figure 5.31: Synthesis of Q evolutions during combined bending and torsional fatigue test with $\varphi=90^\circ$ and $\Lambda=\sqrt{3}$	211
Figure 5.32: Example of strain maps relevant to the fatigue tests A+T, $\varphi=90^\circ$, $\Lambda=\sqrt{3}$ test 8 (See Fig. 28).	212
Figure 5.33: Comparison between the raw DIC data and cubic spline fitting of A+T, $\varphi=0^\circ$, $\Lambda=1$ test 8 (See Fig. 28).	213
Figure 5.34: Hysteresis cycle during axial fatigue test Axial_test4.....	214
Figure 5.35: Hysteresis cycle during axial fatigue test Torsional_test4	214
Figure 5.36: Hysteresis cycles during multiaxial fatigue test A+T, $\varphi=0^\circ$, $\Lambda=1$ test 8	215
Figure 5.37: Hysteresis cycles during multiaxial fatigue test A+T, $\varphi=0^\circ$, $\Lambda=\sqrt{3}$ test 9	215
Figure 5.38: Hysteresis cycles during multiaxial fatigue test A+T, $\varphi=90^\circ$, $\Lambda=1$ test 9 (See Fig. 30)	216
Figure 5.39: Hysteresis cycles during multiaxial fatigue test A+T, $\varphi=90^\circ$, $\Lambda=\sqrt{3}$ test 10 (See Fig. 31)	216
Figure 5.40: Evolution of ΔW and Q during axial and torsional fatigue tests.	217
Figure 5.41: Evolution of ΔW and Q during multiaxial fatigue tests subjected to proportional loading condition.....	217
Figure 5.42: Evolution of ΔW and Q during multiaxial fatigue tests subjected to out-of-phase loads.....	218
Figure 5.43: Synthesis of fatigue test results in terms of Q, compared to the scatter band calibrated in [13].	219
Figure 5.44: Synthesis of fatigue test results in terms of equivalent Von Mises stress amplitude, compared to the scatter band calibrated in [13]	220
Figure 5.45: Comparison with the scatter band previously calibrated in [13], and that one calibrated on all the data obtained in the present work.	221
Figure 6.1: Specimen's geometry adopted for tensile static and fatigue tests on maraging steel produced by DMLS, and (b) two building platforms with the specimens produced by DMLS having specimen's axis oriented at 0° and 90° with respect to the building direction (z axis). [1].....	227

Figure 6.2: (a) Location of strain gauges adopted to evaluate the correlation between deflection f_a and mean axial strain induced by clamping in the axial machine grips and (b) example of a specimen with a strain gauge placed at point A. [1].....	227
Figure 6.3: (a) An example of strain measurement at the midpoint of the inner side of the specimen curvature (point A) and at the opposite side (point B) during the specimen clamping on the test machine and (b) correlation between mean strain measurements at point A and deflection f_a for selected specimens. [1]	228
Figure 6.4: (a) Stress-strain curves of the DMLS specimens tested in the as-built (not-treated NT) and aged (treated T) conditions with different building orientation (0° and 90°) and (b) summary of mechanical properties. [1].....	229
Figure 6.5: (a) Fatigue test results in terms of nominal stress amplitude for the DMLS specimens tested in the as-built (not-treated NT) and aged (heat-treated T) conditions with different building orientations (0° and 90°). Comparison with fatigue test results obtained by [7] by testing vacuum melted maraging steel 300 under push-pull axial loading. (b) Fatigue test results in terms of SWT parameter evaluated individually at the crack initiation point of the specimens. [1].....	230
Figure 6.6: Crack initiation point analysed by means of a stereoscopic microscope for: (a) AD_90°_NT specimen subjected to $\sigma_a = 400$ MPa, having $f_a = 0.73$ mm, and failed at $7.75 \cdot 10^4$ cycles, and (b) AD_90°_NT specimen subjected to $\sigma_a = 400$ MPa, having $f_a = 0.85$ mm, and failed at $2.99 \cdot 10^5$ cycles. [1].....	230
Figure 6.7: Effect of defects size on threshold stress and stress intensity factor [8,12].....	231
Figure 6.8: Comparison between short crack and long crack behaviour [18,19]. ...	232
Figure 6.9: Specimen's geometries	235
Figure 6.10: building orientation of the specimens AMed.	236
Figure 6.11: Example of microhardness measurement ($HV_{0.2}$) on a cross-section of the gross part of the specimens. The detailed view shows the indentation of a 90° -oriented specimens.....	237
Figure 6.12: Microstructure along a normal and parallel plane of the specimen's axis of wrought maraging steel 300 in the annealed (a) and aged condition (b). (heat treatment parameters are reported in Table (5))......	238
Figure 6.13: Microstructure along a normal and parallel plane with respect to the building direction (Z) of the SISMA (S) as built (a), SISMA (SN) in aged condition (b), and EOS in aged condition (c).....	239
Figure 6.14: 90° -oriented as-built specimens (a), detailed view at the support side (b), surface finish of all specimens after polishing and turning the gross ends (c)	240
Figure 6.15: Deflection of the specimen's axis f_a (before turning the gross ends of the specimens) a). Measurements of f_a	241

Figure 6.16: Deflection f_a before machining the gross parts of the AMed specimens (mean value ± 1 standard deviation) (a) and roughness R_a (The mean value ± 1 standard deviation).....	241
Figure 6.17: Synthesis of the fatigue results expressed in terms of nominal stress amplitude.....	242
Figure 6.18: Fatigue results comparison between wrought and the AMed maraging steel for each batch and same heat treatment condition.....	243
Figure 6.19: Examples of fracture surfaces relevant to the test series S_0°_NT and relevant area at the failure origin.....	244
Figure 6.20: Examples of fracture surfaces relevant to the test series S_90°_NT and relevant area at the failure origin.....	245
Figure 6.21: Examples of fracture surfaces relevant to the test series SN_0°_NT and relevant area at the failure origin.....	246
Figure 6.22: Examples of fracture surfaces relevant to the test series SN_90°_NT and relevant area at the failure origin.....	247
Figure 6.23: Examples of fracture surfaces relevant to the test series SN_0°_T and relevant area at the failure origin.....	248
Figure 6.24: Examples of fracture surfaces relevant to the test series SN_90°_T and relevant area at the failure origin.....	249
Figure 6.25: Examples of fracture surfaces relevant to the test series EN_0°_T and relevant area at the failure origin.....	250
Figure 6.26: Examples of fracture surfaces relevant to the test series EN_90°_T and relevant area at the failure origin.....	251
Figure 6.27: Boxplots of the $\sqrt{\text{area}}$ evaluation per each test series.....	252
Figure 6.28: Distribution of residual defects in 90° oriented specimens.	252
Figure 6.29: Matching Eqs. (1) and (5b) according to expression (9) to estimate the El-Haddad-Smith-Topper length parameter a_0 of the test series S_0°/90°_NT.....	253
Figure 6.30: Matching Eqs. (1) and (5b) according to expression (9) to estimate the El-Haddad-Smith-Topper length parameter a_0 of the test series SN_0°/90°_NT.....	253
Figure 6.31: Matching Eqs. (1) and (5b) according to expression (9) to estimate the El-Haddad-Smith-Topper length parameter a_0 of the test series SN_0°/90°_T.....	254
Figure 6.32: Matching Eqs. (1) and (5b) according to expression (9) to estimate the El-Haddad-Smith-Topper length parameter a_0 of the test series EN_0°/90°_T.....	254
Figure 6.33: Fatigue test results in terms of nominal stress amplitude of the test series S_0_NT a). Fatigue test results in terms of ΔK_{corr} of the test series S_0_NT b).....	255

Figure 6.34: Fatigue test results in terms of nominal stress amplitude of the test series S_90_NT a). Fatigue test results in terms of ΔK_{corr} of the test series S_90_NT b).....	255
Figure 6.35: Fatigue test results in terms of nominal stress amplitude of the test series EN_0_T a). Fatigue test results in terms of ΔK_{corr} of the test series EN_0_T b)	256
Figure 6.36: Fatigue test results in terms of nominal stress amplitude of the test series EN_90_T a). Fatigue test results in terms of ΔK_{corr} of the test series EN_90_T b)	256
Figure 6.37: Fatigue test results in terms of nominal stress amplitude of the test series SN_0_NT a). Fatigue test results in terms of ΔK_{corr} of the test series SN_0_NT b).....	256
Figure 6.38: Fatigue test results in terms of nominal stress amplitude of the test series SN_90_NT a). Fatigue test results in terms of ΔK_{corr} of the test series SN_90_NT b).....	257
Figure 6.39: Fatigue test results in terms of nominal stress amplitude of the test series SN_0_T a). Fatigue test results in terms of ΔK_{corr} of the test series SN_0_T b).....	257
Figure 6.40: Fatigue test results in terms of nominal stress amplitude of the test series SN_90_T a). Fatigue test results in terms of ΔK_{corr} of the test series SN_90_T b).....	257
Figure 6.41: pre-crack a_p after fatigue failure.	260
Figure 6.42: precrack observed after fatigue failure of SN_V_0_NT_1 a) SN_V_0_NT_2 b) and SN_V_0_NT_3 c).....	261
Figure 6.43: precrack observed after fatigue failure of SN_V_90_NT_1 a) SN_V_90_NT_2 b) and SN_V_90_NT_3 c).....	261
Figure 6.44: Fatigue test results of maraging steel specimens oriented at 0° in terms of ΔK_{corr} . Additional experimental results on V-notched, 0° -oriented specimens (see geometry in Fig. 9c) are reported.	262
Figure 6.45: Fatigue test results of maraging steel specimens oriented at 90° in terms of ΔK_{corr} . Additional experimental results on V-notched, 90° -oriented specimens (see geometry in Fig. 9c) are reported.	262

List of Tables

Table 1.1: Values of constants and of parameter f_{w1} according to Eq. (12a).....	32
Table 1.2: Values of constants and of parameter f_{w2} according to Eq. (12b).....	32
Table 1.3: Values of constants and of parameter f_{w3} according to Eq. (12c).....	32
Table 2.1: Conditions for applicability of Eqs. (1)-(3) by using ANSYS® FE code [5,7,9].	59
Table 2.2: Values of constants and of parameter f_{w1} according to Eq. (6a).....	61
Table 2.3: Values of constants and of parameter f_{w2} according to Eq. (6b).....	61
Table 2.4: Values of constants and of parameter f_{w3} according to Eq. (6c).....	61
Table 2.5: Information about materials, welding processes and testing conditions of steel welded joints taken from the literature.	66
Table 2.6: Steel welded joint geometries and FE analyses for fatigue strength assessment according to the PSM [2].	67
Table 2.7: Average FE mesh size required in order to comply with the conditions of applicability of the PSM at the weld root and toe, and finally adopted FE mesh size d [2].	73
Table 2.8: Fatigue test details of steel welded joints (joint geometries are reported in Table 6).....	75
Table 2.9: Fatigue test details of steel welded joints (joint geometries are reported in Table 6).....	77
Table 2.10: Materials, welding processes and testing conditions of aluminium welded joints.	82
Table 2.11: Aluminium welded joint geometries and FE analyses for fatigue strength assessment according to the PSM [1]	84
Table 2.12: Fatigue test details of aluminium joints (joint geometries are reported in Table 11).....	84
Table 3.1: Mechanical properties and chemical composition of the hot-rolled AISI 304L stainless steel	108
Table 3.2: Comparison between Q and Q^* calculated for several specimens with $m= 3, 1, \text{ and } 0.5 \text{ mm}$	119
Table 3.3: Value of radius $R_{Q,90\%}$ measured during the fatigue test.....	121
Table 4.1: Chemical composition of AISI 304L cold drawn bars from datasheet.....	137
Table 4.2: Mechanical properties of AISI 304L cold drawn bars from datasheet.....	137
Table 4.3: Experimental protocol for multiaxial fatigue tests by using the flexible test bench (Fig. 4)	140

Table 4.4: Experimental protocol for multiaxial fatigue tests by using MTS axial/torsional machine	142
Table 5.1: Chemical composition of quenched and tempered C45 cold drawn bars from datasheet.	185
Table 5.2: Mechanical properties of quenched and tempered C45 cold drawn bars from data sheet.	185
Table 5.3: Testing protocol and symbols.	187
Table 5.4: Data results of Q and ΔW	218
Table 6.1: Chemical composition of EOS maraging steel MS1 powder from technical EOS datasheet.	226
Table 6.2: Roughness and deflection range values. [1].....	228
Table 6.3: Chemical composition of the powder adopted in the batch EOS and SISMA.	235
Table 6.4: Process parameters adopted to manufacture maraging steel specimens for fatigue testing.....	236
Table 6.5: Summary of the test series.	237
Table 6.6: Synthesis of fatigue test results.....	258
Table 6.7: Synthesis of fatigue data relevant to V-notched AMed MS specimens.	261

Chapter 1: Introduction

It is known that to ensure the structural durability of an entire mechanical system and avoiding even possible catastrophic damages, mechanical parts subjected to cyclic loading must be designed following the fatigue strength assessment guidelines reported in the relevant standards and recommendations [1–3].

The fatigue behavior of metallic component is known to be influenced by several factors which can be subdivided into two categories: internal and external parameter. The first one includes parameters related to components such as material, dimension, shape, surface finishing, and surface treatment condition. The second category is referred to those parameters related to the environment and to the application of the component, i.e. loading condition, mean stress effect, variation mode of loads, temperature and environment.

The classical approach to fatigue design is based on the nominal parameter (such as nominal stress or strain amplitude) requiring several empirical coefficients for the taking into account part of the above-mentioned factors. Considering the guidelines of the fatigue design of welded joints as an example, the standards report several stress-based fatigue design curves each one related to the most common welded structural details under a given loading direction. However, the nowadays industrial applications increasingly require complex welded joints geometries and, moreover, subjected to complex loading condition. For this reason, the choice of the proper design fatigue curve might not be done for certain.

In the last decades, design machine researchers focused on the development of design methods based on local parameters instead of using nominal ones as suggested in the standards. Adopting such parameters, many fatigue influence parameters can be included in either design.

Analysing the literature, several energy-based parameters were proposed and widely adopted to fatigue strength assessment of both plain and weakened by notches metallic materials due to capability of synthesizing most of the above-mentioned affecting factors in a single fatigue design curve for a given material.

Starting from the state of the art of three selected energy-based approaches, the aim of the present dissertation is to extend their applicability by including several factors that influence the fatigue strength of components in addition to those already covered. The first energy-based method, the so-called Peak Stress Method deals with the fatigue assessment of welded joints by means of a numerical FE-oriented application of the Notch- Stress Intensity Factors (N-SIFs). The equivalent peak stress (the fatigue damage parameter used for assessing the fatigue strength of welded joints) can be obtained by invoking the averaged Strain Energy Density (SED) criterion. The

second one deals with the fatigue characterization of metallic component by assuming the specific heat loss per cycles as a fatigue damage parameter which can be evaluated in a standard constant amplitude fatigue test by adopting an easy experimental technique based on temperature measurements of material surface. The third one deals with the fatigue characterization of metallic materials produced by additive manufacturing, one of the most attractive and studied technology nowadays. Since these materials are affected by the presence of irregular defects, energy-related fracture mechanics approaches seem to be the most suitable for fatigue life assessment.

In this chapter, a review of the above energy-based approaches will be presented along with their state of the art.

1.1 PEAK STRESS METHOD

1.1.1 Notch Stress Intensity Factors approach

The local approach based on Notch-Stress Intensity Factors (N-SIFs) has been successfully applied to the analysis of fatigue strength of both in steel and in lightweight alloy welded joints, the weld bead [1-3]. The basic assumption is that the geometric profile of the weld toe can be assimilated as a sharp V-shaped notch with an opening angle that in most cases can be considered close to 135° , as shown in Fig. 1. This assumption is reasonable since the minimum value of the weld toe radius in corner and head-to-head welded joints with traditional technologies varies considerably even along with the same weld bead and the values are typically between 0.05 mm and 0.6 mm [4].

NSIF-based fatigue design of welded joint assumes the notch tip radius $\rho = 0$ for both the weld toe and the weld root considering them as sharp V-notches. This assumption corresponds to the worst condition in local stress analysis and it was shown that it is consistent with the notch rounding approach (1-mm notch case) [4].

Normally the notch opening angle relative to the weld toe is around 135° , while it is equal to zero at the weld root, as shown in Fig. 1 [5–9]. Taking the advantage of this assumptions, it is possible to quantify the magnitude of the asymptotic linear elastic singular stress distribution (NSIFs), and then rationalise fatigue lives at crack initiation of sharp V-notches [10–12], as the SIFs do at crack-like U-notches [13–15]. Since NSIFs are local stress parameter, they correlate fatigue life relevant to nucleation and propagation of short crack inside a small volume in which the NSIFs leading terms govern the stress distributions.

Let us consider the NSIF approach applied to a typical tube-to-flange welded joint under multiaxial fatigue loadings, as shown in Fig. 2. In the figure, the stresses are tied to mode I, II and III only at the toe side, but they act also at the root side. The asymptotic, singular stress distributions ahead of sharp V-notches under mode I and mode II loadings have been determined by Williams [16], while Qian and Hasebe [17] derived the mode III local stress field along with its degree of singularity. The mode

I and mode II NSIFs can be defined according to Gross and Mendelson [18] by means of Eqs. (1) and (2), respectively.

$$K_1 = \sqrt{2\pi} \cdot \lim_{r \rightarrow 0} [(\sigma_{\theta\theta})_{\theta=0} \cdot r^{1-\lambda_1}] \quad (1)$$

$$K_2 = \sqrt{2\pi} \cdot \lim_{r \rightarrow 0} [(\tau_{r\theta})_{\theta=0} \cdot r^{1-\lambda_2}] \quad (2)$$

Similarly, by extending previous definitions, the mode III NSIF can be defined by means of Eq. (3).

$$K_3 = \sqrt{2\pi} \cdot \lim_{r \rightarrow 0} [(\tau_{\theta z})_{\theta=0} \cdot r^{1-\lambda_3}] \quad (3)$$

In previous expressions, λ_1 , λ_2 and λ_3 are the stress singularity exponents [16,17], which depend on the notch opening angle 2α , while the stress components $\sigma_{\theta\theta}$, $\tau_{r\theta}$, and $\tau_{\theta z}$ are calculated along the notch bisector line, identified by the angular coordinate $\theta=0$. Values of λ_1 , λ_2 and λ_3 for different notch opening angles are reported in Tables 1, 2 and 3, respectively.

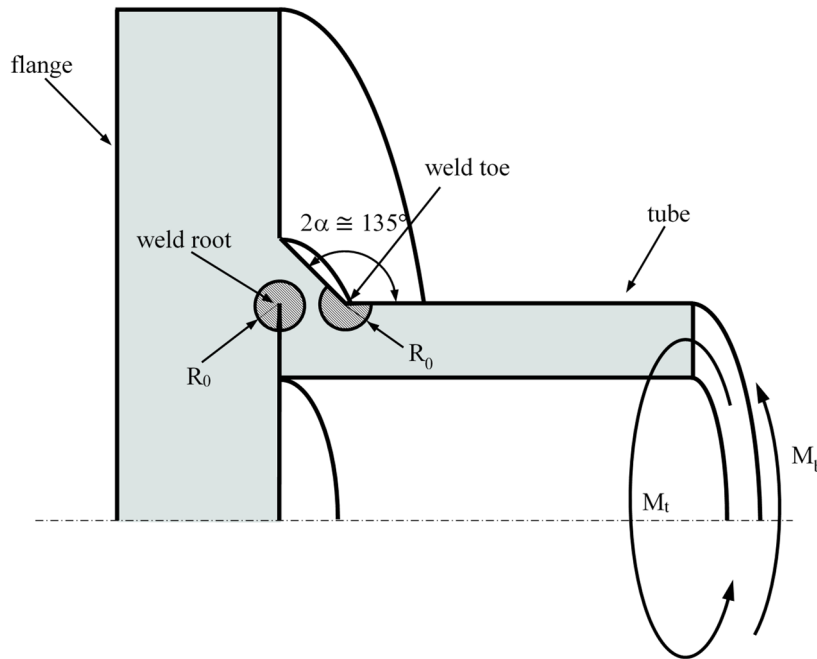


Figure 1.1 Assumptions of the NSIF-based approach in fatigue design of welded joints with reference referring to a tube-to-flange fillet-welded joint under multiaxial fatigue loading. The sharp V-notch opening angle 2α is typically 0° at the weld root and 135° at the weld toe. [Figure taken from [19]].

It has been proved that the mode I NSIF correlates weld toe failures with constant notch opening angle 2α [5,20]; however, since the NSIFs exponents of Eqs. (1)-(3)

change, it is not possible to compare NSIFs with different opening angles 2α . Therefore, the magnitude of the stress field ahead the weld toe and root of welded joint cannot be compared in order to determine the most critical spot.

In the last decades, Lazzarin and co-workers proposed the strain energy density averaged over a structural volume surrounding the weld root or the weld toe as a failure criterion for notched and welded components [21–23], and by adopting this formulation the comparability among notches having different opening angles can be restored. Lazzarin et al. [21–23] assumed a structural volume having a circular shape with radius R_0 as shown in Fig. 1 and provided the closed-form expression of the averaged SED parameter as a function of the relevant NSIFs. Considering a general multiaxial fatigue loading condition (mixed mode I+II+III loading), the strain energy density averaged over the control volume can be expressed as follows [23]:

$$\Delta\bar{W} = \frac{e_1}{E} \left[\frac{\Delta K_1}{R_0^{1-\lambda_1}} \right]^2 + \frac{e_2}{E} \left[\frac{\Delta K_2}{R_0^{1-\lambda_2}} \right]^2 + \frac{e_3}{E} \left[\frac{\Delta K_3}{R_0^{1-\lambda_3}} \right]^2 \quad (4)$$

where E is the modulus of elasticity, e_1 , e_2 , and e_3 are known parameters which depend on the notch opening angle 2α and on the Poisson's ratio ν , while ΔK_1 , ΔK_2 and ΔK_3 are the ranges of the NSIFs (maximum value minus minimum value).

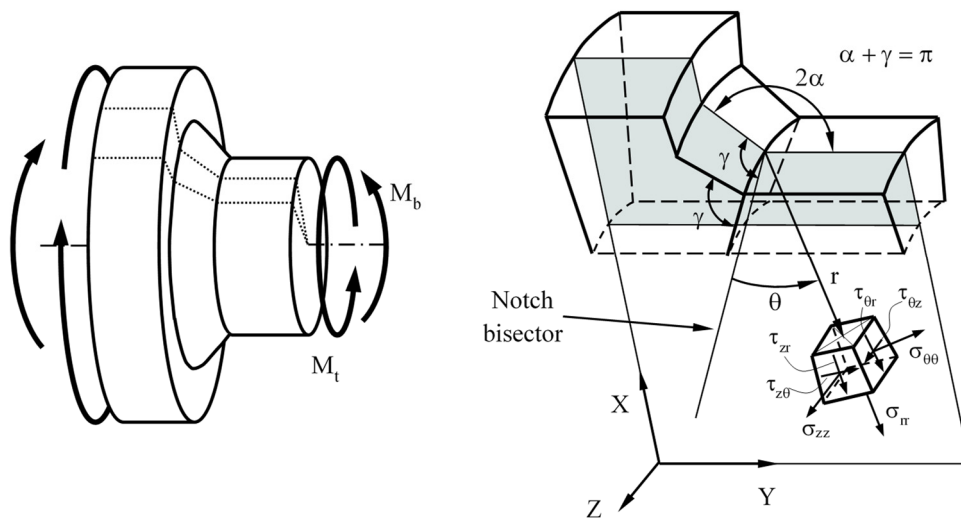


Figure 1.2. Polar reference system centred at the weld toe of a typical tube-to-flange welded joint geometry subjected to multiaxial bending and torsion loading. [Figure taken from [19]]

In Eq. (4), strain energies due to mode I, II and III, respectively, could be simply summed up, mutual terms being null. Moreover, Eq. (4) is valid under the sharp V-notch assumption shown in Figs 1-3. One or both previous conditions of applicability might be violated: this case will be treated in the next section. Tables 1-3 report the values of λ_1 , λ_2 and λ_3 and e_1 , e_2 and e_3 , respectively, for common cases of notch

opening angles 2α and with reference to two values of the Poisson's ratio, namely $\nu = 0.33$ (aluminium alloys) and $\nu = 0.3$ (structural steels) [23]; e_1 and e_2 are referred to plane strain conditions.

The determination of the control radius R_0 can be done by equalling the averaged strain energy density in the high cycle fatigue regime (2 million cycles) of butt ground welded joints and welded joints which failure occurs at the weld toe ($2\alpha \approx 135^\circ$).

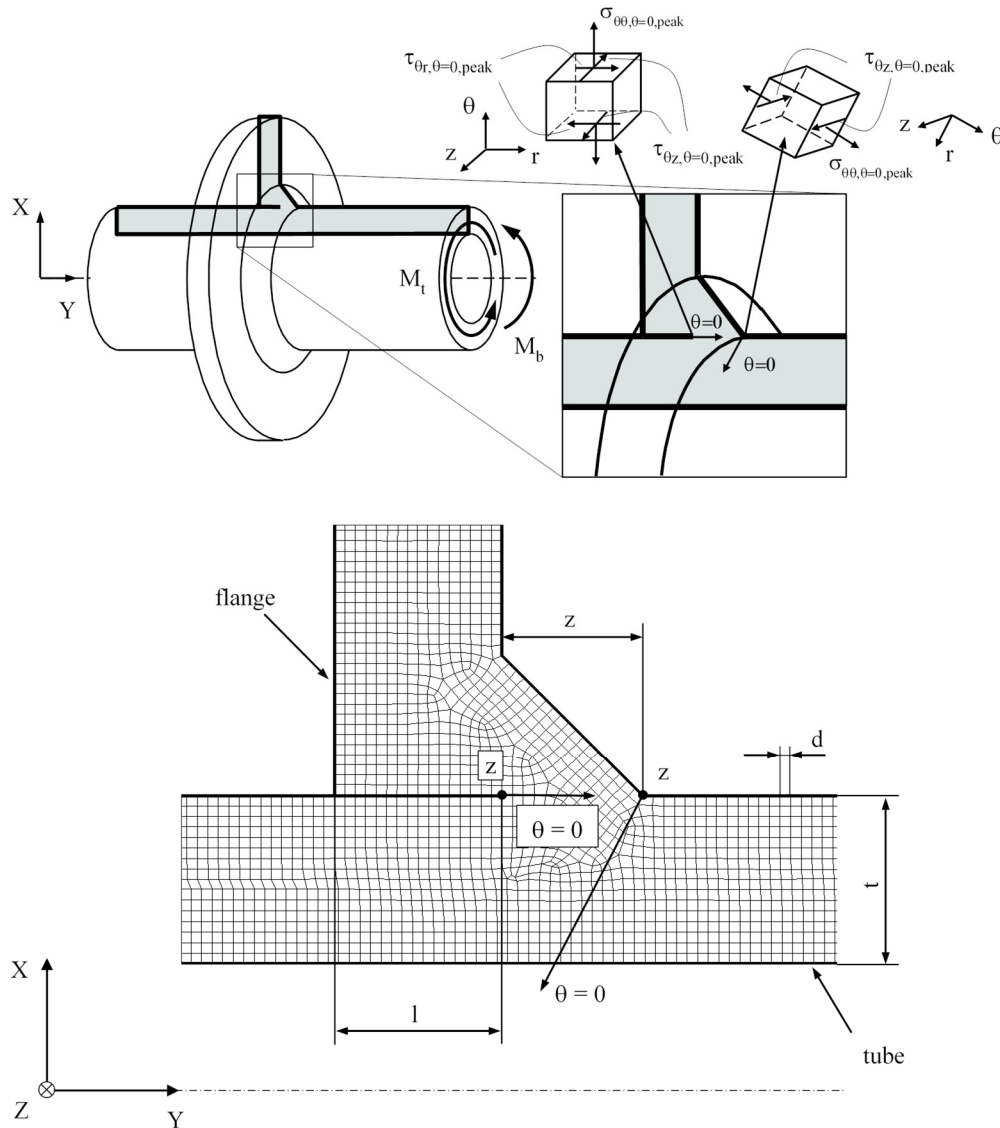


Figure 1.3. Typical 2D FE mesh to apply the PSM according to Eq. (11); the example reported in the figure shows a tube-to-flange fillet welded joint. The four-node, quadrilateral, harmonic PLANE 25 elements available in Ansys® Element Library were adopted to generate the free mesh shown in the figure. The Y -axis coincides with the axis of the tube. [Figure taken from [19]]

As a result, R_0 was found to be 0.28 mm for arc-welded joints made of structural steel and 0.12 mm for those made of aluminum alloy [20,22]. It should be noted that Lazzarin and co-workers [23] adopted a constant value of the control radius R_0 to evaluate the averaged SED of welded joints under mode I, II or III loadings.

Subsequently, Berto and Lazzarin [24,25] adopted a control radius R_0 dependent on the loading mode and used this approach to analyse the multiaxial fatigue strength assessment of notched specimens.

Eq. (4) was used by Lazzarin and co-workers to fit experimental results relevant to joints tested in the as-welded conditions under a load ratio $R \geq 0$ [9,20,22,23]. This approach is consistent with the design recommendations [1–3], where the detail categories of as-welded joints are independent from the applied mean stress, at least for simple as well as complex structural elements loaded with $R \geq -0.25$, and in presence of medium or high tensile residual stresses in relation to the yield strength of the base material [3]. In light of the experimental evidence that residual stresses in as-welded structures make their fatigue behaviour independent from the load ratio of the applied external loads, Eq. (4), which is valid for $R=0$, strictly speaking, was adopted in the extensive re-analysis of experimental data [9,20,22,23], where the endurable values of the SED parameter could be determined, i.e. a fatigue design scatter band for as-welded joints was found. However, in case of stress-relieved joints, sensitivity to the mean stress of the applied external loads is fully effective and therefore it should be taken into account, according to design recommendations [1–3]: according to [12], the load ratio is taken into account by using the following expression to evaluate the SED:

$$\Delta \bar{W} = c_{w1} \frac{e_1}{E} \left[\frac{\Delta K_1}{R_0^{1-\lambda_1}} \right]^2 + c_{w2} \frac{e_2}{E} \left[\frac{\Delta K_2}{R_0^{1-\lambda_2}} \right]^2 + c_{w3} \frac{e_3}{E} \left[\frac{\Delta K_3}{R_0^{1-\lambda_3}} \right]^2 \quad (5)$$

where the coefficients c_{wi} ($i = 1, 2, 3$ indicates the loading mode) depend on the nominal load ratio R according to the following expression [9]:

$$c_w(R) = \begin{cases} \frac{1+R^2}{(1-R)^2} & \text{if } -1 \leq R \leq 0 \\ \frac{1-R^2}{(1-R)^2} & \text{if } 0 \leq R < 1 \end{cases} \quad (6)$$

In particular, the parameter c_w equals 0.5 for $R = -1$.

Application of the NSIF approach to practical engineering problems presents a major drawback, due to the need for very refined FE meshes in order to evaluate the NSIFs using the definitions (1)-(3) [5]. In the case of three-dimensional components, the numerical analyses could be even more time-consuming. While Lazzarin and co-workers underlined that the averaged SED can be calculated numerically by adopting coarse meshes within the control volume characterized by a radius R_0 [26], the Peak Stress Method may also be used to estimate the NSIFs in Eqs (4) and (5) with coarse meshes [27]. One of the advantages of the PSM is that geometrical modeling of the control volume is not required and even coarser meshes can be employed in the FE

analyses as compared to those suggested in [26]. Moreover, only the singular, linear elastic peak stresses must be evaluated at the V-notch tip to apply the PSM, instead of a number of stress-distance numerical results, as required in order to apply definitions (1)-(3).

1.1.2 Equivalent Peak Stress definition

The Peak Stress Method (PSM) takes its origin from the numerical procedure proposed by Nisitani and Teranishi [28,29] which can rapidly estimate the mode I SIF of a crack emanating from an ellipsoidal cavity. In recent papers, the method has been theoretically justified and also extended to estimate the mode I NSIF of sharp and open V-notches [27,30], the mode II SIF of cracks [31] and the mode III NSIF of cracks and open V-notches [32].

Therefore, the PSM was proposed to overcome the numerical application to determine the NSIFs by applying definitions of Eq. (1), (2) and (3). In particular Eq. (1), (2) and (3) require very refined FE meshes to evaluate the local linear elastic singular stresses (finite element size on the order of 10^{-5} m) increasing the computational efforts, especially in 3D models. Furthermore, a set of stress distance FE data must be processed to evaluate the NSIFs according to Eq. (1) (2) and (3) [3–5]. Essentially, the PSM allows to rapidly estimate the NSIFs K_1 , K_2 and K_3 from the singular, linear elastic, opening ($\sigma_{\theta\theta,\theta=0,\text{peak}}$), in-plane shear ($\tau_{r\theta,\theta=0,\text{peak}}$) and anti-plane shear ($\tau_{\theta z,\theta=0,\text{peak}}$) FE peak stresses, which are referred to the V-notch bisector line, according to Fig. 1. The relationship between NSIFs and relevant FE element size and peak stresses previously validated [27,31,32] are the following:

$$K_{\text{FE}}^* = \frac{K_1}{\sigma_{\theta\theta,\theta=0,\text{peak}} \cdot d^{1-\lambda_1}} \quad (7)$$

$$K_{\text{FE}}^{**} = \frac{K_2}{\tau_{r\theta,\theta=0,\text{peak}} \cdot d^{1-\lambda_2}} \quad (8)$$

$$K_{\text{FE}}^{***} = \frac{K_3}{\tau_{\theta z,\theta=0,\text{peak}} \cdot d^{1-\lambda_3}} \quad (9)$$

In Eq. (7-8), d is the so-called ‘global element size’ parameter, which is the average size of the finite elements request by the free mesh generation algorithm of the considered FE-numerical code.

In previous contributions the Eq. (7), (8) and (9) were calibrated [27,31,32] by using ANSYS® FE code and the values $K_{\text{FE}}^* \cong 1.38$, $K_{\text{FE}}^{**} \cong 3.38$ and $K_{\text{FE}}^{***} \cong 1.93$ were obtained under the following condition:

- regarding Eqs. (7) and (8) in 2D FE models, 4-node quadrilateral finite elements with linear shape functions, as implemented in ANSYS® FE code (PLANE 42 or alternatively PLANE 182 with K-option 1 set to 3) should be adopted. For Eq. (9) in 2D FE models, harmonic, 4-node linear quadrilateral elements, as implemented in ANSYS® FE code (PLANE 25) should be adopted. In 3D FE models, eight-node brick elements (SOLID 45 or equivalently SOLID 185 with K-option 2 set to 3 of Ansys Element Library) is allowed for all loading modes, i.e. for Eqs. (1)-(3) should be adopted;
- the FE mesh pattern at the notch or crack tip must be similar that reported in Fig. 3 (see also [27,31,32]); In particular, four elements must share the node located at the notch tip whether the notch opening angle 2α is equal to or lower than 90° (at the weld root $2\alpha \cong 0^\circ$), while two elements must share the node at notch tip when the notch opening angle is greater than 90° (typically at the toe side $2\alpha \cong 135^\circ$), as shown in Fig. 1. It is worth underlining that the mesh patterns according to the PSM shown in Fig. 1, are automatically generated by the free mesh generation algorithm available in ANSYS® software so that only the ‘global element size’ parameter d must be input by the FE analyst;
- Eqs. (7) and (9) can be adopted to V-notches with an opening angle 2α between 0° and 135° ; while Eq. (8) is referred to the crack case ($2\alpha = 0^\circ$);
- for mode I loading (Eq. (7)), the mesh density ratio a/d must be higher than 3 to obtain $K_{FE}^* = 1.38 \pm 3\%$ [27]; for mode II loading (Eq. (8)) the mesh density ratio a/d having to be greater than 14 to obtain $K_{FE}^{**} = 3.38 \pm 3\%$ [31]; finally, in the case of mode III loading (Eq. (9)), the mesh density ratio must be greater than 3 at the weld toe (where $2\alpha \cong 135^\circ$) and 12 at the root side (where $2\alpha = 0^\circ$), to get $K_{FE}^{***} = 1.93 \pm 3\%$ [32]. In previous definitions of the ranges of applicability, the reference dimension a has the following meanings: when the root side is of interest, a is the minimum between the crack length (crack is due to the lack of penetration, i.e. l in Fig. 3), the ligament length (z in Fig. 3) and the thickness (t in Fig. 3), while a is always the thickness (t in Fig. 3) when assessing the toe side.

It is worth noting that Eqs. (7)-(9) should be recalibrated if FE meshes of higher-order elements or characterised by significantly different mesh patterns as compared to the reference one (reported in Fig. 3) were adopted.

By using the PSM relationships (Eqs. (7)-(9)), the averaged SED (Eq. (4)) can be rewritten as a function FE peak stresses $\sigma_{\theta\theta,\theta=0,\text{peak}}$, $\tau_{r\theta,\theta=0,\text{peak}}$ and $\tau_{\theta z,\theta=0,\text{peak}}$. Then, equalling $W = (1 - \nu^2) \sigma_{\text{eq,peak}}^2 / 2E$ valid under plane strain conditions, Eq (4) can be expressed as follow:

$$\Delta \bar{W} = c_{w1} \frac{e_1}{E} \left[K_{FE}^* \cdot \Delta \sigma_{\theta\theta, \theta=0, \text{peak}} \cdot \left(\frac{d}{R_0} \right)^{1-\lambda_1} \right]^2 + c_{w2} \frac{e_2}{E} \left[K_{FE}^{**} \cdot \Delta \tau_{r\theta, \theta=0, \text{peak}} \cdot \left(\frac{d}{R_0} \right)^{1-\lambda_2} \right]^2 + c_{w3} \frac{e_3}{E} \left[K_{FE}^{***} \cdot \Delta \tau_{\theta z, \theta=0, \text{peak}} \cdot \left(\frac{d}{R_0} \right)^{1-\lambda_3} \right]^2 \rightarrow = \frac{1-\nu^2}{2E} \Delta \sigma_{\text{eq, peak}}^2 \quad (10)$$

Finally, the equivalent peak stress can be obtained:

$$\Delta \sigma_{\text{eq, peak}} = \sqrt{c_{w1} \cdot f_{w1}^2 \cdot \Delta \sigma_{\theta\theta, \theta=0, \text{peak}}^2 + c_{w2} \cdot f_{w2}^2 \cdot \Delta \tau_{r\theta, \theta=0, \text{peak}}^2 + c_{w3} \cdot f_{w3}^2 \cdot \Delta \tau_{\theta z, \theta=0, \text{peak}}^2} \quad (11)$$

The parameters f_{w1} , f_{w2} and f_{w3} weight the peak stresses both around the notch tip and along the radial direction, i.e. θ and r coordinates, respectively, in Fig. 2. By comparison between Eqs. (10) and (11), the coefficients f_{w1} , f_{w2} and f_{w3} are defined as follows:

$$f_{w1} = K_{FE}^* \cdot \sqrt{\frac{2e_1}{1-\nu^2}} \cdot \left(\frac{d}{R_0} \right)^{1-\lambda_1} \quad (12a)$$

$$f_{w2} = K_{FE}^{**} \cdot \sqrt{\frac{2e_2}{1-\nu^2}} \cdot \left(\frac{d}{R_0} \right)^{1-\lambda_2} \quad (12b)$$

$$f_{w3} = K_{FE}^{***} \cdot \sqrt{\frac{2e_3}{1-\nu^2}} \cdot \left(\frac{d}{R_0} \right)^{1-\lambda_3} \quad (12c)$$

The values of f_{w1} , f_{w2} , and f_{w3} are reported in Tables 2-4 respectively, according to Eq. (6) where three values of the average FE size, namely $d = 0.2$ mm, 0.50 mm and 1 mm, different notch opening angles 2α and two values of the control radius for SED evaluation, i.e. $R_0 = 0.28$ mm for structural steels and 0.12 mm for aluminium alloys [20,22], have been taken into account. It should be noted that while parameters f_{w1} , f_{w2} , and f_{w3} , as well as the peak stresses depends on the adopted FE size d , the equivalent peak stress defined by Eq. (5) does not.

A large number of fatigue experimental results of steel welded joints found in the literature [19,27,31–37] were taken and expressed in terms of equivalent peak stress, Eq. (1), evaluated at the point of crack initiation (either the toe or the root) as observed experimentally.

The data results relevant to steel welded joints subjected to pure mode I or mode I+II loading conditions were compared in Fig. 4 with the predicting fatigue design scatter band previously calibrated in [38] on fatigue data relevant to T or cruciform steel welded joints subjected to axial or bending loadings in the as-welded conditions

and with a nominal load ratio R close to zero. Fig. (4) show the agreement with approximately 980 experimental results obtained from both weld toe and weld root failures in joints tested in the as-welded as well as stress relieved conditions and the predicting scatter band for mode I+II.

Table 1.1: Values of constants and of parameter f_{w1} according to Eq. (12a).

2α (deg)	$\lambda_1^{(a)}$	$e_1^{(b)}$	$R_0 = 0.28$		$e_1^{(c)}$	$R_0 = 0.12$ mm	
			$f_{w1,d=0.5mm}^{(b)}$	$f_{w1,d=1mm}^{(b)}$		$f_{w1,d=0.2mm}^{(c)}$	$f_{w1,d=1mm}^{(c)}$
0	0.500	0.133	0.997	1.410	0.125	0.944	2.109
90	0.544	0.145	1.015	1.392	0.138	0.969	2.019
120	0.616	0.129	0.918	1.198	0.124	0.886	1.644
135	0.674	0.118	0.849	1.064	0.113	0.821	1.387

^(a): values from [13,14,37]

^(b): values calculated with $\nu = 0.3$, $K_{FE}^* = 1.38$

^(c): values calculated with $\nu = 0.33$, $K_{FE}^* = 1.38$

Table 1.2: Values of constants and of parameter f_{w2} according to Eq. (12b).

2α (deg)	$\lambda_2^{(a)}$	$e_2^{(b)}$	$R_0 = 0.28$		$e_2^{(c)}$	$R_0 = 0.12$ mm	
			$f_{w2,d=0.5mm}^{(b)}$	$f_{w2,d=1mm}^{(b)}$		$f_{w2,d=0.2mm}^{(c)}$	$f_{w2,d=1mm}^{(c)}$
0	0.500	0.340	3.904	5.522	0.337	3.795	8.480

^(a): value from [13,14,37]

^(b): values calculated with $\nu = 0.3$, $K_{FE}^{**} = 3.38$

^(c): values calculated with $\nu = 0.33$, $K_{FE}^{**} = 3.38$

Table 1.3: Values of constants and of parameter f_{w3} according to Eq. (12c).

2α (deg)	$\lambda_3^{(a)}$	$e_3^{(b)}$	$R_0 = 0.28$		$e_3^{(c)}$	$R_0 = 0.12$ mm	
			$f_{w3,d=0.5mm}^{(b)}$	$f_{w3,d=1mm}^{(b)}$		$f_{w3,d=0.2mm}^{(c)}$	$f_{w3,d=1mm}^{(c)}$
0	0.500	0.414	2.459	3.478	0.423	2.428	5.431
90	0.666	0.310	1.933	2.436	0.317	1.931	3.303
120	0.750	0.276	1.737	2.065	0.282	1.745	2.610
135	0.800	0.259	1.634	1.877	0.265	1.649	2.273

^(a): values from [14]

^(b): values calculated with $\nu = 0.3$, $K_{FE}^{***} = 1.93$

^(c): values calculated with $\nu = 0.33$, $K_{FE}^{***} = 1.93$

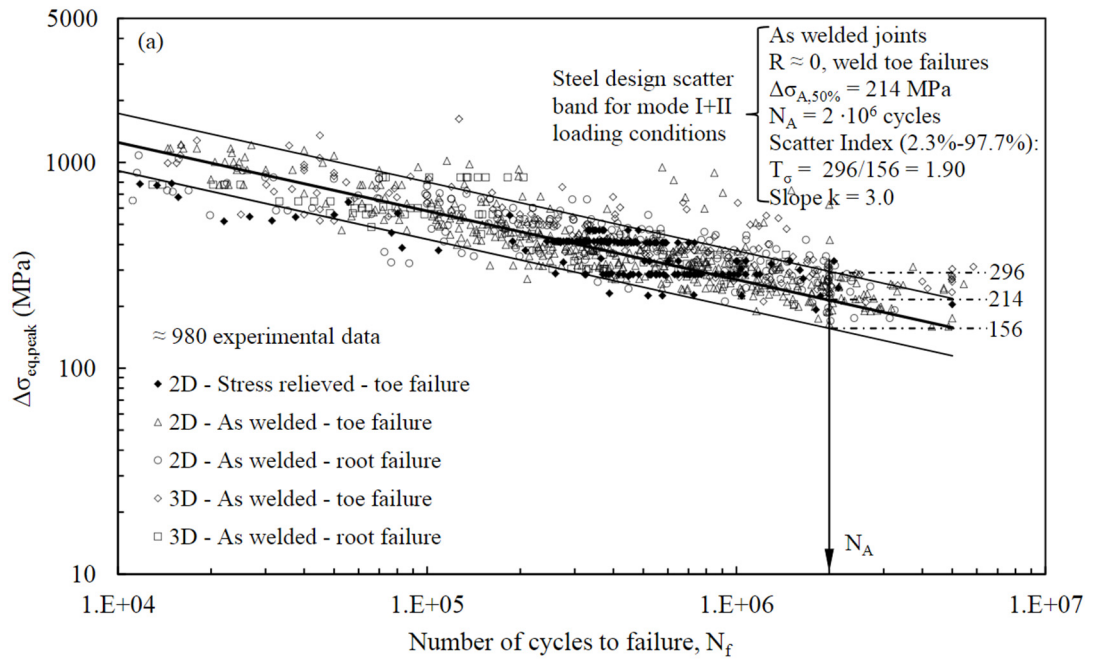


Figure 1.4: Comparison between the fatigue design scatter band and experimental fatigue results relevant to structural steel welded joints obtained under mode I+II [19,27,31–36] (figure taken from [39])

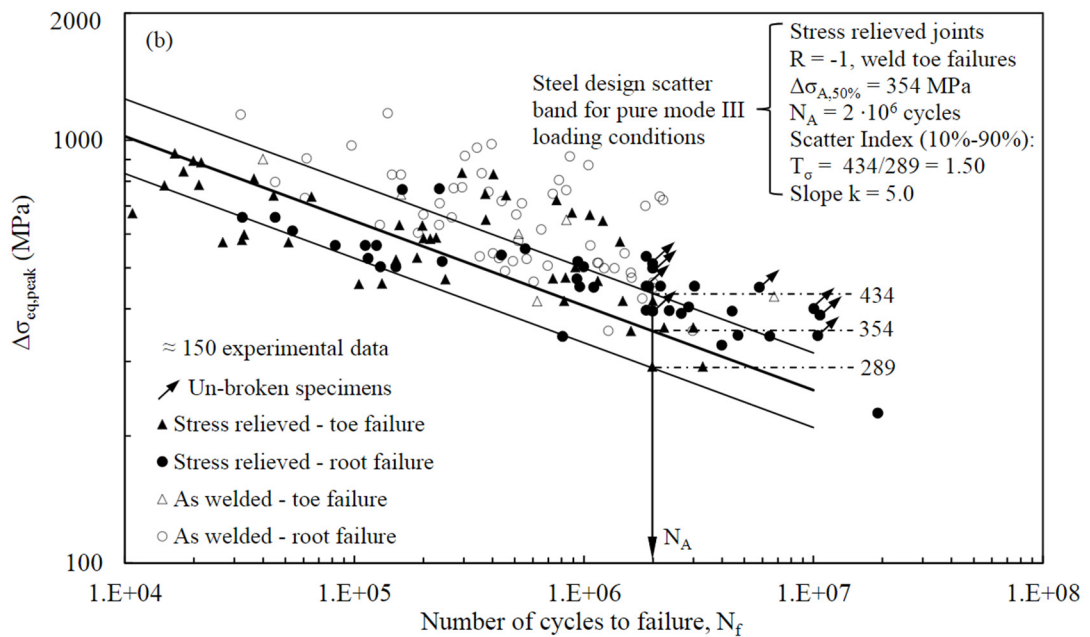


Figure 1.5: Comparison between the fatigue design scatter band and experimental fatigue results relevant to structural steel welded joints obtained under mode III. [19,33,40] (figure taken from [39]).

In the case of pure mode III, experimental results obtained from steel welded joints expressed in terms of equivalent peak stress were compared in Fig. (5) with the fatigue design scatter band, which has been previously calibrated in [16] on experimental results relevant only to weld toe failures in full penetration tube-to-flange steel joints tested under pure torsion loading in the stress-relieved condition and with

a nominal load ratio R equal to -1 . Fig. 5 show a fairly good agreement between the fatigue design scatter band and about 150 experimental results generated from both weld toe and weld root failures in steel joints tested in the as-welded as well as stress relieved conditions.

In Chapter 2, the theoretical framework for developing the Peak Stress Method for the fatigue strength assessment of welded joints subjected to multiaxial loading conditions will be proposed. After that, several multiaxial fatigue data taken from the literature relevant to both aluminium and steel welded joints will be analysed by using the PSM for validating the theoretical prediction.

1.2 THERMAL ENERGY DISSIPATION DUE TO FATIGUE

It is known that fatigue is a dissipative phenomenon, indeed by considering a material subjected to cyclic loading, part of the mechanical input is expended as heat to the surrounding and the remaining part is involved to the increasing of the internal energy of the materials.

In constant amplitude fatigue tests characterized by a given stress amplitude, mean stress and stress state, the temperature of the specimen's surface reaches a stable value that depends on the load test frequency, the specimen's geometry and the temperature of the surroundings. Starting from this experimental evidence, thermographic methods were proposed to estimate the fatigue limit in metallic materials as well as composites and components [41–46], to detect the initiation and propagation of damage in metal materials as well as in composites [47–50] and to analyse the fatigue behaviour under constant amplitude [51–53] as well as block loading [54,55].

For a clear overview of the state of the art of thermomechanical methods present in the literature, the theoretical background outlined in [56] is proposed in the following.

The fatigue is considered as a dissipative and quasi-static process within the framework of the classical continuum mechanics reported in [57,58].

Combining the first and the second law of the thermodynamics, the energy balance equation can be written in terms of power per unit of volume as follows:

$$\begin{aligned} \rho c \dot{T} + \text{div}(-\lambda \text{grad}T) = \sigma : \dot{\varepsilon} - \rho \frac{\partial \Psi}{\partial \varepsilon_e} : \dot{\varepsilon}_e - \rho \frac{\partial \Psi}{\partial \alpha} : \dot{\alpha} + \\ + \rho T \frac{\partial^2 \Psi}{\partial T \partial \varepsilon_e} : \dot{\varepsilon}_e + \rho T \frac{\partial^2 \Psi}{\partial T \partial \alpha} : \dot{\alpha} + \dot{r}_e \end{aligned} \quad (13)$$

where the dot symbol indicates the time derivative of the parameter. In Eq. (13), T is the temperature λ and ρ are the thermal conductivity and material density, respectively, Ψ is the Helmholtz free energy potential, α is the vector of state variable

describing the internal state of the material and \dot{r}_e is the heat generation rate per unit of volume caused by external sources (for instance, Joule effect caused by electric current flow). In Eq. (13) two state variables α were made explicit; one is temperature T and the other one is the strain ε . The remaining α variables are related to phenomena acting to the microstructure of the material such as for instance hardening, damage, and change of state.

Let us describe the right-hand side of Eq. (13): $\sigma : \dot{\varepsilon} - \rho \frac{\partial \Psi}{\partial \varepsilon_e} : \dot{\varepsilon}_e$ is the plastic strain energy rate obtained by subtracting the elastic component ($-\rho \frac{\partial \Psi}{\partial \varepsilon_e} : \dot{\varepsilon}_e$) to the total one ($\sigma : \dot{\varepsilon}$); the term $\rho \frac{\partial \Psi}{\partial \alpha} : \dot{\alpha}$ represents the stored energy rate due to material evolution during the fatigue process: for instance, it includes the residual stresses at the microscopic level due to re-arrangement of the dislocation density as well as strain hardening and damage variables [59]. The terms $\rho T \frac{\partial^2 \Psi}{\partial T \partial \varepsilon_e} : \dot{\varepsilon}_e$ and $\rho T \frac{\partial^2 \Psi}{\partial T \partial \alpha} : \dot{\alpha}$ are the heat rate per unit volume caused by thermoelasticity and the heat rate per unit volume due to the changes in the material state, respectively, and they are referred to as thermomechanical couplings. In particular, $\rho T \frac{\partial^2 \Psi}{\partial T \partial \alpha} : \dot{\alpha}$ can be neglected in metals undergoing fatigue loading when the temperature variations are reduced avoiding changes in the material state [60,61].

According to the second laws of thermodynamics in the form of Clausius-Duhem inequality reported in [57], two dissipative terms can be identified:

$$d_1 = \sigma : \dot{\varepsilon} - \left(\rho \frac{\partial \Psi}{\partial \varepsilon_e} : \dot{\varepsilon}_e + \rho \frac{\partial \Psi}{\partial \alpha} : \dot{\alpha} \right) \quad (14)$$

$$d_2 = -\frac{h}{T} \cdot \text{grad}T \quad (15)$$

in which d_1 is the intrinsic mechanical dissipation and d_2 the thermal dissipation. Finally, it is possible to re-write Eq (13) by introducing Eq. (14):

$$\rho c \dot{T} + \text{div}(-\lambda \text{grad}T) = d_1 + \rho T \frac{\partial^2 \Psi}{\partial T \partial \varepsilon_e} : \dot{\varepsilon}_e \quad (16)$$

in which the thermomechanical coupling and the external heat generation rate were neglected since they are normally not involved during a standard fatigue problem.

Starting from Eq. (16) many research group worked on the determination of the heat sources induced by cyclic loads. In the following, some methods to determine the energy dissipation were briefly summarised and classified according to the purpose of the studies.

1.2.1 Methods for fatigue life and fatigue limit estimation by thermography

An accurate calorimetric analysis of reversible and irreversible heat sources involved in standard fatigue problem was carried out in [62]. In particular, thermoelastic and dissipated heat sources were separately estimated in axial fatigue test on dual phase steel specimens from the temperature field acquired by means of an infrared camera and by adopting a simple differential equation for diffusion problem.

The case study analysed in [62] dealt with the determination of the two terms of the right-hand side of Eq (16) during load-controlled fatigue test performed by adopting different load levels on thin, flat specimens (2.5-mm thick).

By supposing a uniform heat source distribution within the specimen cross-section, which is consistent in axial tests, the Eq. (16) can be simplified as follows:

$$\rho c \left(\frac{dT}{dt} + \frac{T}{\tau_{eq}} \right) \approx d_1 + s_{th} \quad (17)$$

where T is the surface temperature at the center of the specimen and τ_{eq} takes into account the heat losses.

By adopting this model, the experimental thermoelastic response was compared to the theoretical estimation based on the following derived equation:

$$\Delta\theta_{the} = \frac{T_0 \alpha \Delta\sigma}{\rho C} \frac{2\pi f_L}{\sqrt{\tau_{eq}^{-2} + 4\pi^2 f_L^2}} \quad (18)$$

where T_0 is the equilibrium temperature f_L the load frequency and $\Delta\sigma$ the stress range applied in this case, but it is the sum of principal surface stresses in the general one. The results showed the linear dependency between $\Delta\theta_{the}$ and $\Delta\sigma$ and the constancy of $\Delta\theta_{the}$ during constant amplitude fatigue tests.

Regarding the dissipation source d_1 , Eq (17) was used to determine the total energy sources $s = d_1 + s_{th}$, then it was time-integrated for providing the \bar{d}_1 by computing the slope of the linear interpolation along about 500 cycles. This method does not provide any information about the instantaneous dissipation within a cycle. Computing this calculation during the load step fatigue test, it was observed that \bar{d}_1 is higher at the beginning of each loading step indicating a non-uniform heat source field and then it reaches a stabilized value.

By adopting Eq (16) written cycle by cycle, in [63], the dissipative behaviour in the elastic domain of 316L and DP600 steels was studied by using a thermographic method in order to monitor the microstructure variations. It was observed that the dissipation averaged in a cycle \bar{d}_1 increases with the cumulated plastic strain

performed and the relevant relation between them is non-linear. Furthermore, the specific damping capacity $\zeta = \frac{2E}{\sigma_a^2} \bar{d}_1$ increases with σ_a non-linearly and the trend is a material characteristic.

In view of the above, many methods, based on temperature measurements, were proposed to deal with fatigue problems, and some of them will be reviewed here.

In [44], the authors proposed an experimental methodology based on the thermography which can be used to rapidly determinate the fatigue limit of metals as well as composites materials. by using theoretically one specimen. Basically, the method consists in measuring either the initial temperature gradient $\Delta T/\Delta N$ (phase 1 of Fig. 6) or the stabilised temperature difference ΔT_{stab} (phase 2 of Fig. 6) during a step-wise fatigue test with the aim of cross plotting these values with the respective stress amplitude applied (Fig. 7). The intersection of the linear regression model with the abscissa of the plots reported in Fig. 7 provides the fatigue limit of the relevant material.

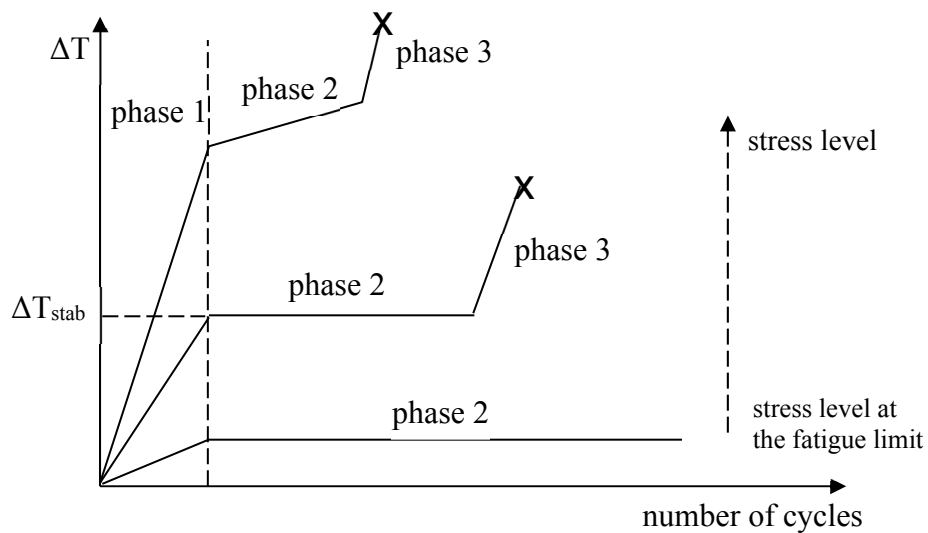


Figure 1.6. Qualitative thermal increments in specimens under fatigue loading at different applied stresses. The three phases are shown.

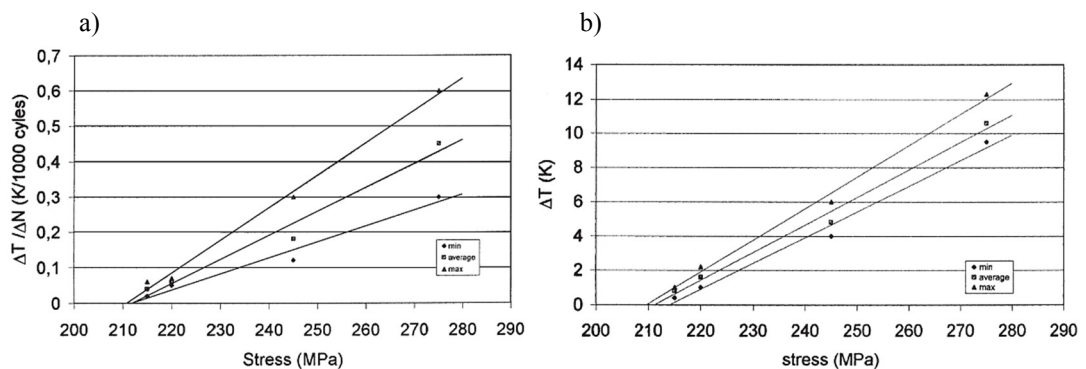


Figure 1.7. Determination of the fatigue limit from the initial temperature gradient $\Delta T/\Delta N$ a) and stabilised temperature ΔT (phase 2 of fig. 6) b). Pictures were taken from [44].

The reason of which this method was mentioned here is that the temperature ΔT is induced by the dissipative source d_1 (Eq. 14). However, according to Eq (16) and for a given stress amplitude level the dissipation d_1 increases with the strain-rate amplitude, i.e with the load frequency.

In [51], an extension of the above-mentioned method was proposed to estimate also the fatigue curve by introducing the energy-related parameter Φ which is the integral of the function $\Delta T=f(N)$ estimable by means of the “step loading process”. Since Φ is proportional to the energy dissipated as heat which is proportional, in turn, to the constant limiting value energy of plastic deformation a constant limiting value (material parameter), after having estimate Φ it is possible to estimate the fatigue life of any other load applied from the relevant temperature ΔT_{stab} measured after few loading cycles based on the following:

$$\Phi \approx \Delta T \cdot N_f \approx \text{const} \quad (19)$$

being N_f the number of cycles to failure.

However, the previous temperature-based methods are sensitive to the thermal boundary conditions of the testing environment, so they have to be carefully controlled during the test.

Regarding the thermoelastic source, a vast amount of works are addressed to the so-called Thermoelastic Stress Analysis (TSA) technique [64–66]. A promising empirical procedure to evaluate the fatigue limit and fatigue damage, which it is worth mentioning, is described in [67]. In particular, some previous works have demonstrated that exists a correlation between fatigue behavior and the phase between the load signal and the thermoelastic temperature variation [68–70]. The phase shift starts when the hypothesis of local adiabatic condition is not satisfied and non-linear behavior due to plasticity occurs.

As stated in [67], The TSA can be applied to the entire fatigue regime, especially at the fatigue limit, where some thermographic methods based on the evaluation of d_1 component could present some limitation due to the low, or even absent, temperature rise. Indeed, if the internal heat source is not present Eq (16) become:

$$\rho c \dot{T} + \text{div}(-\lambda \text{grad}T) = \rho T \frac{\partial^2 \Psi}{\partial T \partial \varepsilon_e} : \dot{\varepsilon}_e \quad (20)$$

and if the temperature gradient or the diffusivity is zero or the load frequency is high, local adiabatic conditions can be achieved, therefore Eq. (20) can be simplified as follow:

$$\dot{T} = -\frac{\alpha T_0}{\rho C} \dot{\sigma}_1 \quad (21)$$

Finally in the case of uniaxial sinusoidal load, Eq. (21) can be written as follow:

$$T = -\frac{\alpha T_0}{\rho C} \sigma_a \sin(\omega t + \varphi) \quad (22)$$

where φ is the above-mentioned phase between the load signal and the thermoelastic temperature variation. Changes in this parameter are due to viscoelastic or plastic behaviour of material and loss of adiabatic conditions.

Therefore in [67], by adopting the load step procedure, the range $\Delta\varphi_{\max}$, which has been defined as maximum difference between the actual phase value and the reference one (the latter taken during the first loading step where there is no damage) were plotted against the load level applied. As it can be seen from the figure taken from [67] a well-defined change of the slope occurs at the fatigue limit.

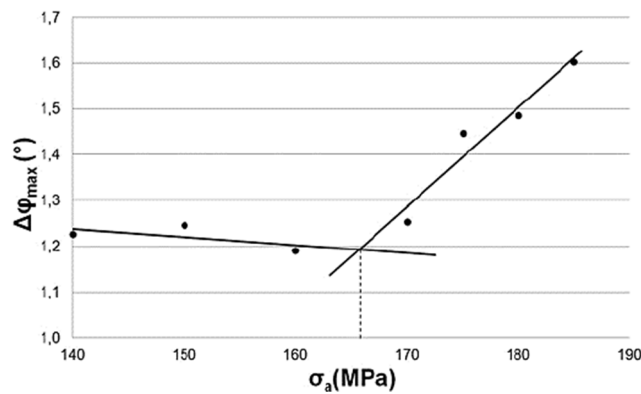


Figure 1.8: $\Delta\varphi_{\max}$ data for fatigue limit estimation. Figure taken from [67].

The present TSA method has the advantage of being independent of the evolution of temperature caused by the internal heat source so it can be applied any time during a fatigue test. The fatigue limit can be estimated with lower uncertainties and it seems to be less sensitive to thermal boundary conditions with respect to the other temperature-based methods. Furthermore, by applying this method pixel-by-pixel of an infrared acquisition, the method seems to provide the local fatigue damage.

1.2.2 Methods for fatigue crack growth and identification of the plastic zone

The estimation of the residual fatigue life of cracked components is challenging due to the small localised plastic area in front of the crack tip, especially for small cracks. Indeed, the smaller the plastic area the lower the temperature increment due to the internal heat source for the same load frequency and cyclic load applied. Therefore, TSA takes advantage of being a methodology which is independent from the mean temperature evolution due to internal dissipation.

In [71], lock-in thermography was adopted to identify the local plasticity, starting from the experimental evidence that the transient cyclic temperature

measurement deviates when plastic deformation occurs. It was found that the resulting waveform obtained by subtracting the temperature waveform measured when plasticity occurs and the relevant thermoelastic one appears in double frequency as shown in Fig. 9 (taken from [71]).

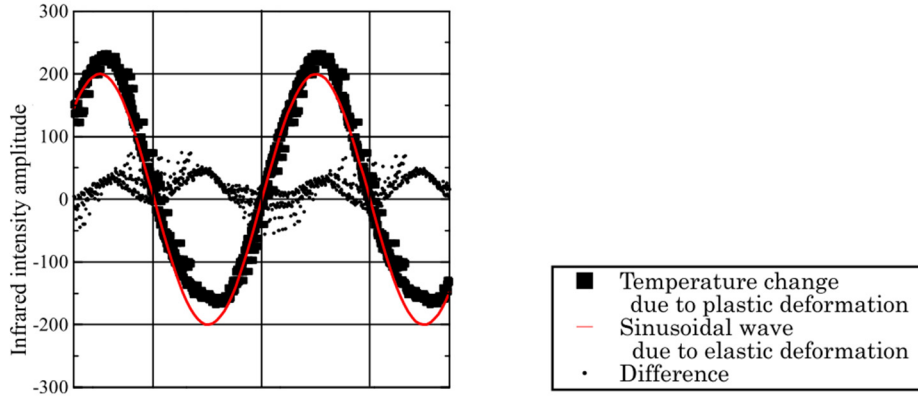


Figure 1.9: Waveform of temperature measurement close to a circular hole under cyclic axial load.
Figure taken from [71]

The double frequency synchronised infrared intensity computed pixel-by-pixel was compared with the sum of principal stresses calculated by means of static elastic-plastic finite element analysis. The size of the plastic zone obtained from the double frequency method was relatively higher than the one obtained numerically. However, this discrepancy can be attributed to the numerical analysis obtained under static loading conditions. This method was also employed to analyse the fatigue crack growth behaviour in [72,73].

On the basis of double frequency related method, a new rapid approach has been proposed recently in [74] to assess the thermal energy dissipated at the crack tip within the plastic zone. In [74], the authors proposed the specific thermal energy dissipated per cycle E_d defined as follows:

$$E_d = \rho c \Delta T_d \quad (23)$$

where ρ is the material density and c the specific heat at constant pressure of the material. The parameter ΔT_d is defined as the total temperature variation in one cycle under the following hypothesis: i) most of the dissipative energy is dissipated as heat, ii) adiabatic condition, iii) and the evolution of the heat dissipated energy is linear from a to b and c to d points of as shown in the picture taken from [74] reported in Fig. 10.

Furthermore, ΔT_d can be analytically correlated to the temperature amplitude of a triangular function $T_{2\omega}$ as illustrated in Fig. 10.

It was shown in [74] that $T_{2\omega}$ can be evaluated by infrared thermography in order to evaluate the total heat dissipated per cycle [J/cycle] as follows:

$$Q_d = E_d V_p \quad (24)$$

in which V_p is the plastic volume at the crack tip.

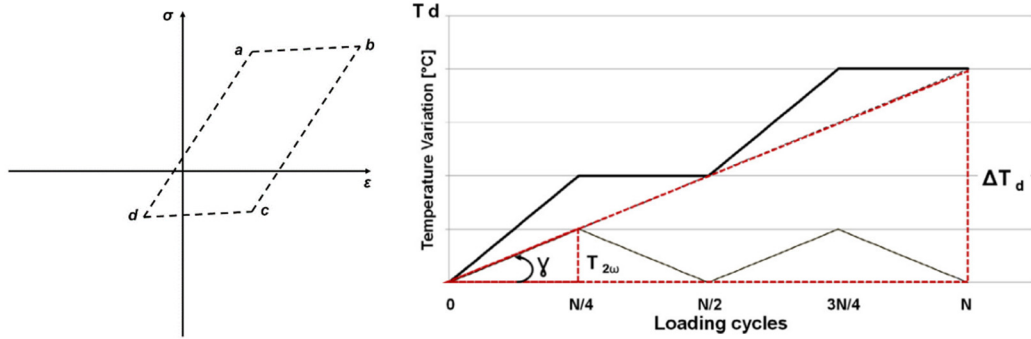


Figure 1.10: Energy dissipation evolution during a loading cycle of a simplified bilinear material model. Figure taken from [74].

1.2.3 Specific thermal energy dissipated per cycle evaluated by using the cooling gradient technique

In [75] a theoretical model and an experimental procedure were proposed to evaluate the Q parameter, taking advantage of temperature measurements, which can be performed by using thermocouples as well as an infrared camera. The specific heat energy per cycle, Q , was assumed as a fatigue damage indicator [75], because it is expected to be a material property, similarly to the plastic strain hysteresis energy [76].

At the beginning of a constant amplitude fatigue test, the material increases its temperature $T(t)$ until to reach a stabilised value, ΔT_{st} , when the thermal equilibrium is achieved between the thermal power “generated” by the material and that dissipated to the surroundings, as shown in Fig. (11b). The alternating component superimposed to $T_m(t)$ is due to the thermoelastic effect. By applying the energy balance equation to a control volume V of a material undergoing a fatigue test Fig. (11a), the first law of thermodynamics applied over one loading cycle can be written as [75]:

$$\int_V W \cdot dV = \int_V (Q + \Delta U) \cdot dV \quad (25)$$

W being the input mechanical energy per cycle (the area within the hysteresis loop), Q the dissipated thermal energy and ΔU the variation of internal energy.

a)

b)

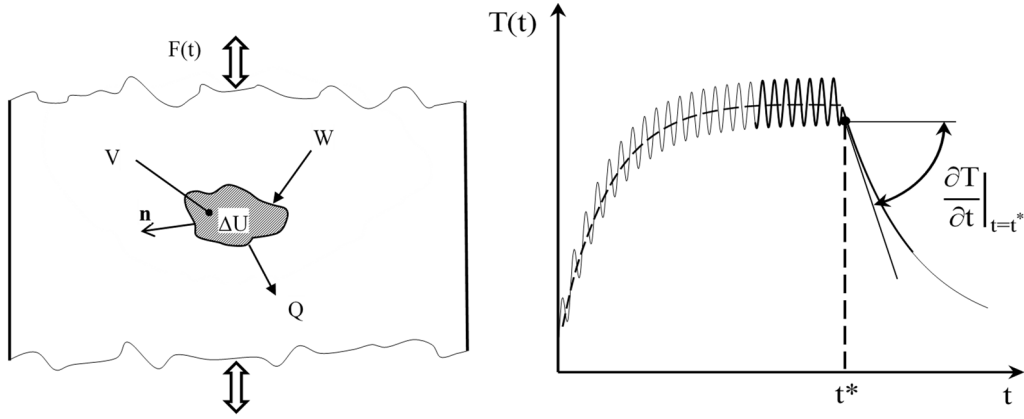


Figure 1.11: Energy balance of a material subjected to cyclic loading (a) Qualitative representation of temperature evolution during a fatigue test and evaluation of the cooling gradient immediately after a test stop (b).

Eq. 25 can be written by considering the mean power exchanged over one loading cycle:

$$\int_V \left(\oint \sigma_{ij} \cdot d\varepsilon_{ij} \right) \cdot f_L \cdot dV = \int_V H \cdot dV + \int_V \left(\rho \cdot c \cdot \frac{\partial T_m(t)}{\partial t} + \dot{E}_p \right) \cdot dV \quad (26)$$

where f_L is load test frequency, $H=Q \cdot f_L$ is the thermal power dissipated by conduction, convection and radiation, ρ the material density, c the specific heat and \dot{E}_p the rate of accumulation of damaging energy in a unit volume of material. Since Eq. (26) considers the rate of energy contributions averaged over one cycle, thermoelasticity does not produce a net energy dissipation or absorption, because it consists of a reversible exchange between mechanical and thermal energy over one loading cycle. Therefore, the mean temperature evolution $T_m(t)$ appears on the right side of Eq. (14). When temperature stabilises ($t > t_s$ in Fig. (11b)), the first derivative of $T_m(t)$ becomes null, therefore Eq.26 simplifies to:

$$\int_V \left(\oint \sigma_{ij} \cdot d\varepsilon_{ij} \right) \cdot f_L \cdot dV = \int_V H \cdot dV + \int_V \dot{E}_p \cdot dV \quad (27)$$

If referred to a point on the specimen's surface, Eq. 27 becomes

$$W \cdot f_L = H + \dot{E}_p \quad (28)$$

Suppose now to stop suddenly the fatigue test at $t=t^*$ (see Fig. (11b)): then just after t^* (i.e. at $t=t^{*+}$) the mechanical input power $W \cdot f_L$ and the rate of accumulation

of fatigue damage \dot{E}_p will vanish. By writing the energy balance equation (26) again, we obtain:

$$\rho \cdot c \cdot \left. \frac{\partial T(t)}{\partial t} \right|_{t=(t^*)^+} = -H \quad (29)$$

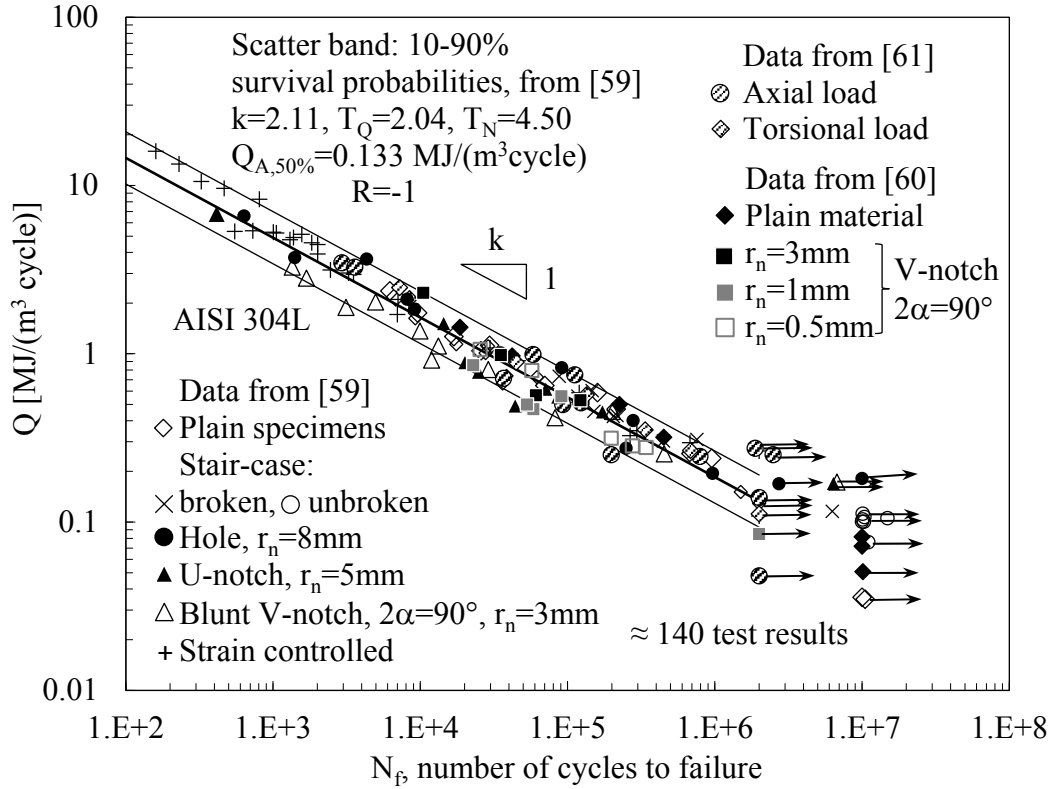


Figure 1.12: Fatigue tests results in terms of specific heat energy. The scatter band was calibrated only on data published in [77].

It is worth noting that the thermal power H dissipated to the surroundings just before and just after t^* is the same in Eq. (28) and in Eq. (29), respectively, because the temperature field is continuous through t^* . Finally, the thermal energy released in a unit volume of material per cycle can be calculated by simply accounting for the load test frequency, f_L :

$$Q = \frac{H}{f_L} = - \frac{\rho \cdot c \cdot \left. \frac{\partial T(t)}{\partial t} \right|_{t=(t^*)^+}}{f_L} \quad (30)$$

Equation (30) enables one to measure readily and in-situ the specific heat loss Q at any point of a specimen or a component undergoing fatigue loadings.

The Q parameter was adopted to synthesise 140 experimental results obtained from constant amplitude, push-pull, stress- or strain-controlled fatigue tests carried out on plain and notched hot rolled AISI 304L stainless steel specimens [77–79] as well as from cold drawn un-notched bars of the same steel, under fully-reversed axial or torsional fatigue loadings [80]. The fatigue test results synthesised in term of Q are reported in Fig. 12: all of them fall in a single energy-based scatter band, which was originally fitted only on the fatigue test results relevant to plain material, hole specimens, U and bluntly V-notched specimens [80].

Adopting the cooling gradient methodology, the Q depends on the material and the stress ratio R as it can be observed in Fig. (13)

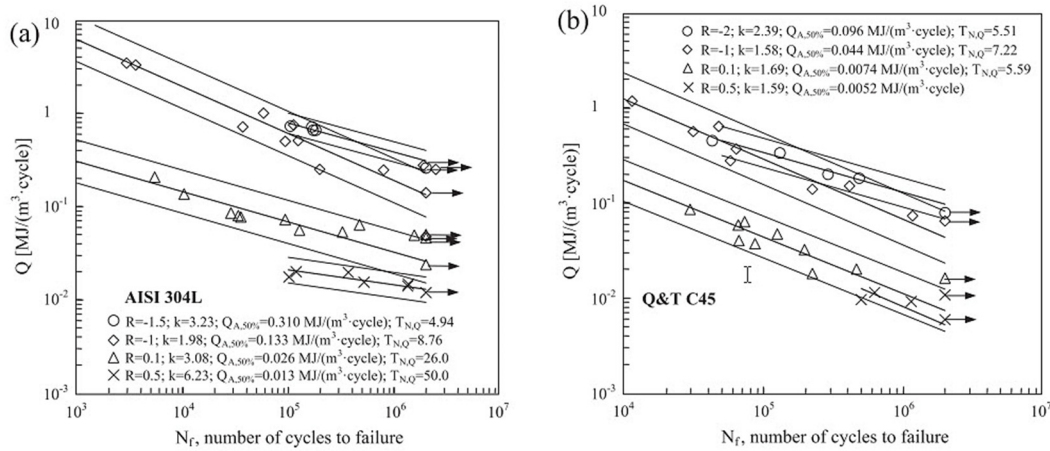


Figure 1.13: Fatigue data analysed in terms of specific heat loss. Scatter bands are defined for 10% and 90% survival probabilities [62]

Later on, the mean stress influence in fatigue has been taken into account [81], by proposing a new two-parameters energy-based approach which combines the specific heat loss and the thermoelastic temperature corresponding to the maximum stress of the load cycle. The main idea takes the origin from the most common stress-based approach to take into account the mean stress/strain effect. More precisely, the common feature of such approaches is to combine two different mechanical parameters. For instance, Smith, Watson and Topper [82] proposed the SWT parameter to include the mean stress effect in the strain-life approach to notch fatigue combining the elastic-plastic strain amplitude and σ_{\max} the maximum stress. Even in Fracture Mechanics (FM) problems [83–86] an equivalent SIF range for long crack growth data generated from fatigue tests with different load ratios including the range and the maximum value of the stress intensity factor was assumed to deal with mean stress/strain effect.

These approaches show that the driving force of both crack nucleation and propagation is governed by two parameters in which one is the range (or amplitude) of the driving force and the relevant maximum value.

Therefore in [81] Q by Eq. 30 was proposed as thermodynamic exchange variable and whereas and the thermoelastic temperature T_{the} as the state variable

assumed equal to the temperature that would be reached by the material when loaded at the maximum stress level of the fatigue cycle, σ_{\max} , in an adiabatic process.

T_{the} can be evaluated experimentally by measuring the corresponding temperature variation by loading the material in its elastic field. The applied stress rate should be properly set to make the loading process adiabatic. The thermoelastic temperature T_{the} can be easily calculated from Eq. (31), which relates T_{the} to the maximum applied stress [87]:

$$\frac{\Delta T_{\text{the}}}{T_0} = -\left(\frac{\alpha}{\rho \cdot c}\right) \cdot \Delta \sigma = -K_m \cdot \Delta \sigma \quad (31)$$

where T_0 is the material temperature at the beginning of the adiabatic loading process and α the material thermal expansion coefficient.

Finally, the following fatigue life equation was proposed to rationalise the mean stress influence on axial fatigue:

$$\left(Q \cdot \left(\frac{|\Delta T_{\text{the}}|}{T_0}\right)^h\right)^m \cdot N_f = (\bar{Q})^m \cdot N_f = \text{const} \quad (32)$$

h and m are material constants to evaluate by best fitting the experimental data.

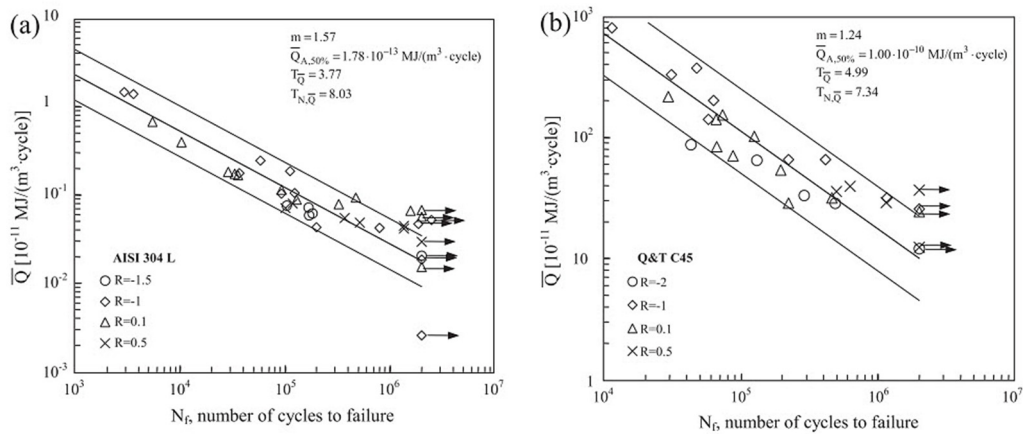


Figure 1.14: Fatigue data of Fig. 13 analysed in terms of the temperature-corrected energy parameter Q . Scatter bands are defined for 10% and 90% survival probabilities. [62]

In [81] all the axial fatigue test results of plain specimens made of cold drawn AISI 304 L and hot-rolled quenched and tempered C45 steel bars under different load ratios in the range $-2 < R < 0.5$ were synthesised by a single scatter band expressed by adopting the corrected Q parameter, as it can be seen in Fig. (14).

In order to extend the applicability of Q evaluated by adopting the cooling gradient technique in chapters 3, the analysis of the thermal energy dissipated was carried out on constant amplitude ($R=-1$) fatigue on severely notched AISI 304L steel specimens having tip radii equal to 3, 1, and 0.5

Furthermore, since Q was able to synthesis both axial and torsional fatigue tests, it is reasonable to assume that the same energy-based scatter may include multiaxial fatigue test results as well. Therefore, in Chapters 4 and 5 fatigue results relevant to constant amplitude multiaxial cyclic loading condition on both AISI 304L and C45 steel specimens will be presented and discussed

1.3 METALLIC MATERIALS PRODUCED BY ADDITIVE MANUFACTURING

Additive manufacturing (AM) technology is known for more than 20 years and it was applied in the first place to rapid production of prototypes, in which the porosity was not an issue [88]. In the last decades, AM of parts has been increased thanks to the improvement of the technology, which led to an increment of part density and quality, with the possibility of producing very complex components by respecting new geometrical constraints completely different from traditional manufacturing [89–92].

AM of metals can be presently performed by using the following methods: Laser Beam Melting (LBM), Electron Beam Melting (EBM) and Laser Metal Deposition (LMD) (also known as Direct Energy Deposition (DED)) [93–95]. Regardless of the adopted technology, the starting point of metal AM processes is a 3D CAD model, which is sliced in the computer virtual environment into thin layers (the layer thickness being in the range $20\ \mu\text{m} - 1\ \text{mm}$). Afterwards, the physical component is built layer-by-layer by deposition and local melting of the material using a heat source (the laser beam or the electron beam depending on the AM process) [89–92]. From the structural point of view, topological optimisation is the key task in design for additive manufacturing to maximise the structural performance of the component for a given set of design loads.

Complex thermal cycles with extremely high cooling rates (i.e. on the order of $10^3-10^8\ \text{K/s}$ in LBM processes [96]) are involved in all AM processes. Furthermore, since the heat conduction is mainly directed towards the build direction, elongated grain shapes have been observed leading to a certain anisotropy of the microstructure and of the resulting mechanical properties.

The first goal in AM process optimisation is to increase the density of the material in order to reduce pore formation [97], which is detrimental for static and, to a larger extent, for fatigue strength. Regarding the static mechanical properties (yield and tensile strengths) in AM metallic materials, they result to be approximately the same or even higher than those relevant ones obtained by means of traditional processes (e.g. casting). This outcome can be found for instance by comparing the static properties of wrought [98] and LMD-manufactured 304L and 316L stainless

steels [99,100], of cast [101] and LBM AlSi10Mg aluminium alloy [102], of wrought [103] and LBM Ti-6Al-4V titanium alloy [104,105].

However, structural durability is of major concern in designing structural components, as the increasing number of fatigue studies reported in the literature testifies (see for instance the recent review on AM of metallic material published in [106]). As a general remark, microstructure, surface roughness, residual stresses and size/distribution of material defects strongly influence the fatigue strength [104,107–112]. The most common defects caused by Selective Laser Melting (SLM) are the so-called Lack Of Fusion (LOF) which are unmelted regions characterized by irregular 3D shapes known. Other defects are pores with elliptical or spherical shape and crack-like defects. The mechanism of formation of such defects is well explained in [113]. Generally, additive manufacturing parts require post-processing to achieve the target properties. Hot isostatic pressure (HIP), heat treatments, machining/micro-machining, surface treatments like sandblasting or micro-shot peening are most used post-processes to reduce remaining porosity, mitigate of inner residual stresses and prepare functional surfaces.

Leuders et al. investigated the fatigue crack propagation resistance of as-built, heat-treated and HIPed SLM-processed Ti-6Al-4V titanium alloy and concluding that microstructure, pore size, and internal residual stresses have a fundamental role in determining the resulting fatigue properties [104]. Mower and Long compared the static strength and fatigue behaviour of additively manufactured AlSi10Mg, Ti-6Al-4V, and two stainless steel (316L and 17-4PH) with the same alloys produced by traditional methods (wrought and machined) [108]. Li et al. highlighted the key role of surface roughness in fatigue performances of Ti-6Al-4V AM specimens [109], while Nicoletto analysed the HCF behaviour of Ti-6Al-4V titanium alloy in-plane bending fatigue [110]. Cyclic plastic behaviour of SLMed maraging steel 300 has been studied in [112]. In ref [111] an overview focused on the challenges and opportunities in fabricating AM materials with increased fatigue resistance is reported. It is highlighted the need for a more complete understanding of the relationship among process, structure, and property performance for several AM processes and materials.

From a design point of view, fatigue strength estimations cannot be performed without taking into account the defects mechanics. Fracture mechanics-based studies of the anisotropic behaviour of SLM-processed metals have been performed recently [114,115]; whereas defect sensitivity of AMed materials has been compared to traditionally manufactured metals in ref. [116]. As it is well-known, the fatigue strength is controlled by the defects having the maximum size and, given the complex geometries of LOF discontinuities, the $\sqrt{\text{area}}$ parameter is appropriate to quantify the effect of defect size [117]. Statistics of extreme values can be applied in order to estimate the maximum size of the defect, which in the most recent applications is performed starting from CT scanning inspections [118–120].

According to the author's knowledge, there was a lack of data in the literature as regards axial fatigue strength of AMed maraging steel. Maraging steels grade 300 (or

18Ni 300) is a high-strength material adopted in aeronautical and tool fields for its superior properties such as high ductility, high yield stress, good hardenability, good weldability and simple heat treatment without deformations. Maraging steel 300 is material that can be produced by additive manufacturing systems. Kempen et al. analysed the influence of the laser speed, the layer thickness and the post-ageing treatment on the hardness and static properties of SLM additively manufactured maraging steel grade 300 and compared them with those obtained from wrought material [121]. Croccolo et al., inspired by the contributions on titanium alloy of Edwards and Ramulu, [122,123], studied the influence of the building orientation on the high cycle rotating bending fatigue life of maraging steel specimens [124].

In a recent paper [125], the author of this dissertation and co-workers investigated the fatigue strength of additively manufactured maraging steel specimens by considering the effect of building orientation and ageing heat treatment. Results were compared with the literature relevant to traditional processes and are reported in Fig. (15), which shows that AM specimens exhibit a lower fatigue strength and a larger scatter as compared to traditionally manufactured specimens.

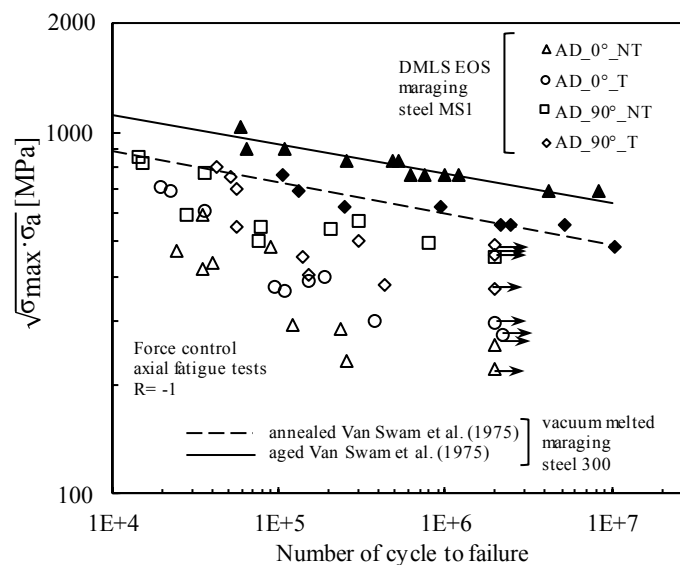


Figure 1.15: Fatigue test results in terms of SWT parameter for DMLS specimens tested in the as-built (not-treated NT) and aged (heat-treated T) conditions with different building orientations (0° and 90°) (from [125]). Comparison with fatigue test results obtained by Van Swam et al. [126] by testing vacuum melted maraging steel 300 under push-pull loading

It should be noted that the SWT parameter [82] has been used to present the results. Indeed, after having detached the specimens from the built platform they exhibited distortions, which caused a mean stress influence on fatigue testing due to clamping in the axial test machine. Geometrical distortion was more pronounced in 90°- than for 0°-oriented specimens in the as-built condition. Distortions in AM components are due to residual stresses generated during the manufacturing process, which can achieve approximately the yield strength of the material; for instance in Ref.

[127], by adopting the hole-drilling strain gauge method, tensile residual stresses of 720 ± 142 MPa are reported in as-built AM maraging steel 300 specimens. In Refs. [128,129] it was shown that residual stresses parallel to the scanning direction are much larger than those parallel to the building direction; therefore thin components laying in the scanning plane are subject to higher deflections.

Furthermore, the large scatter of the results observed Fig. (15) have been attributed to different defects size observed at the origin of the fracture surfaces of the specimens.

For this reason, in chapter (6) the defects mechanics were applied to new batches of maraging steel specimens produced by two different AM system.

Defects triggering fatigue crack initiation have been investigated after fracture by using Scanning Electron Microscope (SEM) analyses.

Since LoF defects can be considered like small cracks the linear elastic SIF based on the $\sqrt{\text{area}}$ parameter [117] has been corrected by using the El Haddad Smith and Topper length parameter a_0 in order to propose a ΔK_{corr} -fatigue life curve.

The definition of the a_0 is the following:

$$a_0 = \frac{1}{\pi} \cdot \left(\frac{\Delta K_{\text{th}}}{\Delta \sigma_0} \right)^2 \quad (21)$$

where ΔK_{th} and $\Delta \sigma_0$ are the threshold range of the stress intensity factor for long cracks and the plain material fatigue limit in a defect-free condition, respectively. In the absence of experimental data to determine ΔK_{th} and $\Delta \sigma_0$, a novel approximated method to determine the a_0 parameter will be proposed in Chapter 6.

Furthermore, the estimation of a_0 adopting such approximated method could also allow to evaluate of the radius R_c of the control volume adopted in the averaged SED approach by adopting the analogy with the Kitagawa and Atzori's diagrams found in [130].

All the theoretical background of this approach is reported in Chapter 6.

1.4 REFERENCES

- [1] Eurocode 3: Design of steel structures – part 1–9: Fatigue. CEN; 2005.
- [2] Eurocode 9: Design of aluminium structures - Part 1-3: Structures susceptible to fatigue. CEN; 2011.
- [3] Hobbacher AF. Recommendations for Fatigue Design of Welded Joints and Components. IIW Collection. Springer International Publishing; 2016. doi:10.1007/978-3-319-23757-2.
- [4] Radaj D, Lazzarin P, Berto F. Generalised Neuber concept of fictitious notch rounding. *Int J Fatigue* 2013;51:105–15. doi:10.1016/j.ijfatigue.2013.01.005.
- [5] Lazzarin P, Tovo R. A notch intensity factor approach to the stress analysis of welds. *Fatigue Fract Eng Mater Struct* 1998;21:1089–103. doi:10.1046/j.1460-

- 2695.1998.00097.x.
- [6] Radaj D, Sonsino CM, Fricke W. *Fatigue Assessment of Welded Joints by Local Approaches*. 2nd ed. Cambridge: Woodhead Publishing; 2006.
 - [7] Radaj D. State-of-the-art review on extended stress intensity factor concepts. *Fatigue Fract Eng Mater Struct* 2014;37:1–28. doi:10.1111/ffe.12120.
 - [8] Lazzarin P, Livieri P. Notch stress intensity factors and fatigue strength of aluminium and steel welded joints. *Int J Fatigue* 2001;23:225–32. doi:10.1016/S0142-1123(00)00086-4.
 - [9] Lazzarin P, Sonsino CM, Zambardi R. A notch stress intensity approach to assess the multiaxial fatigue strength of welded tube-to-flange joints subjected to combined loadings. *Fatigue Fract Eng Mater Struct* 2004;27:127–40. doi:10.1111/j.1460-2695.2004.00733.x.
 - [10] Boukharouba T, Tamine T, Niu L, Chehimi C, Pluvinage G. The use of notch stress intensity factor as a fatigue crack initiation parameter. *Eng Fract Mech* 1995;52:503–12. doi:10.1016/0013-7944(94)00242-A.
 - [11] Verreman Y, Nie B. Early development of fatigue cracking at manual fillet welds. *Fatigue Fract Eng Mater Struct* 1996;19:669–81. doi:10.1111/j.1460-2695.1996.tb01312.x.
 - [12] Radaj D, Vormwald M. *Advanced Methods of Fatigue Assessment*. Berlin, Heidelberg: Springer Berlin Heidelberg; 2013. doi:10.1007/978-3-642-30740-9.
 - [13] Smith RA, Miller KJ. Prediction of fatigue regimes in notched components. *Int J Mech Sci* 1978;20:201–6. doi:10.1016/0020-7403(78)90082-6.
 - [14] Taylor D. Geometrical effects in fatigue: a unifying theoretical model. *Int J Fatigue* 1999;21:413–20. doi:10.1016/S0142-1123(99)00007-9.
 - [15] Atzori B, Lazzarin P, Meneghetti G. Fracture mechanics and notch sensitivity. *Fatigue Fract Eng Mater Struct* 2003;26:257–67. doi:10.1046/j.1460-2695.2003.00633.x.
 - [16] Williams ML. Stress singularities resulting from various boundary conditions in angular corners of plates in tension. *J Appl Mech* 1952;19:526–8.
 - [17] Qian J, Hasebe N. Property of eigenvalues and eigenfunctions for an interface V-notch in antiplane elasticity. *Eng Fract Mech* 1997;56:729–34. doi:10.1016/S0013-7944(97)00004-0.
 - [18] Gross B, Mendelson A. Plane elastostatic analysis of V-notched plates. *Int J Fract Mech* 1972;8:267–76. doi:10.1007/BF00186126.
 - [19] Meneghetti G, Campagnolo A, Rigon D. Multiaxial fatigue strength assessment of welded joints using the Peak Stress Method – Part I: Approach and application to aluminium joints. *Int J Fatigue* 2017;101:328–42. doi:10.1016/j.ijfatigue.2017.03.038.
 - [20] Lazzarin P, Lassen T, Livieri P. A notch stress intensity approach applied to fatigue life predictions of welded joints with different local toe geometry. *Fatigue Fract Eng Mater Struct* 2003;26:49–58. doi:10.1046/j.1460-2695.2003.00586.x.
 - [21] Lazzarin P, Zambardi R. A finite-volume-energy based approach to predict the static and fatigue behavior of components with sharp V-shaped notches. *Int J Fract* 2001;112:275–98. doi:10.1023/A:1013595930617.
 - [22] Livieri P, Lazzarin P. Fatigue strength of steel and aluminium welded joints based on generalised stress intensity factors and local strain energy values. *Int J Fract* 2005;133:247–76. doi:10.1007/s10704-005-4043-3.
 - [23] Lazzarin P, Livieri P, Berto F, Zappalorto M. Local strain energy density and fatigue strength of welded joints under uniaxial and multiaxial loading. *Eng Fract Mech* 2008;75:1875–89. doi:10.1016/j.engfracmech.2006.10.019.
 - [24] Berto F, Lazzarin P, Yates JR. Multiaxial fatigue of V-notched steel specimens: A non-conventional application of the local energy method. *Fatigue Fract Eng Mater Struct* 2011;34:921–43. doi:10.1111/j.1460-2695.2011.01585.x.
 - [25] Berto F, Lazzarin P. Fatigue strength of structural components under multi-axial loading in terms of local energy density averaged on a control volume. *Int J Fatigue*

- 2011;33:1055–65. doi:10.1016/j.ijfatigue.2010.11.019.
- [26] Lazzarin P, Berto F, Zappalorto M. Rapid calculations of notch stress intensity factors based on averaged strain energy density from coarse meshes: Theoretical bases and applications. *Int J Fatigue* 2010;32:1559–67. doi:10.1016/j.ijfatigue.2010.02.017.
- [27] Meneghetti G, Lazzarin P. Significance of the elastic peak stress evaluated by FE analyses at the point of singularity of sharp V-notched components. *Fatigue Fract Eng Mater Struct* 2007;30:95–106. doi:10.1111/j.1460-2695.2006.01084.x.
- [28] Nisitani H, Teranishi T. KI value of a circumferential crack emanating from an ellipsoidal cavity obtained by the crack tip stress method in FEM. In: Guagliano M, Aliabadi MH, editors. *Proc. 2nd Int. Conf. Fract. damage Mech.*, 2001, p. 141–6.
- [29] Nisitani H, Teranishi T. KI of a circumferential crack emanating from an ellipsoidal cavity obtained by the crack tip stress method in FEM. *Eng Fract Mech* 2004;71:579–85. doi:10.1016/S0013-7944(03)00035-3.
- [30] Meneghetti G, Guzzella C. The peak stress method to estimate the mode I notch stress intensity factor in welded joints using three-dimensional finite element models. *Eng Fract Mech* 2014;115:154–71. doi:10.1016/j.engfracmech.2013.11.002.
- [31] Meneghetti G. The use of peak stresses for fatigue strength assessments of welded lap joints and cover plates with toe and root failures. *Eng Fract Mech* 2012;89:40–51. doi:10.1016/j.engfracmech.2012.04.007.
- [32] Meneghetti G. The peak stress method for fatigue strength assessment of tube-to-flange welded joints under torsion loading. *Weld World* 2013;57:265–75. doi:10.1007/s40194-013-0022-x.
- [33] Meneghetti G, Campagnolo A, Rigon D. Multiaxial fatigue strength assessment of welded joints using the Peak Stress Method – Part I: Approach and application to aluminium joints. *Int J Fatigue* 2017;101:328–42. doi:10.1016/j.ijfatigue.2017.03.038.
- [34] Meneghetti G, Campagnolo A, Berto F. Fatigue strength assessment of partial and full-penetration steel and aluminium butt-welded joints according to the peak stress method. *Fatigue Fract Eng Mater Struct* 2015;38:1419–31. doi:10.1111/ffe.12342.
- [35] Meneghetti G, Guzzella C, Atzori B. The peak stress method combined with 3D finite element models for fatigue assessment of toe and root cracking in steel welded joints subjected to axial or bending loading. *Fatigue Fract Eng Mater Struct* 2014;37:722–39. doi:10.1111/ffe.12171.
- [36] Meneghetti G, Marini D, Babini V. Fatigue assessment of weld toe and weld root failures in steel welded joints according to the peak stress method. *Weld World* 2016;1–14. doi:10.1007/s40194-016-0308-x.
- [37] Meneghetti G, De Marchi A, Campagnolo A. Assessment of root failures in tube-to-flange steel welded joints under torsional loading according to the Peak Stress Method. *Theor Appl Fract Mech* 2016;83:19–30. doi:10.1016/j.tafmec.2016.01.013.
- [38] Meneghetti G, Lazzarin P. The Peak Stress Method for Fatigue Strength Assessment of welded joints with weld toe or weld root failures. *Weld World* 2011;55:22–9. doi:10.1007/BF03321304.
- [39] Meneghetti G, Campagnolo A. The Peak Stress Method to assess the fatigue strength of welded joints using linear elastic finite element analyses. *Procedia Eng* 2018;213:392–402. doi:10.1016/j.proeng.2018.02.039.
- [40] Meneghetti G, Campagnolo A, Berto F. Assessment of tensile fatigue limit of notches using sharp and coarse linear elastic finite element models. *Theor Appl Fract Mech* 2016;84:106–18. doi:10.1016/j.tafmec.2016.06.001.
- [41] Stromeyer CE. The Determination of Fatigue Limits under Alternating Stress Conditions. *Proc R Soc A Math Phys Eng Sci* 1914;90:411–25. doi:10.1098/rspa.1914.0066.
- [42] Dengel D, Harig H. Estimation of the fatigue limit by progressively-increasing load tests. *Fatigue Fract Eng Mater Struct* 1980;3:113–28. doi:10.1111/j.1460-2695.1980.tb01108.x.

- [43] Luong MP. Infrared thermographic scanning of fatigue in metals. *Nucl Eng Des* 1995;158:363–76. doi:10.1016/0029-5493(95)01043-H.
- [44] La Rosa G, Risitano A. Thermographic methodology for rapid determination of the fatigue limit of materials and mechanical components. *Int J Fatigue* 2000;22:65–73. doi:10.1016/S0142-1123(99)00088-2.
- [45] Curà F, Curti G, Sesana R. A new iteration method for the thermographic determination of fatigue limit in steels. *Int J Fatigue* 2005;27:453–9. doi:10.1016/j.ijfatigue.2003.12.009.
- [46] Palumbo D, De Finis R, Demelio PG, Galietti U. A new rapid thermographic method to assess the fatigue limit in GFRP composites. *Compos Part B Eng* 2016;103:60–7. doi:10.1016/J.COMPOSITESB.2016.08.007.
- [47] Reifsnider KL, Williams RS. Determination of fatigue-related heat emission in composite materials 1974;14:479–85. doi:10.1007/BF02323148.
- [48] Plekhov O, Palin-Luc T, Saintier N, Uvarov S, Naimark O. Fatigue crack initiation and growth in a 35CrMo4 steel investigated by infrared thermography. *Fatigue Fract Eng Mater Struct* 2005;28:169–78. doi:10.1111/j.1460-2695.2005.00856.x.
- [49] Ummenhofer T, Medgenberg J. On the use of infrared thermography for the analysis of fatigue damage processes in welded joints. *Int J Fatigue* 2009;31:130–7. doi:10.1016/j.ijfatigue.2008.04.005.
- [50] Jones R, Krishnapillai M, Cairns K, Matthews N. Application of infrared thermography to study crack growth and fatigue life extension procedures. *Fatigue Fract Eng Mater Struct* 2010;33:871–84. doi:10.1111/j.1460-2695.2010.01505.x.
- [51] Fargione G, Geraci A, La Rosa G, Risitano A. Rapid determination of the fatigue curve by the thermographic method. *Int J Fatigue* 2002;24:11–9. doi:10.1016/S0142-1123(01)00107-4.
- [52] Starke P, Walther F, Eifler D. Fatigue assessment and fatigue life calculation of quenched and tempered SAE 4140 steel based on stress–strain hysteresis, temperature and electrical resistance measurements. *Fatigue Fract Eng Mater Struct* 2007;30:1044–51. doi:10.1111/j.1460-2695.2007.01174.x.
- [53] Jegou L, Marco Y, Le Saux V, Calloch S. Fast prediction of the Wöhler curve from heat build-up measurements on Short Fiber Reinforced Plastic. *Int J Fatigue* 2013;47:259–67. doi:10.1016/j.ijfatigue.2012.09.007.
- [54] Fan J, Guo X, Wu C. A new application of the infrared thermography for fatigue evaluation and damage assessment. *Int J Fatigue* 2012;44:1–7. doi:10.1016/j.ijfatigue.2012.06.003.
- [55] Risitano A, Risitano G. Cumulative damage evaluation in multiple cycle fatigue tests taking into account energy parameters. *Int J Fatigue* 2013;48:214–22. doi:10.1016/j.ijfatigue.2012.10.020.
- [56] Meneghetti G, Ricotta M. The heat energy dissipated in the material structural volume to correlate the fatigue crack growth rate in stainless steel specimens. *Int J Fatigue* 2018;115:107–19. doi:10.1016/J.IJFATIGUE.2018.07.037.
- [57] Germain P, Nguyen QS, Suquet P. Continuum thermodynamics. *J Appl Mech Trans ASME* 1983;50:1010–20. doi:10.1115/1.3167184.
- [58] Lemaitre J, Chaboche JL. *Mechanics of solid materials*. Cambridge University Press; 1994.
- [59] Rousselier G. Dissipation in porous metal plasticity and ductile fracture. *J Mech Phys Solids* 2001;49:1727–46. doi:10.1016/S0022-5096(01)00013-8.
- [60] Chrysochoos A, Louche H. An infrared image processing to analyse the calorific effects accompanying strain localisation. *Int J Eng Sci* 2000;38:1759–88. doi:10.1016/S0020-7225(00)00002-1.
- [61] Chrysochoos A, Berthel B, Latourte F, Galtier A, Pagano S, Wattrisse B. Local energy analysis of high-cycle fatigue using digital image correlation and infrared thermography. *J Strain Anal Eng Des* 2008;43:411–22. doi:10.1243/03093247JSA374.

- [62] Boulanger T. Calorimetric analysis of dissipative and thermoelastic effects associated with the fatigue behavior of steels. *Int J Fatigue* 2004;26:221–9. doi:10.1016/S0142-1123(03)00171-3.
- [63] Connesson N, Maquin F, Pierron F. Dissipated energy measurements as a marker of microstructural evolution : 316L and DP600 q. *Acta Mater* 2011;59:4100–15. doi:10.1016/j.actamat.2011.03.034.
- [64] Wang WJ, Dulieu-Barton JM, Li Q. Assessment of non-adiabatic behaviour in thermoelastic stress analysis of small scale components. *Exp Mech* 2010;50:449–61. doi:10.1007/s11340-009-9249-2.
- [65] Dulieu-Barton JM. Introduction to thermoelastic stress analysis. *Strain* 1999;35:35–9. doi:10.1111/j.1475-1305.1999.tb01123.x.
- [66] Pitarresi G, Patterson EA. A review of the general theory of thermoelastic stress analysis. *J Strain Anal Eng Des* 2003;38:405–17. doi:10.1243/03093240360713469.
- [67] Palumbo D, Galietti U. Thermoelastic Phase Analysis (TPA): a new method for fatigue behaviour analysis of steels. *Fatigue Fract Eng Mater Struct* 2017;40:523–34. doi:10.1111/ffe.12511.
- [68] Galietti U, Palumbo D, Finis R De, Ancona F. Fatigue damage evaluation of martensitic stainless steel by means of thermal methods Valutazione del danneggiamento a fatica di acciai inossidabili martensitici mediante metodi termici 2013;1560:80–90.
- [69] Casavola C, Galietti U, Modugno D, Pappalettere C. An application of the differential thermographic technique for welded joints fatigue evaluation. *SPIE*, 2006, p. 6250.
- [70] DIAZ FA, Patterson EA, Tomlinson RA, Yates JR. Measuring stress intensity factors during fatigue crack growth using thermoelasticity. *Fatigue Fract Eng Mater Struct* 2004;27:571–83. doi:10.1111/j.1460-2695.2004.00782.x.
- [71] Sakagami T, Kubo S, Tamura E, Nishimura T. Identification of plastic-zone based on double frequency lock-in thermographic temperature measurement. *Proc. 11th Int. Conference Fract. - ICF11, Italy: 2005.*
- [72] Bär J, Seifert S. Investigation of Energy Dissipation and Plastic Zone Size During Fatigue Crack Propagation in a High-Alloyed Steel. *Procedia Mater Sci* 2014;3:408–13. doi:10.1016/j.mspro.2014.06.068.
- [73] Bär J, Vshivkov A, Plekhov O. Combined lock-in thermography and heat flow measurements for analysing heat dissipation during fatigue crack propagation. *Frat Ed Integrita Strutt* 2015;9:456–65. doi:10.3221/IGF-ESIS.34.51.
- [74] Palumbo D, De Finis R, Ancona F, Galietti U. Damage monitoring in fracture mechanics by evaluation of the heat dissipated in the cyclic plastic zone ahead of the crack tip with thermal measurements. *Eng Fract Mech* 2017;181:65–76. doi:10.1016/j.engfracmech.2017.06.017.
- [75] Meneghetti G. Analysis of the fatigue strength of a stainless steel based on the energy dissipation. *Int J Fatigue* 2007;29:81–94. doi:10.1016/j.ijfatigue.2006.02.043.
- [76] Ellyin F. *Fatigue damage, crack growth, and life prediction.* Chapman & Hall; 1997.
- [77] Meneghetti G, Ricotta M, Atzori B. A synthesis of the push-pull fatigue behaviour of plain and notched stainless steel specimens by using the specific heat loss. *Fatigue Fract Eng Mater Struct* 2013;36:1306–22. doi:10.1111/ffe.12071.
- [78] Meneghetti G, Ricotta M. The use of the specific heat loss to analyse the low- and high-cycle fatigue behaviour of plain and notched specimens made of a stainless steel. *Eng Fract Mech* 2012;81:2–16. doi:10.1016/j.engfracmech.2011.06.010.
- [79] Meneghetti G, Ricotta M, Atzori B. The Heat Energy Dissipated in a Control Volume to Correlate the Fatigue Strength of Bluntly and Severely Notched Stainless Steel Specimens. *Proc. 21st Eur. Conf. Fract. ECF21. Catania, Italy, vol. 2, 2016, p. 2076–83.* doi:10.1016/j.prostr.2016.06.260.
- [80] Meneghetti G, Ricotta M, Negrisol L, Atzori B. A Synthesis of the Fatigue Behavior of Stainless Steel Bars under Fully Reversed Axial or Torsion Loading by Using the Specific Heat Loss. *Key Eng Mater* 2013;577–578:453–6. doi:10.4028/www.scientific.net/KEM.577-578.453.

- [81] Meneghetti G, Ricotta M, Atzori B. A two-parameter, heat energy-based approach to analyse the mean stress influence on axial fatigue behaviour of plain steel specimens. *Int J Fatigue* 2016;82:60–70. doi:10.1016/j.ijfatigue.2015.07.028.
- [82] Smith KN, Watson P, Topper TH. A Stress-Strain Function for the Fatigue of Metals. *J Mater ASTM* 1970;5:767–78.
- [83] Walker K. The Effect of Stress Ratio During Crack Propagation and Fatigue for 2024-T3 and 7075-T6 Aluminum. *Eff. Environ. Complex Load Hist. Fatigue Life*, 100 Barr Harbor Drive, PO Box C700, West Conshohocken, PA 19428-2959: ASTM International; n.d., p. 1-1–14. doi:10.1520/STP32032S.
- [84] Vasudevan A., Sadananda K, Glinka G. Critical parameters for fatigue damage. *Int J Fatigue* 2001;23:39–53. doi:10.1016/S0142-1123(01)00171-2.
- [85] Kujawski D. A new $(\Delta K + K_{max})^{0.5}$ driving force parameter for crack growth in aluminum alloys. *Int J Fatigue* 2001;23:733–40. doi:10.1016/S0142-1123(01)00023-8.
- [86] Stoychev S, Kujawski D. Analysis of crack propagation using ΔK and K_{max} . *Int J Fatigue* 2005;27:1425–31. doi:10.1016/J.IJFATIGUE.2005.06.038.
- [87] Audenino A, Goglio L, Rossetto M. *Metodi sperimentali per la progettazione* 1997.
- [88] Beaman JJ, Deckard CR. Selective laser sintering with assisted powder handling. 4938816., 1990.
- [89] Kruth JP, Vandenbroucke B, van Vaerenbergh J, Naert I. Rapid manufacturing of dental prostheses by means of selective laser sintering/ melting. *AFPR*, S4, 2005.
- [90] Rännar L, Glad A, Gustafson C. Efficient cooling with tool inserts manufactured by electron beam melting. *Rapid Prototyp J* 2007;13:128–35. doi:10.1108/13552540710750870.
- [91] Murr LE, Gaytan SM, Ramirez DA, Martinez E, Hernandez J, Amato KN, et al. Metal Fabrication by Additive Manufacturing Using Laser and Electron Beam Melting Technologies. *J Mater Sci Technol* 2012;28:1–14. doi:10.1016/S1005-0302(12)60016-4.
- [92] Kranz J, Herzog D, Emmelmann C. Design guidelines for laser additive manufacturing of lightweight structures in TiAl6V4. *J Laser Appl* 2015;27:S14001. doi:10.2351/1.4885235.
- [93] Yan M, Yu P. An Overview of Densification, Microstructure and Mechanical Property of Additively Manufactured Ti-6Al-4V — Comparison among Selective Laser Melting, Electron Beam Melting, Laser Metal Deposition and Selective Laser Sintering, and with Conventional Powder. *Sinter Tech Mater* 2015. doi:10.5772/59275.
- [94] Murr LE. Metallurgy of additive manufacturing: Examples from electron beam melting. *Addit Manuf* 2015;5:40–53. doi:10.1016/j.addma.2014.12.002.
- [95] Saboori A, Gallo D, Biamino S, Fino P, Lombardi M. An overview of additive manufacturing of titanium components by directed energy deposition: microstructure and mechanical properties. *Appl Sci* 2017;7:883. doi:10.3390/app7090883.
- [96] Gu D, Hagedorn Y-C, Meiners W, Meng G, Batista RJS, Wissenbach K, et al. Densification behavior, microstructure evolution, and wear performance of selective laser melting processed commercially pure titanium. *Acta Mater* 2012;60:3849–60. doi:10.1016/j.actamat.2012.04.006.
- [97] Everton SK, Hirsch M, Stravroulakis P, Leach RK, Clare AT. Review of in-situ process monitoring and in-situ metrology for metal additive manufacturing. *Mater Des* 2016;95:431–45. doi:10.1016/j.matdes.2016.01.099.
- [98] ASTM A276, Standard Specification for Stainless Steel Bars and Shapes n.d.
- [99] Carlton HD, Haboub A, Gallegos GF, Parkinson DY, MacDowell AA. Damage evolution and failure mechanisms in additively manufactured stainless steel. *Mater Sci Eng A* 2016;651:406–14. doi:10.1016/j.msea.2015.10.073.
- [100] Wang Z, Palmer TA, Beese AM. Effect of processing parameters on microstructure and tensile properties of austenitic stainless steel 304L made by directed energy deposition additive manufacturing. *Acta Mater* 2016;110:226–35.

- doi:10.1016/j.actamat.2016.03.019.
- [101] DIN EN 1706, Aluminium and Aluminium Alloys e Castings e Chemical Composition and Mechanical Properties, 2013-12 n.d.
 - [102] Manfredi D, Calignano F, Krishnan M, Canali R, Paola E, Biamino S, et al. Additive Manufacturing of Al Alloys and Aluminium Matrix Composites (AMCs). *Light Met. Alloy. Appl., InTech*; 2014. doi:10.5772/58534.
 - [103] Donachie MJ. *Titanium: A Technical Guide*, 2nd Edition. vol. 99. 2000. doi:10.5772/1844.
 - [104] Leuders S, Thöne M, Riemer A, Niendorf T, Tröster T, Richard HA, et al. On the mechanical behaviour of titanium alloy TiAl6V4 manufactured by selective laser melting: Fatigue resistance and crack growth performance. *Int J Fatigue* 2013;48:300–7. doi:10.1016/j.ijfatigue.2012.11.011.
 - [105] Xu W, Brandt M, Sun S, Elambasseril J, Liu Q, Latham K, et al. Additive manufacturing of strong and ductile Ti-6Al-4V by selective laser melting via in situ martensite decomposition. *Acta Mater* 2015;85:74–84. doi:10.1016/j.actamat.2014.11.028.
 - [106] Herzog D, Seyda V, Wycisk E, Emmelmann C. Additive manufacturing of metals. *Acta Mater* 2016;117:371–92. doi:10.1016/j.actamat.2016.07.019.
 - [107] Mercelis P, Kruth J. Residual stresses in selective laser sintering and selective laser melting. *Rapid Prototyp J* 2006;12:254–65. doi:10.1108/13552540610707013.
 - [108] Mower TM, Long MJ. Mechanical behavior of additive manufactured, powder-bed laser-fused materials. *Mater Sci Eng A* 2016;651:198–213. doi:10.1016/j.msea.2015.10.068.
 - [109] Li P, Warner DH, Fatemi A, Phan N. Critical assessment of the fatigue performance of additively manufactured Ti-6Al-4V and perspective for future research. *Int J Fatigue* 2016;85:130–43. doi:10.1016/j.ijfatigue.2015.12.003.
 - [110] Nicoletto G. Anisotropic high cycle fatigue behavior of Ti-6Al-4V obtained by powder bed laser fusion. *Int J Fatigue* 2016;94:255–62. doi:10.1016/j.ijfatigue.2016.04.032.
 - [111] Yadollahi A, Shamsaei N. Additive manufacturing of fatigue resistant materials: Challenges and opportunities. *Int J Fatigue* 2017;98:14–31. doi:10.1016/j.ijfatigue.2017.01.001.
 - [112] Branco R, Costa J, Berto F, Razavi S, Ferreira J, Capela C, et al. Low-Cycle Fatigue Behaviour of AISI 18Ni300 Maraging Steel Produced by Selective Laser Melting. *Metals (Basel)* 2018;8:32. doi:10.3390/met8010032.
 - [113] Gong H, Rafi K, Gu H, Starr T, Stucker B. Analysis of defect generation in Ti-6Al-4V parts made using powder bed fusion additive manufacturing processes. *Addit Manuf* 2014;1:87–98. doi:10.1016/j.addma.2014.08.002.
 - [114] Konečná R, Kunz L, Nicoletto G, Bača A. Long fatigue crack growth in Inconel 718 produced by selective laser melting. *Int J Fatigue* 2016;92:499–506. doi:10.1016/j.ijfatigue.2016.03.012.
 - [115] Konečná R, Kunz L, Bača A, Nicoletto G. Resistance of direct metal laser sintered Ti6Al4V alloy against growth of fatigue cracks. *Eng Fract Mech* 2017. doi:10.1016/j.engfracmech.2017.03.033.
 - [116] Beretta S, Romano S. A comparison of fatigue strength sensitivity to defects for materials manufactured by AM or traditional processes. *Int J Fatigue* 2017;94:178–91. doi:10.1016/j.ijfatigue.2016.06.020.
 - [117] Murakami Y (Yukitaka). *Metal fatigue : effects of small defects and nonmetallic inclusions*. Elsevier; 2002.
 - [118] Siddique S, Imran M, Rauer M, Kaloudis M, Wycisk E, Emmelmann C, et al. Computed tomography for characterization of fatigue performance of selective laser melted parts. *Mater Des* 2015;83:661–9. doi:10.1016/j.matdes.2015.06.063.
 - [119] Romano S, Brückner-Foit A, Brandão A, Gumpinger J, Ghidini T, Beretta S. Fatigue properties of AlSi10Mg obtained by additive manufacturing: Defect-based modelling and prediction of fatigue strength. *Eng Fract Mech* 2017;187:165–89.

- doi:10.1016/j.engfracmech.2017.11.002.
- [120] Benedetti M, Fontanari V, Bandini M, Zanini F, Carmignato S. Low- and high-cycle fatigue resistance of Ti-6Al-4V ELI additively manufactured via selective laser melting: Mean stress and defect sensitivity. *Int J Fatigue* 2018;107:96–109. doi:10.1016/j.ijfatigue.2017.10.021.
- [121] Kempen K, Yasa E, Thijs L, Kruth JP, Van Humbeeck J. Microstructure and mechanical properties of Selective Laser Melted 18Ni-300 steel. *Phys Procedia* 2011;12:255–63. doi:10.1016/j.phpro.2011.03.033.
- [122] Edwards P, Ramulu M. Fatigue performance evaluation of selective laser melted Ti-6Al-4V. *Mater Sci Eng A* 2014;598:327–37. doi:10.1016/j.msea.2014.01.041.
- [123] Edwards P, Ramulu M. Effect of build direction on the fracture toughness and fatigue crack growth in selective laser melted Ti-6Al-4V. *Fatigue Fract Eng Mater Struct* 2015;38:1228–36. doi:10.1111/ffe.12303.
- [124] Croccolo D, De Agostinis M, Fini S, Olmi G, Vranic A, Ciric-Kostic S. Influence of the build orientation on the fatigue strength of EOS maraging steel produced by additive metal machine. *Fatigue Fract Eng Mater Struct* 2016;39:637–47. doi:10.1111/ffe.12395.
- [125] Meneghetti G, Rigon D, Cozzi D, Waldhauser W, Dabalà M. Influence of build orientation on static and axial fatigue properties of maraging steel specimens produced by additive manufacturing. *Procedia Struct Integr* 2017;7:149–57. doi:10.1016/j.prostr.2017.11.072.
- [126] Van Swam LF, Pelloux RM, Grant NJ. Fatigue behavior of maraging steel 300. *Metall Trans A* 1975;6:45–54. doi:10.1007/BF02673669.
- [127] Hermann Becker T, Dimitrov D. The achievable mechanical properties of SLM produced Maraging Steel 300 components. *Rapid Prototyp J* 2016;22:487–94. doi:10.1108/RPJ-08-2014-0096.
- [128] Wu AS, Brown DW, Kumar M, Gallegos GF, King WE. An Experimental Investigation into Additive Manufacturing-Induced Residual Stresses in 316L Stainless Steel. *Metall Mater Trans A* 2014;45:6260–70. doi:10.1007/s11661-014-2549-x.
- [129] Liu Y, Yang Y, Wang D. A study on the residual stress during selective laser melting (SLM) of metallic powder. *Int J Adv Manuf Technol* 2016:1–10. doi:10.1007/s00170-016-8466-y.
- [130] Lazzarin P, Berto F. From Neuber's Elementary Volume to Kitagawa and Atzori's Diagrams: An Interpretation Based on Local Energy. *Int J Fract* 2005;135:L33–8. doi:10.1007/s10704-005-4393-x.

Chapter 2: Peak Stress Method for multiaxial loading

This chapter describes in the first place the theoretical framework for extending the applicability of Peak Stress Method in order to extend its applicability to the fatigue strength assessment of welded joints subjected to multiaxial loading conditions. After that, several multiaxial fatigue data taken from the literature relevant to both aluminium and steel welded joint will be analysed by using the PSM for validating the theoretical prediction.

This chapter is referred to the following author's papers:

- [1] Meneghetti G, Campagnolo A, Rigon D. *Multiaxial fatigue strength assessment of welded joints using the Peak Stress Method – Part I: Approach and application to aluminium joints. Int J Fatigue 2017;101:328–42. doi:10.1016/j.ijfatigue.2017.03.038*
- [2] Meneghetti G, Campagnolo A, Rigon D. *Multiaxial fatigue strength assessment of welded joints using the Peak Stress Method – Part II: Application to structural steel joints. Int J Fatigue 2017;101: 343-62. doi:10.1016/j.ijfatigue.2017.03.039*

2.1 THEORETICAL FRAMEWORK

The numerical procedure proposed by Nisitani and Teranishi [3,4] has lead the formulation of the PSM which can rapidly estimate the mode I SIF of a crack emanating from an ellipsoidal cavity. The method has been theoretically justified and also extended to estimate the mode I NSIF of sharp and open V-notches [5,6], the mode II SIF of cracks [7] and the mode III NSIF of cracks and open V-notches [8]. Recently, the local SED concept and its relation to the PSM have been thoroughly reviewed by Radaj [9].

Essentially, the PSM allows to rapidly estimate the NSIFs K_1 , K_2 and K_3 from the singular, linear elastic, opening ($\sigma_{\theta\theta,\theta=0,\text{peak}}$), in-plane shear ($\tau_{r\theta,\theta=0,\text{peak}}$) and anti-plane shear ($\tau_{\theta z,\theta=0,\text{peak}}$) FE peak stresses, which are referred to the V-notch bisector line, according to Fig. 1. In more detail, the following expressions were previously validated [5,7,8]:

$$K_{\text{FE}}^* = \frac{K_1}{\sigma_{\theta\theta,\theta=0,\text{peak}} \cdot d^{1-\lambda_1}} \quad (1)$$

$$K_{\text{FE}}^{**} = \frac{K_2}{\tau_{r\theta,\theta=0,\text{peak}} \cdot d^{1-\lambda_2}} \quad (2)$$

$$K_{FE}^{***} = \frac{K_3}{\tau_{\theta z, \theta=0, peak} \cdot d^{1-\lambda_3}} \quad (3)$$

In the previous equations, d is the so-called ‘global element size’ parameter, which is the average size of the finite elements request by the free mesh generation algorithm of the considered FE-numerical code. It should be noted that the ‘exact’ K_1 , K_2 and K_3 NSIFs values in Eqs. (1)-(3) must be meant as the values derived from their definitions applied to the stress-distance numerical results obtained from very refined FE mesh patterns (where the size of the smallest element close to the V-notch tip is on the order of 10^{-5} mm [10,11]).

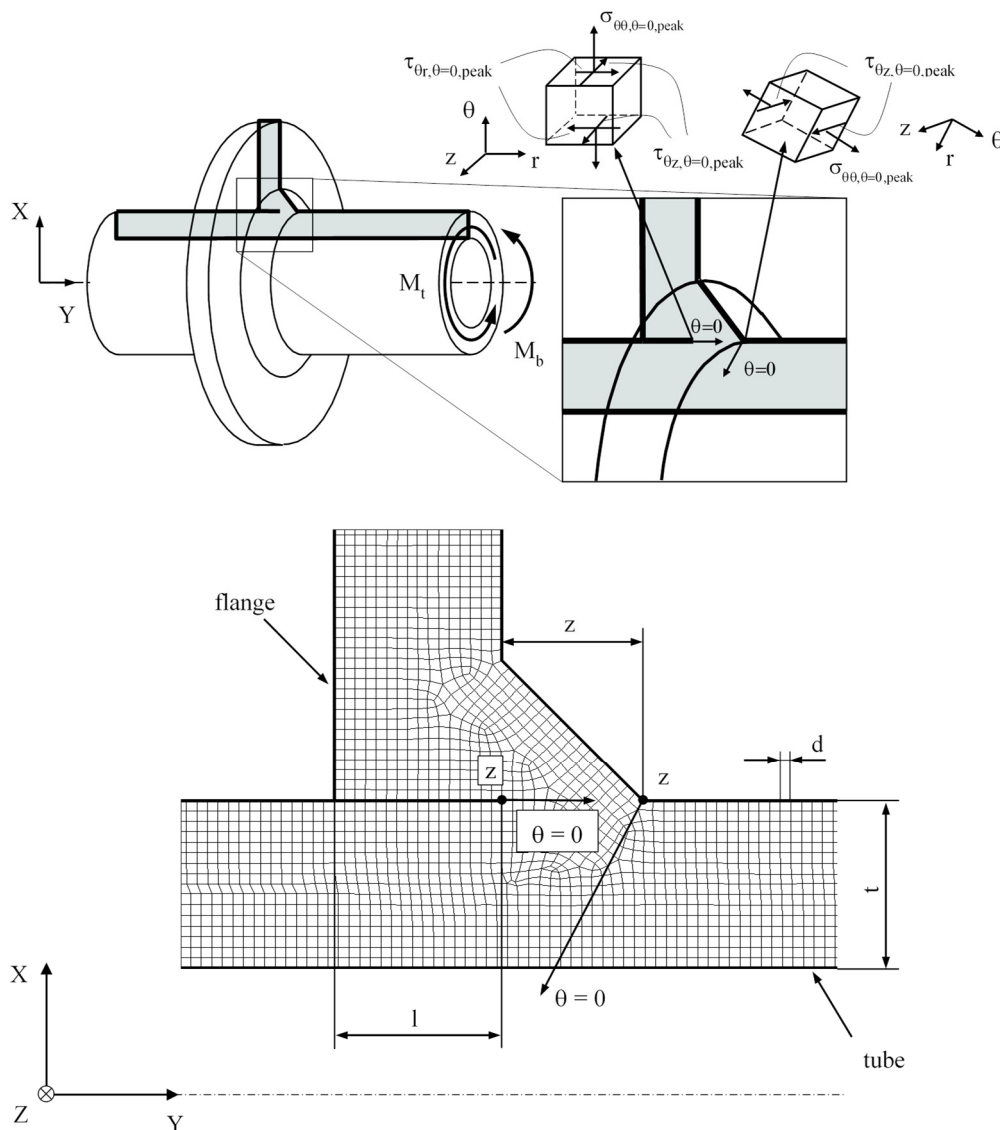


Figure 2.1: Typical 2D FE mesh to apply the PSM according to Eq. (11); the example reported in the figure shows a tube-to-flange fillet welded joint. The four-node, quadrilateral, harmonic PLANE 25 elements available in Ansys® Element Library were adopted to generate the free mesh shown in the figure. The Y-axis coincides with the axis of the tube. [Figure taken from [1]]

The condition of applicability by using ANSYS® FE code were summarized in Table 1. It is worth noting that Eqs. (1)-(3) should be recalibrated if FE meshes of higher-order elements or characterised by significantly different mesh patterns as compared to that one reported in Fig. 1 were adopted.

Equations (1)-(3) are useful to a design engineer, because the N-SIFs K_1 , K_2 and K_3 can be rapidly estimated by taking advantage of the FE peak stresses $\sigma_{\theta\theta, \theta=0, \text{peak}}$, $\tau_{r\theta, \theta=0, \text{peak}}$ and $\tau_{\theta z, \theta=0, \text{peak}}$, respectively.

Table 2.1: Conditions for applicability of Eqs. (1)-(3) by using ANSYS® FE code [5,7,9].

	Loading mode		
	Mode I	Mode II	Mode III
Eq.	(1)	(2)	(3)
K_{FE}	$1.38 \pm 3\%$	$3.38 \pm 3\%$	$1.93 \pm 3\%$
2D FE [^]	PLANE 42 or PLANE 182 (K-option 1 set to 3)		PLANE 25
3D FE [^]	SOLID 45 or SOLID 185 (K-option 2 set to 3)		
2α	$0^\circ \leq 2\alpha \leq 135^\circ$	$2\alpha = 0^\circ$	$0^\circ \leq 2\alpha \leq 135^\circ$
Minimum a/d	3	14	3 (toe, $2\alpha \cong 135^\circ$) 12 (root, $2\alpha = 0^\circ$)
a – root side [°]	$a = \min\{l, z\}$	$a = \min\{l, z\}$	$a = \min\{l, z, t\}$
a – toe side [°]	$a = t$	-	$a = t$

[^] finite elements of Ansys® Element Library

[°] l, z, t are defined in Fig. 1

2.1.1 Definition of PSM-Based design stress for multiaxial loadings by using the SED criterion

By using the PSM relationships (Eqs. (1)-(3)), the averaged SED can be rewritten as a function of the singular, linear elastic FE peak stresses $\sigma_{\theta\theta, \theta=0, \text{peak}}$, $\tau_{r\theta, \theta=0, \text{peak}}$ and $\tau_{\theta z, \theta=0, \text{peak}}$. Then, taking advantage of the equality $W = (1 - \nu^2) \sigma_{\text{eq, peak}}^2 / 2E$ valid under plane strain conditions, it can be written:

$$\Delta \bar{W} = c_{w1} \frac{e_1}{E} \left[K_{FE}^* \cdot \Delta \sigma_{\theta\theta, \theta=0, \text{peak}} \cdot \left(\frac{d}{R_0} \right)^{1-\lambda_1} \right]^2 + c_{w2} \frac{e_2}{E} \left[K_{FE}^{**} \cdot \Delta \tau_{r\theta, \theta=0, \text{peak}} \cdot \left(\frac{d}{R_0} \right)^{1-\lambda_2} \right]^2 + c_{w3} \frac{e_3}{E} \left[K_{FE}^{***} \cdot \Delta \tau_{\theta z, \theta=0, \text{peak}} \cdot \left(\frac{d}{R_0} \right)^{1-\lambda_3} \right]^2 \rightarrow = \frac{1-\nu^2}{2E} \Delta \sigma_{\text{eq, peak}}^2 \quad (4)$$

Therefore, the following expression of the equivalent peak stress is obtained:

$$\Delta\sigma_{\text{eq,peak}} = \sqrt{c_{w1} \cdot f_{w1}^2 \cdot \Delta\sigma_{\theta\theta,\theta=0,\text{peak}}^2 + c_{w2} \cdot f_{w2}^2 \cdot \Delta\tau_{r\theta,\theta=0,\text{peak}}^2 + c_{w3} \cdot f_{w3}^2 \cdot \Delta\tau_{\theta z,\theta=0,\text{peak}}^2} \quad (5)$$

The parameters f_{w1} , f_{w2} and f_{w3} weight the peak stresses both around the notch tip and along the radial direction, i.e. θ and r coordinates, respectively (see Fig. (1)). By comparing Eqs. (4) and (5), the coefficients f_{w1} , f_{w2} and f_{w3} are defined as follows:

$$f_{w1} = K_{\text{FE}}^* \cdot \sqrt{\frac{2e_1}{1-\nu^2}} \cdot \left(\frac{d}{R_0}\right)^{1-\lambda_1} \quad (6a)$$

$$f_{w2} = K_{\text{FE}}^{**} \cdot \sqrt{\frac{2e_2}{1-\nu^2}} \cdot \left(\frac{d}{R_0}\right)^{1-\lambda_2} \quad (6b)$$

$$f_{w3} = K_{\text{FE}}^{***} \cdot \sqrt{\frac{2e_3}{1-\nu^2}} \cdot \left(\frac{d}{R_0}\right)^{1-\lambda_3} \quad (6c)$$

The values of f_{w1} , f_{w2} and f_{w3} are reported in Tables 2-4 respectively, according to Eq. (6) for three values of the average FE size ($d = 0.2$ mm, 0.50 mm and 1 mm), different notch opening angles 2α and two values of the control radius for SED evaluation (i.e. $R_0 = 0.28$ mm for structural steels and 0.12 mm for aluminium alloys) [12,13]. It's worth noticing that f_{w1} , f_{w2} , and f_{w3} , as well as the peak stresses depend on the adopted FE size d , while the equivalent peak stress defined by Eq. (5) does not. When stress components related to mode II loading are null (for instance: pure mode I at the weld root) or non-singular (for example: at the toe side as far as $2\alpha > 102^\circ$ [14,15]), the equivalent peak stress, Eq. (5), can be simplified as follow:

$$\Delta\sigma_{\text{eq,peak}} = \sqrt{c_{w1} \cdot f_{w1}^2 \cdot \Delta\sigma_{\theta\theta,\theta=0,\text{peak}}^2 + c_{w3} \cdot f_{w3}^2 \cdot \Delta\tau_{\theta z,\theta=0,\text{peak}}^2} \quad (7)$$

As aforementioned, in case of as-welded joints tested at any nominal load ratio R , Eqs. (5) and (7) simplify to Eqs. (8) and (9), respectively:

$$\Delta\sigma_{\text{eq,peak}} = \sqrt{f_{w1}^2 \cdot \Delta\sigma_{\theta\theta,\theta=0,\text{peak}}^2 + f_{w2}^2 \cdot \Delta\tau_{r\theta,\theta=0,\text{peak}}^2 + f_{w3}^2 \cdot \Delta\tau_{\theta z,\theta=0,\text{peak}}^2} \quad (8)$$

$$\Delta\sigma_{\text{eq,peak}} = \sqrt{f_{w1}^2 \cdot \Delta\sigma_{\theta\theta,\theta=0,\text{peak}}^2 + f_{w3}^2 \cdot \Delta\tau_{\theta z,\theta=0,\text{peak}}^2} \quad (9)$$

in which, the correction factors c_{wi} ($i = 1, 2, 3$) are equal to 1.

Table 2.2: Values of constants and of parameter f_{w1} according to Eq. (6a).

2α (deg)	$\lambda_1^{(a)}$	$e_1^{(b)}$	$R_0 = 0.28$ mm		$e_1^{(c)}$	$R_0 = 0.12$ mm	
			$f_{w1,d=0.5mm}^{(b)}$	$f_{w1,d=1mm}^{(b)}$		$f_{w1,d=0.2mm}^{(c)}$	$f_{w1,d=1mm}^{(c)}$
0	0.500	0.133	0.997	1.410	0.125	0.944	2.109
90	0.544	0.145	1.015	1.392	0.138	0.969	2.019
120	0.616	0.129	0.918	1.198	0.124	0.886	1.644
135	0.674	0.118	0.849	1.064	0.113	0.821	1.387

(a): values from [13,14,37]

(b): values calculated with $\nu = 0.3$, $K_{FE}^* = 1.38$

(c): values calculated with $\nu = 0.33$, $K_{FE}^* = 1.38$

Table 2.3: Values of constants and of parameter f_{w2} according to Eq. (6b).

2α (deg)	$\lambda_2^{(a)}$	$e_2^{(b)}$	$R_0 = 0.28$ mm		$e_2^{(c)}$	$R_0 = 0.12$ mm	
			$f_{w2,d=0.5mm}^{(b)}$	$f_{w2,d=1mm}^{(b)}$		$f_{w2,d=0.2mm}^{(c)}$	$f_{w2,d=1mm}^{(c)}$
0	0.500	0.340	3.904	5.522	0.337	3.795	8.480

(a): value from [13,14,37]

(b): values calculated with $\nu = 0.3$, $K_{FE}^{**} = 3.38$

(c): values calculated with $\nu = 0.33$, $K_{FE}^{**} = 3.38$

Table 2.4: Values of constants and of parameter f_{w3} according to Eq. (6c).

2α (deg)	$\lambda_3^{(a)}$	$e_3^{(b)}$	$R_0 = 0.28$ mm		$e_3^{(c)}$	$R_0 = 0.12$ mm	
			$f_{w3,d=0.5mm}^{(b)}$	$f_{w3,d=1mm}^{(b)}$		$f_{w3,d=0.2mm}^{(c)}$	$f_{w3,d=1mm}^{(c)}$
0	0.500	0.414	2.459	3.478	0.423	2.428	5.431
90	0.666	0.310	1.933	2.436	0.317	1.931	3.303
120	0.750	0.276	1.737	2.065	0.282	1.745	2.610
135	0.800	0.259	1.634	1.877	0.265	1.649	2.273

(a): values from [14]

(b): values calculated with $\nu = 0.3$, $K_{FE}^{***} = 1.93$

(c): values calculated with $\nu = 0.33$, $K_{FE}^{***} = 1.93$

2.1.2 Special cases of equivalent peak stress

Previous Eqs. (5), (7)-(9) are valid when the weld toe and the weld root profiles can be assumed as sharp V-notches (notch tip radius $\rho \approx 0$), i.e. when local stresses are singular. If these cases are not satisfied, then the analytical expressions should be updated.

More precisely, when the weld toe radius is large enough to induce full notch sensitivity (see as an example Fig. 2 [16]), the equivalent peak stress at the weld toe must be evaluated according to the following expression:

$$\Delta \bar{W} = c_{w1} \cdot \frac{1-\nu^2}{2E} \cdot \Delta \sigma_{\max}^2 + c_{w3} \cdot \frac{(1+\nu) \cdot \Delta \tau_{\max}^2}{E} \Rightarrow \frac{1-\nu^2}{2E} \cdot \Delta \sigma_{\text{eq,peak}}^2$$

$$\Delta \sigma_{\text{eq,peak}} = \sqrt{c_{w1} \cdot \Delta \sigma_{\max}^2 + c_{w3} \cdot \frac{2 \cdot \Delta \tau_{\max}^2}{1-\nu}}$$
(10)

where σ_{\max} and τ_{\max} are the maximum values of the tension and torsion stresses, respectively, evaluated at the weld toe with sufficiently refined FE meshes (see Fig. 2), as it is required to evaluate the stress concentration factor.

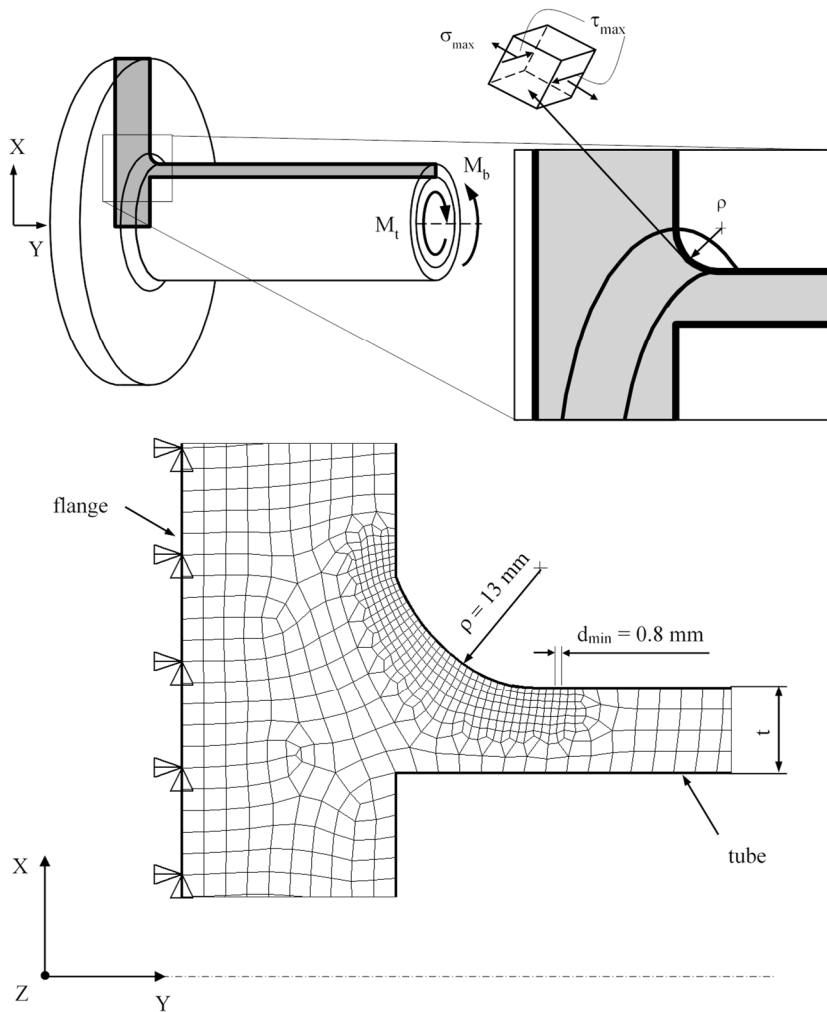


Figure 2.2: 2D FE mesh to apply the PSM according to Eq. (10); the example reported in the figure shows a tube-to-flange full penetration welded joint [16] with a large toe radius ($\rho = 13$ mm). Four-node, quadrilateral, harmonic PLANE 25 elements available in Ansys® Element Library were adopted to generate the free mesh shown in the figure. The Y-axis is the axis of the tube. [Figure taken from [1]]

Another special case, which is not covered by Eqs (5), (7)-(9), is that of box-beam fillet-welded joints under combined bending and torsion multiaxial fatigue loadings shown in Fig. 3 [17].

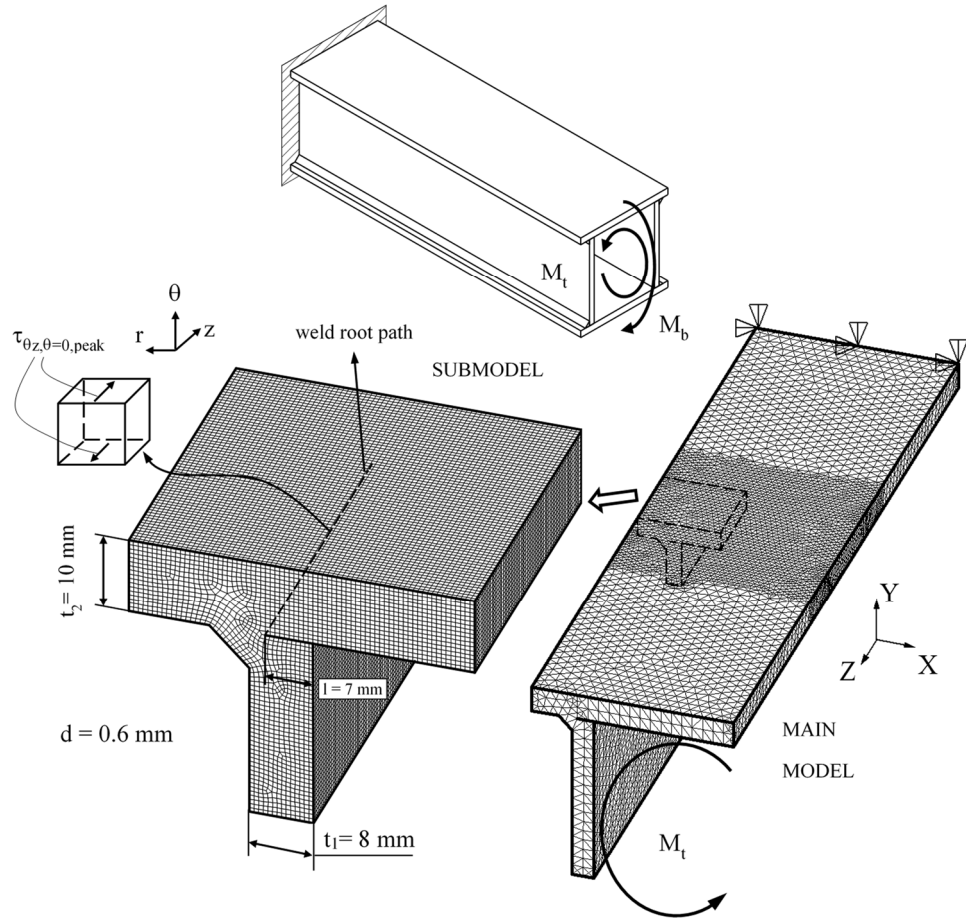


Figure 2.3 3D FE mesh to apply the PSM according to Eq. (11); the example reported in the figure shows a box-beam fillet-welded joint [17]. Eight node brick SOLID 185 elements (with K-option 2 set to 3) available in Ansys® Element Library were adopted to generate the 3D mesh of the submodel shown in the figure. [Figure taken from [1]]

In this case, since the mode I bending stresses are parallel to the weld toe as well as to the weld root paths, they are not singular neither at the weld toe nor at the weld root. By considering the mode I, non-singular, nominal bending stress (σ_{nom}) and the mode III, singular, torsional shear stress ($\tau_{\theta z, \theta=0, peak}$), the equivalent peak stress can be evaluated by using the following expression:

$$\Delta \bar{W} = c_{w1} \cdot \frac{\Delta \sigma_{nom}^2}{2E} + c_{w3} \frac{e_3}{E} \left[\mathbf{K}_{FE}^{***} \cdot \Delta \tau_{\theta z, \theta=0, peak} \cdot \left(\frac{d}{R_0} \right)^{1-\lambda_3} \right]^2 \rightarrow \frac{1-\nu^2}{2E} \cdot \Delta \sigma_{eq, peak}^2$$

$$\Delta \sigma_{eq, peak} = \sqrt{c_{w1} \cdot \frac{\Delta \sigma_{nom}^2}{1-\nu^2} + c_{w3} \cdot f_{w3}^2 \cdot \Delta \tau_{\theta z, \theta=0, peak}^2} \quad (11)$$

in which the nominal stress (σ_{nom}) can be evaluated analytically from classical expressions of solid mechanics, while the singular one ($\tau_{\theta z, \theta=0, peak}$) must be calculated from FE analyses according to the PSM as illustrated in previous Fig. (1).

A further special case is investigated in the following. Eq.s (4) and (5) (chapter 1) sum up the strain energies due to mode I, mode II and mode III singular stresses, because the relevant energy contributions are independent one from the other. Therefore, strictly speaking, they are not applicable when multiple load components do not allow to treat the strain energy as an additive quantity, due to the existence of coupling terms.

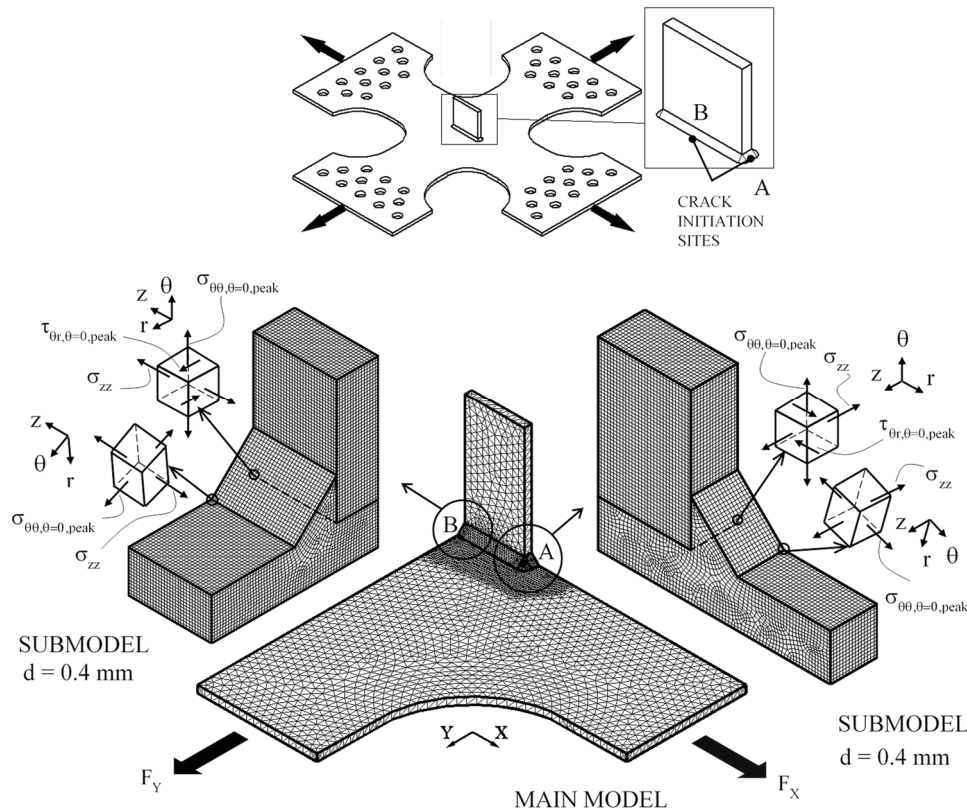


Figure 2.4. 3D FE mesh to apply the PSM according to Eq. (18c); the example reported in the figure shows a plate having a box-welded (wrap-around) joint [27,28]. Eight node brick SOLID 185 elements (with K-option 2 set to 3) available in Ansys® Element Library were adopted to generate the 3D mesh of the submodels shown in the figure. [Figure taken from [1]]

Obviously, the same limitation of applicability applies to Eqs (5) and (7)-(9), they having been derived from Eqs (4) and (5) (chapter 1). However, the summation of energy contribution was seen to be still effective in the design cases analysed in the present work, after having compared it with the averaged SED calculated by modelling the control volume at the relevant weld root and toe which can take into account the coupling terms. An example of such situation is depicted in Fig. 4. It is reported a plate having a box-welded (wrap-around) joint subjected to biaxial fatigue loading due to two orthogonal forces (F_X and F_Y in Fig. 4). The two external forces F_X and F_Y are analysed separately and strain energies due to any single load component are simply added, which is not correct, strictly speaking. Let us consider the weld root side at point A. The single force F_X generates mode I and mode II singular stresses; the single force F_Y generates mode I, mode II singular stresses and also σ_{zz} non-singular stresses (referred to the local coordinate system (r, θ, z) , Fig. 4). Considering the root side at

point B, the single force F_X generates mode I, mode II singular stresses and σ_{zz} non-singular stresses, while F_Y generates mode I and mode II singular stresses. The total averaged SED, $\Delta\bar{W}$ is evaluated by summing the contributions due to the forces F_X and F_Y applied individually:

$$\Delta\bar{W} = \Delta\bar{W}_{F_X} + \Delta\bar{W}_{F_Y} \quad (12a)$$

Now, the general expression applied at point A as well as at point B is the following:

$$\begin{aligned} \Delta\bar{W}_{F_X} &= c_{w,F_X} \left\{ \frac{e_1}{E} \left[K_{FE}^* \cdot \Delta\sigma_{\theta\theta,\theta=0,\text{peak}} \cdot \left(\frac{d}{R_0} \right)^{1-\lambda_1} \right]^2 + \frac{e_2}{E} \left[K_{FE}^{**} \cdot \Delta\tau_{r\theta,\theta=0,\text{peak}} \cdot \left(\frac{d}{R_0} \right)^{1-\lambda_2} \right]^2 + \frac{\Delta\sigma_{zz}^2}{2E} \right\}_{F_X} \\ \Delta\bar{W}_{F_Y} &= c_{w,F_Y} \left\{ \frac{e_1}{E} \left[K_{FE}^* \cdot \Delta\sigma_{\theta\theta,\theta=0,\text{peak}} \cdot \left(\frac{d}{R_0} \right)^{1-\lambda_1} \right]^2 + \frac{e_2}{E} \left[K_{FE}^{**} \cdot \Delta\tau_{r\theta,\theta=0,\text{peak}} \cdot \left(\frac{d}{R_0} \right)^{1-\lambda_2} \right]^2 + \frac{\Delta\sigma_{zz}^2}{2E} \right\}_{F_Y} \end{aligned} \quad (12b)$$

Furthermore, the contributions due to non-singular stresses (σ_{zz}) were evaluated and resulted to be negligible in Eq. (12b); therefore, the equivalent peak stress was derived from Eq. (12a) as follows:

$$\begin{aligned} \Delta\bar{W} &= \frac{1-\nu^2}{2E} \Delta\sigma_{\text{eq,peak}}^2 \rightarrow \\ \Delta\sigma_{\text{eq,peak}} &= \sqrt{c_{w,F_X} \left\{ f_{w1}^2 \cdot \Delta\sigma_{\theta\theta,\theta=0,\text{peak}}^2 + f_{w2}^2 \cdot \Delta\tau_{r\theta,\theta=0,\text{peak}}^2 \right\}_{F_X} + c_{w,F_Y} \left\{ f_{w1}^2 \cdot \Delta\sigma_{\theta\theta,\theta=0,\text{peak}}^2 + f_{w2}^2 \cdot \Delta\tau_{r\theta,\theta=0,\text{peak}}^2 \right\}_{F_Y}} \end{aligned} \quad (12c)$$

2.2 GEOMETRIES AND PSM FE-MODELS

2.2.1 Steel welded joints

Fatigue test data from the literature, on steel welded joints subjected to pure axial, pure bending, pure torsion and multiaxial fatigue loadings are analysed here. All the information about the materials, welding processes and testing conditions of all the considered steel welded joints were reported in Table 5.

Only the contributions in which the authors have reported either the external loads or the expression used for calculating the stresses in the welded joint were considered. This was a fundamental requirement for obtaining the force values necessary in FE model without making any assumption. Therefore, according to the original contributions, the following classical expression for evaluating the axial, bending and torsion nominal stresses in the tubes were adopted:

$$\sigma_{\text{nom,axial}} = \frac{F}{A} = \frac{F}{\frac{\pi}{4} \cdot [d_e^2 - (d_e - 2t)^2]} \quad (13a)$$

$$\sigma_{\text{nom,bending}} = \frac{M_f}{W_f} = \frac{M_f}{\frac{\pi}{32} \cdot \frac{d_e^4 - (d_e - 2t)^4}{d_e}} \quad (13b)$$

$$\tau_{\text{nom}} = \frac{M_t}{W_t} = \frac{M_t}{\frac{\pi}{16} \cdot \frac{d_e^4 - (d_e - 2t)^4}{d_e}} \quad (13c)$$

where F is the axial load, M_f and M_t are the bending and torsional moment, respectively, A is the section area, W_f and W_t are the section moduli, d_e is the tube outer diameter and t is the tube thickness.

Table 2.5: Information about materials, welding processes and testing conditions of steel welded joints taken from the literature.

Ref.	Joint * geometry	Material	Yield strength [MPa]	Ultimate strength [MPa]	Welding process	Testing condition	ρ weld toe [mm]
Siljander et al. [19]	(1)	A519 tube A36 flange	414 tube 250 flange	483 tube 550 flange	MIG	Stress-relieved	0.18
Razmjoo [20]	(2a-2b)	BS 4360-50E	415	577	MMA	As-welded	-
Yousefi et al. [21]	(3)	P 460	520	670	MIG	Stress-relieved	-
Bäckström et al. [22]	(4)	Fe 52	355	490-630	MIG	As-welded	-
Dahle et al. [17]	(5)	DOMEX 350	350	-	MAG	As-welded	-
Sonsino et al. [23,24]	(6)	StE 460	520	670	MAG	Stress-relieved	0.2÷0.8
Bertini et al. [25,26]	(7a-7b)	S355 JR	360	520	-	As-welded	-
Takahashi et al. [27,28]	(8a-8b)	JIS SM400B	283	432	MAG	As-welded	-

*All joints have un-machined welds.

The geometry of the steel welded and the details of the FE model according to the PSM were gathered in Table 6. In the case of axis-symmetric joint geometry (see models 1-3, 6 and 7 of Table 6), a free mesh pattern of 2D quadrilateral four-node harmonic elements (PLANE 25 of the ANSYS® element library) was used to evaluate the peak stresses both at the weld root and at the weld toe sides. Regarding the more complex, non axis-symmetric joint geometries (see models 4, 5 and 8 of Table 2), 3D FE models were needed to calculate the equivalent peak stress, according to the three-dimensional PSM described in [6,18]. In particular, first the whole joint geometry was modelled and solved by means of a main model; subsequently, a submodel of the

critical area of the joint (the weld toe or weld root) was solved by adopting the submodelling technique available in Ansys® numerical software.

Table 2.6: Steel welded joint geometries and FE analyses for fatigue strength assessment according to the PSM [2].

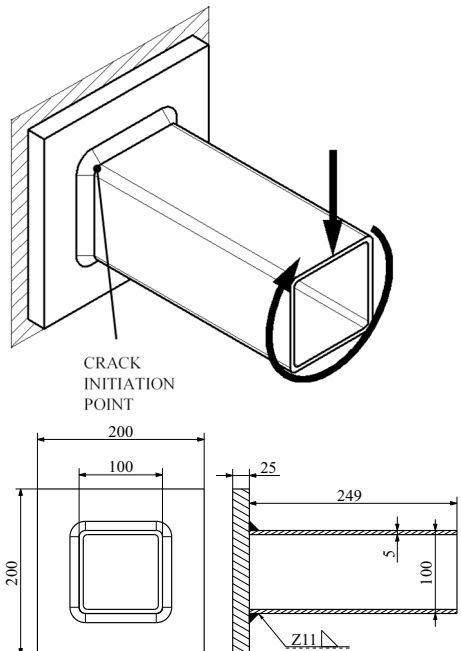
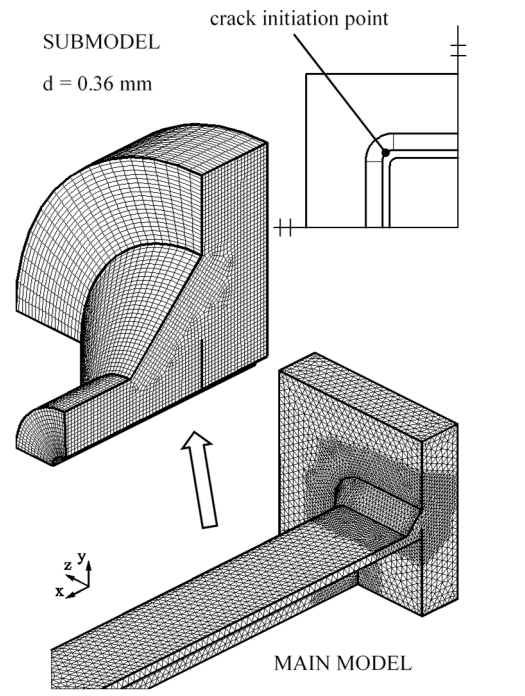
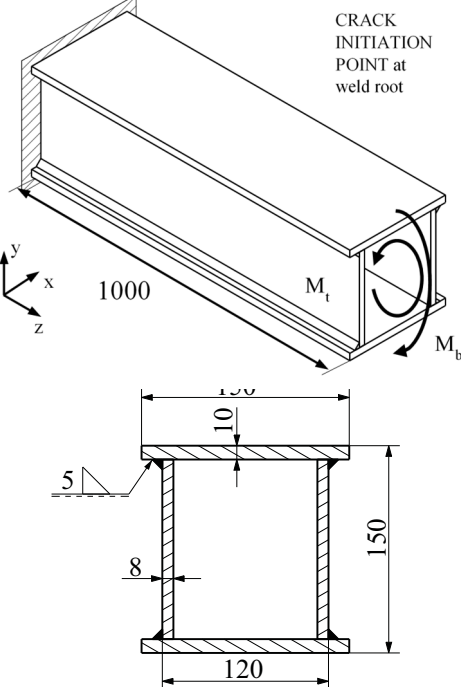
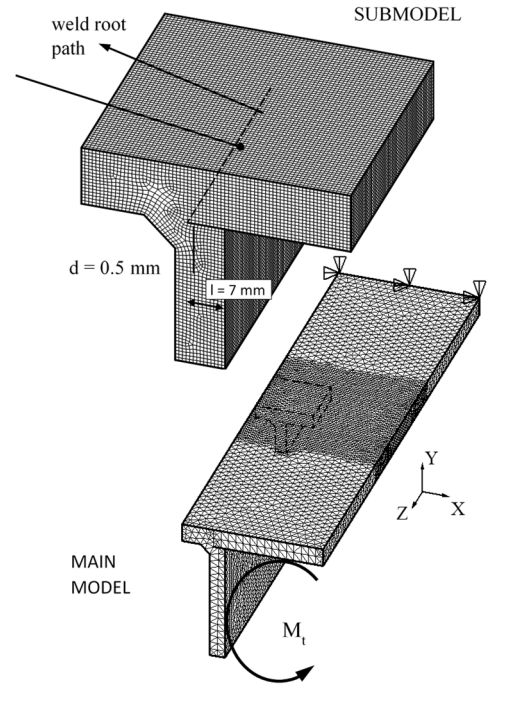
Ref.	Joint * geometry	Material
Model 1 [19]	<p>Geometric drawing of Model 1 joint. It shows a cylindrical tube of diameter $\phi 50.8$ mm welded to a flange. The total length of the tube is 355 mm, with a section of 230 mm. The flange thickness is 114.3 mm. A crack initiation point is indicated at the weld toe. Dimensions include 9.525 mm for the distance from the end to the crack, 9.525 mm for the distance from the crack to the end of the 230 mm section, and a 12 mm fillet radius. A tack weld is also shown.</p>	<p>FE mesh and detail of Model 1 joint. The mesh shows a crack of length $d = 0.57$ mm. The crack is oriented at $\theta = 0$ degrees. The detail shows the weld root and weld toe, with a tube thickness $t = 9.5$ mm. The flange is also shown.</p>
Model 2a [20]	<p>Geometric drawing of Model 2a joint. It shows a cylindrical tube of diameter $\phi 120$ mm welded to a flange. The total length of the tube is 400 mm, with a section of 352 mm. The flange thickness is 48.6 mm. A crack initiation point is indicated at the weld toe. Dimensions include 12 mm for the distance from the end to the crack, 7 mm for the distance from the crack to the end of the 352 mm section, and 3.2 mm for the distance from the crack to the end of the tube. A Z111 fillet is also shown.</p>	<p>FE mesh and detail of Model 2a joint. The mesh shows a crack of length $d = 0.27$ mm. The crack is oriented at $\theta = 0$ degrees. The detail shows the weld root and weld toe, with a tube thickness $t = 9.5$ mm. The flange is also shown.</p>

Table 6 (continued)

Ref.	Joint + geometry	Material
Model 2b [20]		
Model 3 [21]		

The main model can be meshed by employing a free mesh of second-order, ten-node tetra elements (SOLID 95 or equivalently SOLID 187 of the Ansys® element library), as shown for example in the main model 8a of Table 6. After that, the submodel was defined by “cutting” the main model at a distance from the weld toe and root equal to one main plate or tube thickness (see sub model 8a of Table 6).

Table 6 (continued)

Ref.	Joint * geometry	Material
Model 4 [22]	 <p>CRACK INITIATION POINT</p> <p>200</p> <p>100</p> <p>25</p> <p>249</p> <p>100</p> <p>200</p>	<p>SUBMODEL</p> <p>crack initiation point</p> <p>$d = 0.36 \text{ mm}$</p>  <p>MAIN MODEL</p>
Model 5 [17]	 <p>CRACK INITIATION POINT at weld root</p> <p>1000</p> <p>10</p> <p>5</p> <p>8</p> <p>120</p> <p>150</p> <p>M_t</p> <p>M_b</p>	<p>SUBMODEL</p> <p>weld root path</p> <p>$d = 0.5 \text{ mm}$</p> <p>$l = 7 \text{ mm}$</p>  <p>MAIN MODEL</p> <p>M_t</p>

In order to obtain the standard 2D mesh pattern required by the PSM in a 3D solid geometry, first, a 2D free mesh pattern of quadrilateral four-node PLANE 182 elements having average size d was generated (see X-Z plane of the sub model 8a); then, the 2D FE mesh was extruded (along Y axis in the case of sub model 8a) by

setting an extrusion step size equal to the average element size d and by using 3D eight-node brick elements (SOLID45 of the Ansys® element library or equivalently SOLID185 with K-option 2 set to 3).

Table 6 (continued)

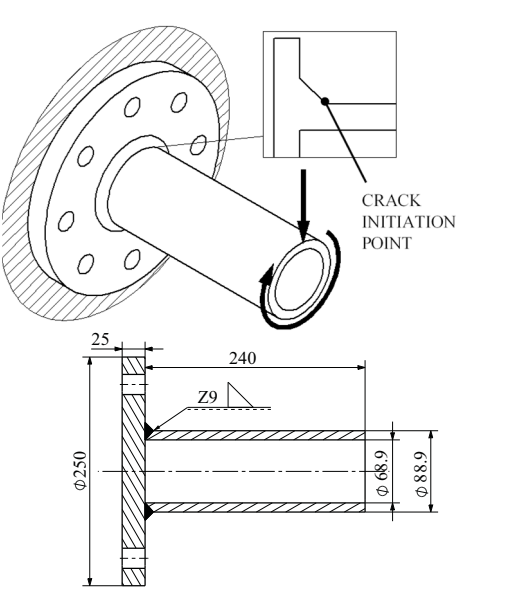
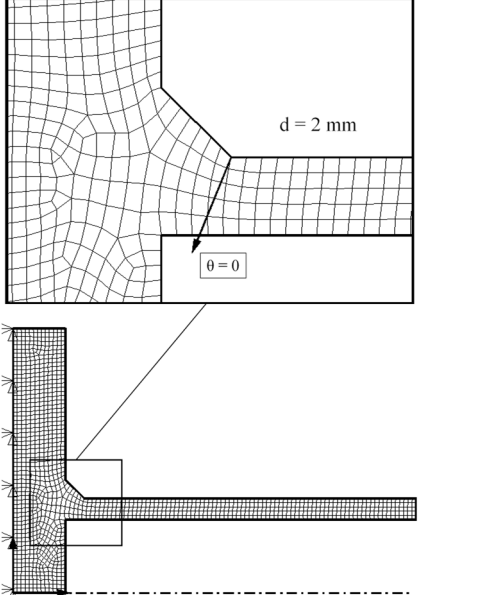
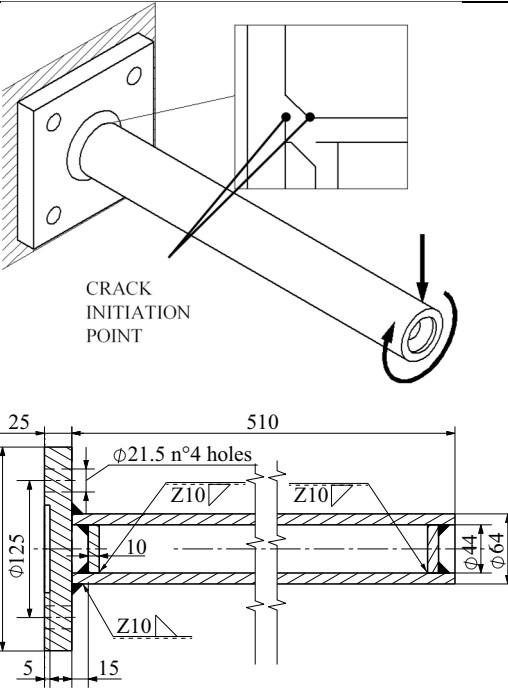
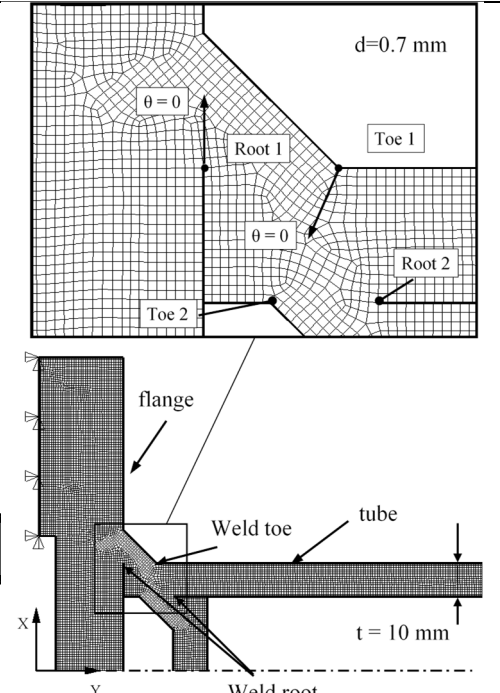
Ref.	Joint * geometry	Material
Model 6 [23,24]		
Model 7 [25]		

Table 7 reports for each model the average FE mesh size required in order to comply with the conditions of applicability of the PSM at the weld root and toe, respectively, while the adopted FE mesh size d has been reported in the last column.

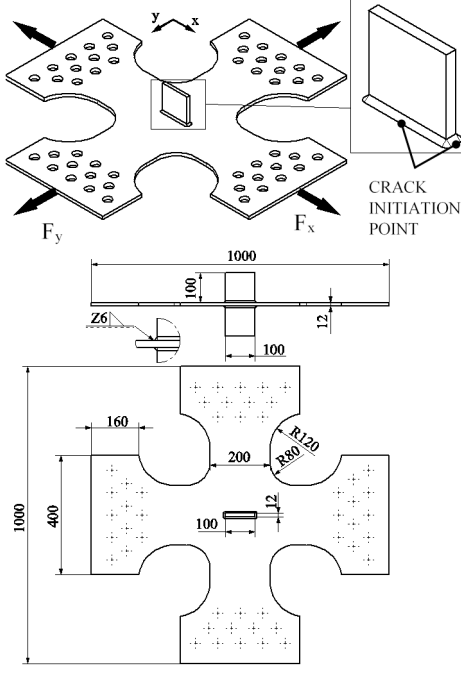
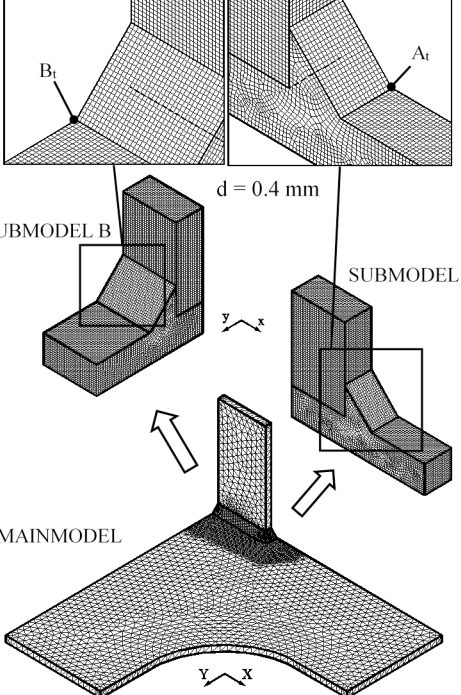
Table 6 (continued)

Ref.	Joint * geometry	Material
Model 7b [26]		
Model 8a [27]		

Regarding the example model 8a of Table 6, a d equal to $6/14 \approx 0.4$ mm was adopted, in which a mesh density ratio $a/d \geq 14$ was the most demanding condition for the applicability of the PSM concerning the weld root under mode II loading, where $a = 6$ mm is the ligament length.

In the following, specific details regarding the experimental fatigue tests and the analysis procedure of each test series were reported.

Table 6 (continued)

Ref.	Joint * geometry	Material
Model 8b [28]		

Siljander et al. [19]

In this contribution tube-to-flange steel fillet-welded joints (model 1 in Table 6) fatigue test data under completely reversed ($R = -1$) and pulsating ($R = 0$) cyclic loadings were reported. The experimental tests were performed applying pure bending, pure torsion and combined in-phase ($\phi = 0^\circ$) as well as out-of-phase (see the loading paths in Fig. 5a and b)) bending-torsion fatigue loadings. Several biaxiality ratios A (A being defined by the ratio σ_{nom}/τ_{nom}) were also analysed, as reported in Table 8. Each test was stopped after having obtained a crack longer than 10 mm [19]. The singular, linear elastic peak stresses were calculated at the weld toe and weld root from 2D axis-symmetric FE models, in which coarse FE mesh patterns according to the PSM have been adopted. The mesh density ratio a/d was chosen equal to 14 to comply with the conditions of applicability of the PSM at the root side in presence of mode II stresses (see Table 7), so that an average element size d equal to $8/14 \approx 0.57$ mm has been adopted, $a = 8$ mm being the ligament length. Due to the reduced weld toe radius ($\rho \approx$

0.18 mm), the worst case assumption $\rho = 0$ was made in the FE analyses and both the toe and the root sides were modelled as sharp notches (V-shaped or crack-like).

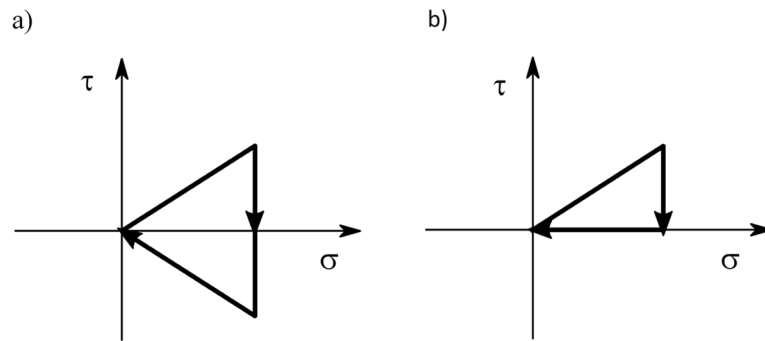


Figure 2.5: Nominal loading paths adopted in out-phase multiaxial fatigue tests in [19]. [Figure taken from [1]]

Table 2.7: Average FE mesh size required in order to comply with the conditions of applicability of the PSM at the weld root and toe, and finally adopted FE mesh size d [2].

Model	d required at root [mm]			d required at toe [mm]		d adopted [mm]
	mode I*	mode II ^o	mode III ⁺	mode I**	mode III**	
(1)	2.67	0.57	0.67	3.17	3.17	0.57
(2a)	3.67	-	0.27	1.07	1.07	0.27
(2b)	-	-	0.58	-	2.33	0.58
(3)	0.33	0.07	0.08	2.67	2.67	0.07
(4)	1.67	0.36	0.42	1.67	1.67	0.36
(5)	-	-	0.50	-	2.67	0.50
(6)	-	-	-	3.33	3.33	2.00
(7a)	3.33	0.71	0.83	3.33	3.33	0.70
(7b)	3.33	0.71	0.83	3.33	3.33	0.70
(8a)	2.00	0.43	-	4.00	-	0.40
(8b)	2.00	0.43	-	4.00	-	0.40

* $a/d \geq 3$, $a = \min\{l, z\}$

^o $a/d \geq 14$, $a = \min\{l, z\}$

⁺ $a/d \geq 12$, $a = \min\{l, z, t\}$

l, z, t are defined in Fig. 1 of Chapter 1

** $a/d \geq 3$, $a = t$

The testing conditions of the joints were not described in detail in the original work [19]. Indeed, it was not explicitly reported where the tube was fixed but it can be deduced that the rear area of the tube was fixed, as shown in Table 6 (model 1).

All tube-to-flange joints were tested under stress-relieved conditions, therefore the equivalent peak stress was calculated at the root side by means of Eq. (7), while Eq. (7) was adopted at the toe side since mode II stresses are non-singular there ($2\alpha > 102^\circ$ [14,15]). According to Siljander et al. [19], fatigue crack initiation always occurred at the toe side. Table 8 highlights that the crack initiation location is properly assessed by means of the PSM, since the equivalent peak stress $\sigma_{eq,peak}$ is always higher at the toe than at the root side. Should the designer have been interested only in fatigue assessment of the weld toe, Table 7 highlights that an increased average FE size equal to 3 mm (in place of 0.57 mm) could have been adopted.

Razmjoo [20], tube-to-flange joints

In [20] the fatigue behaviour of two geometries of tube-to-flange steel fillet-welded joints under pulsating ($R = 0$) fatigue loadings was reported. The joints with 3.2-mm-thick tube (model 2a in Table 6, $t = 3.2$ mm) were subjected to pure tension and combined tension-torsion fatigue loadings with different biaxiality ratios A and with different phase shift angle between the cyclic tension and torsion signal ($\phi = 0^\circ$ and $\phi = 90^\circ$). The joints with 7-mm-thick tube (model 2b in Table 6, $t = 7$ mm) were only subjected to pure torsion fatigue loading. Table 8 reports the synthesis of the loading conditions. Razmjoo [20] reported the number of cycles relevant to the complete separation of the joints.

The numerical analyses consisted in two-dimensional axis-symmetric FE models with coarse meshes according to the PSM were carried out to evaluate the peak stresses at the toe and root sides. The mesh density ratio $a/d \geq 12$ being the most demanding condition for the applicability of the PSM at the root side under mode III loading (see Table 7), an average element size d equal to $3.2/12 \approx 0.27$ mm and $7/12 \approx 0.58$ mm has been adopted for the 3.2-mm-thick and the 7-mm-thick joint geometry (model 2a and 2b in Table 6), respectively. The connection between the flange and the test bench was implemented constraining all the degree of freedom at the back surface of the flange, as indicated in Table 6 (models 2a and 2b).

All specimens were tested in the as-welded condition, so Eq. (8) was adopted to calculate the equivalent peak stress at the weld root, while Eq. (9) was used at the weld toe due to the V-notch opening angle $2\alpha > 102^\circ$.

For the model 2a the fatigue failure always initiated at the toe side, while in model 2b fatigue crack initiation occurred mainly at the root side [20] as reported in Table 8. Furthermore, from Table 8, it is worth noticing that the prediction of the crack initiation location for model 2a was correctly evaluated by means of the PSM, because the equivalent peak stress $\sigma_{eq,peak}$ was always higher at the weld toe than at the weld root. On the contrary, in the case of model 2b, the PSM anticipates the initiation at the toe side, while experimental results show that only 2 among 8 specimens failed at the toe side.

Table 2.8: Fatigue test details of steel welded joints (joint geometries are reported in Table 6)

Joint geometry	Load condition ^o	$\lambda^{\circ\circ}$	R_σ	R_τ	Phase ϕ [°]	N° failures			$\sigma_{eq,peak}^*$	$\sigma_{eq,peak}^*$	Failure criterion	Applied nominal stresses		
						toe	root	tube	[MPa]	[MPa]		$\Delta\sigma_{nom}$ [MPa]	$\Delta\tau_{nom}$ [MPa]	
1	B	∞	-1	-	-	4	-	-	1.030 [^]	0.820 [^]	10-mm-long crack	220 ÷ 440	-	
	B	∞	0	-	-	5	-	-	1.457 [^]	1.160 [^]		140 ÷ 440	-	
	T	0	-	-1	-	4	-	-	1.759	1.755		-	140 ÷ 220	
	T	0	-	0	-	2	-	-	2.488	2.481		-	170 ÷ 220	
	B+T	7.34	0	0	0	}	9	-	-	10.99		8.879	216	29
										4.279		3.721	174 ÷ 260	73 ÷ 109
										2.883		2.739	80 ÷ 136	80 ÷ 136
	B+T	1.2	0	-1	Fig. 1a	4	-	-	2.480	2.240		174	145	
B+T	2.39	0	0	Fig. 1b	3	-	-	4.279	3.721	174	73			
2a	A	∞	0	-	-	7	-	-	2.256 [^]	1.248 [^]	Complete stiffness loss	100 ÷ 245	-	
	A+T	2	0	0	0	}	7	-	-	5.063		2.584	100	50
										3.219		1.415	80	80
										3.141		1.360	107	113
										3.080		1.317	107	118
										2.786		1.099	80 ÷ 82	115 ÷ 118
										2.420		0.790	54	160
										2.420		0.790	54	160
	A+T	2	0	0	90	}	7	-	-	5.063		2.584	100	50
										3.886		1.858	160	115
										3.348		1.504	211	195
										3.219		1.415	80	80
										3.110		1.338	107	115
										2.786		1.099	80	115
										2.420		0.790	54	160
2.420										0.790	54	160		
2b	T	0	-	0	-	2	6	-	2.664	1.579	-	105 ÷ 158		
3	B	∞	-1	-	-	16	-	-	1.856 [^]	1.223 [^]	break-through	104 ÷ 41	-	
	B	∞	0	-	-	6	-	-	2.624 [^]	1.729 [^]		93 ÷ 310	-	
	T	0	-	-1	-	9	-	-	1.985	1.258		-	121 ÷ 201	
	T	0	-	0	-	9	-	-	2.808	1.779		-	104 ÷ 152	
	B+T	1	-1	-1	0	7	-	-	2.718	1.754		73 ÷ 156	73 ÷ 156	
	B+T	1	0	0	0	7	-	-	3.843	2.481		72 ÷ 179	72 ÷ 179	
	B+T	1	-1	-1	90	8	-	-	2.718	1.754		70 ÷ 110	70 ÷ 110	
	B+T	1	0	0	90	9	-	-	3.843	2.481		73 ÷ 156	73 ÷ 156	

^o axial (A), bending (B), torsion (T)

^o $\lambda = \sigma_{nom}/\tau_{nom}$

* calculated with $\tau_{nom} = 1$ MPa, λ as indicated.

[^] calculated with $\sigma_{nom} = 1$ MPa

Table 2.8 (continued)

Joint geometry	Load condition ^o	λ	R_σ	R_τ	Phase ϕ [°]	N° failures			$\sigma_{eq,peak}^*$ toe [MPa]	$\sigma_{eq,peak}^*$ root [MPa]	Failure criterion	Applied nominal stresses		
						toe	root	tube				$\Delta\sigma_{nom}$ [MPa]	$\Delta\tau_{nom}$ [MPa]	
4	B	∞	0.3	-	-	1	-	-	3.565 [^]	2.067 [^]	Complete stiffness loss	266	-	
	B	∞	0.1	-	-	1	-	-				319	-	
	B	∞	0.6	-	-	1	-	-				149	-	
	B	∞	0.7	-	-	2	-	-				98 ÷ 116	-	
	T	0	-	-1	-	-	-	3 [#]	2.758	1.182		-	151 ÷ 327	
	T	0	-	0	-	-	-	1 [#]				-	218	
	B+T	3	-1	-1	0	0	3	-	-	11.04	6.313		414	139
										8.651	4.899		356	155
										4.231	2.204		198	221
	B+T	1.9	-0.8	-1.2	0	1	-	-	7.313	4.102		244	130	
	B+T	1.9	-0.8	-1.3	0	1	-	-				243	129	
	B+T	1.6	0	-0.1	0	1	-	-	6.336	3.512		227	140	
B+T	2.2	0	0	0	3	-	-	8.314	4.699		208 ÷ 348	99 ÷ 160		
B+T	2.3	0	0	90	4	-	-	8.651	4.899		208 ÷ 253	92 ÷ 111		
											<i>Eq. (13b)</i>	<i>Eq. (13c)</i>		
5	B	∞	-1	-	-	3 T ⁺	-	-		1.048 [^]	long crack (200÷500 mm)	194 ÷ 316	-	
	T	0	-	-1	-	-	14 L ⁺	-		6.305		-	111 ÷ 184	
	T	0	-	-1	-	-	5 L ⁺	-				-	131 ÷ 182	
	B+T	0.58	-1	-1	0	3 T ⁺	3 L ⁺	-		6.326			71 ÷ 135	138 ÷ 221
	B+T	0.98	0	0	0	-	1 L ⁺	-		6.326			180	184
	B+T	0.92	-1	-1	90	1 T ⁺	1 L ⁺	2 (L+T) ⁺		6.367			127 ÷ 169	138 ÷ 184
											<i>Eq. (13b)</i>	<i>Eq. (13c)</i>		
6	B	∞	-1	-	-	10	-	-	1.908 [^]	-	crack initiation and break-through	157 ÷ 510	-	
	T	0	-	-1	-	9	-	-	2.034			-	230 ÷ 347	
	B+T	1.72	-1	-1	0	8	-	-	3.861			200 ÷ 270	116 ÷ 156	
	B+T	1.72	-1	-1	90	9	-	-	3.861			149 ÷ 271	86 ÷ 157	
											<i>Eq. (14a)</i>	<i>Eq. (14b)</i>		
7a	B	∞	-1	-	-	10	-	-	4.430 [^]	3.441 [^]	break-through	140 ÷ 229	-	
	B	∞	0	-	-	9	-	-				95 ÷ 214	-	
	T	0	-	-1	-	-	13	-	3.739	4.008		-	111 ÷ 177	
	T	0	-	0	-	-	13	-				-	115 ÷ 192	
	B+T	3.25	-1	-1	0	-	7	-	14.87	11.88		137 ÷ 190	42 ÷ 58	
	B+T	3.25	0	0	0	-	8	-				91 ÷ 194	28 ÷ 60	
	B+T	0.88	-1	-1	0	-	5	-	5.401	5.023		85 ÷ 114	97 ÷ 12	
	B+T	0.88	0	0	0	-	5	-				67 ÷ 84	76 ÷ 95	
											<i>Eq. (14a)</i>	<i>Eq. (14b)</i>		
7b	B+T	3.25	-1	-1	90	10	-	-	16.80	8.936	break-through	98÷187	30 ÷ 57	
	B+T	3.25	0	0	90	9	-	-				78÷178	24 ÷ 55	
	B+T	0.88	-1	-1	90	-	13	-	5.830	4.463			56÷100	64 ÷ 114
	B+T	0.88	0	0	90	-	13	-					50÷90	57 ÷ 103

^o bending (B), torsion (T)

* calculated with $\tau_{nom} = 1$ MPa, λ as indicated.

[^] calculated with $\sigma_{nom} = 1$ MPa

[#] the equivalent peak stress evaluated in the tube resulted $\sigma_{eq,peak,tube} = 1.910$ MPa

⁺(L) corresponds to longitudinal cracks while (T) to transversal cracks, according to the original contribution [17]

Table 2.9: Fatigue test details of steel welded joints (joint geometries are reported in Table 6)

Joint geometry	Load condition ^o	λ	R_x	R_y	Phase ϕ [°]	N° failures			$\sigma_{eq,peak}$ toe [MPa]	$\sigma_{eq,peak}$ root [MPa]	Failure criterion	Applied nominal stresses	
						toe	root	tube				$\Delta\sigma_{nom,xx}$ [MPa]	$\Delta\sigma_{nom,yy}$ [MPa]
8a	Uniaxial	∞	0	-	-	6	-	-	3.117 [^]	1.977 [^]	1÷2 mm technical crack and complete failure	Eq. (13a)	-
8b	Biaxial	1.02 ⁺	0	0	180	4	-	-	2.868 ^A	2.085 ^A	1÷2 mm technical crack and complete failure	Eq. (13a)	Eq. (13a)
	Biaxial	1.02 ⁺	0	0	180	4	-	-	1.613 ^B	0.601 ^B			
		0.85							2.442 ^A	1.834 ^A			
		0.68							1.612 ^B	0.551 ^B			
		0.34							2.032 ^A	1.597 ^A			
									1.612 ^B	0.507 ^B			
									1.293 ^A	1.213 ^A			
									1.612 ^B	0.442 ^B			
	Biaxial	1.52 ⁺	0	∞	0	4	-	-	4.150 ^A	2.881 ^A			
									1.614 ^B	0.767 ^B			
		1.25							3.453 ^A	2.444 ^A			
									1.613 ^B	0.674 ^B			
		1.02							2.868 ^A	2.085 ^A			
									1.613 ^B	0.601 ^B			
		0.85							2.442 ^A	1.834 ^A			
									1.612 ^B	0.551 ^B			

⁺ biaxiality ratio λ calculated as: σ_x/σ_y

^{*} calculated with $\sigma_y = 1$ MPa, σ_x/σ_y as indicated.

[^] calculated with $\sigma_x = 1$ MPa

Yousefi et al. [21]

The fatigue strength of tube-to-flange steel welded joints with partial penetration (model 3 in Table 6) were analysed adopting two stress ratios ($R = -1$ and $R = 0$) under pure bending, pure torsion and combined bending and torsion loadings [21]. Multiaxial loadings were applied with loads in-phase ($\phi = 0^\circ$) and out-of-phase ($\phi = 90^\circ$), by adopting $\lambda = 1$. The number of cycles to obtain a through-the-thickness crack was adopted as failure criterion [21]. The original experimental results were assumed here as expressed in terms of nominal stress range (defined as maximum minus minimum value) evaluated in the tube (see Eq. (13)). This information is not explicit in the fatigue curve reported in the original contribution.

Following the PSM mesh generation guidelines, the relevant peak stresses were calculated at the potential crack initiation sites from 2D axis-symmetric FE models. In this case, the most critical mesh density ratio to apply the PSM is dictated by mode II

loading at the root side (see Table 7), according to which a/d should be greater than or equal to 14, $a = 1$ mm being the root length. Therefore, an average element size d equal to $1/14 \approx 0.07$ mm was adopted in the FE analyses.

Given that the specimens were tested under stress-relieved conditions in this contribution, the equivalent peak stress was calculated by using Eq. (5) at the weld root and Eq. (7) at the toe side. As reported in Table 8, in this case, the PSM enables to correctly estimate the crack initiation location, which always occurred at the toe side according to [21]. Finally, because of the reduced root length, (see model 3 in Table 6), it is known from experience that the failure likely occurs at the weld toe rather than the root. Therefore, the PSM could have been applied only at the toe side. In such a case, Table 7 shows that a much greater average element size equal to $d = 8/3 = 2.67$ mm could have been adopted.

***Bäckström et al.* [22]**

A 5-mm-thick square hollow section (SHS) steel fillet-welded onto a square plate (SP), see model 4 in Table 6, was tested under pure bending, pure torsion and combined bending-torsion fatigue loadings. Both in-phase ($\phi = 0^\circ$) and out-of-phase ($\phi = 90^\circ$) multiaxial loadings condition were applied in the experimental testing. Biaxiality ratios A ranging from 0.9 and 3 and nominal load ratios R between -1.3 and 0.7 were adopted (see Table 8). The complete stiffness loss was chosen as a failure criterion in the original paper [22].

Due to geometrical complexity, 3D FE main model and a proper 3D submodel were necessary to calculate the peak stresses at the toe and root sides. In Table 6 it is shown the locations where the maximum values of the peak stresses relevant to both weld toe and root sides is occurred, more precisely, at the corner of the SHS section. Accordingly, a 3D submodel of that region was generated, by extruding around the corner a 2D mesh prepared according to the PSM. Since a mesh density ratio $a/d \geq 14$ should be guaranteed to comply with the conditions of applicability of the PSM at the root side under mode II loading (see Table 3), then an average element size $d = 5/14 \approx 0.36$ mm was adopted.

All joints were tested in the as-welded conditions [22], therefore Eq. (8) was used at the weld root, while regarding the weld toe, Eq. (9) was adopted. According to the original contribution [22], fatigue failure always occurred at the toe side at the corner of the SHS section, except for the joints tested under pure torsion loading, in which fatigue crack initiated in the tube. Table 8 shows that the crack initiation location was properly assessed by means of the PSM, the equivalent peak stress $\sigma_{eq,peak}$ being always higher at the weld toe than at the weld root. Furthermore, it should be noted that, in the case of joints tested under pure torsion loading, Table 8 shows that the equivalent peak stress $\sigma_{eq,peak}$ calculated in the tube resulted 1.91 MPa (see # symbol) which is not in agreement with the experimental evidence.

Dahle et al. [17]

Fatigue data ($R = -1$ and $R = 0$) on box-beam steel fillet-welded joints (model 5 in Table 6) were reported in [17]. Bending, torsion and combined in phase ($\phi = 0^\circ$) as well as out-of-phase ($\phi = 90^\circ$) bending-torsion fatigue loadings were applied with different biaxiality ratios A , (more detail in Table 8). The number of cycles to initiate a visually detectable crack, which corresponded to a longitudinal crack length between 200 and 500 mm was set a failure criterion for the fatigue testing. Fatigue failure always occurred at the weld toe in pure bending fatigue test, while crack always initiated from the root side in all the other cases.

Since the stress components related to bending load are not singular, they were analytically evaluated from classical expressions of solid mechanics. On the contrary, torsional (mode III) shear stress component is singular and must be calculated from FE analyses performed according to the PSM. A 3D FE main model coupled with a submodel was necessary to calculate the peak stresses relevant to mode III loading at the root side. The submodel was first prepared in the (X,Y) plane shown in Table 6 and meshed according to the PSM; after that, the mesh was extruded in the Z direction. The mesh density ratio $a/d \geq 12$ was adopted to apply the PSM at the root side under mode III loading (see Table 7); therefore an average element size $d = 6/12 \approx 0.5$ mm was used to perform the FE analysis of the submodel, $a = 6$ mm corresponding to the ligament length.

The $c_w = 1$ has been employed to calculate the equivalent peak stress due to the fact that all the specimens were in the as-welded conditions.

Sonsino et al. [23,24]

The fatigue strength of tube-to-flange full-penetration steel welded joints (model 6 in Table 6) subjected to pure bending, pure torsion and combined bending-torsion loadings ($R = -1$) investigated by Sonsino et al. [23,24] were taken into account. The multiaxial fatigue strength, analysing both in-phase ($\phi = 0^\circ$) and out-of-phase ($\phi = 90^\circ$) loading condition with a biaxiality ratio $A = 1.724$ was investigate in the original contributions [23,24].

Two number of cycles were obtained from each test: more precisely, the number of cycles to obtain a 1-mm-long technical crack and also the number of cycles to break-through, in which the latter was determined from the air pressure drop inside the tube. The mean ratio between the number of cycles to crack initiation and that to break-through is approximately 0.50. For this case, the theoretical estimations based on PSM were compared with both values of number of cycles. Fatigue cracks always initiated at the weld toe because of the fully penetrated welding execution.

The peak stresses were calculated at the toe side by employing 2D axis-symmetric FE models. Despite the minimum adoptable mesh density ratio of $a/d = 3$ (see Table 7), a slightly more refined FE mesh with $d = a/5 = 2$ mm ($a = 10$ mm is the tube thickness) was adopted to obtain the standard FE mesh pattern around the weld

toe. Since the weld toe radius was reduced ($\rho \approx 0.2 \div 0.8$ mm, see Table 5), the sharp V-notch configuration ($\rho = 0$) has been assumed in the FE analyses.

Bertini et al. [25] and Frendo and Bertini [26]

The fatigue strength of two geometries of tube-to-flange steel fillet-welded joints (models 7a and 7b in Table 6) under cyclic loadings with two load ratio ($R = -1$ and $R = 0$) were reported in [25,26]. Model 7a [25] was subjected to pure bending, pure torsion and combined in-phase ($\phi = 0^\circ$) bending-torsion fatigue loadings. Out-of-phase ($\phi = 90^\circ$) multiaxial fatigue loading condition were analysed to model 7b [26]. As it can be noted in Table 4, different biaxiality ratios A were adopted in the experimental campaign.

The air pressure drop in the small volume enclosed by the sleeve between the tube and the flange (see models 7a and 7b in Table 6) was set as failure criterion as reported in the original contributions [25,26]. The bending and torsion nominal stresses, reported in the original contributions, were calculated in the weld throat by means of the following expressions [25,26]:

$$\sigma_{\text{nom,bending}} = \frac{M_f}{W_f} = \frac{M_f}{\frac{\pi \cdot \left((d_e + 2 \cdot s)^3 - \frac{d_e^4}{d_e + 2 \cdot s} \right)}{32}} \quad (14a)$$

$$\tau_{\text{nom}} = \frac{M_t}{W_t} = \frac{M_t}{\frac{\pi \cdot \left((d_e + 2 \cdot s)^3 - \frac{d_e^4}{d_e + 2 \cdot s} \right)}{16}} \quad (14b)$$

being d_e the tube outer diameter and $s = 10/\sqrt{2}$ the weld throat thickness.

It is worth noticing that four critical points are present in the considered geometries: two weld toes and two weld roots, as indicated in detail in models 7a and 7b of Table 6. Due to the symmetrical properties of the component, it was possible to model two-dimensional axis-symmetric FE models with coarse meshes to apply the PSM at the weld toes and roots. The mesh density ratio $a/d \geq 14$ being the most demanding condition in order to apply the PSM at the root side under mode II loading (see Table 7), an average FE size $d = 10/14 = 0.7$ mm was employed to analyse both joint geometries, where a represents the tube thickness and equals 10 mm.

The equivalent peak stress was obtained by means of Eq. (8) at the weld roots, on the other hand, Eq. (9) was used at the weld toes because all joints were tested in the as-welded conditions. Only the highest equivalent peak stresses between the two toes and that between the two roots are reported in Table 8. Such highest values always occurred at the toe and root sides relevant to the outer welding (indicated with subscript 1 in Table 6). Dealing with model 7a, Table 8 shows that the PSM properly estimates

the fatigue failure location under pure modes of loading, which occurred at the weld toe side under pure bending and at the weld root side under pure torsion loading [25]. When multiaxial loadings are considered (model 7a or 7b), according to the PSM the weld toe is always more critical than the weld root, the equivalent peak stress being higher there (see Table 4). Nevertheless, cracks initiated in 6 test series among 8 at the root and not at the toe [25,26]. In previous work, it has been observed that difficulties arise in estimating the failure location, when multiple crack initiation sites are in competition in the same joint in presence of highly non-uniform residual stress fields, which the equivalent peak stress does not account for [18].

Takahashi et al. [27,28]

Two geometries consisting of steel plates having a box-fillet-welded (wrap-around) joint were tested under pulsating uniaxial (model 8a in Table 6) and biaxial (model 8b in Table 6) fatigue loadings. Dealing with model 8b, both in-phase ($\phi = 0^\circ$) and out-of-phase ($\phi = 180^\circ$) loadings were applied, by adopting different biaxiality ratios λ as reported in Table 8.

In the original contributions [27,28], the authors reported the number of cycles to obtain a first technically detectable crack, corresponding to a crack depth in the range of 1÷2 mm, as well as the number of cycles to complete failure. Both values of number of cycles will be considered in the reanalysis of the experimental data according to the PSM.

Given the geometrical complexity, a 3D main model, as well as a submodel, were required to evaluate the peak stresses at the weld toe and the weld root (models 8a and 8b of Table 6). It should be noted that the maximum values of the peak stresses referred to the toe and root sides occurred at zone A of model 8a and at zones A and B of model 8b, as indicated in Table 6. Accordingly, the 3D submodels of those regions have been generated and an average element size d equal to $6/14 \approx 0.4$ mm has been adopted according to the PSM. In fact, the mesh density ratio $a/d \geq 14$, $a = 6$ mm being the ligament length at the root side, is the most demanding condition for the applicability of the PSM concerning the weld root under mode II loading (see Table 7). It should be noted that only one eighth of each joint geometry was modelled (see Table 8), taking advantage of the three symmetry planes.

Given that all welded joints were fatigue tested in the as-welded conditions, Eq. (6) (Chapter 1) has been adopted to evaluate the equivalent peak stress at the toe and root sides of both joint geometries ($F_Y = 0$ in the case of uniaxial loading, model 8a), by considering $c_w = 1$. Eq. (12) has been discussed in the companion paper [29]. According to Takahashi et al. [27,28], fatigue failures always occurred at the toe side, i.e. point A_t dealing with model 8a (see Table 6). Considering model 8b (see Table 6) fatigue cracks initiated at point A_t along the weld toe profile, with only one exception where crack initiation occurred at point B_t . Table 9 shows that the failure location is

correctly assessed by means of the PSM in all cases, the equivalent peak stress $\sigma_{eq,peak}$ being always higher at the weld toe, A_t or B_t , from which fatigue cracks were seen to initiate during experiments.

2.2.2 Aluminium welded joints

Several experimental fatigue data referring aluminium welded joints under pure bending, pure torsion and multiaxial fatigue loads were taken from the literature. More precisely, the original data are taken from Kueppers and Sonsino [16] and Costa et al. [30] which are related to tube to flange and overlapped tubes welded joints, respectively. The materials, welding processes and testing conditions taken into consideration are reported in table 10, while in Table 11 the joint geometries and also the details of the stress analyses according to the PSM are illustrated.

Table 2.10: Materials, welding processes and testing conditions of aluminium welded joints.

Ref.	Joint Geometry	Material	Yield strength [MPa]	Ultimate strength [MPa]	Welding process	Testing condition	Weld toe radius ρ [mm]
Kueppers and Sonsino [16]	(1)	EN-AW 6082 T6	315	332	TIG and MIG	As-welded	13÷20
Costa et al. [30]	(2)	EN-AW 6060 T6	215	240	-	Stress-relieved	0.2 minimum 1.3 average

According to the original contributions, the bending and torsion nominal stresses were defined in the tube by means of the Eq.s (13b) and (13c), respectively, where d_e is the outer diameter and t is the tube thickness.

Two-dimensional, axis-symmetric FE models were employed for both models to convert the original experimental data from nominal stresses (Eq. 13) to the equivalent peak stress. A free mesh pattern of quadrilateral four-node harmonic elements PLANE 25 of the ANSYS® element library was adopted to calculate the peak stresses both at the weld root and the weld toe. The employed FE type enables to analyse axis-symmetric components under external loads which are not necessarily axis-symmetric, but they must be expressible with a Fourier series expansion. Therefore, this finite element type can be adopted to model three-dimensional axis-symmetric components subjected to bending or torsion loads, while keeping the advantage of performing two-dimensional FE analyses.

In the following, specific details concerning the experimental fatigue tests and the analysis procedure of each test series are reported.

Kueppers and Sonsino [16]

In [16] the fatigue strength under completely reversed ($R = -1$) pure bending, pure torsion and combined bending and torsion cyclic loads of tube-to-flange full-

penetration aluminium welded joints (Model 1 in Table 11) was analysed. In the multiaxial loading condition, loads both in-phase ($\phi = 0^\circ$) and out-of-phase ($\phi = 90^\circ$) with a biaxiality ratio $\Lambda = 1.72$ were investigated in the experimental campaign (see the details in Table 12).

The number of cycles to obtain a through-the-thickness crack was considered as a failure criterion. Due to the fully penetrated welding, the fatigue crack initiation always occurred at the weld toe (see Table 12).

According to Kueppers and Sonsino [16], the weld toe radius ranged from 13 and 20 mm. In the numerical analyses here reported, the minimum value of weld toe radius ($\rho_{\min} \approx 13$ mm) has been considered. This assumption is justified by the fact that the fatigue crack is expected to initiate at the highest stress concentration and furthermore full notch sensitivity is also expected, so the maximum values of bending (σ_{peak}) and torsion (τ_{peak}) stresses, respectively, have been calculated. Therefore, the FE model consisted in a simply refined mesh (see Model 1 in Table 11) having a minimum FE size about equal to 0.8 mm. All the degree of freedom at the line representing the back face of the flange were fixed in order to simulate the connection between the flange and the test frame, as shown in Table 11 (Model 1).

Eq. (10) with $c_{w1} = c_{w3} = 1$ was used to calculate the equivalent peak stress at the weld toe side due to the fact that all the tested welded joints were in the as-welded conditions (see Table 11).

Costa et al. [30]

Overlap-tubes aluminium fillet-welded joints (Model 2 in Table 11) were tested under rotating bending as well as reversed ($R = -1$) and pulsating ($R = 0$) in-phase bending and torsion fatigue loadings. In addition, one series was tested by applying rotating bending and constant torsion loadings. The biaxiality ratios Λ of the multiaxial testing are reported in Table 12. In [30], 10% stiffness loss of the joints was adopted as failure criterion and it has been considered as fatigue life in the present work.

In the original contribution, the fatigue data were reported in terms of the peak value of the von Mises stresses evaluated at the weld toe. The stress concentration factors relevant to the average and the minimum values of the measured weld toe radii were also reported in the original paper [30]. Therefore, in order to derive the nominal stresses to apply to the FE models, the highest stress concentration factor relevant to the minimum weld toe radius ($\rho_{\min} \approx 0.2$ mm) was adopted. The worst-case assumption $\rho = 0$ was adopted in the present FE analysis due to the very small weld toe radius of the considered welded joints.

Table 2.11: Aluminium welded joint geometries and FE analyses for fatigue strength assessment according to the PSM [1]

Ref.	Joint * geometry	Material
Model 9 [16]		
Model 10 [30]		

Table 2.12: Fatigue test details of aluminium joints (joint geometries are reported in Table 11).

Joint geometry	Load condition ^o	$\Lambda^{\circ\circ}$	$R_{\sigma} = R_{\tau}$	Phase ϕ [°]	N ^o failures			$\sigma_{eq,peak}^*$ toe [MPa]	$\sigma_{eq,peak}^*$ root [MPa]	Failure criterion	Applied nominal stresses	
					Toe	root	tube				$\Delta\sigma_{nom}$ [MPa]	$\Delta\tau_{nom}$ [MPa]
											<i>Eq. (13a)</i>	<i>Eq. (13b)</i>
1	B	∞	-1	-	9	-	-	1.687 [^]	-	break-through	80 ÷ 143	-
	T	0	-1	-	7	-	-	2.002	-		-	72 ÷ 122
	B+T	1.72	-1	0	7	-	-	2.618	-	-	60 ÷ 100	35 ÷ 58
	B+T	1.72	-1	90	8	-	-	-	-	-	59 ÷ 100	35 ÷ 58
											<i>Eq. (13a)</i>	<i>Eq. (13b)</i>
2	rot. B	∞	-1	-	8	-	-	2.154 [^]	2.004 [^]	Stiffness loss (-10%)	65 ÷ 107	-
	B+T	2	-1	0	5	-	-	4.761	4.546		56 ÷ 91	28 ÷ 45
	B+T	0.167	-1	0	3	-	-	2.060	2.173		12 ÷ 15	72 ÷ 88
	B+T	1.33	0	0	5	-	-	4.963	4.840	40 ÷ 64	30 ÷ 48	
	B+T	2	0	0	8	-	-	6.733	6.429	47 ÷ 73	24 ÷ 36	
	B+T	3	0	0	4	-	-	9.576	9.027	52 ÷ 70	17 ÷ 23	
	rot. B + const. T	1	-1	-	8	-	-	2.864	2.665	64 ÷ 86	64 ÷ 86	

^o bending (B), torsion (T), rotating bending (rot B), constant torsion (const. T)

^{oo} $\Lambda = \sigma_{nom} / \tau_{nom}$

* calculated with $\tau_{nom} = 1$ MPa, Λ as indicated.

[^] calculated with $\sigma_{nom} = 1$ MPa

A 2D axis-symmetric FE model was solved to calculate the peak stresses at the weld toe and root sides, which FE mesh pattern related to the PSM is reported in Table 10. The mesh density ratio a/d was chosen equal to 14 to comply with the conditions of applicability of the PSM at the root side under mode II loading conditions; therefore, an average element size d equal to $3/14 \approx 0.20$ mm has been adopted, the ligament length being $a = 3$ mm. In order to simulate the testing conditions described by Costa et al. [30], the outer tube was restrained as shown in Table 11 (Model 2).

The equivalent peak stress was evaluated according to Eq. (11) at the weld root, while Eq. (7) was adopted at the weld toe, 2α being greater than 102° because all welded joints were tested in the stress-relieved conditions. In both equations, the coefficients f_{w1} , f_{w2} and f_{w3} relevant to $R_0 = 0.12$ mm (see Tables 1-3) were adopted.

According to the original contribution [30], fatigue crack initiation always occurred at the weld toe side. It should be noted from Table 11 that the crack initiation location is correctly estimated by the PSM in all but one case, where the equivalent peak stress $\sigma_{eq,peak}$ is slightly higher at the weld root than at the weld toe. In a previous contribution [7], it has been highlighted that reduced differences of the equivalent peak stress calculated at different competing failure locations can hardly anticipate the experimental cracking location [7,18].

2.3 ASSESSMENT OF WELD TOE AND WELD ROOT FAILURES

2.3.1 Steel welded joints

After having solve all the FE model of the abovementioned welded details, the original fatigue data taken from the literature have been expressed in terms of range of the equivalent peak stress calculated at the critical point according to the PSM. Tables 8 and 9 properly report the equivalent peak stress evaluated at the weld toe and at the weld root by means of the appropriate expressions mentioned in the previous section, where $\tau_{nom}=1$ MPa, $\sigma_{nom}=\Lambda \cdot \tau_{nom}$ have been used (if $\Lambda=\infty$, then $\sigma_{nom}=1$ was applied). By using the equivalent peak stress related to the unit of nominal stress, to convert the original data to the local equivalent peak stress, it is possible to multiply the nominal stress range adopted in the original fatigue tests by the relevant equivalent peak stress reported in Tables 8 and 9.

From Figs. 6 to 13 the experimental data relevant to welded joints made of structural steels reconverted in terms of range of equivalent peak stress are compared with the scatter band suggested to design steel welded joints subjected to multiaxial loads. The proposed design scatter here follows what formulated by Lazzarin et al. [31] for the averaged SED criterion. More precisely, the design scatter band was obtained by taking first the high-cycle fatigue strength at $2 \cdot 10^6$ cycles for structural steel joints subjected to pure mode I loading previously found in [32] fitted on about 200 experimental results taken from the literature.

The just mentioned fatigue strength resulted equal to $\Delta\sigma_{A,50\%} = 214$ MPa, and second, adopting the inverse slope of the design scatter band for structural steels relevant to pure mode III loading, i.e. $k = 5$ according to [8].

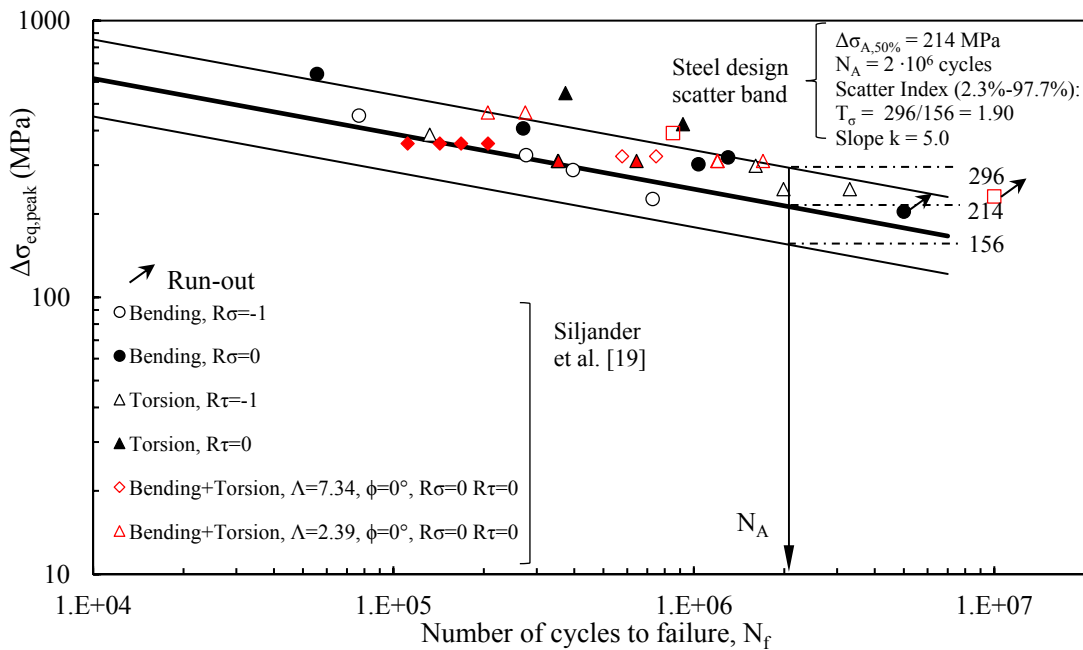


Figure 2.6 Fatigue assessment of tube-to-flange welded joints (model 1) according to the PSM. Comparison between the proposed multiaxial fatigue design scatter band and experimental fatigue results from [19]. [Figure taken from [2]]

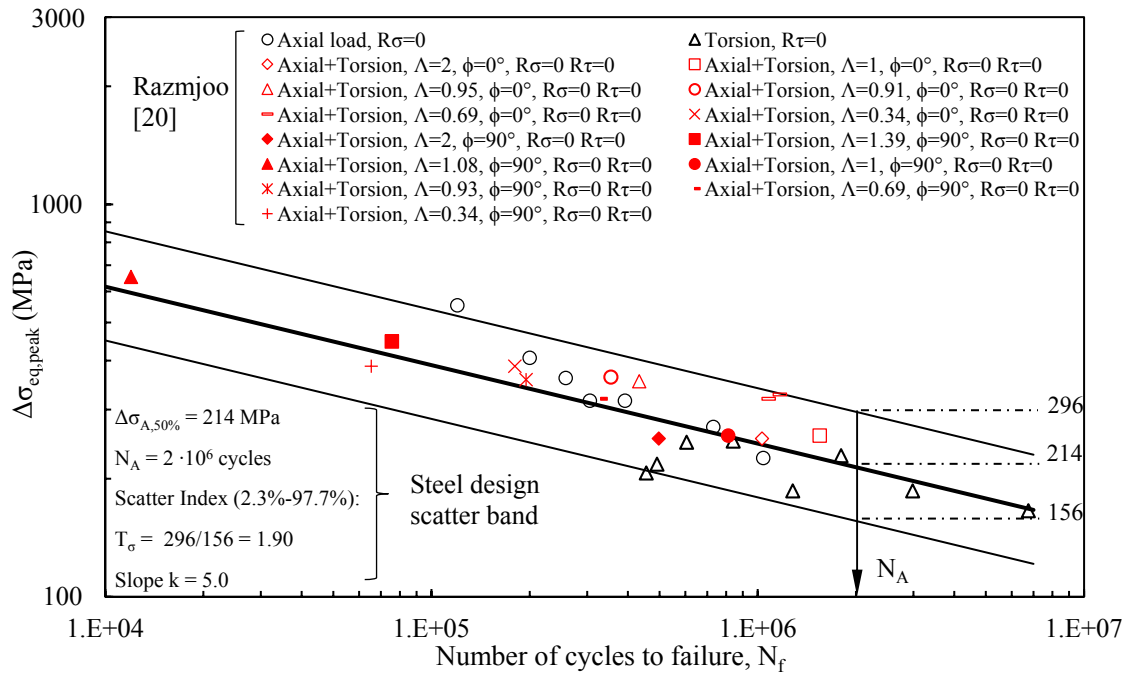


Figure 2.7 Fatigue assessment of tube-to-flange welded joints (model 2a and 2b) according to the PSM. Comparison between the proposed multiaxial fatigue design scatter band and experimental fatigue results from [20]. [Figure taken from [2]]

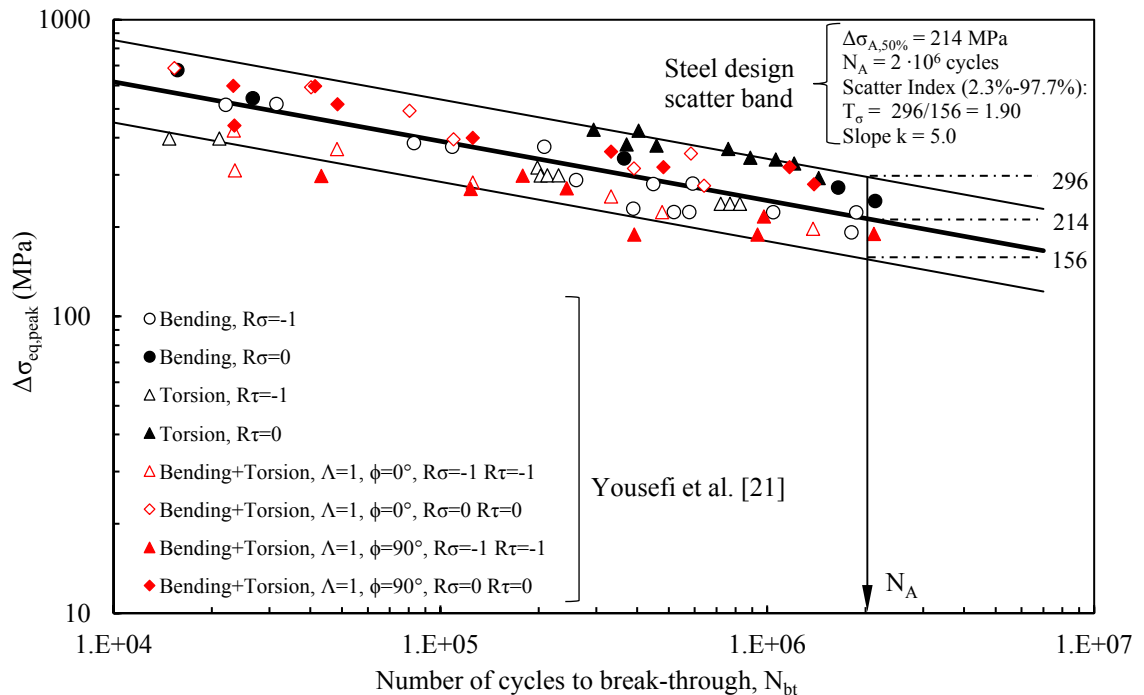


Figure 2.8: Fatigue assessment of tube-to-flange welded joints with partial penetration (model 3), according to the PSM. Comparison between the proposed multiaxial fatigue design scatter band and experimental fatigue results from [21]. [Figure taken from [2]]

The scatter index T_σ of the design scatter band is that one obtained for survival probabilities of 2.3%-97.7% (i.e. mean value \pm two standard deviations). Therefore T_σ resulted being equal to 1.90 [3, 17, 29], which is consistent with the value $T_\sigma = 1.50$,

referred to survival probabilities of 10%-90%, found by Haibach [33] analysing single test series.

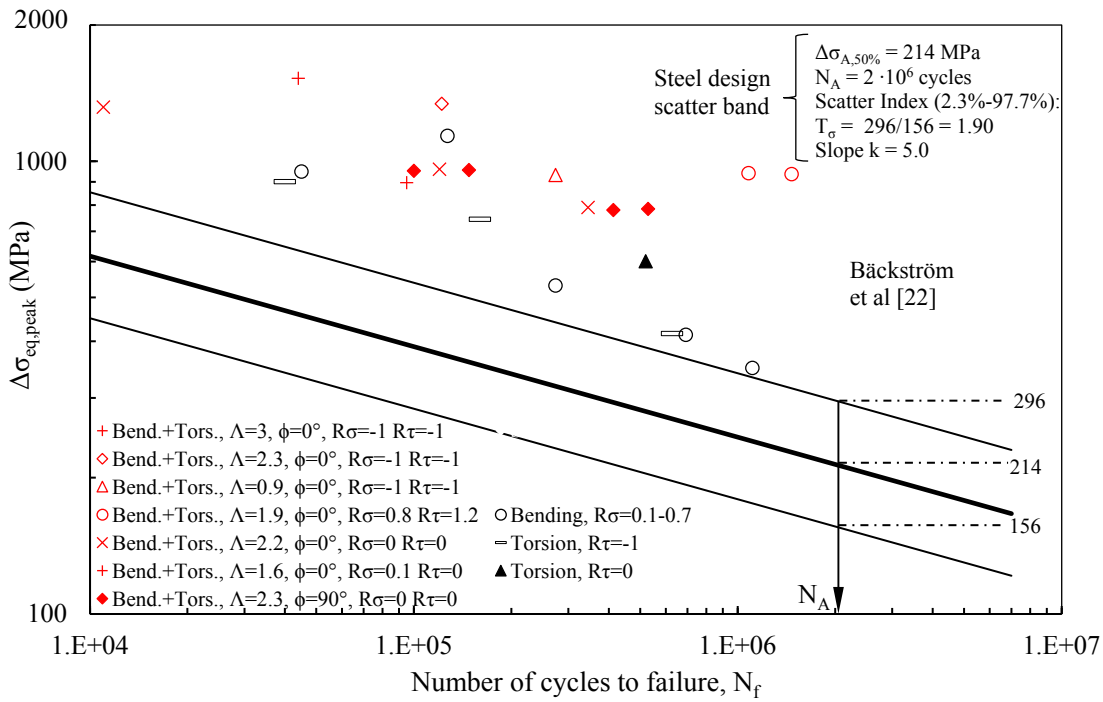


Figure 2.9 Fatigue assessment of square hollow section (SHS) beam fillet-welded onto a square plate (SP), (model 4) according to the PSM. Comparison between the proposed multiaxial fatigue design scatter band and experimental fatigue results from [22]. [Figure taken from [2]]

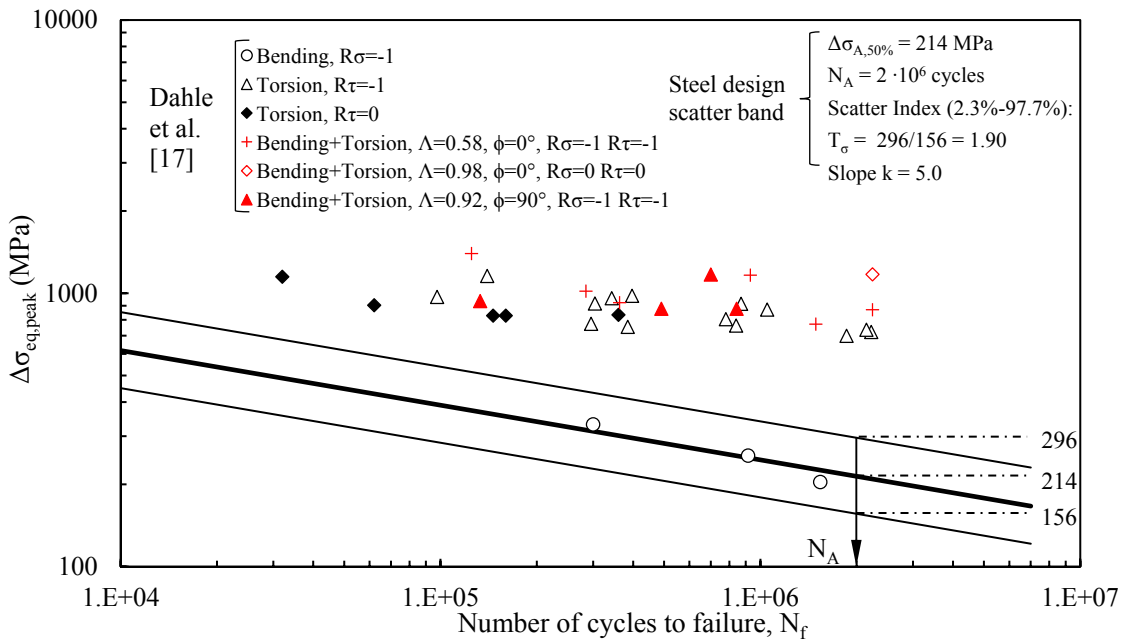


Figure 2.10 Fatigue assessment of box-beam steel fillet welded joints (model 5) according to the PSM. Comparison between the proposed multiaxial fatigue design scatter band and experimental fatigue results from [17]. [Figure taken from [2]]

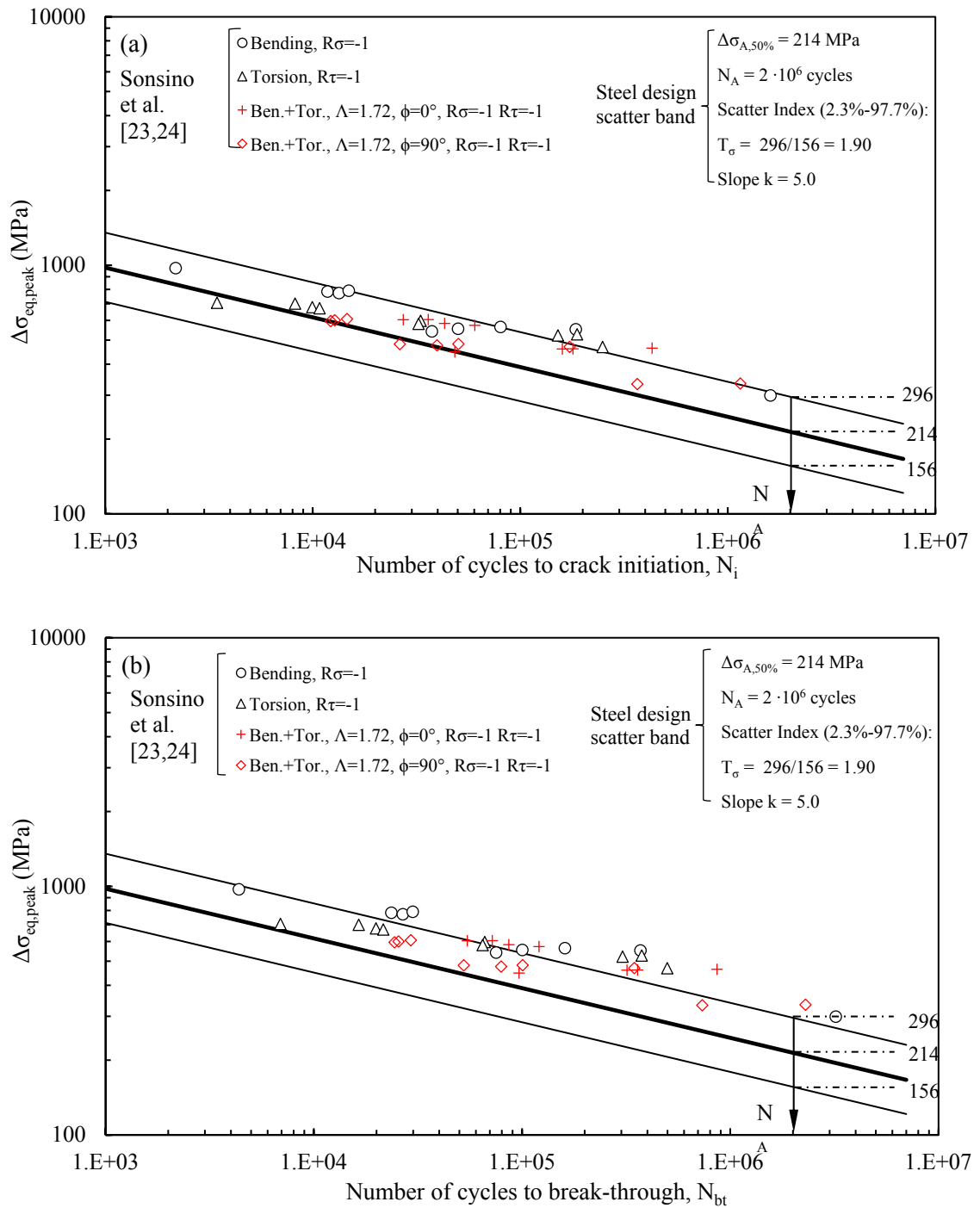


Figure 2.11: Fatigue assessment of tube-to-flange full-penetration welded joints (model 6) according to the PSM. Comparison between the proposed multiaxial fatigue design scatter band and experimental fatigue results from [23,44], expressed in terms of number of cycles to (a) crack initiation and (b) break-through. [Figure taken from [2]]

In most cases, see Figs. 6-8, 11 and 13, a good agreement between experimental fatigue results and theoretical prediction based on PSM for joints tested under uniaxial as well as multiaxial fatigue loadings was found. Only in the cases of Bäckström et al. [22] and Dahle et al. [17] (see Figs. 9 and 10), the design curve is too conservative

with respect to the experimental data. This might be due to the nature of the NSIF parameters which are commonly used to correlate the fatigue life referred to crack initiation and short propagation in the structural volume (see Fig. 1 of [29]), where the NSIFs govern the local stress field. Although the N-SIF based approach should be used for estimating the crack initiation, they correlate fairly well also the total fatigue life of small-scale laboratory specimens NSIF-based approach correlates [12,13,34,35]. Indeed, in the cases of full-size structures, the crack propagation phase out of the region governed by the NSIF leading terms should be treated separately by adopting a Linear Elastic Fracture Mechanics (LEFM) approach. In support to this statement, the fatigue results on welded joints tested by Dahle et al. [17] (model 5 in Table 6) show a significant influence of the crack propagation life on the total fatigue life, where failure criterion was defined at a number of cycles such as to detect up to 500-mm-long cracks. Figs 11a and b allow to appreciate the better correlation between proposed design scatter band and fatigue test results if fatigue life to initiate a 1-mm-long technical crack is considered (Fig. 11a) rather than fatigue life to break-through (Fig. 11b).

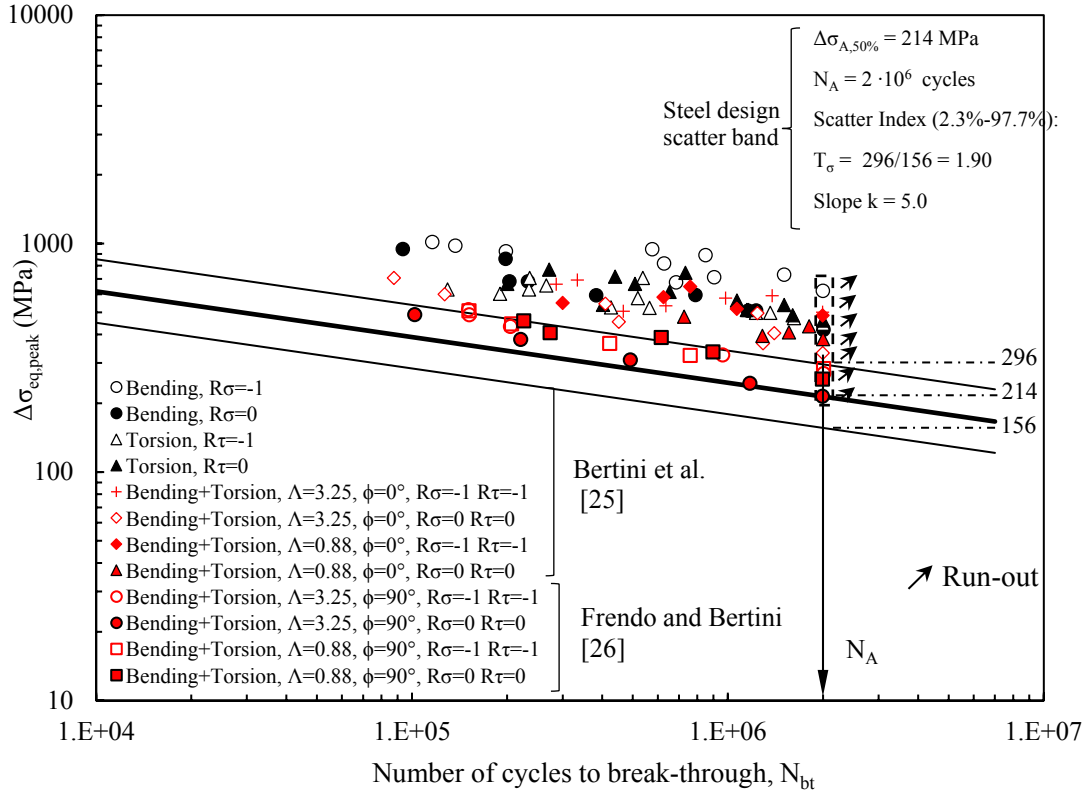


Figure 2.12: Fatigue assessment of tube-to-flange welded joints (model 7a and 7b) according to the PSM. Comparison between the proposed multiaxial fatigue design scatter band and experimental fatigue results from [25,26]. [Figure taken from [2]]

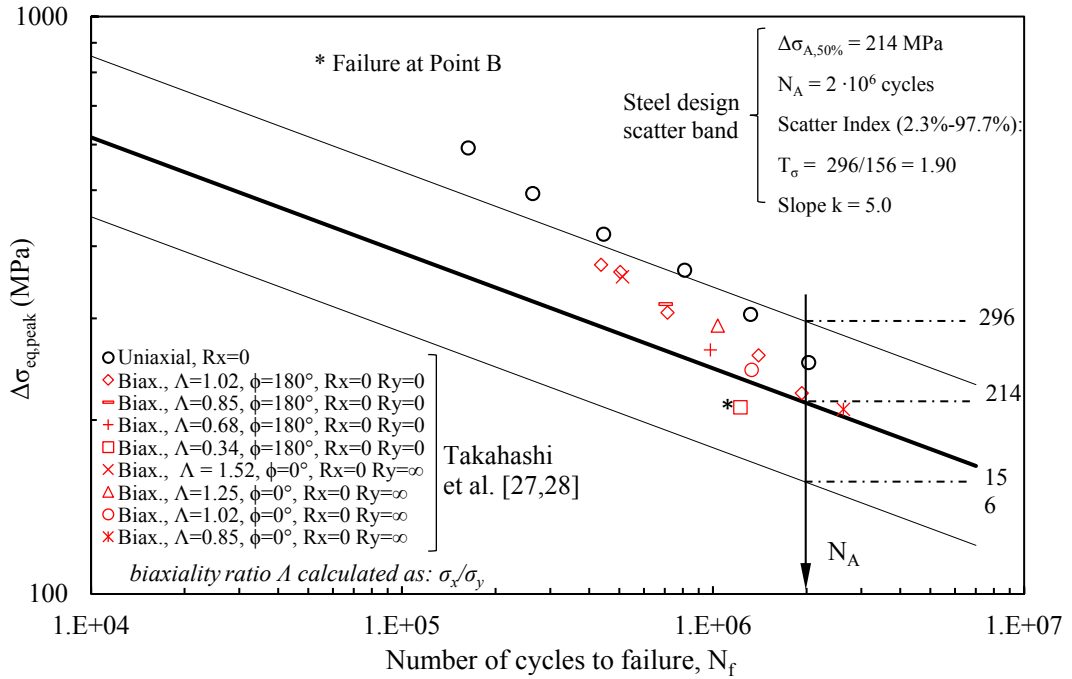


Figure 2.13: Fatigue assessment of plates having a box-fillet-welded (wrap-around) joints (model 8a and 8b) according to the PSM. Comparison between the proposed multiaxial fatigue design scatter band and experimental fatigue results from [27,28]. [Figure taken from [2]]

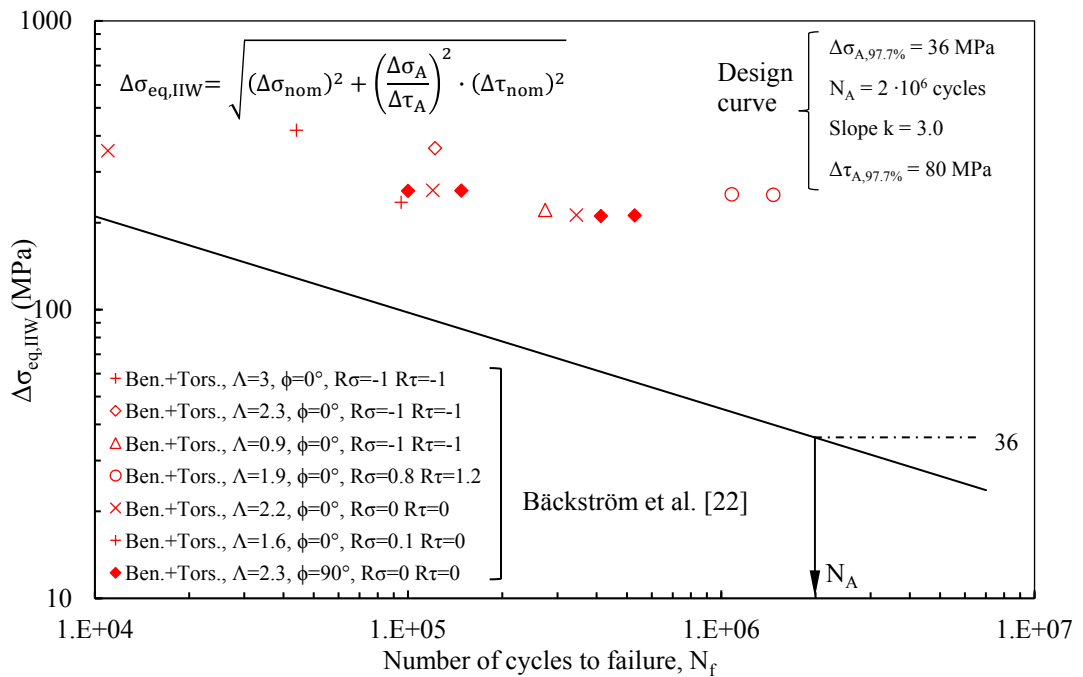


Figure 2.14: Fatigue assessment of square hollow section (SHS) beam fillet-welded onto a square plate (SP), (model 4) based on the nominal stress approach, as formulated for the case of multiaxial loadings according to IIW Recommendations [37]. Comparison between the design curve and experimental fatigue results from [22]. [Figure taken from [2]]

Regarding the results relevant to the joints tested by Bäckström et al. [22] (model 4 in Table 6), it is worth noticing that their fatigue strength is high even compared to

FAT classes of design standards [36,37], as it is seen from Fig. 14, which reports the comparison between the design curve obtained by applying the multiaxial nominal stress approach according to IIW Recommendations [37] and the multiaxial fatigue test results of the original contribution.

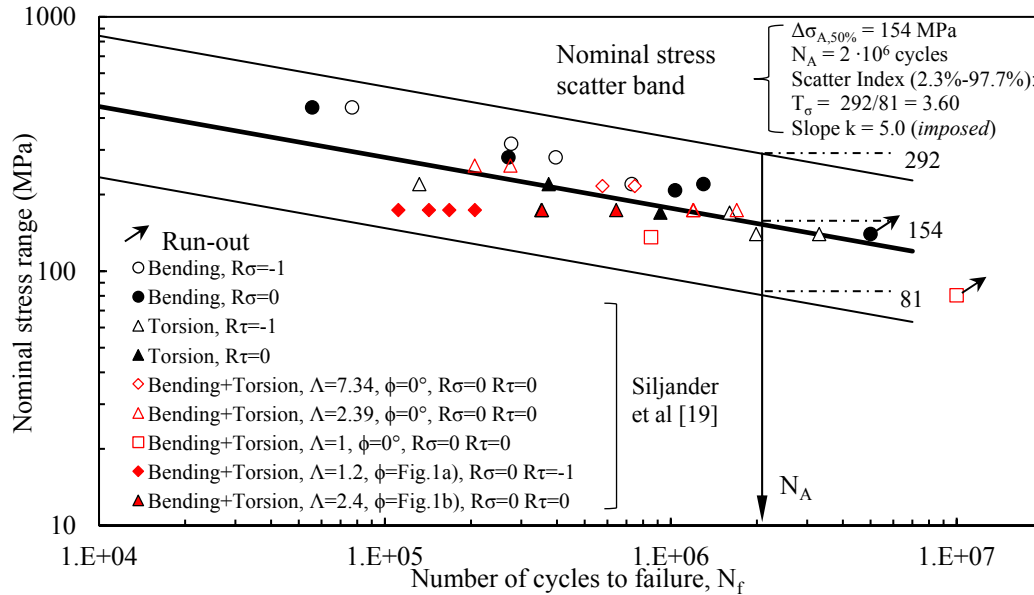


Figure 2.15 Experimental fatigue results relevant to tube-to-flange steel welded joints (model 1) taken from [19] and expressed in terms of shear (for pure torsion) or normal (for all other cases) nominal stress range. See Fig. 6 for comparison. [Figure taken from [2]]

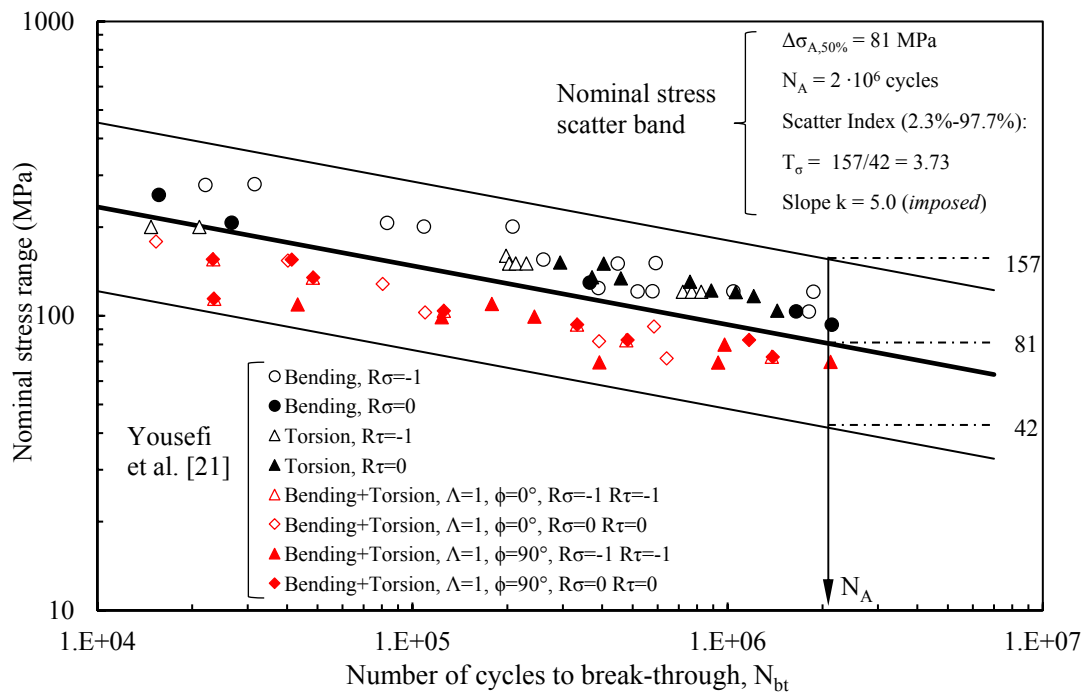


Figure 2.16: Experimental fatigue results relevant to tube-to-flange steel welded joints with partial penetration (model 3) taken from [21] and expressed in terms of shear (for pure torsion) or normal (for all other cases) nominal stress range. See Fig. 8 for comparison. [Figure taken from [2]]

Several multiaxial fatigue data analysed in the present paper were obtained by shifting the torsional (mode III) load with respect to the axial/bending (mode I) load components. This means Eqs. (11) and (12) do not take into account the phase shift between the load applied. Despite the known sensitivity to the phase shift between normal and shear stresses of structural steel joints [21,23,24] (differently from aluminium welded joints), Figure 8 and Figure 11a report the results relevant to stress-relieved joints taken from [21] and [23,24], respectively, analysed according to Eq. (11), which does not take into account the phase shift. These figures show that for the same load ratio of the external load, the influence of the phase shift can be distinguished, but it is not that remarkable.

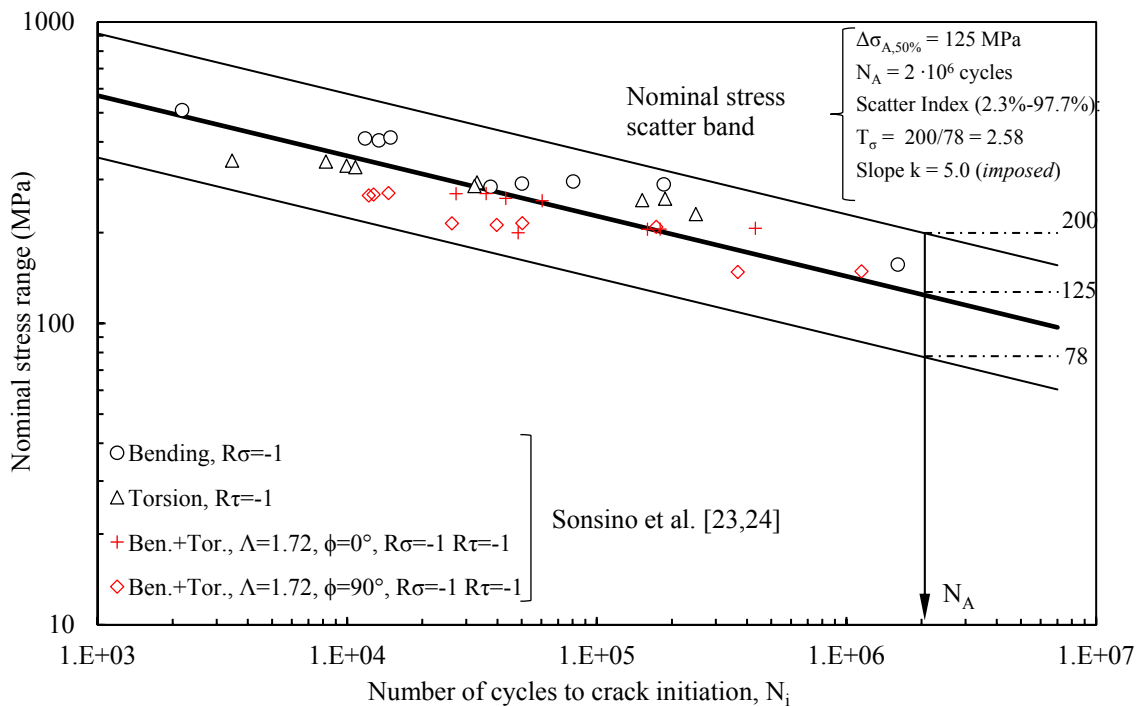


Figure 2.17: Crack initiation experimental fatigue results relevant to tube-to-flange full-penetration steel welded joints (model 6) taken from [23,24] and expressed in terms of shear (for pure torsion) or normal (for all other cases) nominal stress range. See Fig. 11a for comparison. [Figure taken from [2]]

Therefore, the experimental data seem to support the SED approach as proposed by Lazzarin and co-workers [31,38], which does not take into account the phase shift between the different load contributions. To exclude the influence of mean stresses and so the uncertainties in residual stress evaluation, it is convenient to refer again to the stress relieved joints. A comparison among figures 15, 16 and 17, which report the results in terms of nominal stresses, and figures Figs 6, 8 and 11a quantifies the reduction in the scatter indexes obtained. Again it should be noted that a scatter index of 1.90 referred to the 2.3%-97.7% survival probabilities corresponds to the intrinsic scatter of single test series according to Haibach [33] and Sonsino [23,24]. As to the as-welded joints, a general conservatism has been observed between theoretical

estimations and experimental results. It is the authors' opinion that one of the reasons for that is due to the compressive residual stresses that have been measured for example by Yung and Lawrence [39] in tube-to-flange welded joints, who noted that fatigue strength was decreased after performing the post-welding heat treatment to relieve residual stresses.

2.3.2 Aluminium welded joints

The analyses of the previous paragraph has been carried out for the original fatigue data of aluminium welded joint found in the literature. In view of this, Table 12 properly reports the equivalent peak stress evaluated at the weld toe and at the weld root by means of the appropriate expressions mentioned in the previous section, where $\tau_{nom}=1$ MPa, $\sigma_{nom}=\Lambda \cdot \tau_{nom}$ have been used (if $\Lambda=\infty$, then $\sigma_{nom}=1$ was applied). By using the equivalent peak stress related to the unit of nominal stress, to convert the original data to the local equivalent peak stress, it is possible to multiply the nominal stress range adopted in the original fatigue tests by the relevant equivalent peak stress reported in Table 12.

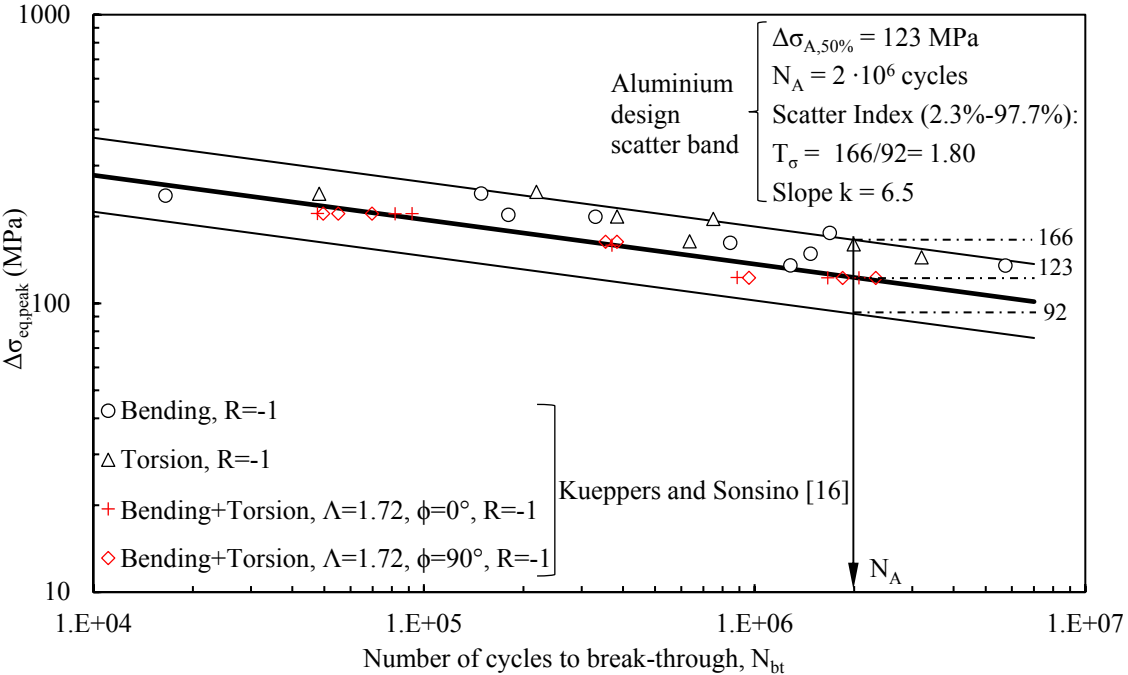


Figure 2.18: Fatigue assessment of tube-to-flange welded joints made of aluminium alloy according to the PSM. Comparison between the proposed multiaxial fatigue design scatter band and experimental fatigue results from [16]. [Figure taken from [1]]

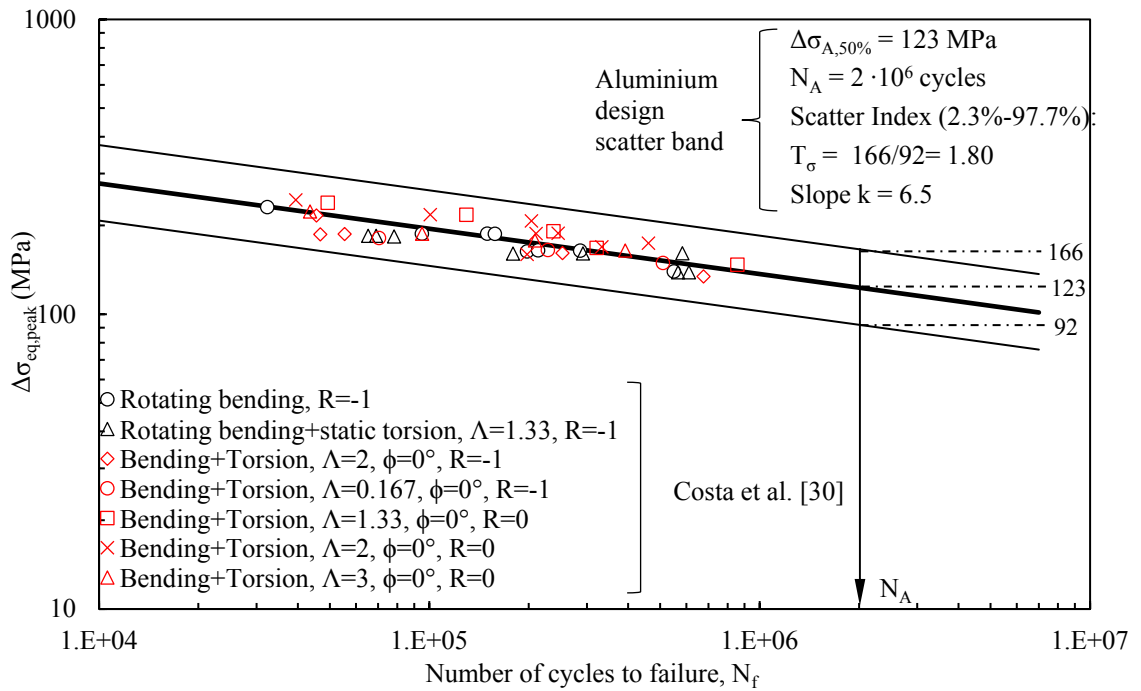


Figure 2.19 Fatigue assessment of overlap-tubes welded joints made of aluminium alloy according to the PSM. Comparison between the proposed multiaxial fatigue design scatter band and experimental fatigue results from [30]. [Figure taken from [1]]

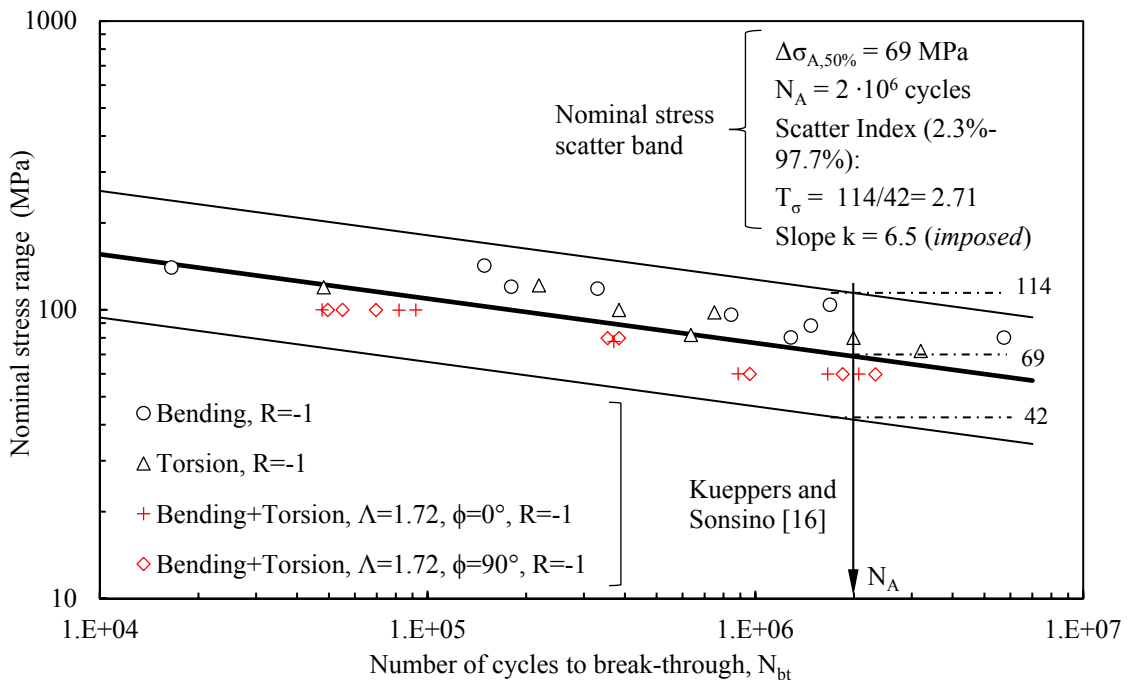


Figure 2.20: Experimental fatigue results relevant to tube-to-flange welded joints made of aluminium alloy taken from [16] and expressed in terms of nominal shear (for pure torsion) or normal (for all other cases) stress range. See Fig. 18 for comparison. [Figure taken from [1]]

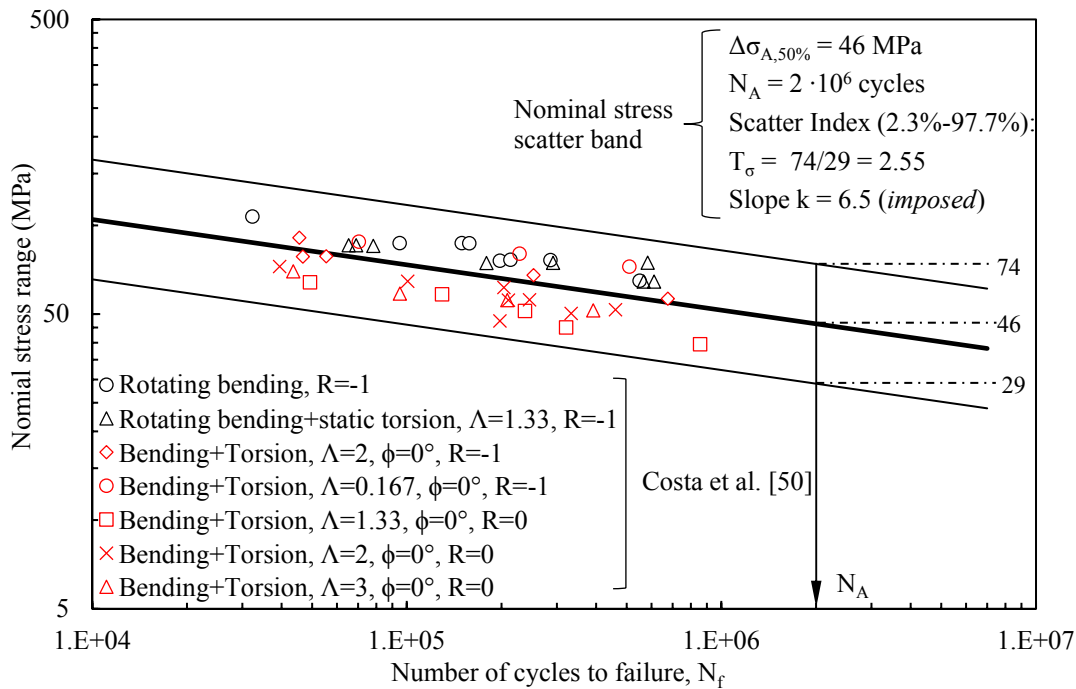


Figure 2.21: Experimental fatigue results relevant to overlap-tubes welded joints made of aluminium alloy taken from [30] and expressed in terms of nominal normal stress range. See Fig. 19 for comparison [Figure taken from [1]]

The scatter band proposed for multiaxial fatigue design of aluminium welded joints is compared in Figs. 18 and 19 to experimental results related to tube-to-flange [16] and overlap-tubes [30] welded joints made of aluminium alloys, respectively. The scatter band reported in Figs. 18 and 19 was defined fatigue stress range at 2 million cycles obtained under pure mode I loading and the inverse slope relevant to pure mode III loading (i.e. pure torsion loading). Such a definition of the design scatter band is according to the SED approach proposed by Lazzarin et al. [31]. The endurable stress ranges for different survival probabilities at $2 \cdot 10^6$ cycles valid for aluminium joints under pure mode I loading and expressed in terms of equivalent peak stress range had it was found $\Delta\sigma_{A,50\%} = 123$ MPa (50% survival probability) by fitting tens of experimental results taken from the literature (Refs. [40]). The value of the inverse slope of the design scatter band of aluminum welded joints subjected to pure mode III loading is equal to 6.5 and it was found experimentally by Lazzarin et al. [41]. The same slope value is also reported in [16]. Figs. 18 and 19 report $T_\sigma = 1.80$ of the design scatter band referred to survival probabilities of 2.3%-97.7% (i.e. mean value \pm two standard deviations). This value is consistent with $T_\sigma = 1.50$ referred to survival probabilities of 10%-90%, which is the intrinsic scatter of single test series, as reported by Haibach [33] and mentioned in ref. [16] were the experimental data analysed in Fig. 18 were taken from.

A good agreement between experimental data and theoretical estimations based on the PSM was obtained for joints tested under uniaxial as well as under multiaxial

fatigue loadings, as it can be noted in Figs. 18 and 21. In particular, Fig. 18 shows that to pure bending and torsion data are a bit shifted in the conservative region and an even higher degree of conservatism of the pure torsion data was observed in the original paper [16], applying critical plane approach by combining the normal and shear stresses according to Von Mises expression. It is worth noting that in [16] any effect of the phase shift between the bending and torsion stresses has been observed. Therefore, the adopted SED approach (Eq. (5) of Chapter 1), which does not explicitly account for any phase shift, is consistent with the observed fatigue behaviour of aluminium welded joints. Concerning the obtained results on stress relieved joints reported in Fig. 19, it can be observed that all data are in excellent agreement with the theoretical predictions. Furthermore, the mean stress effect is correctly accounted for. Indeed, the influence of a static torsion stress superimposed to the rotating bending stress is not taken into account by the SED criterion (see Eq. (5) of Chapter 1); however, the influence of mean stress is only confined in the medium- and high-cycle fatigue regimes, as Fig. 19 and the original paper [30] highlight.

Figures 20 and 21 report the results expressed in terms of nominal stresses rather than in equivalent peak stress (Figs 18 and 19). Comparing the relevant couple of figures, the reduction of the scatter indexes obtained when local stresses according to the PSM are used can be appreciated.

2.4 DISCUSSION

As a result of this development, it is appropriate to highlight the advantages of the present method and its current limitations.

The main advantages of the PSM can be listed as follows:

- it is a local approach, therefore the adopted damage parameter is representative of local linear elastic stress state of the welded structure.
- it is not necessary to model the material-dependent structural volume having size R_0 in order to evaluate numerically the averaged SED;
- relatively coarse FE meshes can be modelled, considerably reducing the computational efforts pertaining to the NSIF approach ;
- only the linear elastic peak stresses evaluated at the point of stress singularity are necessary to evaluate the equivalent peak stress;

It is worth underlining that the parameters K^*_{FE} , K^{**}_{FE} and K^{***}_{FE} of equations (1-3) depend on the following conditions: (i) formulation of the element; (ii) mesh pattern of finite elements and (iii) numerical procedure to extrapolate stresses at FE nodes (well-explained in [42]).

Originally, K^*_{FE} , K^{**}_{FE} and K^{***}_{FE} have been calibrated by adopting ANSYS® FE code and the average values of 1.38, 3.38 and 1.93, respectively, have been derived under the conditions of applicability summarised in Table 1.

More recently, K^*_{FE} , K^{**}_{FE} (Eq. (1) and (2)) have also been calibrated for six commercial FE packages other than Ansys®, namely Abaqus®, Straus 7®, MSC® Patran/Nastran, Lusas®, Hypermesh/Optistruct/Hyperview® and Hypermesh/Ls-Dyna/Hyperview® [42].

Furthermore, for some complex 3D model, it is necessary to adopt the submodelling technique first by solving a main model and then a submodel in which the most stressed weld bead is included. For respecting the required mesh pattern of the PSM, originally the sub model had to be extruded from the 2D cross-section of the weld bead (as done in this work). However, in a more recent paper, the PSM was also calibrated for being applicable by using 10-node tetrahedral elements, overcoming the issue above mentioned [43].

2.5 CONCLUSIONS

The peak stress method (PSM), which was originally formulated for pure axial and bending loadings or pure torsion loadings, has been developed for the first time to welded joints under multiaxial cyclic loading conditions.

Basically, the PSM is based on the NSIF approach, which assumes the weld toe and the weld root as a sharp V-notch and a pre-crack, respectively. It employs the singular, linear elastic peak stresses evaluated at the toe and root sides by means of FE analyses carried out by adopting a given mesh pattern, in which the element type is kept constant and the FE size can be chosen arbitrarily within the applicability range of the method.

A properly defined design stress, the so-called equivalent peak stress, allows to estimate the failure location and to assess the multiaxial fatigue strength of welded joints. When multiple crack initiation sites are in competition in the same joint, comparison among the equivalent peak stresses enables to discern the most critical one.

About 350 experimental data grouped into 78 test series have been considered all in all. When multiple potential failure locations were in competition in the same joint, which is a typical condition in partially penetrated welded joints (this is the case of 68 among 78 test series), the PSM properly assessed the fatigue crack initiation site in 60 test series among 68 (i.e. 88%).

A new scatter band in terms of range of the equivalent peak stress has been proposed for the multiaxial fatigue design of welded joints made of structural steels. It combines the high-cycle fatigue strength of steel welded joints under pure mode I loading and the inverse slope of the design scatter band for pure mode III loading: both of them had been evaluated in previous papers. Thereafter, the multiaxial fatigue strength of the considered welded joints has been assessed by means of the proposed scatter band. For some of the considered test series, consisting of 52 among 350 analysed experimental data, it has been observed that the theoretical predictions based on the PSM were extremely on the safe side. A twofold tentative interpretation has

been put forward: most of those data were characterized by remarkable long crack propagation paths (up to 500 mm) developed during the experimental tests with applied torsional loading. Such long fraction of the total fatigue life can hardly be rationalized by the PSM, because by nature the method captures the fatigue damage induced by the intense NSIF-dominated local stresses existing in the small volume of material surrounding the crack initiation point; Secondly, as far as as-welded joints and tube-to-flange configurations are considered, significant compressive residual stresses might have been generated during the welding process, according to the published literature. Dealing with the remaining test data, a good agreement has been obtained from the comparison of theoretical estimations with the experimental fatigue results, 205 data among 298 (i.e. 69%) falling within the 2.3-97.7% design scatter band.

The proposed approach has been also applied to assess weld toe failures in tube-to-flange and overlap-tubes welded joints made of aluminium alloys and tested under uniaxial as well as multiaxial fatigue loadings, covering in-phase as well as out-of-phase loading situations. All in all, 72 experimental data grouped into 11 test series have been considered. In the case of partially penetrated welded joints, the PSM correctly estimated the location of fatigue failures in 6 among 7 test series (i.e. 86%) subjected to multiaxial loading conditions.

A new scatter band, expressed in terms of range of the equivalent peak stress, has been proposed for the multiaxial fatigue design of aluminium welded joints. It takes the high-cycle fatigue strength of aluminium welded joints under pure mode I loading, which had been found in previous papers, and the inverse slope of the aluminium design scatter band relevant to pure mode III loading, which has been taken from the literature. Comparison between theoretical estimations and the experimental fatigue results was satisfactory, 70 among 72 experimental data (i.e. 97%) successfully falling inside the proposed 2.3-97.7% scatter band. Because of the simplicity of a point-like method combined with the robustness of the NSIF approach, the PSM might be useful in industrial applications.

2.6 REFERENCES

- [1] Meneghetti G, Campagnolo A, Rigon D. Multiaxial fatigue strength assessment of welded joints using the Peak Stress Method – Part I: Approach and application to aluminium joints. *Int J Fatigue* 2017;101:328–42.
doi:10.1016/j.ijfatigue.2017.03.038.
- [2] Meneghetti G, Campagnolo A, Rigon D. Multiaxial fatigue strength assessment of welded joints using the Peak Stress Method – Part I: Approach and application to aluminium joints. *Int J Fatigue* 2017;101:328–42.
doi:10.1016/j.ijfatigue.2017.03.038.
- [3] Nisitani H, Teranishi T. KI value of a circumferential crack emanating from an

- ellipsoidal cavity obtained by the crack tip stress method in FEM. In: Guagliano M, Aliabadi MH, editors. Proc. 2nd Int. Conf. Fract. damage Mech., 2001, p. 141–6.
- [4] Nisitani H, Teranishi T. KI of a circumferential crack emanating from an ellipsoidal cavity obtained by the crack tip stress method in FEM. *Eng Fract Mech* 2004;71:579–85. doi:10.1016/S0013-7944(03)00035-3.
- [5] Meneghetti G, Lazzarin P. Significance of the elastic peak stress evaluated by FE analyses at the point of singularity of sharp V-notched components. *Fatigue Fract Eng Mater Struct* 2007;30:95–106. doi:10.1111/j.1460-2695.2006.01084.x.
- [6] Meneghetti G, Guzzella C. The peak stress method to estimate the mode I notch stress intensity factor in welded joints using three-dimensional finite element models. *Eng Fract Mech* 2014;115:154–71. doi:10.1016/j.engfracmech.2013.11.002.
- [7] Meneghetti G. The use of peak stresses for fatigue strength assessments of welded lap joints and cover plates with toe and root failures. *Eng Fract Mech* 2012;89:40–51. doi:10.1016/j.engfracmech.2012.04.007.
- [8] Meneghetti G. The peak stress method for fatigue strength assessment of tube-to-flange welded joints under torsion loading. *Weld World* 2013;57:265–75. doi:10.1007/s40194-013-0022-x.
- [9] Radaj D. State-of-the-art review on the local strain energy density concept and its relation to the J -integral and peak stress method. *Fatigue Fract Eng Mater Struct* 2015;38:2–28. doi:10.1111/ffe.12231.
- [10] Meneghetti G, Campagnolo A, Berto F, Atzori B. Averaged strain energy density evaluated rapidly from the singular peak stresses by FEM: cracked components under mixed-mode (I+II) loading. *Theor Appl Fract Mech* 2015;79:113–24. doi:10.1016/j.tafmec.2015.08.001.
- [11] Meneghetti G, Campagnolo A, Berto F. Averaged strain energy density estimated rapidly from the singular peak stresses by FEM: Cracked bars under mixed-mode (I+III) loading. *Eng Fract Mech* 2016;167:20–33. doi:10.1016/j.engfracmech.2016.03.040.
- [12] Livieri P, Lazzarin P. Fatigue strength of steel and aluminium welded joints based on generalised stress intensity factors and local strain energy values. *Int J Fract* 2005;133:247–76. doi:10.1007/s10704-005-4043-3.
- [13] Lazzarin P, Lassen T, Livieri P. A notch stress intensity approach applied to fatigue life predictions of welded joints with different local toe geometry. *Fatigue Fract Eng Mater Struct* 2003;26:49–58. doi:10.1046/j.1460-2695.2003.00586.x.
- [14] Williams ML. Stress singularities resulting from various boundary conditions in angular corners of plates in tension. *J Appl Mech* 1952;19:526–8.
- [15] Lazzarin P, Tovo R. A unified approach to the evaluation of linear elastic stress fields in the neighborhood of cracks and notches. *Int J Fract* 1996;78:3–19. doi:10.1007/BF00018497.
- [16] Kueppers M, Sonsino CM. Critical plane approach for the assessment of the fatigue behaviour of welded aluminium under multiaxial loading. *Fatigue Fract Eng Mater Struct* 2003;26:507–13. doi:10.1046/j.1460-2695.2003.00674.x.
- [17] Dahle T, Olsson K-E, Jonsson B, Bäckström M, Siljander A, Kuitunen R, et al. Multiaxial fatigue experiments of square hollow section tube-to plate welded joints. In: Blom AF, editor. Proc. First North Eur. Eng. Sci. Conf. (NESCO I), Welded High strength steel Struct., London, UK: EMAS Ltd; 1997, p. 163–177.
- [18] Meneghetti G, Guzzella C, Atzori B. The peak stress method combined with 3D finite element models for fatigue assessment of toe and root cracking in steel welded joints subjected to axial or bending loading. *Fatigue Fract Eng Mater Struct* 2014;37:722–39. doi:10.1111/ffe.12171.
- [19] Siliander A, Kurath P, Lawrence F V. Nonproportional Fatigue of Welded Structures. In: Mitchel MR, Landgraf R, editors. Adv. Fatigue Lifetime Predict. Tech. ASTM STP 1122, Philadelphia, PA: ASTM; 1992, p. 319–38.
- [20] Razmjoo G. Fatigue of Load-Carrying Fillet Welded Joints Under Multiaxial Loadings. In: Abington, editor. TWI REF. 7309.02/96/909, Cambridge, UK: 1996.

- [21] Yousefi F, Witt M, Zenner H. Fatigue strength of welded joints under multiaxial loading: experiments and calculations. *Fatigue Fract Eng Mater Struct* 2001;24:339–55. doi:10.1046/j.1460-2695.2001.00397.x.
- [22] Bäckström M, Siljander A, Kuitunen R, Ilvonen R. Multiaxial fatigue experiments of square hollow section tube-to plate welded joints. In: Blom AF, editor. *First North Eur. Eng. Sci. Conf. (NESCO I)*, London, UK: Welded High strength steel structures, EMAS; 1997, p. 163–77.
- [23] Sonsino CM. Multiaxial fatigue of welded joints under in-phase and out-of-phase local strains and stresses. *Int J Fatigue* 1995;17:55–70. doi:10.1016/0142-1123(95)93051-3.
- [24] Sonsino CM, Łagoda T. Assessment of multiaxial fatigue behaviour of welded joints under combined bending and torsion by application of a fictitious notch radius. *Int J Fatigue* 2004;26:265–79. doi:10.1016/S0142-1123(03)00143-9.
- [25] Bertini L, Cera A, Frenzo F. Experimental investigation of the fatigue resistance of pipe-to-plate welded connections under bending, torsion and mixed mode loading. *Int J Fatigue* 2014;68:178–85. doi:10.1016/j.ijfatigue.2014.05.005.
- [26] Frenzo F, Bertini L. Fatigue resistance of pipe-to-plate welded joint under in-phase and out-of-phase combined bending and torsion. *Int J Fatigue* 2015;79:46–53. doi:10.1016/j.ijfatigue.2015.04.020.
- [27] Takahashi I, Takada A, Ushijima M, Akiyama S. Fatigue behaviour of a box-welded joint under biaxial cyclic loading: effects of biaxial load range ratio and cyclic compressive loads in the lateral direction. *Fatigue Fract Eng Mater Struct* 2003;26:439–48. doi:10.1046/j.1460-2695.2003.00645.x.
- [28] Takahashi I, Ushijima M, Takada A, Akiyama S, Maenaka H. Fatigue behaviour of a box-welded joint under biaxial cyclic loads. *Fatigue Fract Eng Mater Struct* 1999;22:869–77. doi:10.1046/j.1460-2695.1999.00224.x.
- [29] Meneghetti G, Campagnolo A, Rigon D. Multiaxial fatigue strength assessment of welded joints using the peak stress method – part I: approach and application to aluminium joints. *Int J Fatigue* n.d.:(submitted).
- [30] Costa JDM, Abreu LMP, Pinho ACM, Ferreira JAM. Fatigue behaviour of tubular AlMgSi welded specimens subjected to bending-torsion loading. *Fatigue Fract Eng Mater Struct* 2005;28:399–407. doi:10.1111/j.1460-2695.2005.00875.x.
- [31] Lazzarin P, Livieri P, Berto F, Zappalorto M. Local strain energy density and fatigue strength of welded joints under uniaxial and multiaxial loading. *Eng Fract Mech* 2008;75:1875–89. doi:10.1016/j.engfracmech.2006.10.019.
- [32] Meneghetti G, Lazzarin P. The Peak Stress Method for Fatigue Strength Assessment of welded joints with weld toe or weld root failures. *Weld World* 2011;55:22–9. doi:10.1007/BF03321304.
- [33] Haibach E. *Service fatigue-strength – methods and data for structural analysis*. Dusseldorf: VDI; 1989.
- [34] Lazzarin P, Tovo R. A notch intensity factor approach to the stress analysis of welds. *Fatigue Fract Eng Mater Struct* 1998;21:1089–103. doi:10.1046/j.1460-2695.1998.00097.x.
- [35] Lazzarin P, Zambardi R. A finite-volume-energy based approach to predict the static and fatigue behavior of components with sharp V-shaped notches. *Int J Fract* 2001;112:275–98. doi:10.1023/A:1013595930617.
- [36] Eurocode 3: Design of steel structures – part 1–9: Fatigue. CEN; 2005.
- [37] Hobbacher AF. *Recommendations for Fatigue Design of Welded Joints and Components*. IIW Collection. Springer International Publishing; 2016. doi:10.1007/978-3-319-23757-2.
- [38] Berto F, Lazzarin P. Fatigue strength of structural components under multi-axial loading in terms of local energy density averaged on a control volume. *Int J Fatigue* 2011;33:1055–65. doi:10.1016/j.ijfatigue.2010.11.019.
- [39] Yung JY, Lawrence F V. Predicting the fatigue life of welds under combined bending and torsion. In: Brown M, Miller K, editors. *Biaxial multiaxial fatigue EGF 3.*,

- London: Mechanical Engineering Publications; 1989, p. 53–69.
- [40] Meneghetti G, Campagnolo A, Berto F. Fatigue strength assessment of partial and full-penetration steel and aluminium butt-welded joints according to the peak stress method. *Fatigue Fract Eng Mater Struct* 2015;38:1419–31. doi:10.1111/ffe.12342.
 - [41] Lazzarin P, Sonsino CM, Zambardi R. A notch stress intensity approach to assess the multiaxial fatigue strength of welded tube-to-flange joints subjected to combined loadings. *Fatigue Fract Eng Mater Struct* 2004;27:127–40. doi:10.1111/j.1460-2695.2004.00733.x.
 - [42] Meneghetti G, Campagnolo A, Avalor M, Castagnetti D, Colussi M, Corigliano P, et al. Rapid evaluation of notch stress intensity factors using the peak stress method: Comparison of commercial finite element codes for a range of mesh patterns. *Fatigue Fract Eng Mater Struct* 2018;41:1044–63. doi:10.1111/ffe.12751.
 - [43] Campagnolo A, Meneghetti G. Rapid estimation of notch stress intensity factors in 3D large-scale welded structures using the peak stress method. *MATEC Web Conf* 2018;165:17004. doi:10.1051/mateconf/201816517004.

Chapter 3: The use of the Specific Heat Loss per cycle to correlate the fatigue strength of severely notched stainless steel specimens

This chapter describes the experimental protocol used for validating the Specific Heat Loss per cycle to severely notched components made of AISI 304L stainless steel.

The specific heat loss per cycle (Q parameter) evaluated experimentally by means of the so-called *cooling gradient technique* was used in previous works to synthesise 140 experimental fatigue test results generated from plain and bluntly notched specimens made of AISI 304L stainless steel. Since the cooling gradient was measured by means of thermocouple wires attached to the specimen's surface with a 1.5-to-2 mm glue dot diameter, notches with tip radii greater than 3 mm were considered because the glue dot diameter would have been too large to capture the specific heat loss at the tip of sharper notches. Therefore, in this work the cooling gradient was measured by means of a FLIR SC7600 infrared camera, equipped with proper lens and a spacer ring to achieve a 20 μm /pixel spatial resolution and fully reversed axial fatigue tests were carried out on 4-mm-thick, hot-rolled AISI 304L stainless steel specimens, characterized by 3, 1 and 0.5 mm notch tip radii. The new fatigue data were resulted in good agreement with the existing heat energy-based scatter band previously calibrated.

Then, an automatic data processing technique was developed in the Matlab® code to investigate the distribution of the energy dissipated around the notch tip starting from the evaluation of Q by means of the *cooling gradient technique* pixel-by-pixel of the infrared video recorded. A robust analytical framework and numerical simulations were proposed to provide the applicability of such procedure.

This chapter is referred to the following author's papers:

[1] Rigon, D.; Ricotta, M.; Meneghetti, G. *The use of the heat energy loss to correlate the fatigue strength of severely notched stainless steel specimens. In Proceedings International Symposium on Notch Fracture (ISNF) Santander, Spain, March 2017*

[2] Rigon D; Ricotta M; Meneghetti G, *An analysis of the specific heat loss at the tip of severely notched stainless steel specimens to correlate the fatigue strength. Theoretical And Applied Fracture Mechanics*, 92: 240-251, 2017 - ISSN:0167-8442 (92) doi:10.1016/j.tafmec.2017.09.003.

[3] Rigon D; Ricotta M; Meneghetti G, *Evaluating the specific heat loss in severely notched stainless steel specimens for fatigue strength analyses. pp.151-158. Procedia Structural Integrity*, 9:151-158, 2018 doi:10.1016/J.PROSTR.2018.06.023

[4] Rigon D, Ricotta M, Meneghetti G. Analysis of dissipated energy and temperature fields at severe notches of AISI 304L stainless steel specimens. *Frattura Ed Integrità Strutturale* 2019;13:334–47. doi:10.3221/IGF-ESIS.47.25.

3.1 INTRODUCTION AND THEORETICAL BACKGROUND

In [5–8], the Q parameter was adopted to synthesise 140 experimental results obtained from constant amplitude, push-pull, stress- or strain-controlled fatigue tests carried out on plain and notched hot rolled AISI 304L stainless steel specimens as well as from cold drawn un-notched bars of the same steel, under fully-reversed axial or torsional fatigue loadings. The fatigue test results synthesised in terms of Q are reported in Fig. (1); all of them fall in a single energy-based scatter band, which was fitted only on the fatigue test results relevant to plain material, hole specimens, U and bluntly V notched specimens [6].

Depending on the severity of the stress concentration effect, the heat energy can be evaluated either at a point or averaged in a material volume. More precisely, in case of blunt notches the specific heat loss were evaluated at a point of a specimen (Q), i.e. at the notch tip; in case of severe V-notches or cracks (data from [8], Fig. (1)), the specific heat loss has been averaged in a control volume of material surrounding the tip of the stress raiser (Q*). The need for averaging is reminiscent of Neuber’s finite-size structural volume concept [9].

To evaluate Q or Q*, three experimental techniques have been proposed that will be briefly presented in the following. The first one evaluates Q, while the remaining two ones evaluate Q*.

Point-related cooling gradient technique

A simple experimental evaluation of the Q parameter at a point of a component’s surface was proposed in [10], which consists in measuring the cooling gradient at the time just after the fatigue test has been stopped, according to Eq. (1):

$$Q = \frac{\rho \cdot c \cdot \partial T / \partial t}{f_L} \quad (1)$$

where T(t) is the time-variant temperature at the point, ρ is the material density, c is the material specific heat and f_L is the load test frequency. In [6,7] the cooling gradients were measured by using thermocouple wires having diameter of 0.127 mm, which were attached to the notch tip by means of a 1.5-2 mm silver-loaded glue dot diameter; conversely, in [8] temperature was monitored by means of an infrared camera because of the much more localized temperature field caused by the notch tip radii lower than 3 mm, which were tested in [6,7].

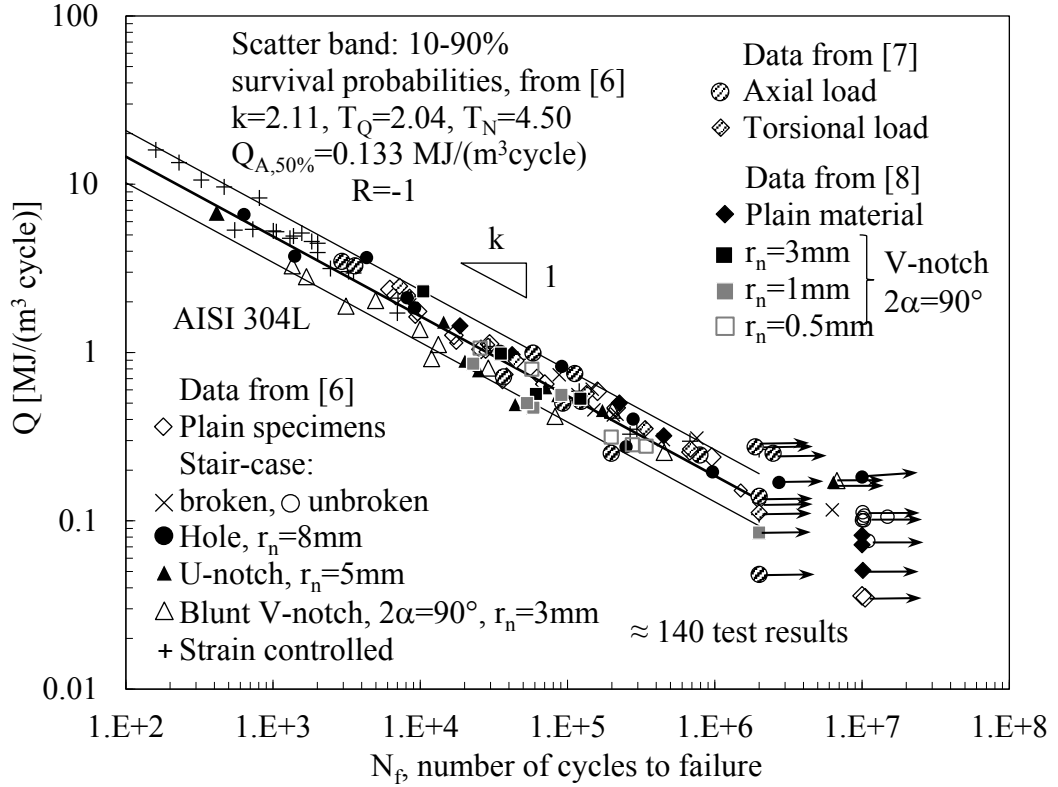


Figure 3.1: Fatigue tests results in terms of specific heat energy. The scatter band was calibrated only on data published in [6].

Spatial gradient technique

In order to extend the heat energy method to severely notched or cracked materials, the specific heat energy per cycle was averaged in a control volume V_c , located at the notch or crack tip according to Fig. (2). The averaged energy per cycle Q^* was defined and was experimentally evaluated using the following equation ([11]):

$$Q^* = \frac{1}{V_c} \int Q \cdot dV = -\frac{1}{f_L V} \cdot \lambda \cdot z \cdot R_c \cdot \int_{-\pi}^{+\pi} \frac{\partial T_m(r, \theta)}{\partial r} \Big|_{r=R_c} \cdot d\theta \quad (2)$$

where λ is the material thermal conductivity, z the specimen's thickness, R_c the radius of the control volume V_c and T_m the mean temperature field evaluated during the test after that thermal equilibrium is achieved, r and θ are the polar coordinates. Fig (3b) shows a typical temperature vs time acquisition at a point of a specimen or component after a fatigue test has started. If the temperature field is monitored by means of an infrared camera, Fig. (3b) might be interpreted as the temperature vs time history of the i -th pixel and it shows that temperature increases until the mean temperature level stabilises, while the alternating component due to the thermoelastic effect still exists. If we consider a sampling window taken after thermal equilibrium

with the surroundings is achieved (between t_s and t^* in figure 3), the mean temperature T_m for i -th pixel, can be defined as follows:

$$T_m^i = \frac{\sum_{j=1}^{n_{\max}} T_j^i}{n_{\max}} \quad (3)$$

where T_j^i are the temperature data acquired at a sampling rate f_{acq} and $n_{\max} = f_{\text{acq}} \cdot (t^* - t_s)$ is the number of picked-up samples between the time t_s ($j=1$) and the time t^* ($j=n_{\max}$).

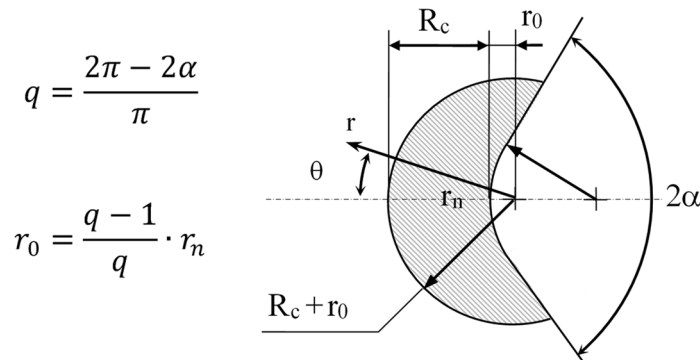


Figure 3.2: Material control volume at a notch tip according to [12] ($r_0=0.2$, $2\alpha=135^\circ$).

If we suppose now that at $t=t^*$ the fatigue test is suddenly interrupted, Fig. (3b) shows the cooling curve leading to the thermal equilibrium with the surroundings. The cooling gradient measured at $t=t^*$ is exactly that appearing in Eq. (1).

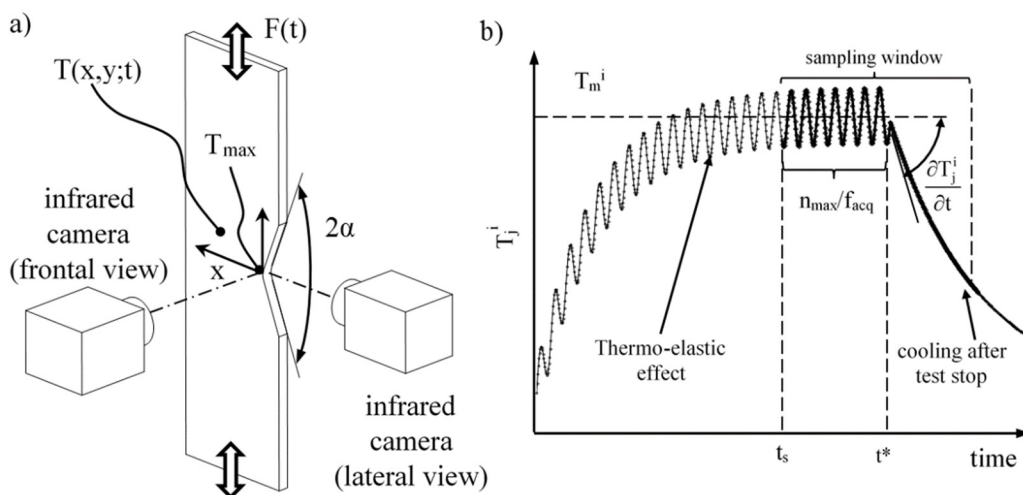


Figure 3.3: Experimental set-up adopted (a) and evaluation of the cooling gradient (from Eq. (1)) during a fatigue test (b).

Regarding V_c , the critical volume size R_c was calibrated in [12], by equating the averaged heat loss Q^* of the plain specimen's case and the cracked specimen's case for the same fatigue life. Calibration of the critical volume size R_c was performed at fatigue lives on the order of 10^5 cycles. The reader is referred to [12] for additional details. As a result, R_c was found equal to 0.52 mm for the hot-rolled AISI 304L stainless steel tested in completely reversed fatigue.

Averaged cooling gradient technique

In [11], it has been demonstrated that Q^* can be calculated according to Eq. (1), provided that the point-related cooling gradient is substituted by the cooling gradient of temperature averaged inside V_c , T^* , as follows:

$$Q^* = \frac{\rho \cdot c \cdot \partial T^* / \partial t}{f_L} \quad (4)$$

the cooling gradient being evaluated at $t=t^*$ indicated in Fig. (3b). The averaged temperature T^* can be calculated starting from the infrared thermal maps where again T_j^i is the j -th sample picked-up at the i -th pixel location:

$$T_j^* = \frac{\sum_{i=1}^{n_{V_c}} T_j^i}{n_{V_c}} \quad (5)$$

where n_{V_c} is the number of pixels inside V_c .

The aim of this research work is to apply the heat energy approach to specimens with notch tip radii equal to 3, 1, and 0.5 mm, and to compare Q from equation (1) with Q^* estimated from equations (2) and (4). Furthermore, an analysis of the Q field around the notch tip will be evaluated starting from cooling measurements by using an infrared camera and analysing data by means of a proper developed Matlab® script. Finally, the Q -field results will be discussed from a theoretical point of view.

3.2 MATERIAL AND METHODS

3.2.1 Experimental protocol

Constant amplitude, completely reversed, stress-controlled fatigue tests were carried out on 4-mm thick, hot rolled AISI 304L stainless steel specimens, having notch tip radii r_n equal to 3, 1, and 0.5 mm, as reported in Fig. (4a). The mechanical properties and the chemical composition are reported in Table 1 [20], while Fig. (4b) shows the austenitic microstructure of the material. The analysed stainless steel had a

material density ρ and the specific heat c equal to 7940 kg/m^3 and 507 J/(kg K) , respectively [15,23].

Starting from $46 \times 150 \text{ mm}$ rectangular plates, notches were obtained by wire electro-discharge machining, followed by electrochemical polishing. After that, the specimen surfaces were polished using progressively finer emery papers (until the maximum paper grade of 4000 was reached), in order to prepare the surface for fatigue crack monitoring. One surface of the specimen, as well as the notch root in the thickness direction, were black painted to increase the material emissivity in view of the infrared thermal acquisitions, as will be discussed in the next sections.

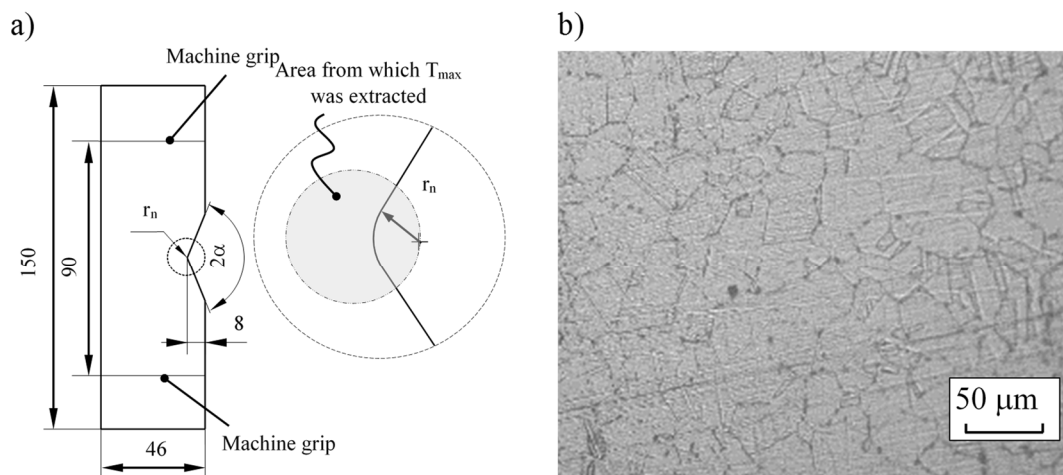


Figure 3.4: Specimen's geometry (units in mm) (a) and microstructure of the AISI 304L stainless steel (b).

Table 3.1: Mechanical properties and chemical composition of the hot-rolled AISI 304L stainless steel

$R_{p0.2\%}$ (MPa)	R_m (MPa)	A (%)	$\sigma_{A,-1.50\%}$ (MPa)	HB	C (%)	Mn (%)	Si (%)	Cr (%)	Ni (%)	P (%)	S (%)	N (%)
279	620	57	202	170	0.026	1.470	0.370	18.1	8.2	0.034	0.001	0.058

The net-section stress concentration factors, K_{tn} , were evaluated by carrying out 3D linear elastic finite element analyses and resulted 3.41, 4.85 and 6.10, for r_n equal to 3, 1 and 0.5 mm, respectively. To take into account the machine grip effect, displacements were applied to the relevant lines shown in Fig (4a).

The fatigue tests were carried out by using a servo-hydraulic Schenck Hydropuls PSA 100 machine having a 100 kN load cell and equipped with a TRIO Sistemi RT3 digital controller. Load test frequencies were set in the range between 3 and 40 Hz, depending on the applied stress level, in order to keep the material temperature below $60 \text{ }^\circ\text{C}$. A total number of 25 specimens were fatigue tested, and the number of cycles to failure, N_f , was equal to that for complete separation.

The temperature field surrounding the notch apex was measured by using a FLIR SC7600 infrared camera, operating at a frame rate, f_{acq} , equal to 200 Hz, having a 1.5-5.1 μm spectral response range, 50 mm focal lens, a noise equivalent temperature difference (NETD) < 25 mK and an overall accuracy of 0.05°C . It was equipped with an analog input interface, which was used to synchronize the force signal coming from the load cell with the measured temperature signal. Furthermore, a 30-mm spatial ring was adopted to achieve a spatial resolution of approximately $20 \mu\text{m}/\text{pixel}$. Lastly, infrared images were analyzed by means of the ALTAIR 5.90.002 commercial software.

To monitor the evolution of Q (and Q^*) during each test, 1 to 10 temperature acquisitions (depending on the applied stress levels) were performed using a 10-second-long sampling window with $f_{acq}=200$ Hz (2000 frames), that consisted of approximately 5 seconds of running test (1000 frames between t_s and t^*) followed by the machine stop at the time t^* , and the remaining 5 seconds of acquisition to capture the cooling gradient (additional 1000 frames after t^*).



Figure 3.5: Test setup consisting of a FLIR SC7600 infrared camera, a AM4115ZT Dino-lite digital microscope and the specimen clamped in the test machine

Regarding the *point-related cooling gradient technique*, the cooling gradient of the maximum temperature inside V_c (see Fig. (4a)), T_{\max} was considered in order to evaluate Q just after the test stop t^* by means of Eq. (1). In addition, the temperature field was measured both on the specimen's surface (frontal view) and in the thickness (lateral view), as illustrated in (see Fig. (3a)).

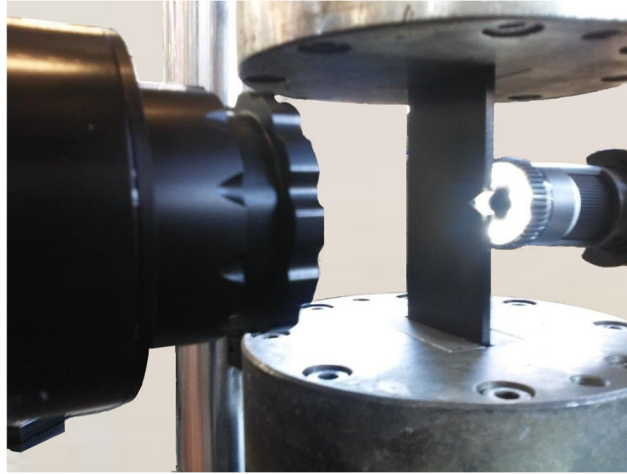


Figure 3.6: Inspection phase of technical crack initiation.

To calculate the averaged heat energy within the control volume V_c , Q^* , by means of the *spatial gradient technique* (Eq. (2)), firstly the initial 1000 frames of the 2000 available were processed by using the FLIR MotionByInterpolation tool, that allows the relative motion between the fixed focal lens and the moving specimen to be compensated. After that, the time-dependent temperature was averaged pixel-by-pixel over the 1000 temperature images by using Eq. (3), thus obtaining the averaged temperature field T_m^i , which in turn was used to calculate the Q^* by means equation (2).

As to the *averaged cooling gradient technique* (Eq. (4)), the temperature averaged inside V_c , T^* , was calculated by the ALTAIR software for each one of the 1000 temperature images available for $t \geq t^*$ by using Eq. (5); having in hands the T^* vs time trend, Q^* was calculated from the cooling gradient of T^* , according to Eq. (4).

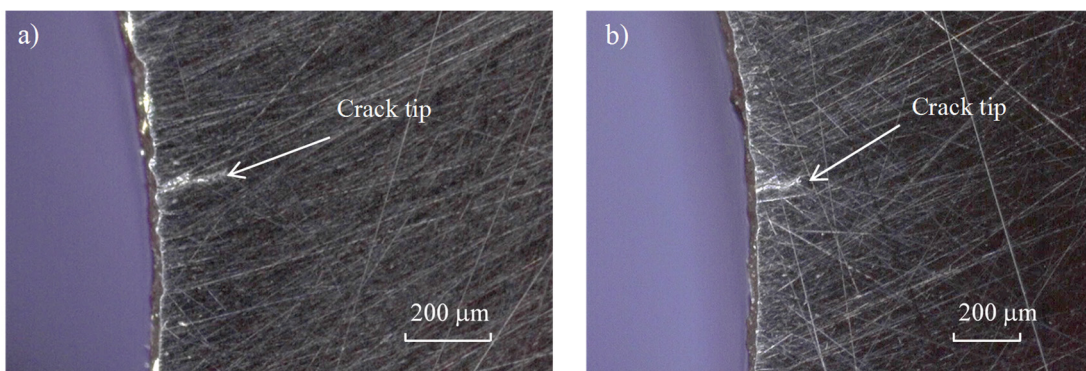


Figure 3.7: A crack observed at the number of cycles of technical crack initiation

At each test stop, the notch tip was monitored by using a AM4115ZT Dino-Lite digital microscope operating with a magnification ranging from 20x to 220x. The microscope and the infrared camera monitored the opposite specimen's surfaces, as shown in Fig. (6).

The technical crack initiation was defined at a number of cycle N_i when a crack a_i was first observed during periodical inspections, as reported in Fig. (7), where a 0.14-mm-long crack emanated from the notch tip can be observed. According to the adopted testing protocol, N_i could not be defined at a fixed crack length; the average technical crack length a_i resulted equal to 0.4 mm.

The effective spatial resolution in each test was evaluated by gently scratching the black painted side of the specimens and measuring both the distance in metric units by using the Digital Microscope DINOLite and the relevant one in pixels by using an infrared image. An example of this procedure is reported in Fig. (8).

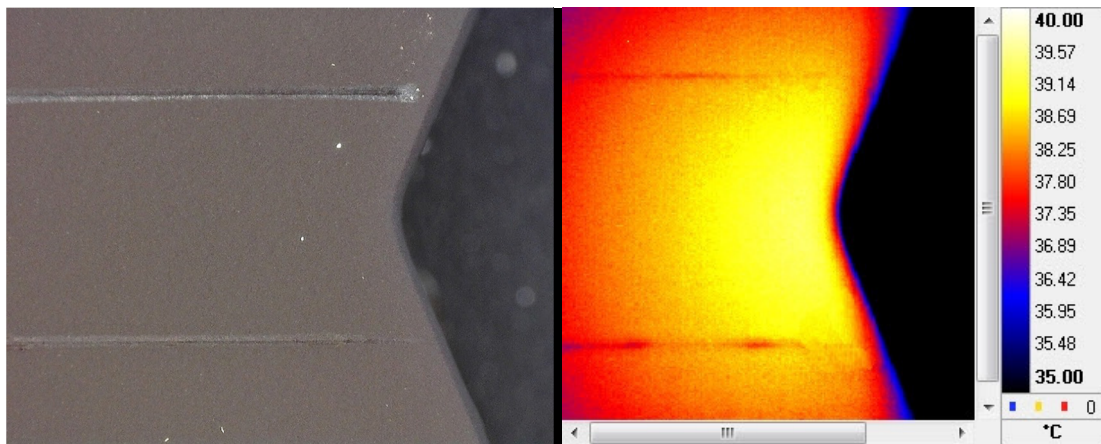


Figure 3.8: Digital microscope image on the left and infrared image on the right used for evaluating the effective spatial resolution before each test.

3.2.2 Data post-processing

The acquired temperature maps and force signal were post-processed by means of the ALTAIR 5.90.002 commercial software and saved as Altair PTW film file (*.ptw). Since the test machine takes some tenth of a second to definitively stop, an engineering definition of t^* was introduced, as follows. The time t^* was defined taking advantage of the data post-processing carried out by using the ALTAIR 5.90.002 commercial software and it was defined as the time when the first peak of the tapered force amplitude signal is within the range of ± 2.7 kN, i.e. below 5% of the force amplitude relevant to the fatigue test in all the acquisitions. Fig. 14 reports an example of t^* evaluation.

In order to obtain the energy distribution at the notch tip of the considered specimens, a numerical procedure was developed by using the Matlab code. First, the Altair video recording file (*.ptw) was converted into an ASCII film file (*.asc), which is readable in Matlab. Next, the ASCII file was input to a dedicated Matlab script, that converts it into a Matlab 3-dimensional array, named $\bar{T}(m,n,p)$, having dimension m -by- n -by- p . The m , n values are the dimensions of the frame expressed in terms of pixels, reduced to avoid vignetting ($m=136$ px, $n=167$ px), and p is the number of

frames acquired by the infrared camera (i.e p is equal to 2000). A schematic illustration of $\bar{T}(m,n,p)$ is shown in Fig. 4a. Let i, j and k be the indexes of $\bar{T}(m,n,p)$. An element of this 3D array corresponds to a temperature value of the n -th pixel having coordinate i and j for the k -th frame. In this way, fixing i and j and plotting T_{ij} against the time (obtained from the division of the k index value by f_{acq}), the time-variant temperature graph, commonly used for evaluated the Q parameter, is obtained for the n -th pixel.

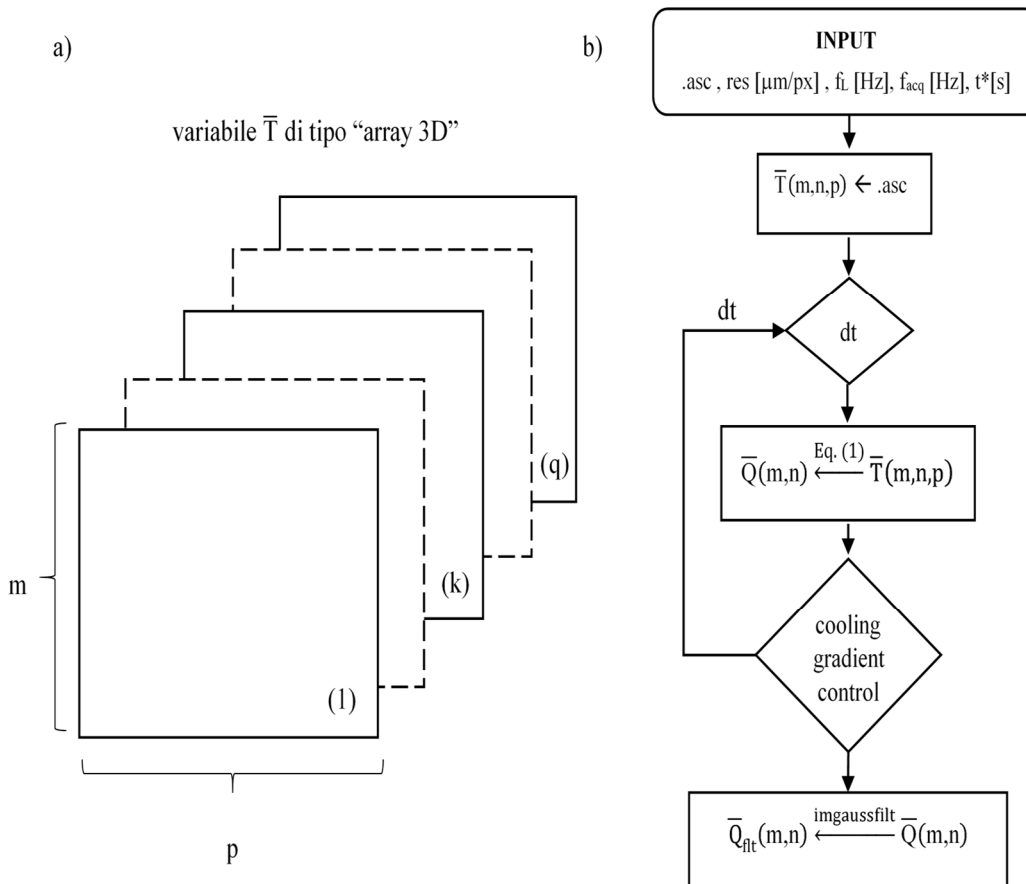


Figure 3.9: Schematic representation of the 3-dimensional array \bar{T} (a). Flowchart of the data analysis to obtain the energy distribution at the notch tip. (b)

A tentative value of 0.1 s was assigned to a numerical variable, named “dt”, for evaluating the cooling gradient of the n -th pixel and it was kept constant for all pixels (see Fig. 4b). In practice, the numerical evaluation of the cooling gradient was performed by the “polyfit” matlab function, which returns the value of the slope of the linear fitting of the data within the time window “dt”. Finally, Q_{ij} is evaluated by applying Eq. (1). This operation was routinely performed for all pixels by a for loop, resulting in a m -by- n matrix composed of Q_{ij} values, called $\bar{Q}(m,n)$. Since the same dt value was fixed for all the pixels and a certain level of noise in the measurements was present, the cooling gradient might result meaningless for some pixels. Therefore, after

plotting the $\bar{Q}(m,n)$ matrix, a check was performed to single-out unrealistic spike-like values.

3.3 ENERGY-BASED SYNTHESIS OF FATIGUE TEST RESULTS

All fatigue test results were summarized in Fig. (10) in terms of net-section stress amplitude, σ_{an} . The scatter band reported in the figure was originally calibrated in [6], considering fatigue test results carried out on U- and V-notched specimens with tip radii equal to 5 mm and 3 mm, respectively, and opening angle $2\alpha = 90^\circ$.

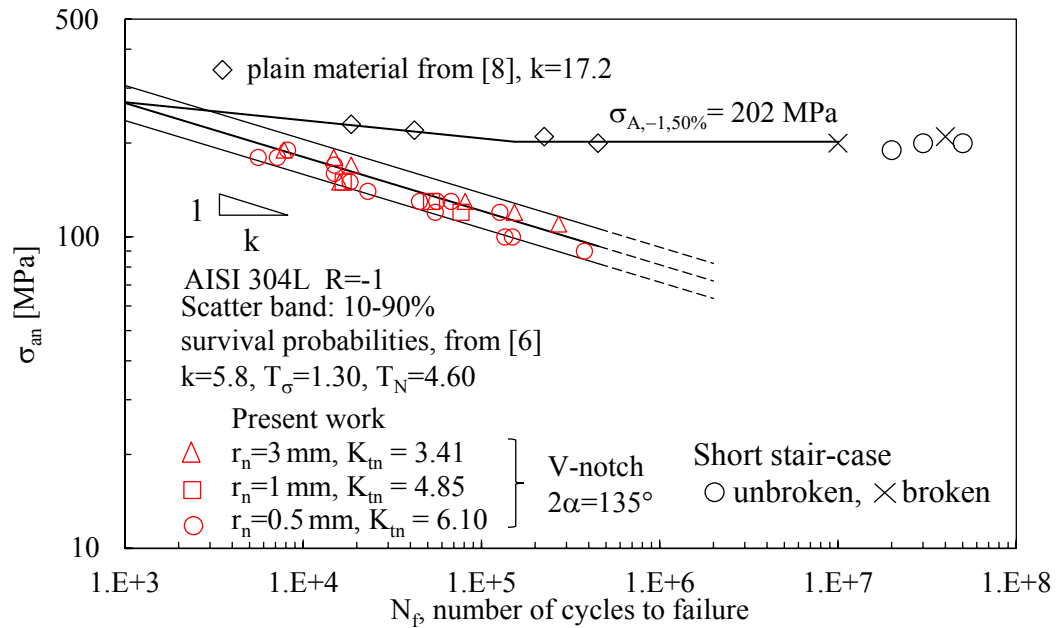


Figure 3.10: Fatigue data analysed in terms of net-section stress amplitude. Scatter band was calibrated in [6].

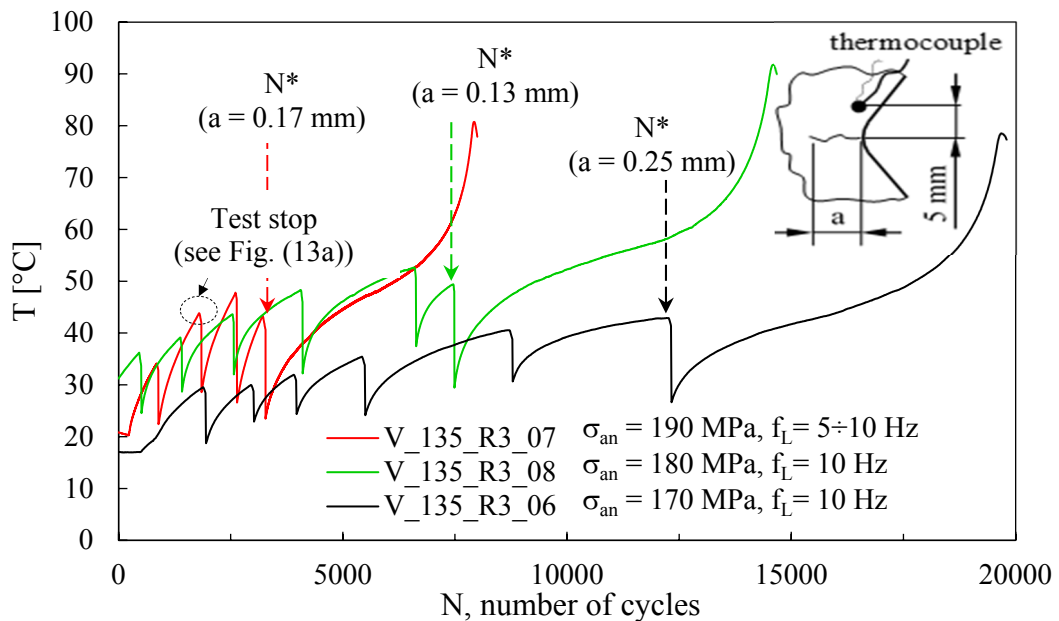


Figure 3.11. Typical temperature evolution measured at a distance of 5 mm from the notch apex by using thermocouples.

As a result, Fig. (10) shows that the new experimental results fall inside the previously defined σ_a -based scatter band. In addition, data relevant to the plain specimens are also reported in Fig. (10). It is worth observing that the data results show the fatigue notch sensitivity of the material which cannot be predicted by the stress concentration factors obtained from a linear elastic analysis (see K_{tn} values in the previous paragraphs).

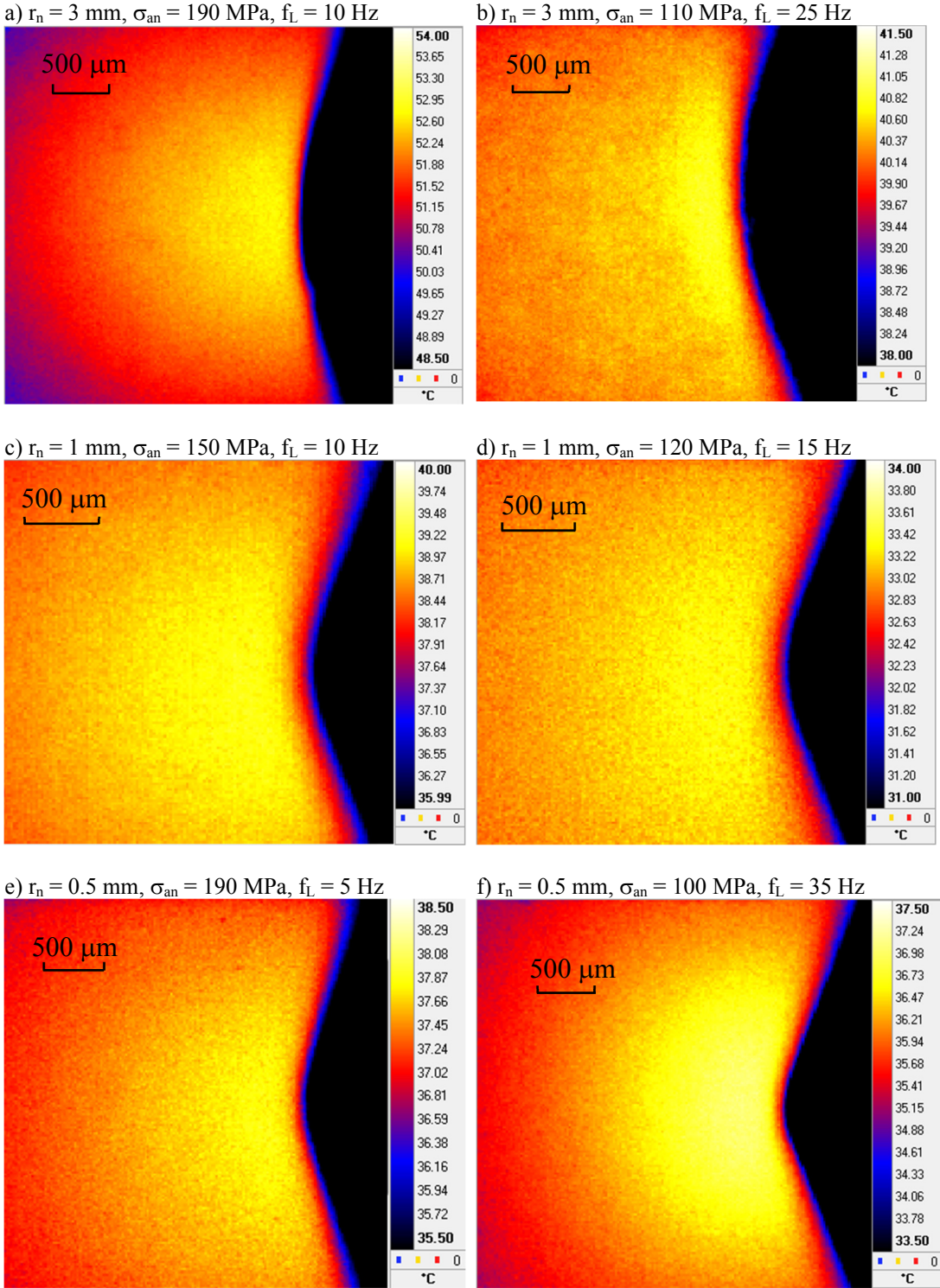


Figure 3.12: Temperature maps observed during the fatigue tests.

To show the temperature evolution during the fatigue test, copper-constantan thermocouple wires having a diameter of 0.127 mm were fixed at a distance of 5 mm from the notch tip only for three tests shown in Fig. (11). A schematic sketch of the thermocouples position was also reported at the the top-right of Fig. (11).

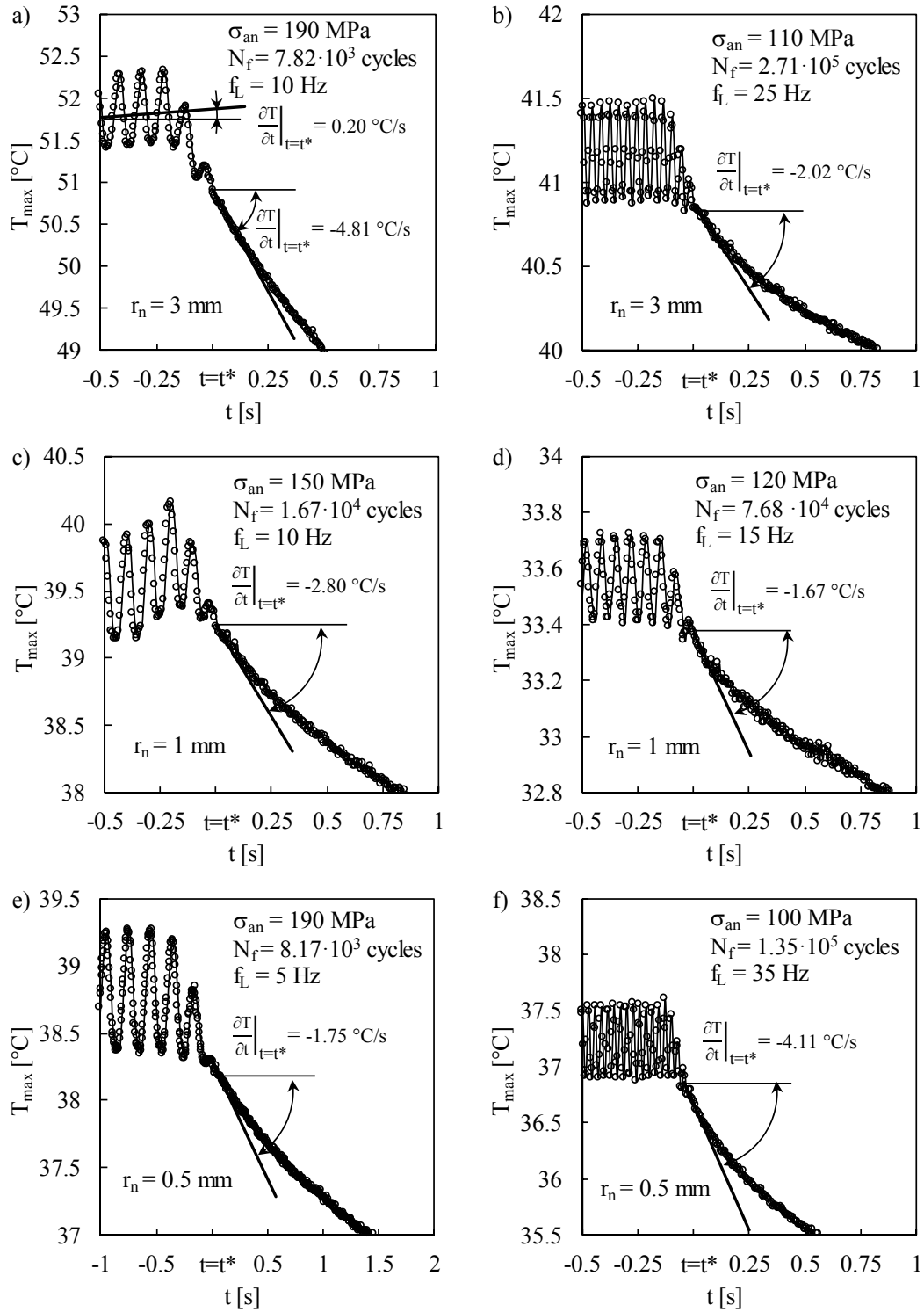


Figure 3.13: Typical cooling gradients at the notch tip measured during the fatigue tests. T_{\max} is the maximum temperature inside a circle area as it is shown in Fig. (4).

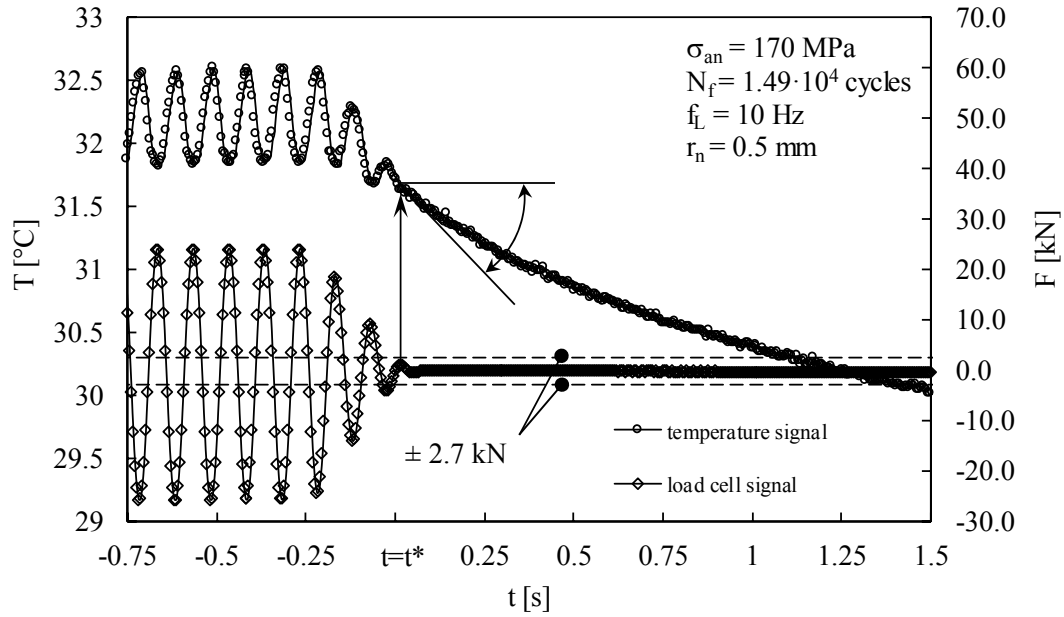


Figure 3.14: Definition of the time t^* when the machine is assumed to stop cycling and the cooling gradient is evaluated.

It is worth noting that several test stops were performed before the technical crack initiation to calculate Q and Q^* by means of the three methods here presented.

Concerning the evaluation of Q by means of Eq. (1), Figs (12) and (13) show examples of a typical temperature map at the time t^* (see Fig. (3)) and the time-dependent T_{\max} profile around the time t^* , respectively. Essentially T_{\max} is the maximum temperature value extracted frame-by-frame from a circular embracing the notch tip (see Fig. (4a)).

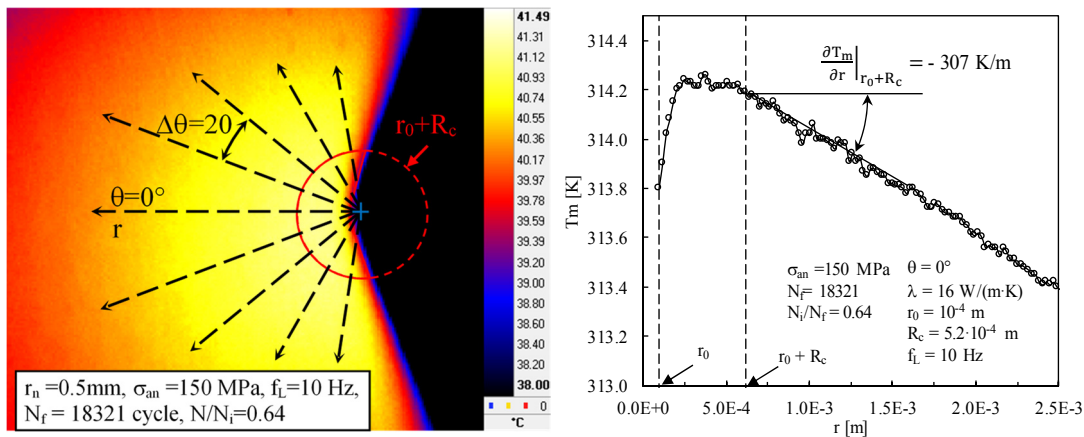


Figure 3.15 Mean temperature field $T_m(r, \theta)$, and radial paths adopted to calculate Q^* from Eq. (2) (a). Radial temperature profile measured at $\theta = 0^\circ$ (b).

The estimation of the cooling gradient and then Q according to Eq. (1) can be observed in Fig. (13). From Fig. (14), it is worth noticing that the servo-hydraulic machine takes tenths of seconds to reach the null force value. Therefore, an operational definition of t^* was necessarily adopted. Such definition is as follows: t^* is the time

when the first peak of force is within a range of ± 2.7 kN. Practically, it was verified that adopting this definition, the first peak value after having triggered the machine stop was below 5% of the amplitude force applied.

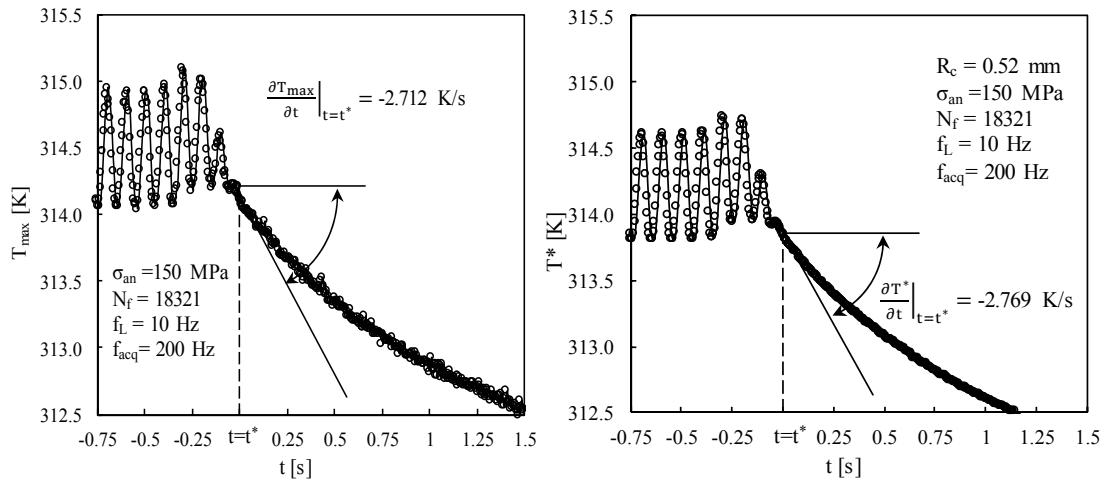


Figure 3.16: Typical cooling gradient of T_{max} measured during the fatigue tests carried out on notched specimens with $r_n = 0.5$ mm (a). Typical cooling gradient of $T^*(t)$ for the same fatigue test on the same notched specimen (b).

Regarding the evaluation of Q^* , Fig. (15a) shows an example of the stabilised mean temperature field $T_m(r, \theta) = T_m^i$ calculated according to Eq. (3) applied to the infrared images, which have been previously processed by means of the MotionByInterpolation tool. Afterwards, the averaged heat energy per cycle Q^* was numerically calculated by using the Eq. (2), taking a finite number of radial temperature profile with a step of 20° , as reported in Fig. (15a). More precisely, 9 radial paths were considered, emanating from the center of the control volume. Fig. (15b) shows as an example the radial temperature profile at the angular coordinate $\theta = 0^\circ$ of Fig. (15a), where it can be appreciated the estimation of the derivative of T_m on radial coordinate which contributes to calculation of Q^* .

Regarding the *averaged cooling gradient technique* (Eq. (4)), Fig. (16) shows the comparison between the cooling gradient from T_{max} (Fig. (16a)) and T^* (Fig. (16b)) in which the latter was used to evaluate Q^* . As it can be observed from Figs (16a) and (16b) the difference of the cooling gradient between T_{max} and T^* is engineering negligible. As support of this statement, the evolutions of Q (Eq. (1)) and Q^* (Eq. (4)) versus the fraction of fatigue life expended to initiate a crack reported in Fig. (17), show the same trend for each test. It can be also noted that the specific heat loss is nearly constant during the test before the technical crack nucleation for both the methodology.

Some Q and Q^* values are reported in Table 2 for comparison purposes: it can be noted that practically coincident values were found by using the present three methods. These results are in agreement with those reported in [12].

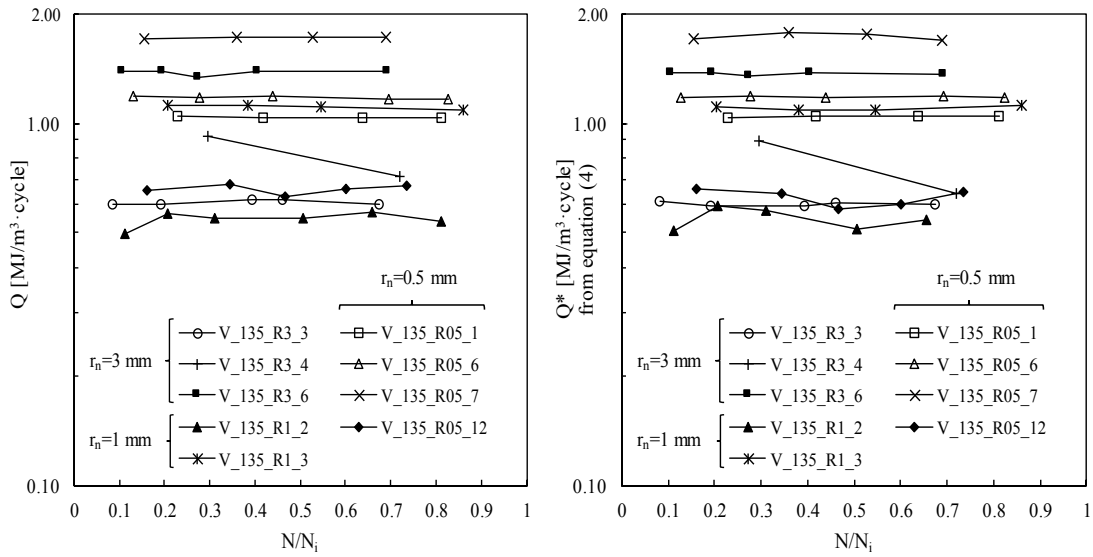


Figure 3.17: Q versus N/N_i , measured during the fatigue tests (a) and Q^* (from equation (4)) versus N/N_i , measured during the fatigue tests (b).

The Q parameter evaluated from Eq. (1) was adopted in order to synthesise all fatigue test results in terms of average heat energy per cycle in Fig. (19).

In particular, Q values reported on the ordinate in Fig. (19) are the average values calculated during a single fatigue test: one example is reported in Fig. (18).

Fig. (19) shows that the energy parameter Q can rationalise the fatigue strength of plain and notched specimens, as opposed to the net-section stress amplitude (see figure 10).

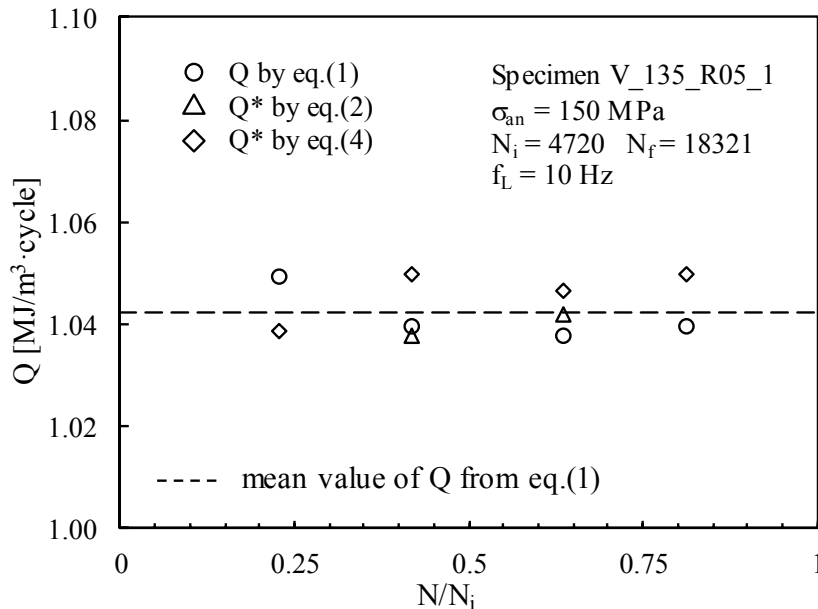


Figure 3.18: Example of Q and Q^* trends evaluated before the technical crack initiation

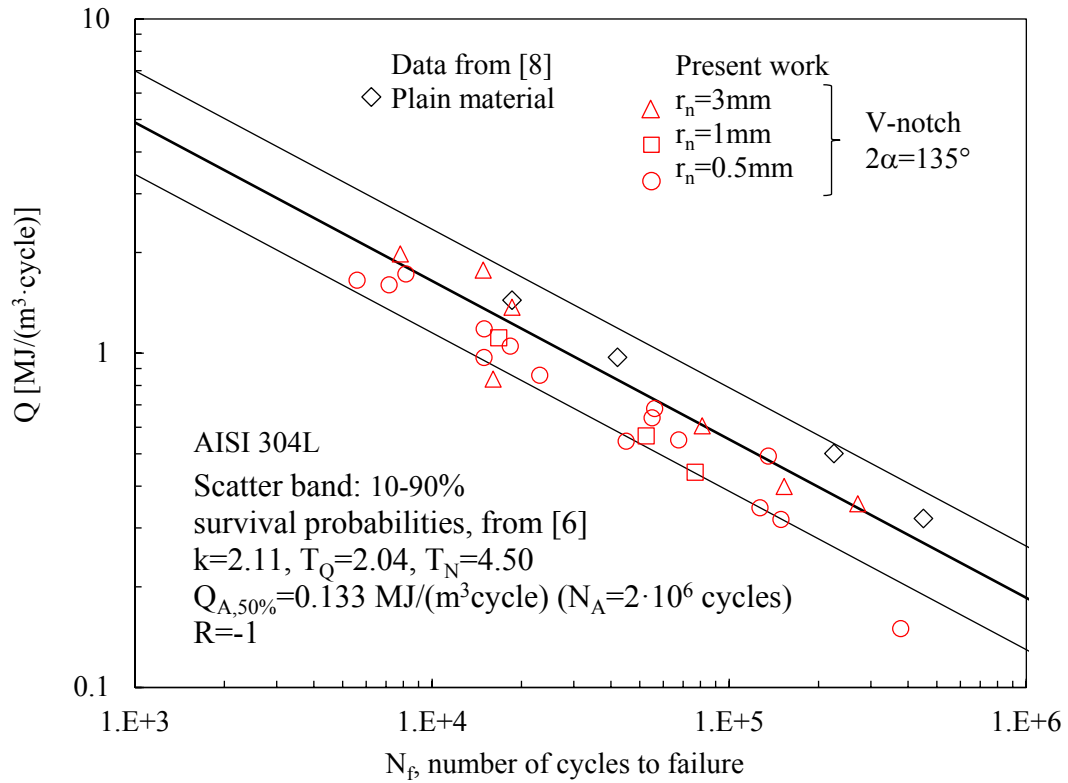


Figure 3.19 Fatigue data reported in figure 8 analysed in terms of specific heat loss per cycle. Scatter band is defined for 10% and 90% survival probabilities (from [6])

Table 3.2: Comparison between Q and Q^* calculated for several specimens with $m=3, 1,$ and 0.5 mm

r_n [mm]	Specimen	σ_{an} [MPa]	N/N_i	$Q^{(a)}$ [MJ/m ³ ·cycle]	$Q^{*(b)}$	$Q^{*(c)}$
0.5	R05_1	150	0.42	1.039	1.037	1.050
0.5	R05_6	170	0.28	1.179	1.193	1.193
0.5	R05_7	190	0.36	1.737	1.780	1.776
0.5	R05_9	160	0.50	0.970	1.036	0.956
0.5	R05_10	180	0.47	1.602	1.612	1.549
0.5	R05_12	130	0.34	0.683	0.761	0.640
0.5	R05_14	120	0.16	0.358	0.357	0.345
1	R1_3	150	0.38	1.119	1.015	1.095
3	R3_3	130	0.39	0.613	/	0.593

(a): from Eq. (1);

(b): from Eq. (2);

(c): from Eq. (4);

The analysis performed in the present work has been limited to the low and medium cycle fatigue regimes, because, despite the improved spatial resolution allowed by the adopted infrared camera, the overall thermal accuracy is still inadequate

to capture the small temperature rise experienced at the notch tip in the high cycle fatigue regime. For this reason, the reference situation to calibrate the material volume size V_c was taken in the medium cycle fatigue, by equalling the averaged heat loss Q^* of the smooth specimen and of the cracked specimen at a fatigue life on the order of 10^5 cycles [12].

Following on a parallel track the stress-averaging approaches (reminiscent of Neuber's finite-size structural volume concept [9]), it has been shown that the point-related specific heat energy Q from equation (1) in proximity of the V-notch apex ($r_n = 3, 1$ and 0.5mm) is comparable with the average heat energy Q^* (from equation (2) and (4)) for the material and the specimens' geometries adopted here.

Therefore, the point related Q estimation has been used for the following analysis.

3.4 THERMAL ENERGY DISSIPATION CLOSE TO THE NOTCH TIP

In this section, the infrared images acquired by the infrared camera were used to study the thermal energy dissipation around the notch tip. In particular, the analysis is referred to the subparagraph *Data Post-Processing* of the paragraph *Material and Methods*.

In Fig. (20a) an example of the $Q(x,y)$ raw data measured at $N = 8.12 \cdot 10^3$ cycles for a specimen having $r_n = 0.5$ mm and subjected to $\sigma_{an} = 130$ MPa ($N_f = 6.76 \cdot 10^4$ cycles) was reported, whereas the relevant distribution $Q(x,0)$ along the notch bisector is illustrated in Fig. (20b). The results were affected by a certain level of noise because the dt variable was maintained constant for all the pixels of the thermal images (see the post-processing analysis in *Materials and Methods*). The relevant $Q_{fit}(x,y)$ filtered results are shown in Fig. (20c), while the comparison between $Q(x,0)$ and $Q_{fit}(x,0)$ along the notch bisector is reported in Fig. (20d).

Let us define Q_0 the energy dissipated at the notch tip (i.e $Q_{fit}(0,0)$). Fig. (20c) shows the constant energy contours normalized with respect to Q_0 . It is worth noting that in Fig. (20c) the iso-energy contours seem to be circular and centered at the notch tip. In particular, a circular contour with radius $R_{Q,90\%}$ has been plotted in order to identify the biggest region where the energy calculated is equal to or greater than 90% of Q_0 . For the example reported in Fig. (20c) $R_{Q,90\%}$ is equal to 0.54 mm.

Fig. (21) shows more examples of energy distribution $Q(x,y)$ and the relevant distribution along the notch bisector $Q(x,0)$, for different notch tip radii and applied stress amplitudes. The evaluation of the $R_{Q,90\%}$ was carried out on selected specimens and the results are summarized in Table 3. Although the estimates of $R_{Q,90\%}$ ranges from 0.53 to 0.87 mm, there may be a link between $R_{Q,90\%}$ and the structural volume size for fatigue strength assessment evaluated in a recent work [12,13] for the same material and testing condition, but more investigation should be carried out.

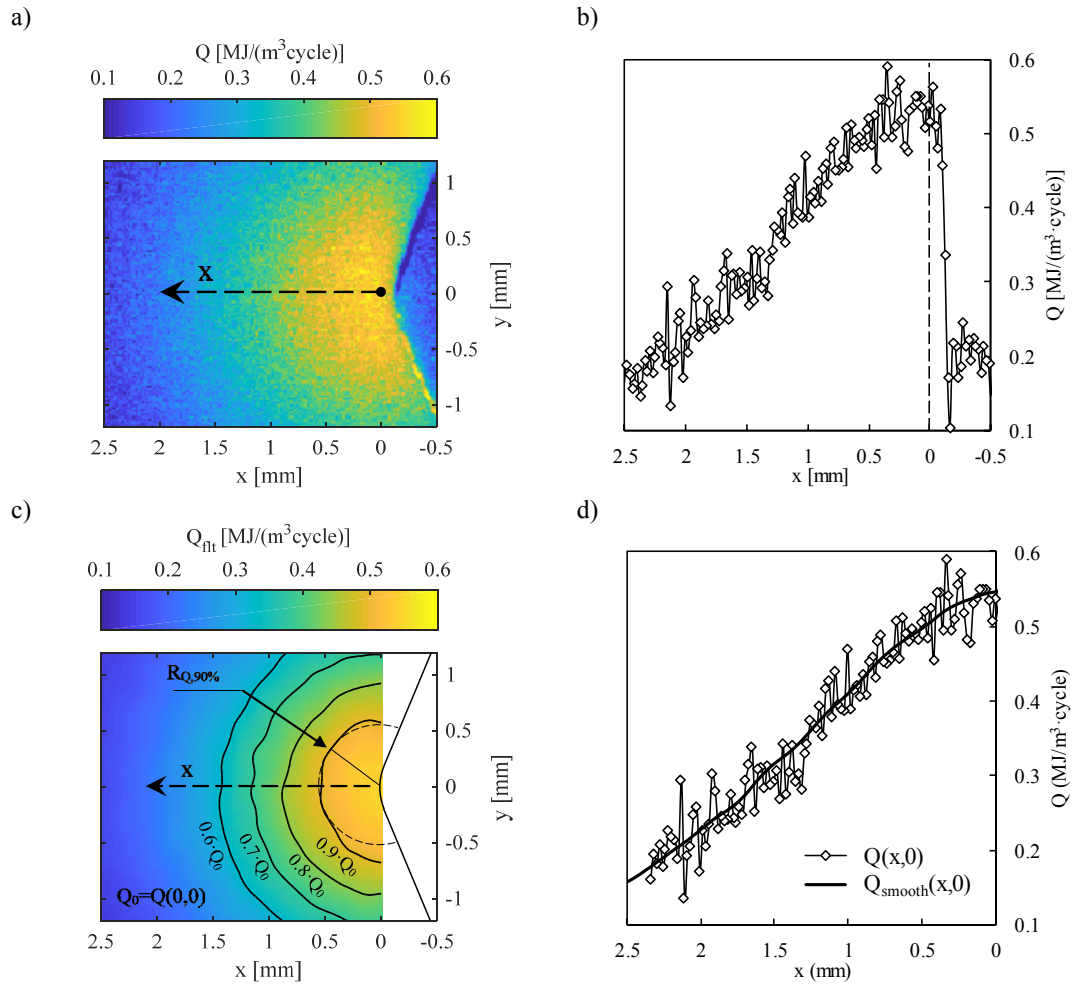
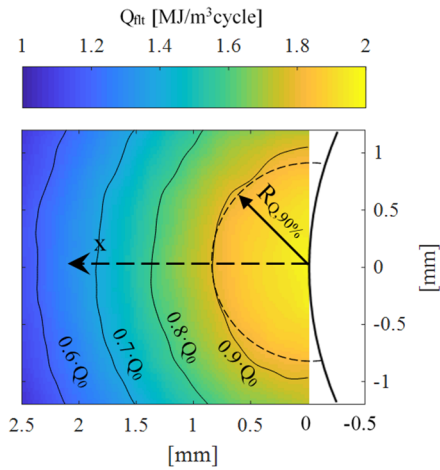


Figure 3.20: Example of raw data of the energy distribution $Q(x,y)$ (a) and along the coordinate $y=0$ (along the notch bisector (b)). The filtered energy distribution $Q_{flt}(x,y)$ (c) and the relevant distribution along the notch bisector ($y=0$) (d). (a-d) data are referred to the acquisition obtained at $N = 8.12 \cdot 10^3$ cycles of the specimen characterised by $r_n=0.5$ mm, $\sigma_{an}=130$ MPa, and $N_f = 6.76 \cdot 10^4$.

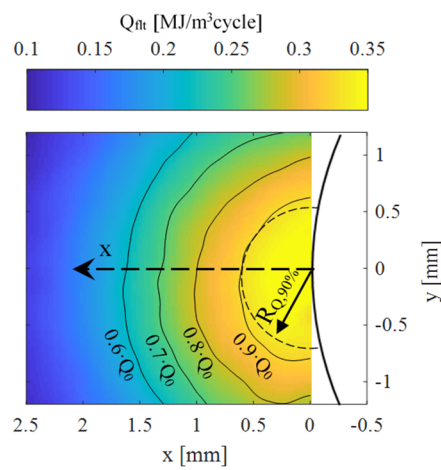
Table 3.3: Value of radius $R_{Q,90\%}$ measured during the fatigue test.

r_n [mm]	σ_{an} [MPa]	f_L [Hz]	N_f	N^*/N_f	Q_0 [MJ/(m³cycle)]	$R_{Q,90\%}$ [mm]	N/N_f
3	190	10	$7.82 \cdot 10^3$	0.41	1.98	0.85	0.24
3	170	10	$1.85 \cdot 10^4$	0.61	1.45	0.87	0.42
3	110	25	$2.71 \cdot 10^5$	0.67	0.38	0.55	0.17
1	150	10	$1.67 \cdot 10^4$	0.33	1.17	0.64	0.28
1	120	15	$7.68 \cdot 10^4$	0.40	0.42	0.55	0.13
0.5	190	5	$8.17 \cdot 10^3$	0.40	1.77	0.83	0.21
0.5	100	35	$1.35 \cdot 10^5$	0.13	0.51	0.53	0.08
0.5	130	25	$6.76 \cdot 10^4$	0.22	0.55	0.54	0.12

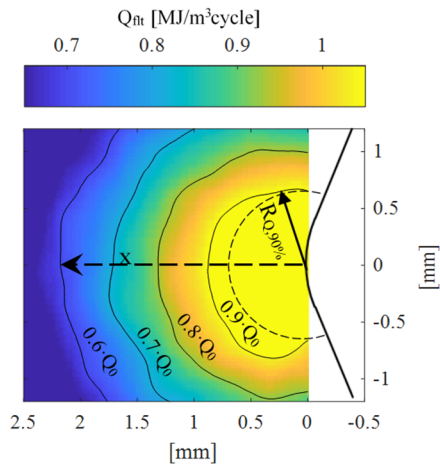
a) $r_n=3\text{ mm}$, $\sigma_{an}=190\text{ MPa}$, $N/N_f=0.24$, $N_f=7.82\cdot 10^3$ cycles, $Q_0=1.98\text{ [MJ/m}^3\text{cycle]}$, $f_L=10\text{ Hz}$



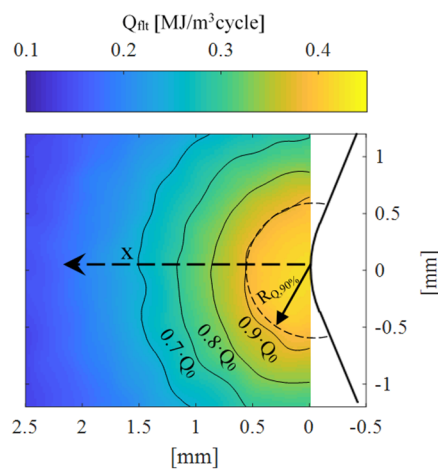
b) $r_n=3\text{ mm}$, $\sigma_{an}=110\text{ MPa}$, $N/N_f=0.42$, $N_f=2.71\cdot 10^5$ cycles, $Q_0=0.38\text{ [MJ/m}^3\text{cycle]}$, $f_L=25\text{ Hz}$



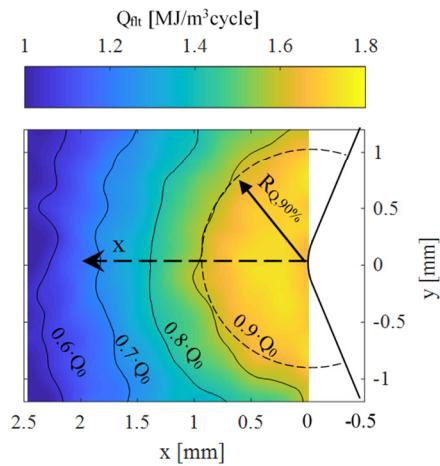
c) $r_n=1\text{ mm}$, $\sigma_{an}=150\text{ MPa}$, $N/N_f=0.28$, $N_f=1.67\cdot 10^4$ cycles, $Q_0=1.17\text{ [MJ/m}^3\text{cycle]}$, $f_L=10\text{ Hz}$



d) $r_n=1\text{ mm}$, $\sigma_{an}=120\text{ MPa}$, $N/N_f=0.13$, $N_f=7.68\cdot 10^4$ cycles, $Q_0=0.42\text{ [MJ/m}^3\text{cycle]}$, $f_L=15\text{ Hz}$



e) $r_n=0.5\text{ mm}$, $\sigma_{an}=190\text{ MPa}$, $N/N_f=0.21$, $N_f=8.17\cdot 10^3$ cycles, $Q_0=1.77\text{ [MJ/m}^3\text{cycle]}$, $f_L=5\text{ Hz}$



f) $r_n=0.5\text{ mm}$, $\sigma_{an}=100\text{ MPa}$, $N/N_f=0.08$, $N_f=1.35\cdot 10^5$ cycles, $Q_0=0.51\text{ [MJ/m}^3\text{cycle]}$, $f_L=35\text{ Hz}$

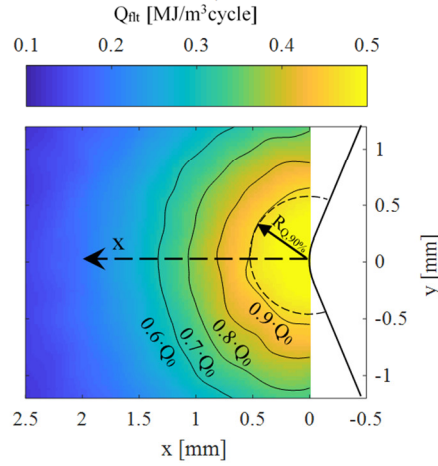


Figure 3.21: Heat energy distributions at the notch tip: (a,b,) $r_n=3\text{ mm}$, $\sigma_{an}=170\text{ MPa}$, $N_f=1.85\cdot 10^4$ cycles; (c,d) $r_n=1\text{ mm}$, $\sigma_{an}=150\text{ MPa}$, $N_f=1.67\cdot 10^4$ cycles; (e,f) $r_n=0.5\text{ mm}$, $\sigma_{an}=100\text{ MPa}$, $N_f=1.35\cdot 10^5$ cycles

To support the peak thermal energy just evaluated at the notch tip, during the fatigue test carried out on the specimen to which Fig. (20) is referred to, thermal maps

were taken both from the frontal and from the lateral views (see Fig. 3a). More precisely, after a given test stop to acquire the cooling phase from the frontal view, the specimen was turned 90° and the test was restarted, followed shortly after by a new stop to acquire the cooling gradient from the lateral view. Fig. (22a) shows the temperature distribution at the notch tip taken from the lateral view and Fig. (22a) shows the Q values measured at different locations along with the specimen thickness, resulting in a mean value $Q = 0.55 \text{ MJ}/(\text{m}^3 \cdot \text{cycle})$. Such a value is seen in excellent agreement with the value calculated at the notch tip from the energy distribution measured at the specimen surface of Fig. (20b).

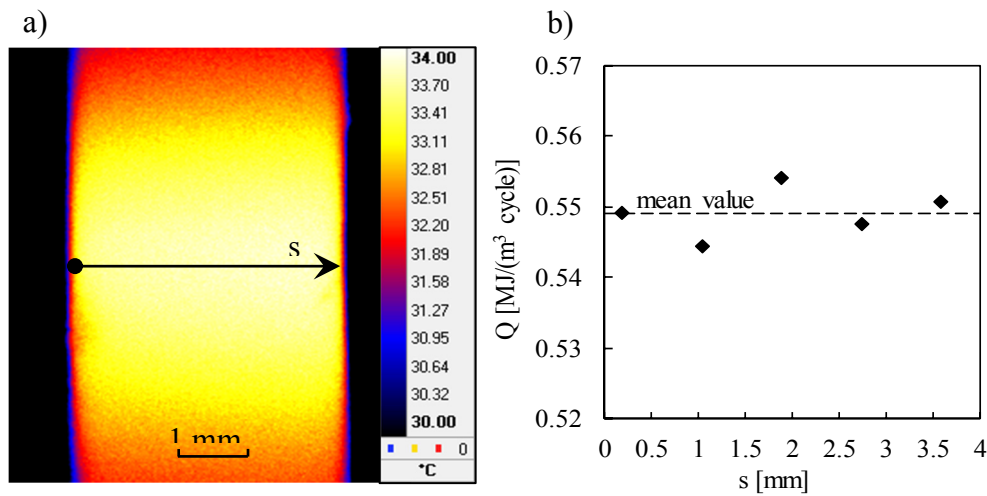


Figure 3.22. Temperature distribution measured along the notch tip from the lateral view (see Fig. (3a)) (a) and the corresponding energy distribution (b)

3.5 ANALYSIS OF ENERGY DISTRIBUTION

Let demonstrate the applicability of the Q field by using the automated technique illustrated in paragraph 3.4.

At an arbitrary point of a material subjected to cyclic stresses, the first law of thermodynamics in terms of a mean power exchanged over one cycle can be written as follow:

$$\left(\oint \sigma_{ij} \cdot \varepsilon_{ij} \right) \cdot f_L = H + \rho \cdot c \cdot \frac{\partial T_m(t)}{\partial t} + \dot{E}_p \quad (6)$$

where $H = Q \cdot f_L$ is the thermal power dissipated by conduction, convection and radiation, $T_m(t)$ is the mean temperature of the alternating thermoelastic effect and \dot{E}_p is the rate of accumulation of damaging energy in a unit of volume. When $T_m(t)$ reaches a constant value Eq. (6) can be rewritten as follows:

$$\left(\oint \sigma_{ij} \cdot \varepsilon_{ij}\right) \cdot f_L = H + \dot{E}_p \quad (7)$$

Stopping the fatigue test machine at $t = t^*$, the mechanical input power and the rate of accumulation of fatigue damage will vanish, therefore the Eq. (6) allow obtaining Eq (1). Evaluating the specific heat loss by means of Eq. (1) pixel-by-pixel of the acquired frame implies that the plastic hysteresis work (i.e H) is not null for all the pixels. In the case of severe notches, this assumption could not be satisfied because the plastic region could be concentrated in a smaller region than the one observed into the frame.

In [10], it was demonstrated that the contributions of Q due to convection and radiation can be neglected with respect the conduction, therefore a temperature field developed by thermal power generation can be described by the Fourier's equation:

$$\rho \cdot c \cdot \frac{\partial T_m(t)}{\partial t} = H + \lambda \cdot \nabla^2 T \quad (8)$$

After stabilization of T_m , if there is no thermal power generation the equation of the temperature field in a steady-state condition becomes:

$$\lambda \cdot \nabla^2 T = 0 \quad (9)$$

whereas if heat generation is occurred, the temperature field is described by the following one:

$$H = -\lambda \cdot \nabla^2 T \quad (10)$$

Let consider AISI 304L steel 2D bar subjected to self-heating just in a portion of volume (see Fig. (23a)) constrained at $T = 0$ °C and the ends. In a steady-state regime, the temperature profile along the longitudinal direction must follow Eq. (10) in the portion of volume subjected to self-heating and Eq. (9) in a position in which there is not heat generation. In the example of Fig. (23a), this means that the temperature profile is a parabola with negative concavity for $a < x < b$, while for $0 < x < a$ and $b < x < L$ it must be linear (see Fig. (23b)).

Let suppose now, that at the time t^* the heat generation become null instantaneously. At the time $t = t^{*+}$, Eq. (8) can be re-written as follows:

$$\rho \cdot c \cdot \frac{\partial T_m(t)}{\partial t} = \lambda \cdot \nabla^2 T \quad (11)$$

where in the region $a < x < b$ the first term is equal to Q, while in $0 < x < a$ and $b < x < L$ must be null. This means that in the second case the initial cooling gradient must be equal to zero $t = t^{*+}$.

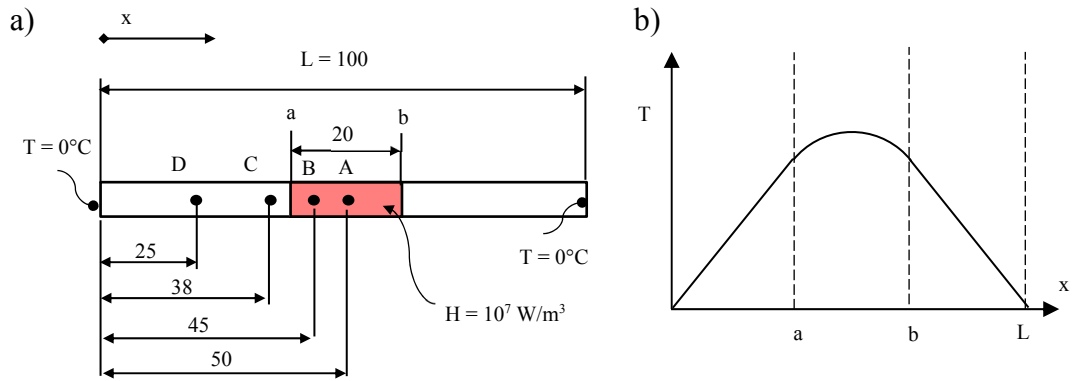


Figure 3.23: a) AISI 304L steel 2D bar subjected to self-heating just in a portion of volume constrained at $T = 0^\circ\text{C}$ and the ends. b) Qualitative representation of temperature profile after stabilization according to Eq. (9) and (10).

In order to prove this, first, a steady-state thermal finite element analysis was performed by applying a heat generation rate $H = 10^7 \text{ W/m}^3$ in the region area included between a and b and by assigning a temperature value at the ends equal to 0°C . The simulation was performed by using ANSYS® software, adopting 2-dimensional four-node element PLANE55 of the Ansys' library. Isotropic thermal conductivity equal to $16 \text{ W/(m}^\circ\text{C)}$ was set as the only material property.

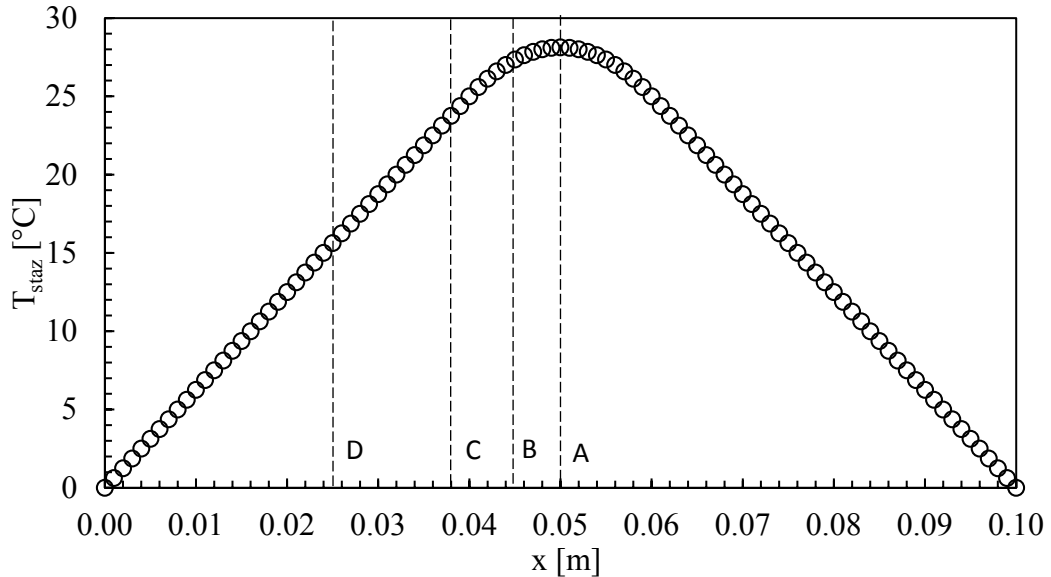


Figure 3.24. Temperature profile obtained from FE steady-state thermal analysis of the bar shown in (Fig. 22a)

The resulting temperature profile along the x coordinate is reported in Fig. (24). After that, the resulting nodal temperature profile was assigned to the same model for solving a transient simulation which was dedicated to simulating the cooling gradient after stopping the heat generation source. A material density ρ equal to 7940 kg/m^3 , specific

heat c 507 J/(kg K) and isotropic thermal conductivity equal to 16 W/m² were given in input to the material model. A “time at the end load step” equal to 1 s with a “time increment” of $2 \cdot 10^{-3}$ s was set in the “Solution control” of the Ansys® solver.

In Fig. (25), the cooling gradients of the points illustrated in Fig. (23a) were plotted. This numerical analysis demonstrated that the analysis of the Q field by adopting the cooling gradient technique in each pixel is valid only in the region of the material subjected to self-heating due to plastic strain energy dissipation.

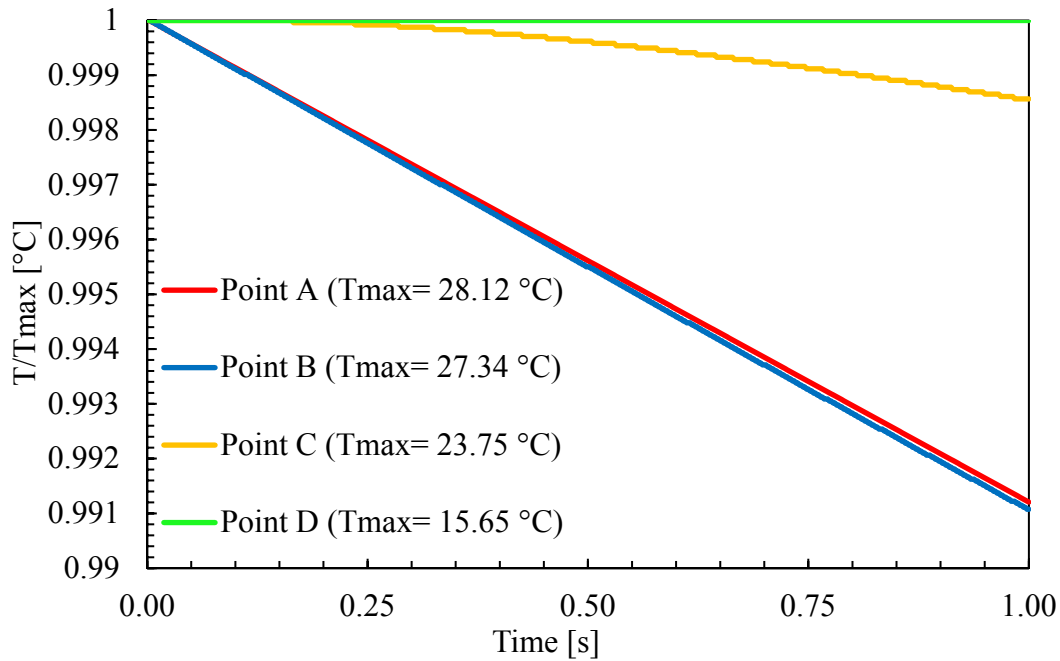


Figure 3.25. Temperature profile on four point (See Fig. 22a) obtained by FE transient analysis.

In order to evaluate the portion of frame in which H is null, the example of Fig. (20) has been taken into account for the following analysis. Firstly, the frames of ten loading cycles between t_s and t^* (see Fig. 3) were processed by using the FLIR MotionByInterpolation tool, which allows the relative motion between the fixed focal lens and the moving of the specimens to be compensated. After that, the time-dependent temperature was averaged pixel-by-pixel over 80 frames (10 loading cycles in this example) and the resulting steady-state temperature (T_m) field and distribution along the notch bisector are shown in Fig. (26a) and (26b). Fig. (26c) shows the same temperature field of Fig. (26a) after filtering by means of a Gaussian smoothing kernel with a standard deviation equal to 8. The comparison between the T_m and $T_{m, \text{filt}}$ profiles along the notch bisector is shown in Fig. (26d).

Assuming that the temperature maps do not vary along with the thickness of the specimen, the 2 dimensional Laplacian of $T_{m, \text{filt}}$ field was numerically calculated by using the Matlab function *del2*. Since the resulting distribution was affected by noise, the Laplacian field was filtered by using the same Gaussian filter used for T_m map. Fig. (27a) reports the Laplacian field with the sign reversed on which the contour

related to the null value of the distribution is also plotted. The comparison between the raw and filtered Laplacian profiles along the notch bisector are shown in Fig. (27b). In Fig. (27a) it can be clearly seen that inside of the contour H is different from zero and positive, whereas in the remaining area is less than zero. The latter case has not physical sense because it would imply that the heat generation is not dissipated to the surroundings. Therefore, only the area with H greater or equal to zero was assumed as heat-generating zone in the following analysis.

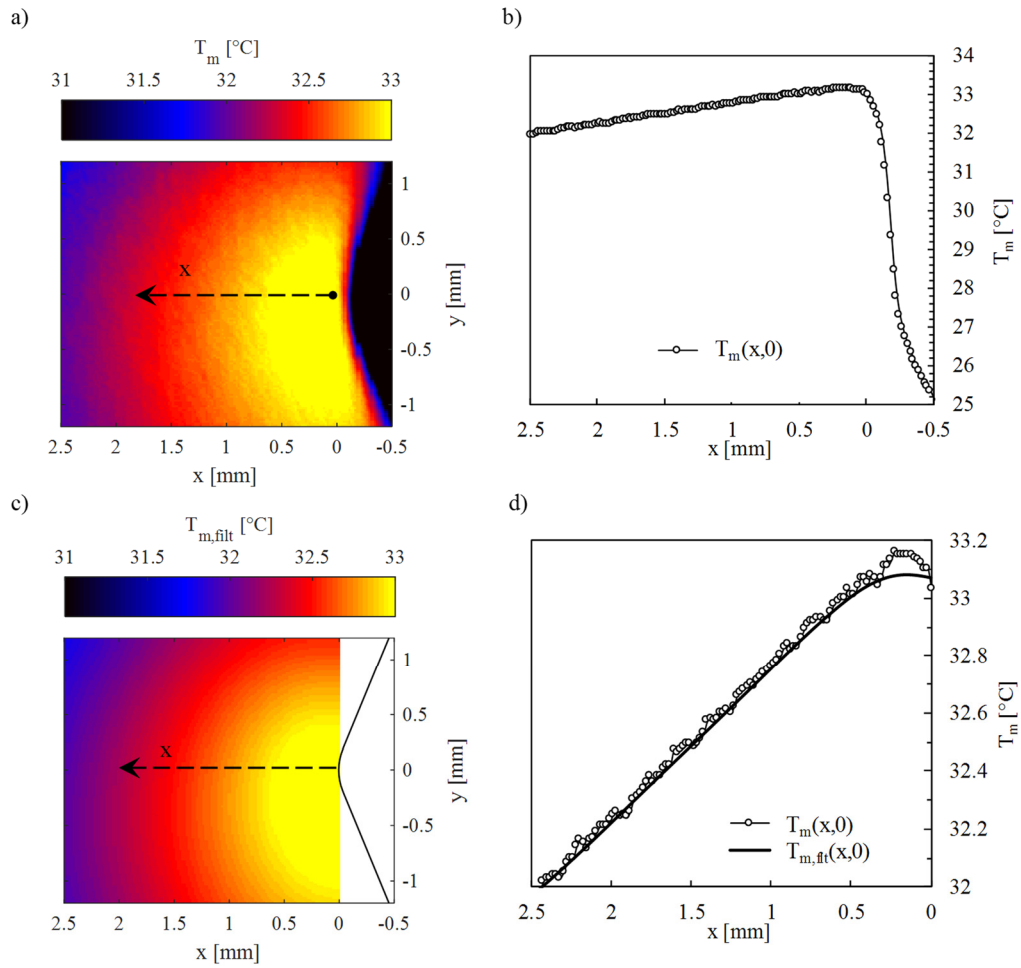


Figure 3.26: Steady-state temperature ($T_m(x,y)$) field (a) and distribution along the notch bisector ($y=0$) (b). Filtered steady-state temperature ($T_{m,flt}(x,y)$) field (c) and the relevant distribution along the notch bisector ($y=0$) (d). The relevant fatigue test details are reported in Fig. 7.

The results, shown in Fig. 25, demonstrate that the analysis of the Q fields obtained by calculating the cooling gradients pixel-by-pixel is valid only in the region subjected to self-heating.

Finite element analysis

Steady-state thermal finite element analysis was carried out for the fatigue test results of Fig (20) in order to verify the experimental temperature map of Fig. (26a),

assigning a non-uniform specific heat power generation obtained from the evaluation of the specific heat loss pixel-by-pixel.

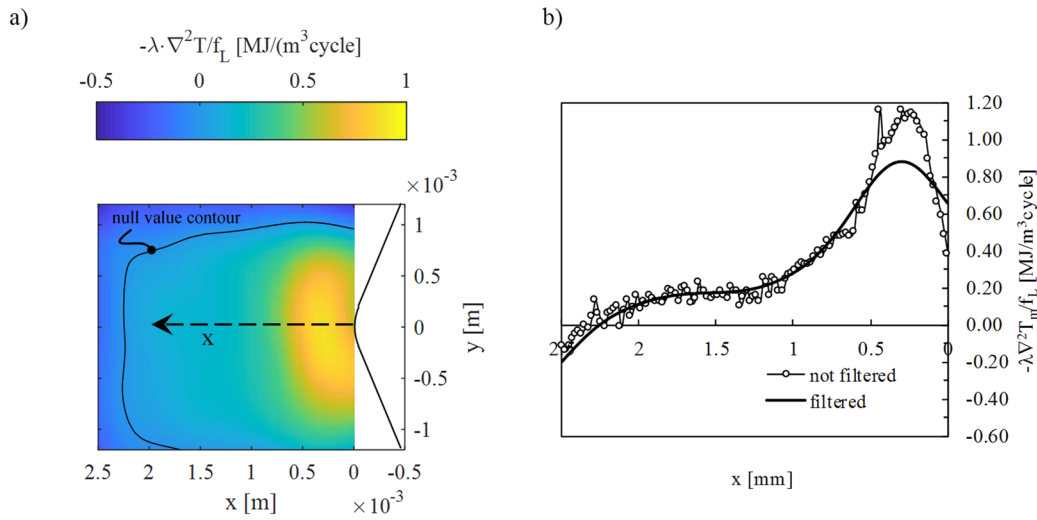


Figure 3.27: Filter Laplacian field (a) and comparison with the not filtered and the filtered Laplacian distributions along the notch bisector ($y=0$) (b).

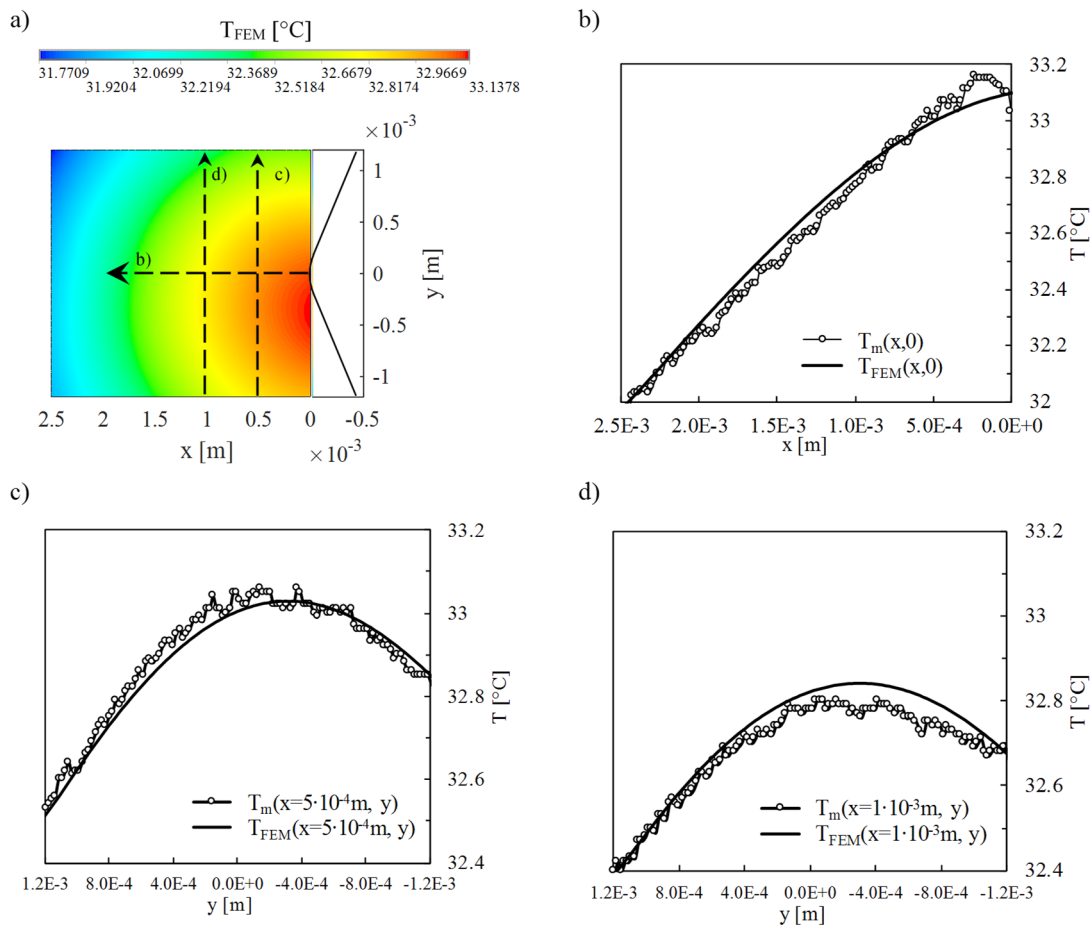


Figure 3.28: Contour plot of the nodal temperature solutions (a) and comparison between the experimental steady-state temperature and nodal solutions along three different path (b,c,d).

The simulation was performed by using ANSYS® software, adopting 2-dimensional four node element PLANE55 of the Ansys' library. Isotropic thermal conductivity equal to 16 W/(m°C) was set as the only material property. A rectangular area having dimension equal to 2.5x2.4 mm (the same dimension of the area analysed in Figs (20) and (21)) was modeled and the element size was set equal to 21 μm in order to obtain a mapped-type mesh having a number of elements equal to the number of pixels analysed in the previous paragraph.

Given the correspondence amongst element size and spatial resolution, it was possible to assign specific heat generation power obtained from the evaluation of Q pixel by pixel in the region with H equal or greater than zero (the inner region of the black contour of Fig (27a)).

The experimental temperature profiles of the borders of Fig. (26a) were assigned at the sides of the FE model.

In Fig. (28a) the contour plot of the nodal temperature values is reported. For comparing the temperature map of Fig. (28a) and the numerical results of Fig. (28a), temperature distributions along three different paths indicated in Fig. (28a) have been reported in Figs. (28b-d). The good correlation between the numerical and experimental data demonstrate that the distribution of Q around a notch tip evaluated by using Eq. (1) pixel-by-pixel is valid only in a limited region in which a heat power generation is developed.

3.6 DISCUSSION

The determination of the specific thermal energy dissipated per cycle Q by using the *cooling gradient technique* is aimed to be proposed as an easy experimental method for assessing the fatigue behavior of components in the prototype phase. Therefore, validation of the present technique to different factors that affect fatigue behavior has to be carried out in order to highlight the robustness of the method and any limitations.

The main advantages of this technique, with attention to the considered material (AISI 304L) weakened by severe notches, are listed here:

- the parameter Q is independent on the thermal-mechanical boundary conditions such as load frequency, temperature of the environment and the testing machine;
- It was experimentally demonstrated that fatigue test results on plain and notched (with different kind of notches and tip radii) under fully reversed cyclic loads are well-synthesised in a single narrow scatter band. The same results were obtained in fully reversed torsion fatigue tests.
- the *cooling gradient technique* can be easily adopted in components having fillet radii greater the 3 mm by using low-cost equipment for the temperature measurement like thermocouples;

- For evaluating Q at the proximity of severe notches an infrared camera with a proper spatial resolution is required in order to record the effective temperature increment more localised close to the notch tip;
- In the case of infrared measurement of the surface temperature, the time-variant profile can be obtained either from temperature values on a fixed pixel or from the mean temperature calculated within a selected area (frame-by-frame). Furthermore, it is not necessary to perform a motion compensation due to the cyclic displacement of the specimens. For these reasons, the cooling gradient technique is not sensitive to the spatial resolution of the equipment for this type of test and for the present material.
- the procedure does not require any information about the load applied and its waveform or the stress state in the material, which is an important experimental advantage.

However, from experience, the cooling gradient technique requires a temperature increment at least $2\text{ }^{\circ}\text{C}$ from the thermal equilibrium (before starting the test). This could be a limit in evaluating Q in high cycle fatigue regimes for materials having a high thermal conductivity because the load frequency required to increase the mean temperature of $2\text{ }^{\circ}\text{C}$ could not be reached by using a standard servo-hydraulic machine. This is more pronounced in severely notched specimens. In the case of the AISI 304L, its thermal conductivity is low enough to guarantee reliable temperature increment even for severely notched specimen (about $14.0 - 16.3\text{ W/m-K}$).

Regarding the applicability of the automated procedure developed in this work, it was demonstrated that it can be adopted to obtain easily the energy distribution within the plastic zone. In the case studied here, the entire frame, in which the thermal energy distribution was evaluated, was included in the plastic zone due to the high ductility of the AISI 304L. In the case of low ductility materials, the procedure can be further developed for instance by identifying the area of the plastic zone by using the double frequency lock-in procedure proposed in [14], and then computing the cooling gradient technique for the pixels related to that area.

3.7 CONCLUSIONS

In order to extend the heat energy-based approach to more severe notched specimens as compared to those tested in the past, constant amplitude, completely reversed, stress-controlled fatigue tests were carried out on hot-rolled 4-thick-mm notched specimens made of stainless steel AISI 304L having notch tip radii equal to 3, 1, and 0.5 mm.

Instead of using thermocouples (the traditional technique of the method) the specific heat energy Q was evaluated by means of an infrared camera with a spatial

resolution equal to 20 $\mu\text{m}/\text{pixel}$ which can measure more localized temperature increments due to the severity of the notches analysed.

In the first place, the aim of the study was only to validate the Q as a damage indicator, expressing the fatigue test results in terms of Q against the number of cycles to failure. Three methodologies of Q evaluation were analysed and compared with each other. The first methodology is the so-called *Point-related cooling gradient technique* which is related to the traditional experimental technique proposed to measure the specific heat loss per cycle Q on plain and bluntly notched specimens. The second one, called *Spatial gradient technique*, which was proposed to extend the thermal energy method to cracked materials (and severely notched specimens) measuring the average thermal energy dissipated per cycle Q^* on a control volume properly calibrated in analogy of the averaged SED criterion proposed by Lazzarin. The third one is the so-called *Averaged cooling gradient technique*, in which the aim is to evaluate Q^* adopting the cooling gradient technique.

The Q and Q^* values were measured several times during a fatigue test, from the beginning of the experiment until the initiation of a technical crack detected by using a digital microscope.

The comparison between Q and Q^* by using all the methods illustrated in this study leads to the conclusion that for both the point-related parameter and the averaged ones allows obtaining the same values even for severely notched specimens when in the classical fatigue approach is commonly not satisfied.

Furthermore, the specific heat loss Q was seen to be approximately constant during an individual fatigue test. This is an important practical consequence because fatigue life can be anticipated starting from measurement performed at the beginning of the fatigue test.

Consequently, it was found that the new fatigue data fall in the energy-based scatter band calibrated previously on the basis of fatigue data obtained on plain material as well as notched specimens, characterised by larger notch tip radii than those tested in this study.

The following part of the study dealt with an investigation about how Q is distributed around the notch tip. Therefore, an automated procedure was proposed to evaluate the specific heat loss (Q parameter) distribution around sharp V-notches, starting from the temperature maps captured around the tip of V notches, by using an infrared camera acquired image.

The automated procedure was developed in Matlab® code taking the video recording file acquired by ALTAIR 5.90.002 commercial software as input file and computing Eq (1) pixel-by-pixel. Then Q distributions ($Q(x,y)$) were analysed for a subset of specimens providing the circular region where the energy dissipated is equal or greater of 90% of the Q value measured at the notch tip.

This automated procedure was validated by an alternative analysis of the Q field carried out by using another post-processing technique. In particular, the Laplacian distribution of the temperature map before the test stop was evaluated in order to

identify the region in which the heat power generation is null. Then a 2D steady-state thermal finite element analysis was performed imposing the distribution of heat generation and the experimental temperature boundary conditions.

3.8 REFERENCES

- [1] Rigon D, Ricotta M, Meneghetti G. The use of the heat energy loss to correlate the fatigue strength of severely notched stainless steel specimens. *Proc. Int. Symp. Notch Fract.*, Santander (Spain): 2017.
- [2] Rigon D, Ricotta M, Meneghetti G. An analysis of the specific heat loss at the tip of severely notched stainless steel specimens to correlate the fatigue strength. *Theor Appl Fract Mech* 2017;92:240–51. doi:10.1016/j.tafmec.2017.09.003.
- [3] Rigon D, Ricotta M, Meneghetti G. Evaluating the specific heat loss in severely notched stainless steel specimens for fatigue strength analyses. *Procedia Struct Integr* 2018;9:151–8. doi:10.1016/J.PROSTR.2018.06.023.
- [4] Rigon D, Ricotta M, Meneghetti G. Analysis of dissipated energy and temperature fields at severe notches of AISI 304L stainless steel specimens. *Frat Ed Integrità Strutt* 2019;13:334–47. doi:10.3221/IGF-ESIS.47.25.
- [5] Meneghetti G, Ricotta M. The use of the specific heat loss to analyse the low- and high-cycle fatigue behaviour of plain and notched specimens made of a stainless steel. *Eng Fract Mech* 2012;81:2–16. doi:10.1016/j.engfracmech.2011.06.010.
- [6] Meneghetti G, Ricotta M, Atzori B. A synthesis of the push-pull fatigue behaviour of plain and notched stainless steel specimens by using the specific heat loss. *Fatigue Fract Eng Mater Struct* 2013;36:1306–22. doi:10.1111/ffe.12071.
- [7] Meneghetti G, Ricotta M, Negrisola L, Atzori B. A Synthesis of the Fatigue Behavior of Stainless Steel Bars under Fully Reversed Axial or Torsion Loading by Using the Specific Heat Loss. *Key Eng Mater* 2013;577–578:453–6. doi:10.4028/www.scientific.net/KEM.577-578.453.
- [8] Meneghetti G, Ricotta M, Atzori B. The Heat Energy Dissipated in a Control Volume to Correlate the Fatigue Strength of Bluntly and Severely Notched Stainless Steel Specimens. *Proc. 21st Eur. Conf. Fract. ECF21*. Catania, Italy, vol. 2, 2016, p. 2076–83. doi:10.1016/j.prostr.2016.06.260.
- [9] Neuber H. *Theory of Notch Stresses*. Berlin: Springer Publishers; 1958.
- [10] Meneghetti G. Analysis of the fatigue strength of a stainless steel based on the energy dissipation. *Int J Fatigue* 2007;29:81–94. doi:10.1016/j.ijfatigue.2006.02.043.
- [11] Meneghetti G, Ricotta M. Evaluating the heat energy dissipated in a small volume surrounding the tip of a fatigue crack. *Int J Fatigue* 2016;92:605–15. doi:10.1016/j.ijfatigue.2016.04.001.
- [12] Meneghetti G, Ricotta M, Rigon D. The heat energy dissipated in a control volume to correlate the fatigue strength of severely notched and cracked stainless steel specimens. *Fatigue 2017*, Cambridge, UK: 2017.
- [13] Meneghetti G, Ricotta M. The heat energy dissipated in the material structural volume to correlate the fatigue crack growth rate in stainless steel specimens. *Int J Fatigue* 2018;115:107–19. doi:10.1016/J.IJFATIGUE.2018.07.037.

- [14] Sakagami T, Kubo S, Tamura E, Nishimura T. Identification of plastic-zone based on double frequency lock-in thermographic temperature measurement. Proc. 11th Int. Conference Fract. - ICF11, Italy: 2005.

Chapter 4: Analysis of the energy dissipation on AISI 304L stainless steel subjected to multiaxial cyclic loading

In this Chapter, the specific heat loss Q has been measured for the first time on AISI 304L specimens subjected to multiaxial fatigue loadings. A test bench consisting of two servo-hydraulic actuators was designed to perform cyclic plane bending, torsion and combined bending torsion. More precisely completely reversed ($R = -1$) pure bending, pure torsion and combined bending and torsion tests were carried out on hourglass-plain specimens. The testing protocol included the analysis of in-phase ($\varphi = 0^\circ$) as well as out-phase ($\varphi = 90^\circ$) loading conditions adopting two different biaxiality ratios ($\Lambda=1$ and $\Lambda=\sqrt{3}$). In addition, the crack initiation was evaluated by adopting the potential drop technique. Thin-walled tubular specimens were tested under completely reversed tension and torsion fatigue loadings for comparative purposes. Afterwards, all fatigue test results were expressed in terms of specific heat loss and compared with the scatter band previously evaluated for plain and notched stainless-steel specimens subjected to uniaxial loading.

This chapter is referred to the following author's papers:

[1] Rigon D., Formilan V., Meneghetti G. *Analysis of the energy dissipation in multiaxial fatigue tests of AISI 304L stainless steel bars. Procedia Structural Integrity 2018;13:1638–43.*
doi:10.1016/j.prostr.2018.12.344

4.1 INTRODUCTION

Considering a volume of metallic material subjected to cyclic stresses, the mechanical input energy is partly stored internally in the material, the remaining part being converted into heat. Regarding the multiaxial fatigue, a general energy-based approach was proposed by [2] by adopting the sum of the plastic strain energy and the positive elastic strain energy as a fatigue damage parameter. Despite the fact that such parameter is a scalar quantity, the severity of the particular multiaxial loading is accounted by a multiaxial constraint function, which takes into account the mean stress effect and non-proportional cyclic loading ([2]). In the case of multiaxial fatigue of notched components and structures, another energy-based approach was proposed by Lazzarin and co-workers, in which the averaged linear elastic strain energy density

within a material dependent and properly defined control volume is assumed as a fatigue damage parameter [3], [4,5].

The internal energy stored within a material, which is indeed correlated to the fatigue damage mechanism, can be evaluated in principle as difference between the mechanical input energy and the thermal energy [6]. However, due to the fact that most of the mechanical input energy is converted into heat, such difference may be affected by uncertainties especially in high cycle fatigue (HCF), where calculating the area of the hysteresis cycle cannot be straightforward [2].

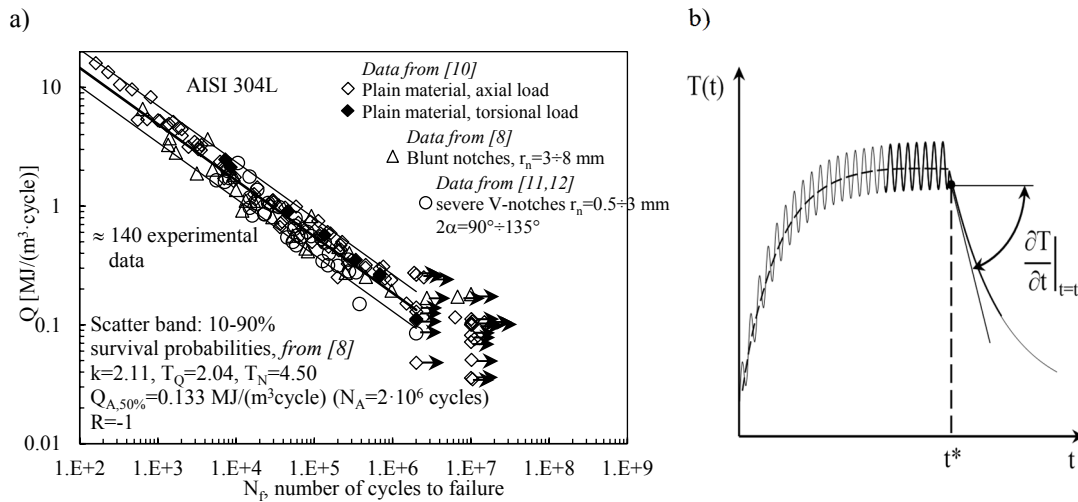


Figure 4.1. Fatigue test results of plain and notched AISI 304L in terms of specific heat loss Q (a). Qualitative representation of temperature evolution during a fatigue test and evaluation of the cooling gradient immediately after a test stop (b).

For this reason, [7] proposed to adopt the specific heat loss per cycle (Q) as a fatigue damage index for fatigue strength analysis, since it can be measured quite easily also in HCF, at least for certain engineering materials. By using Q , more than 140 experimental uniaxial fatigue test results ($R = -1$) on plain, bluntly and severely notched AISI 304L stainless steel specimen were rationalised in a single scatter band calibrated in [8], (Fig.1(a)). The fatigue test details are reported in [8–12].

The specific heat loss per cycle can be evaluated in situ during a fatigue test by means of Eq.(1) ([7]):

$$Q = \frac{\rho \cdot c \cdot \frac{\partial T}{\partial t}}{f_L} \quad (1)$$

where ρ is the material density, c is the material specific heat and f_L is the load test frequency and $\partial T/\partial t$ is the initial cooling gradient after having suddenly interrupted the fatigue test at the time t^* (Fig. 1(b)).

As highlighted in [8], the specific heat loss is a material property for a given load ratio. It is interesting to investigate to which extent it depends on the stress state, the

sole experimental outcome available up to date is that both uniaxial and torsional fatigue results are rationalized in a single scatter band, as reported in previous Fig. 1.

The aim of this investigation is to evaluate for the first time the specific heat loss per cycle Q in multiaxial fatigue test of cold drawn AISI 304L stainless steel bars. Several sets of fatigue tests were carried out to investigate the effect of the biaxiality ratio Λ and of the phase shift angle ϕ between bending and torsion loadings. For comparison purposes, combined axial and torsional fatigue tests were carried out on thin-walled tubular specimens machined from the same material.

By nature, the Q -based approach estimates the fatigue life to initiate crack for theoretical point of view. In the last decades, Ritchie [13,14] classified extrinsic mechanisms that start to operate during crack propagation inducing shielding effect and increasing the resistance of crack growing. Therefore, in this work, the crack nucleation was evaluated by using the potential drop technique during the bending-torsional fatigue tests. The fatigue test results have been compared with the existing scatter band previously calibrated on uniaxial fatigue test results.

4.2 MATERIALS AND METHODS

4.2.1 Material and specimen's geometry

Starting from 25-mm-diameter, AISI 304L cold drawn bars, two sets of specimens were prepared. The first one consists of cylindrical hourglass-shaped specimens (specimen (a)) used for combined bending and torsion fatigue tests whose geometry is reported in Fig. (2a). The second one includes four thin-walled specimens with a net-wall thickness of 1.5 mm (specimen (b)). The geometry of the second set is illustrated in Fig. (2b). The chemical composition and mechanical properties taken from datasheet of the AISI 304L cold drawn bars are summarised in Tables 1 and 2, respectively. Microstructure analyses along the transversal and longitudinal planes were observed by an optical microscope and reported in Fig. (3).

Table 4.1: Chemical composition of AISI 304L cold drawn bars from datasheet.

C %	Si %	Mn %	Cr %	Mo %	Cu %	Ni %	P %	S %	N %
0.013	0.52	1.72	18.27	0.51	0.46	8.11	0.029	0.030	0.091

Table 4.2: Mechanical properties of AISI 304L cold drawn bars from datasheet.

$R_{p,0.2\%}$ [MPa]	R_m [MPa]	KV [J]	HB
475	679	176	227

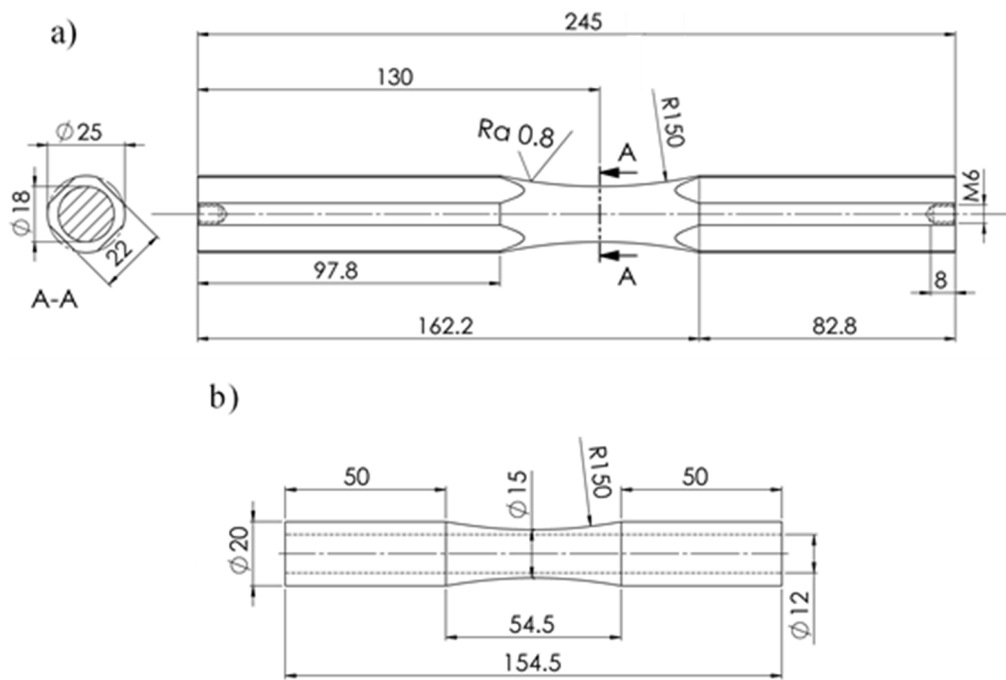


Figure 4.2: (a) Specimen's geometry for bending-torsional fatigue tests; (b) specimen's geometry for axial-torsional fatigue tests (dimensions are given in mm)

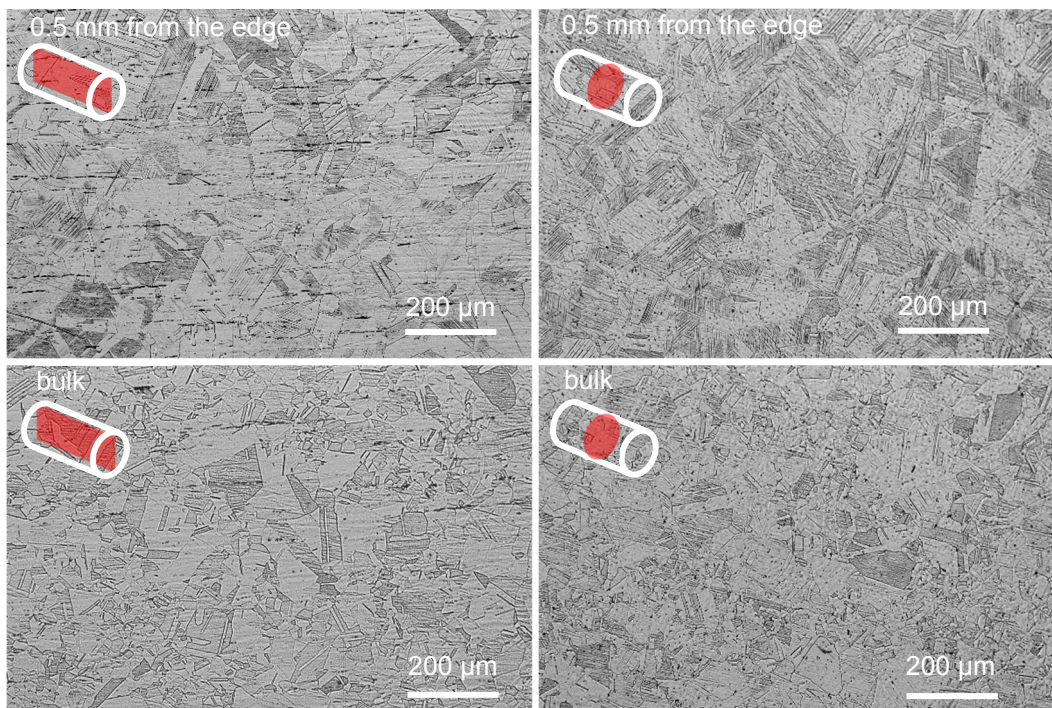
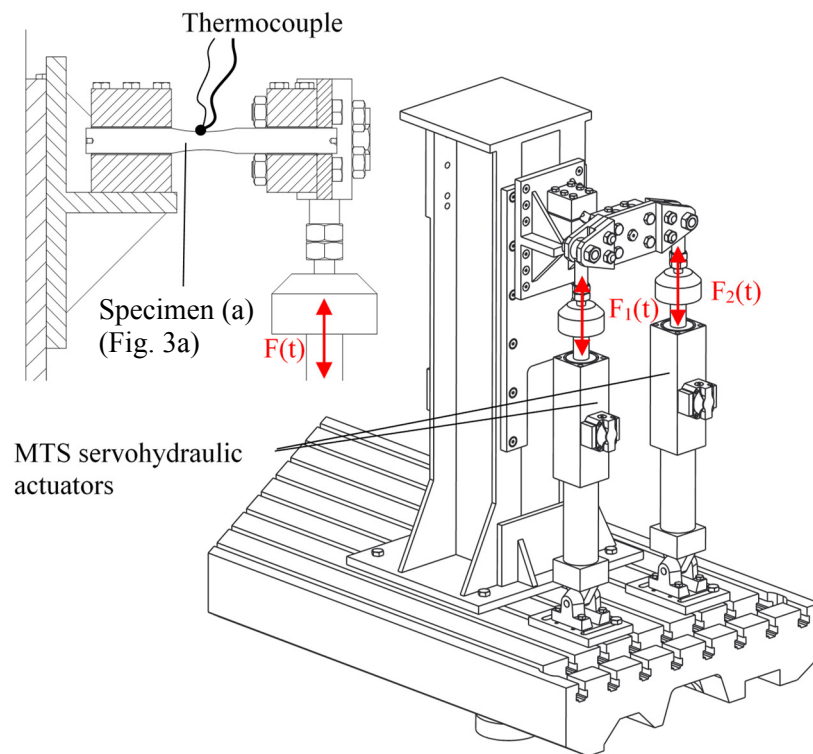


Figure 4.3: Microstructure of cold drawn AISI 304L stainless steel in the longitudinal and transversal planes both close to the edge and in the bulk of the raw bars.

a)



b)

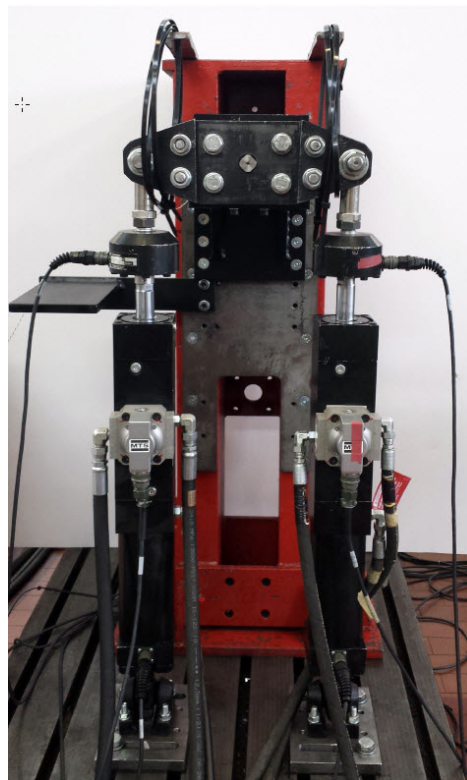


Figure 4.4: Flexible test bench designed for dynamic combined plane bending and torsion on AISI 304L specimens of Fig. (3a) (a). Picture of the relevant test bench placed at the laboratory of Machine Design of University of Padova (b).

4.3 TESTING SETUP: BENDING AND TORSION FATIGUE TESTS

The experimental fatigue tests on the type (a) specimens Fig. (3a) were performed by using a flexible test bench consisting of two MTS servo-hydraulic actuators equipped with 15 kN load cells and controlled by a digital controller MTS Flex Test 60. The test bench was designed to perform combined plane bending and torsion adopting different phase-shift angles between the axial loads of the actuators. An isometric view and a frontal picture of the test bench are reported in Fig (4). One side of the specimen (a) was fixed to the frame while the other one was clamped to a plate linked to the actuators rods by means of rod ends.

Force controlled pure bending (B), pure torsion (T) and combined in-phase and out-of-phase bending-torsion (B+T) fatigue tests were performed according to Table 3, where Λ and ϕ are the stress-based biaxiality ratio (σ_a/τ_a) and the phase-shift angle, respectively. A stiffness loss of 10% was adopted as failure criterion.

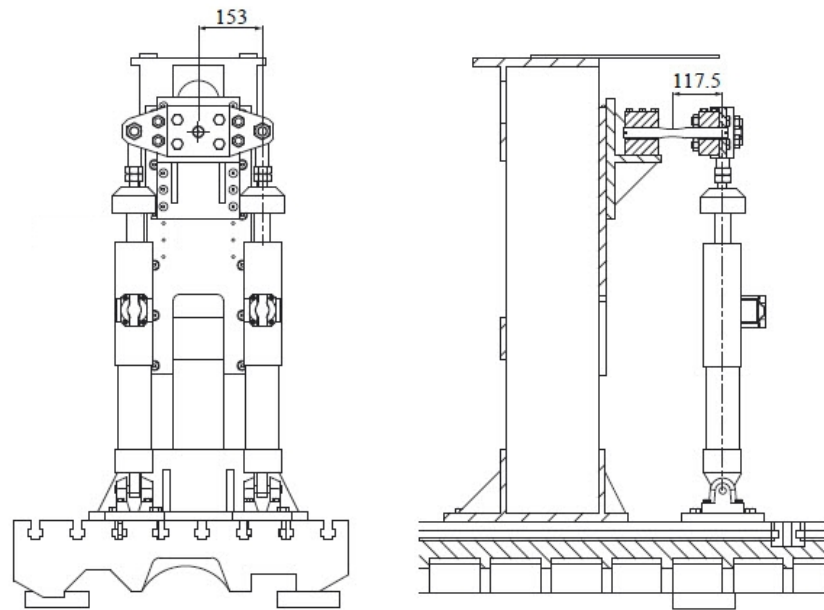
Table 4.3: Experimental protocol for multiaxial fatigue tests by using the flexible test bench (Fig. 4)

Specimen's geometry	Loading type	R	Λ	ϕ [°]	bench configuration*	N. of tests
A (Fig. 3a)	B	-1	∞	\	1	8
	T		0	\	1	3
	B+T		1	0	1	3
	B+T		$\sqrt{3}$	0	2	4
	B+T		1	90	1	4
	B+T		$\sqrt{3}$	90	1	5

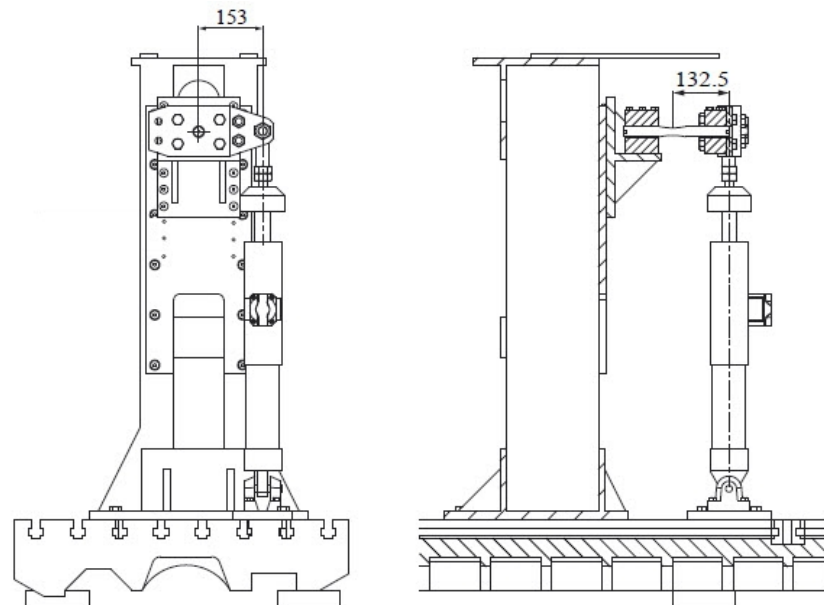
* see Fig. (5)

The dynamic response of the designed testing system (i.e specimen, frame and actuators) does not allow to follow the command signals provided for the B+T loading type characterised by a $\Lambda = \sqrt{3}$ and $\phi = 0^\circ$. Therefore, a different test bench configuration was used in order to guarantee the desired proportional loading condition. The two adopted configurations with the required geometrical parameters are reported in Fig. (5).

The temperature measurements were performed by using copper-constantan thermocouples fixed at the point of maximum bending stress (see Fig. (4a)) by using silver-loaded conductive epoxy glue. The temperature measurements were taken by using a data acquisition/switch unit Agilent 34970A and the data were stored in the PC hard drive by using the software Agilent BenchLink Data Logger. During the fatigue tests, an acquisition rate of 0.1 Hz was set for recording the long-term temperature profile. Several load stops were performed in order to measure the evolution of Q before crack nucleation. Therefore, before each test stop the acquisition rate equal to 22Hz was set for a better measure of the initial cooling gradient necessary to evaluate Q by means of Eq. (1).



test bench configuration 1



test bench configuration 2

Figure 4.5: Test bench configurations.

The damage evolution of some fatigue test (i.e. the crack nucleation and propagation) was monitored adopting the Direct Current Potential Drop (DCPM) technique by using a Matelect DCM-2 device according to the setup illustrated in Fig. (6). The technique requires two specimens: one is the specimen subjected to cyclic loading, while the other one is a reference unloaded specimens. They were connected in series at the ends of each specimen by current probes as shown in Fig. (6) by using M6 bolts. A constant current of 30 A flow on both specimens. The potential drops X, relevant to the loaded specimen, and Y, relevant to the reference unloaded one (see Fig. 6), have been measured by means of potential probes fixed at two points of each

specimen at a distance of about 10 mm from each other see Fig. (6). If a defect nucleates and propagate within the probes the potential increase due to the increment of the electrical resistance caused by the defect. It's worth to underline that the DCPD technique was not used to determine the length of initiating and propagating crack but only to estimate the fraction of total fatigue life expended to technical crack initiation.

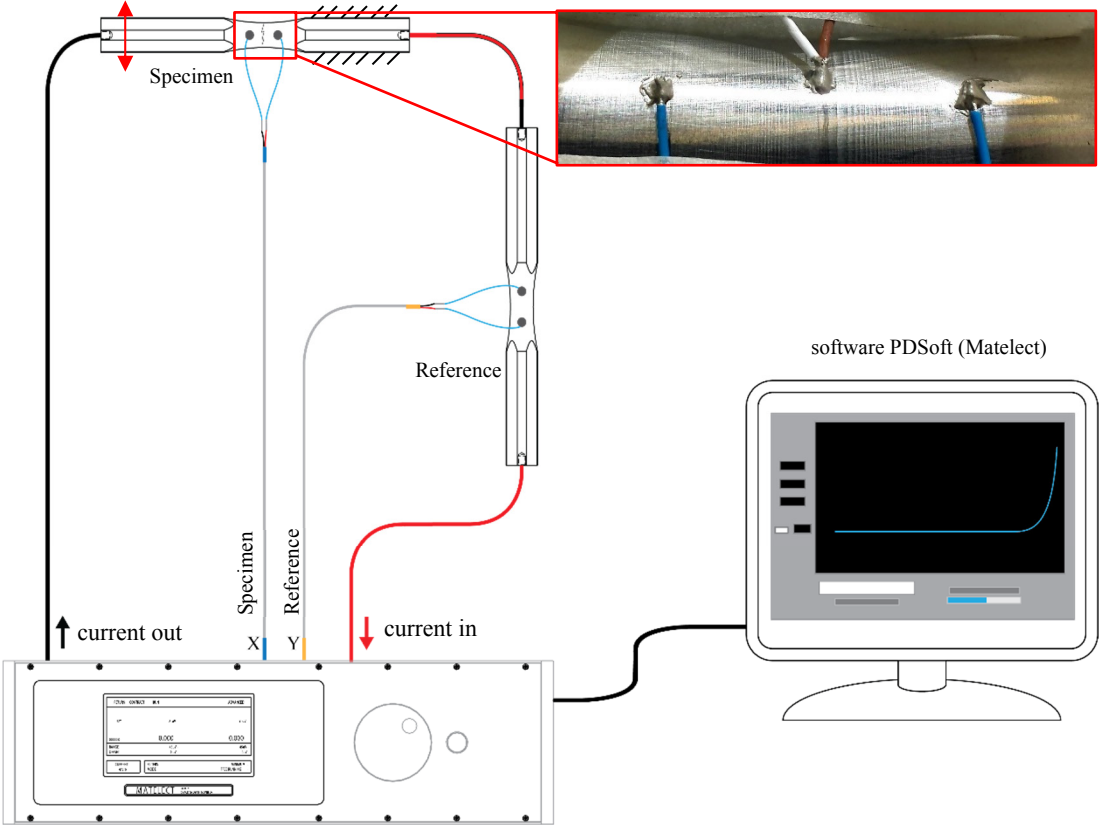


Figure 4.6: Experimental setup of the Matelect DCM-2 DCPD crack growth monitor device.

4.4 TESTING SETUP: AXIAL AND TORSION FATIGUE TESTS

Some dedicated fatigue tests on type (b) specimens (Fig. (3b)) were performed by using a MTS 809 servo-hydraulic biaxial testing machine (± 100 kN, ± 1100 Nm, ± 75 mm/ $\pm 55^\circ$) under load control. In particular, fully reversed ($R=-1$) axial, torsional and combined in-phase ($\phi = 0^\circ$) and out-of-phase ($\phi = 90^\circ$) axial and torsional fatigue tests were performed according to Table 4.

Table 4.4: Experimental protocol for multiaxial fatigue tests by using MTS axial/torsional machine

Specimen's geometry	Loading type	R	Λ	ϕ [°]	N. of tests
B (Fig. (3b))	A	-1	∞	\	1
	T		0	\	1
	A+T		$\sqrt{3}$	0	1
	A+T		$\sqrt{3}$	90	1

The fatigue tests were carried out at a load frequency ranging from 2 to 20 Hz depending on the load level applied and the stiffness loss of about 50% was set as failure criterion.

The surface temperature of type (B) specimens was measured by means of a FLIR SC7600 infrared camera, operating at a sample frequency f_{acq} equal to 100 Hz, having a 1.5–5.1 μm spectral response range, 50mm focal lens, a noise equivalent temperature difference (NETD) < 25 mK and an overall accuracy of 0.05 $^{\circ}\text{C}$. The acquisition time window was set equal to 10 seconds. In particular, the test stop was performed 5 second after triggering the acquisition. For the sake of simplicity, the temperature acquisition was only carried out for the evaluation of Q , so for few multiaxial tests on specimens (B) the long-term temperature profiles are not available. The surface of the type (B) specimens was black painted in order to increase the material emissivity. The fatigue test setup and a picture of the black painted specimens (B) (Fig. 3b) are shown in Fig (7) and (8), respectively.



Figure 4.7: Picture of the experimental setup of multiaxial fatigue testing on type (B) specimens (Fig. 3b)



Figure 4.8. Picture of the specimens (B) of Fig. (3b), used for combined axial and torsional fatigue tests.

4.5 FATIGUE TEST RESULTS

All the fatigue test results are reported in terms of nominal net-section stress amplitude in Fig. (9). In particular, in the case of torsional fatigue test results, they were plotted in terms of net-section shear stress amplitude. More precisely, the shear stress was evaluated by using Eq. (2) for the type (A) specimens, whereas for the type (B) specimens, the shear stress was assumed uniformly distributed over the cross-section and it was evaluated by means Eq. (3):

$$\tau_{an} = \frac{16 \cdot M_{t,a}}{\pi \cdot d_{en}^3} \quad (2)$$

$$\tau_{an} = \frac{16 \cdot M_{t,a}}{\pi (d_{en}^2 - d_{in}^2) (d_{en} + d_{in})} \quad (3)$$

where $M_{t,a}$, d_{en} and d_{in} are the applied torque amplitude, the outer and inner diameters of the net-cross-section, respectively.

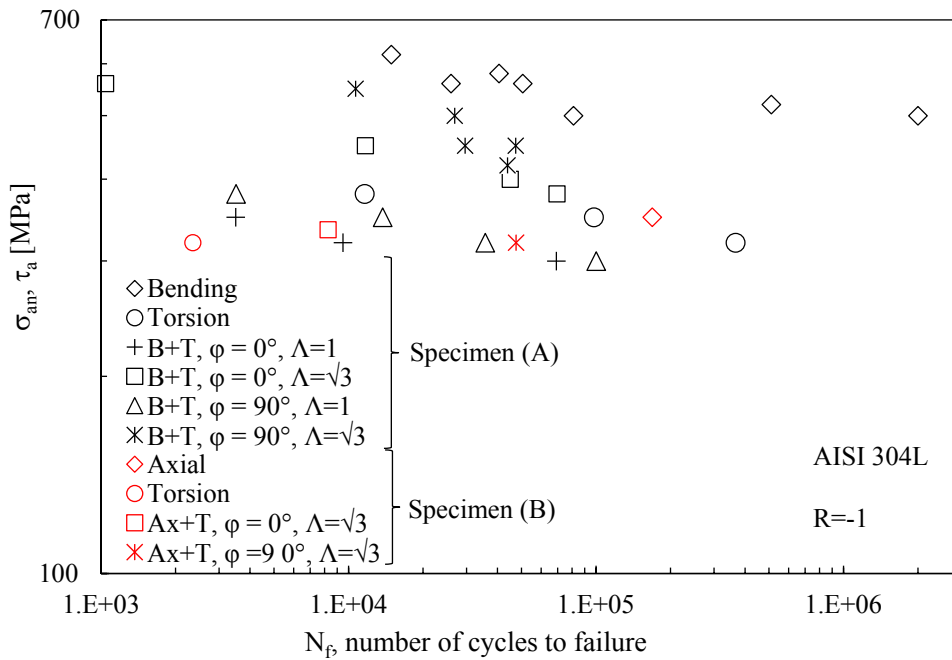


Figure 4.9: Fatigue test results in terms of nominal net-section stress amplitude.

4.5.1 Long-term temperature acquisition and damage analysis of type A specimens

Some examples of long-term temperature acquisitions and potential ratio measured by adopting the potential drop technique were reported in Figs. (10) – (19). More precisely, one or two examples for each loading condition described in Table (3)

were considered. Observing the long-term signals, the common evolution of the temperature consisting in a first increasing of the temperature followed by a stabilization and final increment due to the imminent failure can be appreciated in the examples where the load frequency was kept constant (i.e. Fig. (11)).

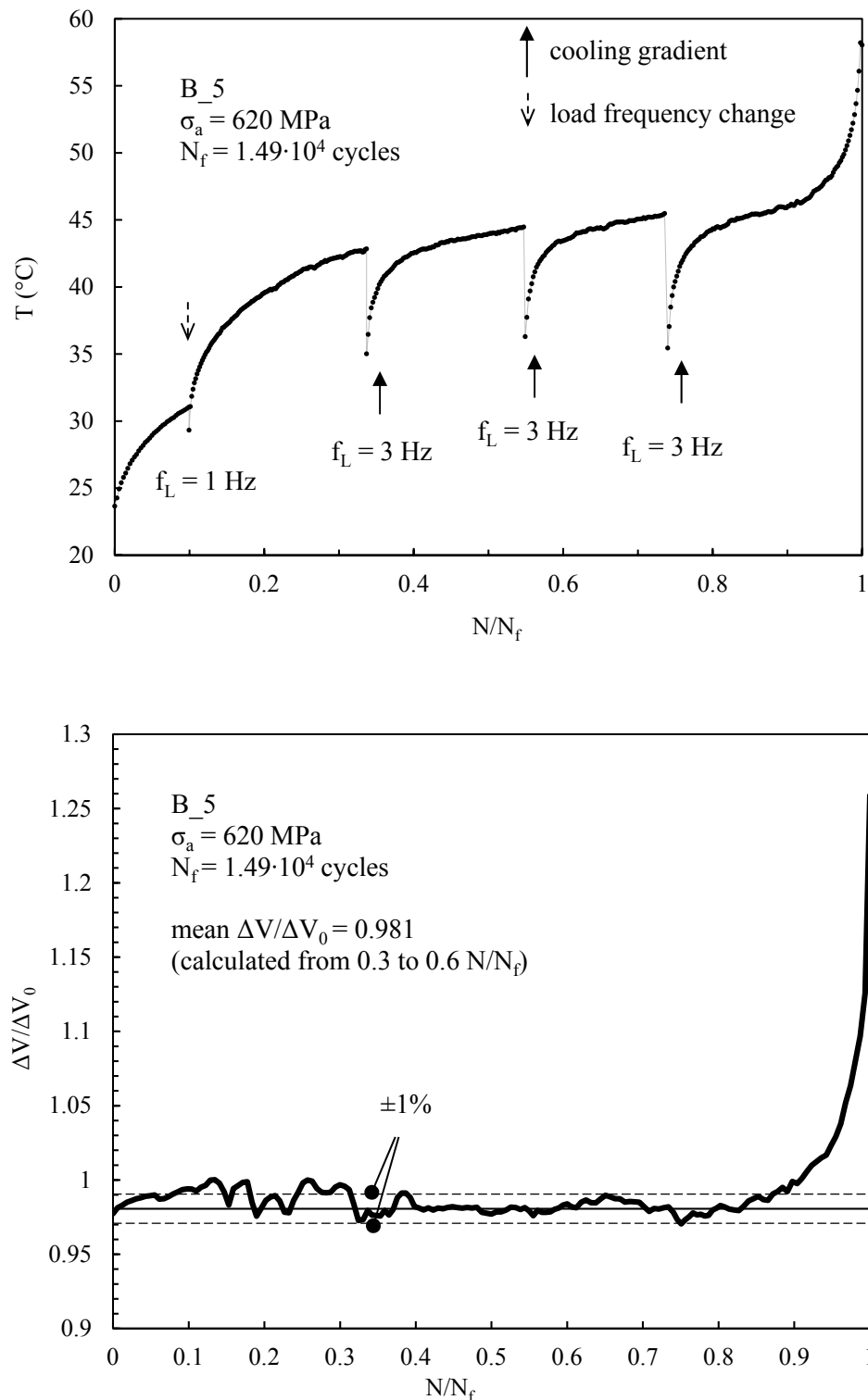


Figure 4.10: Example of long-term temperature acquisition by using thermocouples (a) and potential ratio signal obtained by means of DCPD method (b) on plane bending fatigue tests.

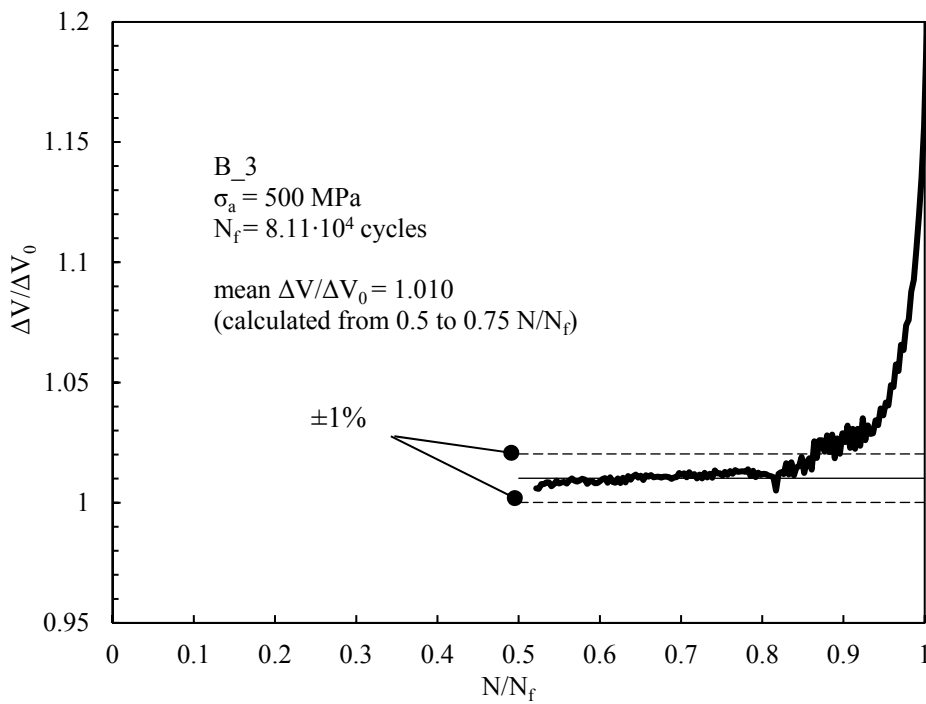
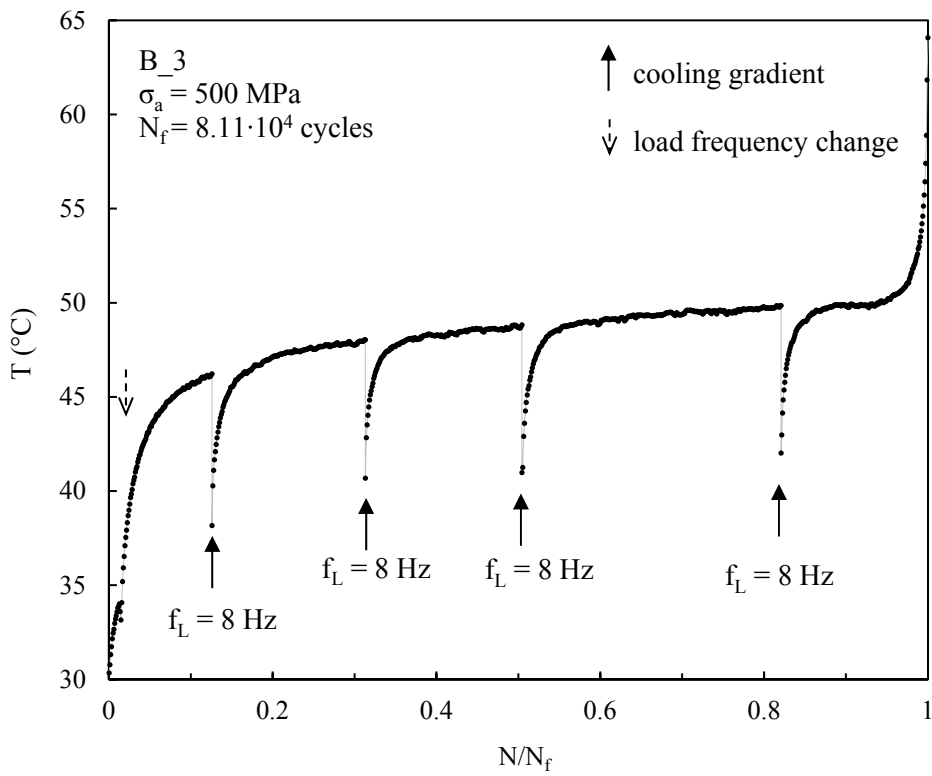


Figure 4.11: Example of long-term temperature acquisition by using thermocouples (a) and potential ratio signal obtained by means of DCPD method (b) on plane bending fatigue tests.

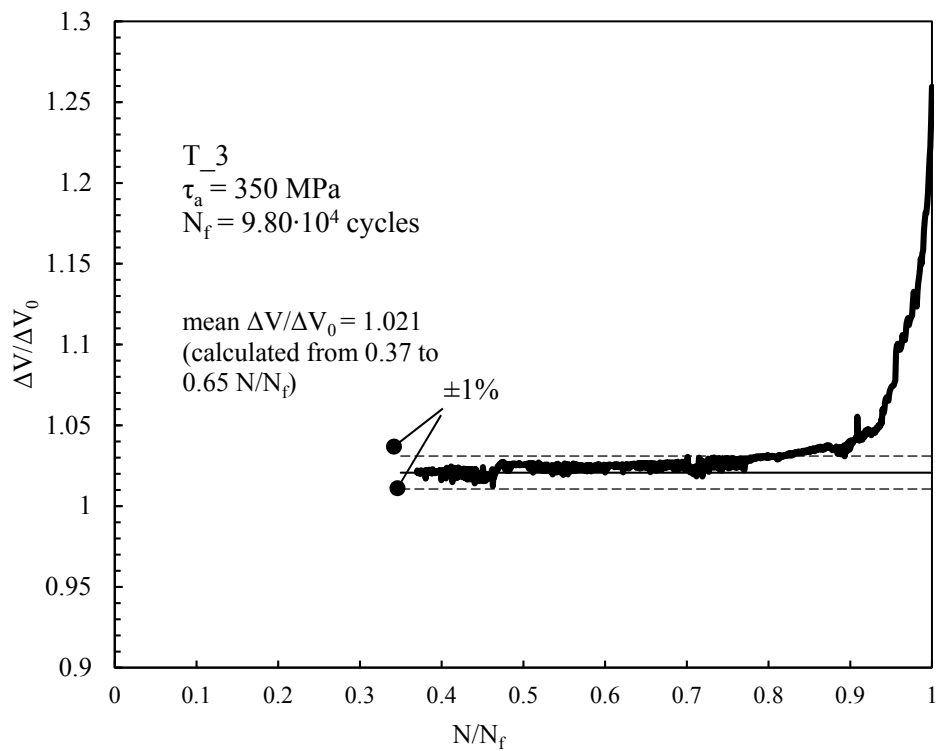
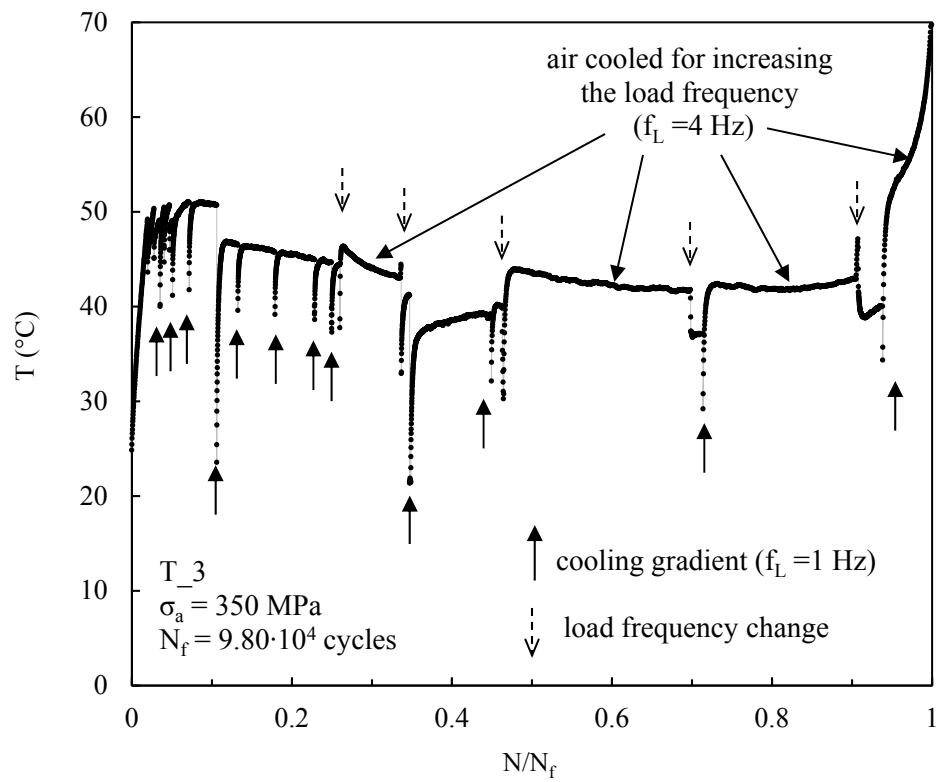


Figure 4.12: Example of long-term temperature acquisition by using thermocouples (a) and potential ratio signal obtained by means of DCPD method (b) on pure torsion fatigue tests.

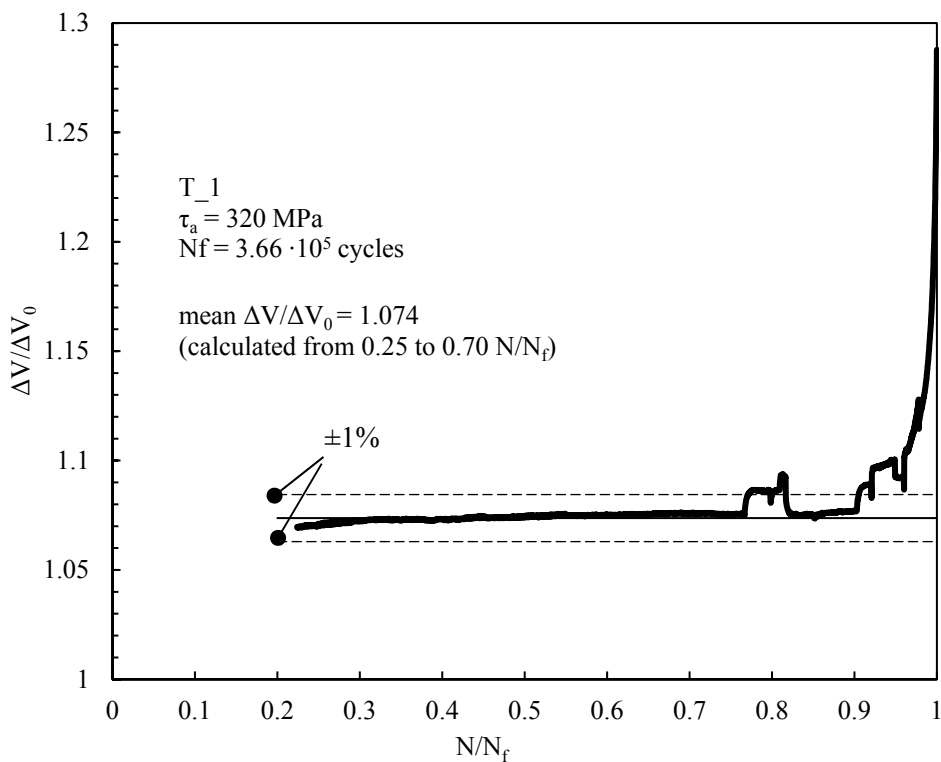
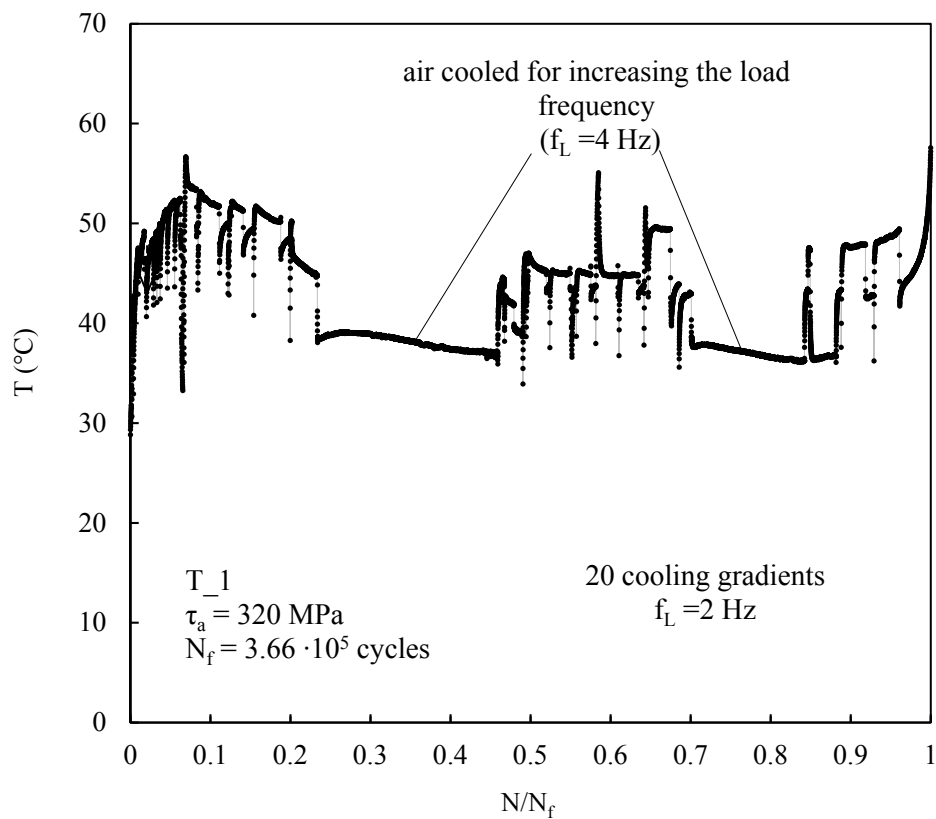


Figure 4.13: Example of long-term temperature acquisition by using thermocouples (a) and potential ratio signal obtained by means of DCPD method (b) on pure torsion fatigue tests.

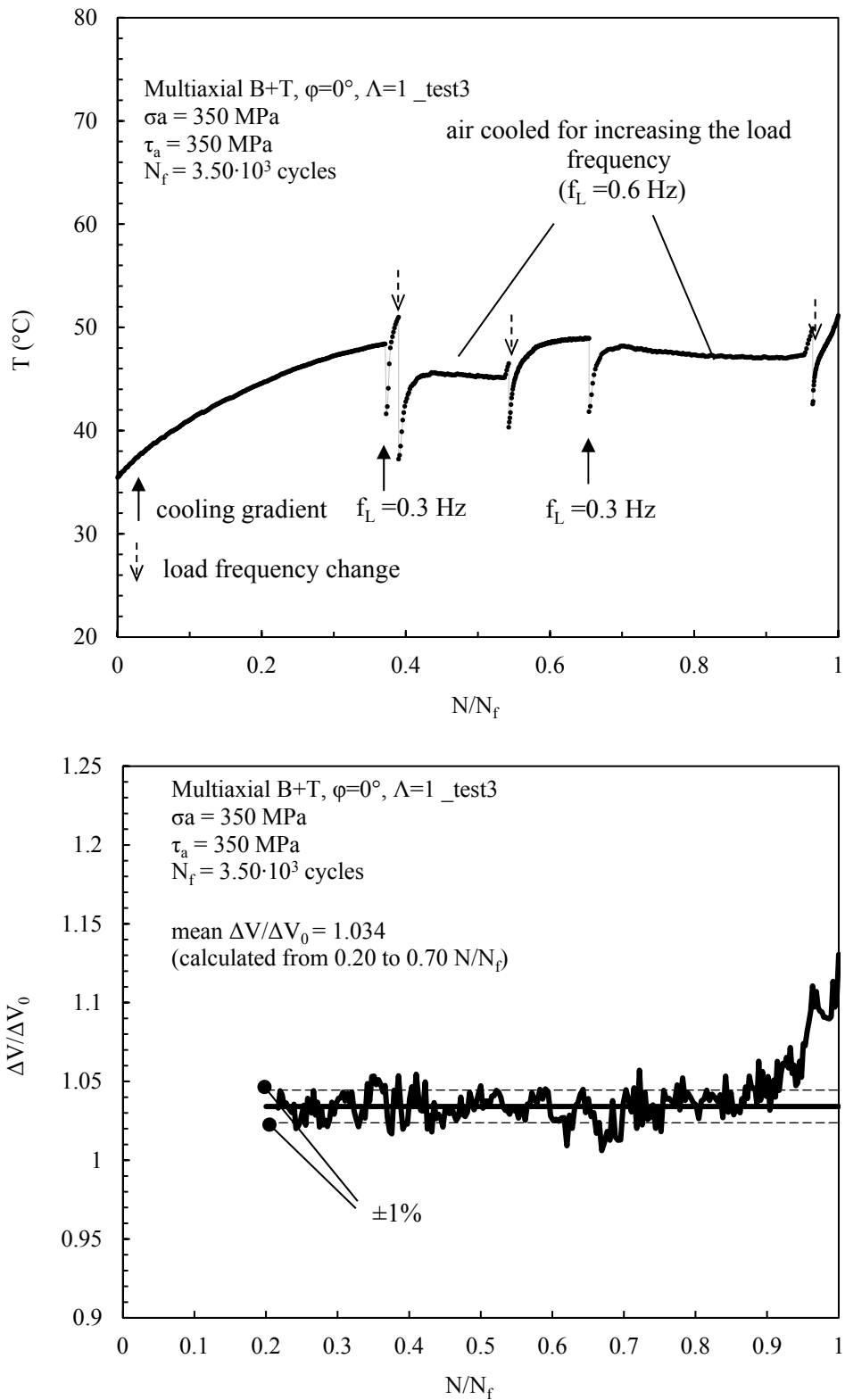


Figure 4.14: Example of long-term temperature acquisition by using thermocouples (a) and potential ratio signal obtained by means of DCPD method (b) on multiaxial B+T, $\varphi=0^\circ$, $\Lambda=1$ fatigue tests.

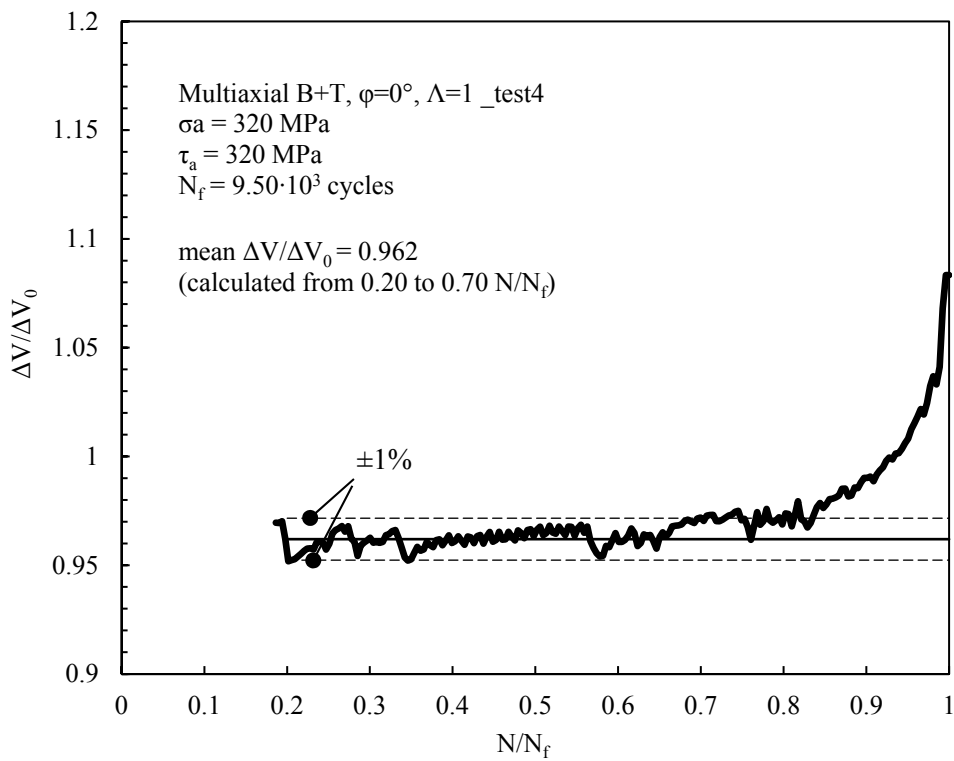
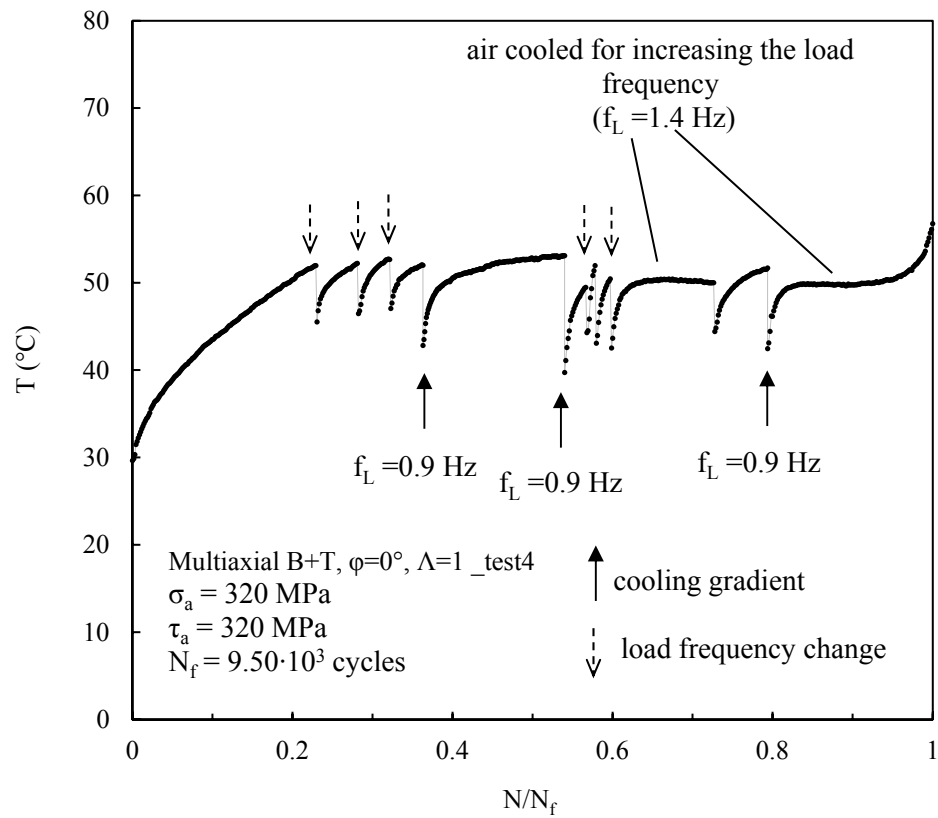


Figure 4.15: Example of long-term temperature acquisition by using thermocouples (a) and potential ratio signal obtained by means of DCPD method (b) on multiaxial B+T, $\varphi=0^\circ$, $\Lambda=1$ fatigue tests.

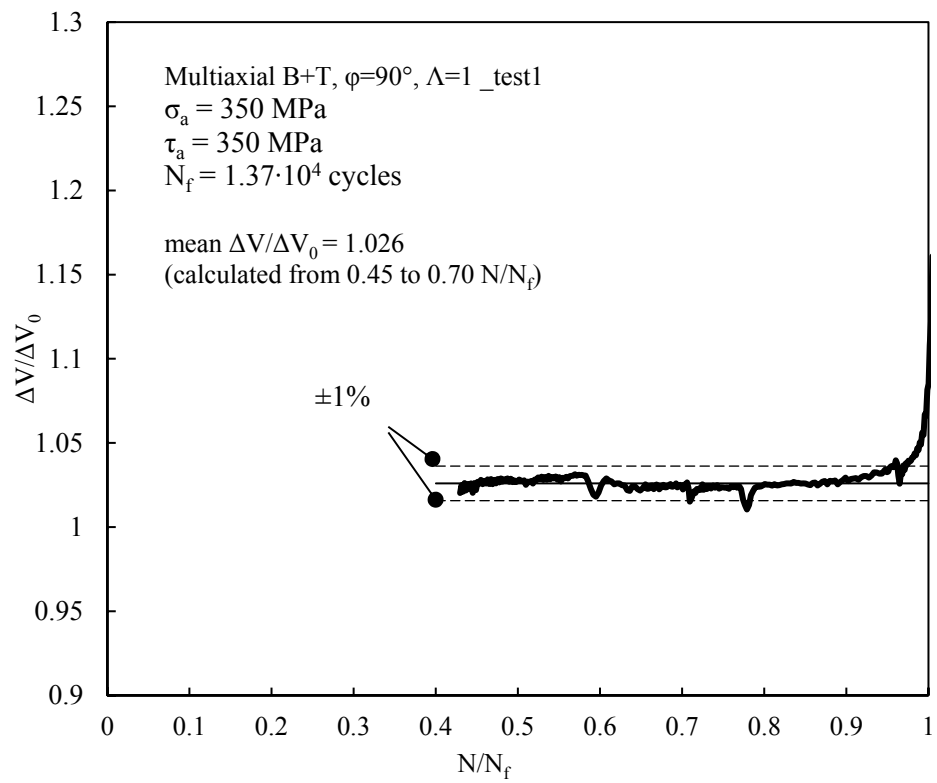
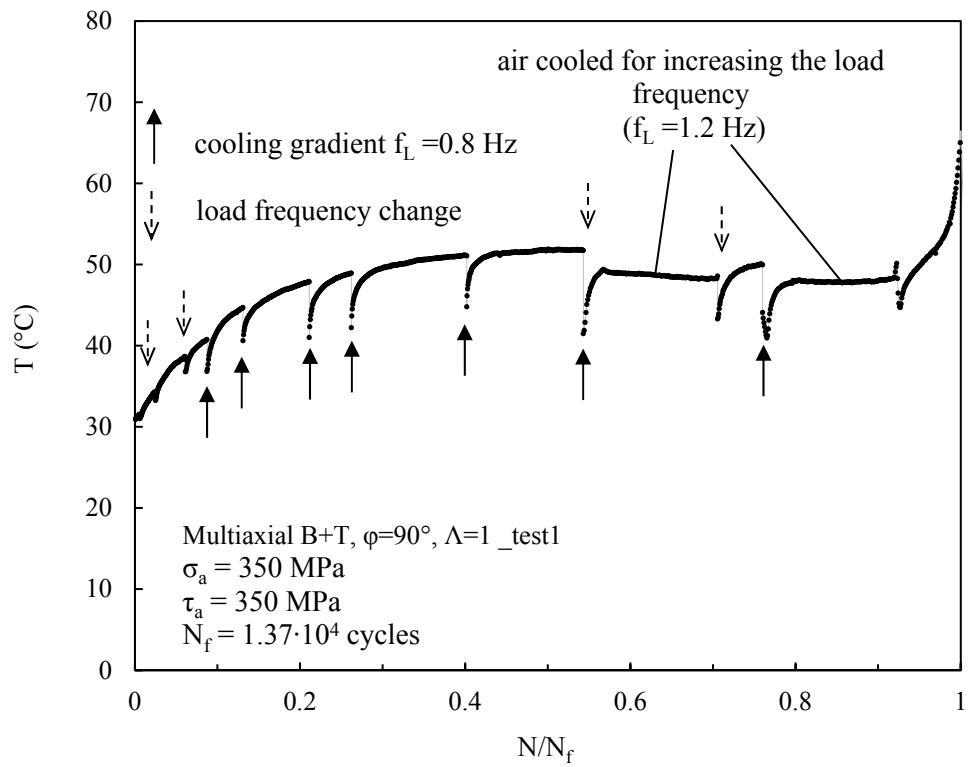


Figure 4.16: Example of long-term temperature acquisition by using thermocouples (a) and potential ratio signal obtained by means of DCPD method (b) on multiaxial B+T, $\phi=90^\circ$, $\Lambda=1$ fatigue tests

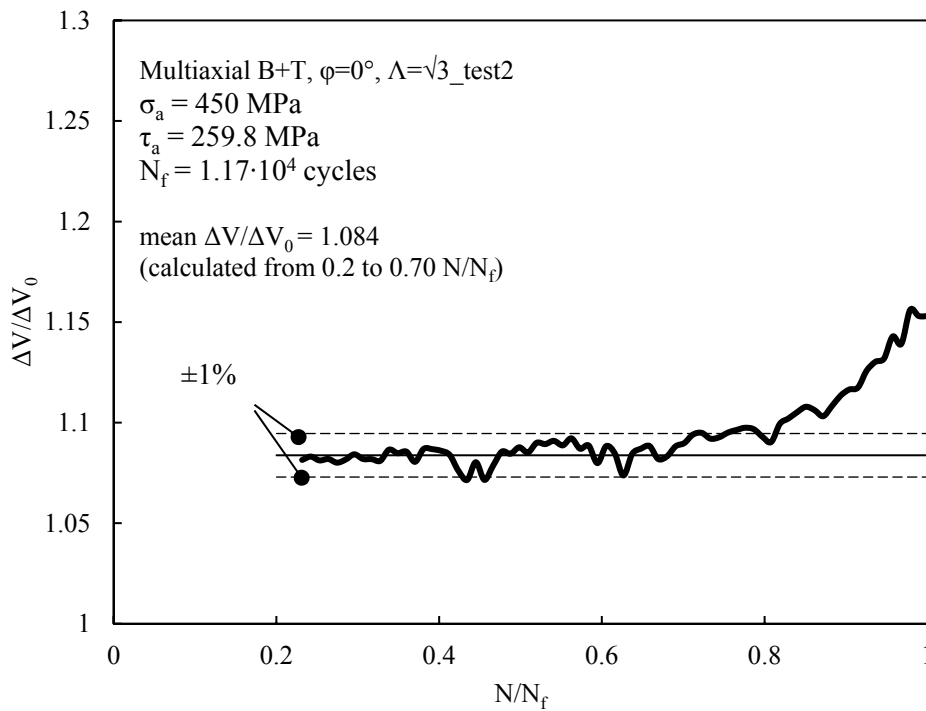
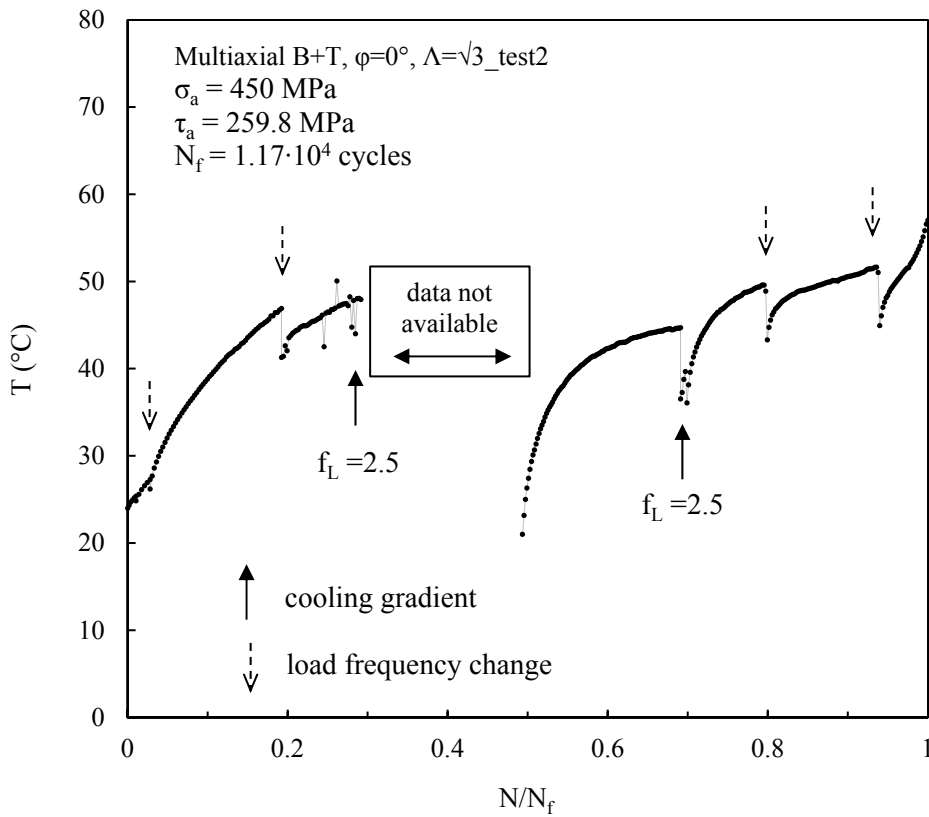


Figure 4.17: Example of long-term temperature acquisition by using thermocouples (a) and potential ratio signal obtained by means of DCPD method (b) on multiaxial B+T, $\varphi=0^\circ$, $\Lambda=\sqrt{3}$ fatigue tests

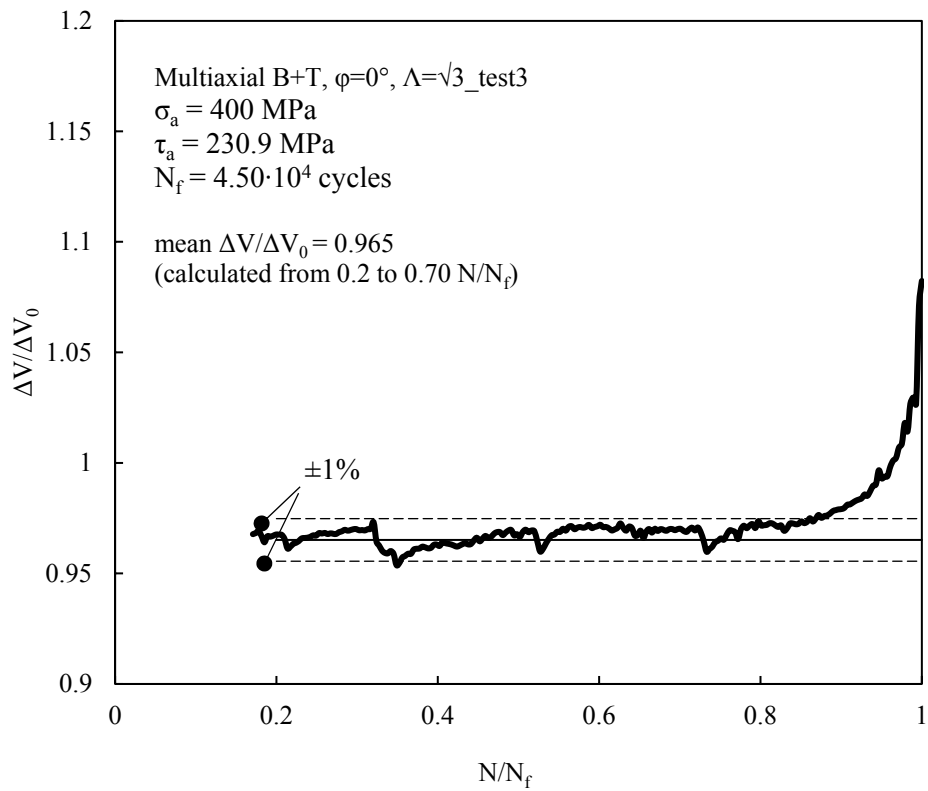
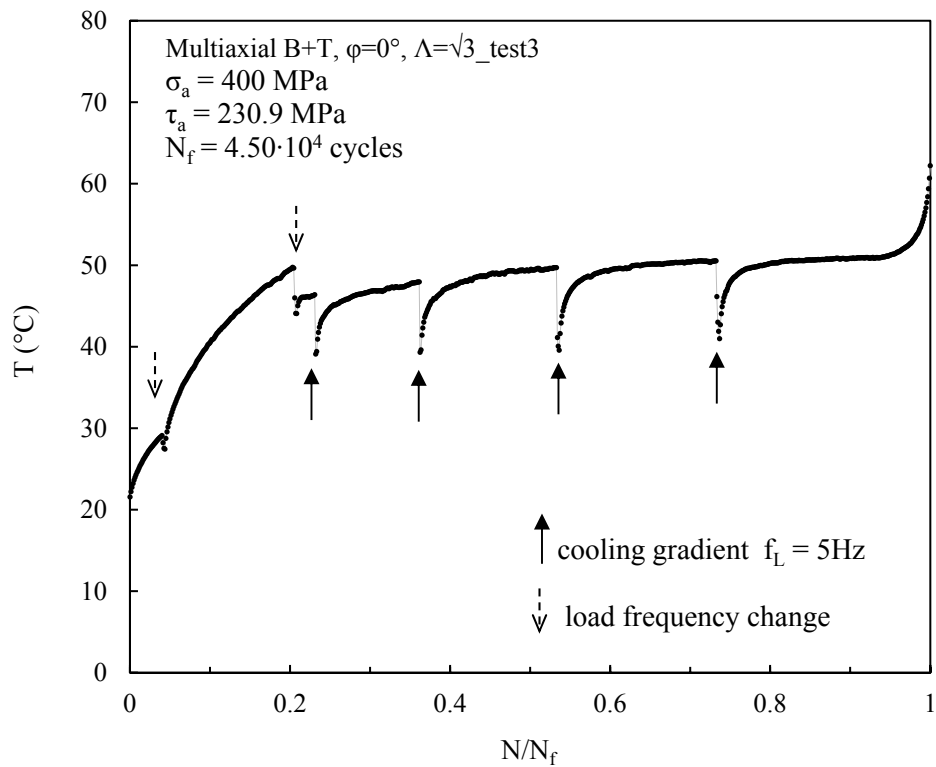


Figure 4.18: Example of long-term temperature acquisition by using thermocouples (a) and potential ratio signal obtained by means of DCPD method (b) on multiaxial B+T, $\phi=0^\circ$, $\Lambda=\sqrt{3}$ fatigue tests

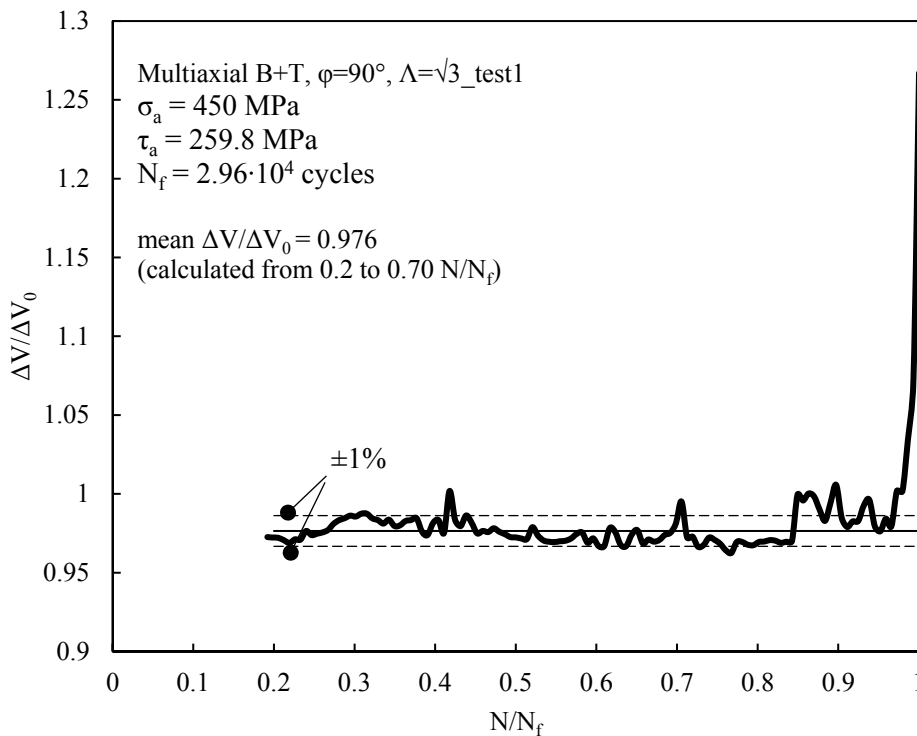
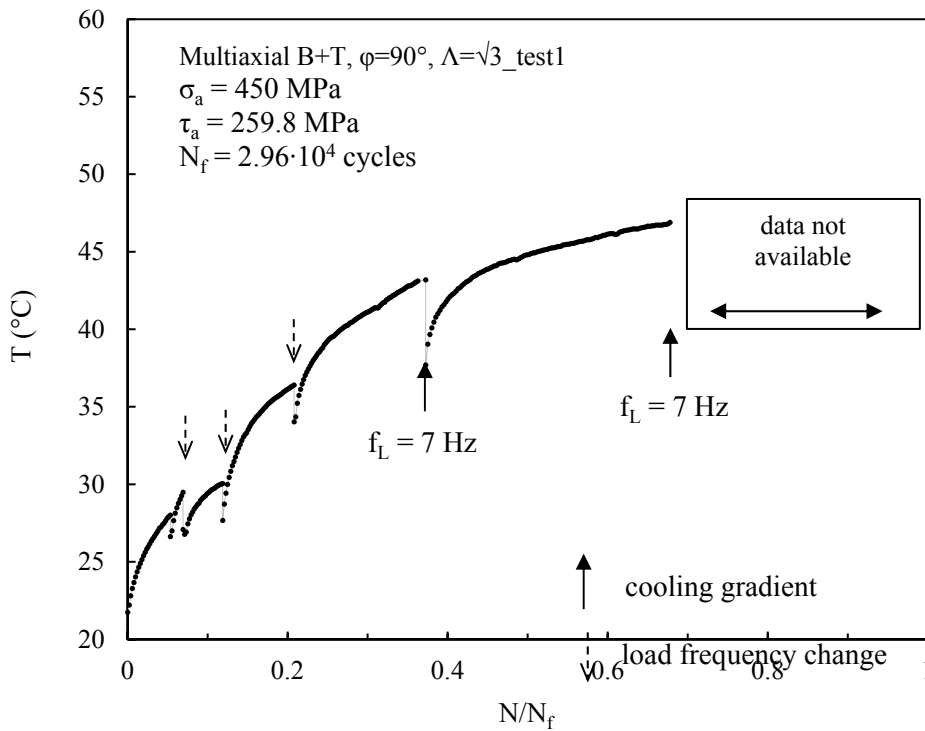


Figure 4.19: Example of long-term temperature acquisition by using thermocouples (a) and potential ratio signal obtained by means of DCPD method (b) on multi-axial B+T, $\varphi=90^\circ$, $\Lambda=\sqrt{3}$ fatigue tests

In Fig.s (10a-19a) the cooling gradients used for evaluating Q were indicated by a black arrow, while a dashed black arrow was adopted for indicating the relevant

cooling gradient which only refers to a load frequency change. Furthermore, in some cases, the specimen was air-cooled by using a fan between two cooling gradient acquisitions for speeding up the fatigue tests keeping, at the same time, the temperature value below 55°C.

It is worth noticing that in fatigue tests relevant to the low cycle fatigue regime (LCF) the temperature does not reach a stabilized value (see Fig.s (10), (17) and (19)). In these cases, the heating gradient before each test stop is at least 90% lower than the cooling gradient measured after having stopped the test. Therefore, Eq (1) can be used without any considerable errors.

Looking at Fig.s (11) and (12) which are related to a plane bending and pure torsion fatigue test, respectively, higher load frequency was adopted in the former one with respect to the latter one for obtaining about the same temperature stabilization. This is mainly due to the fact that the cyclic plastic zone is limited in the two portions of volume where the maximum bending stress occurs, whereas the self-heat generation due to plastic strain energy dissipation in torsional cyclic loading is distributed along the perimeter of the net- cross section of the specimens.

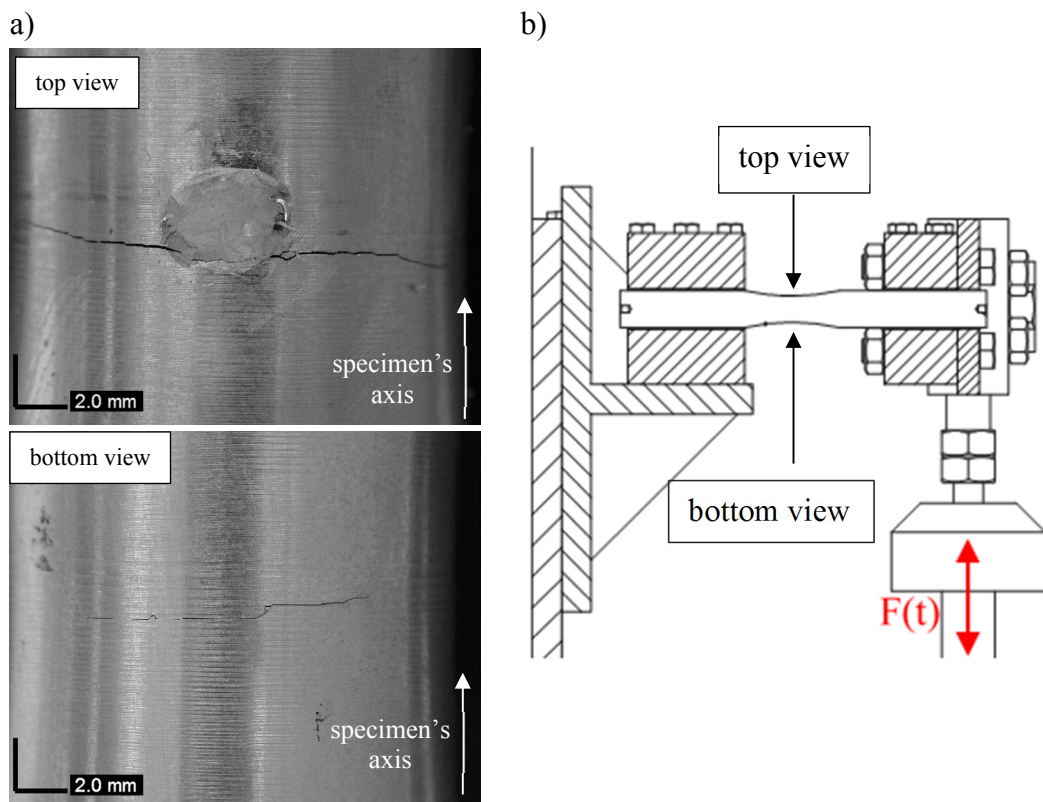


Figure 4.20: Cracks orientation due to cyclic plane bending.

In Fig.s (10b-19b) the ratios between the electrical potentials measured on the loaded and unloaded specimen were reported against the fraction of fatigue life to failure N/N_f . It can be seen that the signals are affected by noise which is not typical in DCPD applications. However, this is probably due to the fact that DCPD is common applied in fatigue crack growth application as well as in fatigue testing on notched

specimens which allow to fix the potential probes by soldering them to the testing samples. Since in this application the DCPD method was applied to plain specimens (without notches), the potential probes could not be attached by soldering.

The number of cycles to the crack initiation N_{in} was here defined as the number of cycles observed when the potential ratio overcome the 1% of its mean value evaluated between a ratio N/N_f of 0.2 and 0.75. As it can be seen from Fig.s (10b-19b), in all the examples N_{in} occurs at N/N_f approximately equal to 0.8 or even higher. Despite the approximated definition of N_{in} , by an engineering point of view, the fatigue life expended to initiate the failure seems to be not affected by the loading condition as well as N_{in} seems to be assumed at N_f .

Damage analysis

An analysis of the crack paths after 50% of stiffness loss was carried out by means of a Digital Microscope DINOLite®.

All the directions of the failures obtained in-plane bending cyclic loading occurred in a plane orthogonal to the maximum principal stress as reported in the example in Fig. (20).

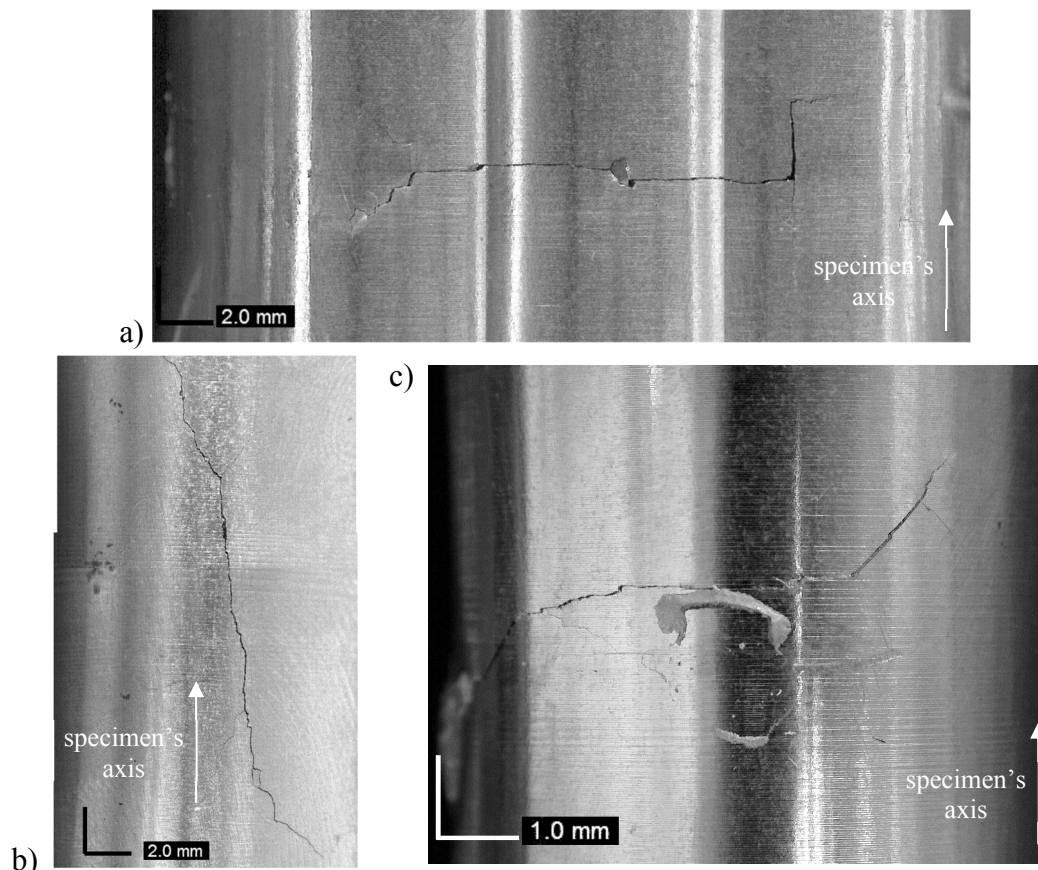


Figure 4.21. Crack orientation due to cyclic pure torsion bending at LCF a) Low-Medium HF b) and HCF regime c).

Fig. (21a-c) reports the crack paths relevant to failures occurred in torsional fatigue tests. All the cracks initiated in a plane of maximum shear strain both in the LCF and HCF regimes.

Regarding the crack orientation under different multiaxial loading conditions, as can be seen in Fig.s (22-25), all the failure initiated on the maximum shear planes.

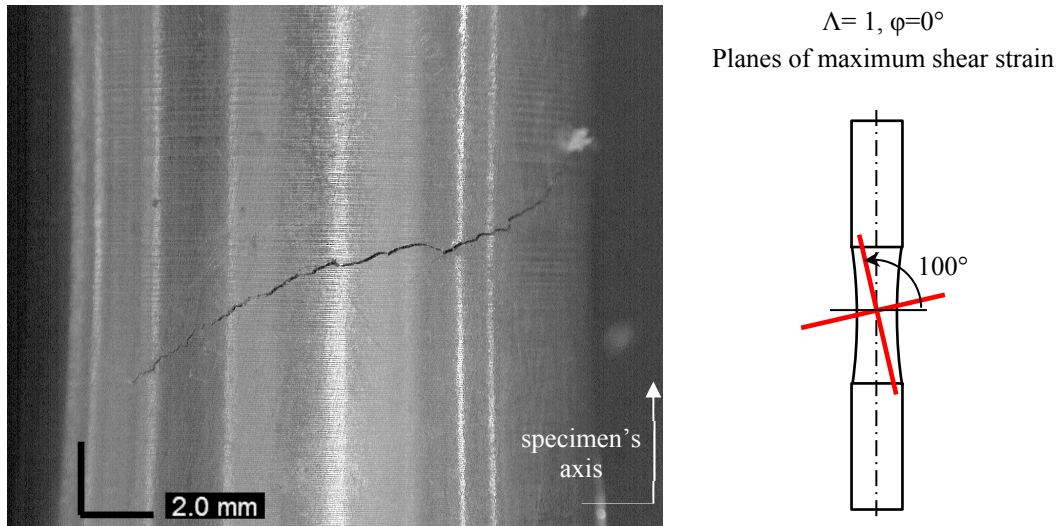


Figure 4.22: Crack orientation due to cyclic combined bending and torsional fatigue loading characterized by $\Lambda = 1, \varphi = 0^\circ$.

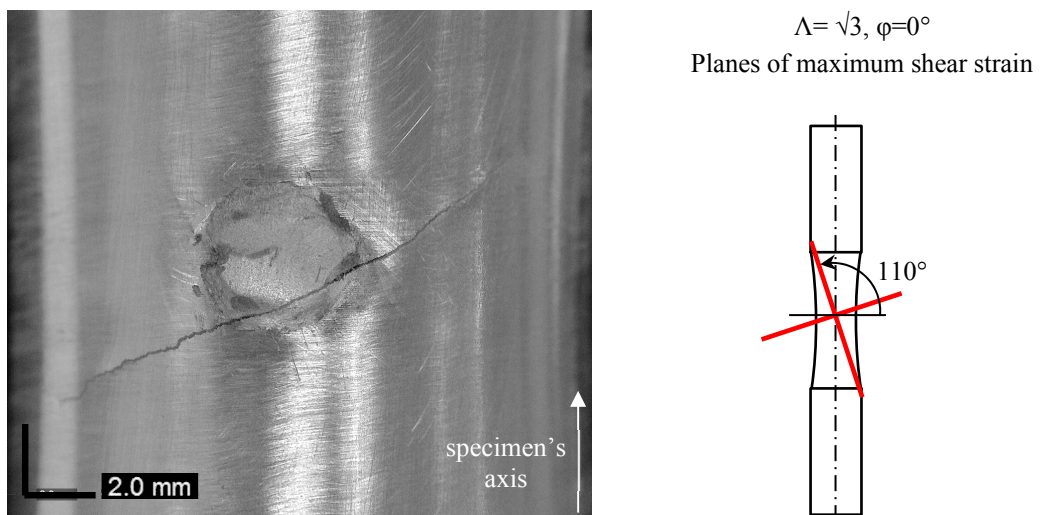


Figure 4.23: Crack orientation due to cyclic combined bending and torsional fatigue loading characterized by $\Lambda = \sqrt{3}, \varphi = 0^\circ$.

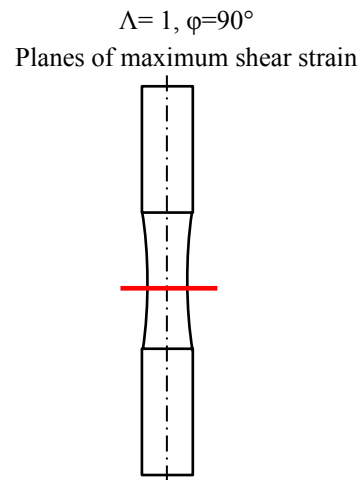
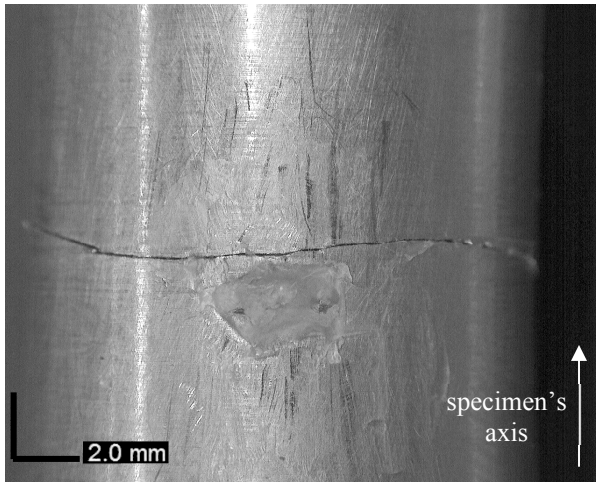


Figure 4.24: Crack orientation due to cyclic combined bending and torsional fatigue loading characterized by $\Lambda = 1, \varphi = 90^\circ$.

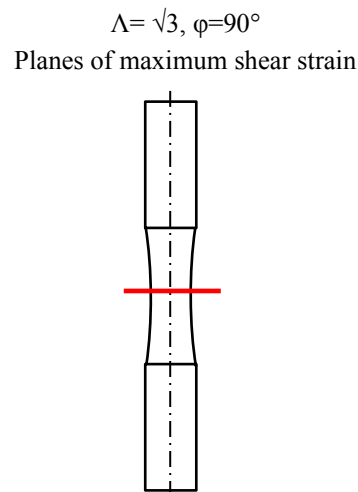
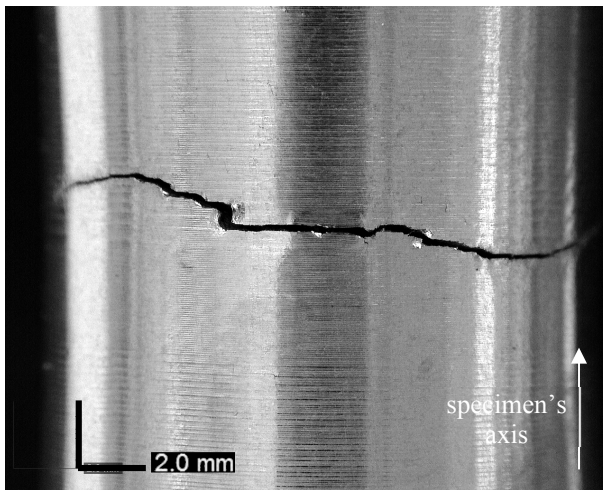


Figure 4.25: Crack orientation due to cyclic combined bending and torsional fatigue loading characterized by $\Lambda = \sqrt{3}, \varphi = 90^\circ$.

4.5.2 Evaluation of the Specific heat loss per cycle Q

In Figs (20-31) two examples of each loading condition were reported. The slope of a linear interpolation of the initial cooling gradient is shown in each relevant cooling gradient. In particular, temperature data related to about 1 s of time window were adopted in order to evaluate the cooling gradient. The choice of the initial time to interpolate the data is done by the operator, but it is easy to observe that changing the set of data to interpolate does not change significantly the value of the slope (i.e. the value of Q).

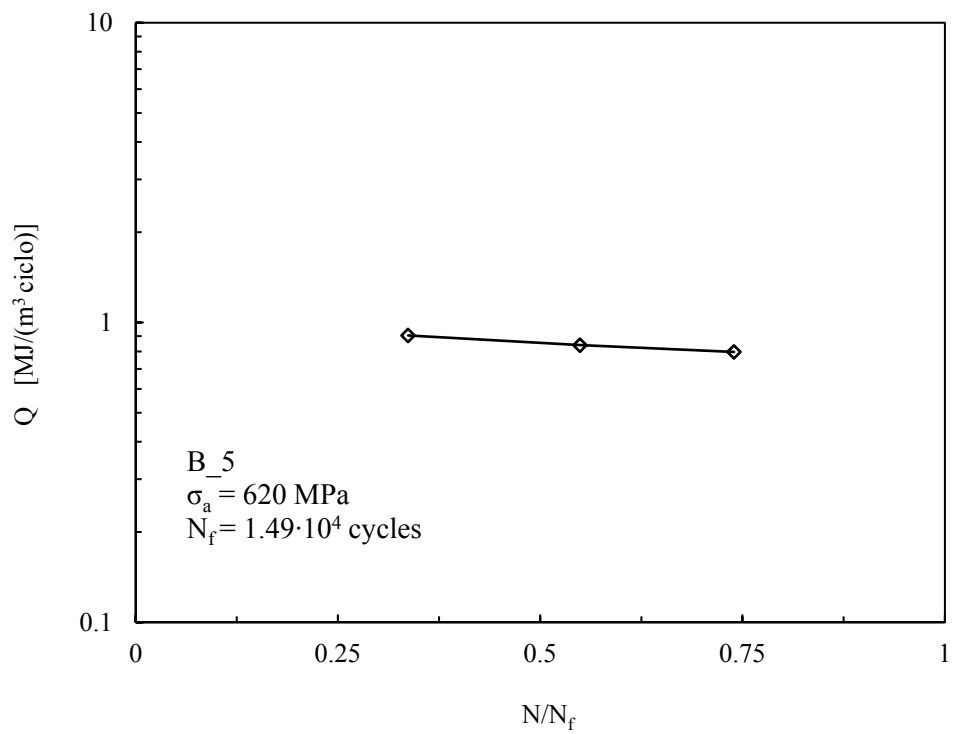
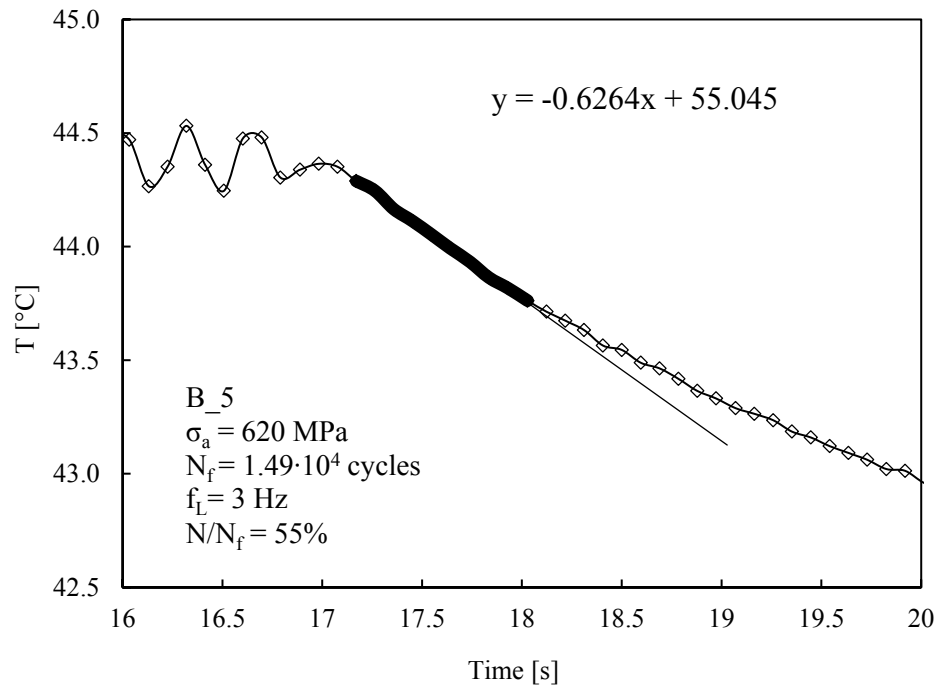


Figure 4.26: Example of cooling gradient measured in plane bending fatigue test and relevant Q evolution.

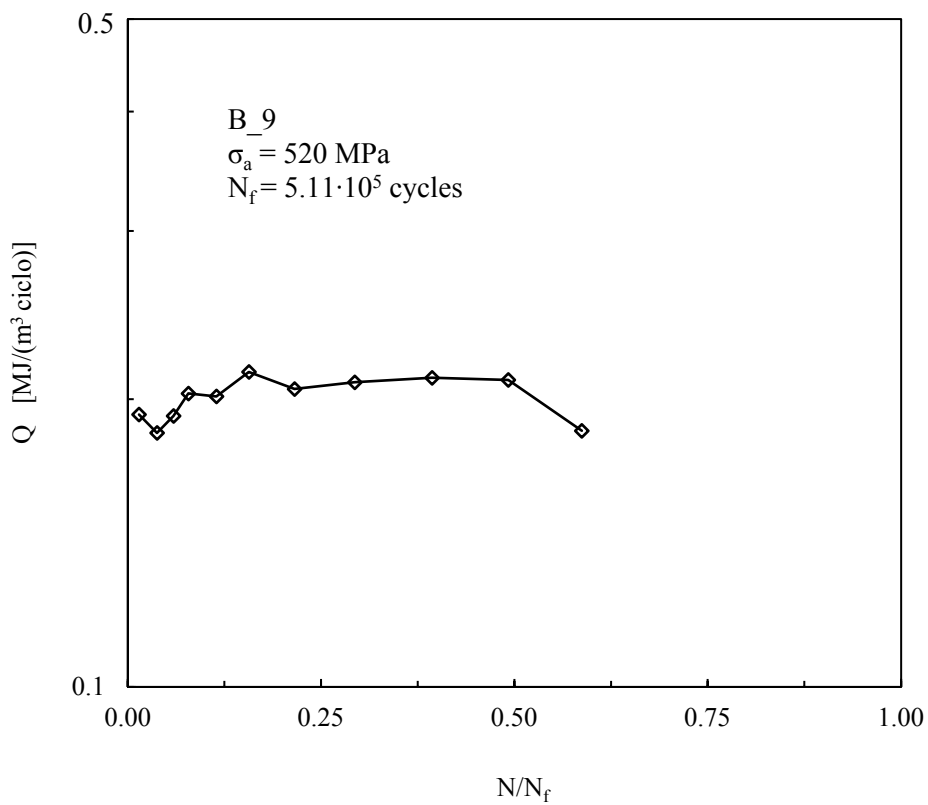
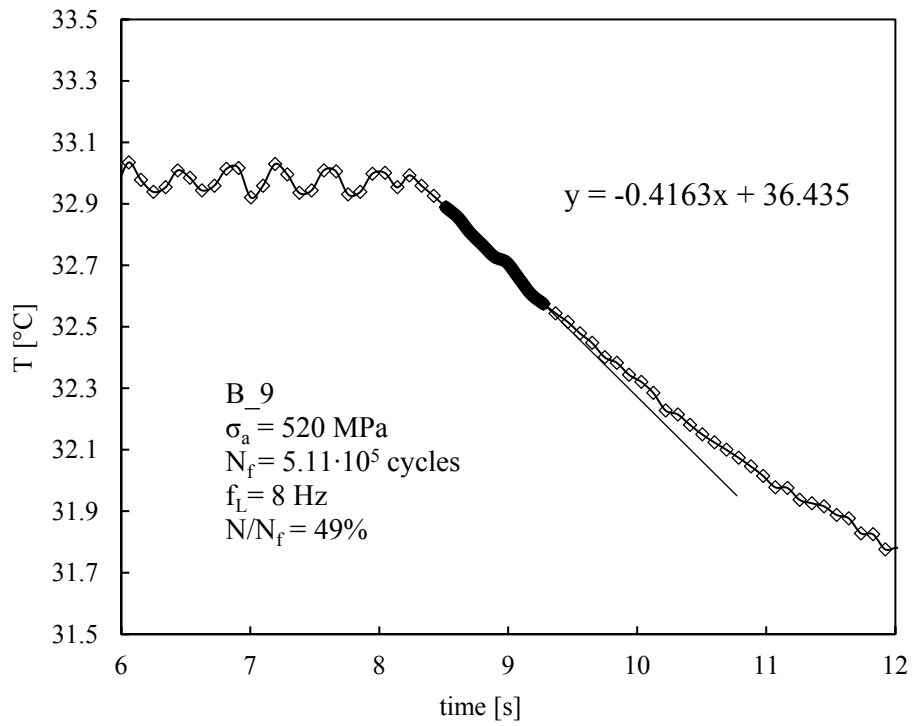


Figure 4.27: Example of cooling gradient measured in plane bending fatigue test and relevant Q evolution.

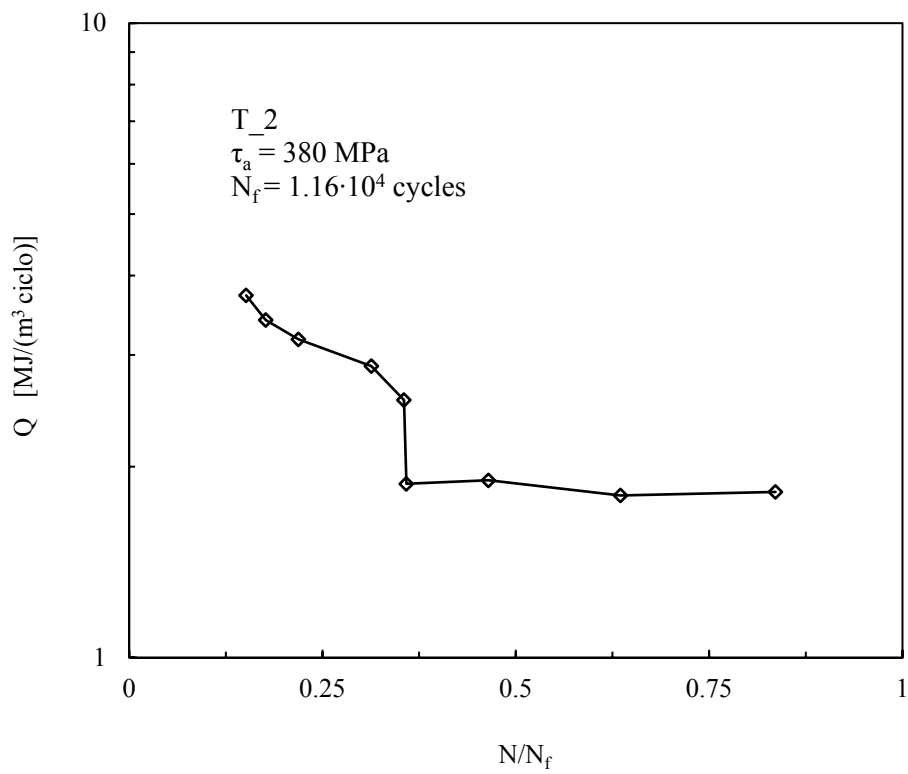
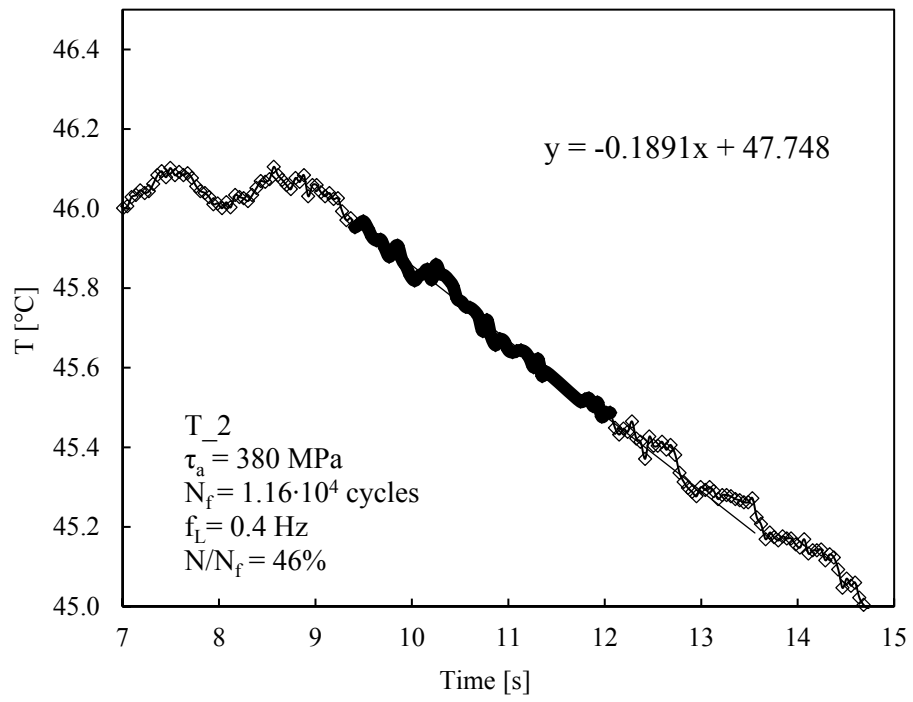


Figure 4.28: Example of cooling gradient measured in pure torsional fatigue test and relevant Q evolution.

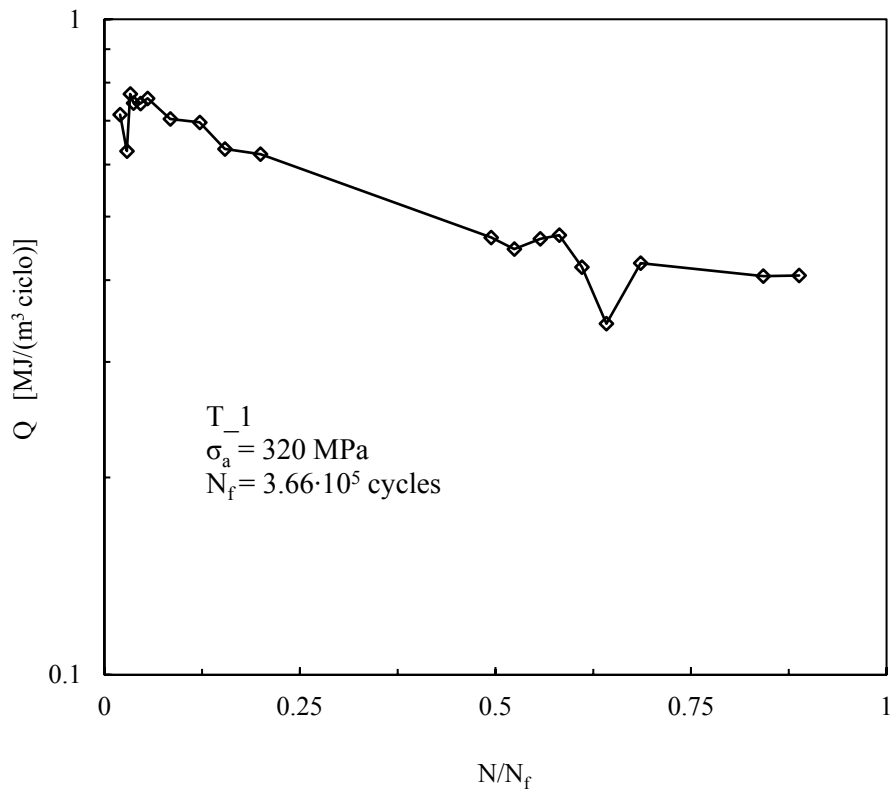
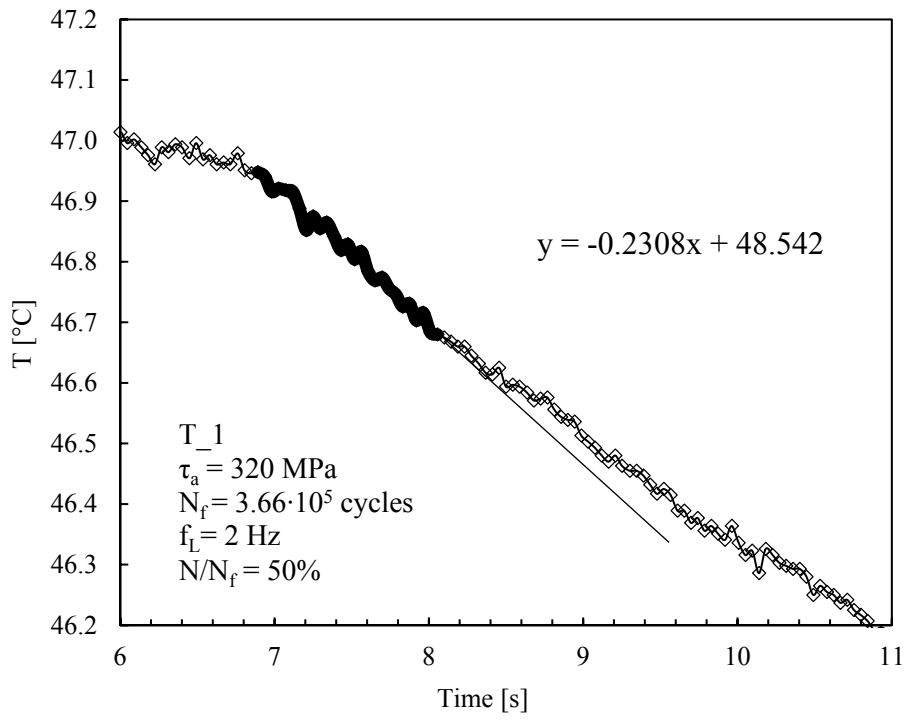


Figure 4.29: Example of cooling gradient measured in pure torsional fatigue test and relevant Q evolution.

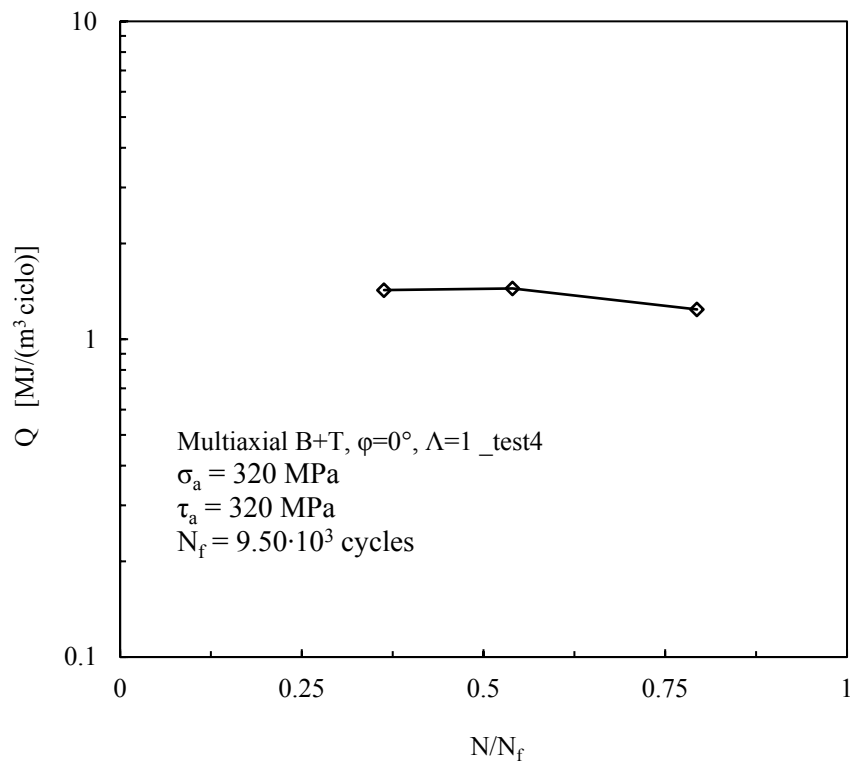
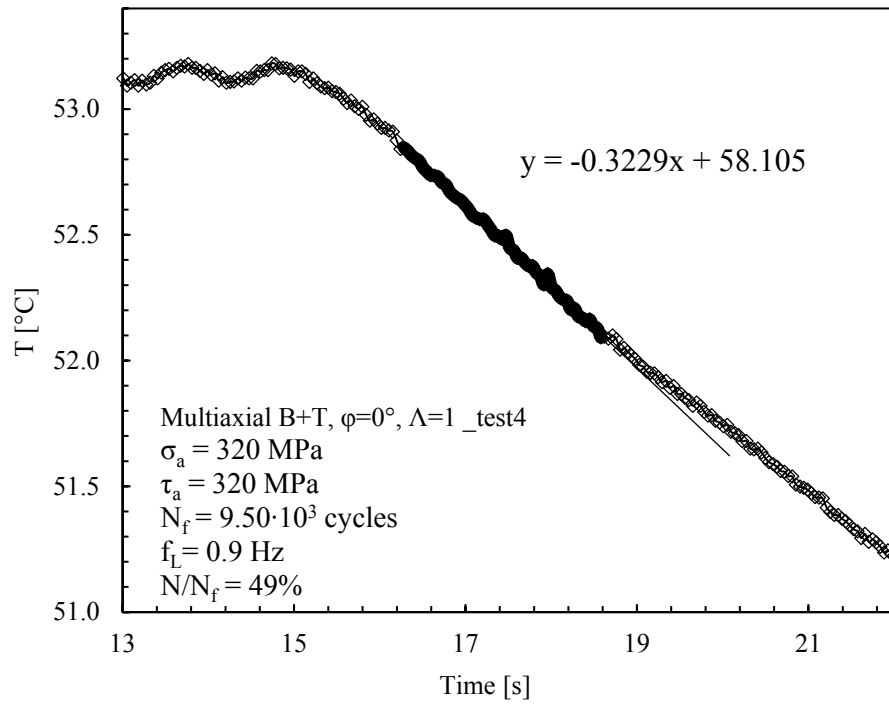


Figure 4.30: Example of cooling gradient measured in B+T, $\varphi=0^{\circ}$, $\Lambda=1$ fatigue test and relevant Q evolution.

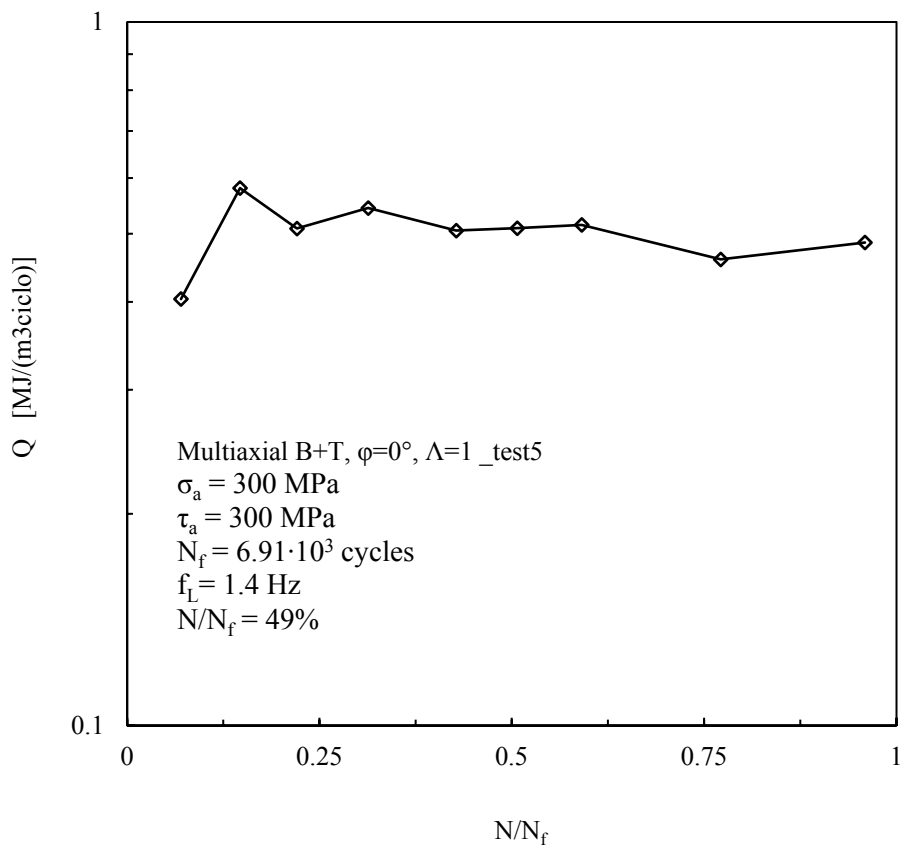
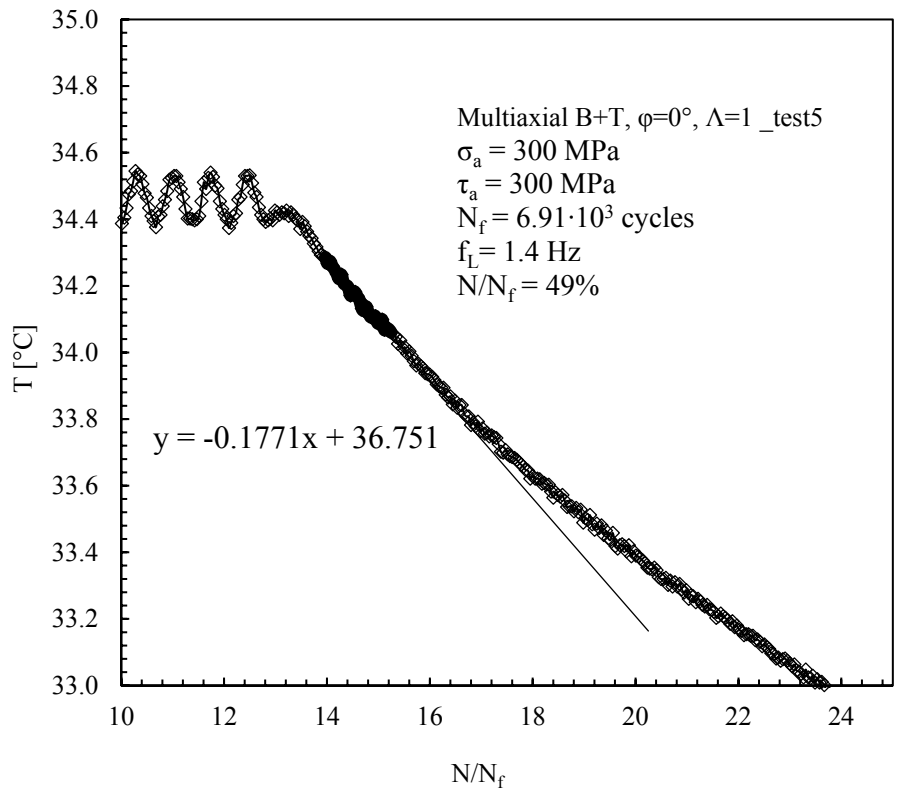


Figure 4.31: Example of cooling gradient measured in B+T, $\varphi=0^\circ$, $\Lambda=1$ fatigue test and relevant Q evolution.

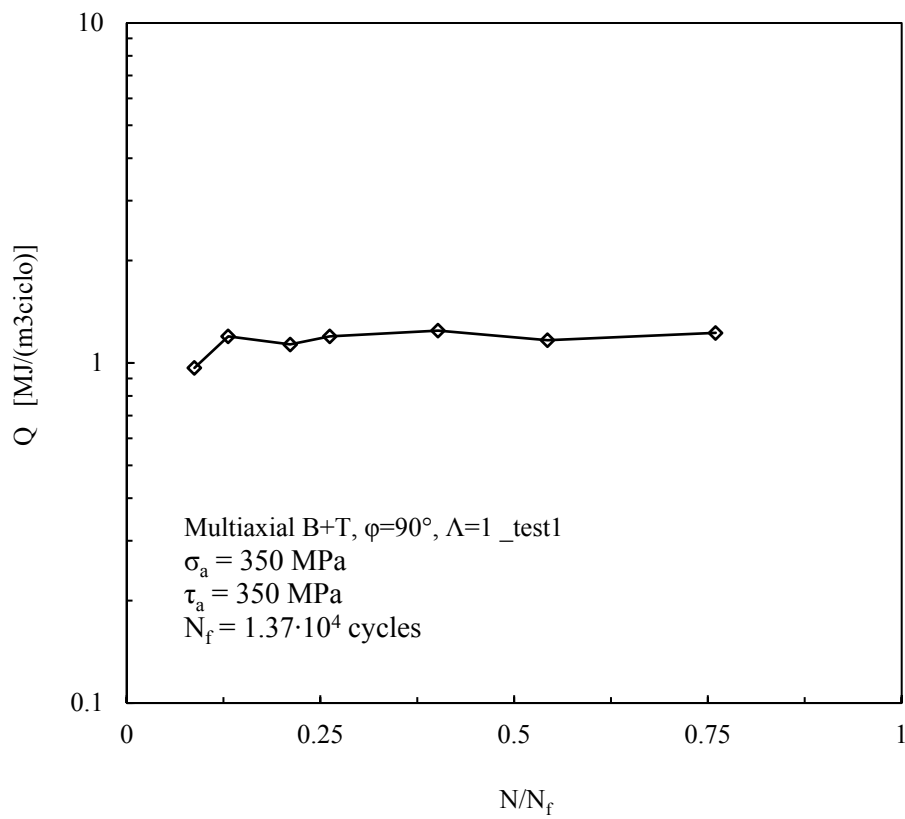
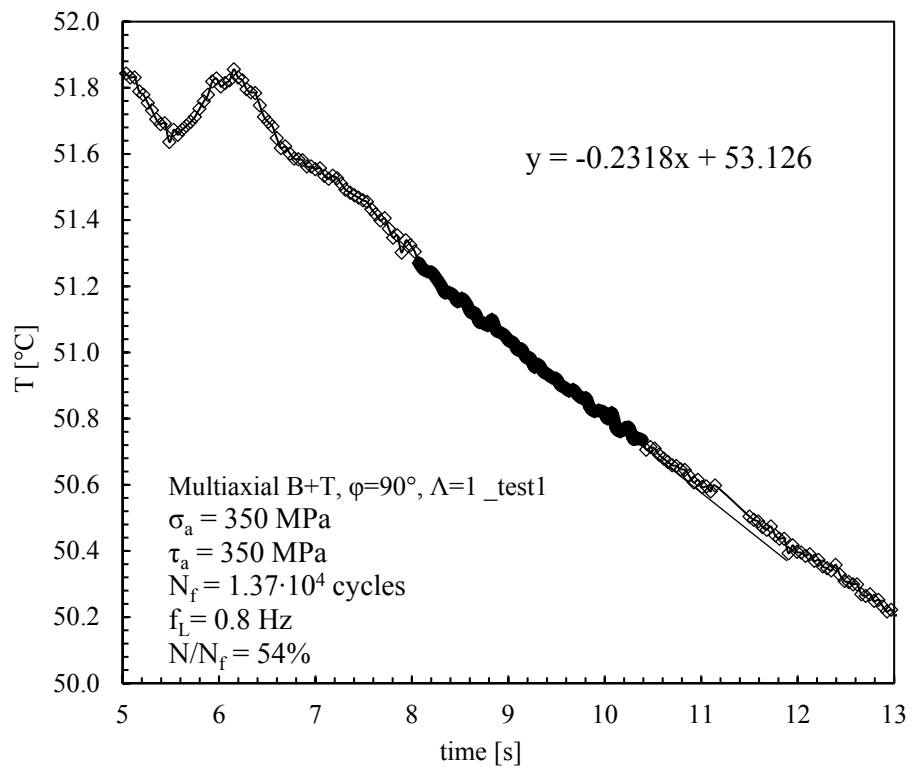


Figure 4.32: Example of cooling gradient measured in B+T, $\varphi=90^{\circ}$, $\Lambda=1$ fatigue test and relevant Q evolution.

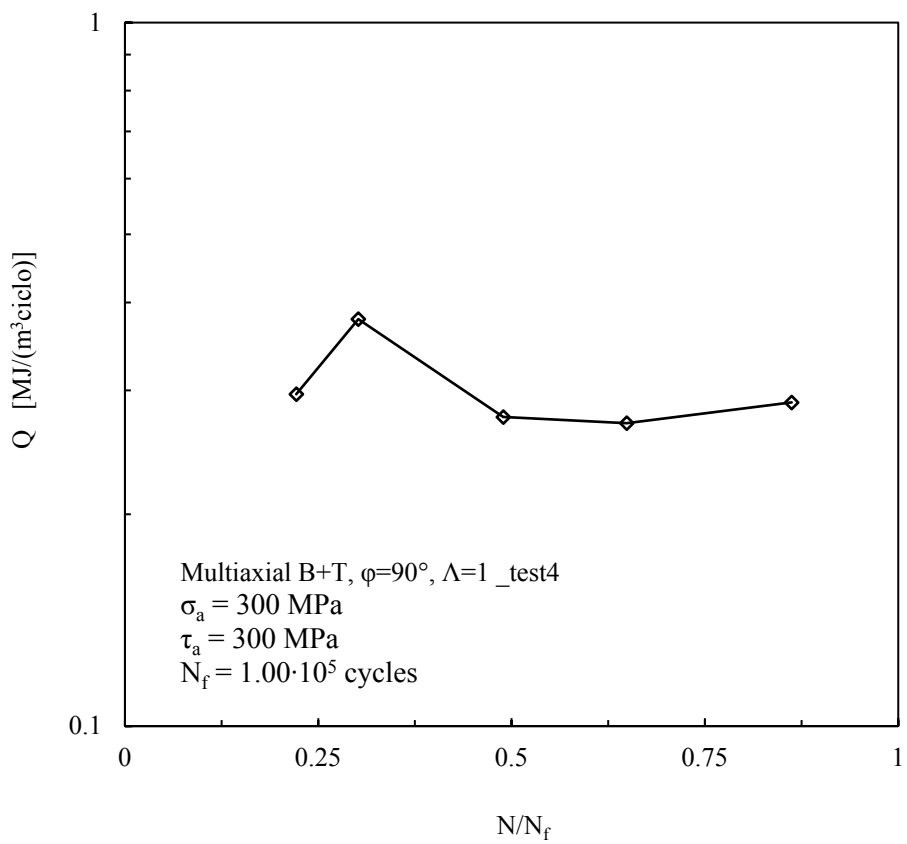
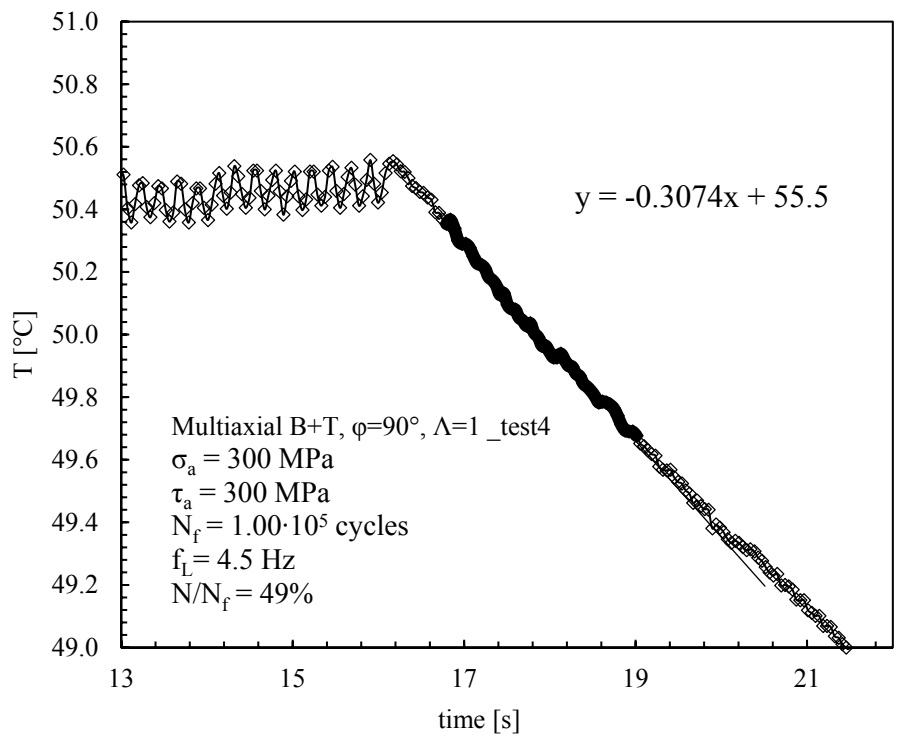


Figure 4.33: Example of cooling gradient measured in B+T, $\varphi=90^{\circ}$, $\Lambda=1$ fatigue test and relevant Q evolution.

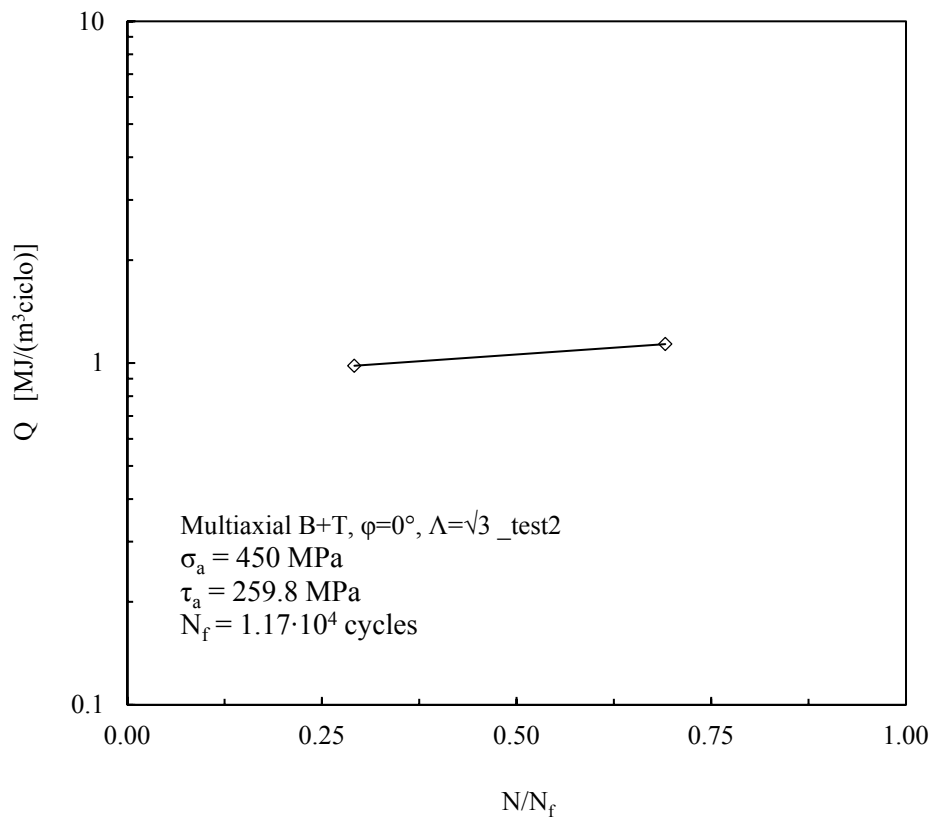
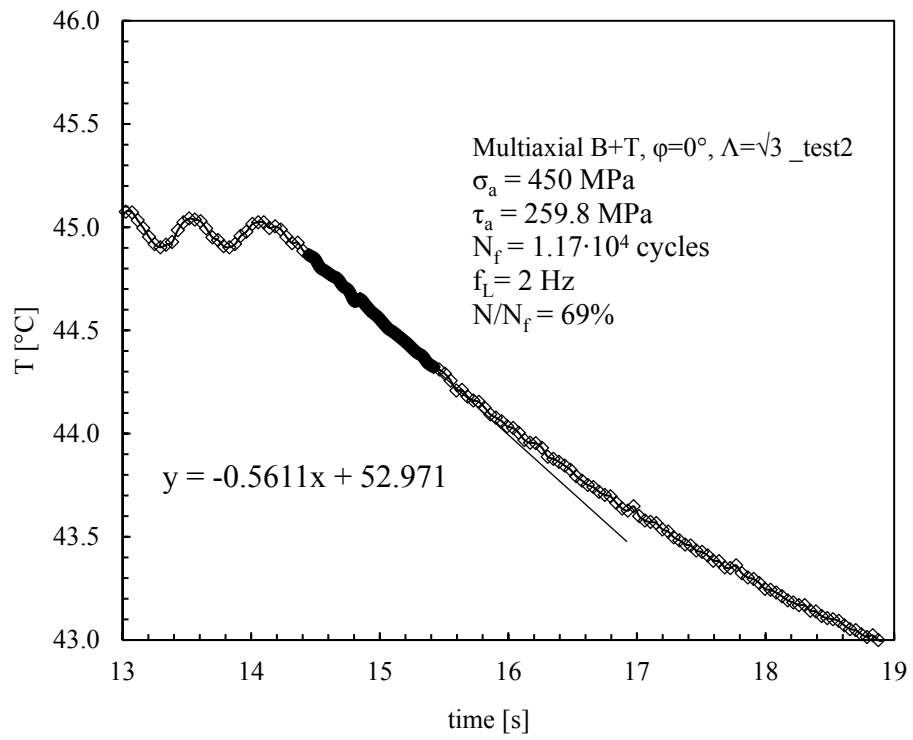


Figure 4.34: Example of cooling gradient measured in B+T, $\varphi=0^\circ$, $\Lambda=\sqrt{3}$ fatigue test and relevant Q evolution.

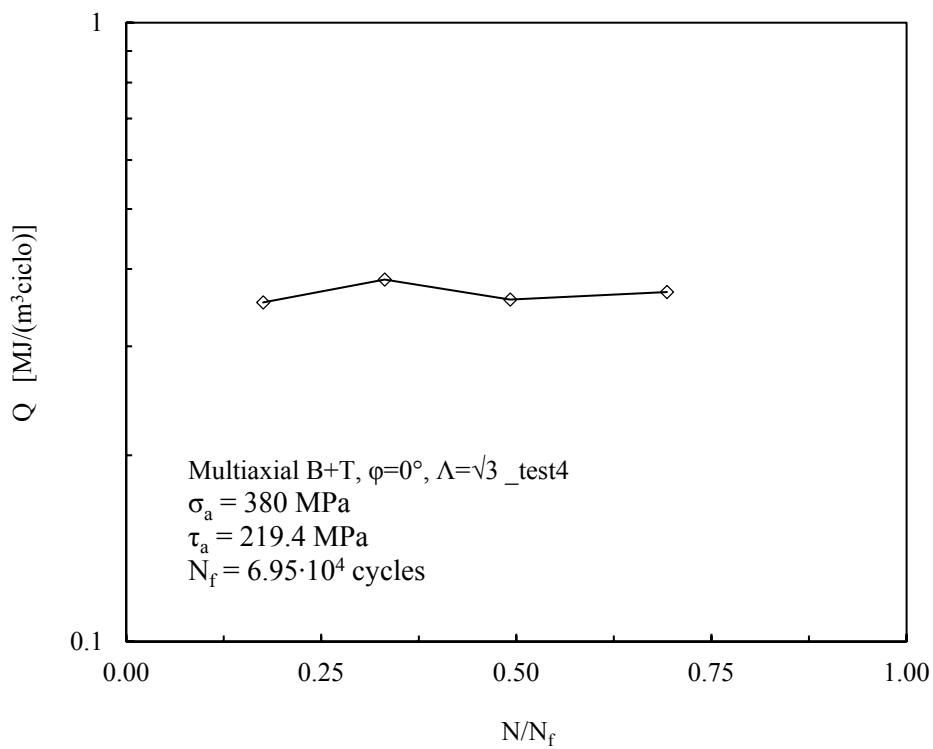
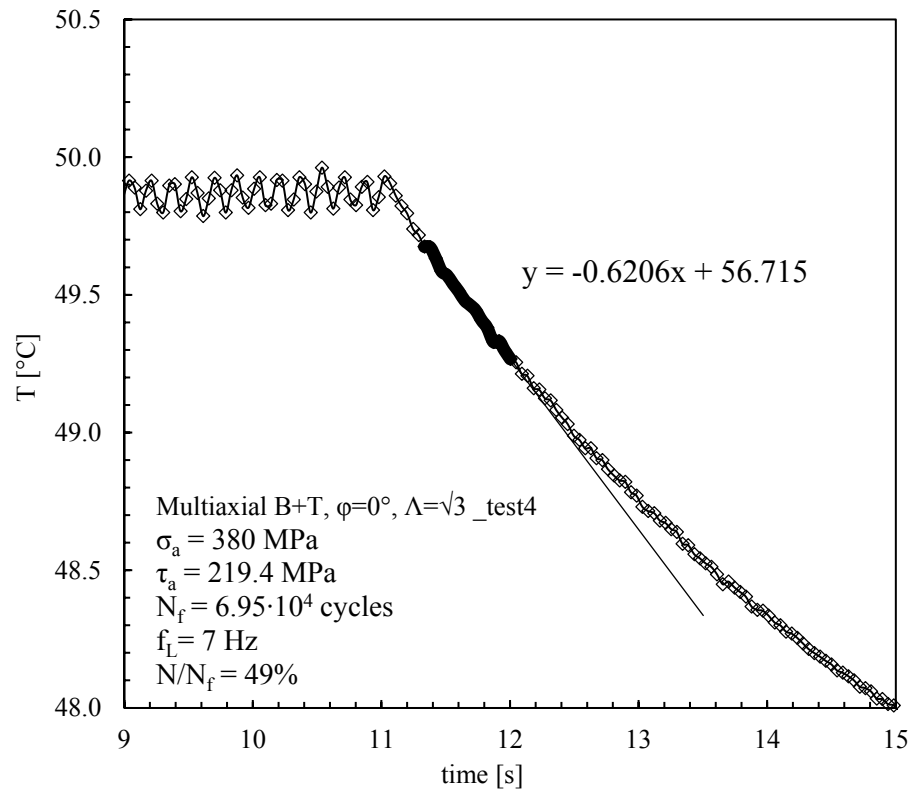


Figure 4.35: Example of cooling gradient measured in B+T, $\varphi=0^{\circ}$, $\Lambda=\sqrt{3}$ fatigue test and relevant Q evolution.

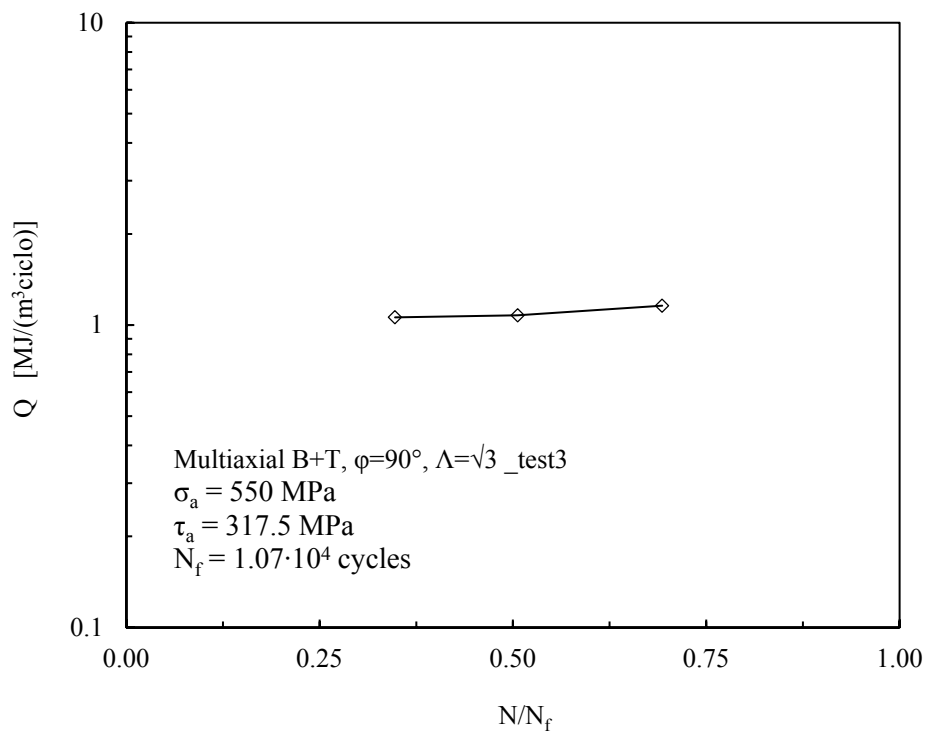
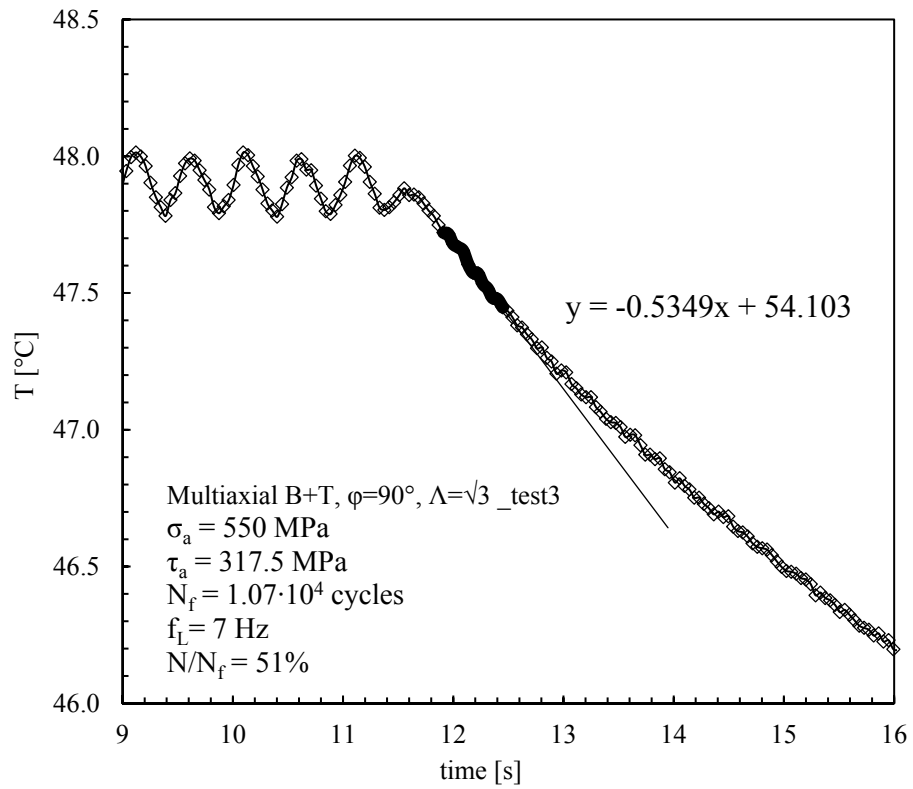


Figure 4.36 Example of cooling gradient measured in B+T, $\varphi=90^{\circ}$, $\Lambda=\sqrt{3}$ fatigue test and relevant Q evolution.

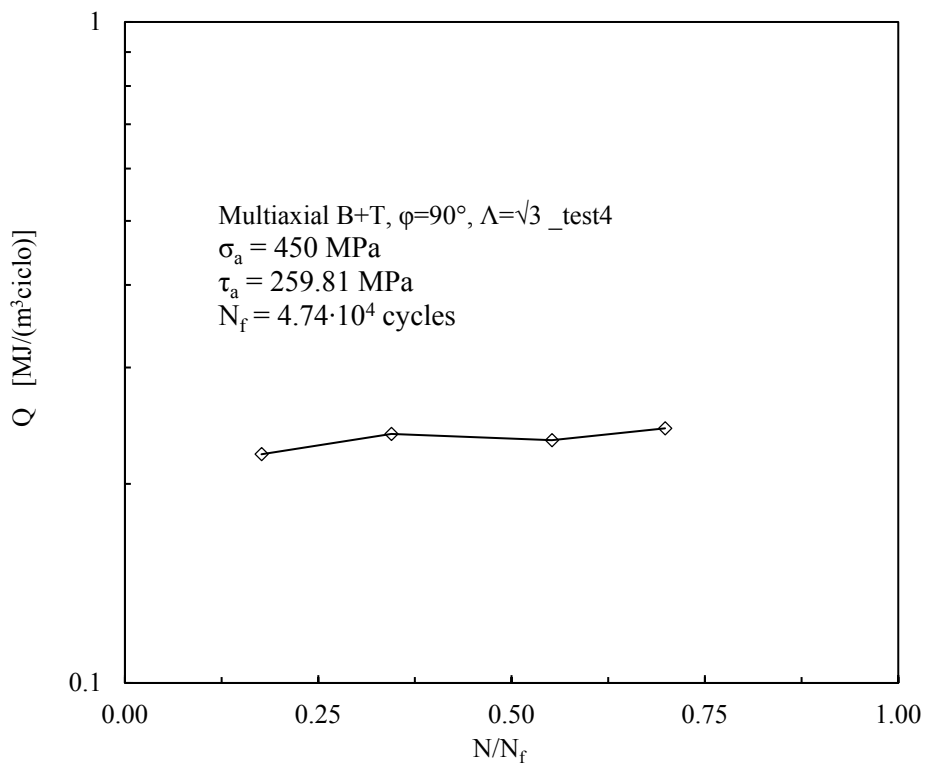
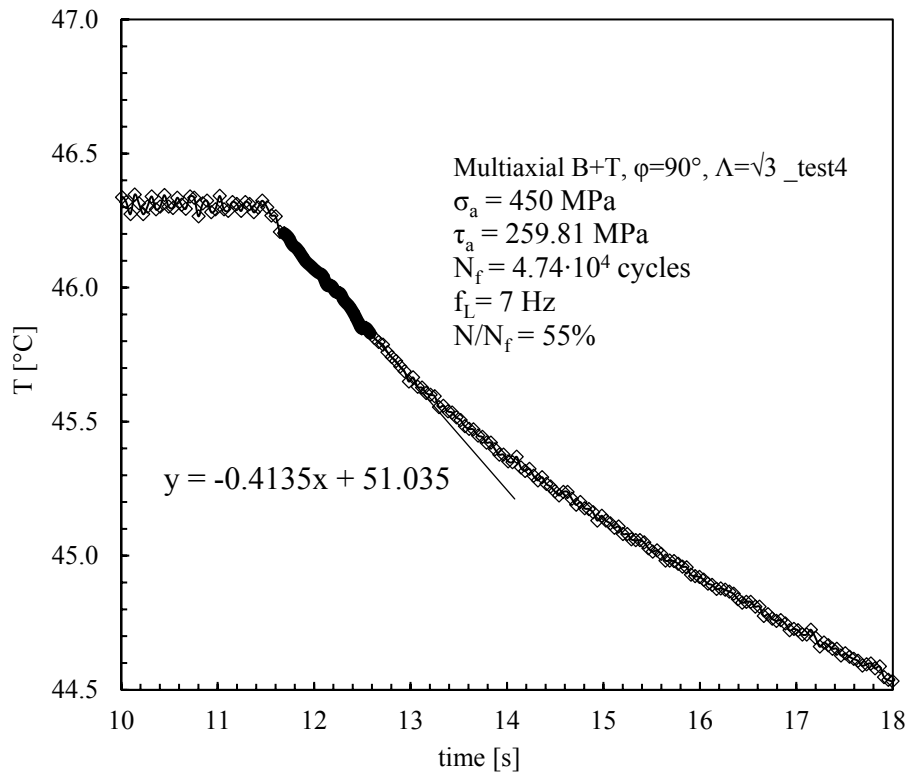


Figure 4.37: Example of cooling gradient measured in B+T, $\phi=90^\circ$, $\Lambda=\sqrt{3}$ fatigue test and relevant Q evolution.

Looking at the Q evolution in Figs (20-31) it can be stated that Q is approximately constant during the fatigue test except for the results relevant to pure torsion (Figs (22, 23)) in which the Q value stabilizes approximately after one third of the total fatigue life of the specimens. Since Q is an indicator of plastic strain energy density dissipated in a cycle, this evolution of Q suggests a different cyclic behaviour between bending and torsional loads.

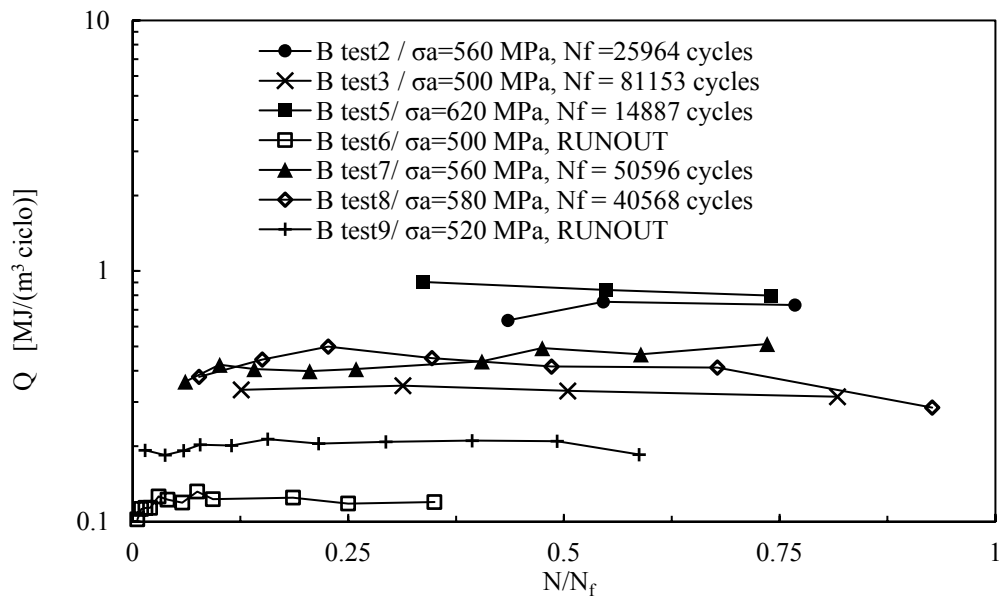


Figure 4.38: Synthesis of Q evolutions during plane bending fatigue tests.

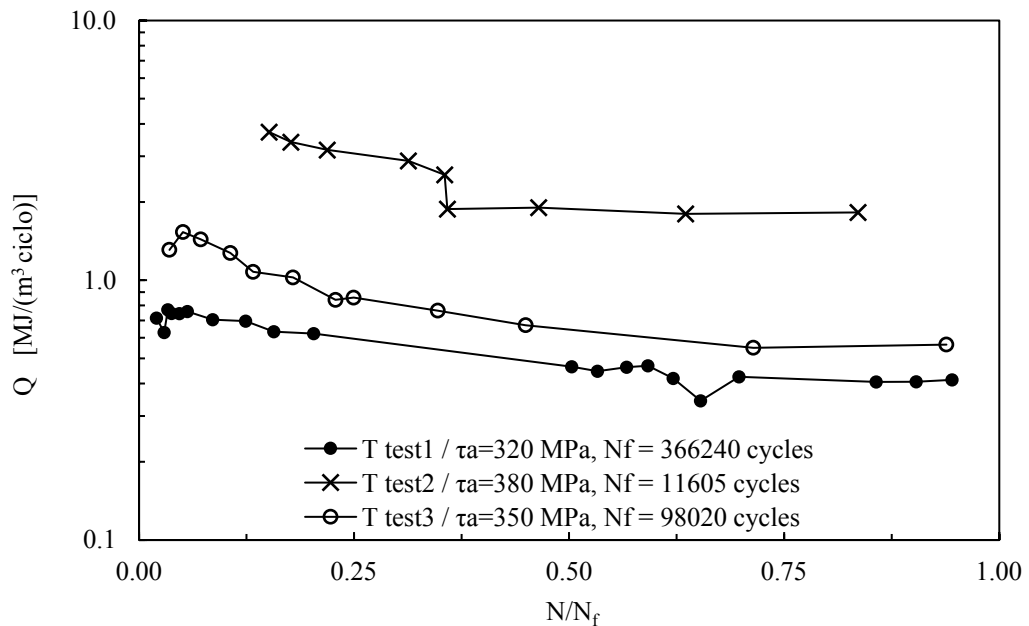


Figure 4.39: Synthesis of Q evolutions during pure torsional fatigue tests.

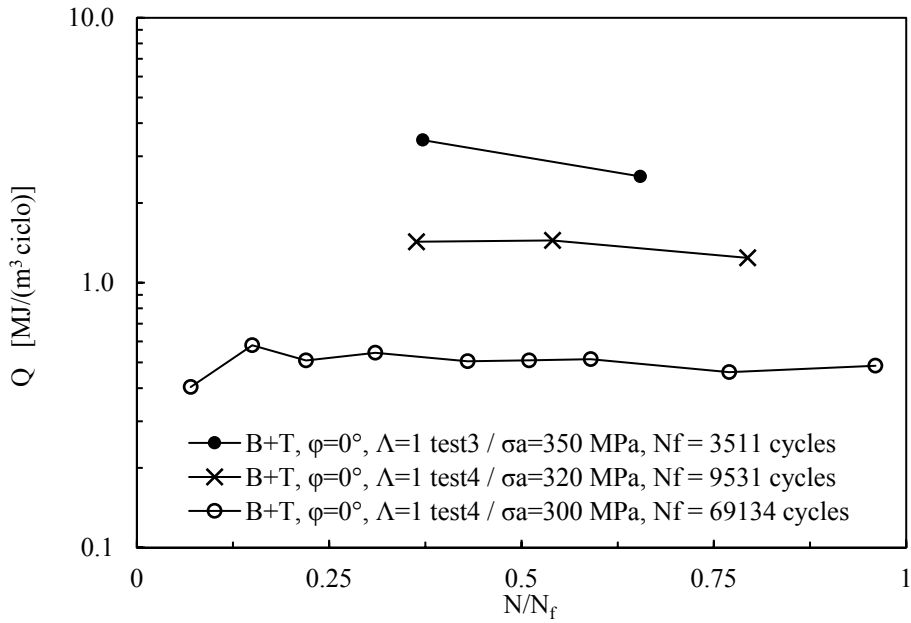


Figure 4.40: Synthesis of Q evolutions during combined bending and torsional fatigue test with $\varphi=0^\circ$ and $\Lambda=1$.

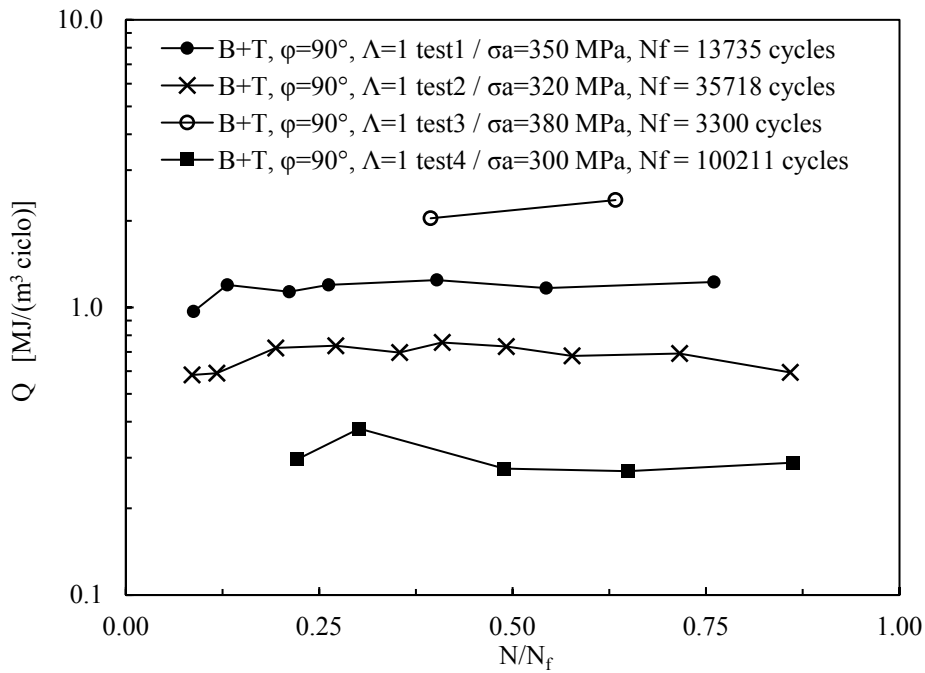


Figure 4.41: Synthesis of Q evolutions during combined bending and torsional fatigue test with $\varphi=90^\circ$ and $\Lambda=1$.

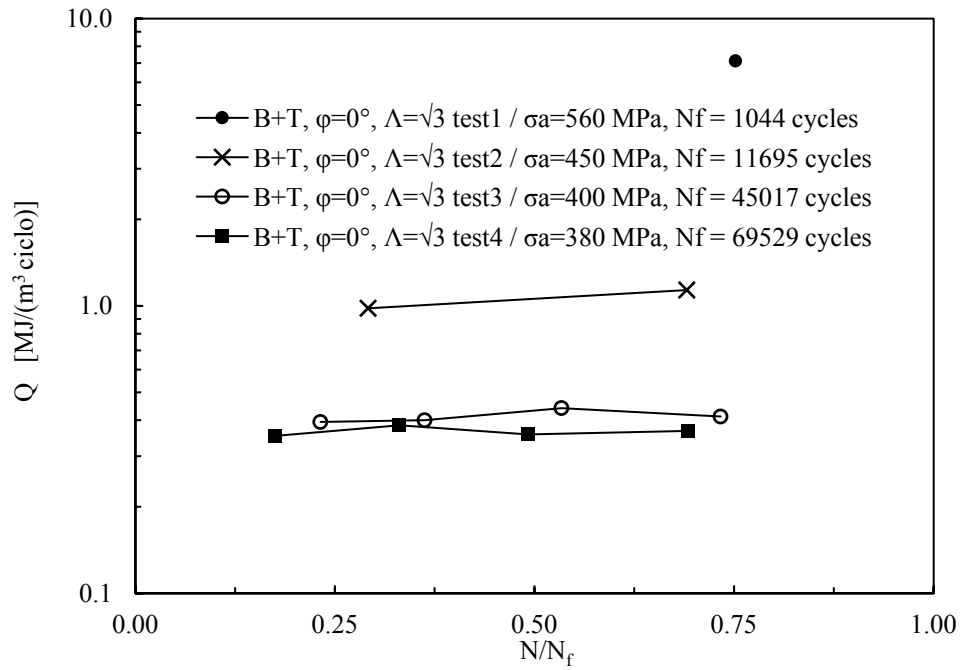


Figure 4.42: Synthesis of Q evolutions during combined bending and torsional fatigue test with $\varphi=0^\circ$ and $\Lambda=\sqrt{3}$

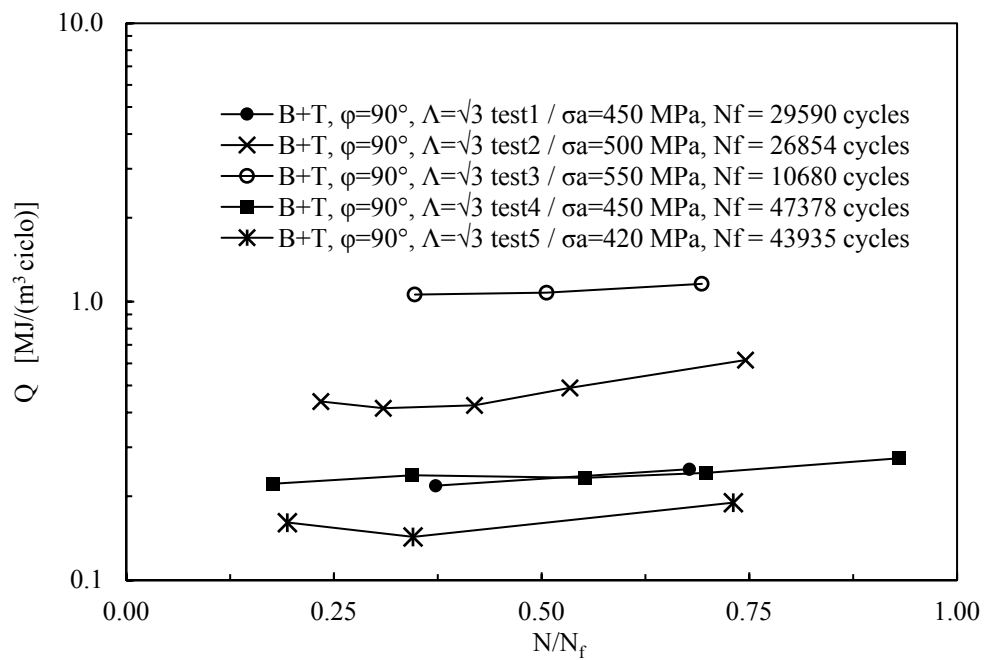


Figure 4.43: Synthesis of Q evolutions during combined bending and torsional fatigue test with $\varphi=90^\circ$ and $\Lambda=\sqrt{3}$

The overall results of the evolution of Q during fatigue tests for each loading condition considered in the present works were reported in Fig.s (38-43).

In agreement with the evaluation of the specific heat loss per cycle carried out in [8], the Q obtained at 50% of total fatigue life was chosen as a representative value for the relevant fatigue test.

4.5.3 Synthesis of multiaxial fatigue test results in terms of Q

In Fig. (44) all the fatigue test results have been expressed in terms of specific heat loss evaluated at half the total fatigue life and compared to the existing heat energy-based scatter band calibrated previously [8]. Concerning the LCF regime, it can be noted that all the Q -based fatigue results of the type (A) specimens are in good agreement with the uniaxial scatter band. As to the HCF regime, it can be observed that the existing scatter band correlates only uniaxial, torsional and in-phase multiaxial fatigue tests with $\Lambda=1$. Conversely, in-phase multiaxial fatigue results with $\Lambda = \sqrt{3}$ as well as out-of-phase multiaxial data with $\Lambda = 1$ fall outside the scatter band in the non-conservative side.

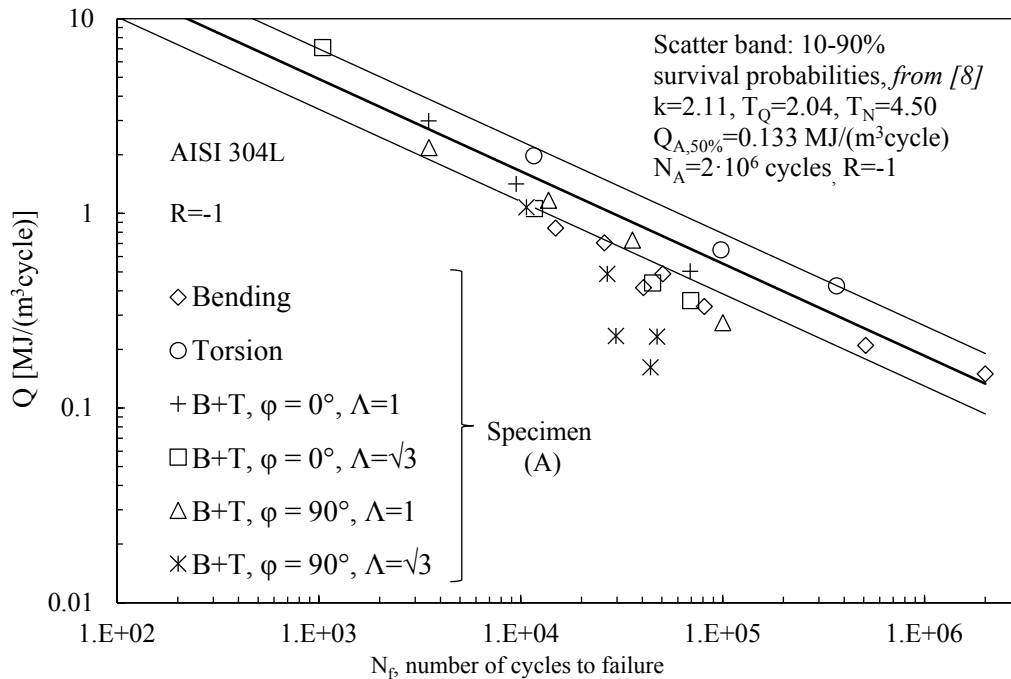


Figure 4.44: Synthesis of fatigue test results in terms of Q , compared to the scatter band calibrated in [8]

As mentioned in Paragraph 4.4, additional few uniaxial and multiaxial fatigue tests were carried out on thin-walled tubular AISI 304L stainless steel specimens (Fig. 3b) for comparison purposes.

The temperature averaged in a rectangular area at the net cross-section of the specimen for each frame was adopted for applying the methodology for evaluating Q . The infrared image at the time t^* (see fig. (1b)) for each loadings condition are shown in Fig. (45).

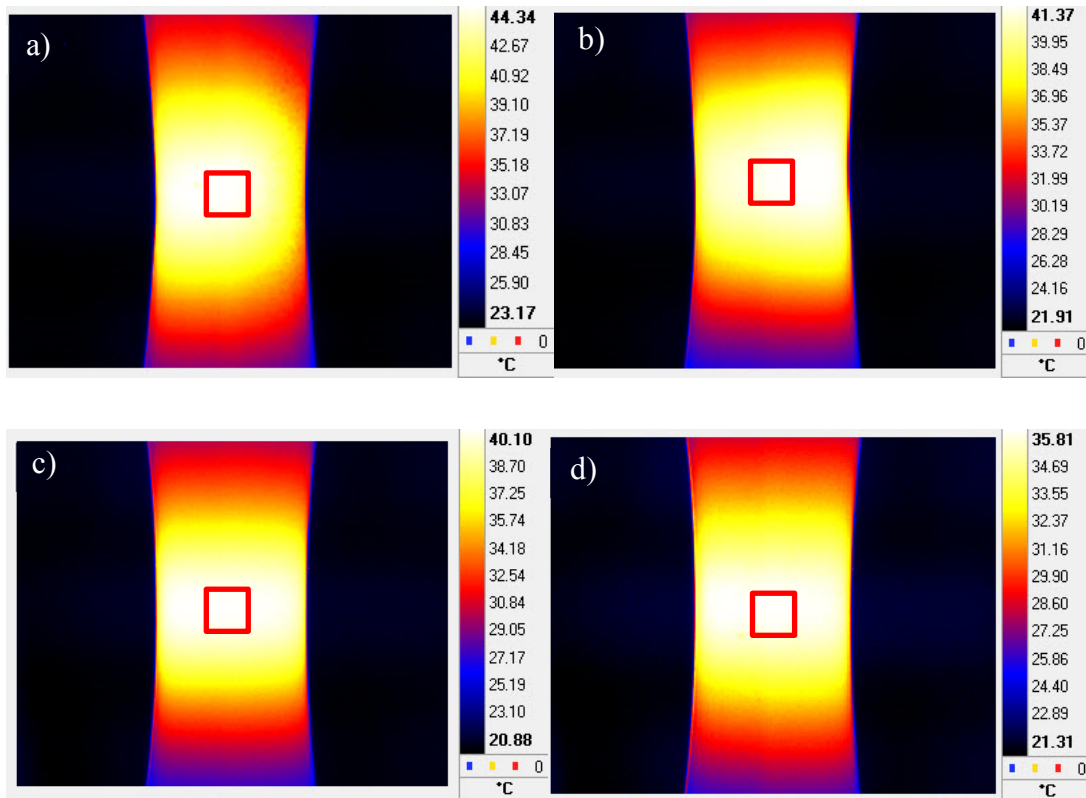


Figure 4.45: Infrared images at time t^* (see Fig. (1b)) for uniaxial (a), torsional (b), multi-axial $\Lambda = \sqrt{3}$ in-phase (c) and out of phase (d) loading conditions on type B specimens. The temperature value was averaged within the red rectangular area for each frame.

As done in the previous section, Figs (46) –(49) show the evaluation of the cooling gradients after a test stop. The uncommon cooling gradient of Fig. (49) is due to the response of the machine after triggering the stop button. This behaviour was observed only in the out of phase multi-axial fatigue test (axial +torsional).

Fig (50) shows the evolution of Q during each fatigue test carried out on type B specimens. As observed in the results obtained for type A specimens the Q value is approximately constant after one third of the total fatigue life.

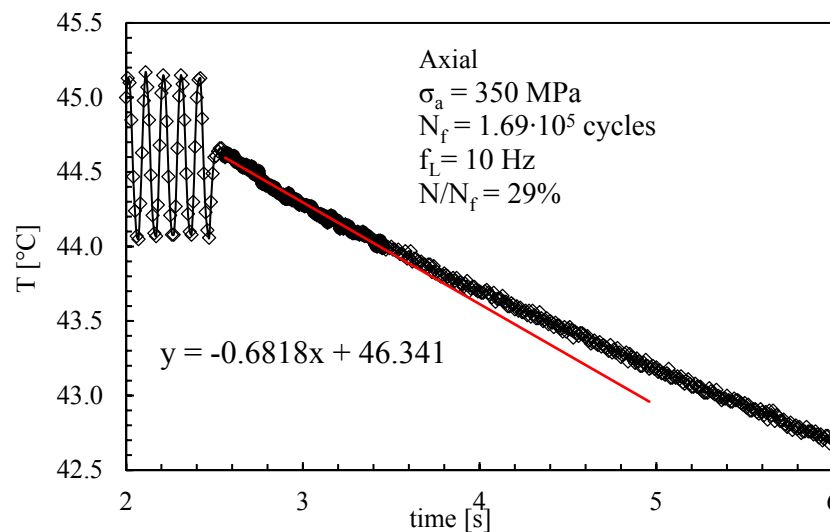


Figure 4.46: Example of cooling gradient measured in uniaxial fatigue test (specimen B)

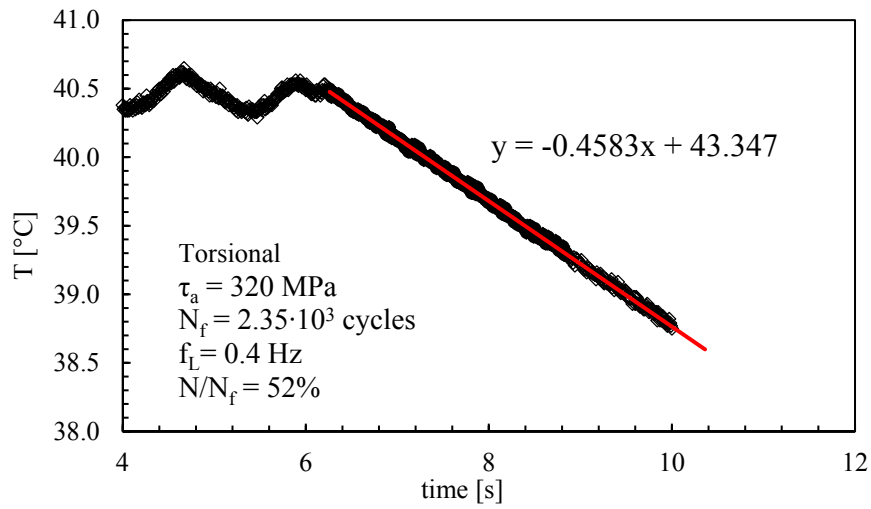


Figure 4.47: Example of cooling gradient measured in pure torsional fatigue test (specimen B)

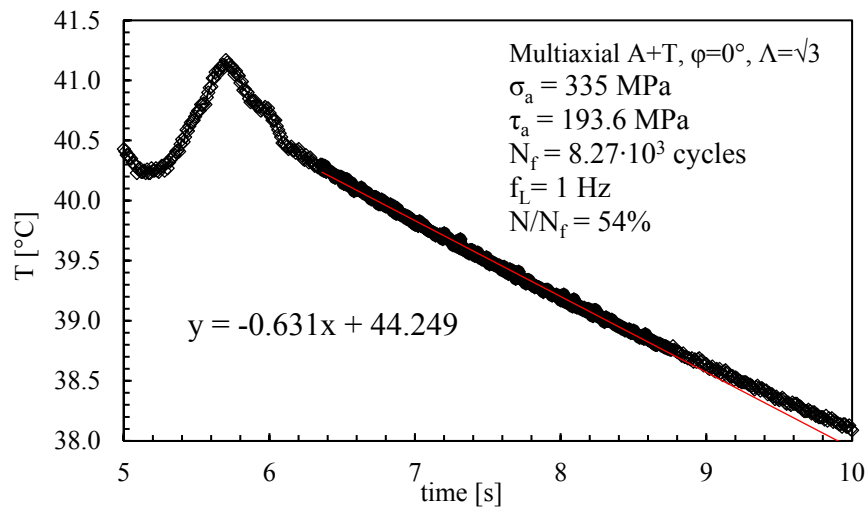


Figure 4.48: Example of cooling gradient measured in A+T, $\varphi=0^\circ$, $\Lambda=\sqrt{3}$ fatigue test (specimen B)

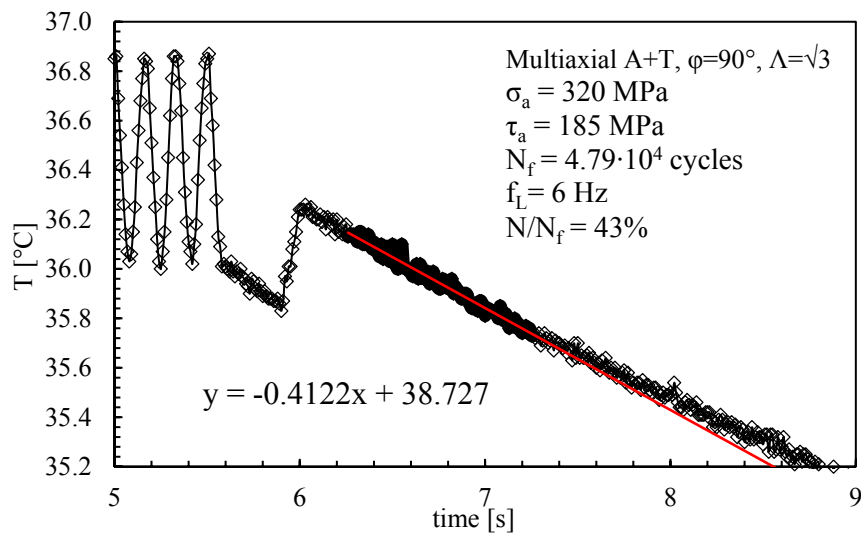


Figure 4.49: Example of cooling gradient measured in A+T, $\varphi=90^\circ$, $\Lambda=\sqrt{3}$ fatigue test (specimen B)

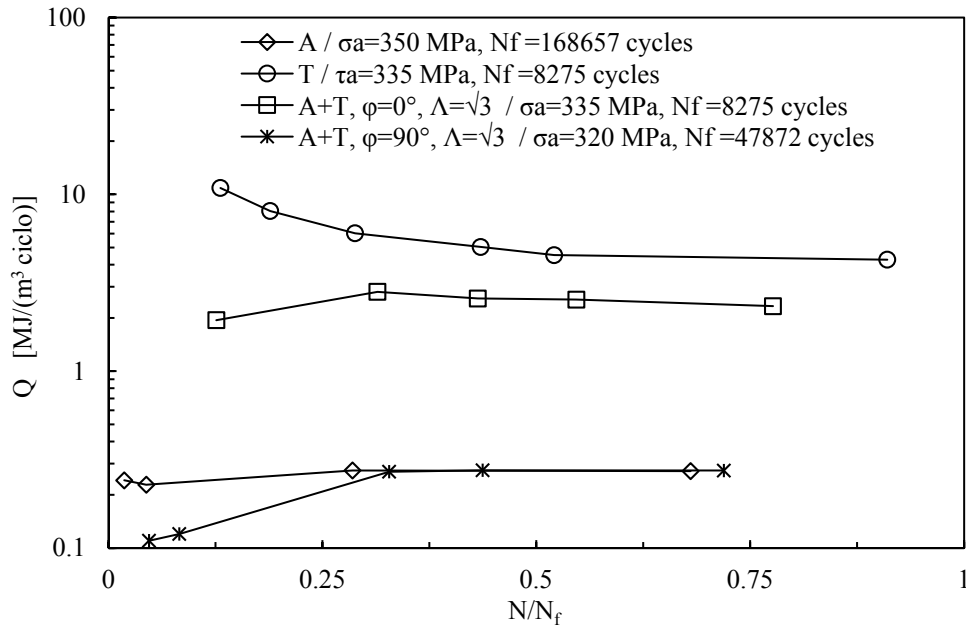


Figure 4.50: Evolution of Q during uniaxial and multiaxial fatigue test on type B specimens

Taking the Q value obtained at 50% of the fatigue life of the specimens, the results relevant to the type B specimens were compared to those relevant to type A in Fig. (51). As it can be seen, the red data (specimen B) confirm the results obtained on specimen A.

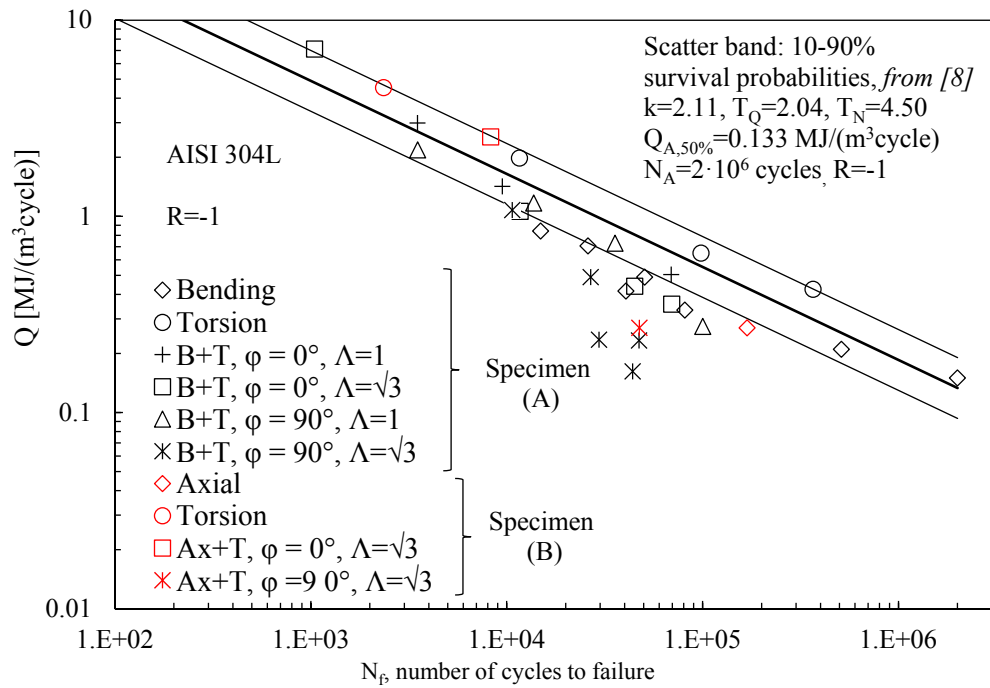


Figure 4.51: Comparison between the results obtained on specimen A and specimen B expressed in terms of Q

Finally, this preliminary study shows that the Q parameter seems to be influenced by the biaxiality ratio Λ and by the phase shift angle φ .

A possible interpretation of the unconservative value of Q related to out of phase loadings, in particular with $\Lambda=\sqrt{3}$, can be deduced from the sensitivity of metastable austenitic stainless steel to exhibit strain-induced martensitic transformation.

Basically, in certain temperatures and loading condition the face-centered γ -austenite transforms to body-centered α' -martensite which modifies significantly the mechanical properties due to its enhanced strength [15,16]. Furthermore, this is an exothermic transformation in which the relevant latent heat can alter the evaluation of Q [17]. Regarding uniaxial cyclic loading martensitic transformation has been demonstrated that depends on the cumulative plastic strain [18,19], strain amplitude [19–24] as well as strain rate [15].

Regarding multiaxial cyclic loading conditions, the cyclic behaviour of stainless steel varies with the grade of proportionality of the loads. In particular, the largest hardening can be obtained in 90° out of phase loading path due to the so-called non-proportional additional hardening. Such behaviour is due to the rotation of maximum shear stress plane which increases the number of activate slip systems, dislocation substructures and mechanical twins [25]. In addition, high value of non-proportionality of the loads leads to finer and more uniformly distributed α' -martensite than to the proportional loading cases.

Supported by the previous literature analysis, the non-proportional Q value could be affected by the α' -martensite transformation. Dedicated multiaxial fatigue tests should be carried out monitoring the growth rate of martensitic content by adopting, for instance, a magnetic induction measuring method [26].

4.6 CONCLUSIONS

In this work, the specific heat loss per cycle (Q parameter) was experimentally evaluated for the first time on cold drawn AISI 304L specimens subjected to multiaxial cyclic loads. A flexible fatigue test bench, consisting of two servo-hydraulic actuators, was adopted for carrying out force-controlled, completely reversed pure bending, pure torsion and combined bending-torsion fatigue tests (specimen's geometry A). Regarding the multiaxial fatigue tests, two phase-shift angles ($\varphi = 0^\circ/ 90^\circ$) and two different biaxiality ratios ($\Lambda=1$ and $\Lambda = \sqrt{3}$) were analysed. For comparison purposes, force-controlled axial, torsional and combined axial-torsional ($\varphi = 0^\circ/ 90^\circ$, $\Lambda = \sqrt{3}$) completely reversed fatigue tests were also carried out on thin-walled specimens (specimen B).

The long-term temperature acquisitions on specimens A showed that higher load frequency was needed in uniaxial cyclic tests with respect to the pure torsional tests for obtaining the same stabilised temperature value for the same environment testing condition.

The damage evolution of some fatigue test (i.e. the crack nucleation and propagation) was monitored adopting the Direct Current Potential Drop (DCPD). The ratio between the electrical potentials measured on the loaded and unloaded specimen presented an uncommon level noise. In fatigue crack growth testing, as well as in fatigue of notched component, the DCPD provides a better signal because of the possibility of soldering the potential probes close to crack without influencing the stress field, while it is not possible in fatigue testing of plain materials. Therefore, the noise of the potential ratio was due to the weak connection between the potential probes and the base material by adopting a silver loaded conductive epoxy glue. From these signals, an approximate definition of crack initiation was defined for evaluating the fraction of total fatigue life expended to initiate a crack. As result, the crack initiation occurs approximately at 80% or higher fraction of total fatigue life. Despite of the approximated definition of N_{in} , by an engineering point of view, the fatigue life expended to initiate the failure seems to be not affected by the loading condition as well as N_{in} seems to be assumed at N_f .

The crack paths at failure were analysed by using a digital microscope and they were oriented to the maximum shear strain plane for all the loading conditions here considered.

After having measured the specific heat loss during individual fatigue tests, it was noted that after approximately one third of the total fatigue life the Q parameter achieves a stationary value, which remains constant during the residual fatigue life. This has been observed both in the uniaxial and multiaxial fatigue tests performed in this contribution.

All fatigue test results have been summarised in terms of specific heat loss taken at half the total fatigue life versus the number of cycles to failure and have been compared with the scatter band previously calibrated on push-pull, uniaxial fatigue tests on plain and notched AISI 304L specimens. As expected, pure bending, axial and torsional fatigue data resulted in good agreement with the existing scatter band. In the LCF regime, a good agreement with the scatter band was found for all multiaxial fatigue results obtained from the type (A) specimens. The same cannot be generalized for the type (B) specimens due to the limited data available up to now. Conversely, fatigue results obtained from out-of-phase multiaxial loading conditions with $\Lambda=1$ and $\sqrt{3}$ as well as in-phase multiaxial with $\Lambda= \sqrt{3}$ fall below the previously calibrated scatter band. The present results suggest that for the present material the specific heat loss per cycle can be adopted for multiaxial stress states in the LCF regimes. Analysing the literature, the unconservative results obtained in this contribution seems to be justified by the strain-induced martensitic transformation, significantly present in out of phase cyclic loading condition.

4.7 REFERENCES

ADDIN Mendeley Bibliography CSL_BIBLIOGRAPHY [1] Rigon D,

- Formilan V, Meneghetti G. Analysis of the energy dissipation in multiaxial fatigue tests of AISI 304L stainless steel bars. *Procedia Struct Integr* 2018;13:1638–43. doi:10.1016/j.prostr.2018.12.344.
- [2] Ellyin F. *Fatigue damage, crack growth, and life prediction*. Chapman & Hall; 1997.
- [3] Lazzarin P, Sonsino CM, Zambardi R. A notch stress intensity approach to assess the multiaxial fatigue strength of welded tube-to-flange joints subjected to combined loadings. *Fatigue Fract Eng Mater Struct* 2004;27:127–40. doi:10.1111/j.1460-2695.2004.00733.x.
- [4] Atzori B, Berto F, Lazzarin P, Quaresimin M. Multi-axial fatigue behaviour of a severely notched carbon steel. *Int J Fatigue* 2006;28:485–93. doi:10.1016/j.ijfatigue.2005.05.010.
- [5] Lazzarin P, Livieri P, Berto F, Zappalorto M. Local strain energy density and fatigue strength of welded joints under uniaxial and multiaxial loading. *Eng Fract Mech* 2008;75:1875–89. doi:10.1016/j.engfracmech.2006.10.019.
- [6] Kaleta J, Blotny R, Harig H. Energy Stored in a Specimen under Fatigue Limit Loading Conditions. *J Test Eval* 1991;19:326–33. doi:10.1520/JTE12577J.
- [7] Meneghetti G. Analysis of the fatigue strength of a stainless steel based on the energy dissipation. *Int J Fatigue* 2007;29:81–94. doi:10.1016/j.ijfatigue.2006.02.043.
- [8] Meneghetti G, Ricotta M, Atzori B. A synthesis of the push-pull fatigue behaviour of plain and notched stainless steel specimens by using the specific heat loss. *Fatigue Fract Eng Mater Struct* 2013;36:1306–22. doi:10.1111/ffe.12071.
- [9] Meneghetti G, Ricotta M. The use of the specific heat loss to analyse the low- and high-cycle fatigue behaviour of plain and notched specimens made of a stainless steel. *Eng Fract Mech* 2012;81:2–16. doi:10.1016/j.engfracmech.2011.06.010.
- [10] Meneghetti G, Ricotta M, Negrisolò L, Atzori B. A Synthesis of the Fatigue Behavior of Stainless Steel Bars under Fully Reversed Axial or Torsion Loading by Using the Specific Heat Loss. *Key Eng Mater* 2013;577–578:453–6. doi:10.4028/www.scientific.net/KEM.577-578.453.
- [11] Meneghetti G, Ricotta M, Atzori B. The Heat Energy Dissipated in a Control Volume to Correlate the Fatigue Strength of Bluntly and Severely Notched Stainless Steel Specimens. *Proc. 21st Eur. Conf. Fract. ECF21*. Catania, Italy, vol. 2, 2016, p. 2076–83. doi:10.1016/j.prostr.2016.06.260.
- [12] Rigon D, Ricotta M, Meneghetti G. An analysis of the specific heat loss at the tip of severely notched stainless steel specimens to correlate the fatigue strength. *Theor Appl Fract Mech* 2017;92:240–51. doi:10.1016/j.tafmec.2017.09.003.
- [13] Ritchie RO. Mechanisms of fatigue crack propagation in metals, ceramics and composites: Role of crack tip shielding. *Mater Sci Eng A* 1988;103:15–28. doi:10.1016/0025-5416(88)90547-2.
- [14] Ritchie RO. Mechanism of Fatigue-Crack Propagation in Ductile and Brittle Materials. *Int J Fract* 1998;100:55–83.
- [15] Pegues JW, Shao S, Shamsaei N, Schneider JA, Moser RD. Cyclic strain rate effect on martensitic transformation and fatigue behaviour of an austenitic stainless steel. *Fatigue Fract Eng Mater Struct* 2017;40:2080–91. doi:10.1111/ffe.12627.
- [16] Yu D, An K, Chen Y, Chen X. Revealing the cyclic hardening mechanism of

- an austenitic stainless steel by real-time in situ neutron diffraction. *Scr Mater* 2014;89:45–8. doi:10.1016/J.SCRIPTAMAT.2014.06.021.
- [17] Bhadeshia HKDH, Wayman CM. Phase Transformations: Nondiffusive. *Phys. Metall. Fifth Ed.*, vol. 1, Elsevier Inc.; 2014, p. 1021–72. doi:10.1016/B978-0-444-53770-6.00009-5.
- [18] Bayerlein M, Christ H-J, Mughrabi H. Plasticity-induced martensitic transformation during cyclic deformation of AISI 304L stainless steel. *Mater Sci Eng A* 1989;114:L11–6. doi:10.1016/0921-5093(89)90871-X.
- [19] Ye D, Xu Y, Xiao L, Cha H. Effects of low-cycle fatigue on static mechanical properties, microstructures and fracture behavior of 304 stainless steel. *Mater Sci Eng A* 2010;527:4092–102. doi:10.1016/J.MSEA.2010.03.027.
- [20] Dey R, Tarafder S, Sivaprasad S. Influence of phase transformation due to temperature on cyclic plastic deformation in 304LN stainless steel. *Int J Fatigue* 2016;90:148–57. doi:10.1016/J.IJFATIGUE.2016.04.030.
- [21] Zeng W, Yuan H. Mechanical behavior and fatigue performance of austenitic stainless steel under consideration of martensitic phase transformation. *Mater Sci Eng A* 2017;679:249–57. doi:10.1016/J.MSEA.2016.10.005.
- [22] Smaga M, Walther F, Eifler D. Deformation-induced martensitic transformation in metastable austenitic steels. *Mater Sci Eng A* 2008;483–484:394–7. doi:10.1016/J.MSEA.2006.09.140.
- [23] Das A. Dislocation configurations through austenite grain misorientations. *Int J Fatigue* 2015;70:473–9. doi:10.1016/J.IJFATIGUE.2014.06.012.
- [24] Das A, Sivaprasad S, Chakraborti PC, Tarafder S. Morphologies and characteristics of deformation induced martensite during low cycle fatigue behaviour of austenitic stainless steel. *Mater Sci Eng A* 2011;528:7909–14. doi:10.1016/J.MSEA.2011.07.011.
- [25] McDowell DL, Stahl OK, Stock SR, Antolovich SD. Biaxial path dependence of deformation substructure of type 304 stainless steel. *Metall Trans A* 1988;19:1277–93. doi:10.1007/BF02662589.
- [26] Talonen J, Aspegren P, Hänninen H. Comparison of different methods for measuring strain induced α -martensite content in austenitic steels. *Mater Sci Technol* 2004;20:1506–12. doi:10.1179/026708304X4367.

Chapter 5: Analysis of the energy dissipation on thin-walled tubular C45 steel specimens subjected to multiaxial loading

In this chapter, Q was evaluated on thin-walled C45 quenched and tempered steel specimens subjected to different multiaxial cyclic loading conditions. The testing protocol includes the analysis of in-phase ($\varphi = 0^\circ$) as well as out-phase ($\varphi = 90^\circ$) loading conditions adopting two different biaxiality ratios ($\Lambda=1$ and $\Lambda=\sqrt{3}$).

In each fatigue test, 2 to 15 Q measurements were performed by using a TELOPS TS-IR MW infrared camera and the representative values of the test were taken at a fraction of total fatigue life equal to 50%. Furthermore, the plastic strain hysteresis energy density per cycle (ΔW) was also measured in some test to compare it with the relevant measured values of Q for the first time. The strain measurements were carried out by means of a Digital Image Correlation (DIC) system synchronized with the load cells of the fatigue test machine. As a result, the experimental results expressed in terms of Q are in excellent agreement with the scatter band calibrated in a previous paper on constant amplitude, axial fatigue test results ($R = -1$) carried out on the same material.

All this work was performed by the author at the Department of Mechanical and Industrial Engineering of the Norwegian University of Science and Technology NTNU (Trondheim, Norway) in collaboration with Prof. Filippo Berto.

5.1 INTRODUCTION

In Chapter 4, the specific heat loss Q was measured for the first time on AISI 304L stainless steel specimens subjected to multiaxial fatigue loadings [1]. A good agreement in LCF regime was found between multiaxial fatigue test results expressed in terms of Q with the scatter band calibrated for plain and notched stainless-steel specimens subjected to uniaxial loading [2] (see Fig. (1)). On the contrary, the data obtained from out-of-phase multiaxial cyclic loads characterized by a biaxiality ratio equal to $\sqrt{3}$ were unconservative with respect to the theoretical prediction. A possible reason of these results can be attributed to the sensitivity of metastable austenitic stainless steel to exhibit strain-induced martensitic transformation especially in cyclic out-of-phase loading conditions as well as to the proportional cyclic hardening effect as discussed in the subparagraph 4.5.3 [3–12].

The aim of the work described in this chapter is to analyse the specific heat loss per cycle in a quenched and tempered medium carbon steel, which is not subjected to remarkable phase transformation during cyclic loading like the metastable austenitic stainless steels. Therefore, in this work, the specific heat loss per cycle was measured on quenched and tempered C45 steel specimens subjected to combined axial and torsional cyclic loads both in-phase ($\varphi = 0^\circ$) and out-of-phase ($\varphi = 90^\circ$) conditions. Also, two different biaxiality ratios ($\Lambda = \sigma_a/\tau_a = 1$ and $\Lambda = \sqrt{3}$) were analysed.

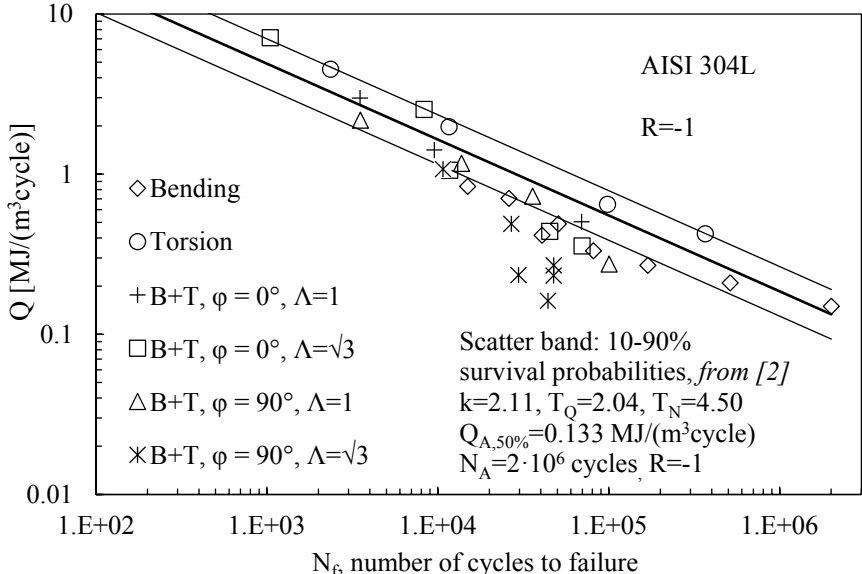


Figure 5.1: Qualitative representation of temperature evolution during a fatigue test and evaluation of the cooling gradient immediately after a test stop (a).

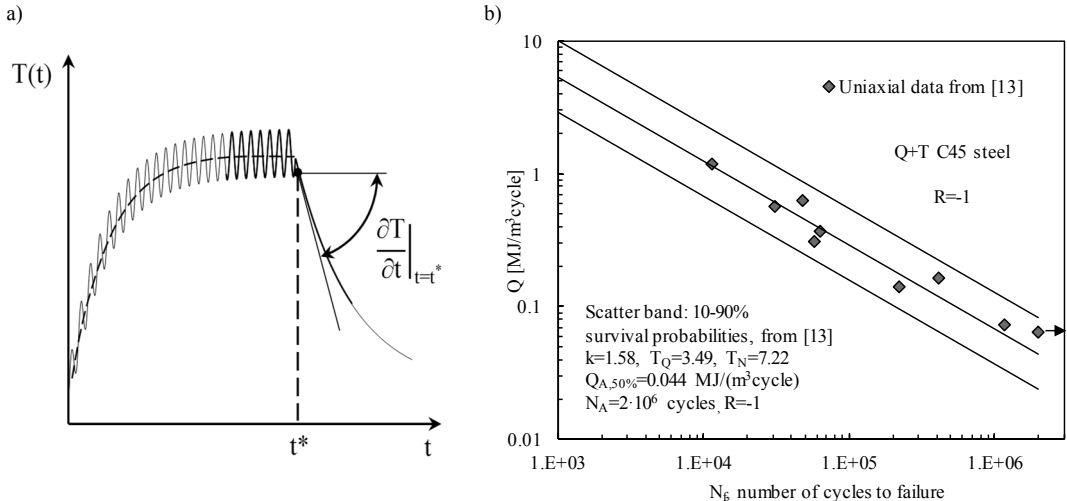


Figure 5.2: Qualitative representation of temperature evolution during a fatigue test and evaluation of the cooling gradient immediately after a test stop (a). Energy-based scatter band calibrated in [13] (b).

The cooling gradient, which occurs after having stopped the test machine, was measured several times during each fatigue test by using an Infrared Camera (IR). Then the specific heat loss per cycle was evaluated by means of Eq. (1):

$$Q = \frac{\rho \cdot c \cdot \partial T / \partial t}{f_L} \quad (1)$$

where ρ is the material density, c is the material specific heat and f_L is the load test frequency and $\partial T / \partial t$ is the initial cooling gradient after having suddenly interrupted the fatigue test at the time t^* (see Fig. (2a)).

Then, the fatigue test results expressed in terms of Q was compared to the energy-based scatter band calibrated in eight axial fatigue test in a recent paper [13] (see Fig. (2b)).

Furthermore, during some LFC fatigue test the strain energy density dissipated in a cycle (ΔW) was evaluated and compared with the relevant Q value in order to determine the fraction of the mechanical input energy is dissipated as heat. In particular, the strain components were measured by using a 3D Digital Image Correlation (DIC) system.

5.2 MATERIALS AND METHODS

The material under investigation is a 25-mm bar of quenched and tempered medium carbon (C45) steel whose chemical composition and mechanical properties, taken from the datasheet, were reported in Table 1 and 2, respectively. A sample taken from the raw rods was sectioned in both longitudinal and transversal plane in order to analyse the microstructure. Both sections were polished to obtain a mirror-like finishing and etched by using 2% Nital. In Fig. (3) the resulting microstructure shows a ferrite and perlite structure without significant differences between the planes.

Microhardness ($HV_{0.1}$) was evaluated on the transversal section of the rod both 0.5 mm far from the section edge and in the bulk of the material. At the edge, the mean value with one standard deviation range of five measurements resulted being equal to 250 ± 10 , whereas in the bulk was 230 ± 13 .

Thin-Walled tubular specimens characterised by a “hourglass”-shape in the gauge section were machined from the rods according to to the specimens’ geometry reported in Fig. (4)

Table 5.1: Chemical composition of quenched and tempered C45 cold drawn bars from datasheet.

C [wt%]	Si [wt%]	Mn [wt%]	Cr [wt%]	Mo [wt%]	Cu [wt%]	Ni [wt%]	P [wt%]	S [wt%]	Al [wt%]
0.46	0.24	0.63	0.15	0.02	0.1	0.08	0.007	0.004	0.027

Table 5.2: Mechanical properties of quenched and tempered C45 cold drawn bars from data sheet.

$R_{p.02\%}$ [MPa]	UTS [MPa]	A [%]	Z [%]
592	779	21.1	64.7

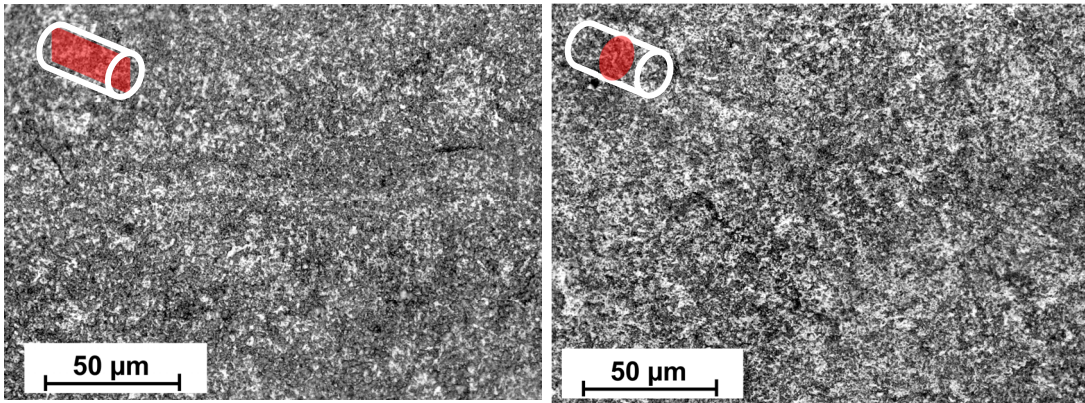


Figure 5.3: Microstructure of quenched and tempered C45 steel in both longitudinal and transversal planes.

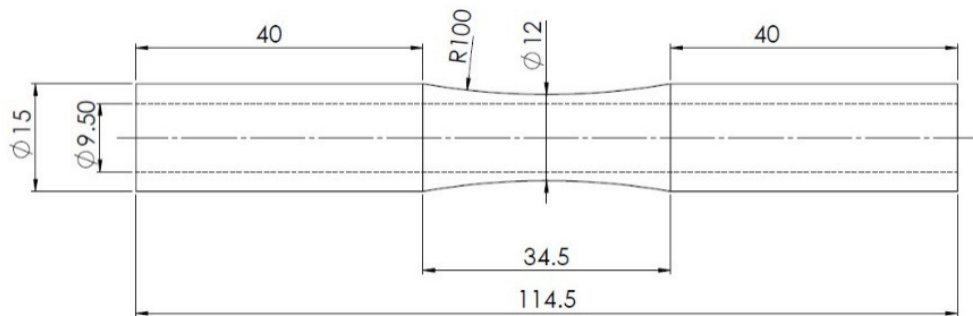


Figure 5.4: Specimen's geometry adopted for multiaxial fatigue testing.

Cylindrical 35 mm long pins having a diameter equal to 9.5 mm were machine and inserted in the gross part of the specimens to avoid deformation due to the clamping system of the testing machine.

The outer and inner surface of the specimens were polished by using progressively finer emery paper starting from grade 400 until grade 1000. The roughness of both surfaces was measured in three longitudinal 5 mm long paths in the gauge part of 4 specimens by using a surface roughness tester Taylor Hobson precision – Surtronic 25. The roughness R_a of the outer and inner surface resulted to be equal to 0.35 ± 0.08 and 0.40 ± 0.06 , respectively.

Constant amplitude, load controlled, multiaxial fatigue tests, with a stress ratio R equal to -1, were performed by using a servo-hydraulic MTS 809 axial/torsional test system controlled by a FlexTest 40 and equipped by load cells having 100 kN of axial load capacity and 2000 N/m of torque capacity. In-phase ($\varphi=0^\circ$) as well as out-of-phase cyclic axial and torsion loads were analysed adopting two different biaxiality ratios ($\Lambda = \sigma_a/\tau_a = 1$ and $\Lambda = \sqrt{3}$). The tests were carried out adopting a load frequency ranging from 5-30 Hz depending on the load level applied and on the level of temperature stabilization which was limited to 55 °C. A 50% stiffness loss was chosen as a failure criterion.

The testing protocol and the here used symbology are reported in Table 3.

Table 5.3: Testing protocol and symbols.

Loading condition	R	$\Lambda = \sigma_a/\tau_a$	φ [°]	Number of tests	
A	-1	∞	\	3	A: uniaxial
T		0	\	4	T: pure torsion
A+T		1	0	8	A+T: combined axial and torsion
A+T		$\sqrt{3}$	0	8	R: stress ratio
A+T		1	90	9	Λ : biaxiality ratio
A+T		$\sqrt{3}$	90	8	φ : phase-shift angle

5.2.1 Infrared camera setup

The surface temperature was measured by means of a TELOPS TS-IR-MW infrared camera, operating at a sample frequency f_{acq} equal to 50 Hz, having a 3-5 μm spectral response range, 25 mm focal lens, a noise equivalent temperature difference (NETD) < 20 mK and an a spatial resolution of 15 $\mu\text{m}/\text{px}$. The acquisition time window was set equal to 10 seconds, in particular, the test stop was performed 5 seconds after triggering the acquisition. The outer surface was covered with matte black paint to uniform and increase its emissivity (see Fig. (5a)). The experimental setup is shown in Fig. (5b).

During each fatigue test, from 2 to 15 rapid load interruptions were performed in order to evaluate the specific heat loss per cycle starting from the measurement of the initial cooling gradient. 250 frames were recorded before the interruption of the load and other 250 frames at zero loads (overall sampling window of 10 seconds). The acquisitions have been set in the full-frame mode (640x512 pixels) framing a portion of the specimen surface as shown in Fig. (6).

The infrared videos were saved on the internal memory of the infrared camera and extracted by using Reveal IR [®] software. Then, the post-processing was carried out by using a Matlab [®] script, properly developed to evaluating the specific heat loss per cycles.

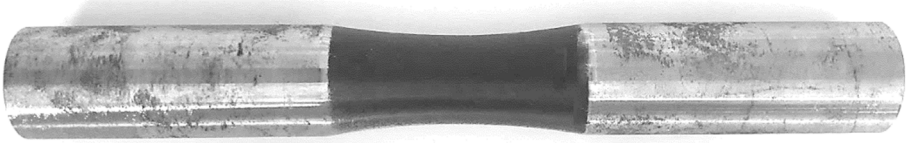
The time-variant temperature profile was generated taking the averaged temperate value within a rectangular area (see Fig (6)) on each frame.

5.2.2 Digital Image Correlation system setup

In one fatigue test per each loading condition, the cyclic strain components were measured by using a Digital Image Correlation (DIC) 3D system synchronised with the load cells of the test machine. The setup consists of two Stingray cameras, equipped by 75-mm lenses and an acquisition unit connected to the cameras and loads cells. A schematic illustration of the setup and a picture of the equipment is shown in Fig (7).

Correlated Solution® SNAP-3D software was used for storing the data, while VIC-3D® was adopted for the post-processing.

a)



b)

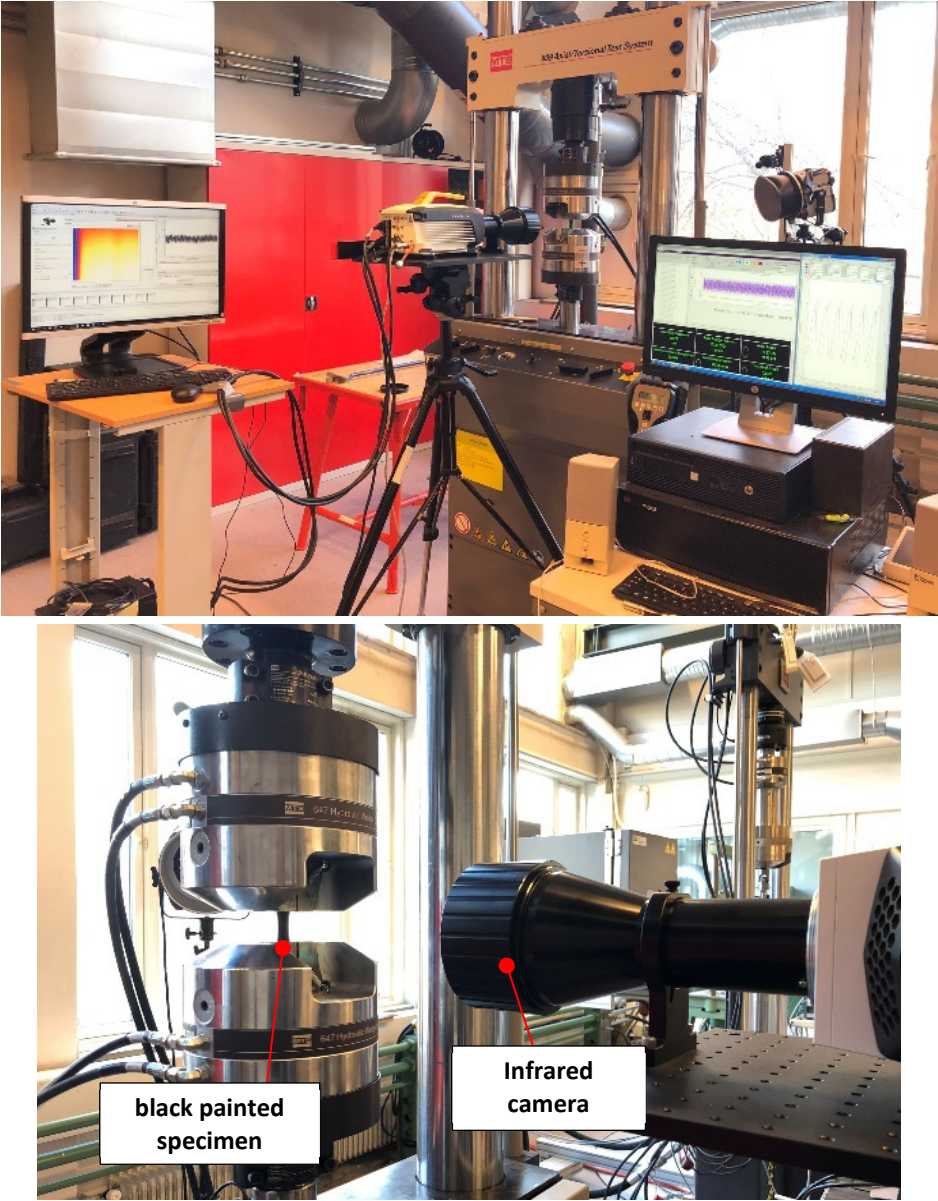


Figure 5.5: Black painted specimens surface (a) and experimental setup for evaluating the specific heat loss per cycles (b) at Fatigue Lab of NTNU (Norway).

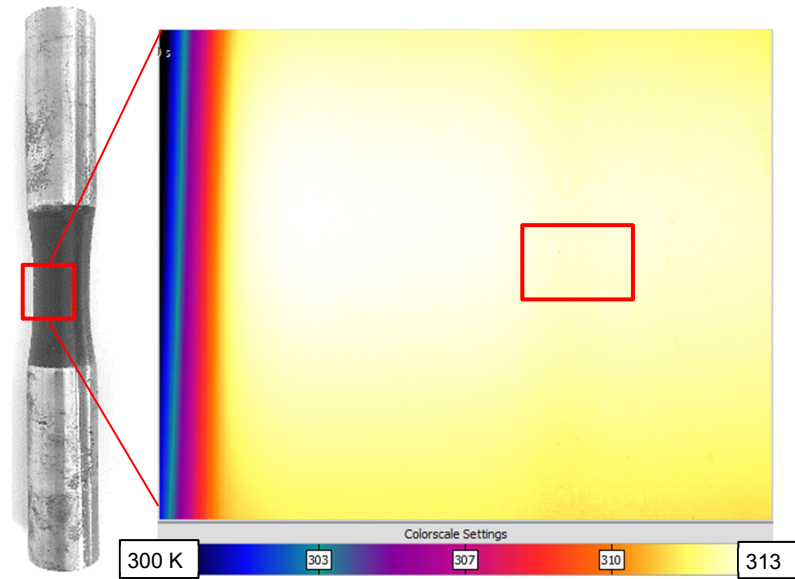


Figure 5.6: Portion of surface area framed by the infrared camera with the relevant temperature map recorded by the infrared camera. The selected rectangular area at the net section of the specimens for extracting the mean temperature value.

In these dedicated tests, the specimen's surface dedicated to strain measurement was first white-coated and then a black refined speckle pattern was created by an airbrush gun (see Fig (8)).

DIC 3D systems require a calibration which involves moving, imaging, and analysing a rigid calibration target in front of a stereo camera pair. Therefore, before mounting the specimens on the test machine 30 pairs of images of the calibration target with orientation and position within the field of view were taken and given in input to the calibration tools of VIC 3D. Some examples of calibration images were reported in Fig. (9).

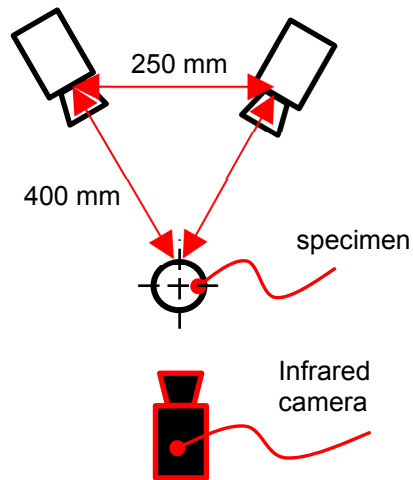
Before each fatigue test, the reference image was taken with zero axial and torsional load applied.

The test procedure consists in:

1. run the fatigue test at a load frequency ranging from 5-30 Hz depending on the load level applied;
2. trigger the test stop for evaluating the cooling gradient (to evaluate Q)
3. change the load frequency to 0.1 Hz;
4. Recording images related to one loading cycle by using SNAP-3D adopting acquisition frequency equal to 7 Hz;
5. change the frequency to the same value of point 1;
6. repeating from points 1 to 5 until specimen failure.

The DIC analyses were carried out adopting a subset size ranging from 48 to 52 pixels and a step size equal to 8 in a rectangular area embracing the net cross-section of the specimen as represented in Fig. (10). These values were obtained by using the *Subset Size Suggestion tool* of VIC 3D ® before each DIC analysis.

a)



b)

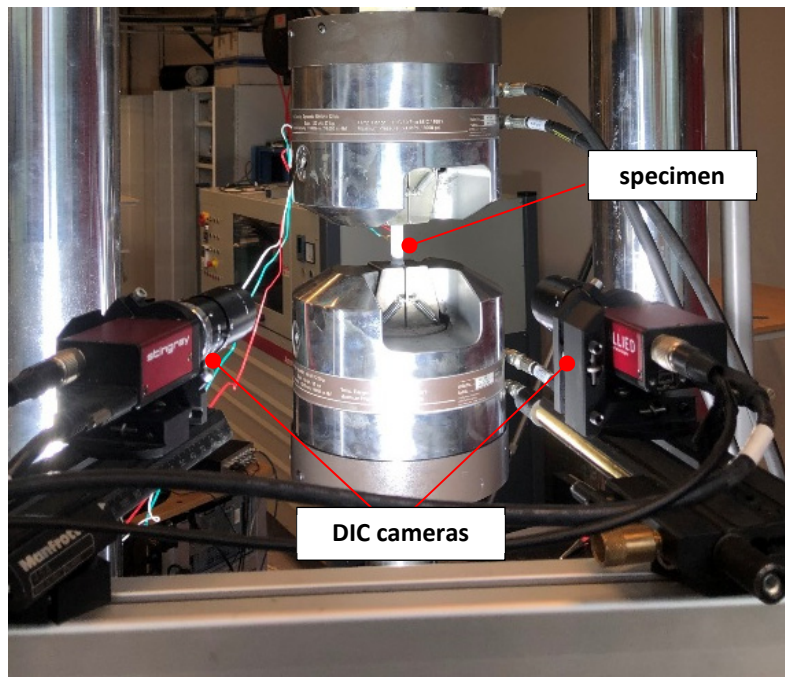


Figure 5.7: Schematic illustration of the experimental setup for evaluating Q and ΔW (a) and picture of the DIC system adopted (b).



Figure 5.8: Example of speckle pattern.

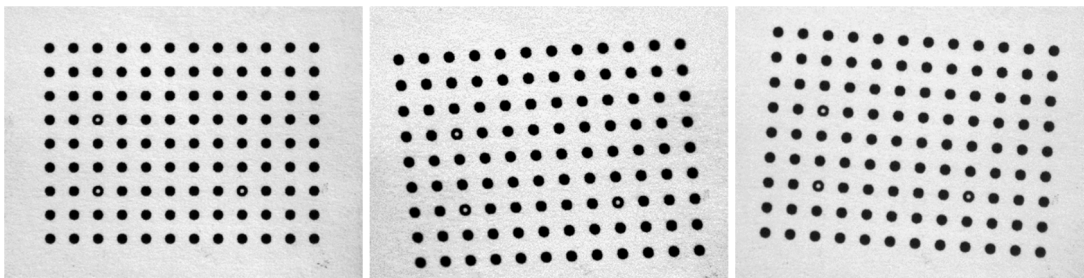


Figure 5.9: Examples of DIC calibration images of the calibration target.

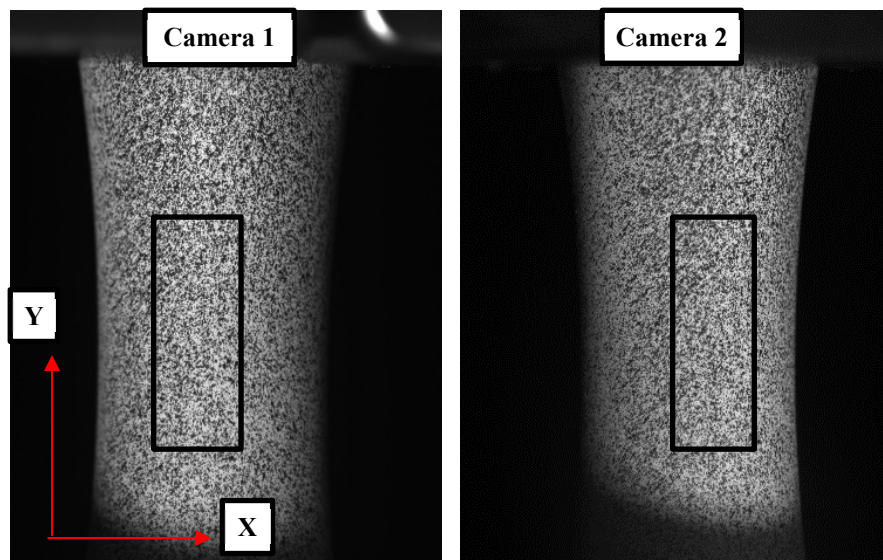
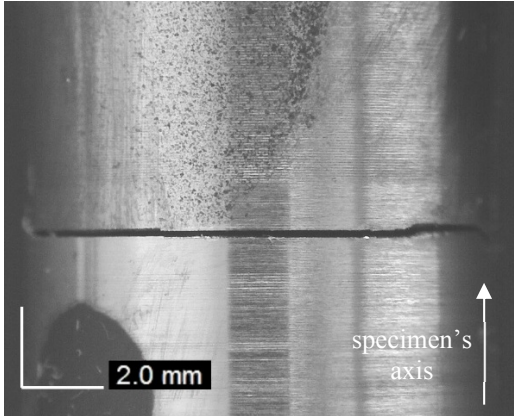


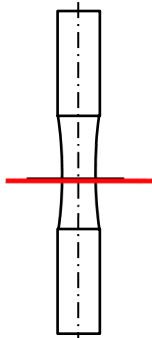
Figure 5.10: Picture taken by the DIC cameras. The correlation algorithm was run within the black rectangular area adopting a subset size of 50 pixels.

5.3 DAMAGE ANALYSIS

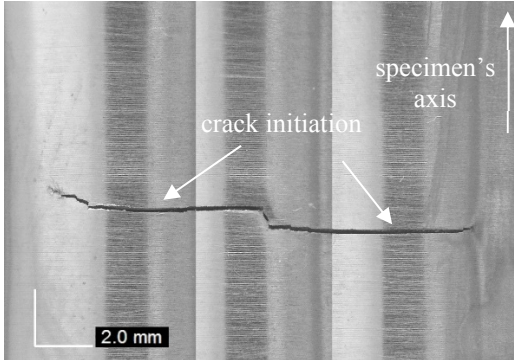
a) Axial, $N_f = 3.87 \cdot 10^5$ cycles



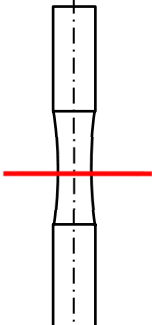
Plane of maximum principal strain



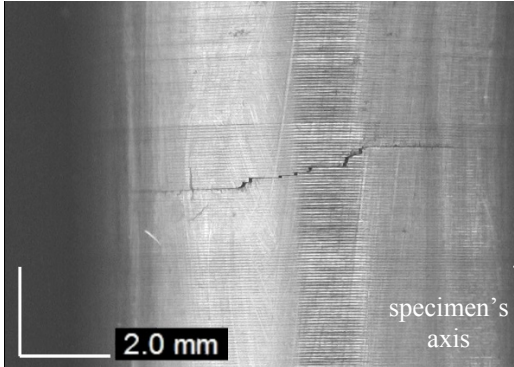
b) Axial, $N_f = 5.54 \cdot 10^4$ cycles



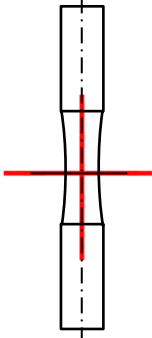
Plane of maximum principal strain



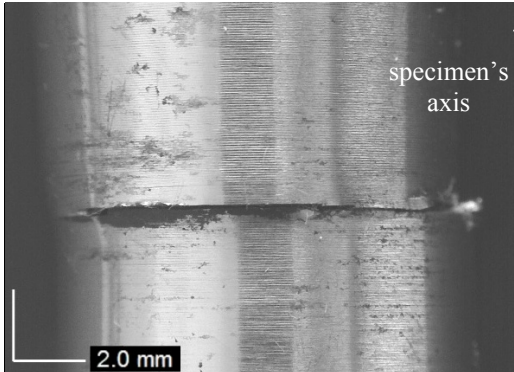
c) Pure torsion, $N_f = 3.87 \cdot 10^5$ cycles



Planes of maximum shear strain



d) Pure torsion, $N_f = 1.21 \cdot 10^3$ cycles



Planes of maximum shear strain

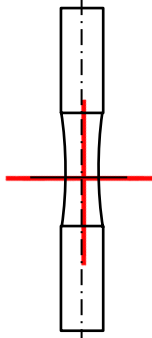
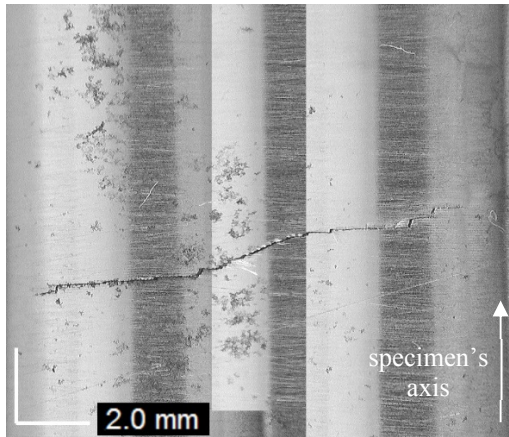
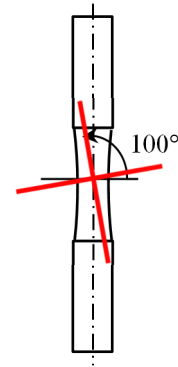


Figure 5.11: crack paths relevant to uniaxial (a,b) and pure torsion (c,d) loading conditions.

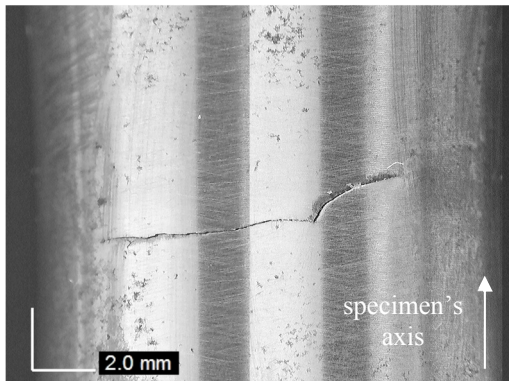
a) A+T, $\Lambda = 1$, $\varphi = 0^\circ$ $N_f = 4.27 \cdot 10^5$ cycles



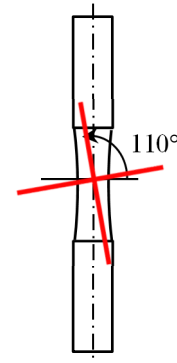
Planes of maximum shear strain



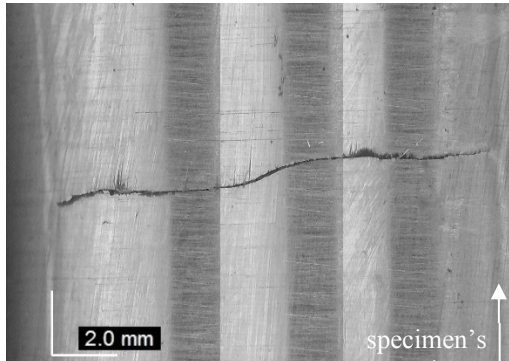
b) A+T, $\Lambda = 1$, $\varphi = 0^\circ$ $N_f = 3.06 \cdot 10^4$ cycles



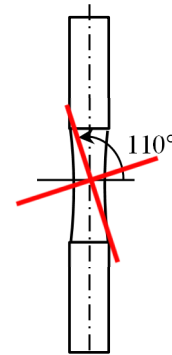
Planes of maximum shear strain



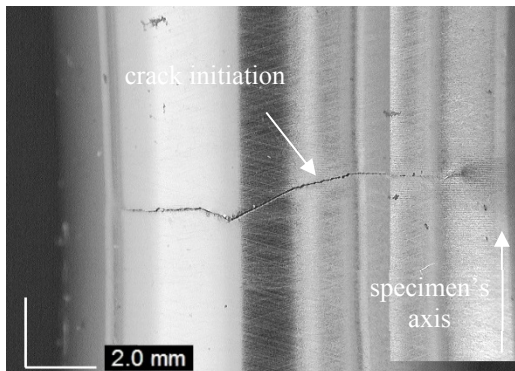
c) A+T, $\Lambda = \sqrt{3}$, $\varphi = 0^\circ$ $N_f = 5.12 \cdot 10^5$ cycles



Planes of maximum shear strain



d) A+T, $\Lambda = \sqrt{3}$, $\varphi = 0^\circ$ $N_f = 3.54 \cdot 10^4$ cycles



Planes of maximum shear strain

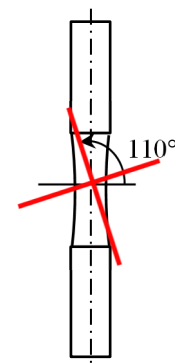
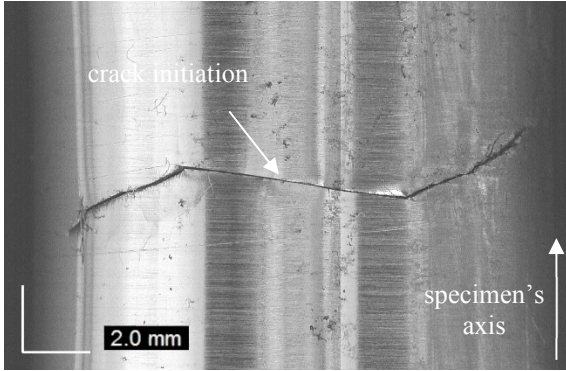
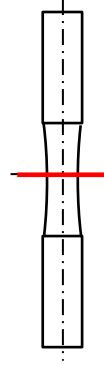


Figure 5.12: crack paths relevant to multiaxial A+T, $\Lambda = 1$, $\varphi = 0^\circ$ (a,b) and A+T, $\Lambda = \sqrt{3}$, $\varphi = 0^\circ$ (c,d) loading conditions

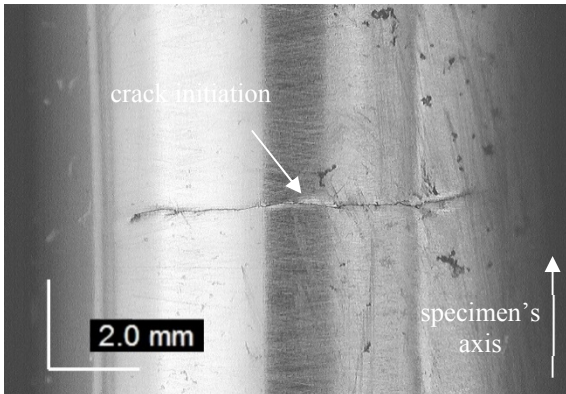
a) A+T, $\Lambda=1$, $\varphi=90^\circ$ $N_f = 1.04 \cdot 10^4$ cycles



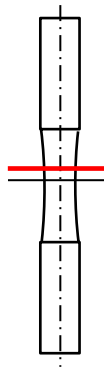
Planes of maximum shear strain



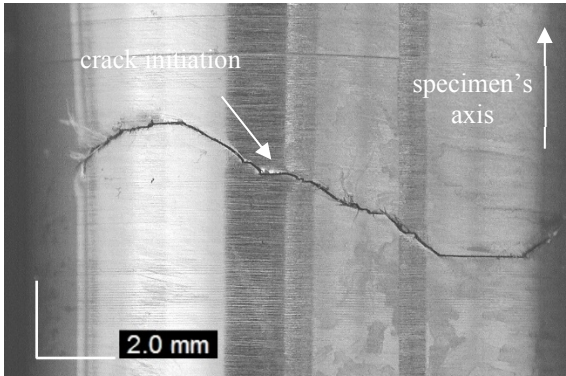
b) A+T, $\Lambda=1$, $\varphi=90^\circ$ $N_f = 5.19 \cdot 10^4$ cycles



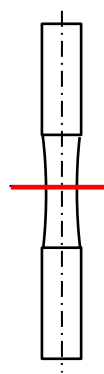
Planes of maximum shear strain



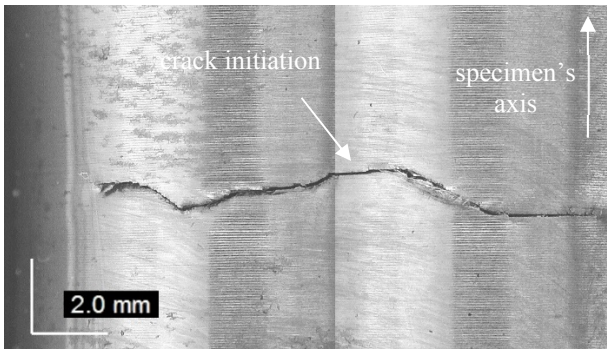
c) A+T, $\Lambda=\sqrt{3}$, $\varphi=90^\circ$ $N_f = 5.19 \cdot 10^4$ cycles



Planes of maximum shear strain



d) A+T, $\Lambda=\sqrt{3}$, $\varphi=90^\circ$ $N_f = 1.18 \cdot 10^4$ cycles



Planes of maximum shear strain

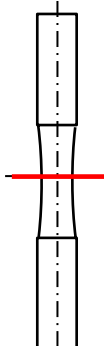


Figure 5.13: crack paths relevant to multiaxial A+T, $\Lambda=1$, $\varphi=90^\circ$ (a,b) and A+T, $\Lambda=\sqrt{3}$, $\varphi=90^\circ$ (c,d) loading conditions

An analysis of the crack paths after 50% of stiffness loss was carried out by means of a Digital Microscope DINOLite®.

All the directions of the failures obtained from uniaxial cyclic loading occurred in a plane orthogonal to the maximum principal stress as reported in the example in Fig. (11a,b). In particular Fig. (11b) shows an example of multi crack initiation at the net cross-section of the specimens.

Fig. (11c,d) reports some example of the crack paths relevant to failures occurred in torsional fatigue tests. All the cracks initiated in a plane of maximum shear strain both in the LCF and HCF regimes. Fig. (11c) highlights the propagation of the crack on mutual planes of maximum shear strain.

Regarding the crack paths relevant to proportional multiaxial loading conditions, as can be seen in Figs (12a-d), all the failure initiated on the maximum shear planes.

Since the direction of maximum principal stresses changes over a loading cycle in out-of-phase multiaxial fatigue testing the failure direction can occur within an interval of angle. Typically, the plane of maximum shear strain amplitude is the crack initiation plane, then the crack follows different directions which depend on the local stress level. In Fig. (13), most of the failures start in the maximum shear strain plane (Fig. (13b-d)), except for the only case of high out-of-phase load level with $\Lambda=1$ (Fig. 13a).

5.4 FATIGUE TEST RESULTS

All the fatigue test results are reported in terms of nominal net-section stress amplitude in Fig. (14).

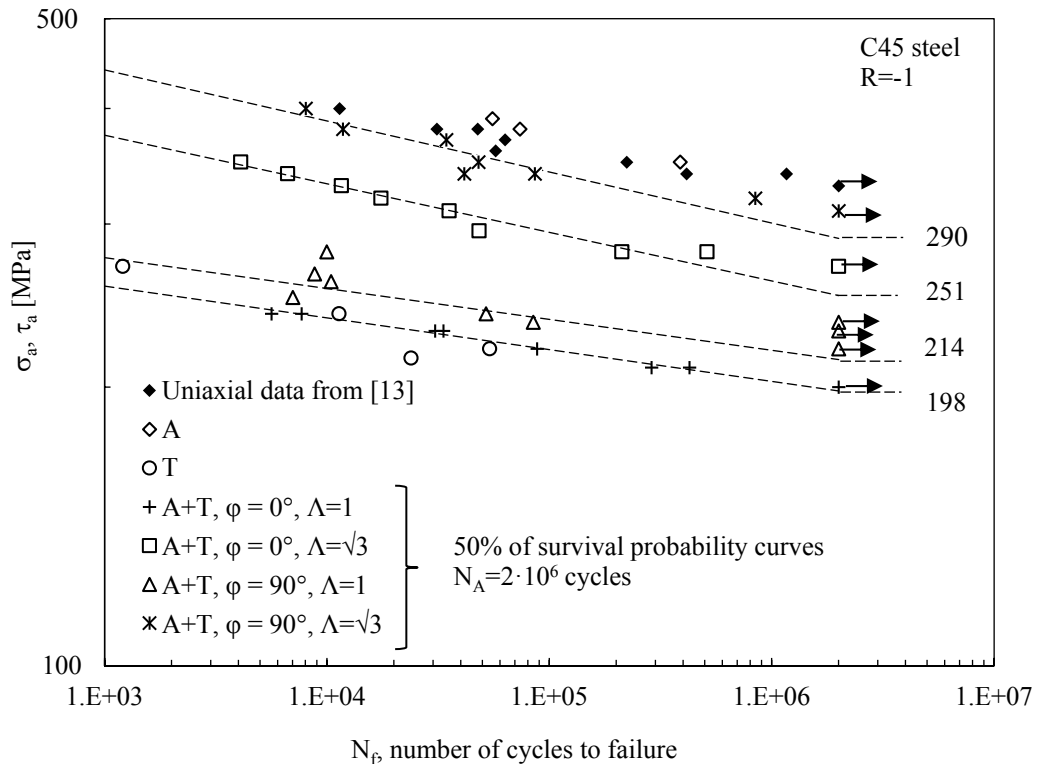


Figure 5.14: Fatigue test results in terms of nominal net-section stress amplitude

In particular, in the case of torsional fatigue tests results, they were plotted in terms of net-section shear stress amplitude assumed uniformly distributed over the cross-section and adopting Eq. (2):

$$\tau_{an} = \frac{16 \cdot M_{t,a}}{\pi(d_{en}^2 - d_{in}^2)(d_{en} + d_{in})} \quad (2)$$

where $M_{t,a}$, d_{en} and d_{in} are the applied torque amplitude, the outer and inner diameters of the net-cross-section, respectively.

In Fig. (14) the test series relevant to multiaxial loading condition were statically analysed to determine the fatigue curves to the 50% of survival probability setting the upper limit to $2 \cdot 10^6$ cycles.

Analysing the multiaxial curves, the lowest fatigue strength was obtained in proportional fatigue testing with $\Lambda = 1$ tests. For the same Λ , out-of-phase loading presents a fatigue strength of 8% higher. Proportional loading condition resulted more damaging also in multiaxial fatigue with $\Lambda = \sqrt{3}$ which is characterized by a fatigue strength at $2 \cdot 10^6$ cycles 14% lower than the relevant out-of-phase loads.

5.4.1 Cooling gradient evaluation and evolution of Q during fatigue tests

In Figs (15-26) two examples per each loading condition of cooling gradient and evolution of Q during the relevant fatigue test were reported. The slope of a linear interpolation of the initial cooling gradient is shown in each relevant cooling gradient. In particular, temperature data related to about 0.4 s of time window were adopted in order to evaluate the cooling gradient. The choice of the initial time to interpolate the data is done by the operator, but it is easy to observe that changing the set of data to interpolate does not change significantly the value of the slope (i.e. the value of Q)

The Q evolutions reported in Figs (15-26) are related to fatigue tests in which the failure occurred. Regarding all the tests characterized by a number of cycles to failure ranging from 10^3 and $3 \cdot 10^5$, Q is approximately constant during the whole tests, whereas for a number of cycles to failure ranging from $3 \cdot 10^5$ and 10^6 it tends to stabilise after one third of total life.

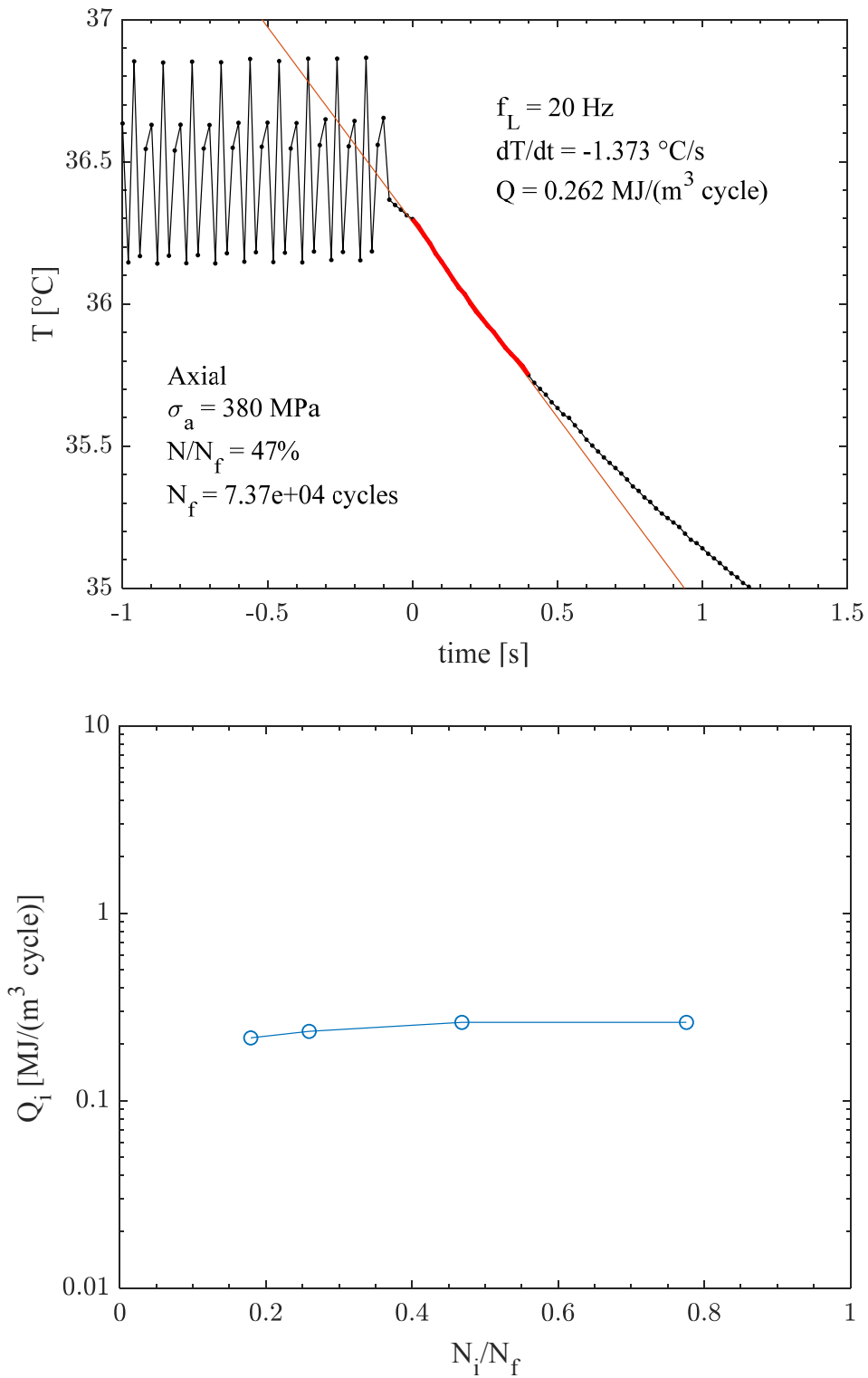


Figure 5.15: Example of cooling gradient measured of axial fatigue test and relevant Q evolution.

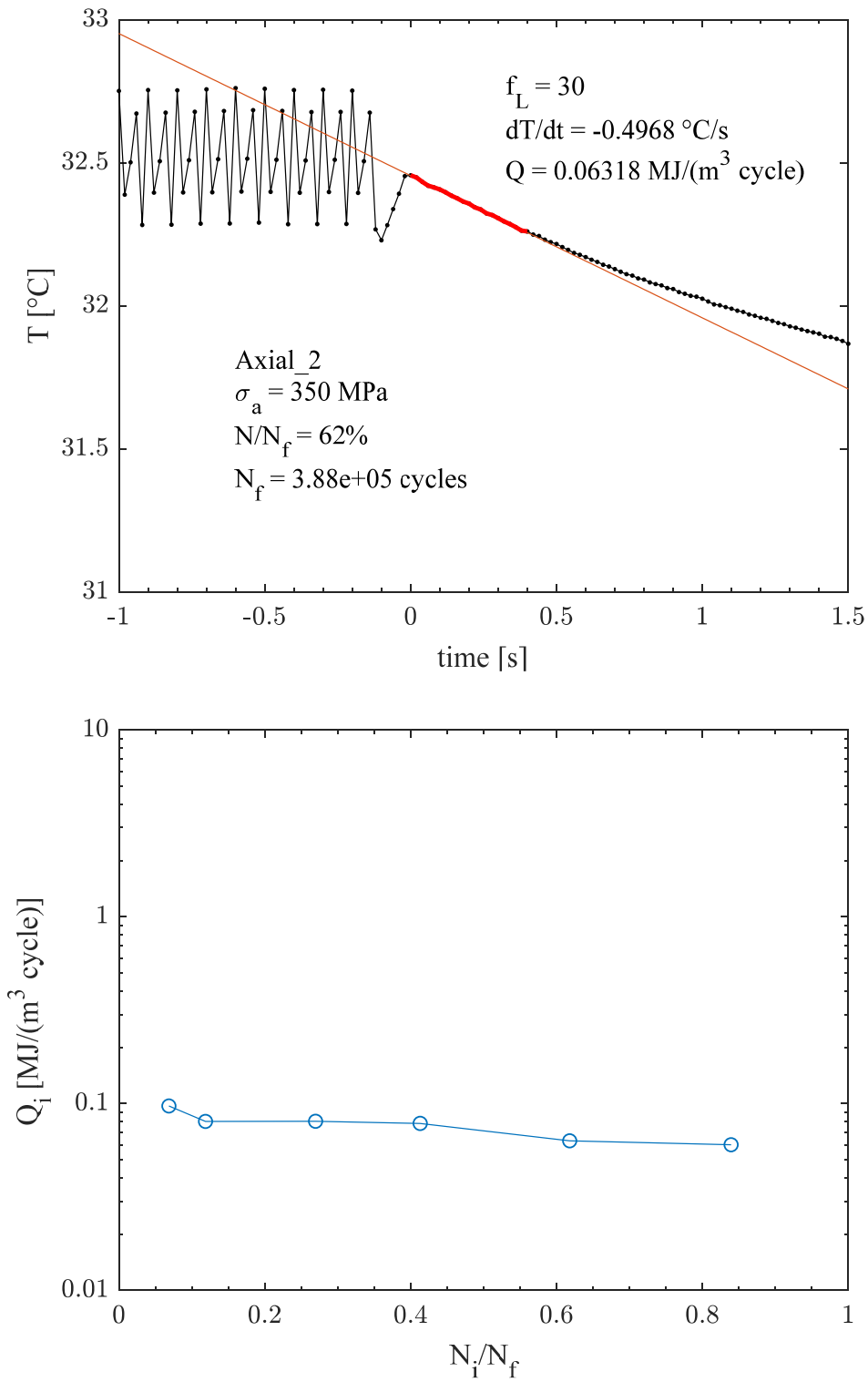


Figure 5.16: Example of cooling gradient measured of axial fatigue test and relevant Q evolution.

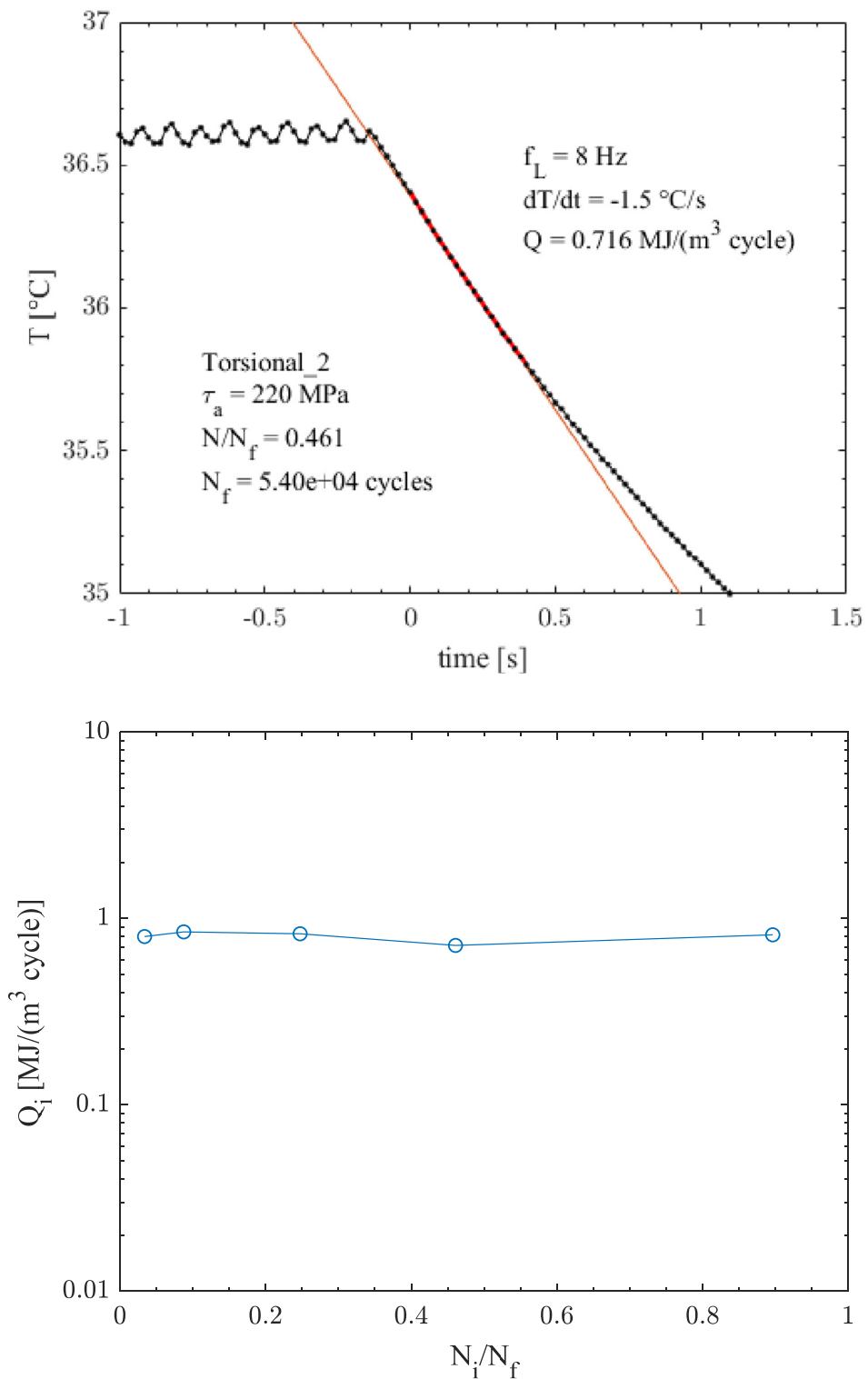


Figure 5.17: Example of cooling gradient measured of pure torsion fatigue test and relevant Q evolution.

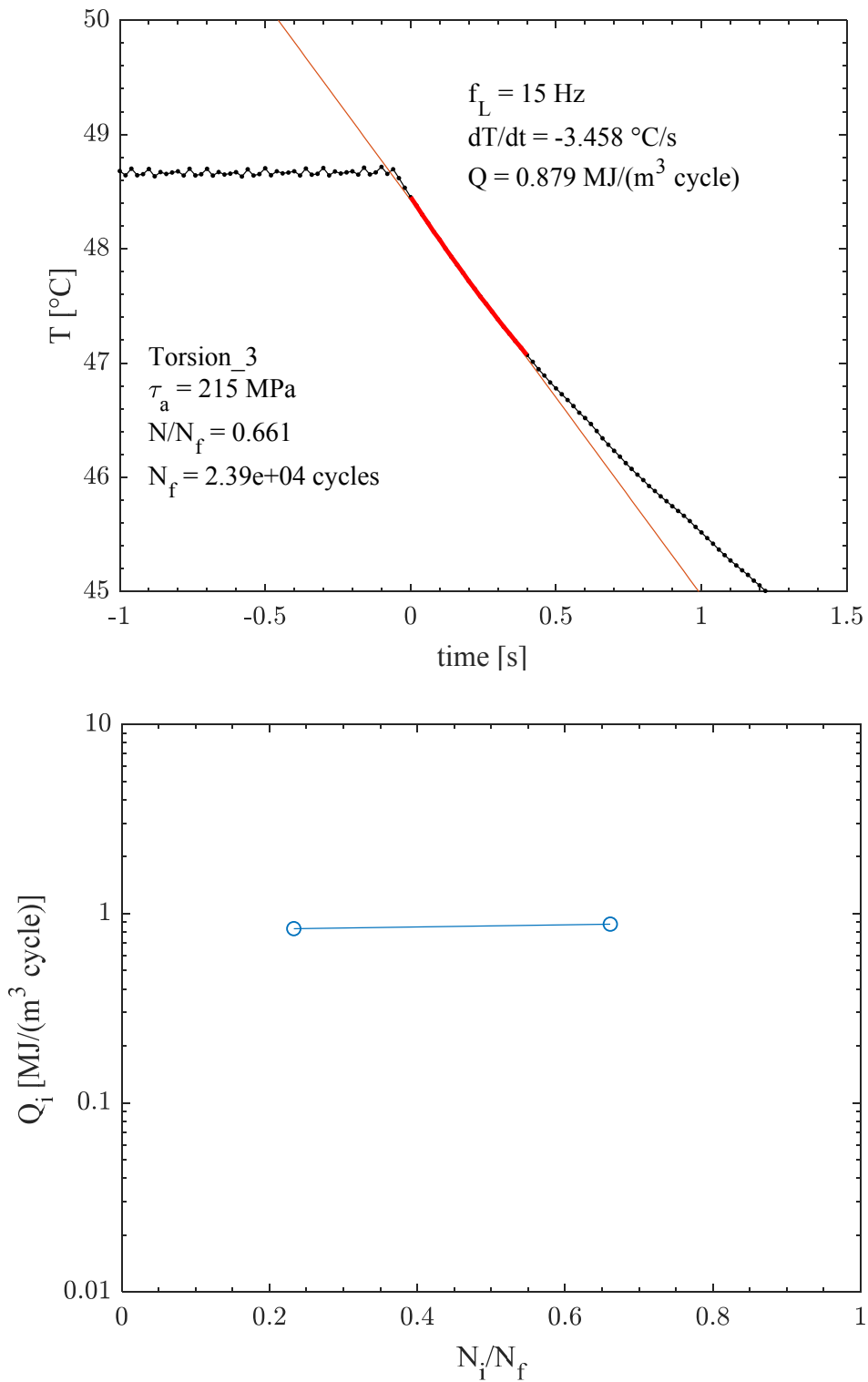


Figure 5.18: Example of cooling gradient measured of pure torsion fatigue test and relevant Q evolution.

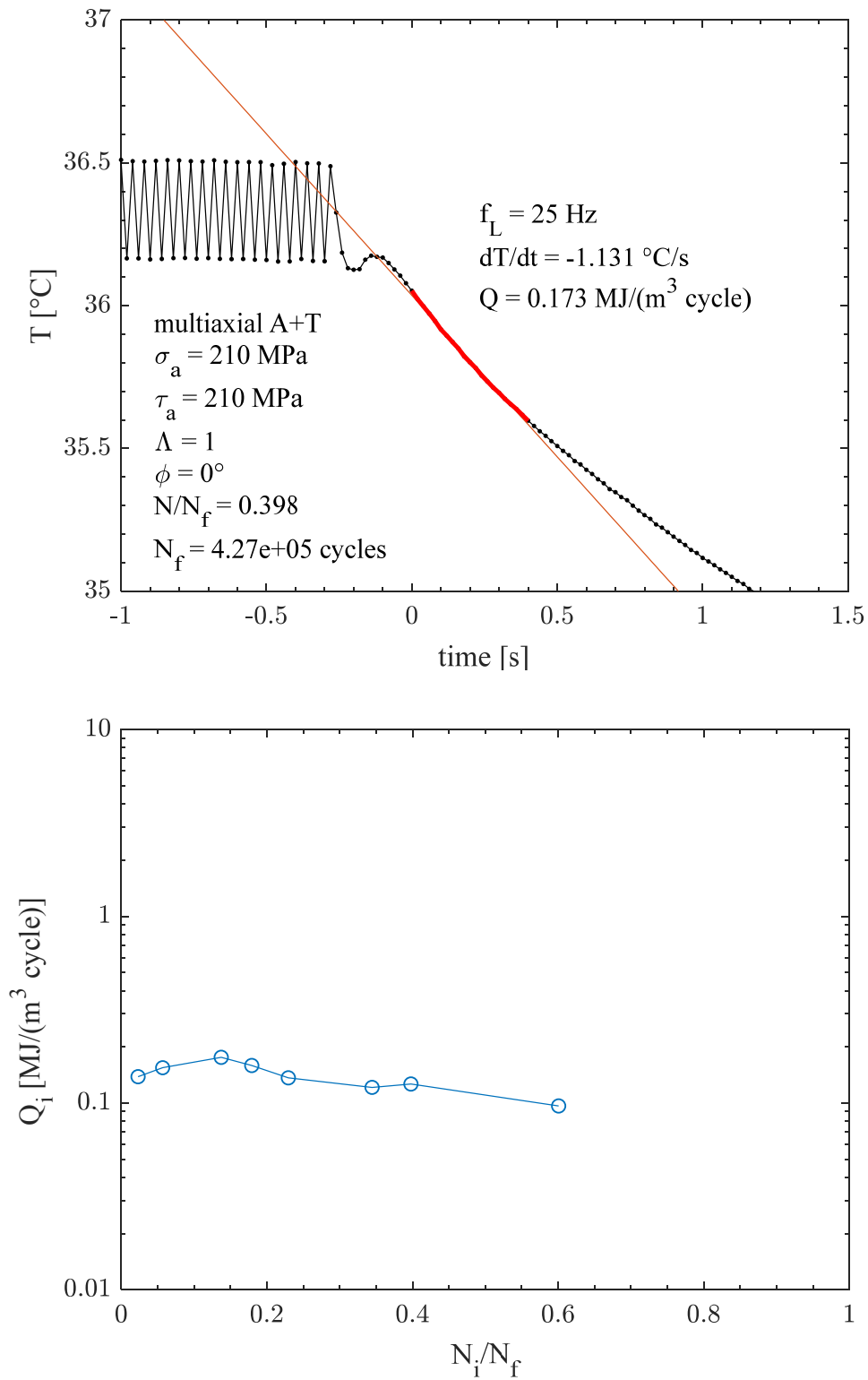


Figure 5.19: Example of cooling gradient measured in A+T, $\phi=0^\circ$, $\Lambda=1$ fatigue test and relevant Q evolution

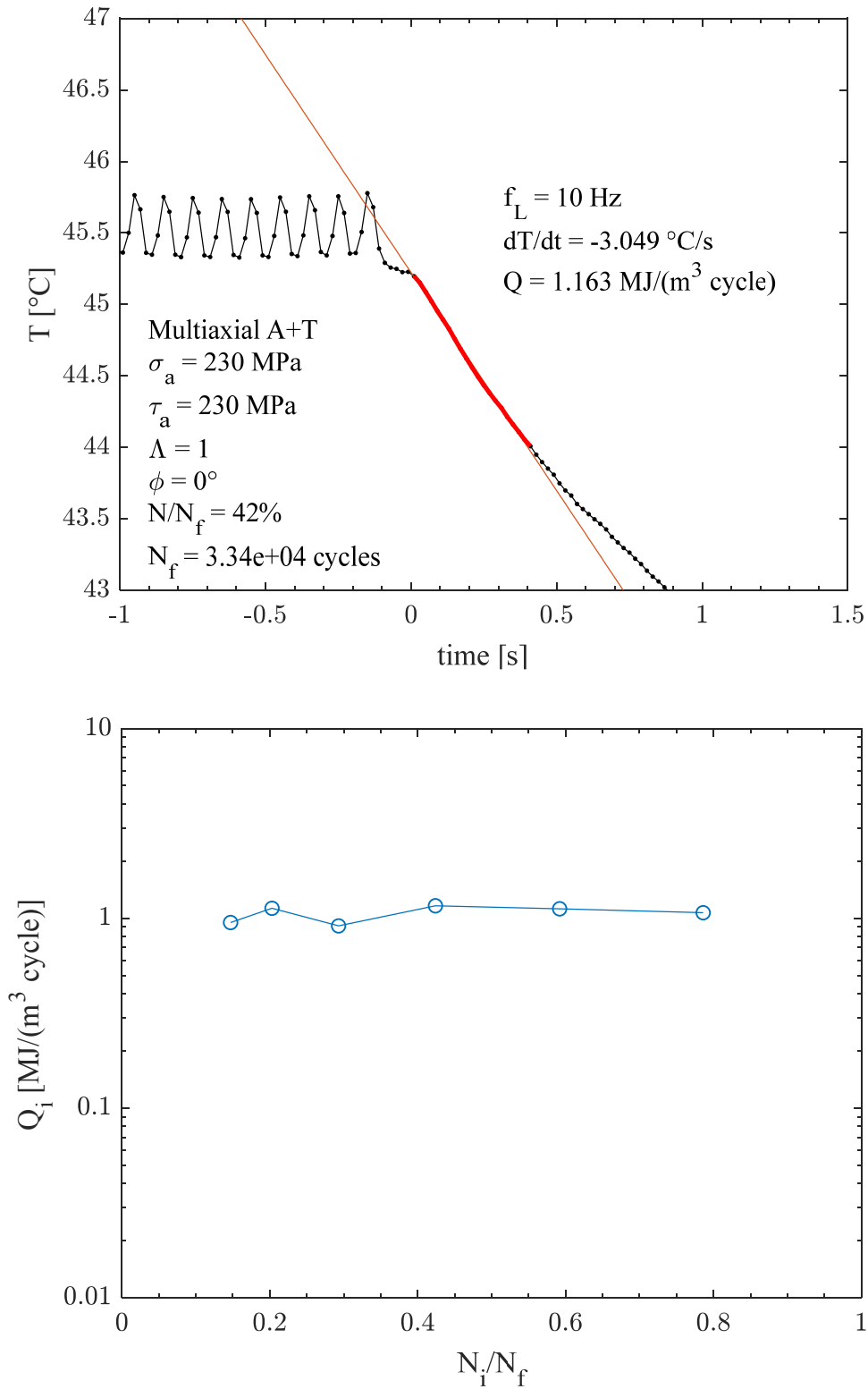


Figure 5.20: Example of cooling gradient measured in A+T, $\phi=0^\circ$, $\Lambda=1$ fatigue test and relevant Q evolution.

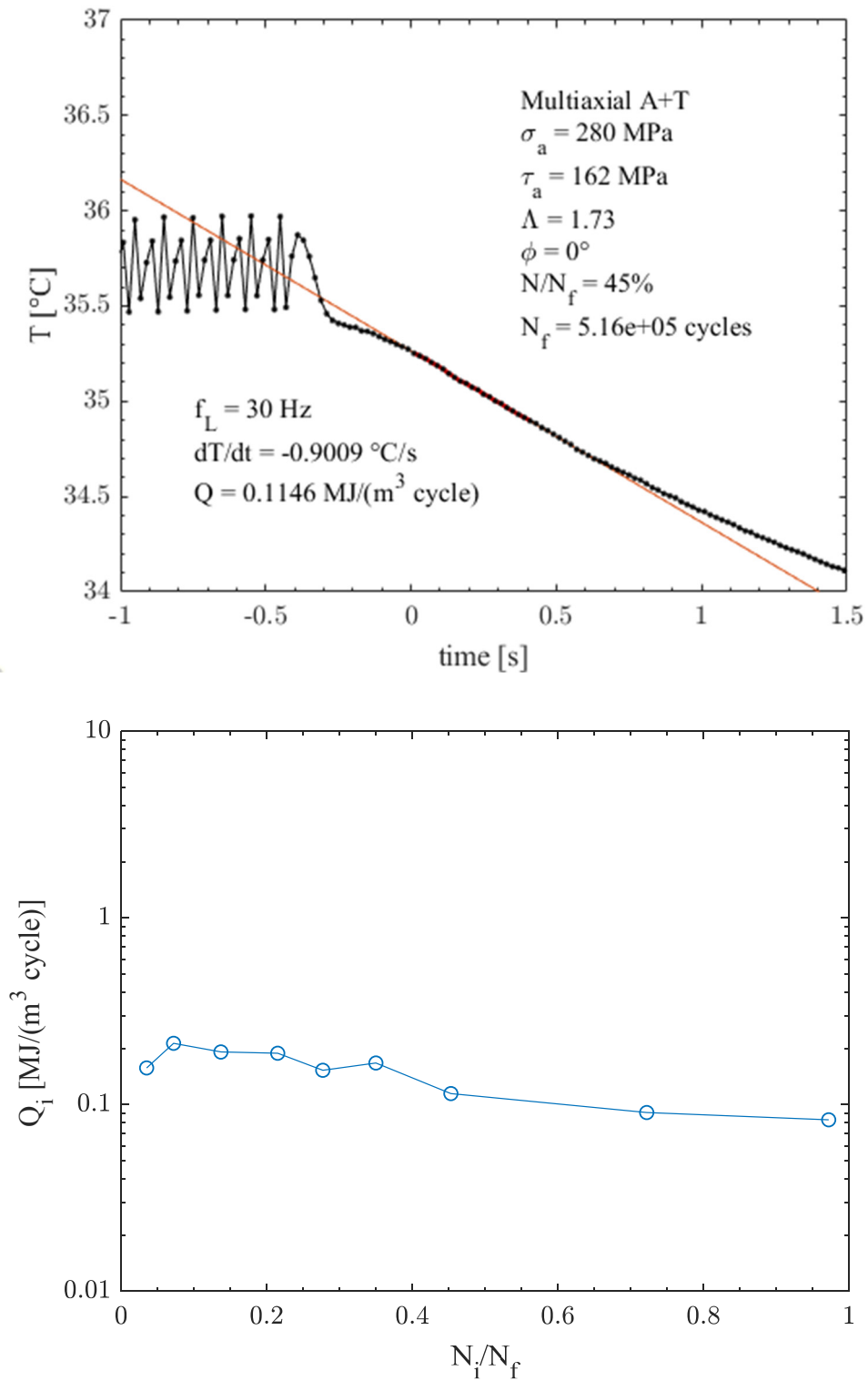


Figure 5.21: Example of cooling gradient measured in A+T, $\phi=0^\circ$, $\Lambda=\sqrt{3}$ fatigue test and relevant Q evolution.

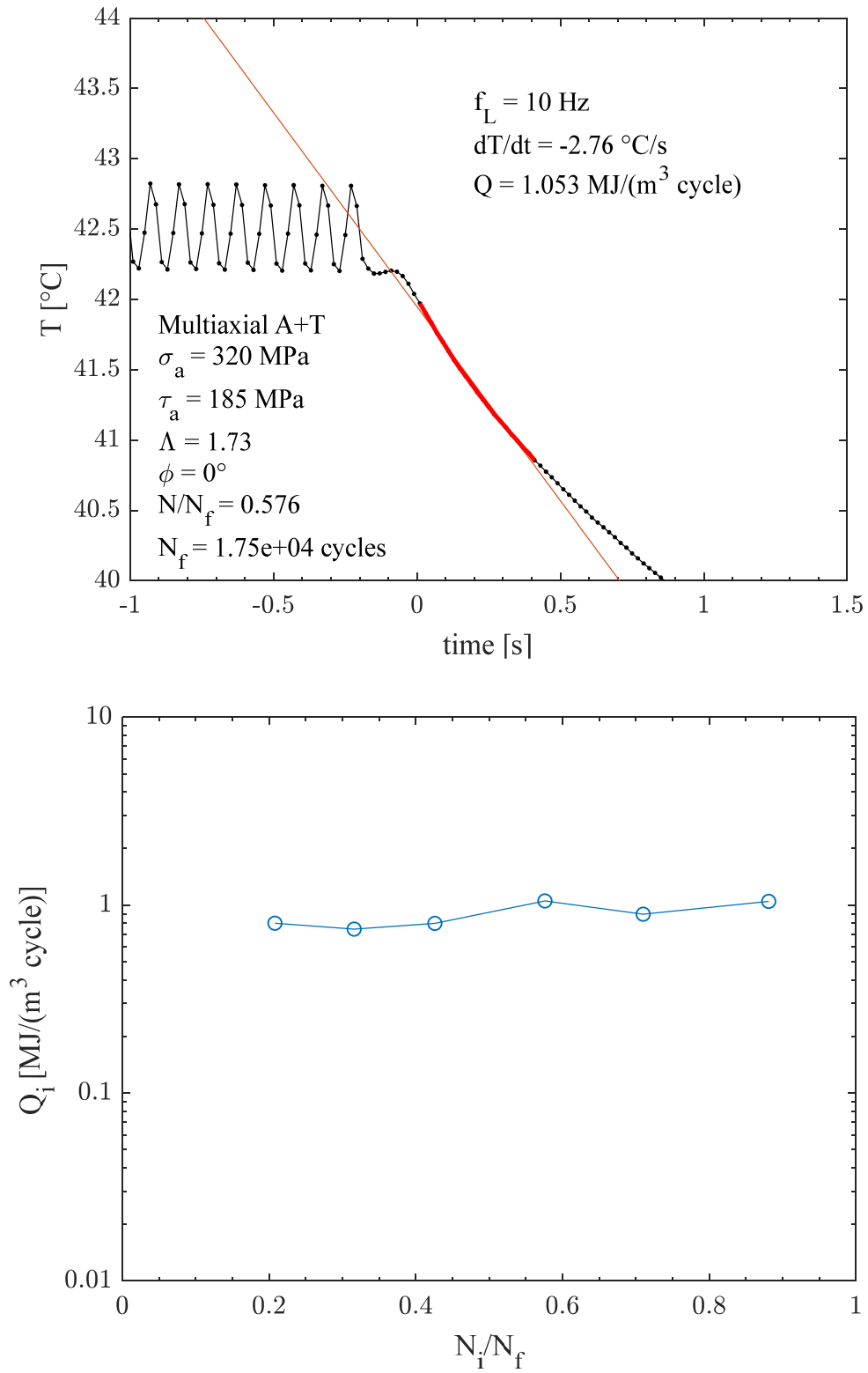


Figure 5.22: Example of cooling gradient measured in A+T, $\phi=0^\circ$, $\Lambda=\sqrt{3}$ fatigue test and relevant Q evolution.

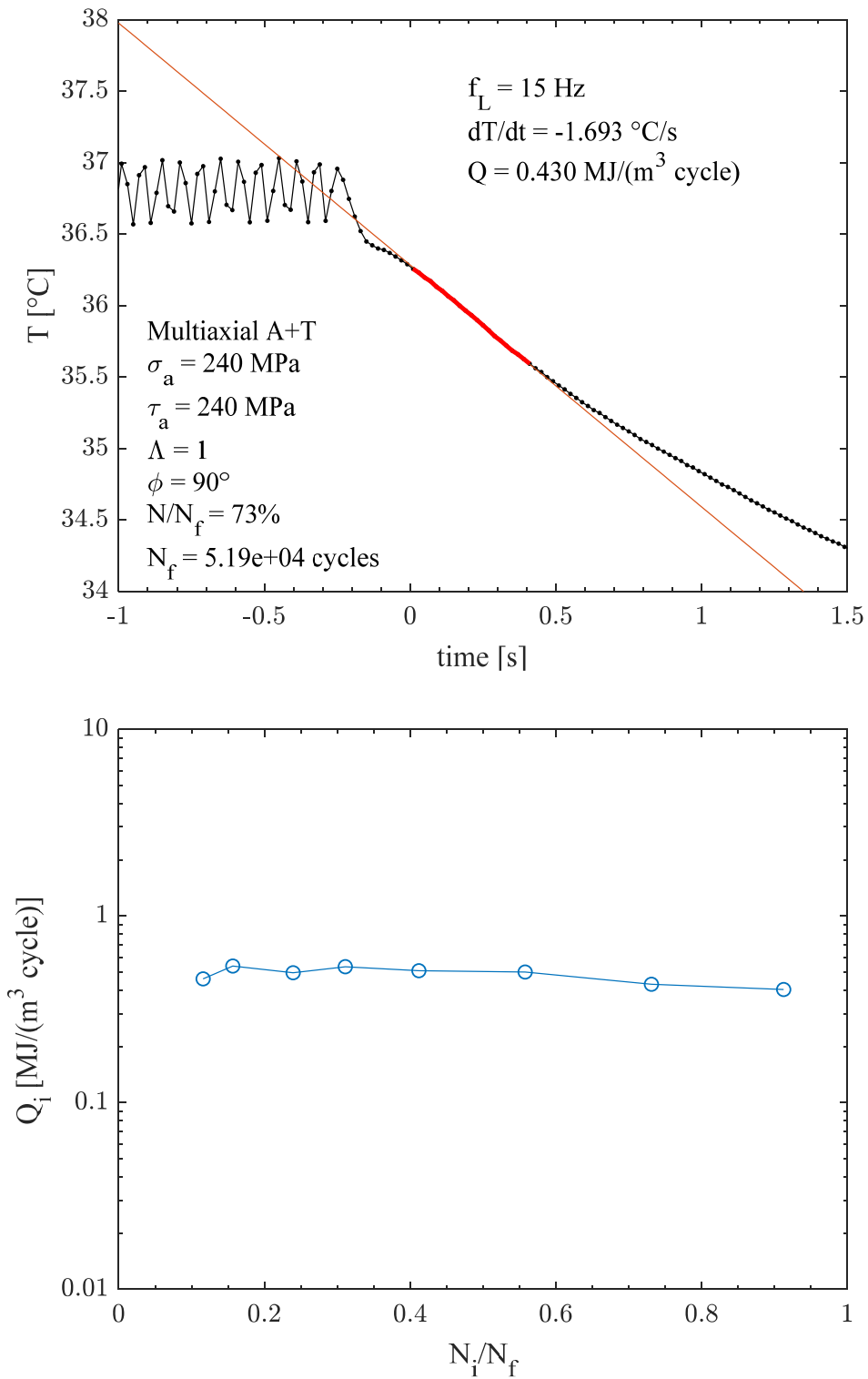


Figure 5.23: Example of cooling gradient measured in A+T, $\phi=90^\circ$, $\Lambda=1$ fatigue test and relevant Q evolution.

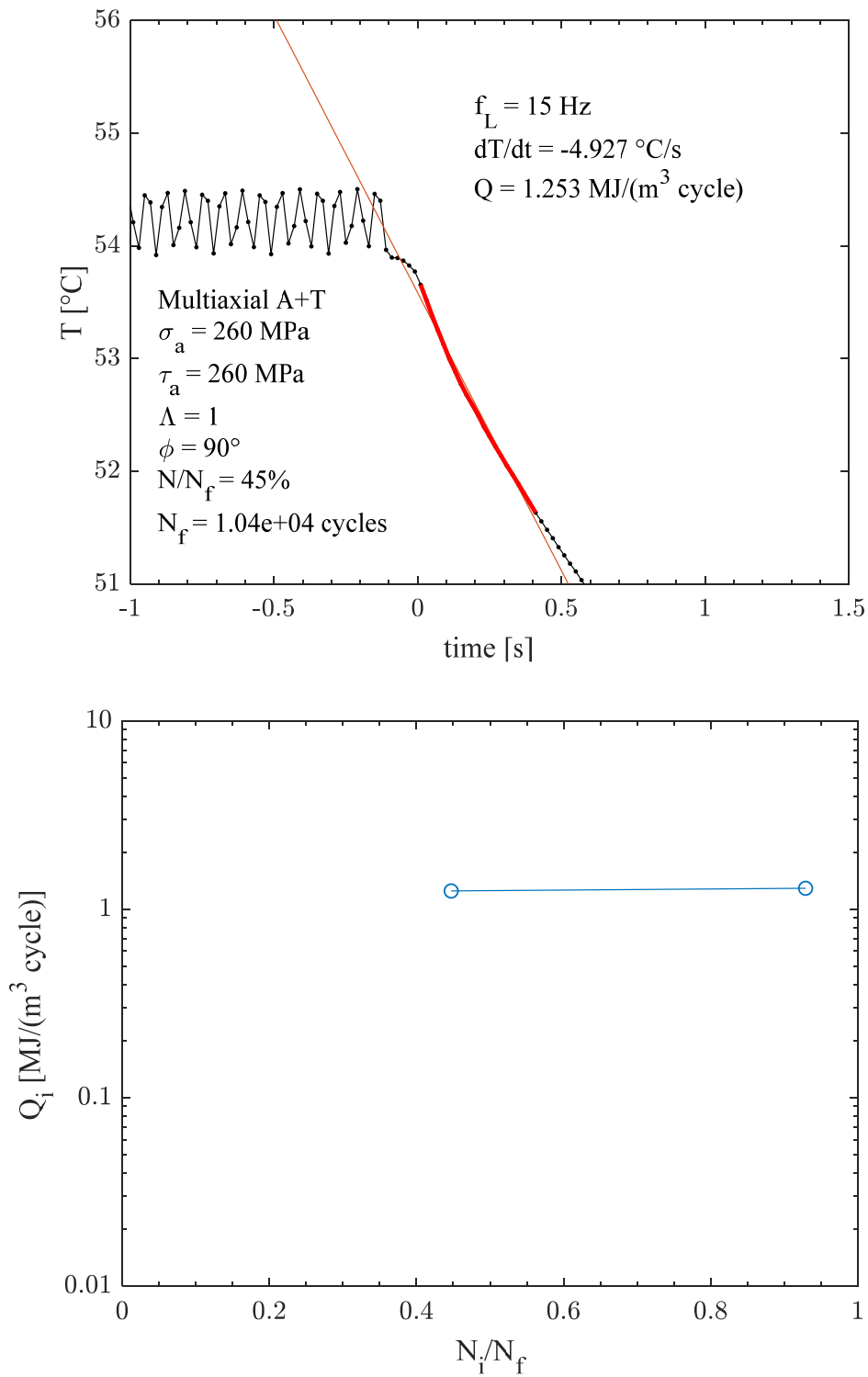


Figure 5.24: Example of cooling gradient measured in A+T, $\phi=90^\circ$, $\Lambda=1$ fatigue test and relevant Q evolution.

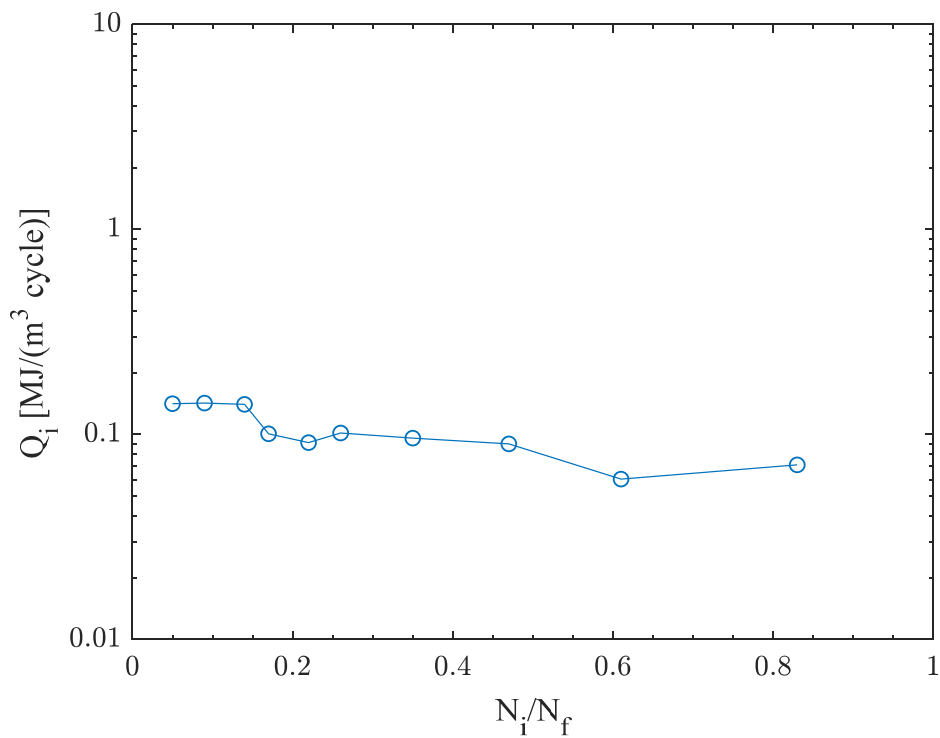
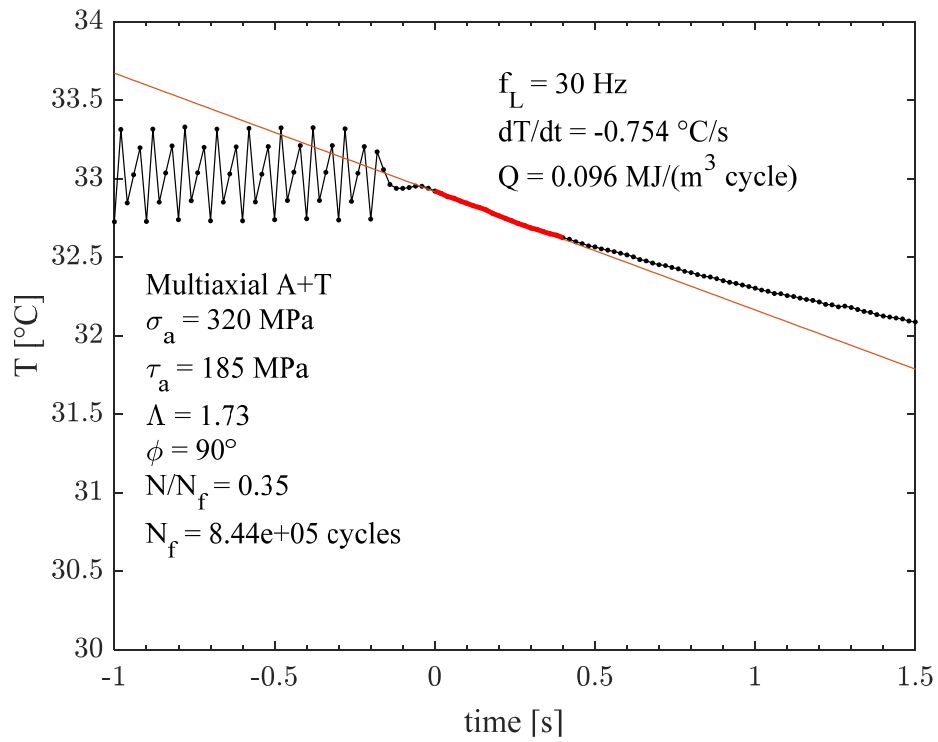


Figure 5.25: Example of cooling gradient measured in A+T, $\phi=90^\circ$, $\Lambda=\sqrt{3}$ fatigue test and relevant Q evolution.

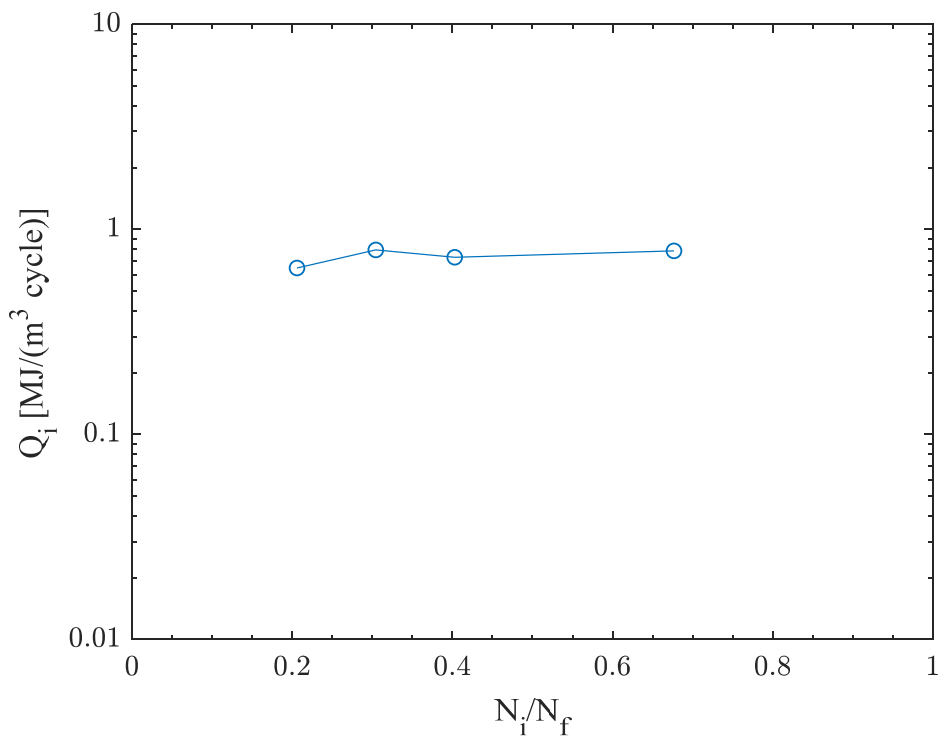
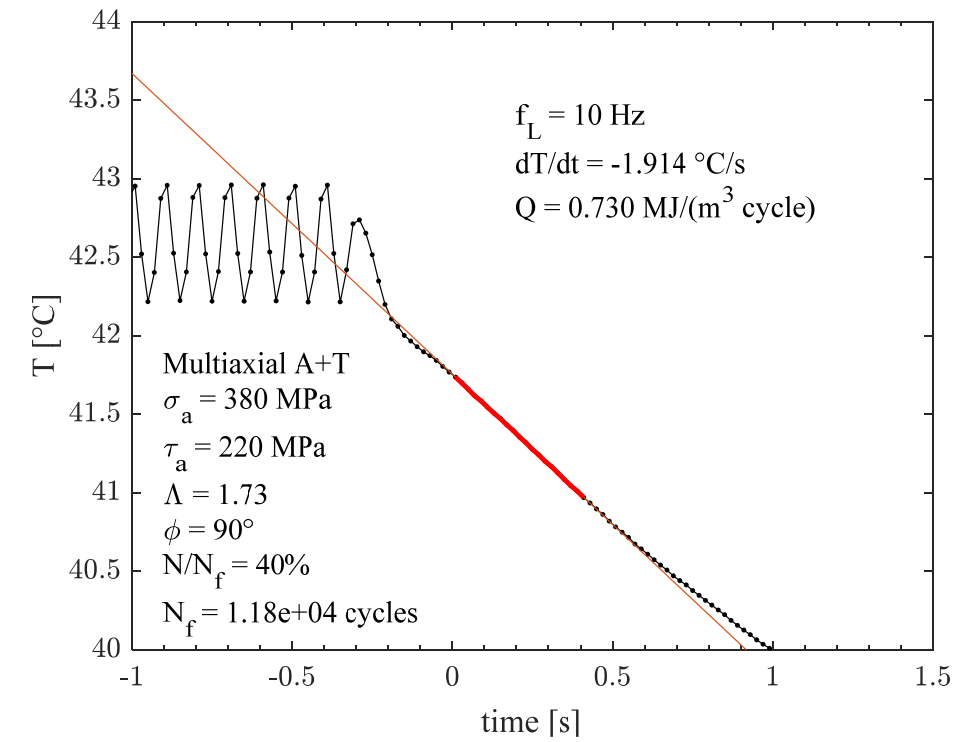


Figure 5.26: Example of cooling gradient measured in A+T, $\phi=90^\circ$, $\Lambda=\sqrt{3}$ fatigue test and relevant Q evolution.

Figs (27-31) show the synthesis of the evolution of Q for each loading condition. The results obtained for uniaxial and torsional loads (Fig. (27)). Focusing on multiaxial tests, a different behavior between runout fatigue tests with $\Lambda = 1$ and $\Lambda = \sqrt{3}$ can be observed. The Q evolutions of runout specimens subjected to a $\Lambda = 1$ (Fig. (28) and (30)) presented high values at the beginning of the test and then they decreased until $2 \cdot 10^6$ cycles. Conversely, runout fatigue tests with $\Lambda = \sqrt{3}$ showed an initial increment until they reach a maximum value at about 20% of $2 \cdot 10^6$ cycles and then a slight decrease occurred. The latter case was also observed in the fatigue test results obtained on fully-reversed axial fatigue tests carried out on the same material in [13]. This suggests a different cyclic behavior, exclusively in the HCF regime, between axial and torsional cyclic loading and the biaxiality ratio is the parameter that determines the cyclic evolution mode. Furthermore, having set the runout at $2 \cdot 10^6$ cycles the stabilized Q value could be reached for a higher number of cycles to failure assuming that the plateau of the nominal stress amplitude fatigue curve occurs at about 10^7 cycles. According to the latter hypothesis, the Q value obtained at 10^6 cycles in runout tests is an engineering approximation.

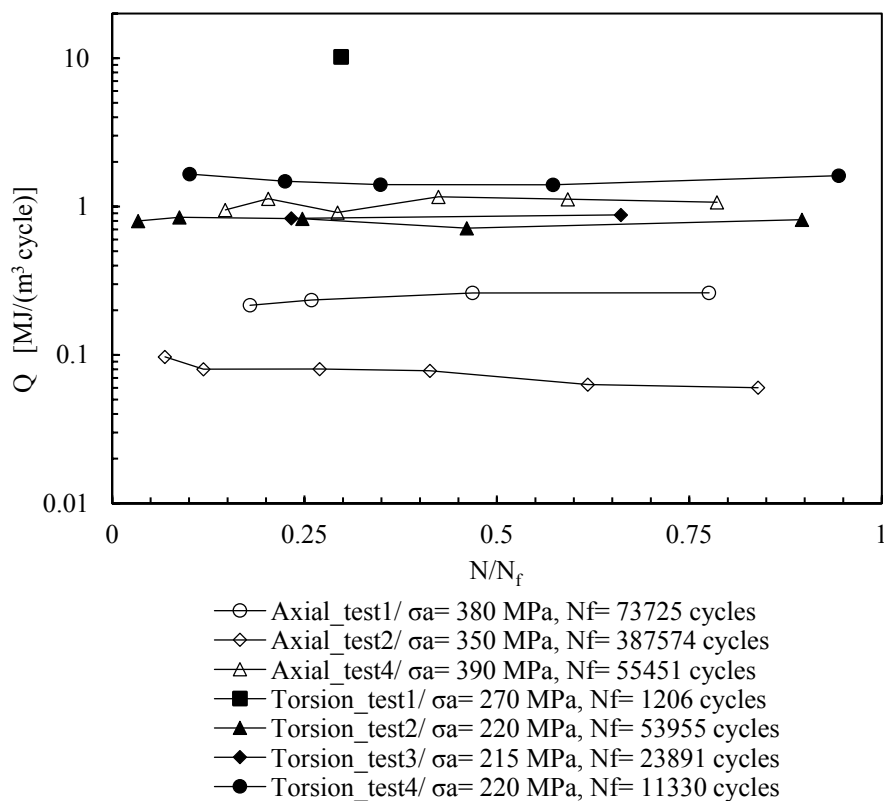


Figure 5.27: Synthesis of Q evolutions during axial and pure torsion fatigue tests.

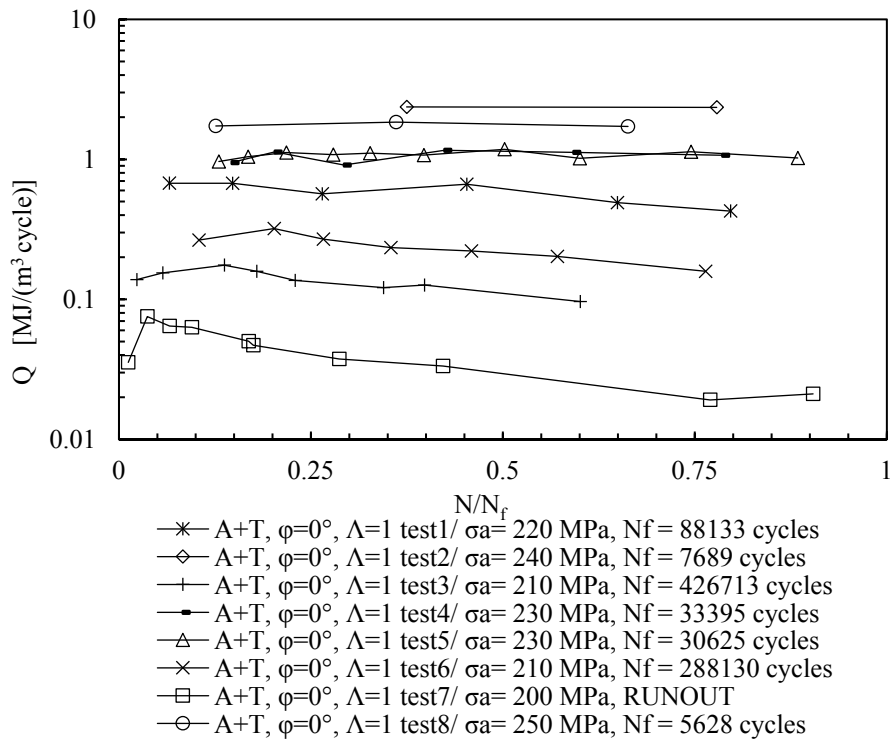


Figure 5.28: Synthesis of Q evolutions during combined axial and torsional fatigue test with $\varphi=0^\circ$ and $\Lambda=1$

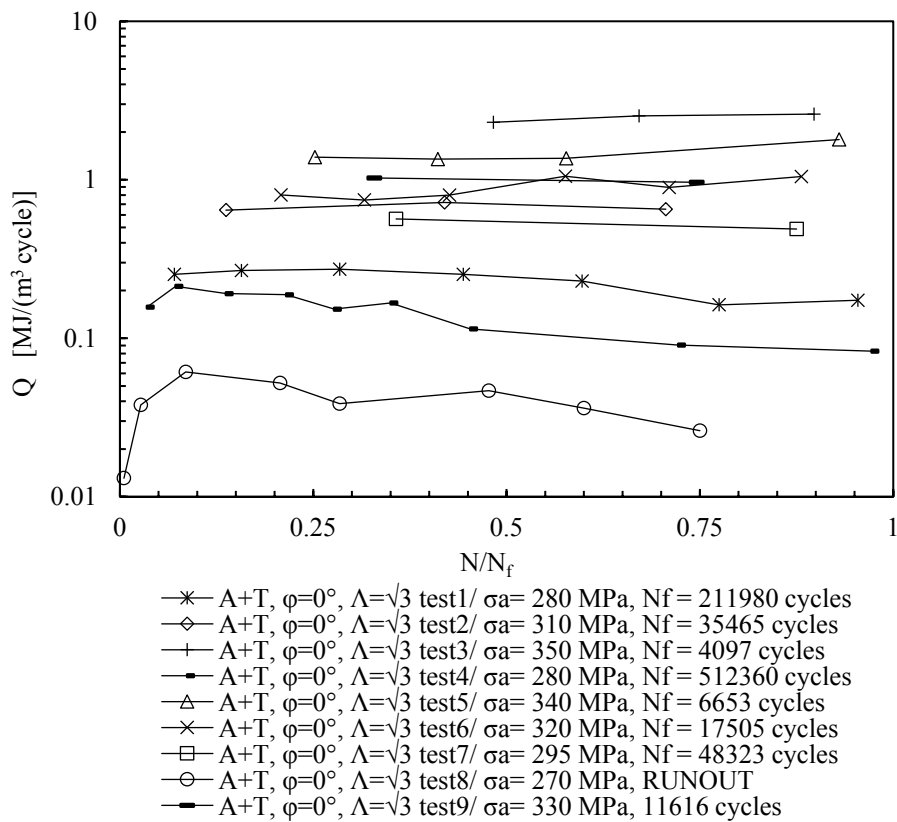


Figure 5.29: Synthesis of Q evolutions during combined bending and torsional fatigue test with $\varphi=0^\circ$ and $\Lambda=\sqrt{3}$

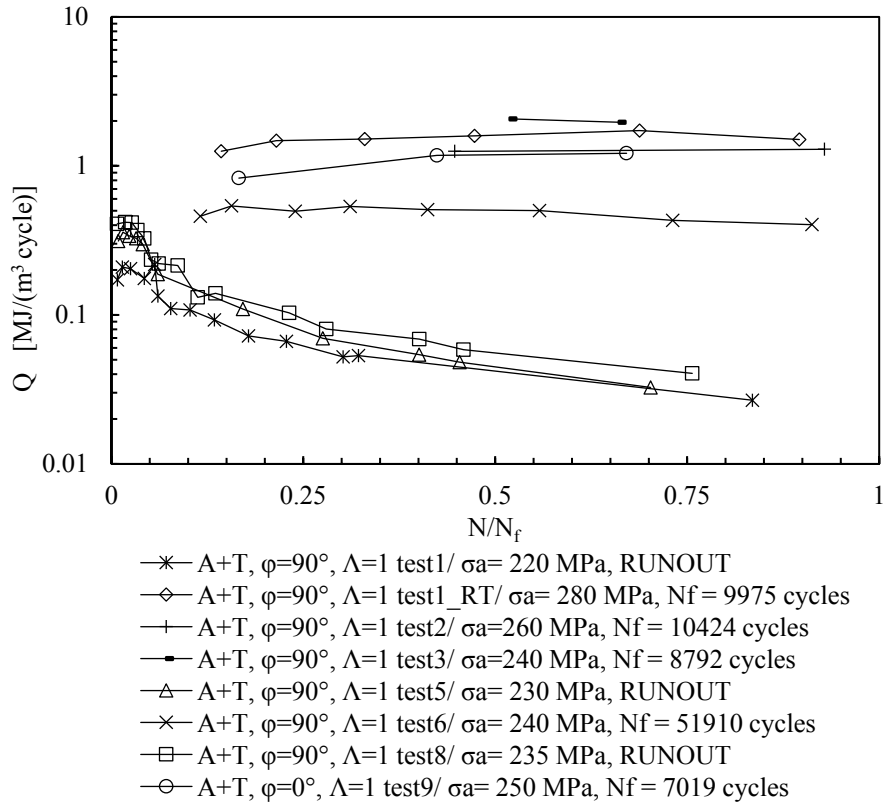


Figure 5.30: Synthesis of Q evolutions during combined bending and torsional fatigue test with $\phi=90^\circ$ and $\Lambda=1$

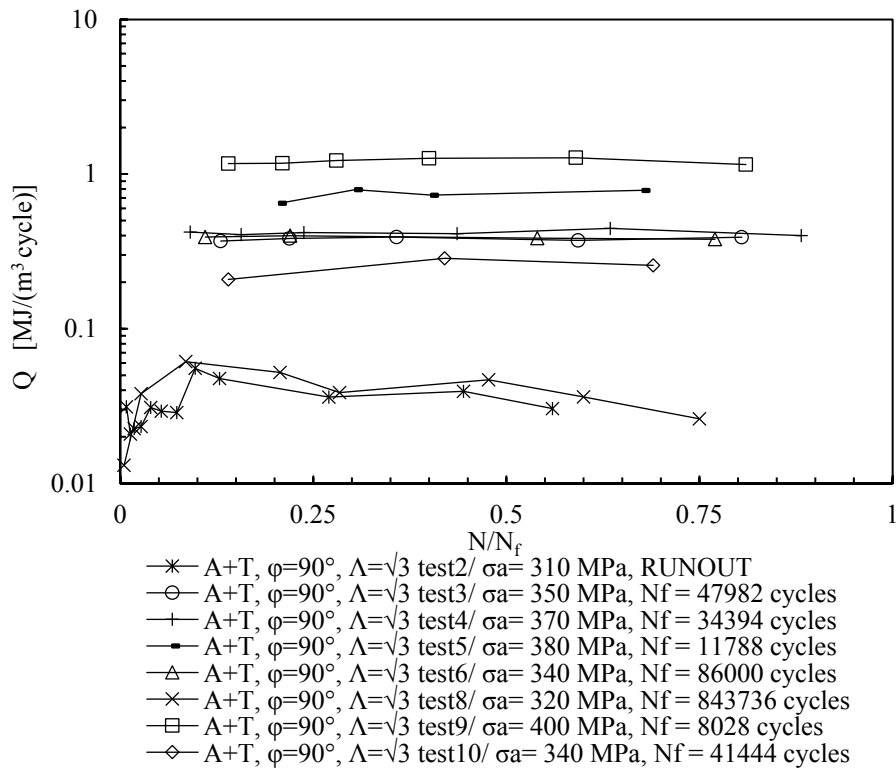


Figure 5.31: Synthesis of Q evolutions during combined bending and torsional fatigue test with $\phi=90^\circ$ and $\Lambda=\sqrt{3}$

5.4.2 Strain energy density dissipated in a cycle ΔW

In one test of each loading condition the strain energy density dissipated in a cycle (ΔW), was evaluated several times during the fatigue test by measuring the strain components with a DIC system.

A typical strain map of both ϵ_{yy} and ϵ_{xy} corresponding to the maximum loads applied in an A+T, $\varphi=0^\circ$ and $\Lambda=1$ test was reported in Fig (32). It's worth noticing that the correlation was carried out in a portion of the frame localised at the net cross-section of the specimen due to the curvature of the surface and for reducing out-of-plane deformation error. Furthermore, the ϵ_{xy} output corresponds to the commonly used definition of tangential strain in continuum mechanics $\gamma_{xy}/2$.

The ϵ_{yy} and ϵ_{xy} (or $\gamma_{xy}/2$) averaged in an area placed at the net cross-section were fitted in the time domain by a cubic spline function in order to eliminate the noise of the cyclic strain measurements. Some examples of the comparison between raw averaged ϵ_{yy} and $\gamma_{xy}/2$ and the relevant fitting are reported in Fig. (33)

After that, the fitted strain components were cross plotted with the relevant stress component and the ΔW was numerically evaluated as follows:

$$\Delta W = \oint_{\text{cycle}} \sigma \cdot d\epsilon = \oint_{\text{cycle}} \sigma_{yy} \cdot d\epsilon_{yy} + 2 \cdot \oint_{\text{cycle}} \tau_{xy} \cdot d(\gamma_{xy}/2) = \Delta W_{\text{axial}} + \Delta W_{\text{tors}} \quad (3)$$

In Fig.s (34-39) shows an example per each loading condition the hysteresis cycles for a certain fraction of fatigue life of the relevant specimen.

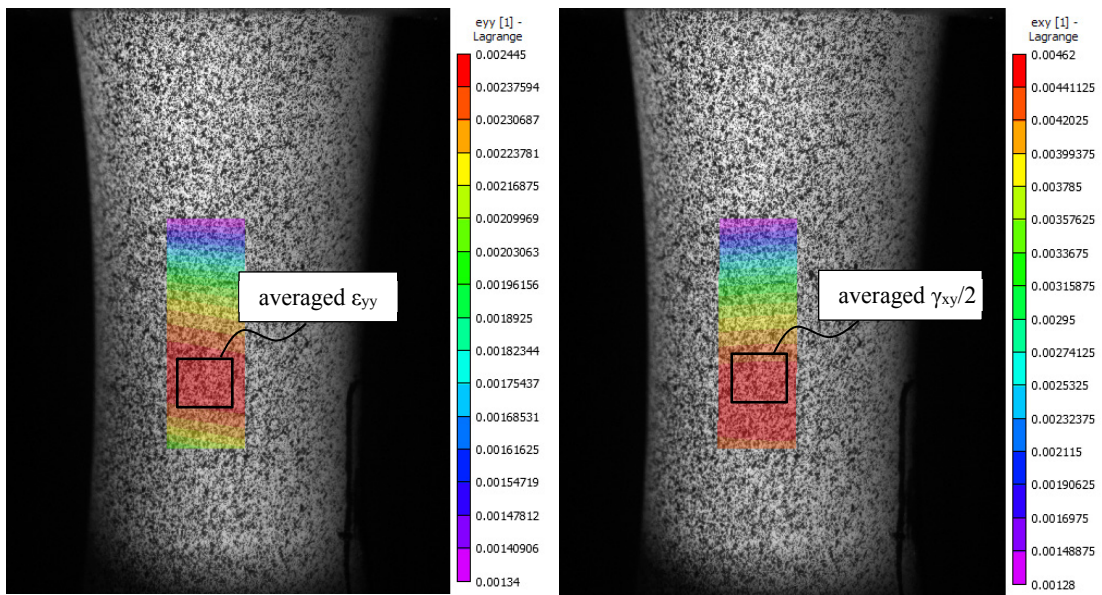


Figure 5.32: Example of strain maps relevant to the fatigue tests A+T, $\varphi=90^\circ$, $\Lambda=\sqrt{3}$ test 8 (See Fig. 28).

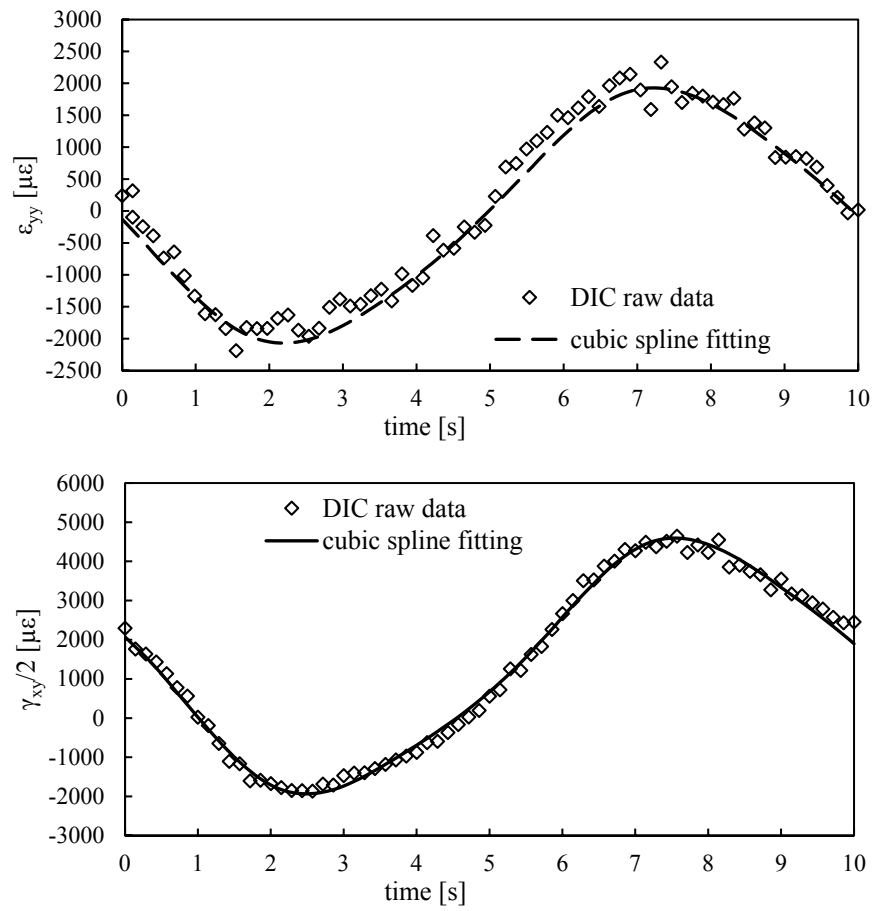


Figure 5.33: Comparison between the raw DIC data and cubic spline fitting of A+T, $\phi=0^\circ$, $\Lambda=1$ test 8 (See Fig. 28).

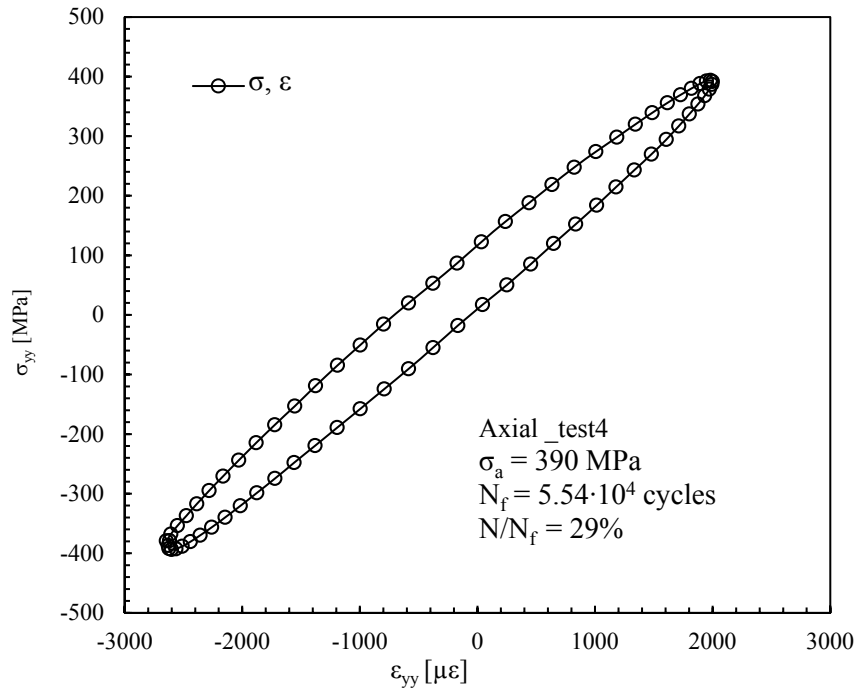


Figure 5.34: Hysteresis cycle during axial fatigue test Axial_test4.

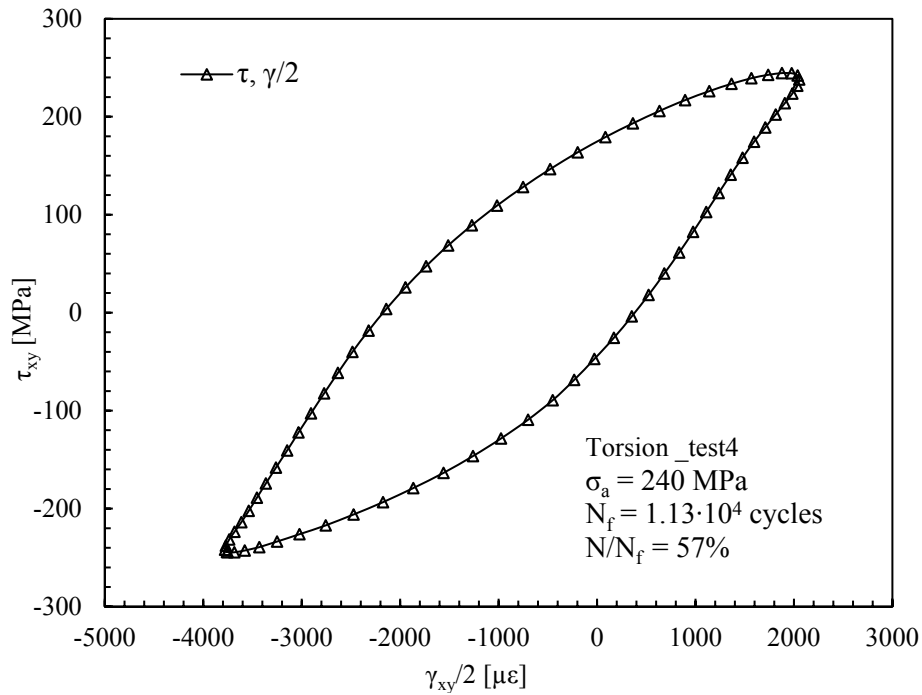


Figure 5.35: Hysteresis cycle during axial fatigue test Torsional_test4 .

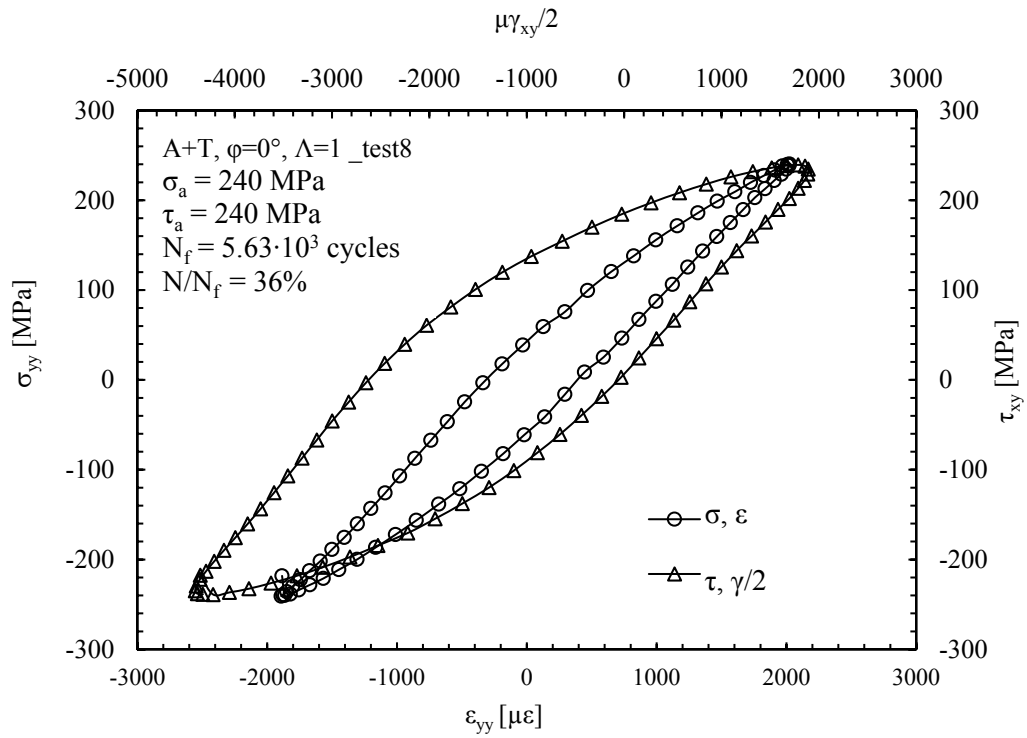


Figure 5.36: Hysteresis cycles during multiaxial fatigue test A+T, $\varphi=0^\circ$, $\Lambda=1$ test 8 .

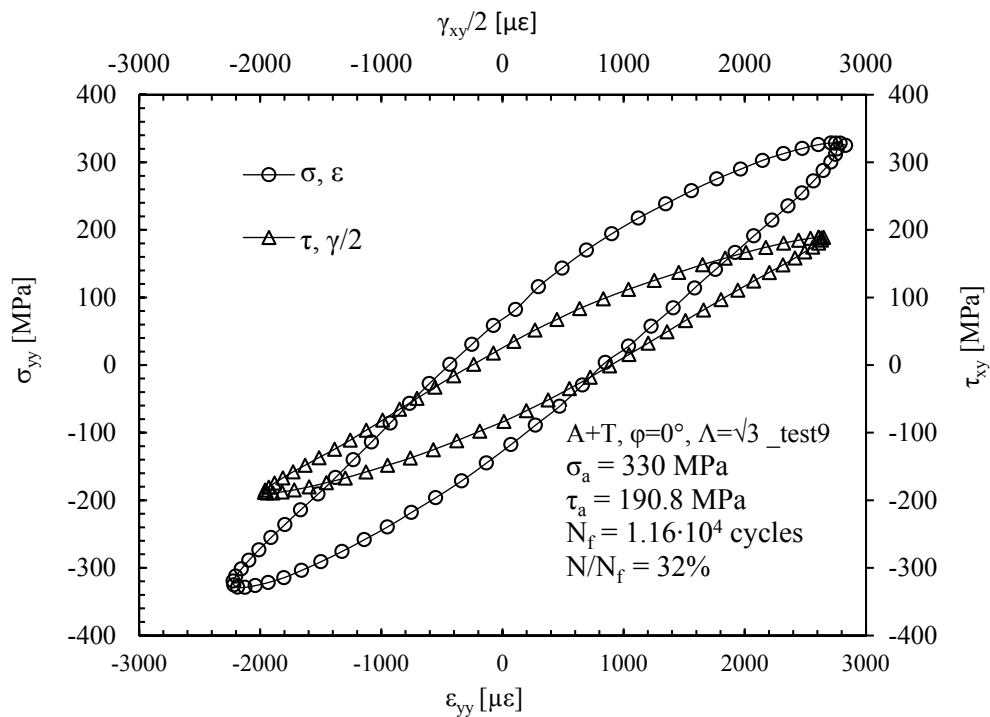


Figure 5.37: Hysteresis cycles during multiaxial fatigue test A+T, $\varphi=0^\circ$, $\Lambda=\sqrt{3}$ test 9

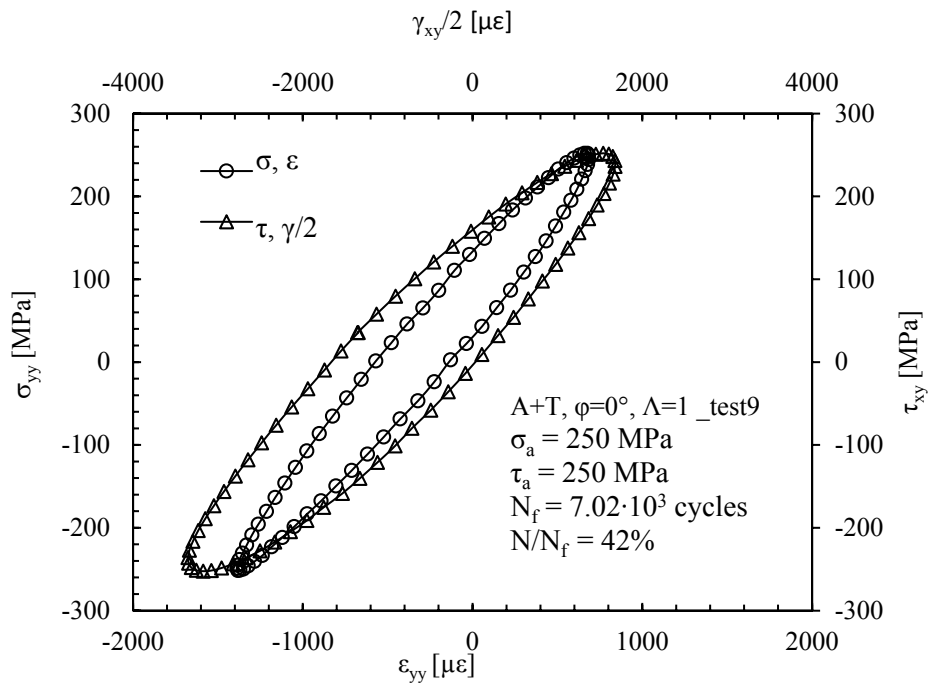


Figure 5.38: Hysteresis cycles during multiaxial fatigue test A+T, $\varphi=90^\circ$, $\Lambda=1$ test 9 (See Fig. 30)

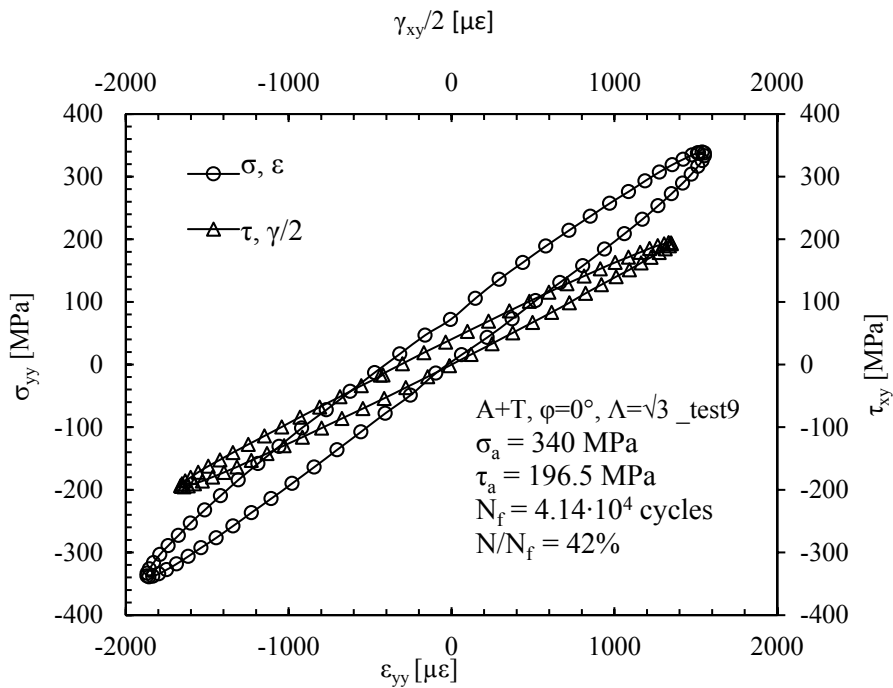


Figure 5.39: Hysteresis cycles during multiaxial fatigue test A+T, $\varphi=90^\circ$, $\Lambda=\sqrt{3}$ test 10 (See Fig. 31)

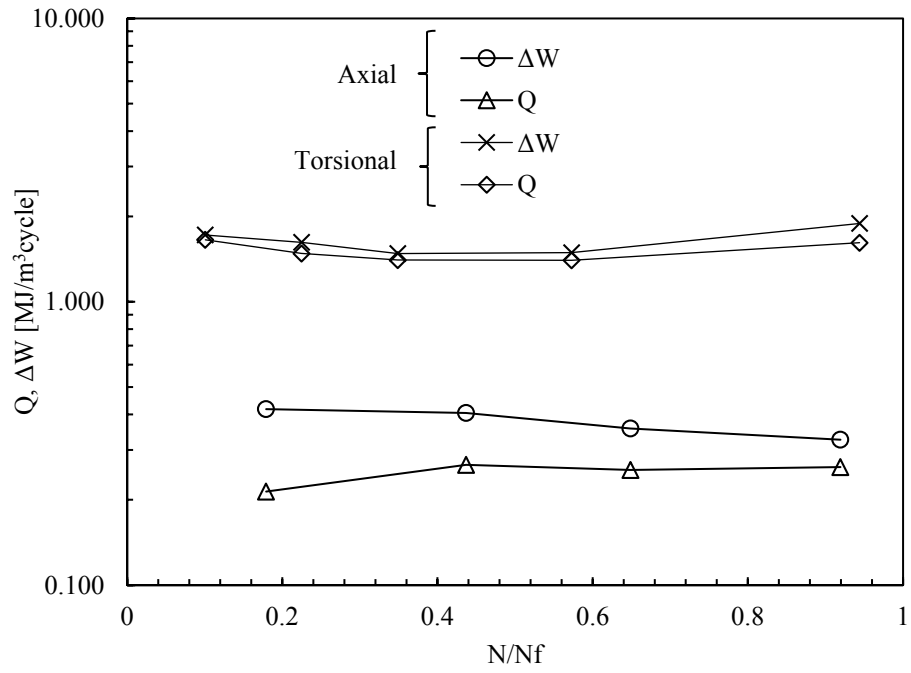


Figure 5.40: Evolution of ΔW and Q during axial and torsional fatigue tests.

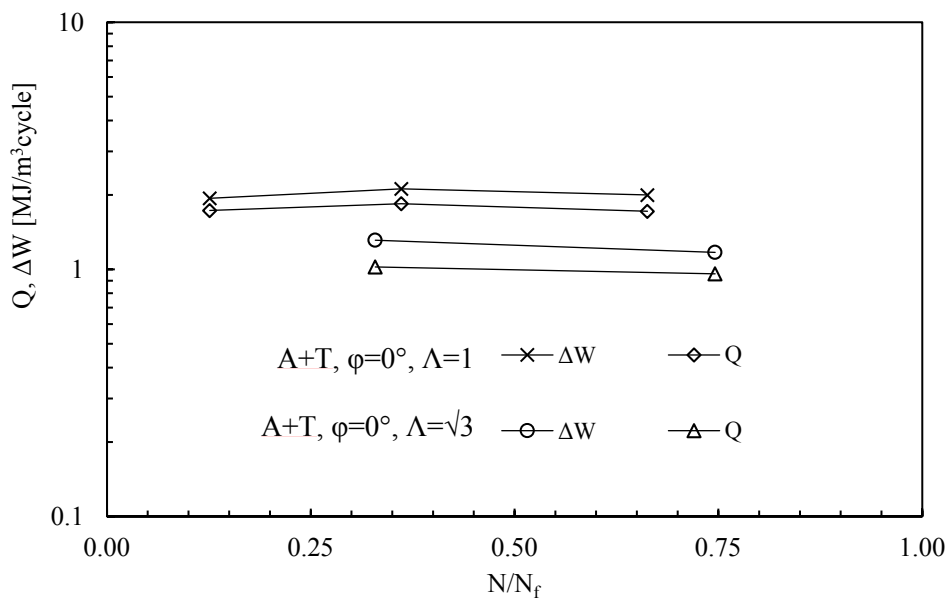


Figure 5.41: Evolution of ΔW and Q during multiaxial fatigue tests subjected to proportional loading condition.

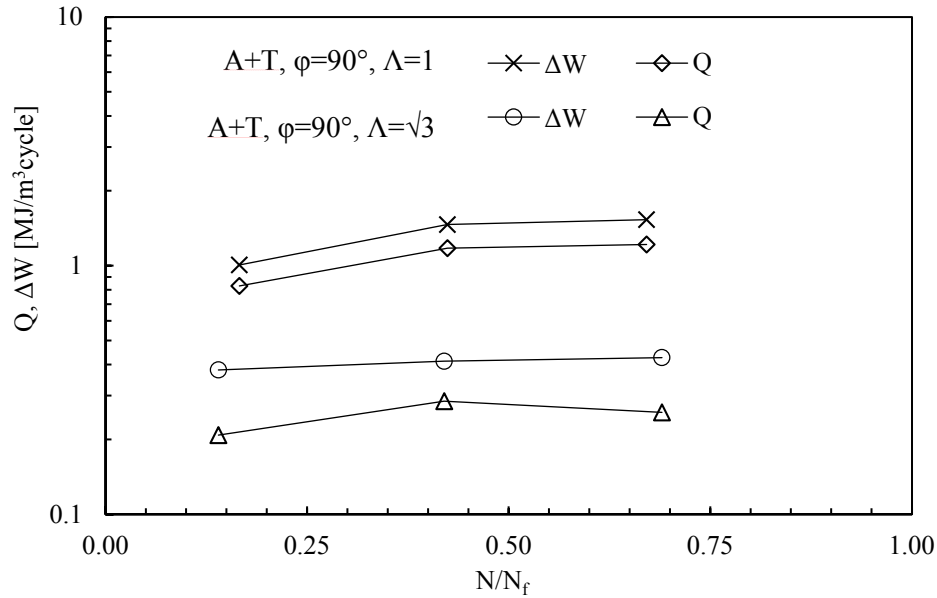


Figure 5.42: Evolution of ΔW and Q during multiaxial fatigue tests subjected to out-of-phase loads.

Table 5.4: Data results of Q and ΔW .

Loading condition	φ [°]	Λ	σ_a [MPa]	τ_a [MPa]	N_f [cycles]	N/N_f	Q [MJ/m ³ cycle]	ΔW [MJ/m ³ cycle]	$Q/\Delta W$ [%]
Axial	/	∞	390	0	$5.5 \cdot 10^4$	0.18	0.214	0.418	51
						0.44	0.266	0.405	66
						0.65	0.255	0.357	71
						0.92	0.261	0.326	80
Torsion	/	0	0	220	$1.6 \cdot 10^4$	0.10	1.654	1.723	96
						0.22	1.480	1.624	91
						0.35	1.403	1.482	95
						0.57	1.401	1.492	94
						0.94	1.615	1.891	85
A+T	0	1	240	240	$5.8 \cdot 10^3$	0.13	1.730	1.94	89
						0.36	1.845	2.12	87
						0.66	1.718	2.00	85
A+T	90	1	250	250	$7.0 \cdot 10^3$	0.17	0.829	1.13	73
						0.42	1.175	1.53	77
						0.67	1.217	1.60	76
A+T	0	1.73	330	190.8	$1.2 \cdot 10^4$	0.33	1.023	1.313	75
						0.75	0.960	1.172	78
A+T	90	1.73	340	196.5	$4.1 \cdot 10^4$	0.14	0.208	0.381	55
						0.42	0.285	0.413	69
						0.69	0.257	0.427	60

The evolutions of ΔW during axial, pure torsion and multiaxial fatigue test were reported in Fig. (38-42), whereas the ratios $Q/\Delta W$ are summarised in Table 4. From Fig. (38-42) it can be observed that the trend of ΔW follows the one relevant to Q and

they are both approximately constant during all fatigue tests. Furthermore, the difference between ΔW and Q seems to depend on the biaxiality ratio. Indeed, the lowest $Q/\Delta W$ (51%) was obtained in axial fatigue tests while the highest one (96%) was measured in pure torsion cyclic test. Intermediate values were obtained in multiaxial loading condition and in particular if Λ is equal to 1, the $Q/\Delta W$ values tend to those obtained in torsional fatigue tests, otherwise, they tend to those obtained in axial fatigue tests. Concerning the phase-shift, about 10 % lower value were observed in out-of-phase loading condition with respect to the proportional load for the same Λ .

Indeed, some studies [14] demonstrate that steels having finer grain size and high hardness value are less sensitive to non-proportional cyclic hardening that can be noted in a further decreasing of strain energy density dissipation as well. Since the 90°-out-of-phase loading generates the maximum degree of non-proportionality because of the wide range slip systems activated caused by continuous rotation of maximum shear plane in all directions, the dislocation in steels having finer grain size cannot split easily with respect to those with coarse grain microstructure [14].

5.4.3 Synthesis of the fatigue test results in terms of Q

In Fig. (44) all the fatigue test results have been expressed in terms of specific heat loss evaluated at half the total fatigue life and compared to the existing heat energy-based scatter band calibrated previously on few axial fatigue test results [13]. On the contrary to the outcomes obtained for AISI 304L steel specimen (Chapter 4), all the fatigue test results on Q+T C45 steel resulted in excellent agreement with the predicting scatter even for out-of-phase loading condition data.

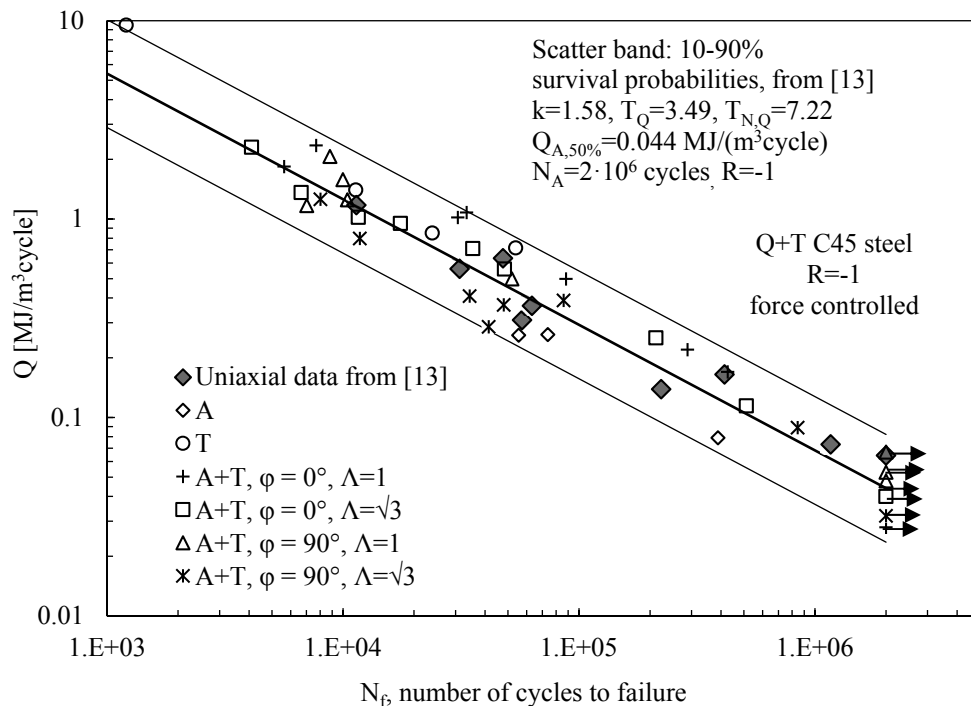


Figure 5.43: Synthesis of fatigue test results in terms of Q , compared to the scatter band calibrated in [13].

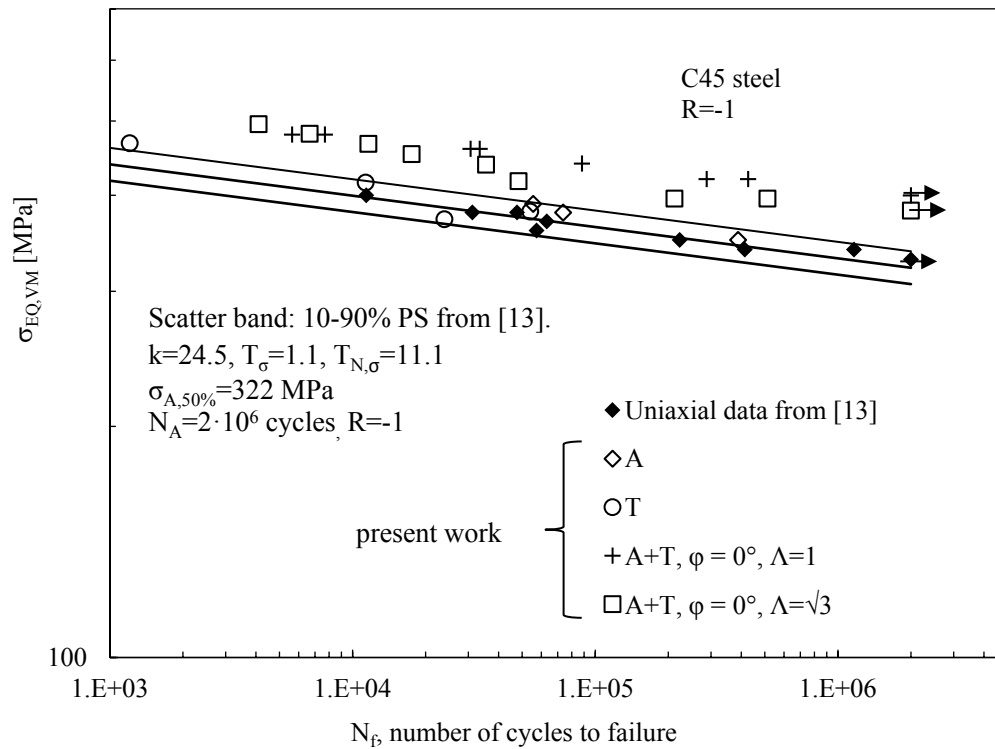


Figure 5.44: Synthesis of fatigue test results in terms of equivalent Von Mises stress amplitude, compared to the scatter band calibrated in [13]

It is worth noticing that the scatter band was calibrated with 8 axial fatigue test results data expressed in terms of energy which lead to an energy-scatter index T_Q equal to 3.49 and a life-scatter index $T_{N,Q}$ equal to 7.22.

For comparative purposes, in Fig. (44) the axial fatigue tests results expressed in terms of nominal stress amplitude with the relevant calibrated scatter band were reported and compared to the fatigue test results obtained in this work expressed in terms of Von Mises equivalent stress amplitude $\sigma_{ea,VM}$ [13]. Since $\sigma_{ea,VM}$ does not include the phase-shift effect, so non-proportional data were not reported in Fig. (44). It is worth noticing that although the sigma scatter index T_σ (Fig. (44)) is about 3 times lower than the energy-based one (T_Q), the life scatter index is 2 times higher than the relevant energy ones. Furthermore, from Fig (44) it can be noted that the torsional fatigue tests in terms of $\sigma_{ea,VM}$ are synthesised in the stress-based scatter, whereas the predictions are conservative of about a factor 46 in fatigue life considering the proportional multiaxial fatigue test results.

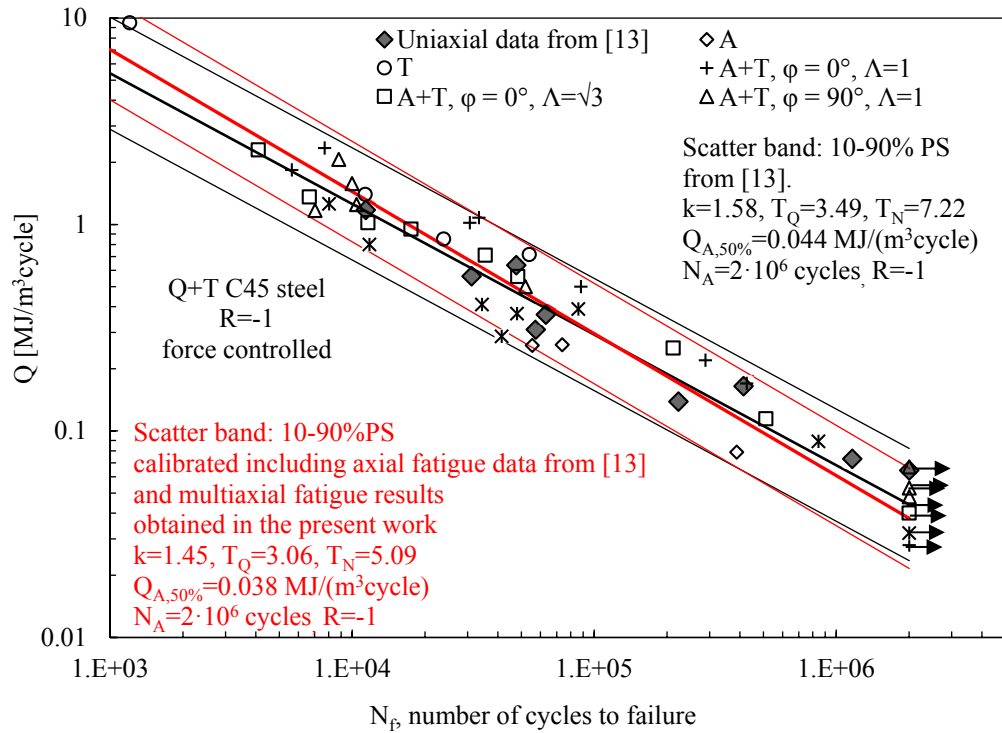


Figure 5.45: Comparison with the scatter band previously calibrated in [13], and that one calibrated on all the data obtained in the present work.

In order to validate the energy-scatter band previously calibrated in [13], a new one was statistically evaluated on all the data obtained in the present work and axial data from taken from [13] and reported in Fig. (45). It is worth noticing that the scatter indexes T_Q and $T_{N,Q}$ were reduced to 3.06 and 5.09, respectively. Slightly changes were also obtained both in inverse slope k and in Q limit of 50% of survival probability $Q_{A,50\%}$. However, the new energy-based scatter band is included in the previous one demonstrating the capability of the specific heat loss per cycle to synthesise uniaxial as well as multiaxial loading condition at least for the present material.

5.5 DISCUSSION

As already stated in the paragraph “Discussion” of Chapter 3, the Q evaluation by using the cooling gradient technique requires validations in order to highlight the capability and any limitations of the method. In Chapters 4 and 5, an huge amount of data were obtained to extend the applicability of the method to multiaxial stress state.

In addition to the advantages and limitations summarised in Chapter 3, an update has been reported in the following:

- the Q parameter can also synthesise multiaxial fatigue test results on materials which are not sensitive to change of phase due to plastic deformation (like the C45 steel) in the same scatter band calibrated on few

axial fatigue data. This is currently valid for the multiaxial loading condition analysed in the present work.

- It was demonstrated that most of the mechanical input energy is dissipated as heat for the C45 steel.

However, in the case of multiaxial fatigue tests carried out on AISI 304L stainless steel (sensitive to strain-induced martensitic transformation during multiaxial fatigue test), the method is still valid only in the LCF regime.

5.6 CONCLUSIONS

In this work, the specific heat loss per cycle (Q parameter) was experimentally evaluated for the first time on thin-walled quenched and tempered C45 steel specimens subjected to multiaxial cyclic loads. Force-controlled axial, torsional and combined axial-torsional completely reversed fatigue tests were carried out considering both proportional ($\varphi = 0^\circ$) and out-of-phase ($\varphi = 90^\circ$) loading conditions adopting two different biaxiality ratios ($\Lambda = \sigma_a/\tau_a = 1$ and $\Lambda = \sqrt{3}$). In addition, in some tests the strain energy density dissipated per cycle ΔW by adopting a Digital Image Correlation DIC system synchronized with the load cells of the test machine in order to verify how much of the mechanical input energy is dissipated as heat.

Having imposed the 50% of stiffness loss as a failure criterion, the crack paths at failure were analysed by using a digital microscope and they were oriented to the maximum shear strain plane for all the loading conditions except in some cases related to 90° out-of-phase loading condition.

After having measured the specific heat loss during individual fatigue tests, it was noted that as regards the tests characterized by a number of cycles to failure ranging from 10^3 and $3 \cdot 10^5$, Q is approximately constant during the whole tests, whereas for a number of cycles to failure ranging from $3 \cdot 10^5$ and 10^6 it tends to stabilise after one third of total life. Different behavior between runout fatigue tests with $\Lambda = 1$ and $\Lambda = \sqrt{3}$ was observed. The Q evolutions of runout specimens subjected to multiaxial $\Lambda = 1$ (Fig. (28) and (30)) presented high values at the beginning of the test and then they decreased until $2 \cdot 10^6$ cycles. Conversely, runout fatigue tests with $\Lambda = \sqrt{3}$ showed an initial increment until they reach a maximum value at about 20% of $2 \cdot 10^6$ cycles and then a slight decrease occurred. These behaviors of Q in runout tests can be attributed to the fact that having set the runout at $2 \cdot 10^6$ cycles, the stabilized Q value could be reached for a higher number of cycles to failure assuming that the plateau of the nominal stress amplitude fatigue curve occurs at about 10^7 cycles.

As regards the ΔW measured on one fatigue test per each loading condition, it resulted approximately constant during fatigue as the relevant Q value. In particular, the evolutions of the ratio $Q/\Delta W$ show a dependency on the biaxiality ratio, Λ , in which the lowest value was observed in axial fatigue test while the highest in torsional fatigue test.

All fatigue test results have been summarised in terms of specific heat loss taken at half the total fatigue life versus the number of cycles to failure and have been compared with the scatter band previously calibrated on few axial fatigue tests on the same material. An excellent agreement between all experimental data and the predicting scatter band was observed.

5.7 REFERENCES

- [1] Rigon D, Formilan V, Meneghetti G. Analysis of the energy dissipation in multiaxial fatigue tests of AISI 304L stainless steel bars. *Procedia Struct Integr* 2018;13:1638–43. doi:10.1016/j.prostr.2018.12.344.
- [2] Meneghetti G, Ricotta M, Atzori B. A synthesis of the push-pull fatigue behaviour of plain and notched stainless steel specimens by using the specific heat loss. *Fatigue Fract Eng Mater Struct* 2013;36:1306–22. doi:10.1111/ffe.12071.
- [3] Pegues JW, Shao S, Shamsaei N, Schneider JA, Moser RD. Cyclic strain rate effect on martensitic transformation and fatigue behaviour of an austenitic stainless steel. *Fatigue Fract Eng Mater Struct* 2017;40:2080–91. doi:10.1111/ffe.12627.
- [4] Yu D, An K, Chen Y, Chen X. Revealing the cyclic hardening mechanism of an austenitic stainless steel by real-time in situ neutron diffraction. *Scr Mater* 2014;89:45–8. doi:10.1016/J.SCRIPTAMAT.2014.06.021.
- [5] Bayerlein M, Christ H-J, Mughrabi H. Plasticity-induced martensitic transformation during cyclic deformation of AISI 304L stainless steel. *Mater Sci Eng A* 1989;114:L11–6. doi:10.1016/0921-5093(89)90871-X.
- [6] Ye D, Xu Y, Xiao L, Cha H. Effects of low-cycle fatigue on static mechanical properties, microstructures and fracture behavior of 304 stainless steel. *Mater Sci Eng A* 2010;527:4092–102. doi:10.1016/J.MSEA.2010.03.027.
- [7] Dey R, Tarafder S, Sivaprasad S. Influence of phase transformation due to temperature on cyclic plastic deformation in 304LN stainless steel. *Int J Fatigue* 2016;90:148–57. doi:10.1016/J.IJFATIGUE.2016.04.030.
- [8] Zeng W, Yuan H. Mechanical behavior and fatigue performance of austenitic stainless steel under consideration of martensitic phase transformation. *Mater Sci Eng A* 2017;679:249–57. doi:10.1016/J.MSEA.2016.10.005.
- [9] Smaga M, Walther F, Eifler D. Deformation-induced martensitic transformation in metastable austenitic steels. *Mater Sci Eng A* 2008;483–484:394–7. doi:10.1016/J.MSEA.2006.09.140.
- [10] Das A. Dislocation configurations through austenite grain misorientations. *Int J Fatigue* 2015;70:473–9. doi:10.1016/J.IJFATIGUE.2014.06.012.
- [11] Das A, Sivaprasad S, Chakraborti PC, Tarafder S. Morphologies and characteristics of deformation induced martensite during low cycle fatigue behaviour of austenitic stainless steel. *Mater Sci Eng A* 2011;528:7909–14. doi:10.1016/J.MSEA.2011.07.011.
- [12] McDowell DL, Stahl OK, Stock SR, Antolovich SD. Biaxial path dependence of deformation substructure of type 304 stainless steel. *Metall Trans A* 1988;19:1277–93. doi:10.1007/BF02662589.
- [13] Meneghetti G, Ricotta M, Atzori B. A two-parameter, heat energy-based approach to analyse the mean stress influence on axial fatigue behaviour of

- plain steel specimens. *Int J Fatigue* 2016;82:60–70.
doi:10.1016/j.ijfatigue.2015.07.028.
- [14] Shamsaei N, Fatemi A. Effect of microstructure and hardness on non-proportional cyclic hardening coefficient and predictions. *Mater Sci Eng A* 2010;527:3015–24. doi:10.1016/j.msea.2010.01.056.

Chapter 6: Analysis of defects influence on structural durability of maraging steel specimens produced by additive manufacturing

The effect of building orientation and ageing heat treatment on the fatigue strength of the first batch of additively manufactured (AMed) maraging steel specimens will be summarized in the introduction of this chapter. The main outcome of this preliminary study highlighted the importance of adopting a local damage parameter due to the presence of defects within AMed materials, such as the maraging steel, here considered. Since the defects can be considered as a short crack-like, Linear Elastic Fracture Mechanic (LEFM) approaches are more suitable than classical nominal approaches to characterize the fatigue behavior of AMed material. Therefore, Stress Intensity Factor (SIF) based on the Murakami's parameter \sqrt{area} was selected as a fatigue damage parameter.

New axial fatigue tests were carried out on three batches of AMed maraging steel specimens produced by two different AM systems (EOS GmbH and SISMA SpA). Furthermore, axial fatigue tests were carried out on wrought maraging steel specimens both in annealed and in aged condition. After failure, the \sqrt{area} of the killer defects was examined by SEM observations of the fracture surfaces. A stress intensity factor-based design curve for all the test series was obtained taking into account the short crack effect by means of the El-Haddad-Smith-Topper model. Due to the lack of expensive experimental data to determine the relevant material length parameter a_0 , a novel rapid method to approximately evaluate a_0 has been proposed. In particular, it consists in matching El-Haddad-Smith-Topper model with Murakami's expression of the threshold range of mechanically short cracks. The advantage of the adopted engineering approach is that only Vickers hardness of the material is necessary. Theoretically, this rapid method can be also adopted to estimate the size of the control volume of the averaged SED approach due to the analogy of the latter to the material length parameter a_0 . In the end, the stress intensity factor-based design curve was adopted to estimate the fatigue strength of sharp V-shaped notches characterized by a reduced notch opening angle.

This chapter is referred to the following author's papers:

[1] Meneghetti G, Rigon D, Cozzi D, Waldhauser W, Dabalà M. Influence of build orientation on static and axial fatigue properties of maraging steel specimens produced by additive manufacturing. *Procedia Struct Integr* 2017;7:149–57. doi:10.1016/j.prostr.2017.11.072.

[2] Meneghetti G, Rigon D, Gennari C. An analysis of defects influence on axial fatigue strength of maraging steel specimens produced by additive manufacturing. *Int J Fatigue* 2019;118:54–64. doi:10.1016/j.ijfatigue.2018.08.034.

6.1 INTRODUCTION

Maraging steels grade 300 (or 18Ni 300) is a high-strength material adopted in aeronautical and tool fields for its superior properties such as high ductility, high yield stress, good hardenability, good weldability and simple heat treatment without deformations. Maraging steel 300 is also one of the materials that can be produced by additive manufacturing systems.

Several studies can be found on literature about the influence of the main process parameter on mechanical properties [3], the influence of the building orientation on rotating bending High Cycle Fatigue (HCF) [4] as well as on Low Cycle fatigue strength of AMed maraging steels [5].

According to the authors knowledge, there is a lack of data in the literature concerning axial fatigue strength of AMed maraging steel. Therefore, in a recent paper [1] tensile static tests and fully reversed ($R = -1$), load-controlled axial fatigue tests were performed on cylindrical specimens additively manufactured by DMLS by adopting EOS maraging steel MS1 powder, whose chemical composition is reported in Table 1. The adopted specimen's geometry is shown in Fig.1a. Specimens were manufactured by using an EOSINT M280, adopting a set of parameters called "Performance 1.0" as optimized by EOS GmbH with the aim of obtaining the best compromise between the manufacturing time and the resulting mechanical properties as stated in the AM system datasheet.

The specimens were built with their axis oriented at 0° and 90° with respect to the building direction (Z-axis Fig. (1b)), by setting a layer thickness equals to $40 \mu\text{m}$, a laser power of 400 W. After manufacturing, half of the specimens, i.e. 24 specimens, were subjected to age hardening heat treatment at 490°C for 6 hours, followed by air cooling as recommended by the powder manufacturer, while the remaining half of them were kept in as-built conditions.

Table 6.1: Chemical composition of EOS maraging steel MS1 powder from technical EOS datasheet.

Fe	Ni	Co	Mo	Ti	Al	Cr	Cu	C	Mn	Si	P	S
(wt-%)	(wt-%)	(wt-%)	(wt-%)	(wt-%)	(wt-%)	(wt-%)	(wt-%)	(wt-%)	(wt-%)	(wt-%)	(wt-%)	(wt-%)
balance	17-19	8.5-9.5	4.5-5.2	0.6-0.8	0.05-0.15	≤ 0.5	≤ 0.5	≤ 0.03	≤ 0.1	≤ 0.1	≤ 0.01	≤ 0.01

Then, the specimens were detached from the building platform by using a liquid-cooled band saw and after that, the lattice supports were removed by using an abrasive grinding wheel. The specimen's surface has been accurately polished by using progressively finer emery paper, starting from grade 100 up to grade 800.



Figure 6.1: Specimen's geometry adopted for tensile static and fatigue tests on maraging steel produced by DMLS, and (b) two building platforms with the specimens produced by DMLS having specimen's axis oriented at 0° and 90° with respect to the building direction (z axis). [1]

Due to residual stresses formed during the manufacturing process, specimen distortions were observed after detaching them from the platform. Therefore, the resulting deflection f_a (see Fig. (2a)) was measured by clamping one side of each specimen and by using a digital dial gauge in contact with the opposite side of the specimen. Distortion caused a secondary bending when specimens are clamped in the axial test machine grips, thus resulting in a mean axial strain, which was measured by using KYOWA strain gauges having a gauge length of 3 mm. Strain measurements were performed only for selected specimens having different values of deflection f_a so that the relation between f_a and the mean strain could be determined. The strain gauges have been applied in the middle of the specimen at locations A and B, as shown in Fig. (2a-b).

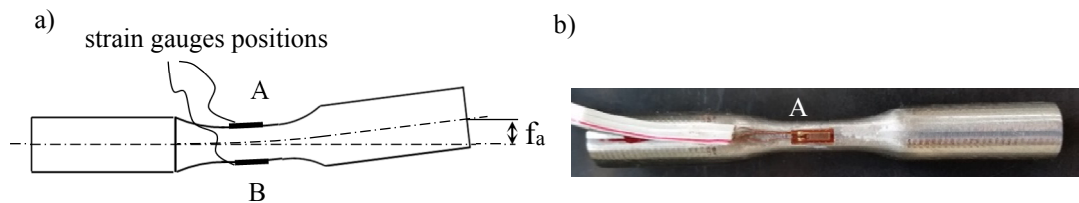


Figure 6.2: (a) Location of strain gauges adopted to evaluate the correlation between deflection f_a and mean axial strain induced by clamping in the axial machine grips and (b) example of a specimen with a strain gauge placed at point A. [1]

Each test series can be identified according to the nomenclature $AD_{0^\circ/90^\circ}_{NT/T_specimen's_number}$, where AD represents the additively manufactured series, 0° and 90° are the orientations of the building directions with respect to the specimen's longitudinal axis, while NT and T identify the series tested in the as-built and in the heat-treated conditions, respectively.

The range of R_a and the deflection f_a values as obtained for each test series are summarized in Table 2. It should be noted that the deflection values f_a obtained from heat-treated specimens (T) were lower than those obtained from as-built specimens since residual stresses induced by DMLS process are likely to be relieved by the aging treatment.

Table 6.2: Roughness and deflection range values. [1]

Series identifier	R_a^* [μm]	f_a° [mm]
AD_0°_NT_#	0.45-0.77	0.22-1.03
AD_0°_T_#	0.53-0.52	0.11-0.25
AD_90°_NT_#	0.36-0.56	0.58-0.98
AD_90°_T_#	0.25-0.57	0.27-0.57

* Measurements carried out for 5 specimens per series

° Measurements carried out for all specimens

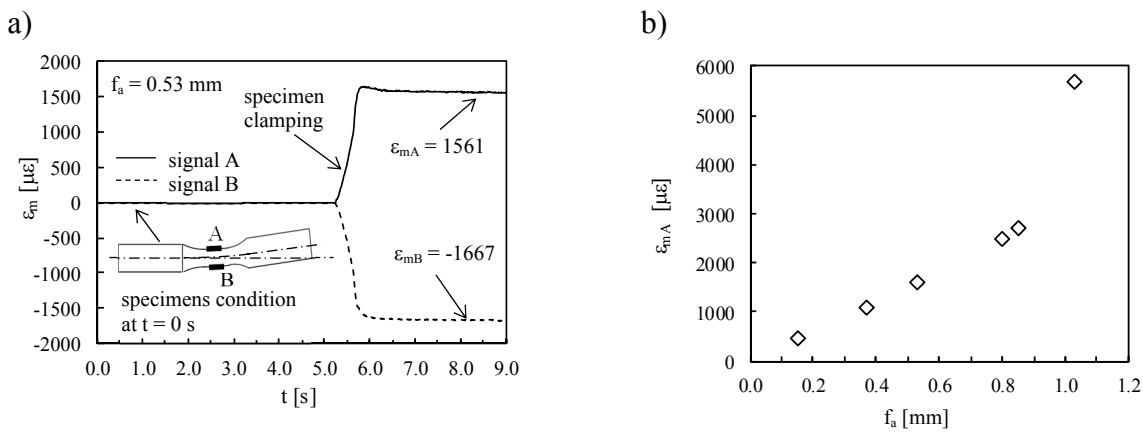


Figure 6.3: (a) An example of strain measurement at the midpoint of the inner side of the specimen curvature (point A) and at the opposite side (point B) during the specimen clamping on the test machine and (b) correlation between mean strain measurements at point A and deflection f_a for selected specimens. [1]

Fig. (3a) reports the strain measurements at points A and B referred to a specimen with $f_a = 0.53$ mm before and after clamping. As expected, after clamping plane bending was induced, being ϵ_m almost equal in modulus but with opposite sign at points A and B. Fig. (3b) reports the correlation between the axial strain ϵ_{mA} as measured at point A and the bending deflection f_a for selected specimens.

6.1.1 Static mechanical properties of AMed maraging steel 300

A tensile stress-strain curve obtained from the static test of one specimen for each test series is reported in Fig. (4a). The starting point of the dashed lines is the point when the extensometer was removed, as its full scale having been achieved. The mechanical properties obtained from the tensile tests are reported in Fig. (4b) for each test series. As a result, the Young's modulus E , the yield strength $\sigma_{p,02}$ and the ultimate tensile strength σ_R were in good agreement with those reported in [3]. Fig. 4b also reports the values of elongation after fracture ϵ_R , which were higher than those reported in [3].

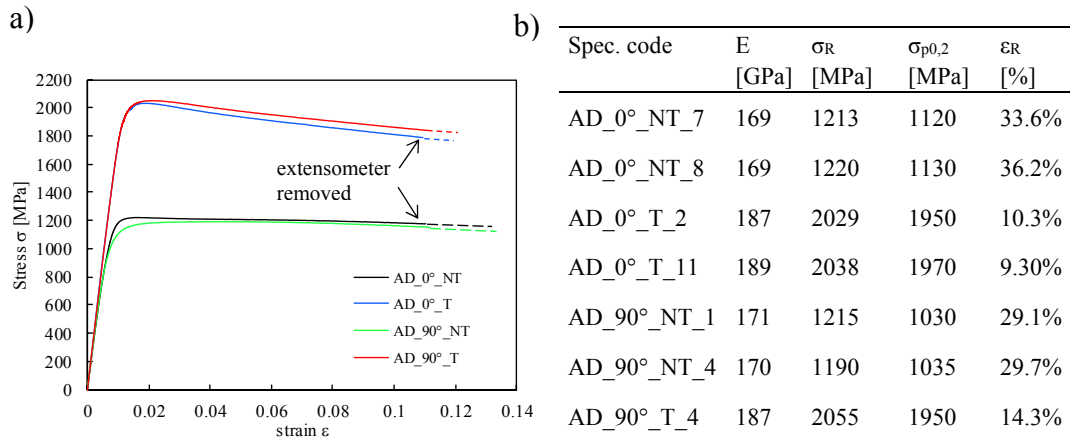


Figure 6.4: (a) Stress-strain curves of the DMLS specimens tested in the as-built (not-treated NT) and aged (treated T) conditions with different building orientation (0° and 90°) and (b) summary of mechanical properties. [1]

6.1.2 Fatigue strength of AMed maraging steel 300

The experimental results obtained from fully reversed ($R=-1$) load-controlled fatigue tests, were presented in Fig. (5a) for the four tests series in terms of nominal stress amplitude. In order to take into account the different mean stresses caused by specimens' distortion illustrated previously, the SWT parameter was evaluated for each specimen at the crack initiation point (Fig (5b)) [6].

For comparison purposes, Fig. (5a) and (b) reported also push-pull axial fatigue data relevant to vacuum melted maraging steel 300 in dry argon environment [7], tested under both annealed (1 h at 820°C air-cooled) or annealed followed by aged condition (3 h at 480°C air-cooled). In Fig. (5b) it is worth noting that the AM fatigue test results are closer to the results of the vacuum melted maraging steel with respect to those in terms of nominal amplitude stress, but the scatters of the single series are not decreased. More precisely, by taking the fatigue strengths at $5.0 \cdot 10^5$ cycles as reference values, the test series AD_0°_NT and AD_90°_NT show 72% and 33% lower fatigue strength with respect to that of vacuum melted maraging in the annealed condition, respectively. The test series AD_0°_T and AD_90°_T show 68% and 61% lower fatigue strengths as compared to that of vacuum melted maraging steel in annealed followed by age-hardened conditions.

However, it was highlighted that some DMLS specimens showed a premature fatigue failure as compared to the trend shown by the other tested specimens belonging to the same test series. An inspection of the fracture surfaces has been carried out by means of a stereoscopic microscope to investigate these particular cases. Analyzing the fracture surfaces of two specimens of the series AD_90°_NT subjected to the same amplitude stress level and having approximately the same f_a (i.e. the same superimposed mean stress), one of them underwent premature failure due to a surface defect relatively larger than the one found on the other fracture surface (see Fig (6a)

and Fig. (6b)). Consequently, the local evaluated SWT parameter is not able to reduce the scatter of the fatigue test results.

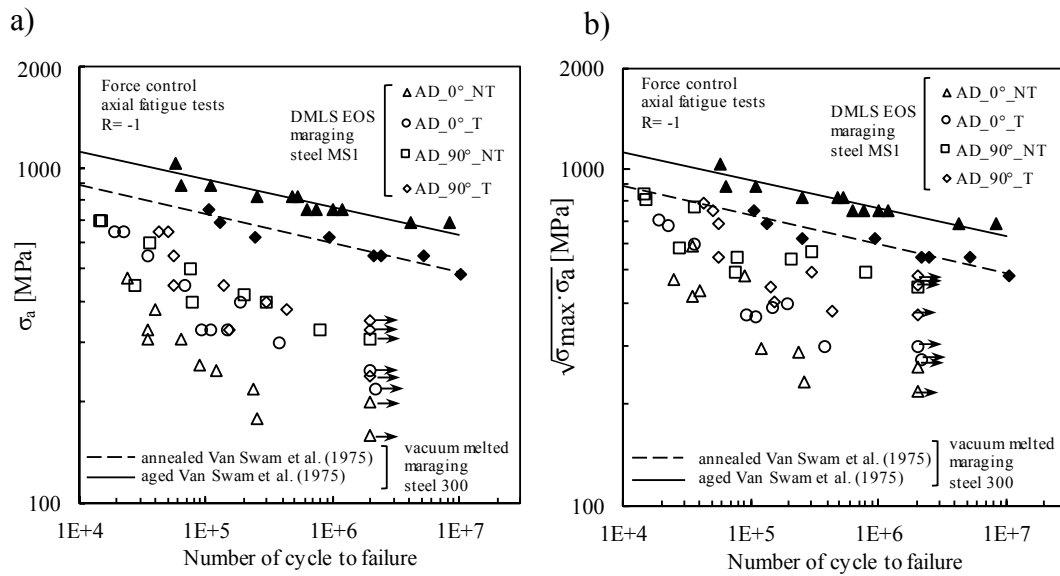


Figure 6.5: (a) Fatigue test results in terms of nominal stress amplitude for the DMLS specimens tested in the as-built (not-treated NT) and aged (heat-treated T) conditions with different building orientations (0° and 90°). Comparison with fatigue test results obtained by [7] by testing vacuum melted maraging steel 300 under push-pull axial loading. (b) Fatigue test results in terms of SWT parameter evaluated individually at the crack initiation point of the specimens. [1]

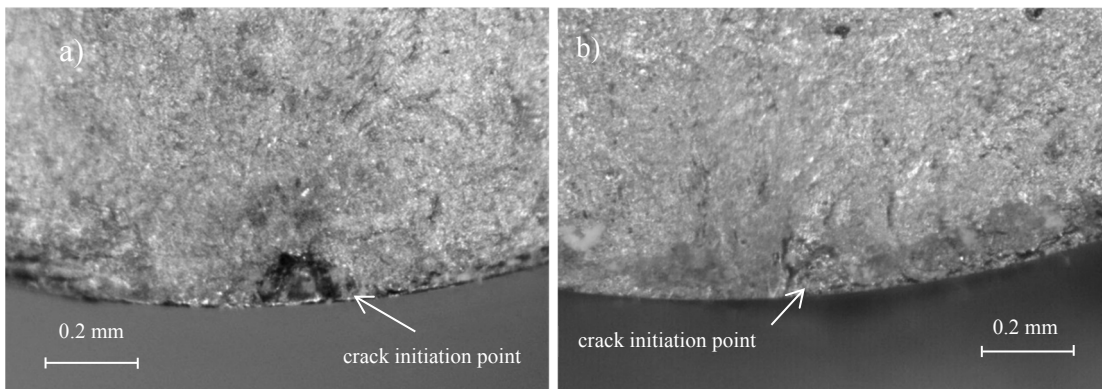


Figure 6.6: Crack initiation point analysed by means of a stereoscopic microscope for: (a) AD_90°_NT specimen subjected to $\sigma_a = 400$ MPa, having $f_a = 0.73$ mm, and failed at $7.75 \cdot 10^4$ cycles, and (b) AD_90°_NT specimen subjected to $\sigma_a = 400$ MPa, having $f_a = 0.85$ mm, and failed at $2.99 \cdot 10^5$ cycles. [1]

In the light of the above, in this chapter further axial fatigue tests results will be proposed on three new batches of AMed maraging steel specimens produced by two different AM system (EOS GmbH and SISMA SpA) as well as on wrought maraging steel specimens both in annealed and in aged condition for comparison purposes. The effect of geometrical distortions was removed by machining the gross ends of the specimens prior to testing in the axial test machine. Defects which caused fatigue crack initiation were analysed after failure by using Scanning Electron Microscope (SEM)

short crack-corrected stress intensity factors were adopted to re-analyse the experimental results.

6.2 THEORETICAL BACKGROUND

It is known that short cracks present lower threshold values of SIF range than long cracks. The smooth transition from long crack to short crack regime as a function of the crack length is illustrated by the Kitagawa-Takahashi diagram [8] (see Fig. (7a)), in with $\Delta\sigma_{g,th}$ is the stress range at the threshold, ΔK_{th} is the stress intensity factor range at the threshold of long cracks. As regards small defects, it was demonstrated that the maximum stress intensity factor along the tip of 2D elliptical defects is proportional to the \sqrt{area} parameter [9–11] in which *area* is the projected area of the 2D defect in a plane normal to the stress flow. Therefore, the Kitagawa-Takahashi diagram was confirmed by Murakami taking into account the influence of natural as well as artificial small defects on constant amplitude fatigue limit of metal materials by adopting the \sqrt{area} parameter instead of short crack length, *a* [12]. In particular for 3D defects, *area* is the projected area of the 3D volume of the defect in a plane normal to the stress flow) [12].

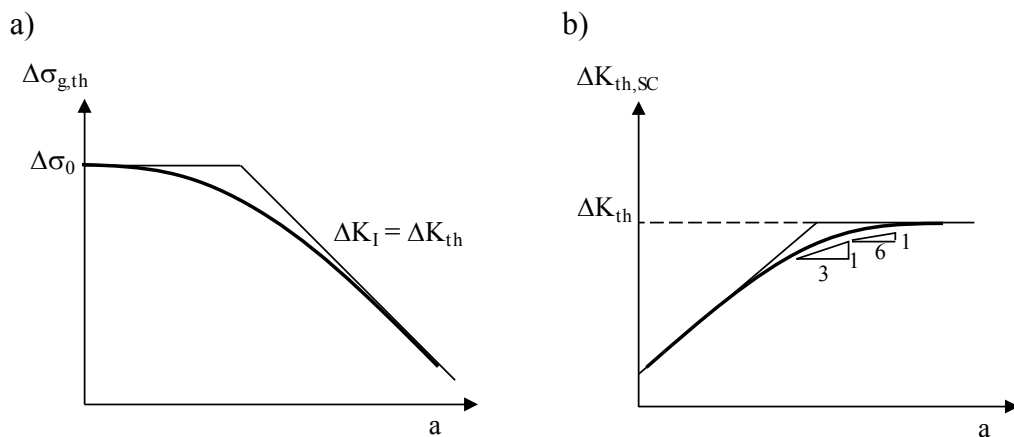


Figure 6.7: Effect of defects size on threshold stress and stress intensity factor [8,12].

The diagram reflecting the Kitagawa-Takahashi diagram is reported in Fig. (7b), which shows the increasing behaviour of the threshold range of the stress intensity factor for short cracks. In the range of defect size $10 \mu\text{m} < \sqrt{area} < 1000 \mu\text{m}$, Murakami found a correlation between the influence of material microstructure on the threshold stress intensity factor range by using simply the Vickers hardness HV and the $\Delta K_{th,SC}$ (short crack-like SC), according to Eq. (1) [12]:

$$\Delta K_{th,SC} = 3.3 \cdot 10^{-3} \cdot (HV + 120) \cdot (\sqrt{area})^{1/3} \quad (1)$$

In the previous expression, $\sqrt{\text{area}}$ is in [μm] and $\Delta K_{\text{th,SC}}$ is in [$\text{MPa}\cdot\sqrt{\text{m}}$].

Incidentally, by using arguments based on the geometrical scale effect, Atzori and Lazzarin [13,14] reasoned that small rounded defects become standard macro-notches as their absolute dimensions increase while keeping the shape unchanged. Therefore, a new diagram was proposed, which includes also sharp/blunt U-shaped notches, besides short/long cracks. An extension of this diagram was later proposed and validated by Atzori, Lazzarin and Meneghetti [15], by including further sharp/blunt V-shaped notches. The diagram proposed by Atzori, Lazzarin and Meneghetti was conceived by taking advantage of non-conventional extensions to sharp V-notches of the Linear Elastic Fracture Mechanics. Such extensions are based on William's solution, who provided the stress singularity exponents of the linear elastic stress distributions close to sharp V-notches [16], and on the Notch-Stress Intensity Factors defined by Gross and Mendelson [17].

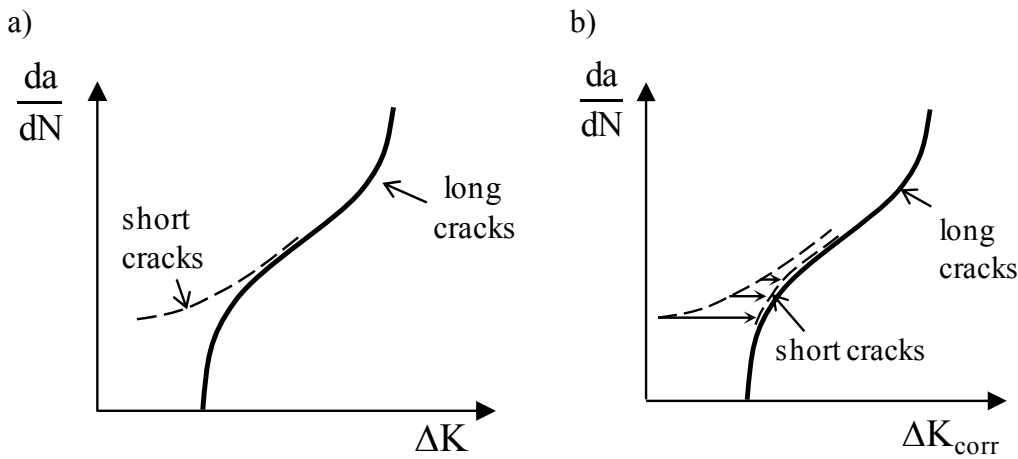


Figure 6.8: Comparison between short crack and long crack behaviour [18,19].

Back to the short crack effect, the higher crack propagation rate exhibited by short cracks, as compared to long cracks subjected to the same linear elastic stress intensity factor range (see the sketch reported in Fig. (8a)) was investigated by El-Haddad, Smith and Topper. They proposed to account for the short crack effect by means of the following 'short crack-corrected' stress intensity factor range ΔK_{corr} [18,19]:

$$\Delta K_{\text{corr}} = \Delta \sigma_g \cdot \sqrt{\pi \cdot (a + a_0)} \quad (2)$$

where a is the crack physical length, $\Delta \sigma_g$ is the applied gross nominal stress range and a_0 is a material parameter, also known as material intrinsic crack length, defined as:

$$a_0 = \frac{1}{\pi} \cdot \left(\frac{\Delta K_{\text{th}}}{\Delta \sigma_0} \right)^2 \quad (3)$$

where ΔK_{th} and $\Delta\sigma_0$ are the threshold range of the stress intensity factor for long cracks and the plain material fatigue limit in a defect-free condition, respectively. At the threshold, in Eq. (2) we have $\Delta K_{corr} = \Delta K_{th}$, $\Delta\sigma_g = \Delta\sigma_{g,th}$, so that the Kitagawa-Takahashi diagram reported in Fig. (7a) is obtained. In the same way, the threshold of small cracks reported in Fig. (7b) immediately follows as:

$$\Delta K_{th,SC} = \Delta K_{th} \sqrt{\frac{a}{a + a_0}} \quad (4)$$

By calculating the stress intensity factor range according to Eq. (2), short crack data in Fig (8a) match long crack data, as shown schematically in Fig (8b) [18,19].

It is worth underlining that Eq. (2) and (4) are referred to a crack centred in an infinitely wide plate; therefore it is necessary to include a shape factor α which takes into account shape dimension and position of the crack (or defect), according to the following expressions [14,15]:

$$\Delta K_{corr} = \Delta\sigma_g \cdot \sqrt{\pi \cdot (\alpha^2 a + a_0)} \rightarrow = \Delta\sigma_g \cdot \sqrt{\pi \cdot (a_{eff} + a_0)} \quad (5a)$$

$$\Delta K_{th,SC} = \Delta K_{th} \sqrt{\frac{a_{eff}}{a_{eff} + a_0}} \quad (5b)$$

where the effective size a_{eff} is defined by the SIF equality:

$$a_{eff} = \frac{1}{\pi} \cdot \left(\frac{K_I}{\sigma_g} \right)^2 \quad (6)$$

Murakami showed that K_I , for surface or sub-surface defects, can be estimated as follows [12]:

$$K_I = 0.65 \cdot \sigma_g \cdot \sqrt{\pi \cdot \sqrt{area}} \quad (7)$$

Therefore, by substituting in Eq. (6), the effective size of a surface or a sub-surface defect is obtained as:

$$a_{eff} = 0.65^2 \cdot \sqrt{area} \quad (8)$$

6.2.1 Rapid estimation of a_0

The original contribution of this work is related to the link between microstructure and fatigue behaviour of material affected by defects. In particular, an empirical relationship was found in the El-Haddad-Smith-Topper model and the Murakami's model to determine the a_0 parameter for the appropriate load ratio R (Eq. (3)) in the absence of relevant experimental data.

In fact, by considering Eq (1) (Murakami model) and (5b) (El-Haddad-Smith-Topper model) in the range of defect size $10 \mu\text{m} < \sqrt{\text{area}} < 1000 \mu\text{m}$, they must provide the same value of $\Delta K_{\text{th,SC}}$ for a given material on which are known the HV, ΔK_{th} , and $\Delta\sigma_0$. However, ΔK_{th} in Eq. (5b) can be expressed by means of definition (3), and the effective plain material fatigue limit (excluding any influence of defects) can further be estimated as $\Delta\sigma_0/2 = 1.6 \cdot \text{HV}$ [12]. Therefore, by equalling Eq. (1) and (5b), the following expression can be obtained:

$$3.3 \cdot 10^{-3} \cdot (\text{HV} + 120) \cdot (\sqrt{\text{area}})^{1/3} = 2 \cdot (1.6 \cdot \text{HV}) \cdot \sqrt{\pi \cdot a_0} \cdot \sqrt{\frac{0.65^2 \cdot \sqrt{\text{area}}}{0.65^2 \cdot \sqrt{\text{area}} + a_0}} \quad (9)$$

where the only unknown parameter is the a_0 .

By using expression (9), a_0 can be found with the method of least squares applied in the range $10 \mu\text{m} < \sqrt{\text{area}} < 1000 \mu\text{m}$, where expression (1) is valid.

The link between this fracture mechanics analyses and the main topics of the present dissertation was found in a technical note published by Lazzaring e Berto [20].

In particular [20] the Kitagawa and Atzori's diagrams were derived by using the averaged Strain Energy Density (SED) in a circular control volume which is a material property. The critical radius R_c , in plane strain condition, can be derived as follows:

$$R_c = \frac{(1+\nu)(5-8\nu)}{4\pi} \left(\frac{\Delta K_{\text{th}}}{\Delta\sigma_0} \right)^2 \quad (10)$$

where ΔK_{th} and $\Delta\sigma_0$ are the threshold range of the SIF for long cracks subjected to mode I, and the plain material fatigue limit in a defect-free condition, respectively.

Therefore, by adopting the definition of a_0 (Eq. (3)), the critical radius R_c can be re-written as follows:

$$R_c = 0.845 \cdot a_0 \quad (11)$$

In this work, the SED approach was not taken into account, but it will be subject of future investigations.

6.3 MATERIALS AND METHODS

The material under investigation is a 18Ni-300 maraging steel produced by the following three different manufacturing technologies:

- wrought maraging steel specimens (TM), machined from a hot rolled raw bars.
- Direct Melting Laser Sintered (DLMSed) maraging steel specimens produced by an EOSINT M280 system (EOS GmbH)
- Selective Laser Melted (SLMed) maraging steel specimens produced by an MYSINT 100 system (SISMA S.p.A.).

The chemical compositions of the relevant materials as taken from datasheets are reported in Table (3).

Plain specimen geometries adopted for fatigue testing of wrought and AMed maraging steels are shown in Fig. (9a) and (9b) respectively. In addition, cylindrical 80-mm-long bars having a nominal diameter equal to 12 mm were SLMed within the SISMA batch and afterwards V-notched specimens were machined according to the geometry of Fig (9c).

Table 6.3: Chemical composition of the powder adopted in the batch EOS and SISMA.

Batch	Fe (wt-%)	Ni (wt-%)	Co (wt-%)	Mo (wt-%)	Ti (wt-%)	Al (wt-%)	Cr (wt-%)	Cu (wt-%)	C (wt-%)	Mn (wt-%)	Si (wt-%)	P (wt-%)	S (wt-%)
wrought	balance	18.5	9.0	5.3	0.6	0.1	/	/	≤ 0.03	≤ 0.1	≤ 0.1	/	/
EOS	balance	17-19	8.5-9.5	4.5-5.2	0.6-0.8	0.05-0.15	≤ 0.5	≤ 0.5	≤ 0.03	≤ 0.1	≤ 0.1	≤ 0.01	≤ 0.01
SISMA	balance	17-19	8.5-10	4.5-5.2	0.8-1.2	/	≤ 0.25	/	≤ 0.03	≤ 0.15	≤ 0.1	≤ 0.01	≤ 0.01

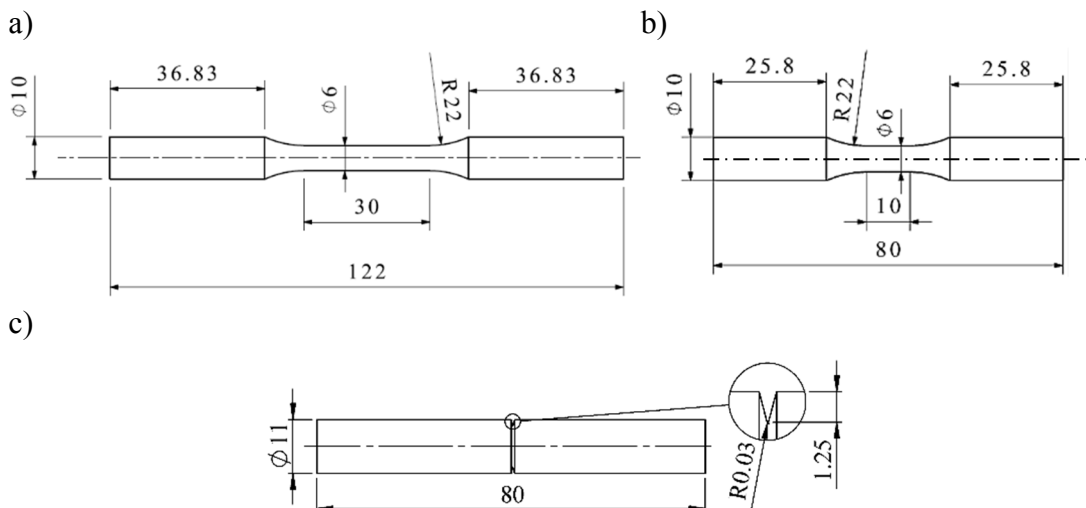


Figure 6.9: Specimen's geometries

All process parameters available from the manufacturers were reported in Table (4). Regarding the scanning strategies, the EOS AM system adopts parallel scanning

paths to melt the powder of a single layer. In the subsequent layer, the scanning paths are rotated by 67.7° . This rotation ensures the minimum repeatability of layers having the same scanning direction. SISMA AM system adopts the so-called islands scanning strategy, but details on process parameters such as islands' sizes and the scanning direction within the "islands" are not available for confidentiality reasons. Furthermore, SISMA provided two batches of plain specimens (Fig. (9b)), one produced adopting a proper set of unavailable process parameter in order to form large Lack of Fusion (LoF) defects and the second with optimized parameter to minimize LoFs.

Table 6.4: Process parameters adopted to manufacture maraging steel specimens for fatigue testing.

Batch	Laser power [W]	Layer thickness [μm]	Laser spot diameter [μm]	Laser scan rate [mm/s]	Powder dimension [μm]	Temperature of the platform	Scanning strategy
EOS ⁺	400	40	100	unknown	60	40 °C	parallel vectors
SISMA (S)*	120	20	55	500	15÷45	Not heated	island
SISMA (SN) [°]	120	20	55	500	15÷45	Not heated	island

⁺ set of parameters called "Performance 1.0"

* further process parameter properly set to form large LoF defects (company know-how)

[°] further process parameter properly set to minimize LoF defects (company know-how)

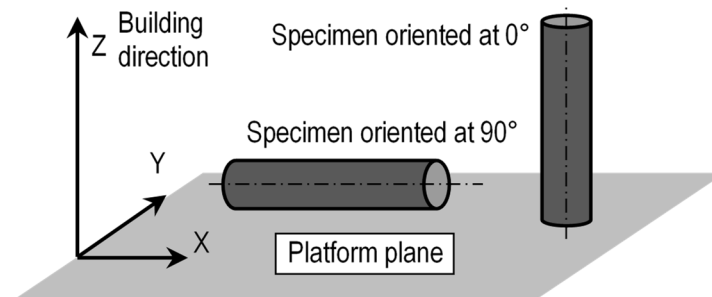


Figure 6.10: building orientation of the specimens AMed.

All SLMed specimens were manufactured with their axis oriented at 0° or 90° with respect to the build direction, i.e. the Z-axis of Fig. (10). Some specimens have been aged at 490°C for 6 hours while the remaining ones were tested in as-built condition. Regarding the wrought maraging steel (TM), all the specimens were first annealed at 820°C for 1 hour and then they were subjected to the aging heat treatment at 490°C for 3 hours, as reported in the technical datasheet.

Micro-Vickers hardness ($\text{HV}_{0.2}$) was measured as the mean ± 1 standard deviation of 5 measurements carried out at a distance of about 0.5 mm from the perimeter of the cross-section by using Leitz Vickers Microhardness indenter as shown in Fig. (11). The results were reported in Table (5) which also provides a nomenclature of the test series and summarizes all the previous information.

Table 6.5: Summary of the test series.

Batch	Technology	N° of samples	Geometry	Building direction	Heat treatment	HV _{0.2}
TM_NT	Wrought	12	Fig. 9a)	/	NT* (annealed 8200°C/1h)	318±9
TM_T		12		/	T* (annealed 820°C/1h + aged 490°C/3h air cooled)	652±29
EN_0°_T	DMLS (EOS)	5	Fig. 9b)	0°	T (aged 490°C/6h air cooled)	614±9
EN_90°_T		3		90°	T (aged 490°C/6h air cooled)	623±5
S_0°_NT	SLM (SISMA)*	15		0°	NT (as-built)	367±28
S_90°_NT		18		90°	NT (as-built)	370±25
SN_0°_NT	SLM (SISMA)°	10		0°	NT (as-built)	358±15
SN_90°_NT		8		90°	NT (as-built)	358±18
SN_0°_T		8		0°	T (aged 490°C/6h air cooled)	558±23
SN_90°_T		10		90°	T (aged 490°C/6h air cooled)	553±20
SN_V_0°_NT		4	Fig. 9c)	0°	NT (as-built)	/
SN_V_90°_NT		3		90°	NT (as-built)	/

* parameter set to form large LoF defects

° parameter set to minimize LoF defects

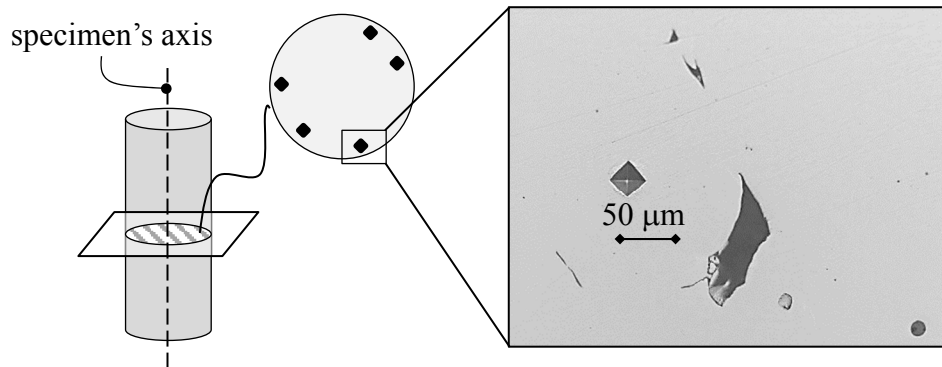
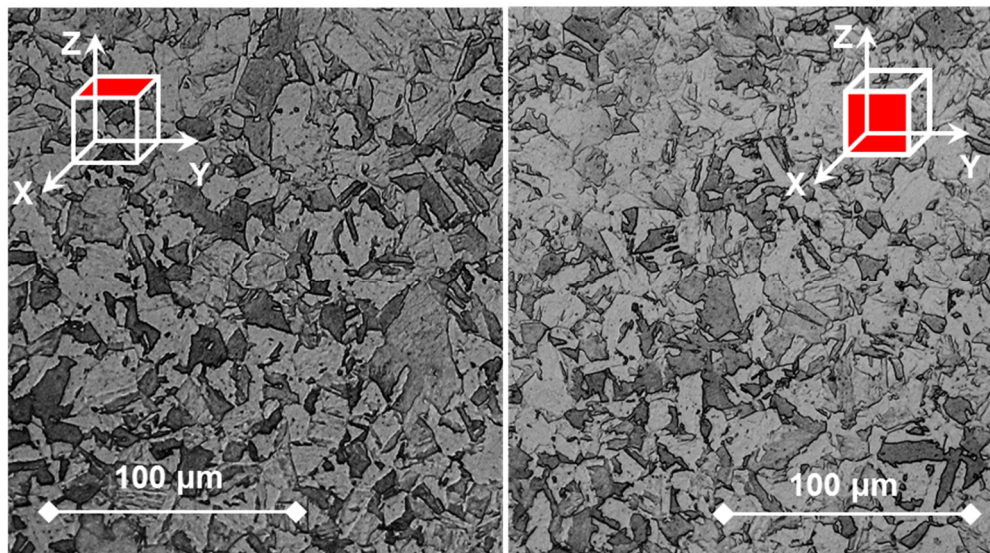


Figure 6.11: Example of microhardness measurement (HV_{0.2}) on a cross-section of the gross part of the specimens. The detailed view shows the indentation of a 90°-oriented specimens.

a)



b)

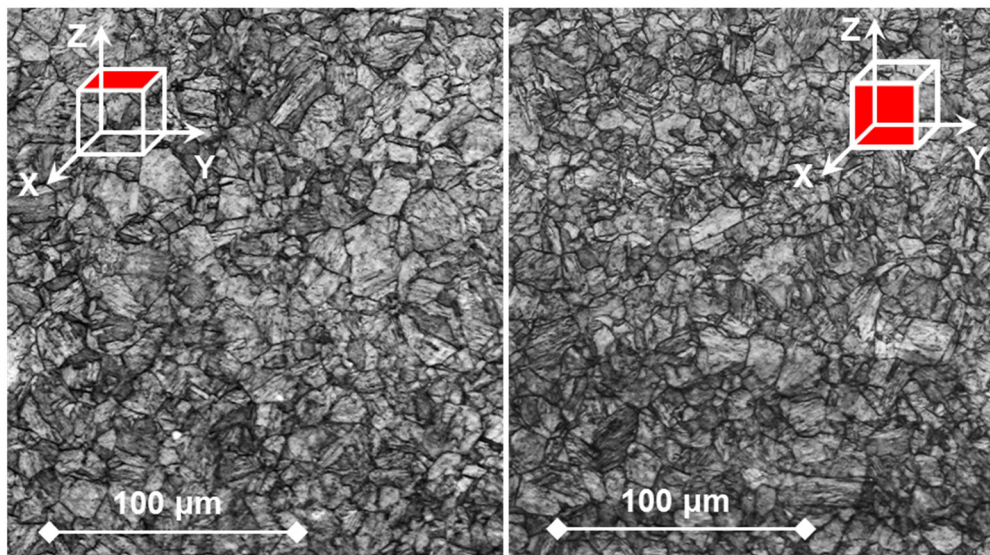
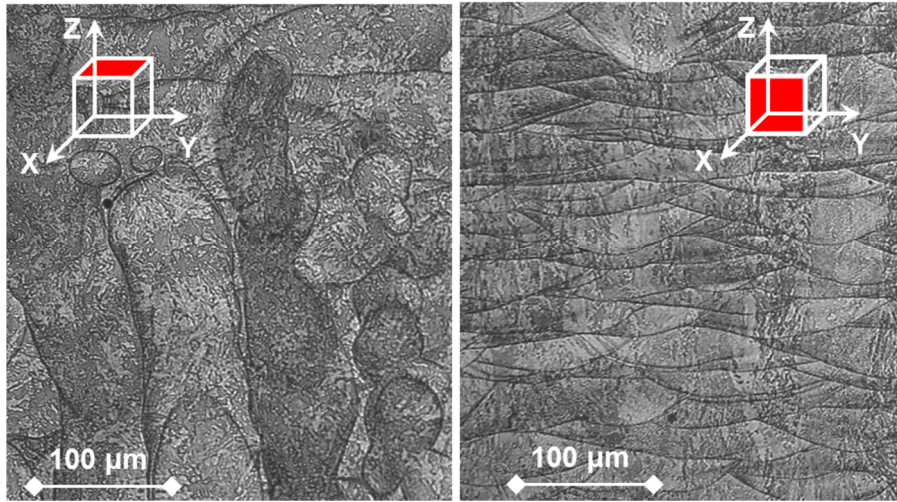


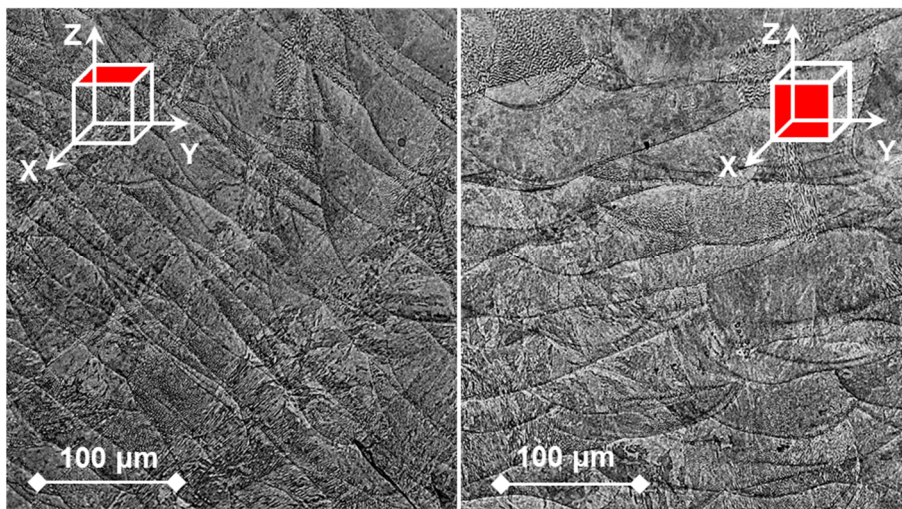
Figure 6.12: Microstructure along a normal and parallel plane of the specimen's axis of wrought maraging steel 300 in the annealed (a) and aged condition (b). (heat treatment parameters are reported in Table (5)).

The analyses of the microstructure along a normal and parallel plane with respect to the specimen's axis (Z axis) of wrought maraging steel 300 both in the annealed and aged condition were reported in Fig. (12). The solution annealed one shows a microstructure constituted by soft, lath martensite in equiaxed grains in both planes (Fig. (12a)). The lath martensite structure is more visible in aged conditions (Fig. (12b)). Furthermore, aging heat treatment produces the precipitation of intermetallic compounds that strengthen the alloy.

a)



b)



c)

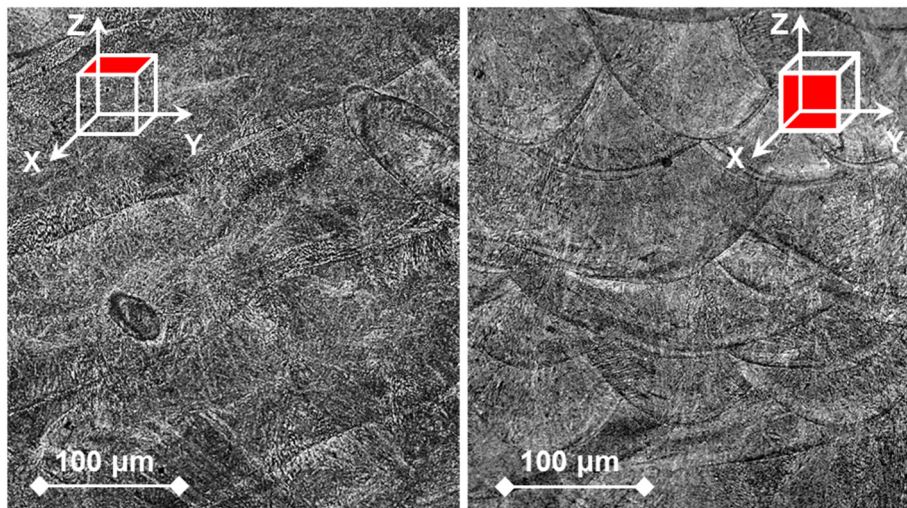


Figure 6.13: Microstructure along a normal and parallel plane with respect to the building direction (Z) of the SISMA (S) as built (a), SISMA (SN) in aged condition (b), and EOS in aged condition (c).

The microstructure analysis was also carried out on the AMed maraging steel. In Fig. (13a, b, and c) normal and parallel planes with respect to the building direction (Z-axis) were reported for SISMA batch in a-built condition (test series S, see table 5), SISMA batch in aged condition (test series SN, see table 5) and the EOS batch in the aged condition (test series EN, see table 5). Fig. (13a and b) show different scanning paths in the normal plane to the build direction due to the different sets of parameters adopted to form large LoF and to minimize them. Whereas, in the parallel plane the melting pools are similar having adopted the same laser power and layer thickness. Concerning the EOS batch (Fig 13c), deeper melting pools can be observed due to the higher value of the laser power and the layer thickness. The microstructure within the melting pools consists of fine columnar/dendritic grains, whose intercellular spacing is smaller than 1 μm , which formed due to the rapid solidification of the melting pools. Such microstructure is in agreement with those reported in the literature for as-built maraging steel produced by SLM [3,21].

Prior to testing, all specimens were polished by using progressively finer emery paper from grade 80 up to grade 800. Fig. (14) shows as an example the surface finish of a 90°-oriented, as-received specimen (which is also representative of 0°-oriented specimens) (a), the side of a 90°-oriented specimen where the support structure was attached (b) and the final surface condition after polishing the gauge portion and turning in a lathe the gross ends of all specimens, in order to remove misalignments between the specimen ends (c). Before turning the gross ends of the AMed specimens, deflection of the specimen's axis f_a (Fig. (15a)) was measured for all samples, by clamping one side of the specimen and by using a digital dial indicator in contact with the opposite end (see Fig. (15b)). The mean values of f_a (± 1 standard deviation) were reported in Fig. (16a). After machining the gross ends of the specimens the deflection f_a was measured again and the resulting mean value of each test series was lower than 0.05 mm.

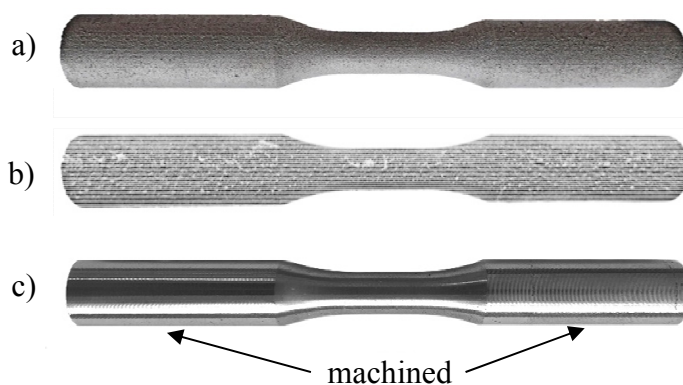


Figure 6.14: 90°-oriented as-built specimens (a), detailed view at the support side (b), surface finish of all specimens after polishing and turning the gross ends (c)

The roughness parameter R_a was measured along four diametrically opposite paths parallel to the specimen axis. Measurements were performed on five specimens for each test series by using a surface roughness tester (Taylor Hobson precision – Surtronic 25) having a resolution of $0.01 \mu\text{m}$.

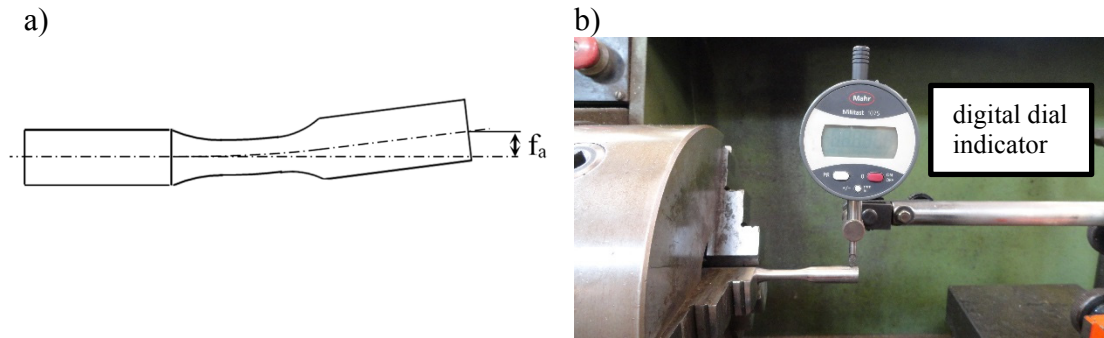


Figure 6.15: Deflection of the specimen's axis f_a (before turning the gross ends of the specimens) a). Measurements of f_a .

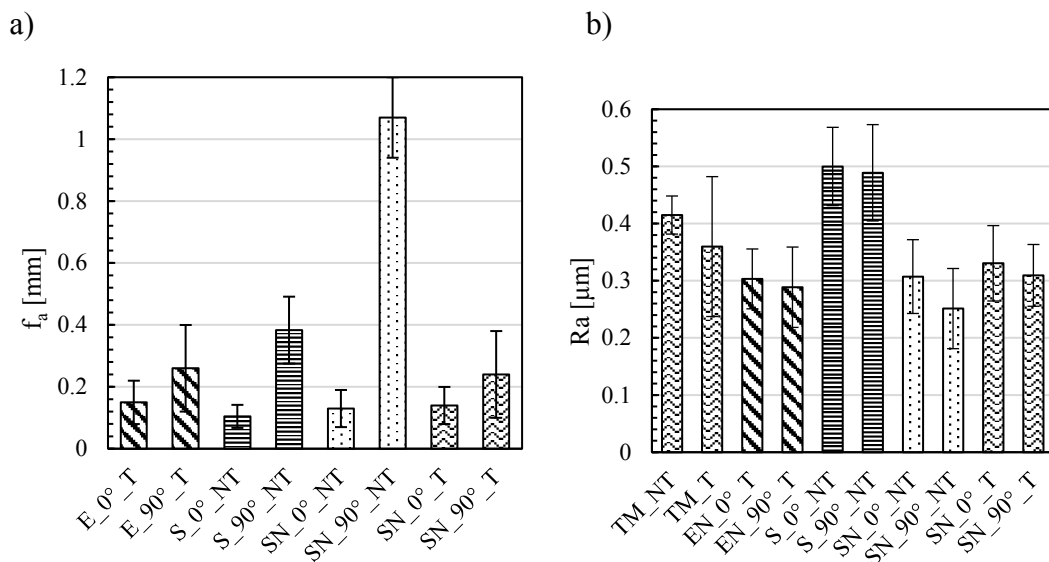


Figure 6.16: Deflection f_a before machining the gross parts of the AMed specimens (mean value ± 1 standard deviation) (a) and roughness R_a (The mean value ± 1 standard deviation).

The mean values of R_a (± 1 standard deviation) were reported in Fig. (16b). Fully reversed ($R = -1$), load-controlled, axial fatigue tests were carried out by using a servo-hydraulic SCHENCK HYDROPULS PSA 100 machine having a 100 kN load cell and equipped with a TRIO Sistemi RT3 digital controller. The load frequency was set in the range between 10 Hz and 30 Hz, depending on the applied load level. The fatigue test was stopped either when the complete separation of the specimen occurred or at 2 million cycles.

After fatigue testing, a subset of fracture surfaces (eight for 0° -oriented specimens and eleven for 90° -oriented specimens) were observed by means of Scanning Electron Microscope (SEM), in order to single out the crack initiation point and to evaluate the

$\sqrt{\text{area}}$ of either the single killer defect or the cluster of defects, which caused fatigue failure.

6.4 FATIGUE TEST RESULTS

Fig. (17) shows the overall fatigue test results of each test series relevant to plain Maraging Steel (MS) specimens in terms of nominal stress amplitude.

Starting with the wrought (TM series) MS in the annealed and aged condition, fatigue curve relevant to 10%, 50% and 90% survival probabilities were obtained and referring to the 50% PS curve the fatigue strength of TM aged MS is 11% higher than the same material in the annealed condition at a number of cycle N_A equal to $4 \cdot 10^5$. Furthermore, the TM_T series is characterized by a higher scatter index T_σ due to the lack of fatigue results for a number of cycles starting from 10^4 to $5 \cdot 10^4$ which could have lead to a slightly higher inverse slope k as well.

All the AMed fatigue results present a higher scatter and lower fatigue strength compared to the wrought MS, especially in the HCF regime.

For the sake of clarity, the singles AMed test series characterised by the same heat treatment condition were compared to the wrought MS separately in Fig. (18a-d). Generally speaking, what emerges from Fig. (18a-d) is that the test series relevant to 0° -oriented specimens presents higher fatigue strength than the 90° -ones except for the test series SN which does not seem to be affected by the building orientation (Fig. 18c). It is worth noticing that most of AMed fatigue results present a knee between $2 \cdot 10^5$ and $2 \cdot 10^6$ cycles therefore in figure of Fig. (18) the fatigue strengths relevant to the lowest knee was reported.

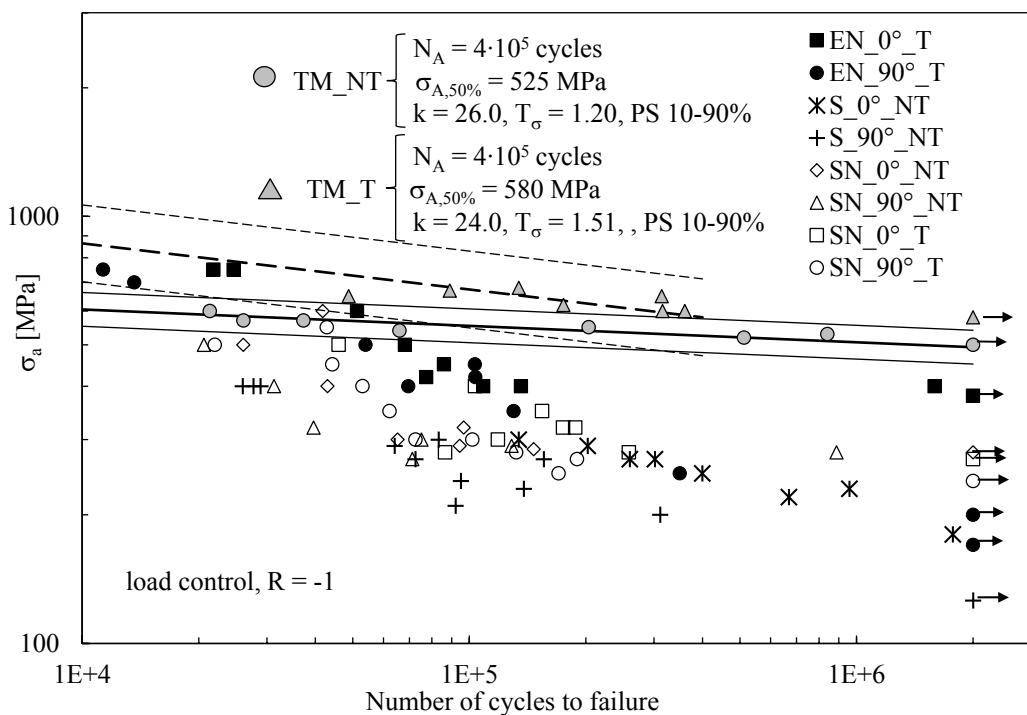


Figure 6.17: Synthesis of the fatigue results expressed in terms of nominal stress amplitude.

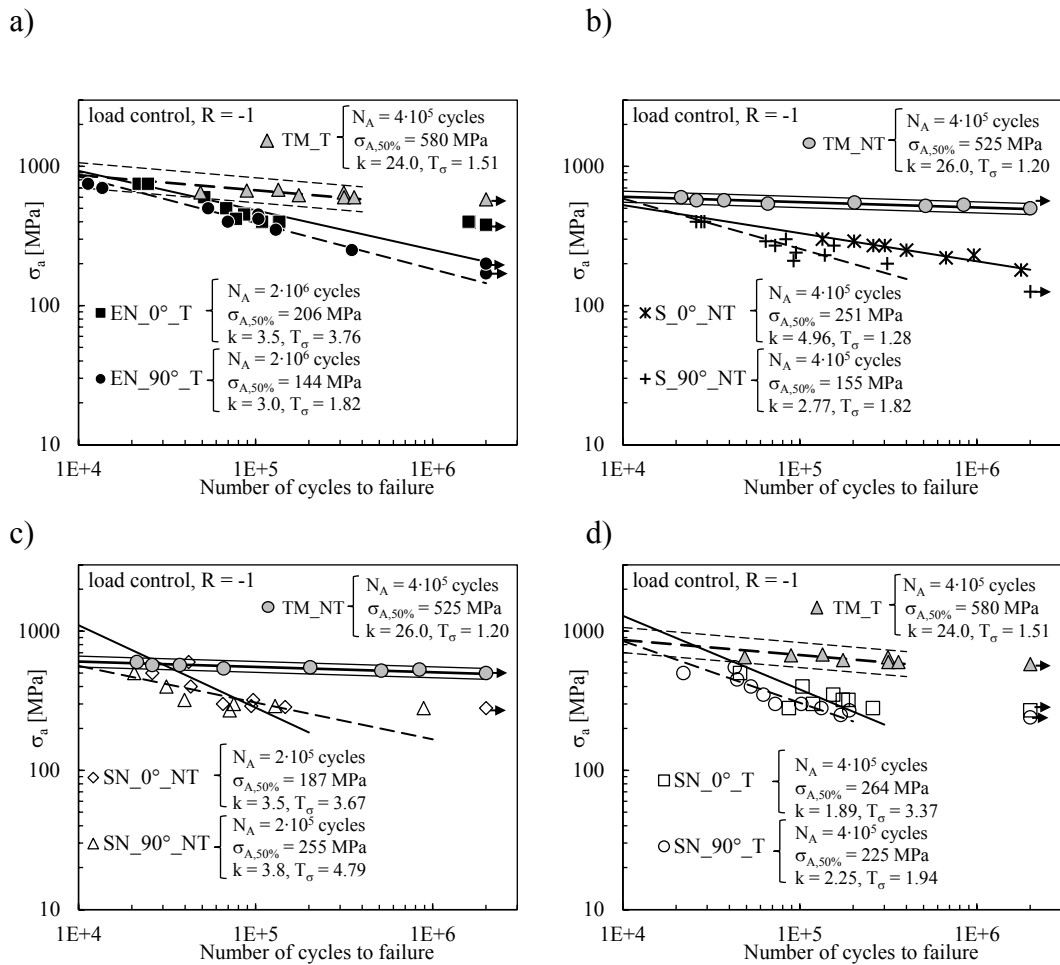


Figure 6.18: Fatigue results comparison between wrought and the AMed maraging steel for each batch and same heat treatment condition.

6.4.1 Fracture surface analysis

Fig. (19-26) show a selection of fracture surfaces per each test series observed by SEM and the detailed views report the contours to evaluate the effective $\sqrt{\text{area}}$ parameter, according to the recommendations in [12]. Fig. 19 shows that in some cases a cluster of sub-surface defects exists along the perimeter of the fracture surface. If the ratio l/c between the length of the defected area (l) and the depth perpendicular to the specimen's surface (c) is equal to or greater than 10 (see the fracture surfaces of the specimen S_0°_NT_15) or the cluster of defects involve the entire perimeter (see the fracture surfaces of the specimen S_0°_NT_2), then $\sqrt{\text{area}}$ is equal to $\sqrt{10} \cdot c$ [12].

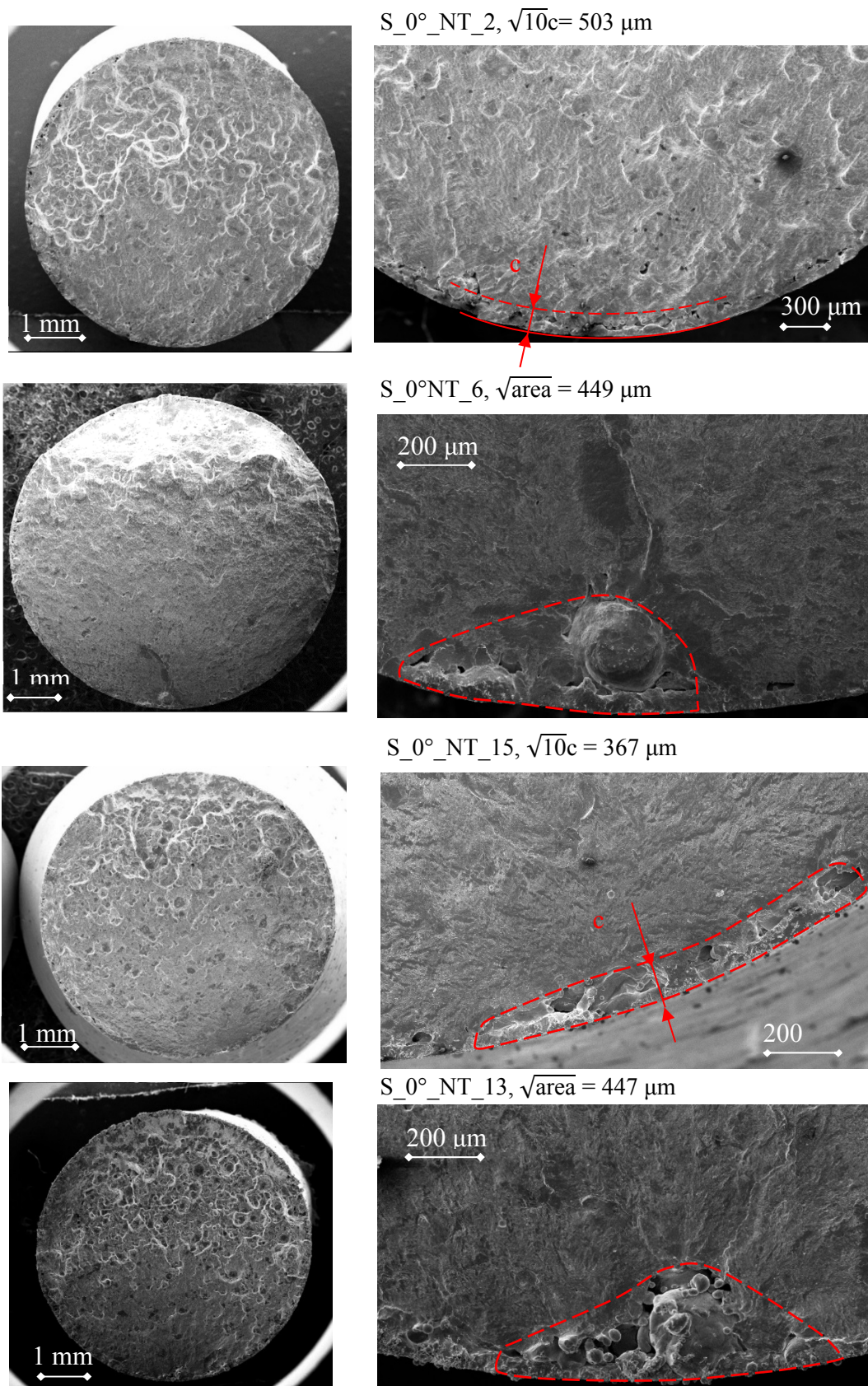
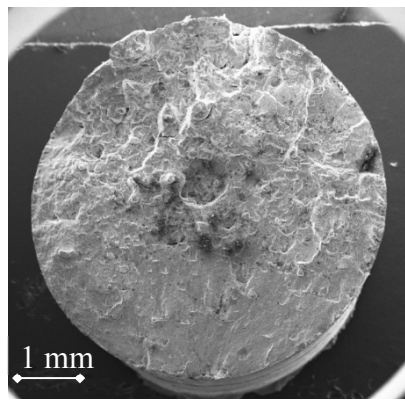
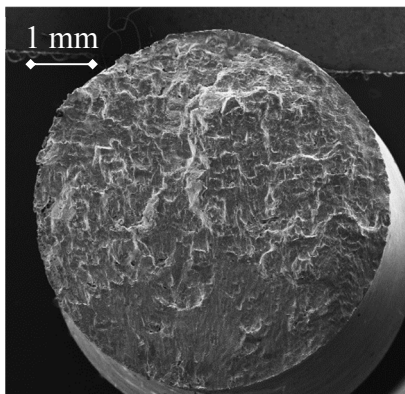
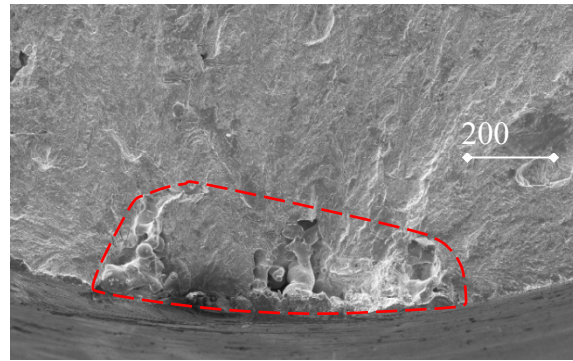


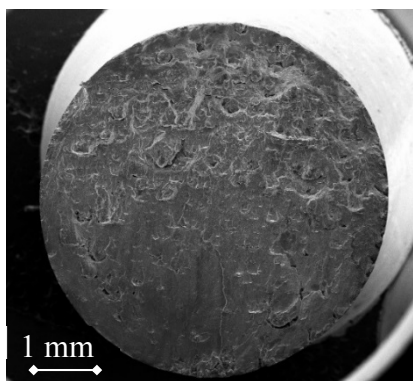
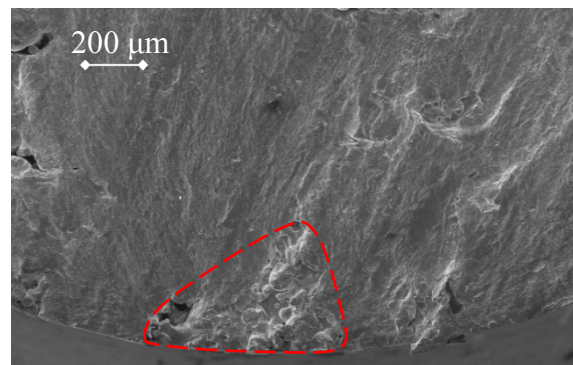
Figure 6.19: Examples of fracture surfaces relevant to the test series S_0°_NT and relevant $\sqrt{\text{area}}$ at the failure origin.



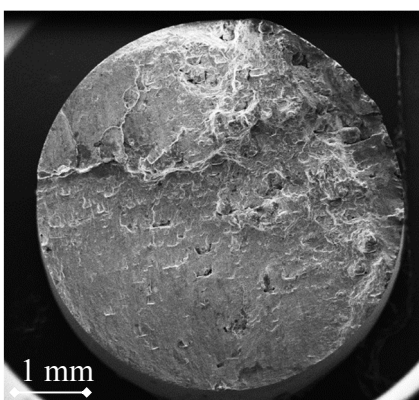
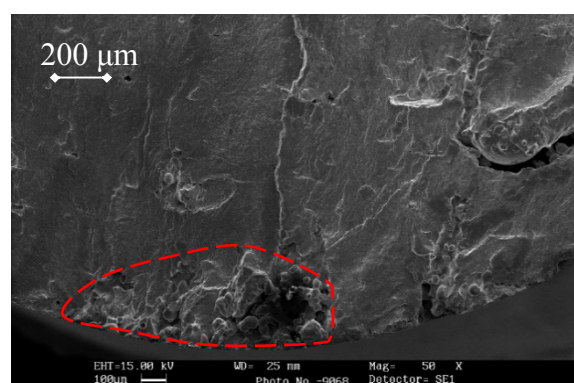
S_90_NT_3, $\sqrt{\text{area}} = 430 \mu\text{m}$



S_90_NT_2, $\sqrt{\text{area}} = 442 \mu\text{m}$



S_90_NT_15, $\sqrt{\text{area}} = 551 \mu\text{m}$



S_90_NT_13, $\sqrt{\text{area}} = 237 \mu\text{m}$

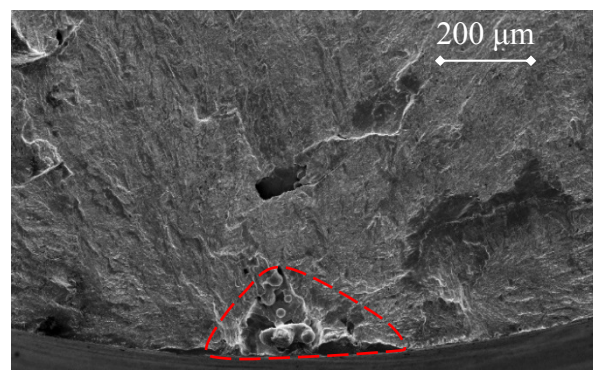
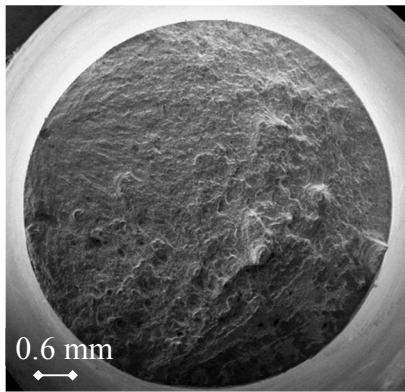
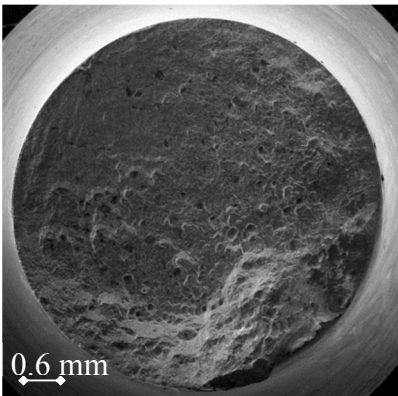
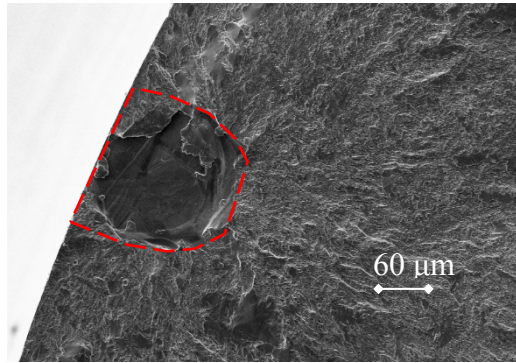


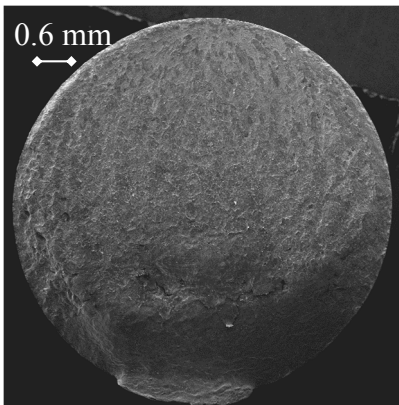
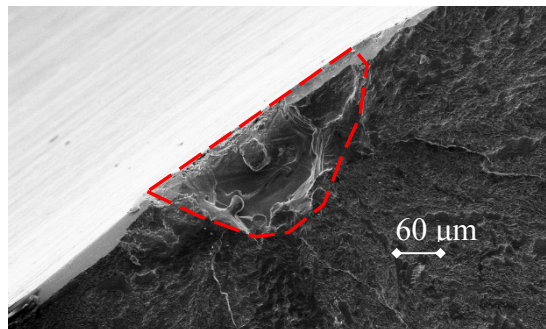
Figure 6.20: Examples of fracture surfaces relevant to the test series S_90°_NT and relevant $\sqrt{\text{area}}$ at the failure origin.



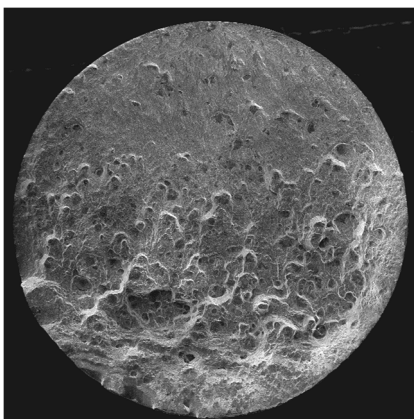
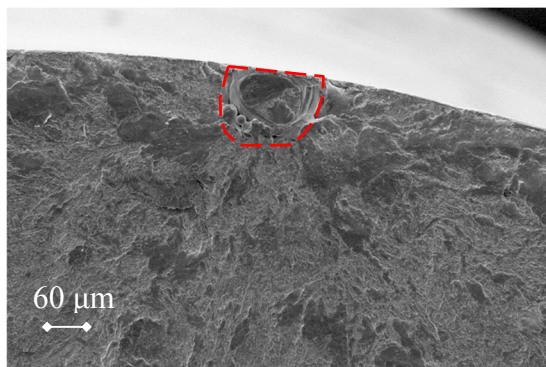
SN_0_NT_4, $\sqrt{\text{area}} = 179 \mu\text{m}$



SN_0_NT_2, $\sqrt{\text{area}} = 161 \mu\text{m}$



SN_0_NT_7, $\sqrt{\text{area}} = 124 \mu\text{m}$



SN_90_NT_5, $\sqrt{\text{area}} = 156 \mu\text{m}$

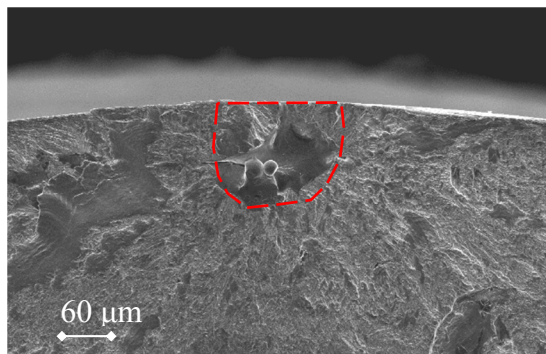
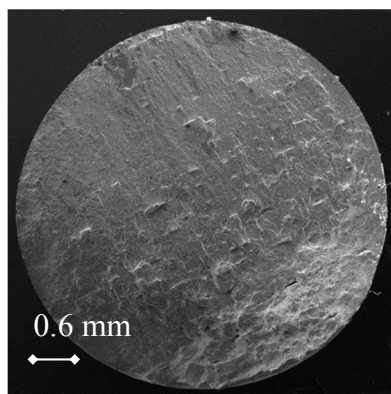
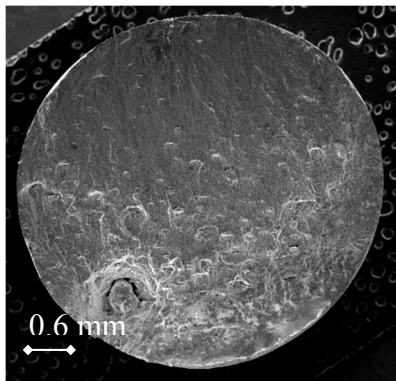
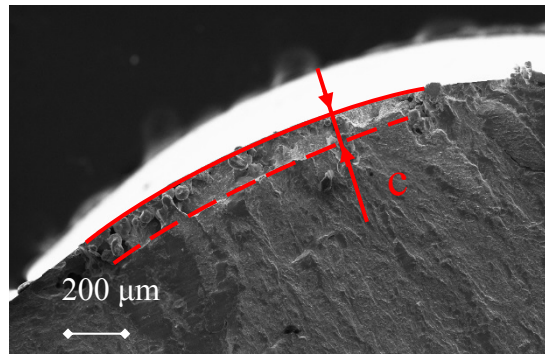


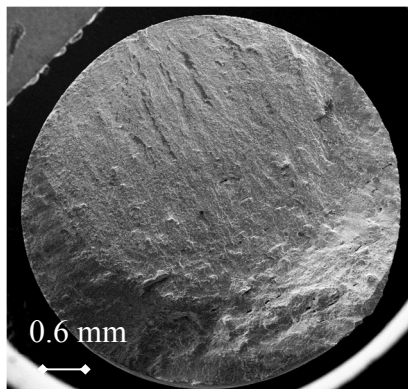
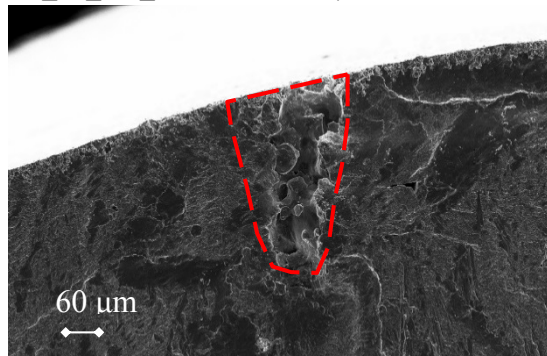
Figure 6.21: Examples of fracture surfaces relevant to the test series SN_0°_NT and relevant $\sqrt{\text{area}}$ at the failure origin.



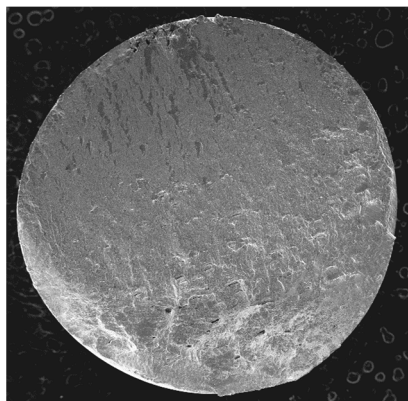
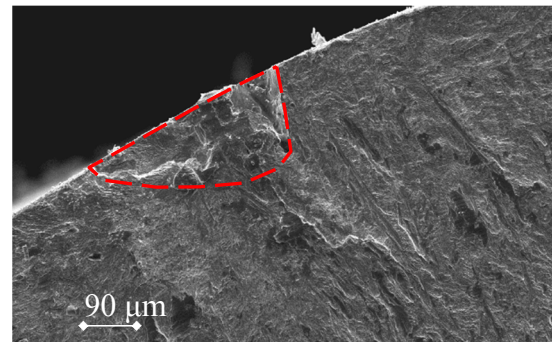
SN_90_NT_1, $\sqrt{\text{area}} = 408 \mu\text{m}$



SN_90_NT_5, $\sqrt{\text{area}} = 221 \mu\text{m}$



SN_90_NT_3, $\sqrt{\text{area}} = 203 \mu\text{m}$



SN_90_NT_7, $\sqrt{\text{area}} = 560 \mu\text{m}$

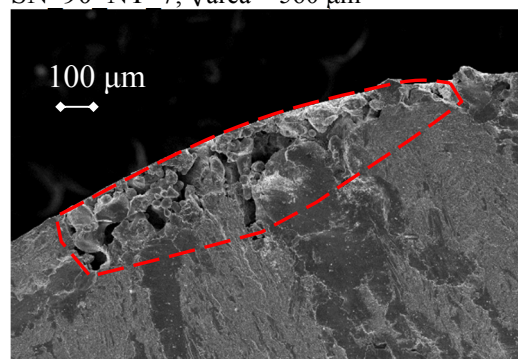
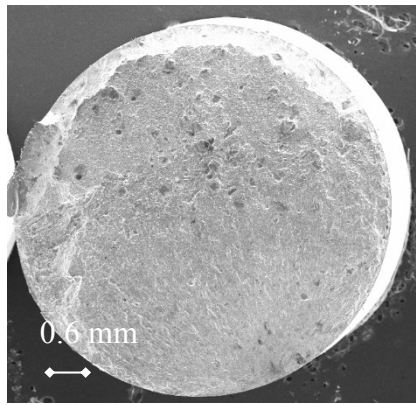
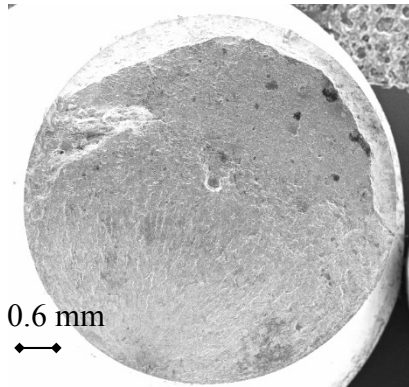
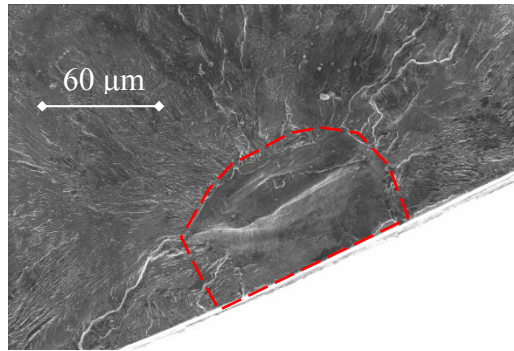


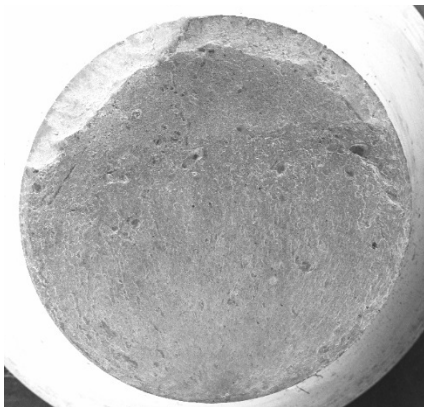
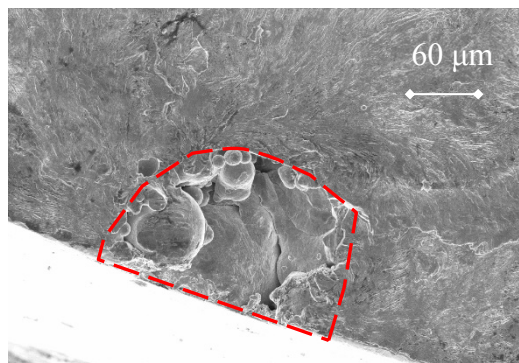
Figure 6.22: Examples of fracture surfaces relevant to the test series SN_90°_NT and relevant $\sqrt{\text{area}}$ at the failure origin.



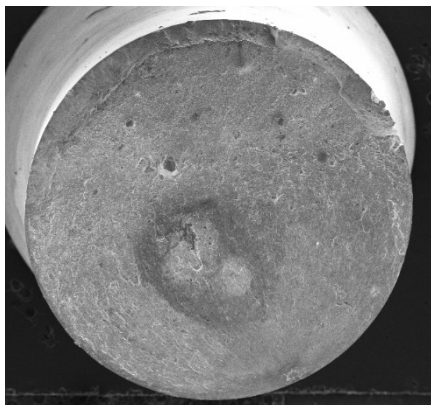
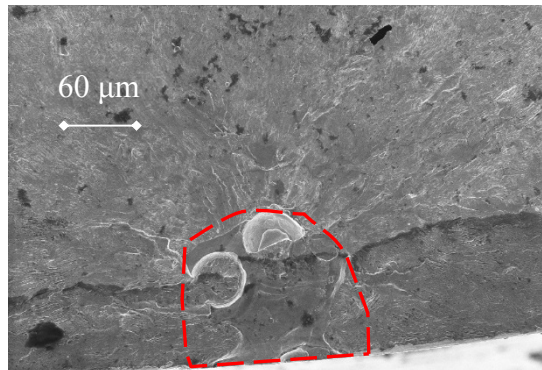
SN_0_T_2, $\sqrt{\text{area}} = 78 \mu\text{m}$



SN_0_T_3, $\sqrt{\text{area}} = 159 \mu\text{m}$



SN_0_T_4, $\sqrt{\text{area}} = 130 \mu\text{m}$



SN_0_NT_5, $\sqrt{\text{area}} = 185 \mu\text{m}$

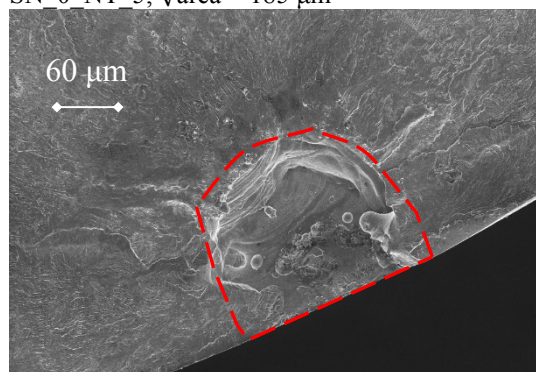
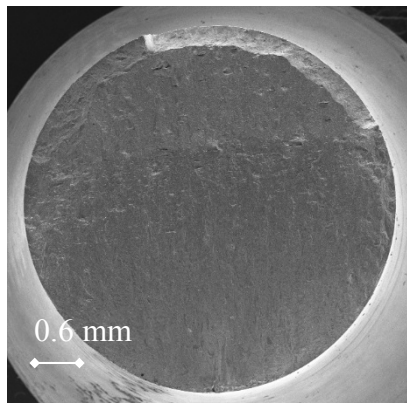
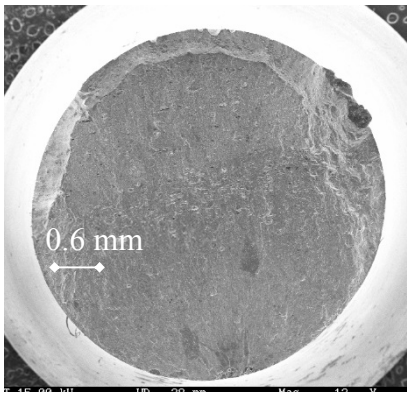
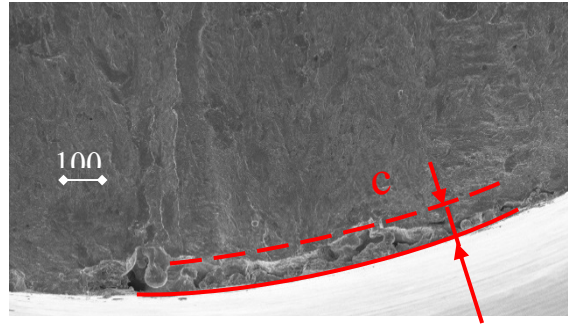


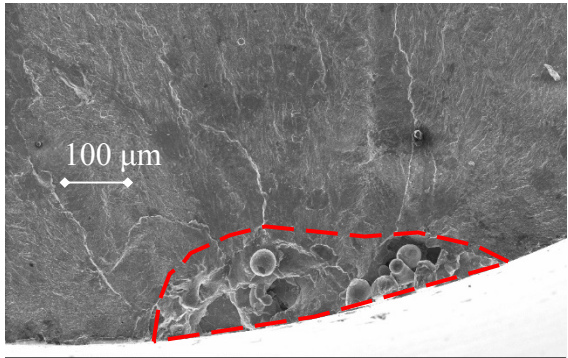
Figure 6.23: Examples of fracture surfaces relevant to the test series SN₀^o_T and relevant $\sqrt{\text{area}}$ at the failure origin.



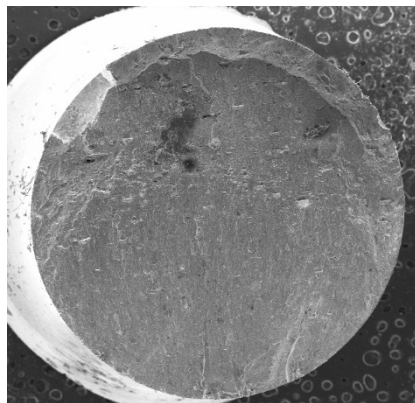
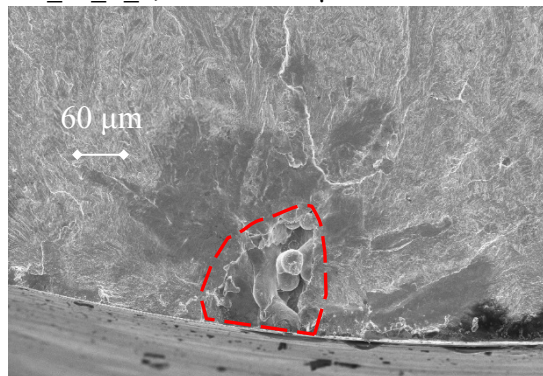
SN_90_T_6, $\sqrt{\text{area}} = 373 \mu\text{m}$



SN_90_T_2, $\sqrt{\text{area}} = 269 \mu\text{m}$



SN_90_T_1, $\sqrt{\text{area}} = 152 \mu\text{m}$



SN_90_T_3, $\sqrt{\text{area}} = 381 \mu\text{m}$

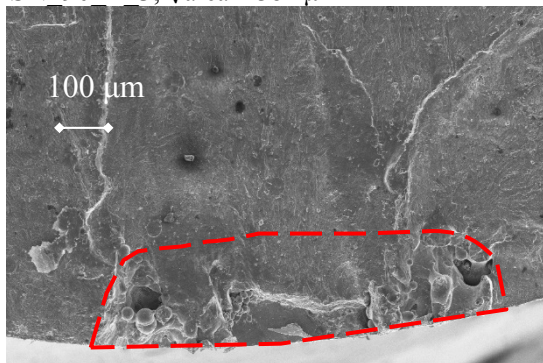
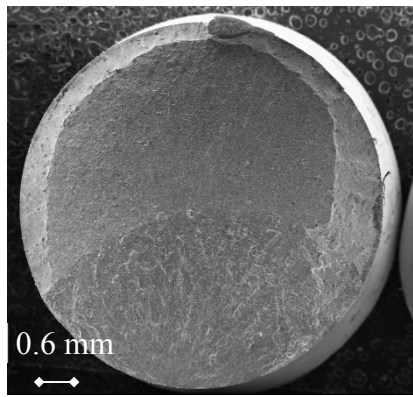
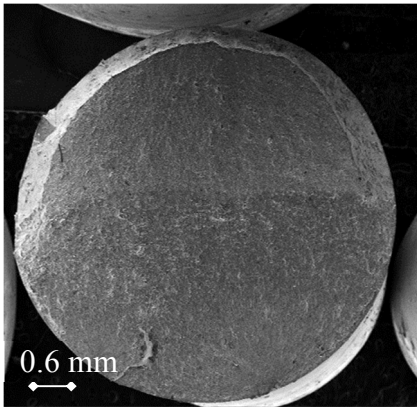
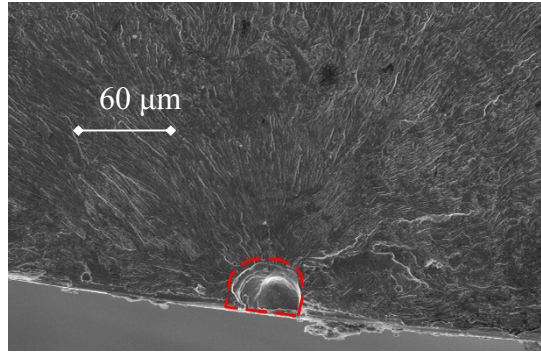


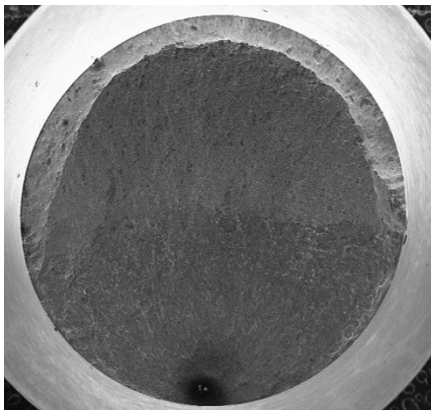
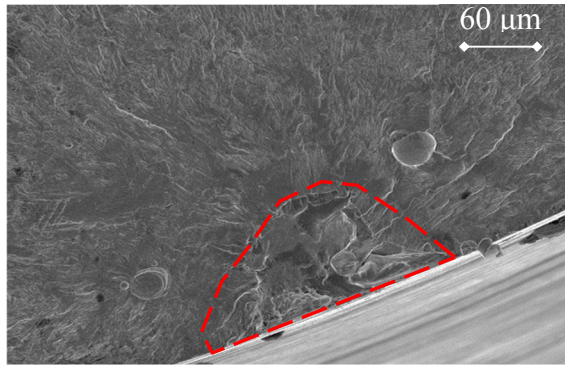
Figure 6.24: Examples of fracture surfaces relevant to the test series SN_90°_T and relevant $\sqrt{\text{area}}$ at the failure origin.



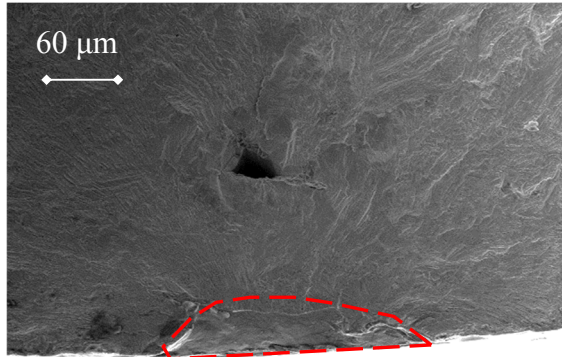
EN_0_T_2, $\sqrt{\text{area}} = 39 \mu\text{m}$



EN_0_T_4, $\sqrt{\text{area}} = 104 \mu\text{m}$



EN_0_T_3, $\sqrt{\text{area}} = 79 \mu\text{m}$



EN_0_T_5_5, $\sqrt{\text{area}} = 83 \mu\text{m}$

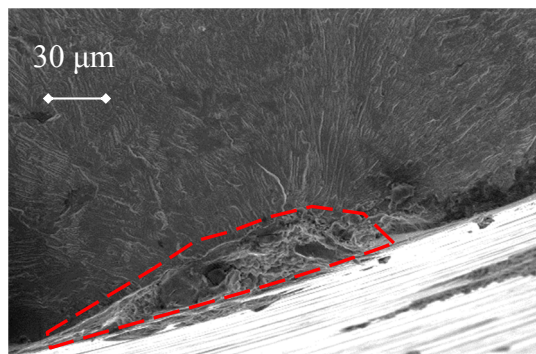
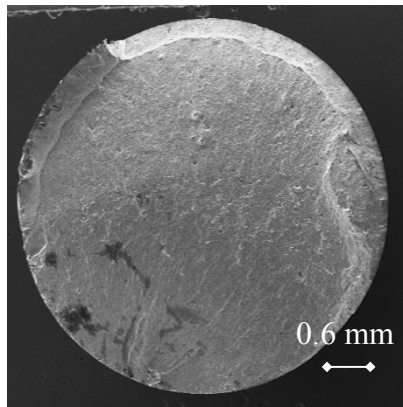
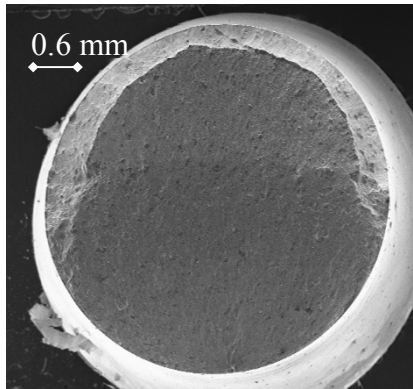
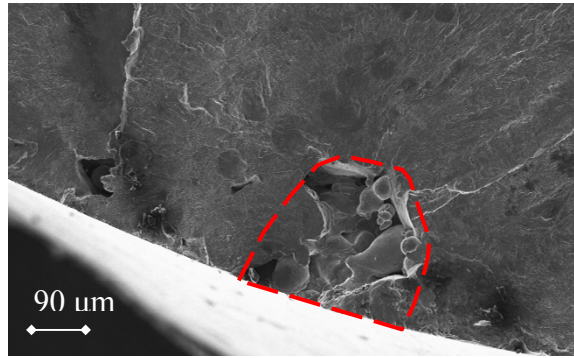


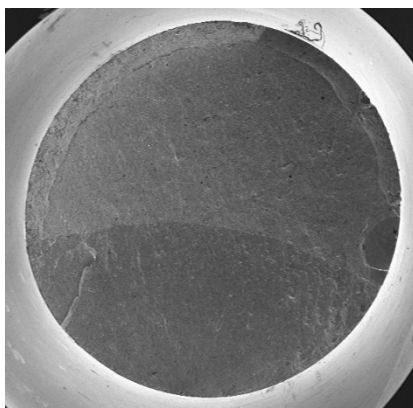
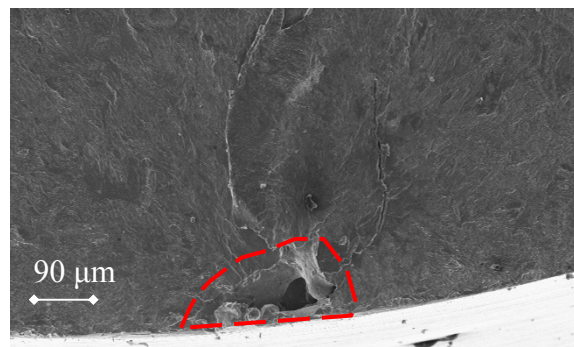
Figure 6.25: Examples of fracture surfaces relevant to the test series EN_0°_T and relevant $\sqrt{\text{area}}$ at the failure origin.



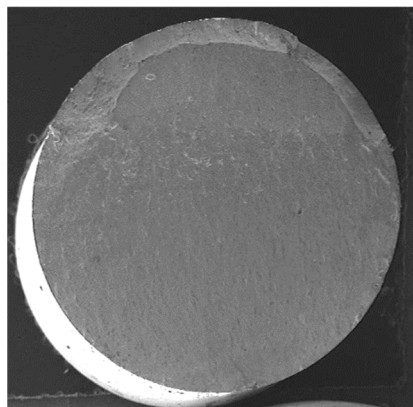
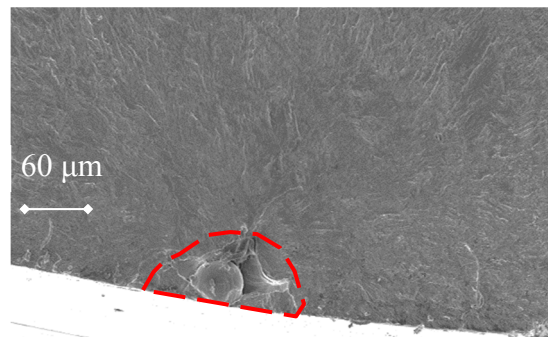
EN_90_T_4, $\sqrt{\text{area}} = 207 \mu\text{m}$



EN_90_T_5, $\sqrt{\text{area}} = 127 \mu\text{m}$



EN_90_T_3, $\sqrt{\text{area}} = 98 \mu\text{m}$



EN_90_T_6, $\sqrt{\text{area}} = 206 \mu\text{m}$

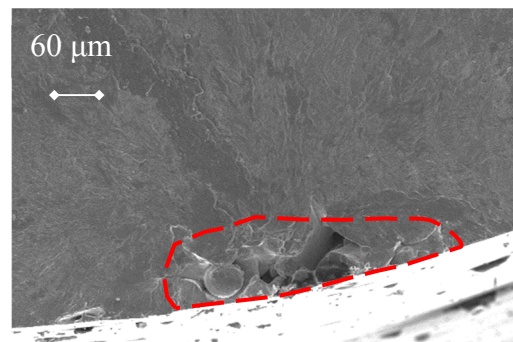


Figure 6.26: Examples of fracture surfaces relevant to the test series EN_90°_T and relevant $\sqrt{\text{area}}$ at the failure origin.

Fig. (27) reports the boxplots of the $\sqrt{\text{area}}$ per each test series in which it can be seen clearly that 90° oriented specimens present higher values than the 0° oriented ones. Only the series (S) present a median value approximately equal. Most of the failure in the 90°-oriented occurs at the surface where the support structures were removed. In this regard, Fig. 28 shows an example of the lateral surface where it can be appreciated the distribution of defects remained after polishing the specimens.

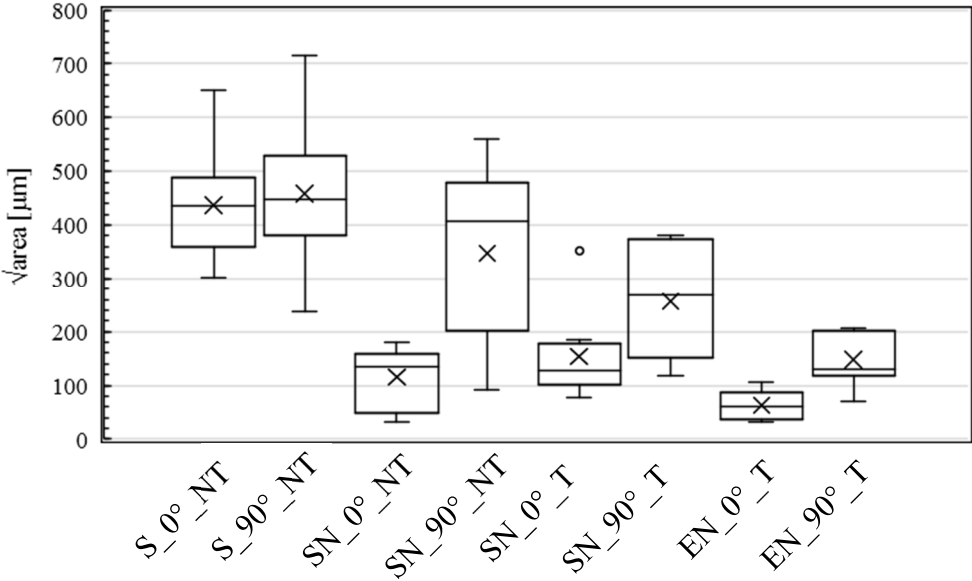


Figure 6.27: Boxplots of the $\sqrt{\text{area}}$ evaluation per each test series.

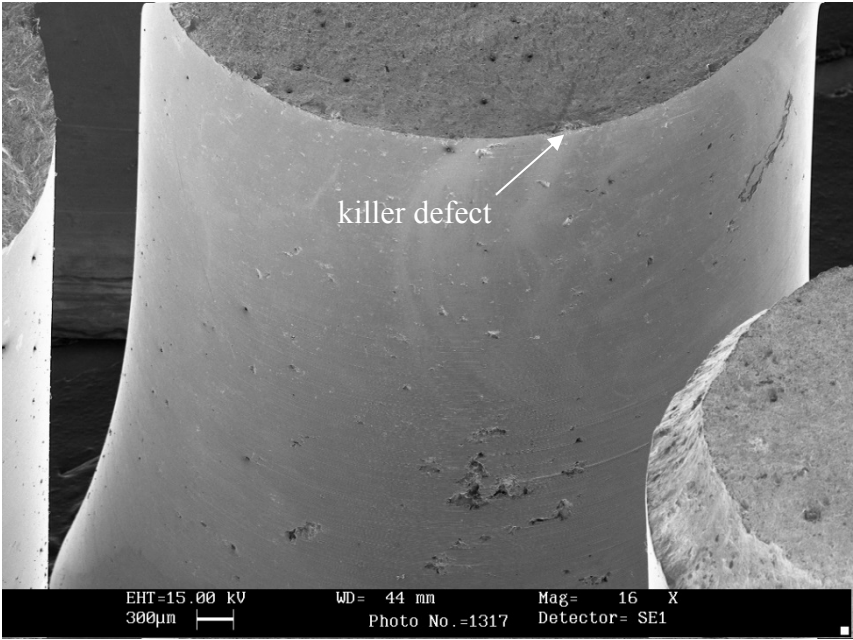


Figure 6.28: Distribution of residual defects in 90° oriented specimens.

6.4.2 Evaluation of a_0

Figs (29-32) show the results of the least square method adopted to match the left and the right-hand sides of Eq. (9) by using a_0 as calibration parameter per each test series for the same heat treatment condition. The mean hardness value between the 0° and 90° oriented test series for the same heat treatment condition was given as input of Matlab® Curve Fitting tool. As output, the fitting provided $a_0 = 50 \pm 1 \mu\text{m}$ for the test series S_0°/90°_NT and SN_0°/90°_NT (with 95% confidence bounds). Whereas, the a_0 obtained for SN_0°/90°_T and SN_0°/90°_T was equal to $40 \pm 1 \mu\text{m}$ and $38 \pm 1 \mu\text{m}$, respectively.

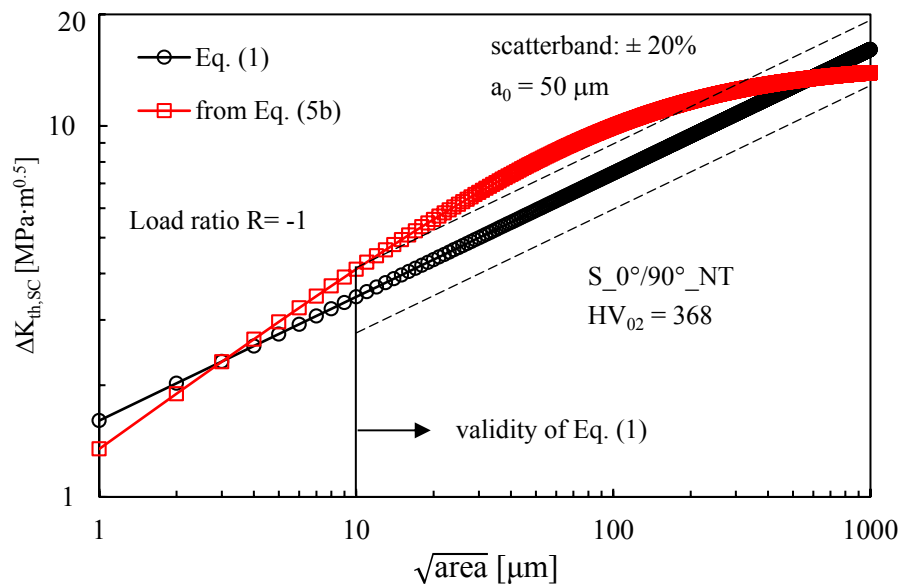


Figure 6.29: Matching Eqs. (1) and (5b) according to expression (9) to estimate the El-Haddad-Smith-Topper length parameter a_0 of the test series S_0°/90°_NT

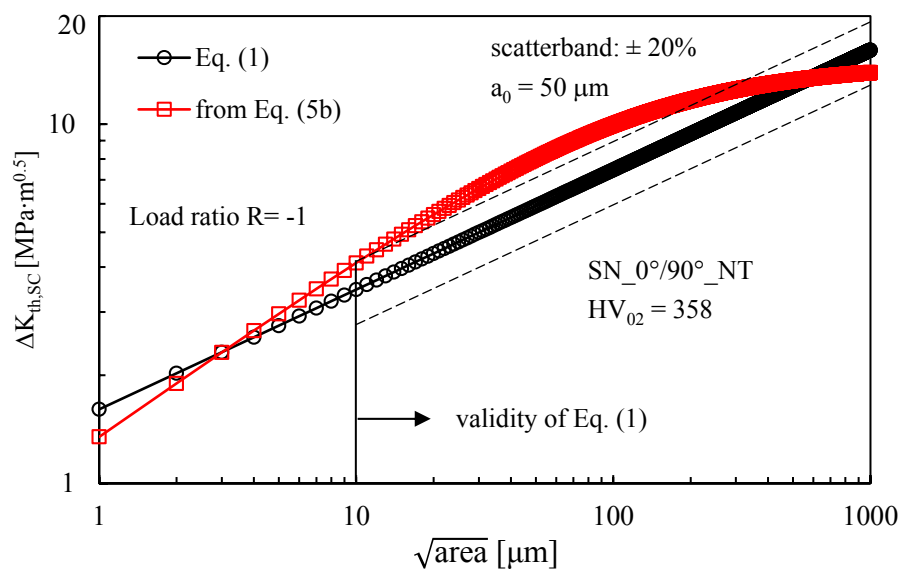


Figure 6.30: Matching Eqs. (1) and (5b) according to expression (9) to estimate the El-Haddad-Smith-Topper length parameter a_0 of the test series SN_0°/90°_NT

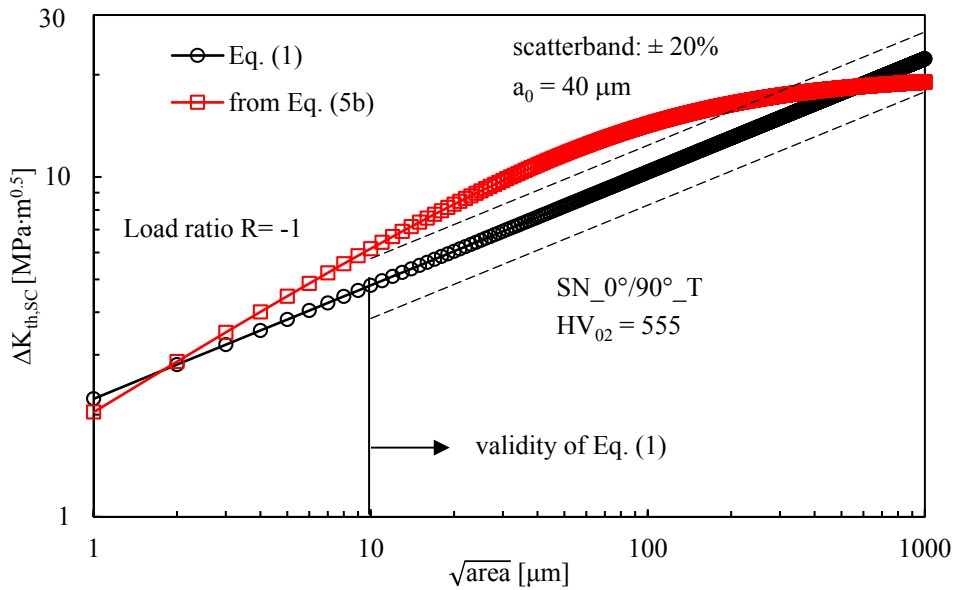


Figure 6.31: Matching Eqs. (1) and (5b) according to expression (9) to estimate the El-Haddad-Smith-Topper length parameter a_0 of the test series $SN_{0^\circ/90^\circ}_T$

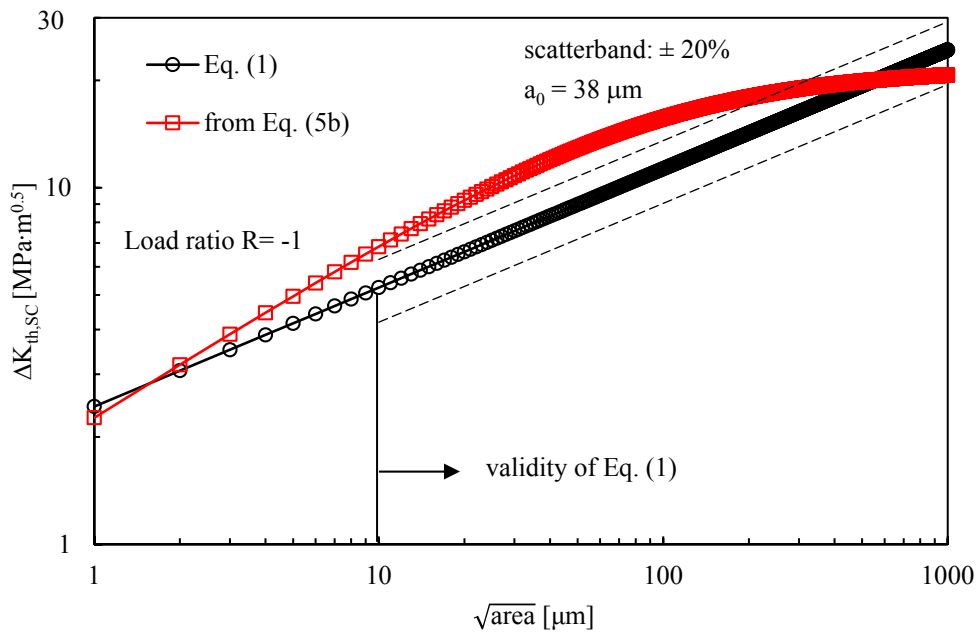


Figure 6.32: Matching Eqs. (1) and (5b) according to expression (9) to estimate the El-Haddad-Smith-Topper length parameter a_0 of the test series $EN_{0^\circ/90^\circ}_T$

Fig. (29-32) highlights the different functional form of Eq. (1) and Eq. (5b), the former having a constant slope of $1/3$ in the range $10 \mu\text{m} < \sqrt{area} < 1000 \mu\text{m}$, while the latter covering the full range of slopes from $1/2$ for very small cracks to 0 for long cracks. Previous Fig. (7b) illustrates this concept.

6.4.3 Fatigue test results expressed in terms of ΔK_{corr}

Figs (33a)-(40a) reports the data results of each test series in terms of nominal stress amplitude: the colour bar reported in the figure represents the value of the $\sqrt{\text{area}}$ for each specimen. Figs (33b)-(40b) report the results of Figs (33a)-(40a) adopting ΔK_{corr} from Eq. (2) as a damage parameter. ΔK -based scatter bands have been statistically calculated in agreement with Figs (33a)-(40a). It is worth noticing that all the ΔK -based scatter indexes are lower than the σ -based ones allowing a better fatigue life prediction. Furthermore, considering ΔK_{corr} in the HCF regime (i.e. at the fatigue limit), it might be possible to approximately evaluate the ΔK_{th} . In a recent paper, the influence of the aging heat treatment on the fatigue crack growth of AMed MS (0° -oriented) was experimentally documented. The ΔK_{th} for a load ratio $R=0.05$ was about equal to 3 $\text{MPa}\sqrt{\text{m}}$ and 4 $\text{MPa}\sqrt{\text{m}}$ for the as-built and aged condition, respectively. Analysing the ΔK_{corr} obtained for the 0° -oriented batches with a load ratio $R = -1$, the estimated ΔK_{th} ranges from 7.9 to 8.4 $\text{MPa}\sqrt{\text{m}}$ for the NT series whereas it ranges from 7.7 to 8.8 $\text{MPa}\sqrt{\text{m}}$ for the T test series.

For the sake of completeness, all the fatigue data were reported in Table 6.

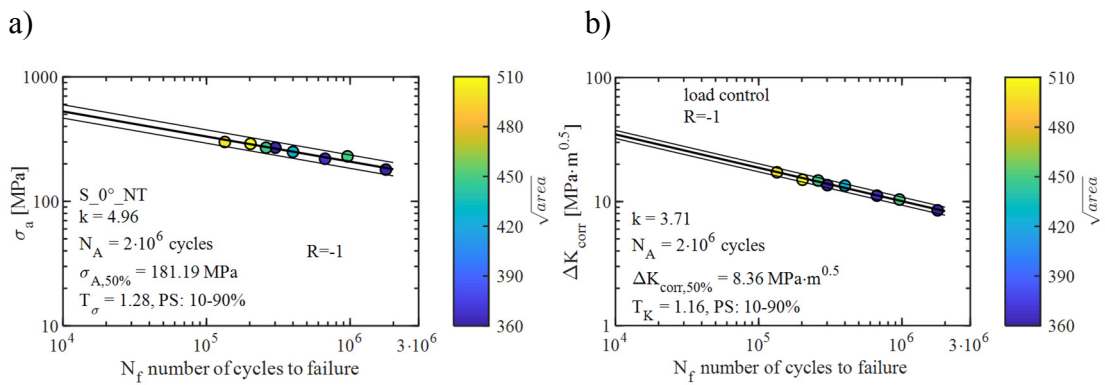


Figure 6.33: Fatigue test results in terms of nominal stress amplitude of the test series S₀_NT a). Fatigue test results in terms of ΔK_{corr} of the test series S₀_NT b)

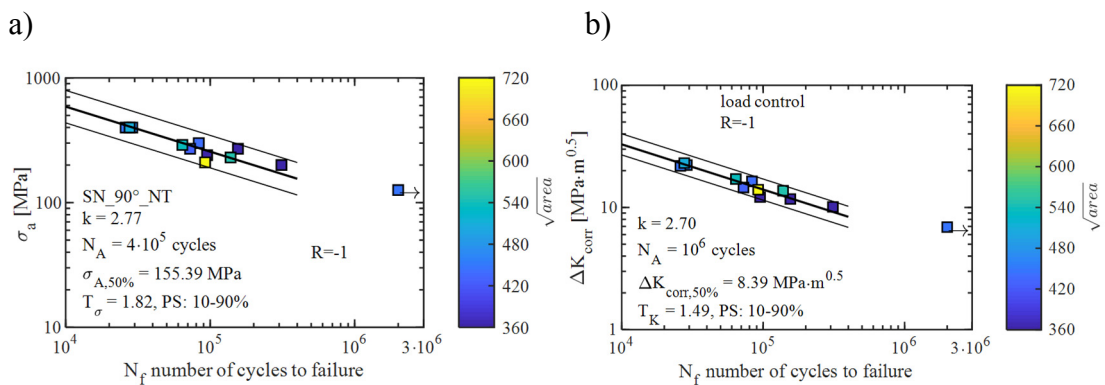


Figure 6.34: Fatigue test results in terms of nominal stress amplitude of the test series S₉₀_NT a). Fatigue test results in terms of ΔK_{corr} of the test series S₉₀_NT b)

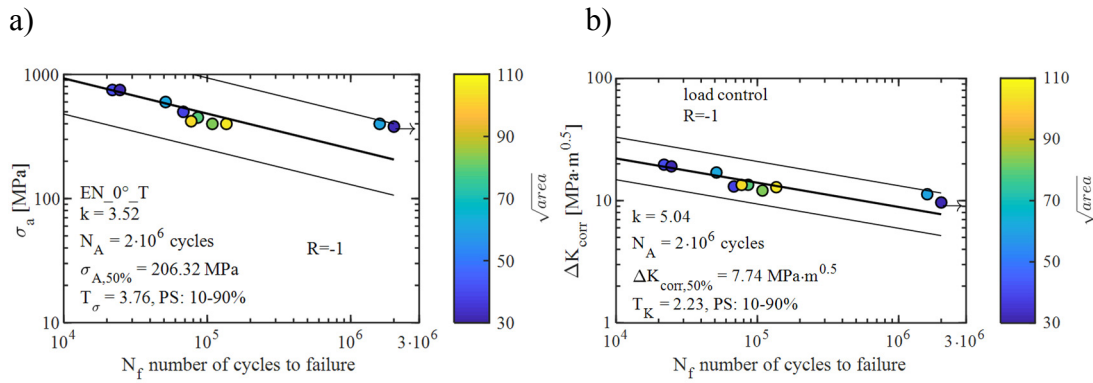


Figure 6.35: Fatigue test results in terms of nominal stress amplitude of the test series EN_0_T a). Fatigue test results in terms of ΔK_{corr} of the test series EN_0_T b)

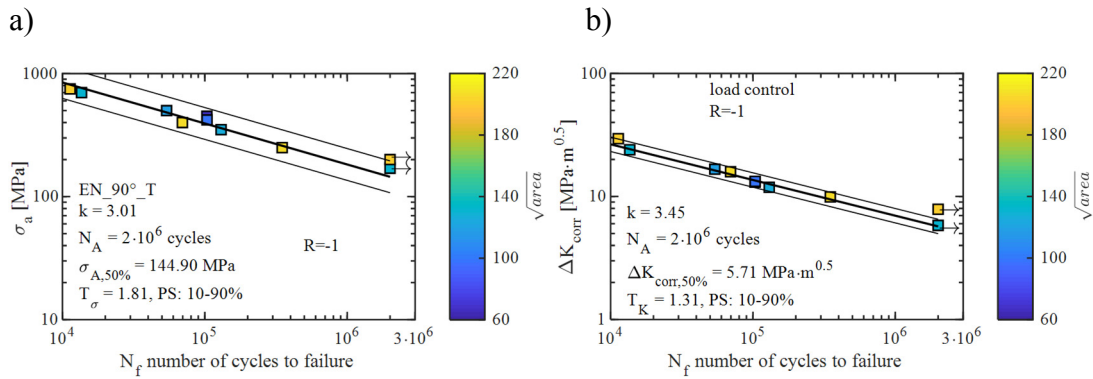


Figure 6.36: Fatigue test results in terms of nominal stress amplitude of the test series EN_90_T a). Fatigue test results in terms of ΔK_{corr} of the test series EN_90_T b)

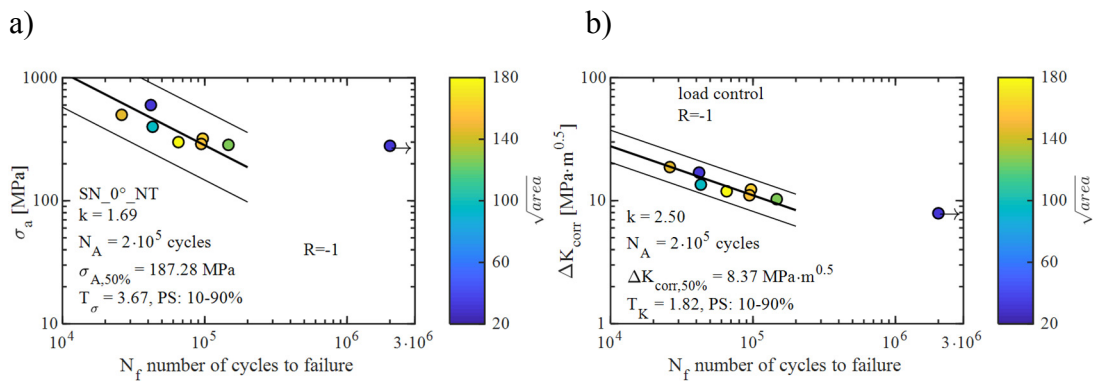


Figure 6.37: Fatigue test results in terms of nominal stress amplitude of the test series SN_0_NT a). Fatigue test results in terms of ΔK_{corr} of the test series SN_0_NT b)

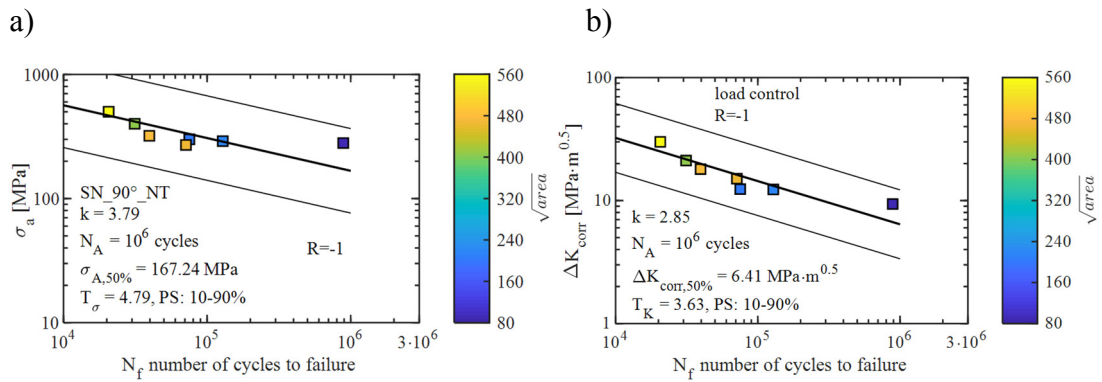


Figure 6.38: Fatigue test results in terms of nominal stress amplitude of the test series SN₉₀_NT a). Fatigue test results in terms of ΔK_{corr} of the test series SN₉₀_NT b)

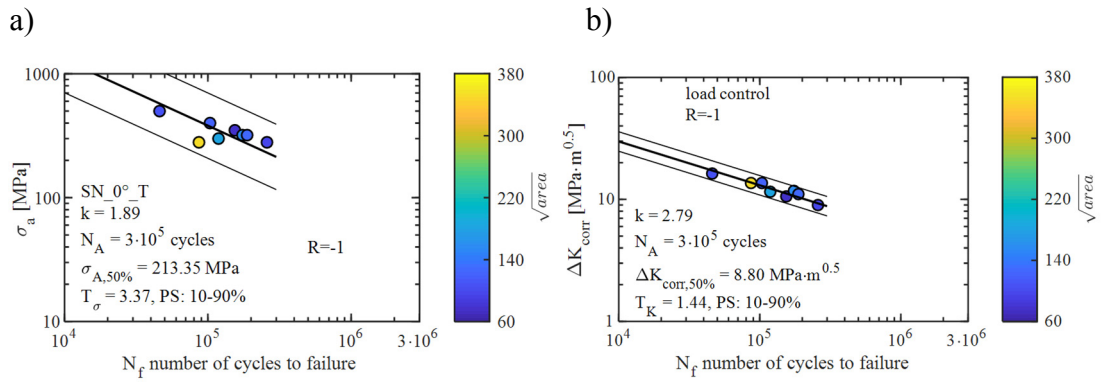


Figure 6.39: Fatigue test results in terms of nominal stress amplitude of the test series SN₀_T a). Fatigue test results in terms of ΔK_{corr} of the test series SN₀_T b)

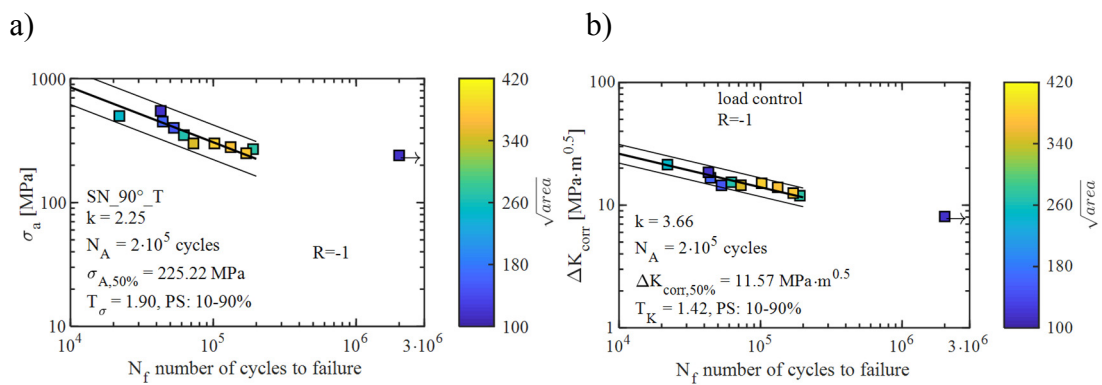


Figure 6.40: Fatigue test results in terms of nominal stress amplitude of the test series SN₉₀_T a). Fatigue test results in terms of ΔK_{corr} of the test series SN₉₀_T b)

Table 6.6: Synthesis of fatigue test results.

Batch	building orientation	Heat treatment	σ_a	$\sqrt{\text{area}}$	a_{eff}	ΔK_{corr}	N_f
	[°]		[MPa]	[μm]	[μm]	[$\text{MPa}\cdot\text{m}^{0.5}$]	[cycles]
S	0°	NT	300	502.8	212.4	17.23	1.34E+05
			270	358.2	151.4	13.58	3.01E+05
			250	426.4	180.2	13.44	4.00E+05
			230	449.4	112.4	10.39	9.59E+05
			180	302.2	127.7	8.51	1.77E+06
			290	652.1	163.0	15.00	2.02E+05
			270	447.2	188.9	14.80	2.60E+05
			220	367.3	155.2	11.17	6.69E+05
			S	90°	NT	400	463.7
300	442.3	186.9				16.37	8.33E+04
270	429.7	181.5				14.56	7.26E+04
200	362.8	153.3				10.11	3.11E+05
126	447.0°	188.9				6.90	2.00E+06
400	447.0	188.9				21.91	2.60E+04
400	509.9	215.4				23.10	2.77E+04
290	536.0	226.4				17.09	6.41E+04
270	237.2	100.2				11.73	1.56E+05
240	364.5	154.0				12.15	9.51E+04
230	551.0	232.8				13.71	1.38E+05
210	715.6	302.3				13.97	9.22E+04
EN	0°	T				400	60
			500	39	16	13.1	6.81E+04
			450	79	34	13.5	8.60E+04
			420	103	44	13.5	7.74E+04
			400	83	35	12.1	1.09E+05
			600	61	26	17.0	5.13E+04
			750	40	17	19.7	2.18E+04
			400	105	45	12.9	1.36E+05
			380	32	14	9.7	2.00E+06
			750	32	14	19.1	2.46E+04
EN	90°	T	500	119	50	16.7	5.39E+04
			450	69	29	13.1	1.03E+05
			420	98	42	13.3	1.04E+05
			400	207	88	15.9	6.96E+04
			350	127	53	11.9	1.30E+05
			250	206	87	9.9	3.50E+05
			170	131	55	5.8	2.00E+06
			700	131	55	24.0	1.36E+04
			200	202	85	7.9	2.00E+06
750	202	85	29.5	1.13E+04			

Table 6.6 continued

Batch	building orientation	Heat treatment	σ_a	$\sqrt{\text{area}}$	a_{eff}	ΔK_{corr}	N_f
	[°]		[MPa]	[μm]	[μm]	[$\text{MPa}\cdot\text{m}^{0.5}$]	[cycles]
SN	0°	NT	400	96	41	13.5	4.30E+04
			320	161	68	12.3	9.67E+04
			280	32	14	7.9	2.00E+06
			300	179	76	11.9	6.53E+04
			290	156	66	11.1	9.44E+04
			500	147	62	18.8	2.61E+04
			285	124	52	10.2	1.47E+05
			600	32	14	17.0	4.18E+04
SN	90°	NT	400	408	172	21.2	3.13E+04
			320	479	203	18.0	3.96E+04
			300	203	86	12.4	7.52E+04
			280	93	39	9.4	8.88E+05
			290	221	93	12.3	1.29E+05
			270	470	198	15.1	7.13E+04
			500	560	237	30.0	2.06E+04
			SN	0°	T	400	124
350	78	33				10.6	1.54E+05
320	159	67				11.8	1.75E+05
320	130	55				11.0	1.88E+05
300	185	78				11.6	1.19E+05
280	352	149				13.6	8.66E+04
500	105	44				16.3	4.60E+04
280	100	42				9.0	2.58E+05
SN	90°	T	400	152	400	14.5	5.30E+04
			350	269	350	15.4	6.22E+04
			300	381	300	15.1	1.02E+05
			500	250	500	21.4	2.20E+04
			300	347	300	14.5	7.26E+04
			280	373	280	14.0	1.32E+05
			450	165	450	16.7	4.42E+04
			270	273	270	11.9	1.90E+05
			250	378	250	12.5	1.70E+05
			240	119	240	8.1	2.00E+06
550	119	550	18.5	4.28E+04			

6.4.4 Sharp V-notch results

Constant amplitude, load controlled fatigue tests were carried out on V-notched specimens of the test series SN_0°/90°_NT (Fig (9c) and table 5) both with and without pre-cracking.

It is known from the literature that applying a compression pulsating cyclic load, a non-propagating crack having length theoretically equal to the radius of the plastic zone $r_{p,\varepsilon}$ can emanate from the notch[22]. Pre-cracking was carried out only for the test series VS_90°_NT by adopting a load ratio R equal to 20 and a minimum load ables to emanate a circumferential crack from the notch having a length equal to 0.13 mm according to the Dugdale Eq. (3) in plane strain condition [23] :

$$r_{p,\varepsilon} = \frac{\pi}{3 \cdot 8} \cdot \left(\frac{|K_{\min}|}{\sigma_0} \right)^2 \quad (3)$$

where the yield strength σ_0 was determined in a previous paper as 1100 MPa [1]. The resulting pre-crack was measured after fatigue failure, by analysing the fracture surfaces with an optical microscope. After measuring the notch-plus-pre-crack length a_p , (Fig. 41) the initial elastic stress intensity factor range could be calculated by means of analytical expression of a circumferential crack in a cylindrical bar under tension from [24] according to the following equation.

$$\Delta K = \alpha \cdot \Delta \sigma_g \cdot \sqrt{\pi \cdot (a + a_p)} \quad (11)$$

The precracking was effective in all the specimens except for the SN_V_0_NT_1 as it can be observed in Fig. (42) and (43).

The synthesis of the fatigue data relevant to V-notched MS was reported in table 7.



Figure 6.41: pre-crack a_p after fatigue failure.

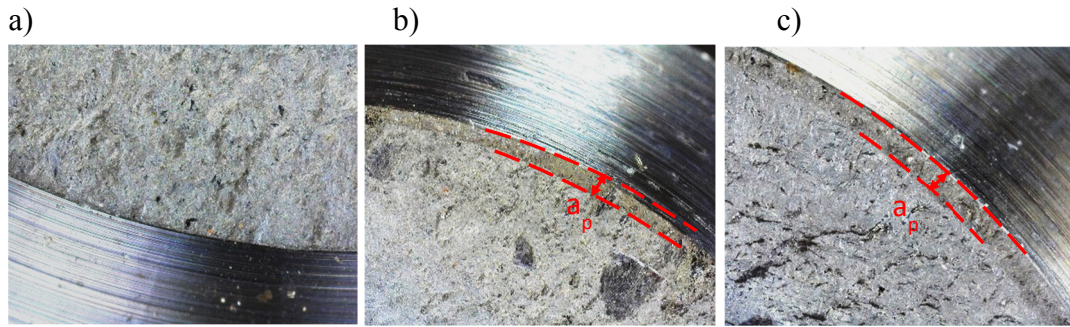


Figure 6.42: precrack observed after fatigue failure of SN_V_0_NT_1 a) SN_V_0_NT_2 b) and SN_V_0_NT_3 c).

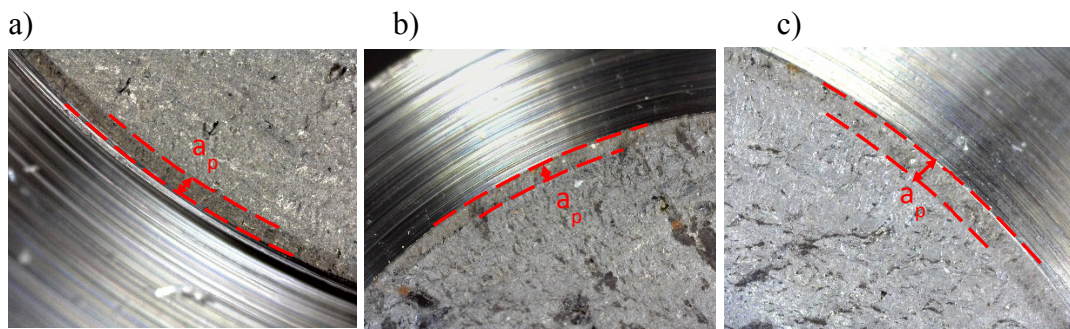


Figure 6.43: precrack observed after fatigue failure of SN_V_90_NT_1 a) SN_V_90_NT_2 b) and SN_V_90_NT_3 c).

Table 6.7: Synthesis of fatigue data relevant to V-notched AMed MS specimens.

Specimen	R	D_g	a	a_p	α	F_{max}	F_{min}	f_L	ΔK_I	N
		[mm]	[mm]	[mm]		[kN]	[kN]	[Hz]	[MPa \sqrt{m}]	[cycles]
SN_V_0_NT_1	-1	11.18	1.24	\	1.290	6.32	-6.32	20.0	10.45	2.00E+06*
SN_V_0_NT_1_RETEST	-1	11.18	1.24	\	1.290	8.04	-8.04	30.0	13.25	2.36E+05
SN_V_0_NT_2	-1	11.09	1.19	0.13	1.311	9.721	-9.721	30.0	16.98	9.78E+04
SN_V_0_NT_3	-1	11.17	1.09	0.14	1.288	10.193	-10.193	30.0	16.81	1.75E+05
SN_V_90_NT_1	-1	11.05	1.15	0.1	1.296	15.56	-15.56	20.0	26.30	2.26E+04
SN_V_90_NT_2	-1	11.08	1.2	0.14	1.316	6.158	-6.16	30.0	10.95	1.24E+05
SN_V_90_NT_3	-1	10.44	1.44	0.14	1.386	4.358	-4.358	30.0	10.10	2.22E+05

In Fig. 44 and 45 the experimental results of the fatigue tests expressed in terms of applied ΔK_I versus the observed number of cycles to failure relevant to the test series SN_V_0°/90°_NT are reported with filled markers along with scatter band calibrated on experimental results generated from the natural defects (Fig. 37b and 38b). Even though further experiments on crack-like notches would be necessary to validate the endurable stress intensity factors reported in Fig. (44) and (45), the same figures suggest that for the 0° and 90°-oriented specimens the difference between the estimated resistance of the material to long cracks/crack-like notches and the

experimental data is not that substantial to be revealed by just the reduced number of validation tests performed here.

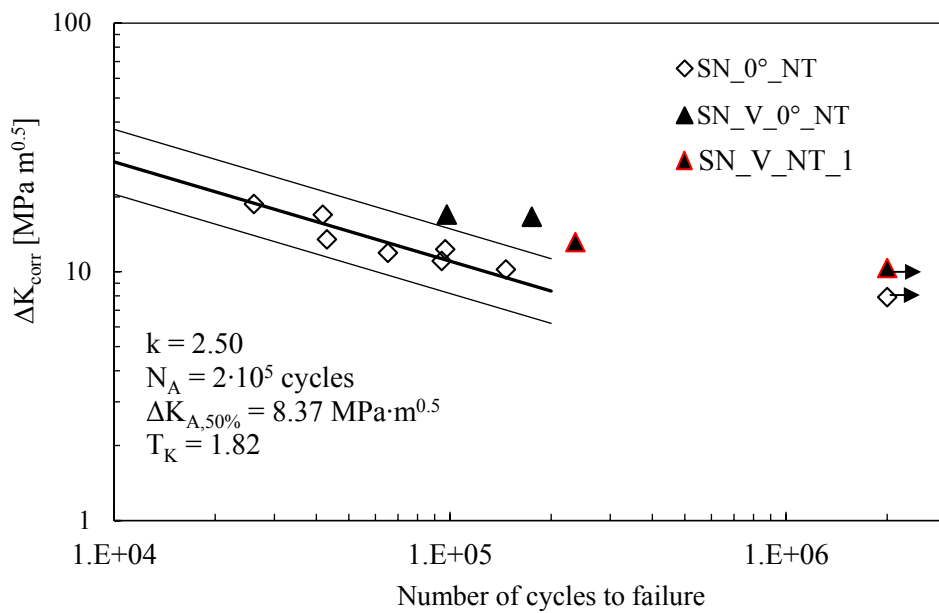


Figure 6.44: Fatigue test results of maraging steel specimens oriented at 0° in terms of ΔK_{corr} . Additional experimental results on V-notched, 0° -oriented specimens (see geometry in Fig. 9c) are reported.

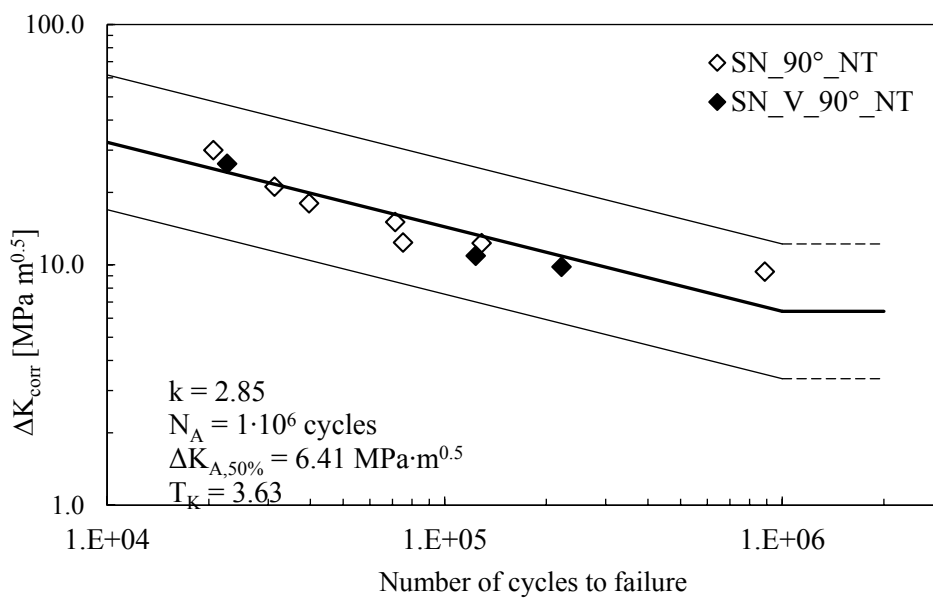


Figure 6.45: Fatigue test results of maraging steel specimens oriented at 90° in terms of ΔK_{corr} . Additional experimental results on V-notched, 90° -oriented specimens (see geometry in Fig. 9c) are reported.

6.5 CONCLUSIONS

Constant amplitude fatigue test results on wrought and AMed maraging steel specimens have been presented. In particular, three batches of AMed specimens were produced by two different AM systems (EOS Gmbh and SISMA Spa). Both 0°-oriented and 90°-oriented specimens were tested. Two batches provided by SISMA were produced by adopting different process parameter in order to produced large Lack of Fusion defects in one (test series S) and minimize the size of them in the other one (test series SN). For the wrought and SN maraging steel, the influence of the aging heat treatment was also analysed.

The fatigue strength of wrought (TM series) aged MS resulted in 11% higher than the same material in the annealed condition.

All the AMed fatigue results present a higher scatter and lower fatigue strength compared to the wrought MS, especially in the HCF regime. The test series relevant to 0°-oriented specimens presents higher fatigue strength than the 90°-ones except for the test series SN which does not seem to be affected by the building orientation (Fig. 18c). For the same building orientation, aged specimens have roughly 20%-30% higher fatigue strength than as-built specimens in the medium cycle fatigue range, while the few data available do not allow to draw a conclusion in the high cycle fatigue range, even if the experimental results seem to suggest a weak influence of the aging heat treatment on the fatigue limit.

After failure, all the fracture surfaces were analysed by a SEM, and the \sqrt{area} parameter of the killer defects was evaluated. In parallel, the a_0 material parameter was evaluated by fitting the Murakami and El Haddad -Smith-Topper models and the resulting values were 50 μm (for S batch and SN batch, not heat-treated), 40 μm (for SN batch in aged condition) and 38 μm (for EN batch in aged condition).

Stress intensity factor-based design curve for all the test series was then derived, by taking into account the short crack effect by means of the El-Haddad-Smith-Topper model. By adopting the latter parameter, the scatter indexes of the 10%-90% survival probability curves for all the test series were reduced as compared to the nominal stress-based curves. The relevant ratio $T_{\Delta K}/T_{\sigma}$ are the following

- S_0°_NT, $T_{\Delta K}/T_{\sigma} = 0.91$
- S_90°_NT, $T_{\Delta K}/T_{\sigma} = 0.81$
- EN_0°_T, $T_{\Delta K}/T_{\sigma} = 0.59$
- EN_90°_T, $T_{\Delta K}/T_{\sigma} = 0.72$
- SN_0°_NT, $T_{\Delta K}/T_{\sigma} = 0.49$
- SN_90°_NT, $T_{\Delta K}/T_{\sigma} = 0.75$
- SN_0°_T, $T_{\Delta K}/T_{\sigma} = 0.42$
- SN_90°_T, $T_{\Delta K}/T_{\sigma} = 0.74$

Finally, the ΔK_{corr} -based scatter bands were compared to the fatigue test results relevant to V-notched and pre-cracked specimens of the SN not heat-treated batch. In

particular, results of V-notched 90° oriented specimens fit the ΔK_{corr} -based scatter band of SN 90° whereas the fatigue life obtained from V-notched 0° oriented specimens was underestimated by the relevant predicting scatter band

6.6 REFERENCES

- [1] Meneghetti G, Rigon D, Cozzi D, Waldhauser W, Dabalà M. Influence of build orientation on static and axial fatigue properties of maraging steel specimens produced by additive manufacturing. *Procedia Struct Integr* 2017;7:149–57. doi:10.1016/j.prostr.2017.11.072.
- [2] Meneghetti G, Rigon D, Gennari C. An analysis of defects influence on axial fatigue strength of maraging steel specimens produced by additive manufacturing. *Int J Fatigue* 2019;118:54–64. doi:10.1016/j.ijfatigue.2018.08.034.
- [3] Kempen K, Yasa E, Thijs L, Kruth JP, Van Humbeeck J. Microstructure and mechanical properties of Selective Laser Melted 18Ni-300 steel. *Phys Procedia* 2011;12:255–63. doi:10.1016/j.phpro.2011.03.033.
- [4] Croccolo D, De Agostinis M, Fini S, Olmi G, Vranic A, Ciric-Kostic S. Influence of the build orientation on the fatigue strength of EOS maraging steel produced by additive metal machine. *Fatigue Fract Eng Mater Struct* 2016;39:637–47. doi:10.1111/ffe.12395.
- [5] Branco R, Costa J, Berto F, Razavi S, Ferreira J, Capela C, et al. Low-Cycle Fatigue Behaviour of AISI 18Ni300 Maraging Steel Produced by Selective Laser Melting. *Metals (Basel)* 2018;8:32. doi:10.3390/met8010032.
- [6] Smith KN, Watson P, Topper TH. A Stress-Strain Function for the Fatigue of Metals. *J Mater ASTM* 1970;5:767–78.
- [7] Van Swam LF, Pelloux RM, Grant NJ. Fatigue behavior of maraging steel 300. *Metall Trans A* 1975;6:45–54. doi:10.1007/BF02673669.
- [8] Kitagawa H, Takahashi S. Applicability of fracture mechanics to very small cracks or the cracks in the early stage. *Proc 2nd int conf mech Behav. Mater. - ICM2*, 1976, p. 627–31.
- [9] Murakami Y, Endo M. Quantitative evaluation of fatigue strength of metals containing various small defects or cracks. *Eng Fract Mech* 1983;17:1–15. doi:10.1016/0013-7944(83)90018-8.
- [10] Murakami Y. Analysis of stress intensity factors of modes I, II and III for inclined surface cracks of arbitrary shape. *Eng Fract Mech* 1985;22:101–14. doi:10.1016/0013-7944(85)90163-8.
- [11] Murakami Y, Endo M. Effects of defects, inclusions and inhomogeneities on fatigue strength. *Int J Fatigue* 1994;16:163–82. doi:10.1016/0142-1123(94)90001-9.
- [12] Murakami Y (Yukitaka). *Metal fatigue : effects of small defects and nonmetallic inclusions*. Elsevier; 2002.
- [13] Atzori B, Lazzarin P. Notch sensitivity and defect sensitivity under fatigue loading.pdf. *Int J Fract* 2000;107:L3–8. doi:10.1023/A:1007686727207.
- [14] Atzori B, Lazzarin P, Meneghetti G. Fracture mechanics and notch sensitivity. *Fatigue Fract Eng Mater Struct* 2003;26:257–67. doi:10.1046/j.1460-2695.2003.00633.x.
- [15] Atzori B, Lazzarin P, Meneghetti G. A unified treatment of the mode I fatigue limit of components containing notches or defects. *Int J Fract* 2005;133:61–

87. doi:10.1007/s10704-005-2183-0.
- [16] Williams ML. Stress singularities resulting from various boundary conditions in angular corners of plates in tension. *J Appl Mech* 1952;19:526–8.
- [17] Gross B, Mendelson A. Plane elastostatic analysis of V-notched plates. *Int J Fract Mech* 1972;8:267–76. doi:10.1007/BF00186126.
- [18] El Haddad MH, Smith KN, Topper TH. Fatigue Crack Propagation of Short Cracks. *J Eng Mater Technol* 1979;101:42. doi:10.1115/1.3443647.
- [19] El Haddad MH, Topper TH, Smith KN. Prediction of non propagating cracks. *Eng Fract Mech* 1979;11:573–84. doi:10.1016/0013-7944(79)90081-X.
- [20] Lazzarin P, Berto F. From Neuber’s Elementary Volume to Kitagawa and Atzori’s Diagrams: An Interpretation Based on Local Energy. *Int J Fract* 2005;135:L33–8. doi:10.1007/s10704-005-4393-x.
- [21] Mutua J, Nakata S, Onda T, Chen ZC. Optimization of selective laser melting parameters and influence of post heat treatment on microstructure and mechanical properties of maraging steel. *Mater Des* 2018;139:486–97. doi:10.1016/j.matdes.2017.11.042.
- [22] Maierhofer J, Kolitsch S, Pippan R, Gänser HP, Madia M, Zerbst U. The cyclic R-curve – Determination, problems, limitations and application. *Eng Fract Mech* 2018;198:45–64. doi:10.1016/j.engfracmech.2017.09.032.
- [23] Anderson TL. *Fracture mechanics: fundamentals and applications*. 3rd ed. CRC Press; 2005.
- [24] Murakami Y (Yukitaka). *Stress intensity factors handbook*. Pergamon; 1987.

Conclusions

This dissertation deals with fatigue assessment of metallic material and components by adopting local energy-based parameters which are widely proposed and adopted in the literature. More precisely, an extension of the applicability of three energy-based approaches to several factors that influence the fatigue strength of material and components, in addition to those already included on the relevant approach, was the aim of the present dissertation.

Regarding the first one, the Peak Stress Method was extended to assess the fatigue strength of both steel and aluminum welded joints subjected to multiaxial loading conditions. A new scatter band expressed in terms of range of the equivalent peak stress has been proposed per each material. For validating the scatter bands, about 420 multiaxial fatigue data taken from the literature relevant to both steel and aluminum welded joints were analysed by using the PSM. As regards steel welded joint (350 fatigue data), on about 50 fatigue results the theoretical predictions based on the PSM were extremely on the safe side. Most of those data were characterized by remarkable long crack propagation paths (up to 500 mm) developed during the experimental tests with applied torsional loading. Such a long fraction of the total fatigue life can hardly be rationalized by the PSM, because by nature the method captures the fatigue damage induced by the intense NSIF-dominated local stresses existing in the small volume of material surrounding the crack initiation point. Dealing with the remaining test data, a good agreement has been obtained from the comparison of theoretical estimations with the experimental fatigue results, 205 data among 298 (i.e. 69%) falling within the 2.3-97.7% design scatter band. As regard aluminum welded joints, 70 among 72 experimental data (i.e. 97%) successfully falling inside the proposed 2.3-97.7% scatter band. Because of the simplicity of a point-like method combined with the robustness of the NSIF approach, the PSM might be useful in industrial applications.

The second energy-based approach assumes the specific heat loss per cycle Q as a fatigue damage indicator. The specific heat loss per cycle (Q parameter) evaluated experimentally by means of the so-called cooling gradient technique was used in previous works to synthesise 140 experimental fatigue test results generated from plain and bluntly notched specimens made of AISI 304L stainless steel. In this work the cooling gradient was measured by means of a FLIR SC7600 infrared camera, equipped with proper lens and a spacer ring to achieve a 20 $\mu\text{m}/\text{pixel}$ spatial resolution and fully reversed axial fatigue tests were carried out on 4-mm-thick, hot-rolled AISI 304L stainless steel specimens, characterized by 3, 1 and 0.5 mm notch tip radii. A good agreement between the new fatigue test results and the existing heat energy-based

scatter band previously calibrated was found. Finally, the analysis of the thermal energy distribution around the notch tip was performed and discussed

Regarding the same approach, the specific heat loss was also measured in constant amplitude multiaxial fatigue tests on both AISI 304L stainless steel and C45 steel specimens. Two phase-shift angle between the loads (0° and 90°) and two biaxiality ratios (1 and $\sqrt{3}$) were analysed. All the fatigue test results on both materials resulted in good agreements with the relevant scatter band previously calibrated except for the out of phase multiaxial fatigue results relevant to the AISI 304L steel. These results seem to be justified by the strain-induced martensitic transformation in metastable austenitic stainless steel, significantly present in out of phase cyclic loading condition.

Finally, the influence of defects on fatigue behaviour of maraging steel specimens has been investigated. Axial fatigue tests were carried out on three batches of AMed maraging steel specimens produced by two different AM systems. Furthermore, axial fatigue tests were carried out on wrought maraging steel specimens both in annealed and in aged condition. After failure, the $\sqrt{\text{area}}$ of the killer defects was examined by SEM observations of the fracture surfaces. A stress intensity factor-based design curve for the all the test series was obtained taking into account the short crack effect by means of the El-Haddad-Smith-Topper model. The ΔK_{corr} -based scatter bands were characterized by a scatter index significantly lower than that one stress-based. Due to the lack of expensive experimental data to determine the relevant material length parameter a_0 , a novel rapid method to approximately evaluate a_0 has been proposed. In particular, it consists in matching El-Haddad-Smith-Topper model with Murakami's expression of the threshold range of mechanically short cracks. The advantage of the adopted engineering approach is that only Vickers hardness of the material is necessary. Theoretically, this rapid method can be also adopted to estimate the size of the control volume of the averaged SED approach due to the analogy of the latter to the material length parameter a_0 . In the end, the stress intensity factor-based design curve was adopted to estimate the fatigue strength of sharp V-shaped notches characterized by a reduced notch opening angle.

Bibliography

For a better reading, numbered references have been included at the end of each Chapter. Below, the complete list of references is reported in alphabetical order.

Anderson TL. Fracture mechanics: fundamentals and applications. 3rd ed. CRC Press; 2005.

ASTM A276, Standard Specification for Stainless Steel Bars and Shapes n.d.

Atzori B, Berto F, Lazzarin P, Quaresimin M. Multi-axial fatigue behaviour of a severely notched carbon steel. *Int J Fatigue* 2006;28:485–93. doi:10.1016/j.ijfatigue.2005.05.010.

Atzori B, Lazzarin P, Meneghetti G. A unified treatment of the mode I fatigue limit of components containing notches or defects. *Int J Fract* 2005;133:61–87. doi:10.1007/s10704-005-2183-0.

Atzori B, Lazzarin P, Meneghetti G. Fracture mechanics and notch sensitivity. *Fatigue Fract Eng Mater Struct* 2003;26:257–67. doi:10.1046/j.1460-2695.2003.00633.x.

Atzori B, Lazzarin P. Notch sensitivity and defect sensitivity under fatigue loading.pdf. *Int J Fract* 2000;107:L3–8. doi:10.1023/A:1007686727207.

Audenino A, Goglio L, Rossetto M. *Metodi sperimentali per la progettazione* 1997.

Bäckström M, Siljander A, Kuitunen R, Ilvonen R. Multiaxial fatigue experiments of square hollow section tube-to plate welded joints. In: Blom AF, editor. *First North Eur. Eng. Sci. Conf. (NESCO I)*, London, UK: Welded High strength steel structures, EMAS; 1997, p. 163–77.

Bär J, Seifert S. Investigation of Energy Dissipation and Plastic Zone Size During Fatigue Crack Propagation in a High-Alloyed Steel. *Procedia Mater Sci* 2014;3:408–13. doi:10.1016/j.mspro.2014.06.068.

Bär J, Vshivkov A, Plekhov O. Combined lock-in thermography and heat flow measurements for analysing heat dissipation during fatigue crack propagation. *Frat Ed Integrita Strutt* 2015;9:456–65. doi:10.3221/IGF-ESIS.34.51.

- Bayerlein M, Christ H-J, Mughrabi H. Plasticity-induced martensitic transformation during cyclic deformation of AISI 304L stainless steel. *Mater Sci Eng A* 1989;114:L11–6. doi:10.1016/0921-5093(89)90871-X.
- Beaman JJ, Deckard CR. Selective laser sintering with assisted powder handling. 4938816., 1990.
- Benedetti M, Fontanari V, Bandini M, Zanini F, Carmignato S. Low- and high-cycle fatigue resistance of Ti-6Al-4V ELI additively manufactured via selective laser melting: Mean stress and defect sensitivity. *Int J Fatigue* 2018;107:96–109. doi:10.1016/j.ijfatigue.2017.10.021.
- Beretta S, Romano S. A comparison of fatigue strength sensitivity to defects for materials manufactured by AM or traditional processes. *Int J Fatigue* 2017;94:178–91. doi:10.1016/j.ijfatigue.2016.06.020.
- Bertini L, Cera A, Frenzo F. Experimental investigation of the fatigue resistance of pipe-to-plate welded connections under bending, torsion and mixed mode loading. *Int J Fatigue* 2014;68:178–85. doi:10.1016/j.ijfatigue.2014.05.005.
- Berto F, Lazzarin P, Yates JR. Multiaxial fatigue of V-notched steel specimens: A non-conventional application of the local energy method. *Fatigue Fract Eng Mater Struct* 2011;34:921–43. doi:10.1111/j.1460-2695.2011.01585.x.
- Berto F, Lazzarin P. Fatigue strength of structural components under multi-axial loading in terms of local energy density averaged on a control volume. *Int J Fatigue* 2011;33:1055–65. doi:10.1016/j.ijfatigue.2010.11.019.
- Bhadeshia HKDH, Wayman CM. Phase Transformations: Nondiffusive. *Phys. Metall.* Fifth Ed., vol. 1, Elsevier Inc.; 2014, p. 1021–72. doi:10.1016/B978-0-444-53770-6.00009-5.
- Boukharouba T, Tamine T, Niu L, Chehimi C, Pluvinage G. The use of notch stress intensity factor as a fatigue crack initiation parameter. *Eng Fract Mech* 1995;52:503–12. doi:10.1016/0013-7944(94)00242-A.
- Boulanger T. Calorimetric analysis of dissipative and thermoelastic effects associated with the fatigue behavior of steels. *Int J Fatigue* 2004;26:221–9. doi:10.1016/S0142-1123(03)00171-3.
- Branco R, Costa J, Berto F, Razavi S, Ferreira J, Capela C, et al. Low-Cycle Fatigue Behaviour of AISI 18Ni300 Maraging Steel Produced by Selective Laser Melting. *Metals (Basel)* 2018;8:32. doi:10.3390/met8010032.

- Campagnolo A, Meneghetti G. Rapid estimation of notch stress intensity factors in 3D large-scale welded structures using the peak stress method. *MATEC Web Conf* 2018;165:17004. doi:10.1051/mateconf/201816517004.
- Carlton HD, Haboub A, Gallegos GF, Parkinson DY, MacDowell AA. Damage evolution and failure mechanisms in additively manufactured stainless steel. *Mater Sci Eng A* 2016;651:406–14. doi:10.1016/j.msea.2015.10.073.
- Casavola C, Galietti U, Modugno D, Pappalettere C. An application of the differential thermographic technique for welded joints fatigue evaluation. *SPIE*, 2006, p. 6250.
- Chrysochoos A, Berthel B, Latourte F, Galtier A, Pagano S, Wattrisse B. Local energy analysis of high-cycle fatigue using digital image correlation and infrared thermography. *J Strain Anal Eng Des* 2008;43:411–22. doi:10.1243/03093247JSA374.
- Chrysochoos A, Louche H. An infrared image processing to analyse the calorific effects accompanying strain localisation. *Int J Eng Sci* 2000;38:1759–88. doi:10.1016/S0020-7225(00)00002-1.
- Connesson N, Maquin F, Pierron F. Dissipated energy measurements as a marker of microstructural evolution : 316L and DP600 q. *Acta Mater* 2011;59:4100–15. doi:10.1016/j.actamat.2011.03.034.
- Costa JDM, Abreu LMP, Pinho ACM, Ferreira JAM. Fatigue behaviour of tubular AlMgSi welded specimens subjected to bending-torsion loading. *Fatigue Fract Eng Mater Struct* 2005;28:399–407. doi:10.1111/j.1460-2695.2005.00875.x.
- Croccolo D, De Agostinis M, Fini S, Olmi G, Vranic A, Ciric-Kostic S. Influence of the build orientation on the fatigue strength of EOS maraging steel produced by additive metal machine. *Fatigue Fract Eng Mater Struct* 2016;39:637–47. doi:10.1111/ffe.12395.
- Curà F, Curti G, Sesana R. A new iteration method for the thermographic determination of fatigue limit in steels. *Int J Fatigue* 2005;27:453–9. doi:10.1016/j.ijfatigue.2003.12.009.
- Dahle T, Olsson K-E, Jonsson B, Bäckström M, Siljander A, Kuitunen R, et al. Multiaxial fatigue experiments of square hollow section tube-to plate welded joints. In: Blom AF, editor. *Proc. First North Eur. Eng. Sci. Conf. (NESCO I), Welded High strength steel Struct.*, London, UK: EMAS Ltd; 1997, p. 163–177.
- Das A, Sivaprasad S, Chakraborti PC, Tarafder S. Morphologies and characteristics of deformation induced martensite during low cycle fatigue behaviour of austenitic

- stainless steel. *Mater Sci Eng A* 2011;528:7909–14. doi:10.1016/J.MSEA.2011.07.011.
- Das A. Dislocation configurations through austenite grain misorientations. *Int J Fatigue* 2015;70:473–9. doi:10.1016/J.IJFATIGUE.2014.06.012.
- Dengel D, Harig H. Estimation of the fatigue limit by progressively-increasing load tests. *Fatigue Fract Eng Mater Struct* 1980;3:113–28. doi:10.1111/j.1460-2695.1980.tb01108.x.
- Dey R, Tarafder S, Sivaprasad S. Influence of phase transformation due to temperature on cyclic plastic deformation in 304LN stainless steel. *Int J Fatigue* 2016;90:148–57. doi:10.1016/J.IJFATIGUE.2016.04.030.
- DIAZ FA, Patterson EA, Tomlinson RA, Yates JR. Measuring stress intensity factors during fatigue crack growth using thermoelasticity. *Fatigue Fract Eng Mater Struct* 2004;27:571–83. doi:10.1111/j.1460-2695.2004.00782.x.
- DIN EN 1706, Aluminium and Aluminium Alloys e Castings e Chemical Composition and Mechanical Properties, 2013-12 n.d.
- Donachie MJ. *Titanium: A Technical Guide*, 2nd Edition. vol. 99. 2000. doi:10.5772/1844.
- Dulieu-Barton JM. Introduction to thermoelastic stress analysis. *Strain* 1999;35:35–9. doi:10.1111/j.1475-1305.1999.tb01123.x.
- Edwards P, Ramulu M. Effect of build direction on the fracture toughness and fatigue crack growth in selective laser melted Ti-6Al-4V. *Fatigue Fract Eng Mater Struct* 2015;38:1228–36. doi:10.1111/ffe.12303.
- Edwards P, Ramulu M. Fatigue performance evaluation of selective laser melted Ti-6Al-4V. *Mater Sci Eng A* 2014;598:327–37. doi:10.1016/j.msea.2014.01.041.
- El Haddad MH, Smith KN, Topper TH. Fatigue Crack Propagation of Short Cracks. *J Eng Mater Technol* 1979;101:42. doi:10.1115/1.3443647.
- El Haddad MH, Topper TH, Smith KN. Prediction of non propagating cracks. *Eng Fract Mech* 1979;11:573–84. doi:10.1016/0013-7944(79)90081-X.
- Ellyin F. *Fatigue damage, crack growth, and life prediction*. Chapman & Hall; 1997.
- Eurocode 3: Design of steel structures – part 1–9: Fatigue. CEN; 2005.
- Eurocode 9: Design of aluminium structures - Part 1-3: Structures susceptible to fatigue. CEN; 2011.

- Everton SK, Hirsch M, Stravroulakis P, Leach RK, Clare AT. Review of in-situ process monitoring and in-situ metrology for metal additive manufacturing. *Mater Des* 2016;95:431–45. doi:10.1016/j.matdes.2016.01.099.
- Fan J, Guo X, Wu C. A new application of the infrared thermography for fatigue evaluation and damage assessment. *Int J Fatigue* 2012;44:1–7. doi:10.1016/j.ijfatigue.2012.06.003.
- Fargione G, Geraci A, La Rosa G, Risitano A. Rapid determination of the fatigue curve by the thermographic method. *Int J Fatigue* 2002;24:11–9. doi:10.1016/S0142-1123(01)00107-4.
- Frendo F, Bertini L. Fatigue resistance of pipe-to-plate welded joint under in-phase and out-of-phase combined bending and torsion. *Int J Fatigue* 2015;79:46–53. doi:10.1016/j.ijfatigue.2015.04.020.
- Galietti U, Palumbo D, Finis R De, Ancona F. Fatigue damage evaluation of martensitic stainless steel by means of thermal methods Valutazione del danneggiamento a fatica di acciai inossidabili martensitici mediante metodi termici 2013;1560:80–90.
- Germain P, Nguyen QS, Suquet P. Continuum thermodynamics. *J Appl Mech Trans ASME* 1983;50:1010–20. doi:10.1115/1.3167184.
- Gong H, Rafi K, Gu H, Starr T, Stucker B. Analysis of defect generation in Ti-6Al-4V parts made using powder bed fusion additive manufacturing processes. *Addit Manuf* 2014;1:87–98. doi:10.1016/j.addma.2014.08.002.
- Gross B, Mendelson A. Plane elastostatic analysis of V-notched plates. *Int J Fract Mech* 1972;8:267–76. doi:10.1007/BF00186126.
- Gu D, Hagedorn Y-C, Meiners W, Meng G, Batista RJS, Wissenbach K, et al. Densification behavior, microstructure evolution, and wear performance of selective laser melting processed commercially pure titanium. *Acta Mater* 2012;60:3849–60. doi:10.1016/j.actamat.2012.04.006.
- Haibach E. Service fatigue-strength – methods and data for structural analysis. Dusseldorf: VDI; 1989.
- Hermann Becker T, Dimitrov D. The achievable mechanical properties of SLM produced Maraging Steel 300 components. *Rapid Prototyp J* 2016;22:487–94. doi:10.1108/RPJ-08-2014-0096.
- Herzog D, Seyda V, Wycisk E, Emmelmann C. Additive manufacturing of metals. *Acta Mater* 2016;117:371–92. doi:10.1016/j.actamat.2016.07.019.

- Hobbacher AF. Recommendations for Fatigue Design of Welded Joints and Components. IIW Collection. Springer International Publishing; 2016. doi:10.1007/978-3-319-23757-2.
- Jegou L, Marco Y, Le Saux V, Calloch S. Fast prediction of the Wöhler curve from heat build-up measurements on Short Fiber Reinforced Plastic. *Int J Fatigue* 2013;47:259–67. doi:10.1016/j.ijfatigue.2012.09.007.
- Jones R, Krishnapillai M, Cairns K, Matthews N. Application of infrared thermography to study crack growth and fatigue life extension procedures. *Fatigue Fract Eng Mater Struct* 2010;33:871–84. doi:10.1111/j.1460-2695.2010.01505.x.
- Kaleta J, Blotny R, Harig H. Energy Stored in a Specimen under Fatigue Limit Loading Conditions. *J Test Eval* 1991;19:326–33. doi:10.1520/JTE12577J.
- Kempen K, Yasa E, Thijs L, Kruth JP, Van Humbeeck J. Microstructure and mechanical properties of Selective Laser Melted 18Ni-300 steel. *Phys Procedia* 2011;12:255–63. doi:10.1016/j.phpro.2011.03.033.
- Kitagawa H, Takahashi S. Applicability of fracture mechanics to very small cracks or the cracks in the early stage. *Proc 2nd int conf mech Behav. Mater. - ICM2*, 1976, p. 627–31.
- Konečná R, Kunz L, Bača A, Nicoletto G. Resistance of direct metal laser sintered Ti6Al4V alloy against growth of fatigue cracks. *Eng Fract Mech* 2017. doi:10.1016/j.engfracmech.2017.03.033.
- Konečná R, Kunz L, Nicoletto G, Bača A. Long fatigue crack growth in Inconel 718 produced by selective laser melting. *Int J Fatigue* 2016;92:499–506. doi:10.1016/j.ijfatigue.2016.03.012.
- Kranz J, Herzog D, Emmelmann C. Design guidelines for laser additive manufacturing of lightweight structures in TiAl6V4. *J Laser Appl* 2015;27:S14001. doi:10.2351/1.4885235.
- Kruth JP, Vandenbroucke B, van Vaerenbergh J, Naert I. Rapid manufacturing of dental prostheses by means of selective laser sintering/ melting. *AFPR*, S4, 2005.
- Kueppers M, Sonsino CM. Critical plane approach for the assessment of the fatigue behaviour of welded aluminium under multiaxial loading. *Fatigue Fract Eng Mater Struct* 2003;26:507–13. doi:10.1046/j.1460-2695.2003.00674.x.

- Kujawski D. A new $(\Delta K + K_{max})^{0.5}$ driving force parameter for crack growth in aluminum alloys. *Int J Fatigue* 2001;23:733–40. doi:10.1016/S0142-1123(01)00023-8.
- La Rosa G, Risitano A. Thermographic methodology for rapid determination of the fatigue limit of materials and mechanical components. *Int J Fatigue* 2000;22:65–73. doi:10.1016/S0142-1123(99)00088-2.
- Lazzarin P, Berto F, Zappalorto M. Rapid calculations of notch stress intensity factors based on averaged strain energy density from coarse meshes: Theoretical bases and applications. *Int J Fatigue* 2010;32:1559–67. doi:10.1016/j.ijfatigue.2010.02.017.
- Lazzarin P, Berto F. From Neuber's Elementary Volume to Kitagawa and Atzori's Diagrams: An Interpretation Based on Local Energy. *Int J Fract* 2005;135:L33–8. doi:10.1007/s10704-005-4393-x.
- Lazzarin P, Lassen T, Livieri P. A notch stress intensity approach applied to fatigue life predictions of welded joints with different local toe geometry. *Fatigue Fract Eng Mater Struct* 2003;26:49–58. doi:10.1046/j.1460-2695.2003.00586.x.
- Lazzarin P, Livieri P, Berto F, Zappalorto M. Local strain energy density and fatigue strength of welded joints under uniaxial and multiaxial loading. *Eng Fract Mech* 2008;75:1875–89. doi:10.1016/j.engfracmech.2006.10.019.
- Lazzarin P, Livieri P. Notch stress intensity factors and fatigue strength of aluminium and steel welded joints. *Int J Fatigue* 2001;23:225–32. doi:10.1016/S0142-1123(00)00086-4.
- Lazzarin P, Sonsino CM, Zambardi R. A notch stress intensity approach to assess the multiaxial fatigue strength of welded tube-to-flange joints subjected to combined loadings. *Fatigue Fract Eng Mater Struct* 2004;27:127–40. doi:10.1111/j.1460-2695.2004.00733.x.
- Lazzarin P, Tovo R. A notch intensity factor approach to the stress analysis of welds. *Fatigue Fract Eng Mater Struct* 1998;21:1089–103. doi:10.1046/j.1460-2695.1998.00097.x.
- Lazzarin P, Tovo R. A unified approach to the evaluation of linear elastic stress fields in the neighborhood of cracks and notches. *Int J Fract* 1996;78:3–19. doi:10.1007/BF00018497.
- Lazzarin P, Zambardi R. A finite-volume-energy based approach to predict the static and fatigue behavior of components with sharp V-shaped notches. *Int J Fract* 2001;112:275–98. doi:10.1023/A:1013595930617.

- Lemaitre J, Chaboche JL. *Mechanics of solid materials*. Cambridge University Press; 1994.
- Leuders S, Thöne M, Riemer A, Niendorf T, Tröster T, Richard HA, et al. On the mechanical behaviour of titanium alloy TiAl6V4 manufactured by selective laser melting: Fatigue resistance and crack growth performance. *Int J Fatigue* 2013;48:300–7. doi:10.1016/j.ijfatigue.2012.11.011.
- Li P, Warner DH, Fatemi A, Phan N. Critical assessment of the fatigue performance of additively manufactured Ti-6Al-4V and perspective for future research. *Int J Fatigue* 2016;85:130–43. doi:10.1016/j.ijfatigue.2015.12.003.
- Liu Y, Yang Y, Wang D. A study on the residual stress during selective laser melting (SLM) of metallic powder. *Int J Adv Manuf Technol* 2016:1–10. doi:10.1007/s00170-016-8466-y.
- Livieri P, Lazzarin P. Fatigue strength of steel and aluminium welded joints based on generalised stress intensity factors and local strain energy values. *Int J Fract* 2005;133:247–76. doi:10.1007/s10704-005-4043-3.
- Luong MP. Infrared thermographic scanning of fatigue in metals. *Nucl Eng Des* 1995;158:363–76. doi:10.1016/0029-5493(95)01043-H.
- Maierhofer J, Kolitsch S, Pippan R, Gänser HP, Madia M, Zerbst U. The cyclic R-curve – Determination, problems, limitations and application. *Eng Fract Mech* 2018;198:45–64. doi:10.1016/j.engfracmech.2017.09.032.
- Manfredi D, Calignano F, Krishnan M, Canali R, Paola E, Biamino S, et al. Additive Manufacturing of Al Alloys and Aluminium Matrix Composites (AMCs). *Light Met. Alloy. Appl., InTech*; 2014. doi:10.5772/58534.
- McDowell DL, Stahl OK, Stock SR, Antolovich SD. Biaxial path dependence of deformation substructure of type 304 stainless steel. *Metall Trans A* 1988;19:1277–93. doi:10.1007/BF02662589.
- Meneghetti G, Campagnolo A, Avalle M, Castagnetti D, Colussi M, Corigliano P, et al. Rapid evaluation of notch stress intensity factors using the peak stress method: Comparison of commercial finite element codes for a range of mesh patterns. *Fatigue Fract Eng Mater Struct* 2018;41:1044–63. doi:10.1111/ffe.12751.
- Meneghetti G, Campagnolo A, Berto F, Atzori B. Averaged strain energy density evaluated rapidly from the singular peak stresses by FEM: cracked components under mixed-mode (I+II) loading. *Theor Appl Fract Mech* 2015;79:113–24. doi:10.1016/j.tafmec.2015.08.001.

- Meneghetti G, Campagnolo A, Berto F. Assessment of tensile fatigue limit of notches using sharp and coarse linear elastic finite element models. *Theor Appl Fract Mech* 2016;84:106–18. doi:10.1016/j.tafmec.2016.06.001.
- Meneghetti G, Campagnolo A, Berto F. Averaged strain energy density estimated rapidly from the singular peak stresses by FEM: Cracked bars under mixed-mode (I+III) loading. *Eng Fract Mech* 2016;167:20–33. doi:10.1016/j.engfracmech.2016.03.040.
- Meneghetti G, Campagnolo A, Berto F. Fatigue strength assessment of partial and full-penetration steel and aluminium butt-welded joints according to the peak stress method. *Fatigue Fract Eng Mater Struct* 2015;38:1419–31. doi:10.1111/ffe.12342.
- Meneghetti G, Campagnolo A, Rigon D. Multiaxial fatigue strength assessment of welded joints using the Peak Stress Method – Part I: Approach and application to aluminium joints. *Int J Fatigue* 2017;101:328–42. doi:10.1016/j.ijfatigue.2017.03.038.
- Meneghetti G, Campagnolo A, Rigon D. Multiaxial fatigue strength assessment of welded joints using the Peak Stress Method – Part I: Approach and application to aluminium joints. *Int J Fatigue* 2017;101:328–42. doi:10.1016/j.ijfatigue.2017.03.038.
- Meneghetti G, Campagnolo A, Rigon D. Multiaxial fatigue strength assessment of welded joints using the peak stress method – part I: approach and application to aluminium joints. *Int J Fatigue* n.d.:(submitted).
- Meneghetti G, Campagnolo A. The Peak Stress Method to assess the fatigue strength of welded joints using linear elastic finite element analyses. *Procedia Eng* 2018;213:392–402. doi:10.1016/j.proeng.2018.02.039.
- Meneghetti G, De Marchi A, Campagnolo A. Assessment of root failures in tube-to-flange steel welded joints under torsional loading according to the Peak Stress Method. *Theor Appl Fract Mech* 2016;83:19–30. doi:10.1016/j.tafmec.2016.01.013.
- Meneghetti G, Guzzella C, Atzori B. The peak stress method combined with 3D finite element models for fatigue assessment of toe and root cracking in steel welded joints subjected to axial or bending loading. *Fatigue Fract Eng Mater Struct* 2014;37:722–39. doi:10.1111/ffe.12171.

- Meneghetti G, Guzzella C. The peak stress method to estimate the mode I notch stress intensity factor in welded joints using three-dimensional finite element models. *Eng Fract Mech* 2014;115:154–71. doi:10.1016/j.engfracmech.2013.11.002.
- Meneghetti G, Lazzarin P. Significance of the elastic peak stress evaluated by FE analyses at the point of singularity of sharp V-notched components. *Fatigue Fract Eng Mater Struct* 2007;30:95–106. doi:10.1111/j.1460-2695.2006.01084.x.
- Meneghetti G, Lazzarin P. The Peak Stress Method for Fatigue Strength Assessment of welded joints with weld toe or weld root failures. *Weld World* 2011;55:22–9. doi:10.1007/BF03321304.
- Meneghetti G, Marini D, Babini V. Fatigue assessment of weld toe and weld root failures in steel welded joints according to the peak stress method. *Weld World* 2016:1–14. doi:10.1007/s40194-016-0308-x.
- Meneghetti G, Ricotta M, Atzori B. A synthesis of the push-pull fatigue behaviour of plain and notched stainless steel specimens by using the specific heat loss. *Fatigue Fract Eng Mater Struct* 2013;36:1306–22. doi:10.1111/ffe.12071.
- Meneghetti G, Ricotta M, Atzori B. A two-parameter, heat energy-based approach to analyse the mean stress influence on axial fatigue behaviour of plain steel specimens. *Int J Fatigue* 2016;82:60–70. doi:10.1016/j.ijfatigue.2015.07.028.
- Meneghetti G, Ricotta M, Atzori B. The Heat Energy Dissipated in a Control Volume to Correlate the Fatigue Strength of Bluntly and Severely Notched Stainless Steel Specimens. *Proc. 21st Eur. Conf. Fract. ECF21. Catania, Italy, vol. 2, 2016, p. 2076–83.* doi:10.1016/j.prostr.2016.06.260.
- Meneghetti G, Ricotta M, Negrisolo L, Atzori B. A Synthesis of the Fatigue Behavior of Stainless Steel Bars under Fully Reversed Axial or Torsion Loading by Using the Specific Heat Loss. *Key Eng Mater* 2013;577–578:453–6. doi:10.4028/www.scientific.net/KEM.577-578.453.
- Meneghetti G, Ricotta M, Rigon D. The heat energy dissipated in a control volume to correlate the fatigue strength of severely notched and cracked stainless steel specimens. *Fatigue 2017, Cambridge, UK: 2017.*
- Meneghetti G, Ricotta M. Evaluating the heat energy dissipated in a small volume surrounding the tip of a fatigue crack. *Int J Fatigue* 2016;92:605–15. doi:10.1016/j.ijfatigue.2016.04.001.

- Meneghetti G, Ricotta M. The heat energy dissipated in the material structural volume to correlate the fatigue crack growth rate in stainless steel specimens. *Int J Fatigue* 2018;115:107–19. doi:10.1016/J.IJFATIGUE.2018.07.037.
- Meneghetti G, Ricotta M. The use of the specific heat loss to analyse the low- and high-cycle fatigue behaviour of plain and notched specimens made of a stainless steel. *Eng Fract Mech* 2012;81:2–16. doi:10.1016/j.engfracmech.2011.06.010.
- Meneghetti G, Rigon D, Cozzi D, Waldhauser W, Dabalà M. Influence of build orientation on static and axial fatigue properties of maraging steel specimens produced by additive manufacturing. *Procedia Struct Integr* 2017;7:149–57. doi:10.1016/j.prostr.2017.11.072.
- Meneghetti G, Rigon D, Gennari C. An analysis of defects influence on axial fatigue strength of maraging steel specimens produced by additive manufacturing. *Int J Fatigue* 2019;118:54–64. doi:10.1016/j.ijfatigue.2018.08.034.
- Meneghetti G. Analysis of the fatigue strength of a stainless steel based on the energy dissipation. *Int J Fatigue* 2007;29:81–94. doi:10.1016/j.ijfatigue.2006.02.043.
- Meneghetti G. The peak stress method for fatigue strength assessment of tube-to-flange welded joints under torsion loading. *Weld World* 2013;57:265–75. doi:10.1007/s40194-013-0022-x.
- Meneghetti G. The use of peak stresses for fatigue strength assessments of welded lap joints and cover plates with toe and root failures. *Eng Fract Mech* 2012;89:40–51. doi:10.1016/j.engfracmech.2012.04.007.
- Mercelis P, Kruth J. Residual stresses in selective laser sintering and selective laser melting. *Rapid Prototyp J* 2006;12:254–65. doi:10.1108/13552540610707013.
- Mower TM, Long MJ. Mechanical behavior of additive manufactured, powder-bed laser-fused materials. *Mater Sci Eng A* 2016;651:198–213. doi:10.1016/j.msea.2015.10.068.
- Murakami Y (Yukitaka). *Metal fatigue : effects of small defects and nonmetallic inclusions*. Elsevier; 2002.
- Murakami Y (Yukitaka). *Stress intensity factors handbook*. Pergamon; 1987.
- Murakami Y, Endo M. Effects of defects, inclusions and inhomogeneities on fatigue strength. *Int J Fatigue* 1994;16:163–82. doi:10.1016/0142-1123(94)90001-9.

- Murakami Y, Endo M. Quantitative evaluation of fatigue strength of metals containing various small defects or cracks. *Eng Fract Mech* 1983;17:1–15. doi:10.1016/0013-7944(83)90018-8.
- Murakami Y. Analysis of stress intensity factors of modes I, II and III for inclined surface cracks of arbitrary shape. *Eng Fract Mech* 1985;22:101–14. doi:10.1016/0013-7944(85)90163-8.
- Murr LE, Gaytan SM, Ramirez DA, Martinez E, Hernandez J, Amato KN, et al. Metal Fabrication by Additive Manufacturing Using Laser and Electron Beam Melting Technologies. *J Mater Sci Technol* 2012;28:1–14. doi:10.1016/S1005-0302(12)60016-4.
- Murr LE. Metallurgy of additive manufacturing: Examples from electron beam melting. *Addit Manuf* 2015;5:40–53. doi:10.1016/j.addma.2014.12.002.
- Mutua J, Nakata S, Onda T, Chen ZC. Optimization of selective laser melting parameters and influence of post heat treatment on microstructure and mechanical properties of maraging steel. *Mater Des* 2018;139:486–97. doi:10.1016/j.matdes.2017.11.042.
- Neuber H. *Theory of Notch Stresses*. Berlin: Springer Publishers; 1958.
- Nicoletto G. Anisotropic high cycle fatigue behavior of Ti-6Al-4V obtained by powder bed laser fusion. *Int J Fatigue* 2016;94:255–62. doi:10.1016/j.ijfatigue.2016.04.032.
- Nisitani H, Teranishi T. KI of a circumferential crack emanating from an ellipsoidal cavity obtained by the crack tip stress method in FEM. *Eng Fract Mech* 2004;71:579–85. doi:10.1016/S0013-7944(03)00035-3.
- Nisitani H, Teranishi T. KI value of a circumferential crack emanating from an ellipsoidal cavity obtained by the crack tip stress method in FEM. In: Guagliano M, Aliabadi MH, editors. *Proc. 2nd Int. Conf. Fract. damage Mech.*, 2001, p. 141–6.
- Palumbo D, De Finis R, Ancona F, Galietti U. Damage monitoring in fracture mechanics by evaluation of the heat dissipated in the cyclic plastic zone ahead of the crack tip with thermal measurements. *Eng Fract Mech* 2017;181:65–76. doi:10.1016/j.engfracmech.2017.06.017.
- Palumbo D, De Finis R, Demelio PG, Galietti U. A new rapid thermographic method to assess the fatigue limit in GFRP composites. *Compos Part B Eng* 2016;103:60–7. doi:10.1016/J.COMPOSITESB.2016.08.007.

- Palumbo D, Galietti U. Thermoelastic Phase Analysis (TPA): a new method for fatigue behaviour analysis of steels. *Fatigue Fract Eng Mater Struct* 2017;40:523–34. doi:10.1111/ffe.12511.
- Pegues JW, Shao S, Shamsaei N, Schneider JA, Moser RD. Cyclic strain rate effect on martensitic transformation and fatigue behaviour of an austenitic stainless steel. *Fatigue Fract Eng Mater Struct* 2017;40:2080–91. doi:10.1111/ffe.12627.
- Pitarresi G, Patterson EA. A review of the general theory of thermoelastic stress analysis. *J Strain Anal Eng Des* 2003;38:405–17. doi:10.1243/03093240360713469.
- Plekhov O, Palin-Luc T, Saintier N, Uvarov S, Naimark O. Fatigue crack initiation and growth in a 35CrMo4 steel investigated by infrared thermography. *Fatigue Fract Eng Mater Struct* 2005;28:169–78. doi:10.1111/j.1460-2695.2005.00856.x.
- Qian J, Hasebe N. Property of eigenvalues and eigenfunctions for an interface V-notch in antiplane elasticity. *Eng Fract Mech* 1997;56:729–34. doi:10.1016/S0013-7944(97)00004-0.
- Radaj D, Lazzarin P, Berto F. Generalised Neuber concept of fictitious notch rounding. *Int J Fatigue* 2013;51:105–15. doi:10.1016/j.ijfatigue.2013.01.005.
- Radaj D, Sonsino CM, Fricke W. *Fatigue Assessment of Welded Joints by Local Approaches*. 2nd ed. Cambridge: Woodhead Publishing; 2006.
- Radaj D, Vormwald M. *Advanced Methods of Fatigue Assessment*. Berlin, Heidelberg: Springer Berlin Heidelberg; 2013. doi:10.1007/978-3-642-30740-9.
- Radaj D. State-of-the-art review on extended stress intensity factor concepts. *Fatigue Fract Eng Mater Struct* 2014;37:1–28. doi:10.1111/ffe.12120.
- Radaj D. State-of-the-art review on the local strain energy density concept and its relation to the J -integral and peak stress method. *Fatigue Fract Eng Mater Struct* 2015;38:2–28. doi:10.1111/ffe.12231.
- Rännar L, Glad A, Gustafson C. Efficient cooling with tool inserts manufactured by electron beam melting. *Rapid Prototyp J* 2007;13:128–35. doi:10.1108/13552540710750870.
- Razmjoo G. Fatigue of Load-Carrying Fillet Welded Joints Under Multiaxial Loadings. In: Abington, editor. TWI REF. 7309.02/96/909, Cambridge, UK: 1996.

- Reifsnider KL, Williams RS. Determination of fatigue-related heat emission in composite materials 1974;14:479–85. doi:10.1007/BF02323148.
- Rigon D, Formilan V, Meneghetti G. Analysis of the energy dissipation in multiaxial fatigue tests of AISI 304L stainless steel bars. *Procedia Struct Integr* 2018;13:1638–43. doi:10.1016/j.prostr.2018.12.344.
- Rigon D, Ricotta M, Meneghetti G. An analysis of the specific heat loss at the tip of severely notched stainless steel specimens to correlate the fatigue strength. *Theor Appl Fract Mech* 2017;92:240–51. doi:10.1016/j.tafmec.2017.09.003.
- Rigon D, Ricotta M, Meneghetti G. An analysis of the specific heat loss at the tip of severely notched stainless steel specimens to correlate the fatigue strength. *Theor Appl Fract Mech* 2017;92:240–51. doi:10.1016/j.tafmec.2017.09.003.
- Rigon D, Ricotta M, Meneghetti G. Analysis of dissipated energy and temperature fields at severe notches of AISI 304L stainless steel specimens. *Frat Ed Integrità Strutt* 2019;13:334–47. doi:10.3221/IGF-ESIS.47.25.
- Rigon D, Ricotta M, Meneghetti G. Evaluating the specific heat loss in severely notched stainless steel specimens for fatigue strength analyses. *Procedia Struct Integr* 2018;9:151–8. doi:10.1016/J.PROSTR.2018.06.023.
- Rigon D, Ricotta M, Meneghetti G. The use of the heat energy loss to correlate the fatigue strength of severely notched stainless steel specimens. *Proc. Int. Symp. Notch Fract., Santander (Spain): 2017.*
- Risitano A, Risitano G. Cumulative damage evaluation in multiple cycle fatigue tests taking into account energy parameters. *Int J Fatigue* 2013;48:214–22. doi:10.1016/j.ijfatigue.2012.10.020.
- Ritchie RO. Mechanism of Fatigue-Crack Propagation in Ductile and Brittle Materials. *Int J Fract* 1998;100:55–83.
- Ritchie RO. Mechanisms of fatigue crack propagation in metals, ceramics and composites: Role of crack tip shielding. *Mater Sci Eng A* 1988;103:15–28. doi:10.1016/0025-5416(88)90547-2.
- Romano S, Brückner-Foit A, Brandão A, Gumpinger J, Ghidini T, Beretta S. Fatigue properties of AlSi10Mg obtained by additive manufacturing: Defect-based modelling and prediction of fatigue strength. *Eng Fract Mech* 2017;187:165–89. doi:10.1016/j.engfracmech.2017.11.002.
- Rousselier G. Dissipation in porous metal plasticity and ductile fracture. *J Mech Phys Solids* 2001;49:1727–46. doi:10.1016/S0022-5096(01)00013-8.

- Saboori A, Gallo D, Biamino S, Fino P, Lombardi M. An overview of additive manufacturing of titanium components by directed energy deposition: microstructure and mechanical properties. *Appl Sci* 2017;7:883. doi:10.3390/app7090883.
- Sakagami T, Kubo S, Tamura E, Nishimura T. Identification of plastic-zone based on double frequency lock-in thermographic temperature measurement. *Proc. 11th Int. Conference Fract. - ICF11, Italy: 2005.*
- Shamsaei N, Fatemi A. Effect of microstructure and hardness on non-proportional cyclic hardening coefficient and predictions. *Mater Sci Eng A* 2010;527:3015–24. doi:10.1016/j.msea.2010.01.056.
- Siddique S, Imran M, Rauer M, Kaloudis M, Wycisk E, Emmelmann C, et al. Computed tomography for characterization of fatigue performance of selective laser melted parts. *Mater Des* 2015;83:661–9. doi:10.1016/j.matdes.2015.06.063.
- Siliander A, Kurath P, Lawrence F V. Nonproportional Fatigue of Welded Structures. In: Mitchel MR, Landgraf R, editors. *Adv. Fatigue Lifetime Predict. Tech. ASTM STP 1122*, Philadelphia, PA: ASTM; 1992, p. 319–38.
- Smaga M, Walther F, Eifler D. Deformation-induced martensitic transformation in metastable austenitic steels. *Mater Sci Eng A* 2008;483–484:394–7. doi:10.1016/J.MSEA.2006.09.140.
- Smith KN, Watson P, Topper TH. A Stress-Strain Function for the Fatigue of Metals. *J Mater ASTM* 1970;5:767–78.
- Smith RA, Miller KJ. Prediction of fatigue regimes in notched components. *Int J Mech Sci* 1978;20:201–6. doi:10.1016/0020-7403(78)90082-6.
- Sonsino CM, Łagoda T. Assessment of multiaxial fatigue behaviour of welded joints under combined bending and torsion by application of a fictitious notch radius. *Int J Fatigue* 2004;26:265–79. doi:10.1016/S0142-1123(03)00143-9.
- Sonsino CM. Multiaxial fatigue of welded joints under in-phase and out-of-phase local strains and stresses. *Int J Fatigue* 1995;17:55–70. doi:10.1016/0142-1123(95)93051-3.
- Starke P, Walther F, Eifler D. Fatigue assessment and fatigue life calculation of quenched and tempered SAE 4140 steel based on stress–strain hysteresis, temperature and electrical resistance measurements. *Fatigue Fract Eng Mater Struct* 2007;30:1044–51. doi:10.1111/j.1460-2695.2007.01174.x.

- Stoychev S, Kujawski D. Analysis of crack propagation using ΔK and K_{max} . *Int J Fatigue* 2005;27:1425–31. doi:10.1016/J.IJFATIGUE.2005.06.038.
- Stromeyer CE. The Determination of Fatigue Limits under Alternating Stress Conditions. *Proc R Soc A Math Phys Eng Sci* 1914;90:411–25. doi:10.1098/rspa.1914.0066.
- Takahashi I, Takada A, Ushijima M, Akiyama S. Fatigue behaviour of a box-welded joint under biaxial cyclic loading: effects of biaxial load range ratio and cyclic compressive loads in the lateral direction. *Fatigue Fract Eng Mater Struct* 2003;26:439–48. doi:10.1046/j.1460-2695.2003.00645.x.
- Takahashi I, Ushijima M, Takada A, Akiyama S, Maenaka H. Fatigue behaviour of a box-welded joint under biaxial cyclic loads. *Fatigue Fract Eng Mater Struct* 1999;22:869–77. doi:10.1046/j.1460-2695.1999.00224.x.
- Talonen J, Aspegren P, Hänninen H. Comparison of different methods for measuring strain induced α -martensite content in austenitic steels. *Mater Sci Technol* 2004;20:1506–12. doi:10.1179/026708304X4367.
- Taylor D. Geometrical effects in fatigue: a unifying theoretical model. *Int J Fatigue* 1999;21:413–20. doi:10.1016/S0142-1123(99)00007-9.
- Ummenhofer T, Medgenberg J. On the use of infrared thermography for the analysis of fatigue damage processes in welded joints. *Int J Fatigue* 2009;31:130–7. doi:10.1016/j.ijfatigue.2008.04.005.
- Van Swam LF, Pelloux RM, Grant NJ. Fatigue behavior of maraging steel 300. *Metall Trans A* 1975;6:45–54. doi:10.1007/BF02673669.
- Vasudevan A., Sadananda K, Glinka G. Critical parameters for fatigue damage. *Int J Fatigue* 2001;23:39–53. doi:10.1016/S0142-1123(01)00171-2.
- Verreman Y, Nie B. Early development of fatigue cracking at manual fillet welds. *Fatigue Fract Eng Mater Struct* 1996;19:669–81. doi:10.1111/j.1460-2695.1996.tb01312.x.
- Walker K. The Effect of Stress Ratio During Crack Propagation and Fatigue for 2024-T3 and 7075-T6 Aluminum. *Eff. Environ. Complex Load Hist. Fatigue Life*, 100 Barr Harbor Drive, PO Box C700, West Conshohocken, PA 19428-2959: ASTM International; n.d., p. 1-1–14. doi:10.1520/STP32032S.
- Wang WJ, Dulieu-Barton JM, Li Q. Assessment of non-adiabatic behaviour in thermoelastic stress analysis of small scale components. *Exp Mech* 2010;50:449–61. doi:10.1007/s11340-009-9249-2.

- Wang Z, Palmer TA, Beese AM. Effect of processing parameters on microstructure and tensile properties of austenitic stainless steel 304L made by directed energy deposition additive manufacturing. *Acta Mater* 2016;110:226–35. doi:10.1016/j.actamat.2016.03.019.
- Williams ML. Stress singularities resulting from various boundary conditions in angular corners of plates in tension. *J Appl Mech* 1952;19:526–8.
- Wu AS, Brown DW, Kumar M, Gallegos GF, King WE. An Experimental Investigation into Additive Manufacturing-Induced Residual Stresses in 316L Stainless Steel. *Metall Mater Trans A* 2014;45:6260–70. doi:10.1007/s11661-014-2549-x.
- Xu W, Brandt M, Sun S, Elambasseril J, Liu Q, Latham K, et al. Additive manufacturing of strong and ductile Ti-6Al-4V by selective laser melting via in situ martensite decomposition. *Acta Mater* 2015;85:74–84. doi:10.1016/j.actamat.2014.11.028.
- Yadollahi A, Shamsaei N. Additive manufacturing of fatigue resistant materials: Challenges and opportunities. *Int J Fatigue* 2017;98:14–31. doi:10.1016/j.ijfatigue.2017.01.001.
- Yan M, Yu P. An Overview of Densification, Microstructure and Mechanical Property of Additively Manufactured Ti-6Al-4V — Comparison among Selective Laser Melting, Electron Beam Melting, Laser Metal Deposition and Selective Laser Sintering, and with Conventional Powder. *Sinter Tech Mater* 2015. doi:10.5772/59275.
- Ye D, Xu Y, Xiao L, Cha H. Effects of low-cycle fatigue on static mechanical properties, microstructures and fracture behavior of 304 stainless steel. *Mater Sci Eng A* 2010;527:4092–102. doi:10.1016/J.MSEA.2010.03.027.
- Yousefi F, Witt M, Zenner H. Fatigue strength of welded joints under multiaxial loading: experiments and calculations. *Fatigue Fract Eng Mater Struct* 2001;24:339–55. doi:10.1046/j.1460-2695.2001.00397.x.
- Yu D, An K, Chen Y, Chen X. Revealing the cyclic hardening mechanism of an austenitic stainless steel by real-time in situ neutron diffraction. *Scr Mater* 2014;89:45–8. doi:10.1016/J.SCRIPTAMAT.2014.06.021.
- Yung JY, Lawrence F V. Predicting the fatigue life of welds under combined bending and torsion. In: Brown M, Miller K, editors. *Biaxial multiaxial fatigue EGF 3.*, London: Mechanical Engineering Publications; 1989, p. 53–69.

Zeng W, Yuan H. Mechanical behavior and fatigue performance of austenitic stainless steel under consideration of martensitic phase transformation. *Mater Sci Eng A* 2017;679:249–57. doi:10.1016/J.MSEA.2016.10.005.

Ringraziamenti

Vorrei dedicare qualche riga a coloro che hanno contribuito alla realizzazione della presente tesi di dottorato.

Inizio con il ringraziare il Prof. Giovanni Meneghetti che nella veste di supervisore ha sempre saputo motivarmi con la sua enorme passione e dedizione per il lavoro durante tutta l'attività di ricerca. Inoltre, lo ringrazio per essere sempre stato disponibile a fornire preziosi suggerimenti e consigli per lo sviluppo del presente lavoro.

Un sentito ringraziamento va ai colleghi del gruppo di ricerca: per primo, Alberto Campagnolo che ha sempre saputo darmi consigli preziosi sia a livello lavorativo che a livello morale. Inoltre, lo ringrazio per il prezioso supporto per la parte riguardante il Peak Stress Method. Ringrazio poi il Prof. Mauro Ricotta per essere sempre stato disponibile a offrire suggerimenti e supporto per la parte della tesi riguardante l'energia termica dissipata. Un sentito grazie va anche al Prof. Bruno Atzori che con la sua enorme esperienza e passione per la tematica mi ha offerto spesso interessanti spunti di riflessione per sviluppi futuri nella ricerca.

Per quanto riguarda l'esperienza a Trondheim, ringrazio il Prof. Filippo Berto che mi ha seguito nel lavoro condotto presso NTNU per la preziosa collaborazione che ha avvalorato il contenuto della tesi con i risultati sperimentali ottenuti.

Non posso non menzionare i miei genitori che da sempre mi sostengono nella realizzazione dei miei progetti. Non finirò mai di ringraziarli per avermi permesso di arrivare fin qui.

Un ringraziamento speciale va a mio fratello Emanuele e a mia cognata Anna Chiara che per me sono sempre stati un punto di riferimento.

Ringrazio le persone che hanno condiviso l'esperienza a Trondheim rendendola unica e speciale: Dario S., Daniele D., Mirco P., Francesco L., Pietro F., Javad R., Federico U., Giulia M., Ambra C., Cecilia P., Emanuele S., Marco G., Andrea F., Filippo D., Matteo C., Luigi P., Lorenzo G.

Ringrazio gli amici che anche con una semplice parola di incoraggiamento mi hanno sostenuto. Non posso citare tutti per motivi di brevità ma un ringraziamento particolare va a Andrea A., amico da una vita, che è sempre stato presente anche durante questa ultima fase del mio percorso.

Infine, un grazie davvero di cuore va a Chiara, per avermi sempre sostenuto con il suo amore incondizionato, per avermi sopportato nei momenti difficili e soprattutto per aver sempre creduto in me.